

The past and future of the  
monkeypox virus pp. 1252 & 1261

Testing the strength of weak  
social ties pp. 1256 & 1304

Target RNA-guided RNA and protein  
cleavage by Craspase p. 1278

# Science

\$15  
16 SEPTEMBER 2022  
science.org

AAAS



## GROUNDWATER OF LIFE

Subsurface capture of seasonal  
rainfall supports Bangladeshi  
agriculture pp. 1258 & 1315



“CST<sup>®</sup> research products perform – beautifully.”

The precise contribution of neuroinflammation to Alzheimer's Disease (AD) progression is poorly understood. Microglia are likely to play an important role in initiating and maintaining neuroinflammatory responses that contribute to AD etiology. Cathepsin D is enriched in microglia, particularly in the context of disease. This confocal immunofluorescent analysis of brain from an amyloid mouse model of AD shows Cathepsin D (E7Z4L) XP<sup>®</sup> Rabbit mAb #88239 (green), Iba1/AIF-1 (E404W) XP Rabbit mAb #36618 (red), GFAP (GAS) Mouse mAb #36657 (cyan), and  $\beta$ -Amyloid (D54D2) XP Rabbit mAb #36363 (blue).

We hear it from researchers all the time. They trust CST antibodies and other research tools to work the way they're supposed to. Every time. And to provide them with results that are clear, unambiguous and reproducible. As scientists ourselves, nothing less is acceptable.

[www.cellsignal.com](http://www.cellsignal.com)



© 2022 Cell Signaling Technology, Inc. All rights reserved. | For Research Use Only. Not For Use In Diagnostic Procedures. | 22-BCH-61229-AUG22



Antibodies for Research



Immunoassay Kits



Customs & Services



Application Workflow Solutions



Industry-leading Validation Process

# CONTENTS

16 SEPTEMBER 2022 • VOLUME 377 • ISSUE 6612

1252 & 1261

## NEWS

### IN BRIEF

**1242** News at a glance

### IN DEPTH

**1244** Europe's energy crisis hits science hard

Supercomputing and accelerator centers struggle with surging gas and electricity prices *By J. Kwan*

**1245** Private venture tackles Long Covid, aims to test drugs soon

Initiative to explore whether coronavirus lingers in patients *By J. Couzin-Frankel*

**1246** U.S. Antarctic Program has ignored sexual harassment

Decades of complaints have gone unheeded by NSF and contractors managing operations, employees say *By J. Mervis*

**1247** Polio returns in rich countries, but big outbreaks are unlikely

As New York state declares an emergency, experts are far more worried about a resurgence in low-income countries *By L. Roberts*

**1248** Record salinity and low water imperil Great Salt Lake

Drought spurs efforts to restore shrinking lake's water supplies *By E. Kintisch*

**1250** NASA's asteroid deflection mission takes aim

Target's structure will sway outcome of upcoming test collision, simulations show *By Z. Savitsky*  
PODCAST

**1251** Reviewers award higher marks when a paper's author is famous

"Matthew effect" is powerful, unusually large study finds *By J. Brainard*

## FEATURES

**1252** Moving target

The global monkeypox outbreak is giving the virus an unprecedented opportunity to adapt to humans. Will it change for the worse?

*By K. Kupferschmidt*

PERSPECTIVE p. 1261

## INSIGHTS

### PERSPECTIVES

**1256** Weak ties, failed tries, and success

A large-scale study provides a causal test for a cornerstone of social science

*By D. Wang and B. Uzzi*

REPORT p. 1304

**1258** The "water machine" of Bengal

A data-driven and policy-supported strategic use of aquifers for irrigation is needed to maximize their benefits

*By A. Mukherji*

REPORT p. 1315

**1259** Replication timing and genetic instability

Synchronized activation of DNA replication origins induces genetic instability in lymphoma

*By M. Méchali*

RESEARCH ARTICLE p. 1277

**1261** Monkeypox: The consequences of neglecting a disease, anywhere

A disease anywhere can spread everywhere, if neglected *By O. Tomori and D. Ogoina*

NEWS STORY p. 1252

**1263** Loyal gut microbes

Bacterial strains in the gut microbiota diversified as humans spread across the globe

*By A. H. Moeller*

REPORT p. 1328

**1264** How Saturn got its tilt and its rings

The destruction of a hypothetical moon may help explain the origin of both *By M. El Moutamid*

RESEARCH ARTICLE p. 1285

### POLICY FORUM

**1266** Risks of decoupling from China on low-carbon technologies

For most technologies, the cure is likely worse than the disease *By M. R. Davidson et al.*

### BOOKS ET AL.

**1270** Whom is real science for?

Skip the metaphors—physics needn't be diluted for nonexperts to achieve real understanding

*By A. E. Motter*

**1271** Dos and don'ts for achieving managerial diversity

A pair of sociologists turn to data to determine how to diversify organizations' upper ranks

*By E. H. Chang*

LETTERS

**1272 A genomics revolution in amphibian taxonomy** *By C. Dufresnes and D. Jablonski*

**1272 Comprehensive support for diversity in STEM** *By T. Mourad and G. Middendorf*

**1273 Ecological footprint of Russia's Ukraine invasion** *By M. Zheleznyak et al.*

**1273 In memoriam**

RESEARCH

IN BRIEF

**1274** From *Science* and other journals

RESEARCH ARTICLES

**1277 Cancer genetics**

DNA replication timing directly regulates the frequency of oncogenic chromosomal translocations *M. Peycheva et al.*

RESEARCH ARTICLE SUMMARY; FOR FULL TEXT: DOI.ORG/10.1126/SCIENCE.ABJ5502

PERSPECTIVE p. 1259

**1278 CRISPR**

Craspe is a CRISPR RNA-guided, RNA-activated protease *C. Hu et al.*

**1285 Gas giant planets**

Loss of a satellite could explain Saturn's obliquity and young rings *J. Wisdom et al.*  
PERSPECTIVE p. 1264

**1290 Signal transduction**

Lysosomal GPCR-like protein LYCHOS signals cholesterol sufficiency to mTORC1 *H. R. Shin et al.*

**1298 Structural biology**

Structural basis for strychnine activation of human bitter taste receptor TAS2R46 *W. Xu et al.*

REPORTS

**1304 Social networks**

A causal test of the strength of weak ties *K. Rajkumar et al.*  
PERSPECTIVE p. 1256

**1311 Evolution**

Exceptional preservation of organs in Devonian placoderms from the Gogo lagerstätte *K. Trinajstić et al.*

**1315 Groundwater**

The Bengal Water Machine: Quantified freshwater capture in Bangladesh *M. Shamsudduha et al.*  
PERSPECTIVE p. 1258; PODCAST



**1319 Quantum simulation**

Direct geometric probe of singularities in band structure *C. D. Brown et al.*

**1323 Organic chemistry**

Halogen-atom and group transfer reactivity enabled by hydrogen tunneling *T. Constantin et al.*

**1328 Microbiome**

Codiversification of gut microbiota with humans *T. A. Suzuki et al.*  
PERSPECTIVE p. 1263

**1333 Nanophotonics**

Few-cycle vacuum squeezing in nanophotonics *R. Nehra et al.*

DEPARTMENTS

**1241 Editorial**

High seas treaty within reach *By K. M. Gjerde et al.*

**1354 Working Life**

The meaning of home *By D. Boglajenko*

ON THE COVER

The irrigation of rice fields by smallholder farmers in Bangladesh, like the one in Sylhet pictured here, has transformed this densely populated, once famine-prone land to a food-secure nation over the past three decades. This type of agriculture depends on groundwater withdrawals made possible by subsurface recharge by the highly seasonal rainfall. This cycle sustains irrigated food production under a changing climate. See pages 1258 and 1315. *Photo: K. M. Asad*



Gordon Research Conferences.....1338  
Science Careers.....1343



SCIENCE (ISSN 0036-8075) is published weekly on Friday, except last week in December, by the American Association for the Advancement of Science, 1200 New York Avenue, NW, Washington, DC 20005. Periodicals mail postage (publication No. 484460) paid at Washington, DC, and additional mailing offices. Copyright © 2022 by the American Association for the Advancement of Science. The title SCIENCE is a registered trademark of the AAAS. Domestic individual membership, including subscription (12 months): \$165 (\$74 allocated to subscription). Domestic institutional subscription (51 issues): \$2212; Foreign postage extra: Air assist delivery: \$98. First class, airmail, student, and emeritus rates on request. Canadian rates with GST available upon request, GST #125488122. Publications Mail Agreement Number 1069624. Printed in the U.S.A.

Change of address: Allow 4 weeks, giving old and new addresses and 8-digit account number. Postmaster: Send change of address to AAAS, P.O. Box 96178, Washington, DC 20090-6178. Single-copy sales: \$15 each plus shipping and handling available from backissues.science.org; bulk rate on request. Authorization to reproduce material for internal or personal use under circumstances not falling within the fair use provisions of the Copyright Act can be obtained through the Copyright Clearance Center (CCC), www.copyright.com. The identification code for Science is 0036-8075. Science is indexed in the Reader's Guide to Periodical Literature and in several specialized indexes.

# High seas treaty within reach

The ocean is Earth's greatest climate mitigator, but it cannot do its work without biodiversity. Yet, accelerating climate change, unsustainable fishing, and widespread plastic and other pollutants, combined with increased resource demands, are threatening life throughout our global ocean. This is particularly acute in the two-thirds of the ocean (the high seas and seabed below) located beyond national boundaries, and as such, no state can solve these problems alone. Since 2018, member states of the United Nations have been crafting an international treaty to protect high-seas biodiversity and to ensure that human pressures are kept to a level that sustains this variety. Last month, the fifth and supposedly final session of the UN Intergovernmental Conference fell short of this goal. Unfortunately, disagreements on fundamental issues meant that negotiators ran out of time. Achieving a timely treaty requires resuming the dialogue as soon as possible with more visible public and political support to surmount remaining hurdles.

These little-known negotiations should compel a sense of urgency because at risk are vital ecosystem services that keep Earth's climate livable. Existing regional and global organizations for managing fishing, shipping, or deep-sea mining lack a global focus on marine biodiversity that the new treaty could provide.

The good news is that despite the delay, negotiators made meaningful progress. This includes accepting key principles and approaches to advance ecosystem-based management, recognizing roles for science as well as traditional knowledge of Indigenous peoples and local communities, and agreeing to establish key institutions such as regular meetings of the states parties to maintain progress. Yet negotiators face many daunting divides. They have to find an acceptable balance between state autonomy and collective action to effectively manage marine protected areas, review environmental impact assessments, and hold each other accountable for harm. Also debated is how to more equitably share benefits derived from marine genetic resources. Potentially valuable genetic material from marine life has prospective applications in agriculture, industry, and biomedicine and can inform research, assessments, and monitoring of the ocean.

Equity—both within and across generations—is at the heart of sharing the benefits of marine genetic material,

empowering participation in decision-making, and enabling sufficient capacity, technology, and financial resources. Richer nations have yet to commit to delivering the capacity building, technology, and funds necessary to assist developing nations, such as small island states, to fully participate in the treaty. Facilitating individual and collective responses to stresses on the global ocean, which these less technologically equipped nations did little to cause, is essential.

The next several months offer a narrowing window to find solutions. The treaty is an opportunity to foster mutually beneficial partnerships that acquire scientific information and leverage technology to monitor cumulative impacts on the global ocean. As the ocean is interconnected, all nations have the right and responsibility to act as stewards of the ocean commons now and for future generations. The current treaty draft offers an innovative pathway for this collective stewardship: strategic environmental assessments of marine ecosystems and activities that are regionally focused, at an ecologically meaningful scale. That is, by bringing together interested states, scientific institutions, sectoral organizations (such as bodies for regional fisheries, international shipping, and seabed mining), financial institutions, civil society, and other stakeholders, these assessments could forge a common understanding while also redressing gaps in capacity. The results could guide coherent climate-resilient management that includes networks of protected areas for safeguarding life in a dynamic ocean.

Scientists can play a role by calling on world leaders to promptly produce a treaty that will inject science-based decision-making, equity, and stewardship into the heart of how the vast majority of Earth's ocean is managed. New activities, from geoengineering to deep-sea mining, are being proposed to address the climate emergency that could imperil high-seas biodiversity. Nations will require sound assessment and accountable decision-making processes so that such new approaches do not cause more harm than good. By finalizing the treaty soon, ideally in 2022, world leaders can further reaffirm faith in the power of global multilateral processes and steer all countries together through the challenges of a changing ocean and planet.

—Kristina M. Gjerde, Harriet Harden-Davies, Kahlil Hassanali

“...at risk are vital ecosystem services that keep Earth's climate livable.”

**Kristina M. Gjerde** is the senior high seas adviser of the Ocean Team at the International Union for Conservation of Nature, Cambridge, MA, USA. [kgjerde@iucn.org](mailto:kgjerde@iucn.org)

**Harriet Harden-Davies** is the director of the Nippon Foundation Ocean Voices Programme, University of Edinburgh, Edinburgh Climate Change Institute, Edinburgh, UK. [harriet.harden-davies@ed.ac.uk](mailto:harriet.harden-davies@ed.ac.uk)

**Kahlil Hassanali** is a research officer at the Institute of Marine Affairs, Chaguaramas, Trinidad and Tobago. [khassanali@ima.gov.tt](mailto:khassanali@ima.gov.tt)

“They need to acknowledge their role in spreading disinformation, and choose a different path.”

University of California, Santa Barbara, energy policy expert Leah Stokes, to *Grist* about her research on utility companies' role in climate change denialism.

## IN BRIEF

Edited by Shraddha Chakradhar

## POLICY

## First ARPA-H director named

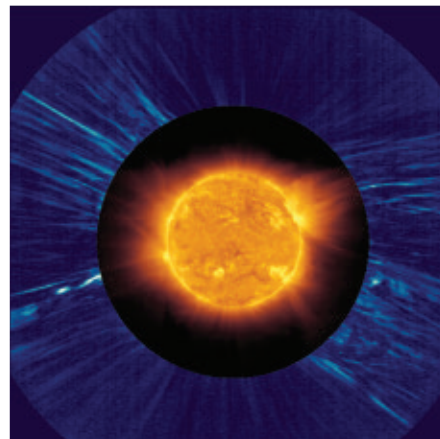
President Joe Biden has picked Renee Wegrzyn, an applied biologist with a background in industry and government, to head his new agency for biomedical innovation, the Advanced Research Projects Agency for Health (ARPA-H). Wegrzyn, 45, served 4 years as a program manager in the biological technologies office of the Defense Advanced Research Projects Agency, the model for ARPA-H, where she led programs in synthetic biology and gene editing. She is currently vice president of business development at the Boston-based Ginkgo Bioworks, which focuses on cell engineering; she also has expertise in biosecurity. ARPA-H, which has a \$1 billion budget this year, was created by Congress in March to develop cutting-edge medical technologies and is currently part of the National Institutes of Health.

## Cancer treatment tackles lupus

**IMMUNOTHERAPY** | Suggesting a new way to battle certain autoimmune conditions, five people with lupus have been successfully treated with engineered immune cells. A team in Germany reports this week in *Nature Medicine* that the patients—four women and a man who had serious organ complications from the autoimmune disease—received chimeric antigen receptor T cell (CAR-T) therapy. The strategy, which was approved 5 years ago in the United States for people with cancers of the immune system's B cells, involves isolating T cells, genetically modifying them outside the body to target specific cells—in this case the B cells that spur lupus—and infusing them back in. All five patients tolerated the treatment well, and their impaired organ function, such as kidney problems, improved or resolved. The patients also discontinued other drugs they were taking, such as immune suppressants. The researchers note that although promising, CAR-T therapy needs to be studied in more people with lupus over time to ensure it's safe and effective.

## The Sun's kinky magnetism

**ASTRONOMY** | New images from the European Solar Orbiter may shed light on mysterious shifts in the Sun's magnetic field and could help explain why the solar wind blows at two different speeds. In March, the spacecraft spotted an S-shaped vortex of ejecting plasma in the Sun's corona—an



The Sun's magnetic fluxes might help explain the solar wind's different speeds.

observation that jibes with previous predictions that the star's looping magnetic field lines sometimes crash into rarer straight ones, causing straight lines of emanating plasma to develop a telltale kink known as a switchback. Scientists had previously seen evidence of switchbacks in magnetic field data, but the images of them reported last week in *The Astrophysical Journal Letters* are a first. The findings support the idea that slower solar winds arise from switchbacks in looping magnetic field lines. The work could help scientists better predict the impact of powerful solar storms on Earth, which can wreak havoc on communications systems and navigational equipment.

## Racism's effects in real time

**RACISM** | A study testing an innovative way to assess racism's impact on health has found stress hormone levels in saliva spike almost immediately after someone experiences a racist interaction. In a pilot study, researchers had 12 Black participants in the United States collect their saliva four times a day over 4 days. Over the same period, participants used a phone app to record perceived discrimination and microaggressions—such as being mistaken for a service worker because of their race. Levels of cortisol—a hormone released during emotional distress—increased in the participants' saliva the morning after they reported racial discrimination events, the team reports this week in *PLOS ONE*. Microaggressions seemed to have a faster effect, increasing cortisol levels the very same day. The study authors, led by Soohyun Nam at Yale University's School of Nursing, say the strength of their strategy lies in being able to follow participants in real time and analyze their hormone levels throughout the day and are planning other similar studies.

## Women faculty paid less

**SCIENTIFIC COMMUNITY** | Echoing previous findings, women faculty members, even those with a stellar publication record, are paid less than their male colleagues, a new study has found. After examining publicly available salary data



**IN FOCUS** Among this year's Wildlife Photographer of the Year winners is this portrait of a southern right whale calf off New Zealand's coast. After circling and inspecting photographer Richard Robinson, the calf reportedly returned for a second look. New Zealand's right whale population had been hunted to near-extinction, but recent protections have helped revive it from a group with 13 breeding females to more than 2000 animals. The contest is developed and produced by the Natural History Museum in London.

for more than 2300 tenured or tenure-track professors who work in science, technology, engineering, and math fields at 17 research-intensive U.S. universities, researchers identified a gender pay gap that persists even after accounting for factors such as the average pay in a department and an individual's h-index, a metric that reflects how many papers they have published and how many times those papers have been cited. Among faculty members with a relatively high h-index of 49, for instance, women were paid roughly \$6000 less per year than their male counterparts. The authors of the study, which is in press at *Scientometrics* and available as a preprint on ResearchGate, say the findings underscore the need for universities to examine equity in faculty pay.

## U.S. alters offensive place names

**GEOGRAPHY** | The Department of the Interior (DOI) last week removed a name used as a slur for Native American women from some 650 peaks, creeks, buttes, and other geographic features across the United States. Secretary Deb Haaland, the first Native American Cabinet member in the U.S. government, set up a committee that considered more than 1000 suggestions for new names. Federal agencies, including the U.S. Geological Survey, will update their maps. Museums will also update databases for specimens collected

near the places on the list. "Having our collections information reflect diversity and inclusion values is important," says Carol Butler, assistant director for collections for the Smithsonian Institution's National Museum of Natural History. The museum will change hundreds of instances in its online database, mostly for plant specimens collected at sites with the offensive names. DOI will continue to accept suggestions for other names that need changing.

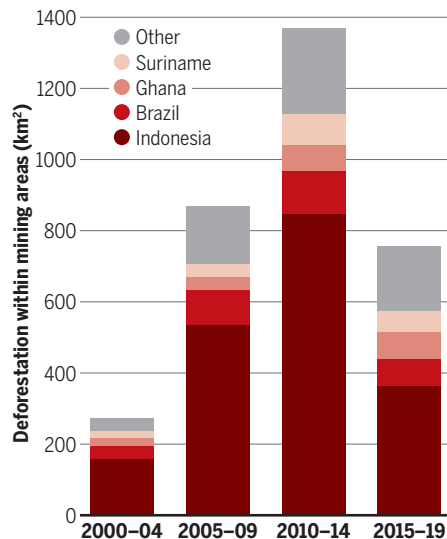
## Sexual assaults' hidden costs

**HEALTH CARE** | People seeking emergency care following a sexual assault may also be burdened with a hefty medical bill. Looking at nearly 113,000 emergency department visits in 2019 for sexual violence, researchers found that nearly 16% of those assaulted didn't have health insurance and had to pay, on average, nearly \$3700. Pregnant individuals who were sexually assaulted incurred the highest charges, of more than \$4500, on average. Such expenses may discourage people from reporting their experience or seeking help, warn the authors of the study, published this week in *The New England Journal of Medicine*. They also write that low-income women and girls—who are disproportionately subject to sexual violence—may be particularly hard hit by the medical charges.

## BY THE NUMBERS

### Dug up and deforested

Just four countries accounted for 81% of tropical forest loss caused by industrial mining as of 2019, according to a study published this week in the *Proceedings of the National Academy of Sciences*. The largest contributor, Indonesia, digs mainly coal, whereas others mine gold and aluminum ore. Forest losses have dropped 45% since 2014, mainly because of declining prices for the mined materials and coal mining restrictions in Indonesia. Overall, agriculture remains a bigger cause of deforestation.





IN DEPTH

Energy budgets at the Dutch Low-Frequency Array are stretched to the breaking point.

EUROPE

# Europe's energy crisis hits science hard

Supercomputing and accelerator centers struggle with surging gas and electricity prices

By Jacklin Kwan

Soon after Jessica Dempsey became director of the Netherlands Institute for Radio Astronomy (ASTRON) in December 2021, she was forced to focus not on the stars, but on the electric bill. ASTRON operates the Low-Frequency Array (LOFAR), which relies on large computer clusters to process radio astronomy data. They consume about 2000 megawatt-hours per year—the equivalent of 800 households. When Dempsey sought to renew ASTRON's energy contracts this summer, she was shocked to find costs had tripled from 2021 levels. She now plans to seek emergency energy funding from the Dutch government; without it, she may have to scale back observations. "It's certainly an existential crisis if these [price] increases continue," she says.

Surging energy prices are hitting Europe hard—and not just households. Institutes that operate energy-hungry supercomputers, accelerators, and laser beamlines are also struggling—and may be harbingers for the rest of science. If prices continue to soar this fall and winter, "The impact for science is going to be significant," says Martin Freer, a nuclear physicist who directs the University of Birmingham's energy institute.

The primary cause of the crisis is a rebound from an economic slowdown during the

COVID-19 pandemic. Power stations that had been shut down could not ramp up in time to meet renewed demand, says Jonathan Stern, who studies natural gas at the Oxford Institute for Energy Studies. Russia's invasion of Ukraine in February worsened the situation. Sanctions and Russian retaliation crimped supplies of Russian natural gas, which generates electricity and heats buildings, pushing European gas prices to more than 10 times their average historical values.

Early science casualties came in January, even before the Ukraine war, when Lumius, an energy contractor in the Czech Republic, declared bankruptcy, driving up energy prices for many Czech universities and research facilities. IT4Innovations, a national supercomputing center, was compelled to run its most powerful supercomputer at one-third of its capacity—creating delays for the 1500 users who used it for climate modeling and drug discovery. ELI Beamlines, a Czech facility that hosts high-power laser beams, had to shut down operations for a few weeks.

By May, the Czech government had agreed to bail out both facilities until the end of 2023, but their fate remains uncertain. Roman Hvězda, ELI Beamlines deputy director, worries the government will declare a state of emergency, which could restrict the gas the facility needs to heat its buildings. But electricity to power the beamlines is the

bigger concern. If supplies are restricted, the facility may have to shut down again, for up to 6 months—which would not only curtail ongoing experiments for hundreds of users, but also delay calls for future ones, he says. "So, you're effectively losing not 6 months, but maybe 12, maybe even 18 months."

There's a similar concern at DESY, Germany's largest accelerator center. DESY has bought enough energy in advance to last into 2023 but might not be able to use those supplies if the German government imposes national energy restrictions, says Wim Leemans, who leads DESY's accelerator programs.

Leemans says DESY is exploring options to run its machines at lower energies. For example, it could turn down its synchrotron, a circular particle accelerator that produces bright x-rays for imaging proteins and materials, so that it only generates lower energy "soft" x-rays. That way it could continue to serve some users, he says. But its two large linear accelerators, used to produce laserlike pulses of x-ray light, would need to be shut down completely if the restrictions are severe. They rely on superconducting modules that need constant power-hungry cooling, Leemans says. "We cannot say, 'Well, we're only going to run some parts of the machine.'"

Reducing operations would hurt important research, he adds. During the pandemic, vaccinemaker BioNTech used DESY's x-ray



facilities to reveal how the SARS-CoV-2 virus uses its surface protein, spike, to dock with human cells. Other DESY researchers study materials used in solar panels and batteries. “It will have ramifications for slowing down innovations, right at the moment when we need them the most,” Leemans says.

Big legacy machines may be hard to restart after a shutdown, adds Anke-Susanne Müller, who heads accelerator physics and technology at the Karlsruhe Institute of Technology. Turning off vacuums may damage delicate systems, stopping the flow of water in cooling systems may cause corrosion, and older control electronics might not turn on again. “If you suddenly switch a component off, they might not easily come back,” she says.

CERN, the world’s largest particle physics laboratory, in Switzerland, is also nervously watching the energy crisis unfold. CERN purchases energy from the French grid years in advance, but now the concern is supply. “For this autumn, it is not a price issue, it’s an availability issue,” says Serge Claudet, chair of CERN’s energy management panel.

CERN uses 1.3 terawatt-hours of energy annually, roughly the equivalent of 250,000 households. French energy authorities might order CERN to not operate at times when the electric grid is least stable—typically mornings and evenings. If frequent, those requests could significantly reduce CERN’s data output, Claudet says. He says CERN may have to shut down smaller accelerators in order to sustain the Large Hadron Collider, the world’s most powerful accelerator.

Even with energy procured for the short term, Claudet says CERN’s budgets will be stretched to pay for it. “This is a financial concern because the energy prices on the market are very high, up to 10 times higher.”

Stern predicts it will take at least 2 years for prices to fall to typical levels. Meanwhile, peak prices will depend on the severity of Europe’s winter and whether Asian countries bid against Europe for global supplies of liquid natural gas. Stern says it’s unclear whether governments will keep research labs afloat, or prioritize aiding industry. Smaller research laboratories in universities may be left to fend for themselves, he says.

Freer warns of real-world consequences. He gives the example of accelerators at Birmingham that produce isotopes for medical imaging—programs that would either need to be suspended, run at a loss, or pass on their costs to local hospitals. “It’s going to be a challenging time to get through,” he says. “It may mean, like with COVID, there will be a hiatus in science programs.” ■

Jacklin Kwan is a science communications graduate student at Imperial College London.

## COVID-19

# Private venture tackles Long Covid, aims to test drugs soon

## Initiative to explore whether coronavirus lingers in patients

By Jennifer Couzin-Frankel

**A** new, privately funded venture announced last week has recruited more than 20 top scientists and is pouring \$15 million raised so far into Long Covid research. It plans to explore whether lingering virus causes symptoms and to launch clinical trials as soon as possible. The scientist who spearheaded the Long Covid Research Initiative (LCRI), microbiologist Amy Proal at the nonprofit PolyBio Research Foundation, says the goal is to bring in \$100 million, with half of that going to trials.

That sum will still be dwarfed by the behemoth RECOVER initiative at the National Institutes of Health (NIH), which has more than \$1 billion to fund Long Covid projects. But RECOVER has come under fire for its sluggish pace. Proal and others say new strategies are needed to distribute funds faster and to embrace higher risk, higher payoff research.

“We need a spark, we need a philanthropic organization that has a risk tolerance much greater than NIH,” says E. John Wherry, an immunologist at the University of Pennsylvania who is part of LCRI and has advised on RECOVER grants. Wherry compares NIH money to the bonds in an investor’s portfolio—“lumbering, slow-changing things that give you the core of what you need.” But sometimes, “bonds are not going to be the tool you use,” he says.



An 18-year-old hospitalized with Long Covid.

NIH said in a statement it welcomes the private initiative because “the public can only benefit from multiple research efforts.” However, NIH also called RECOVER “unprecedented” in scale and crucial to giving researchers “a fighting chance at identifying the underlying mechanisms of Long COVID.”

LCRI was born after several patient advocates with Long Covid and a professional background in technology startups approached Proal early this year. “The enormity of the problem really outweighs the size of the response,” says one, Henry Scott-Green, a Google product manager. The Centers for Disease Control and Prevention estimates that nearly one in five people who contracted COVID-19 may have persistent symptoms, which can include fatigue and brain fog.

So far, LCRI has received \$15 million from investors including the Chan Soon-Shiong Family Foundation; more commitments are expected soon, Proal says. That first batch of funding will support basic research by participating scientists. They will focus on whether SARS-CoV-2 persists in Long Covid patients and drives their symptoms. Studies include a hunt for virus in intestinal, nerve, vascular, and other tissues, including those procured from autopsies. Researchers will also dig deep into immune cell behavior that may reflect viral persistence.

If virus lingers in the body, antiviral therapies might reduce symptoms. Proal hopes the collaborative can soon begin clinical trials of such therapies, and that its scientists can nail down the kind of biomarkers drug companies crave for assessing a candidate treatment, such as immune signatures or other measures in blood.

NIH has said that it, too, expects to launch several Long Covid trials this fall. Those involved in LCRI—and often RECOVER as well—stress they want to complement each other, not work at cross purposes. David Putrino, an LCRI member and neurophysiologist at the Icahn School of Medicine at Mount Sinai who is also on a RECOVER subcommittee, has criticized the NIH initiative but now hopes at least for détente. “No matter ... what’s gone before, we need to swallow our pride and work together.” ■

With reporting by Jocelyn Kaiser.



## SCIENTIFIC COMMUNITY

# U.S. Antarctic Program has ignored sexual harassment

Decades of complaints have gone unheeded by NSF and contractors managing operations, employees say

By Jeffrey Mervis

**W**hen a report last month documented pervasive sexual harassment in the U.S. Antarctic Program, many polar researchers and USAP employees said it confirmed their own experiences of being assaulted, ignored, and sometimes punished for speaking out. They also said the 25 August report wasn't the first time the National Science Foundation (NSF), which manages the program through contracts to private companies and commissioned the report, had been told about the problem.

"There are a million examples of guys being obnoxious and inappropriate," says Joni Zisman, who in April quit her job as IT manager at McMurdo Station, the largest of the three U.S. Antarctic bases, after 13 years with the program. "But what really pissed me off was that leadership has spent the past 2 decades laughing it off and retaliating against anybody who has tried to make things better."

Zisman is one of at least four senior employees who have recently left Leidos, the lead contractor for the Antarctic Support Contract (ASC) awarded by NSF. All told

*Science* about their frustration with how sexual harassment has been allowed to fester. "The unwritten rule ever since I started in the 1990s has been to keep your mouth shut ... or you will be blacklisted," says Elaine Hood, who resigned in July after more than 20 years in corporate communications for a series of lead contractors.

The report, by Leading and Dynamic Services and Solutions (LDSS), doesn't quantify the extent of the sexual misconduct but offers stark anecdotal accounts. "Every woman I knew down there had an assault or harassment experience," one interviewee said.

Since 2019, an informal and fluctuating network of USAP employees called the Ice Allies have put their jobs and their careers at risk in hopes of bringing about change. In addition to sexual harassment, they have also looked into wage disparities and other forms of discrimination against USAP employees—many of them young women in a culture dominated by older men.

One veteran member of McMurdo leadership who befriended the group was Julie Grundberg, who in 2016 became ASC area station manager after many years working in Antarctica. The group's efforts gained

McMurdo Station "is the training ground for bad behavior," according to a new report.

momentum in the fall of 2019, after a rape survivor began sharing her story with colleagues. The survivor's courage, Grundberg says, "led to other people being brave, too. And so I sat in my office for days, and had person after person after person come and talk to me."

Grundberg and the Ice Allies compiled a folder of more than two dozen cases, which they forwarded to NSF after removing identifying features and getting the survivors' permission. At the same time, the woman who had come forward about her rape started to receive unfavorable performance reviews. Within weeks she was fired and flown home.

Those events compelled the Ice Allies to emerge from the shadows. In early 2020 they set up a table outside the dining room in the station's main building to collect signatures on a petition urging NSF and the contractors to take sexual harassment more seriously. It asked for better training, a clear channel for reporting assaults, psychological support for survivors, and evidence that disciplinary actions had been taken when warranted. "It is inexcusable that such a forward-looking institution"—referring to NSF—has "fallen behind in taking such common-sense measures," the petition concluded.

More than 200 people signed the petition. Stephanie Short, NSF's head of Antarctic logistics, says that plea and other informal reports led NSF to commission the LDSS report. "It was important to us not only to understand where the challenges were, but where we needed to focus resources to start to address any challenges," Short says.

Grundberg also kept her Leidos bosses in the loop. "I wanted them to know that [sexual harassment] is a rampant problem down here," she says. "And I wanted them to explain what they were doing to address it."

Grundberg says her barrage of emails and phone calls led superiors to decide she wasn't a team player. On 28 July 2020 Leidos sent her a memo saying she was being terminated for "an inability to meet job expectations."

Leidos declined comment. But Grundberg's former colleagues say her dismissal was a huge loss. "She was beloved by everybody except her ASC bosses," Zisman says.

In a memo to all employees immediately after NSF released the LDSS report, Leidos's Michael Raabe, director of the ASC contract, cited the company's "deep concern with the findings ... and our commitment to ensuring all its [job] sites are a safe and welcoming place for employees." The memo invited employees to avail themselves of "multiple reporting channels," including Raabe himself, an anonymous

Leidos hotline, and the human resources departments for all six subcontractors.

But many USAP employees say offering so many reporting paths has allowed the lead contractor and its subcontractors to ignore complaints or pass the buck and misreads a key finding in the report. “The report makes it clear that people don’t trust their human resource departments and those other entities,” Hood says.

Who actually investigates sexual assault—and how—is murky. NSF’s station manager at McMurdo is also a U.S. marshal and must report any criminal activity among a community that can exceed 1000 in the busy season. But many survivors don’t want to take that route, says Jessica Mindlin, a lawyer with the Victim Rights Law Center and a member of the LDSS team that wrote the report. And the U.S. military, which provides logistical support for USAP operations, has its own system for handling complaints involving service members.

A board of senior managers in NSF’s Office of Polar Programs oversees adherence to its polar code of conduct, which covers a range of behaviors that includes sexual assault. But the body operates in near-total secrecy; none of the USAP employees interviewed for this story, for example, even knew it existed. Mindlin adds that the review board “does not have authority to take action, and it is not an investigative body.” The LDSS report notes that the board relies on information submitted by contractors, which “contains scant (if any) references to sexual assaults.” When such an incident is reported, it adds, the materials submitted “do not convey a full and accurate picture of what occurred.”

“We report serious incidents to the NSF as they occur,” a Leidos spokesperson says. “The NSF determines whether additional reporting is warranted.”

Current and former USAP employees say they want to believe NSF is committed to making things better and praise the agency for asking LDSS to follow up its report with a survey on how often sexual assaults and harassment occur. “The NSF has certainly been accused of complicity and sweeping incidents under the rug,” says one current employee who requested anonymity. “But the fact that they commissioned the report and are pursuing this survey indicates that they’re embracing accountability and seeking a path to positive change.”

“The problem,” the advocate continued, “is that, to this point, they’ve outsourced the mission to private companies who have a vested interest in silencing us. Our fear is that these entities will pay lip service to culture change, implement a new training program, and do nothing substantial to make real culture change.” ■

## GLOBAL HEALTH

# Polio returns in rich countries, but big outbreaks are unlikely

As New York state declares an emergency, experts are far more worried about a resurgence in low-income countries

By **Leslie Roberts**

**H**ere’s how this year’s closely related polio outbreaks in New York state, London, and greater Jerusalem might have started. A child in Afghanistan or Pakistan received two drops of Albert Sabin’s oral polio vaccine (OPV), which contains a weakened, live virus, in December 2021 or so. Soon after, when the child was still shedding some virus in their stool, their family traveled to the United Kingdom, where the vaccine virus found fertile ground in an undervaccinated Orthodox Jewish community in London and began to circulate person to person. Somewhere along the way, it also began to change, picking up mutations that can turn the vaccine virus into one that, in rare instances, can paralyze.

That virus then jumped to Israel and to an Orthodox Jewish community in Rockland County, northwest of New York City, says Nicholas Grassly, an epidemiologist at Imperial College London and member of the U.K. National Authority for the Containment of Poliovirus. He reconstructed the “plausible” scenario based on the epidemiological timeline and viral sequences detected in sewage. In Rockland County, an unvaccinated young

man in the Orthodox community sought care for weakness in his legs in June—the first U.S. polio case in a decade.

The outbreak, which is continuing, underscores the risks facing unvaccinated and undervaccinated people even in wealthy economies. All three countries have ramped up vaccinations, and on 9 September, New York Governor Kathy Hochul declared a state of emergency in an attempt to curb the outbreak.

But Grassly and other polio experts stress that big outbreaks of paralytic polio cases remain highly unlikely in rich countries, thanks to high vaccination coverage and good sanitation. “There is a risk we will end up reporting one or two cases in London,” Grassly says. Mark Pallansch, a polio virologist who recently retired from the U.S. Centers for Disease Control and Prevention (CDC), thinks the same is true for New York state. Both are far more concerned about similar outbreaks in low-income countries—which get far less press coverage but have already paralyzed almost 300 children this year, mostly in Yemen and Africa—and about a resurgence of the wild poliovirus in Africa.

OPV remains the workhorse of the global eradication program because it’s cheap,



Health workers wait for children to vaccinate against polio at a pop-up clinic in Rockland County in New York.

easy to use, and confers robust gut immunity that helps stop polio transmission. But where immunization rates are low, the vaccine virus can continue to spread from person to person and over time acquire enough mutations to regain its ability to paralyze, just like the wild virus. As few as six nucleotide changes in the region encoding a viral capsid protein named VP1 are enough to transform a harmless Sabin virus into what is known as a vaccine-derived poliovirus (VDPV). That's why wealthy countries instead use Jonas Salk's inactivated polio vaccine (IPV), which must be injected. That vaccine cannot revert.

Most VDPV outbreaks are caused by one of the three polioviruses, type 2. Because type 2 has been eradicated in the wild, that component of the vaccine has been removed from general use and is deployed only to fight type 2 outbreaks. Both Afghanistan and Pakistan used type 2 OPV during mass campaigns in December 2021.

The viruses that arrived in New York, London and Israel did not come as full-fledged VDPVs; they were only part way along their journey, with just a few genetic changes from the Sabin type 2 virus. In London, Grassly says, sequence analysis of virus samples collected from wastewater shows a gradual evolution to a VDPV between February and June. Through retrospective analyses, New York state health authorities have found traces of a type 2 Sabin-like virus in wastewater collected to hunt for SARS-CoV-2 as early as April. The virus that paralyzed the young man in June had 10 nucleotide changes in the critical VP1 region. New York officials keep finding Sabin-like viruses in a growing number of counties, some with a few nucleotide changes, others full-fledged VDPVs.

Vaccination rates are high in the U.S. and the U.K. overall, but low in some communities. In Rockland County, where antivaccination sentiment runs high, just 60% of children under age 2 had received the full three doses of IPV in August. In one zip code, coverage is just 37%. (Rockland was also the site of a huge measles outbreak in 2019 that almost cost the United States its measles-free status.) The June polio case is “tragic but totally predictable and preventable,” Pallansch says.

The state has launched an all-out push to get children vaccinated with IPV. Although excellent at preventing paralysis, IPV is not as good as OPV at stopping outbreaks, but U.K. and U.S. experts think it can probably do the job. The idea is to build a wall of immunity around the virus then evaluate how well it works, says Andrew Pollard, director of the Oxford Vaccine Group and chair of the

U.K. Joint Committee on Vaccination and Immunisation. “There is reason to think it will [work]. So end of story.”

New York state has so far had limited success vaccinating the most resistant communities, says Rockland County Health Commissioner Patricia Schnabel Ruppert. But even in pockets where vaccine coverage remains low, the virus may burn itself out because the susceptible population won't be large enough to sustain spread, Grassly says.

Besides, “The kind of sanitation issues that we see [in poor countries] simply don't exist” in wealthy ones, says Aidan O'Leary, head of the Global Polio Eradication Initiative. The poliovirus spreads easily through fecal-oral contact and thrives in places where sanitation is lacking and clean water scarce. In high-income countries, the primary route of transmission is respiratory, which is less efficient, Pallansch says.

If vaccination with IPV isn't enough, contingency planning is underway in both the U.S. and the U.K. to evaluate the possible use of a new vaccine, known as novel OPV2 (nOPV2), designed to be just as good at stopping outbreaks as OPV but significantly less likely

to revert to its neurovirulent form (*Science*, 13 November 2020, p. 751). The vaccine is now being used in 22 low-income countries fighting polio outbreaks under a World Health Organization emergency use authorization. But the U.S. and U.K. would have to jump through big regulatory hoops to get approval to use nOPV2. “We are a long way from reaching for” nOPV2, says Janell Routh, who is leading CDC's investigation into the New York case.

Vaccine-derived polioviruses are not the only threat to the global eradication effort. Cases caused by the wild poliovirus are also up: Pakistan has already reported 17 this year, up from one in all of 2021. After being confined for years to Afghanistan and Pakistan, the wild virus leapt to Africa in 2021, where it was last seen 5 years ago. It has already paralyzed six children in Malawi and Mozambique. The risk of further spread is high, O'Leary says. Mozambique is also battling outbreaks of type 2 and type 3 vaccine-derived strains.

The global priority remains to “stop polio at the source,” while New York state and London deal with the “spillover” effects, O'Leary says. With ramped up surveillance and catch-up vaccination campaigns in place, “They are doing everything right at the right time,” he says. ■

Leslie Roberts is a science journalist in Washington, D.C.

**“This case is tragic but totally preventable and predictable.”**

**Mark Pallansch,**  
polio virologist



## ENVIRONMENTAL SCIENCE

# Record salinity and low water imperil Great Salt Lake

## Drought spurs efforts to restore shrinking lake's water supplies

By **Eli Kintisch**

Utah's Great Salt Lake is smaller and saltier than at any time in recorded history. In July, the U.S. Geological Survey (USGS) reported that the world's third-largest saline lake had dropped to the lowest level ever documented. And this week researchers measured the highest salt concentrations ever seen in the lake's southern arm, a key bird habitat. Salinity has climbed to 18.4%, exceeding a threshold at which essential microorganisms begin to die.

The trends, driven by drought and water diversion, have scientists warning that a critical feeding ground for millions of migrating birds is at risk of collapse.

“We're into uncharted waters,” says biochemist Bonnie Baxter of Westminster College, who has been documenting the lake's alarming changes. “One week the birds are gone from a spot we usually see them. The next week we see dead flies along the shore. And each week we have to walk further to reach the water.”

After years of inaction, the prospect of a



A runner traverses reeflike structures, called microbialites, exposed by the receding waters of the Great Salt Lake. They provide important habitat for insects that feed millions of migrating birds.

dying lake, plus the risk of harmful dust blowing from the dry lakebed, is galvanizing policymakers to find ways to restore water to the shrinking lake.

The Great Salt Lake is really two lakes, divided in 1959 by a railroad causeway. Over time, the northern arm, which has few sources of fresh water, became saltier than the southern arm, which is fed by three rivers. Historically, salinity in the northern arm has hovered around 32%—too salty to support more than microorganisms—and about 14% in the southern arm.

Although the southern part is about four times saltier than seawater, it supports a vibrant ecosystem characterized by billions of brine shrimp and brine flies, which feed on photosynthetic cyanobacteria and other microorganisms. Birds, in turn, devour prodigious numbers of flies and shrimp when they arrive at the lake to nest, molt, or rest during migrations. A diving waterbird called the eared grebe, for example, needs 28,000 adult brine shrimp each day to survive.

The low water and rising salinity threaten to destroy the base of this food web, researchers say. The receding shoreline has already dried out many reeflike mats of cyanobacteria, known as microbialites, that dot the lake bottom. Baxter fears the saltier water now threatens even the microbialite communities that remain submerged. “In laboratory tests, when the salinity passes 17% we see the cyanobacteria start to die off,” she says.

Loss of the mats could also harm brine fly populations, Baxter says. The flies lay eggs on the lake surface, producing larvae that swim down to the microbialites, where they pupate before maturing into adults. Some bird species feed on the larvae or adults, whereas others eat the pupae—which have been showing up dead by the billions during this fall’s migration season.

Soon the brine shrimp could dwindle as well. “The fear is that in some future year, [the lake] will become so salty that its

populations ... will collapse,” a pair of state ecologists wrote recently.

In the meantime, researchers are mobilizing to track the unfolding crisis. Baxter is bringing in a brine fly expert to assess the situation. Conservation groups are tracking shorebird populations across the intermountain West. And USGS has established a program to monitor hydrology and ecology at other saline lakes in Oregon, California, Nevada, and Utah, which are facing similar stress.

The shrinkage of the lake threatens people as well as wildlife. In a 2019 state-funded report, atmospheric scientist Kevin Perry of the University of Utah estimated that 9% of the exposed lakebed sediments contain problematic levels of arsenic or metals, thought to be derived from industry, wastewater treatment, or agriculture. Winds are likely to erode the crust that holds the sediment

in place and carry dust far and wide. With more than 1 million residents living near the lake, in Salt Lake City and its suburbs, the worst-case scenario would be an air pollution disaster—akin to those experienced by communities in Iran near other saline lakes. Even Utah’s famed ski slopes are imperiled by the dust; scientists have documented how storms are already dumping lakebed particles onto the snow, darkening it and hastening the melt.

For years, conservationists have urged policymakers to reduce the water that farmers and other users divert from streams that flow into the lake. But, “Conventional wisdom has been it’s just a salty lake—we should be using the water upstream,” says Utah State Representative Tim Hawkes (R). “For many in Utah the lake’s been a little bit out of sight, out of mind.”

This year, however, policymakers sprang into action. In April, Utah Governor Spencer Cox signed a landmark series of bills aimed at rescuing the lake and addressing the drought. They include new rules that allow farmers to sell water rights they are not using to groups that will allow the water to flow to the lake. The state earmarked \$450 million for water infrastructure and conservation projects, including a \$40 million fund that could acquire water for the lake in the future.

Such policies could take years to have a noticeable impact, especially if the current drought continues. Baxter, for one, wonders: “Is any of this enough?” But Marcelle Shoop, who heads the Saline Lakes Program for the National Audubon Society, says she is “optimistic, because there are so many people trying to develop solutions.”

In the meantime, the lake may get temporary relief from a different source: the upcoming winter wet season. If it produces a good snowpack in nearby mountains, the runoff could help refill the region’s parched streams. ■



A NASA satellite image taken in July shows the Great Salt Lake has shrunk since a high water mark in 1985.

PHOTO: NASA EARTH OBSERVATORY IMAGES BY JOSHUA STEVENS, USING LANDSAT DATA FROM THE U.S. GEOLOGICAL SURVEY AND DATA FROM THE NATIONAL WATER INFORMATION SYSTEM, ADAPTED BY K. FRANKLIN/SCIENCE

## SPACE SCIENCE

# NASA's asteroid deflection mission takes aim

Target's structure will sway outcome of upcoming test collision, simulations show

By Zack Savitsky

On 26 September, an act of targeted violence will unfold 11 million kilometers from Earth, as a spacecraft about the size of a vending machine smashes into a small asteroid at 6 kilometers per second. Unlike some asteroids that stray worryingly close to Earth's orbit, Dimorphos—the 160-meter moon of a larger body—is an innocent bystander, posing no threat to our world. But the looming assault represents humanity's first-ever field test of a planetary defense mission: NASA's Double Asteroid Redirection Test, or DART.

The hope is that the collision will nudge Dimorphos toward its 780-meter partner, Didymos, shortening a nearly 12-hour orbital period by minutes. A successful strike would support the idea that, in the future, similar efforts could deflect threatening asteroids onto safer courses. But simulations and lab experiments show the fate of the mission depends on a crucial question: Are such small asteroids solid boulders or—as astronomers increasingly believe—loose heaps of rubble?

The answer, which should be revealed from the crater and ejecta produced by DART's collision, could determine just how hard to hit an asteroid when the exercise is not a test. "It's going to be thrilling—and very stressful—but ultimately, I think we're going to learn a lot," says Cristina Thomas, a planetary scientist at Northern Arizona University who leads the observation team for the DART mission.

Dimorphos-size asteroids are thousands of times more likely to strike Earth than the larger ones that have triggered mass extinction events in the geologic past, and they are still capable of devastating a state or small country, making these smaller bodies the top priority for planetary defense efforts. But they are no more than pinpricks of light to earthbound telescopes, making them hard to detect, let alone study.

When spotted, binary asteroid systems are more revealing, because their light dims whenever one body blocks the other. By monitoring

small fluctuations in the light from Dimorphos and Didymos, NASA scientists and others have managed to learn how fast they spin and the frequency of the smaller body's orbit. This knowledge allowed them to design an autonomous navigation system that will steer DART as it closes in on its prey.

What will happen next is anyone's guess. "People assume it's a solid rock, we have a solid spacecraft, and we're essentially playing a giant game of billiards in space ... and you can basically just solve that out as a simple physics equation," Thomas says. "But there's so much else that's happening that makes that not true."

The biggest uncertainty is the "strength" of Dimorphos, according to DART lead investigator Andy Cheng of the Johns Hopkins

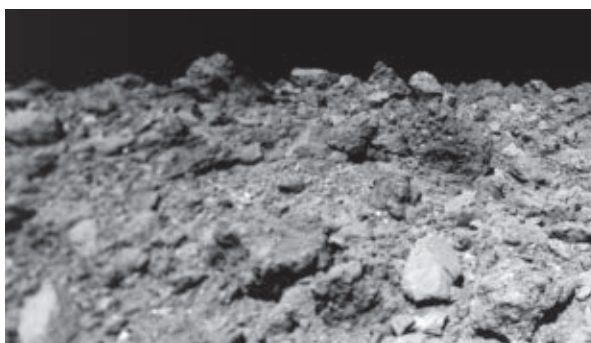
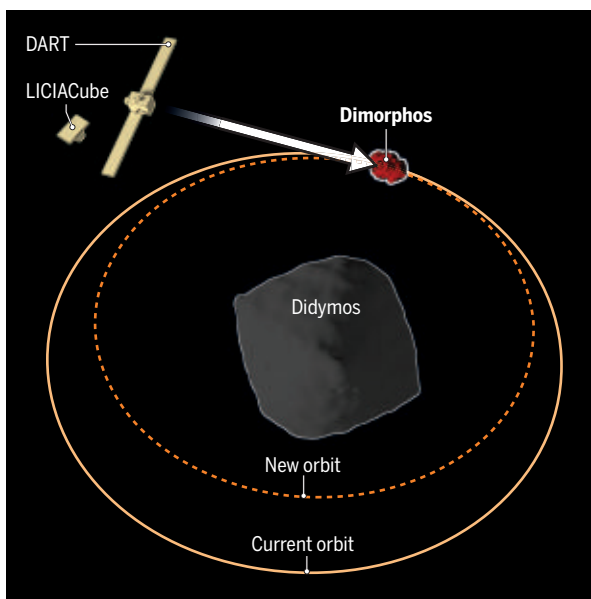
University Applied Physics Laboratory. "And that makes a huge difference in terms of the outcome," he says.

Clues that not all asteroids are solid, monolithic rocks have piled up in recent years. In 2019, Japan's Hayabusa2 probe shot a 2-kilogram copper projectile into the asteroid Ryugu, blasting a surprisingly large crater, 14 meters across. The experiment indicated that Ryugu's surface was held together much more weakly than expected. The following year, NASA's OSIRIS-REx probe landed on the Bennu asteroid and sank right in with little resistance. These missions confirmed the idea of weak asteroids and put constraints on their surface strength—how much force is needed to deform the objects. Scientists estimated these asteroids were held together by

about 1 pascal—the pressure from a piece of paper resting on your hand. "I'm an old-timer, and I find it hard to believe that anything can be so weak," Cheng says. "It's reinforced a lesson we've learned from planetary geology for decades: You cannot tell whether something is a rock by looking at pictures."

Unfortunately, forecasting the consequences of an impact is much more difficult when the target is made up of thousands of loosely bound rocks than when it's a solid boulder. If DART does hit a weak rubble pile, the resulting crater would develop over a few hours in a process so complex it would take months or even years to model with traditional computer simulations, says Sabina Raducan, a planetary scientist at the University of Bern.

Recently, she and her colleague optimized a computer code modeling a 3D shock wave to speed up the calculation to a few weeks. Unexpectedly, the new simulations show the DART impact could transfer four to five times more momentum to a weak rubble-pile target than a consolidated one—enough to reshape the entire asteroid rather than simply leaving a small impact crater, they reported in *The Planetary Science Journal* in June. DART would also have a greater effect on a weak target because the loose rubble structure would allow more material



A trailing spacecraft will document DART's attempt to push Dimorphos into a shorter orbit (graphic). The outcome may hinge on whether the target is solid or a rubble pile like asteroids such as Ryugu (bottom).

to spurt from the impact—propelling the asteroid forward like a rocket thruster.

“This [modeling] is cutting-edge,” says planetary scientist Julie Brisset of the Florida Space Institute, who is not involved in the DART mission. “You don’t want to stick to the old monolithic [rock] story.”

The push to model rubble-pile asteroids extends beyond computer screens. Scientists often calibrate their impact simulations with lab experiments—shooting high-velocity projectiles at different targets, as James Walker has done at the Southwest Research Institute for more than a decade. Recently, Walker’s and Raducan’s teams have both constructed the first makeshift rubble-pile asteroids for these tests. Walker has been launching masses horizontally at a panel of rocks covered in cement and suspended on a pendulum, whereas Raducan has been firing straight down into a 7-meter-wide sand pit embedded with small boulders. Both teams have analyses awaiting publication, and one thing is clear: The weaker targets show much more dramatic explosions from the impacts.

A crew of instruments will be watching how well the actual collision matches the simulations. On Sunday, DART deployed a toaster-size craft, LICIACube, that will record the event with two optical cameras. The James Webb and Hubble space telescopes, along with four ground-based observatories, will take turns monitoring the dot of light. If Dimorphos is a weak rubble pile and its ejecta plume is as large as Raducan predicts, Thomas thinks the observatories should be able to catch it lighting up within hours after the crash. “That final cloud ... is really going to tell us a lot about the actual physical properties of the target,” she says. “It’s not going to take much time for Dimorphos to give us the answers; it’s going to take us more time to figure out what it was telling.”

The full picture won’t come into view for 4 years, though, when the European Space Agency’s Hera mission arrives to survey Dimorphos’s surface and measure its mass. This will help diagnose the asteroid’s internal structure and aid future planetary defense missions. In the event of a real asteroid threat, the goal is to hit the body just hard enough to divert it, without sending a hailstorm of small rock fragments toward Earth.

Confirming that Dimorphos has a rubble-pile structure would also shed light on a bigger question: how the Solar System took shape. “Understanding what these small bodies went through helps us understand how planetary systems formed,” Brisset says. “They’re the remnants of this process.”

For now, however, the scientists must wait anxiously as DART approaches its bull’s-eye, hoping their preparation work will be the key to unlocking its secrets. ■

## PUBLISHING

# Reviewers award higher marks when a paper’s author is famous

“Matthew effect” is powerful, unusually large study finds

By Jeffrey Brainard

**Y**es, having a big name in science will help get your paper published, an unusually robust new study confirms. Just 10% of reviewers of a test paper recommended acceptance when the sole listed author was obscure—but 59% endorsed the same manuscript when it carried the name of a Nobel laureate.

The study, which involved recruiting hundreds of researchers to review an economics manuscript, is “incredible,” says Mario Malički, a postdoctoral researcher at Stanford University and editor-in-chief of *Research Integrity and Peer Review*, who was not involved in the research. “It is the largest randomized controlled trial we have seen on publication bias.”

For years, scientists have griped about the Matthew effect, a term coined in 1968 by sociologists Robert Merton and Harriet Zuckerman to describe how high-status researchers—those who already have many citations and grants, for example—tend to get disproportionately more of the same. (The name comes from a parable about abundance in the biblical Gospel of Matthew.)

But efforts to document such bias often had weaknesses, such as a small sample size or lack of randomization. To avoid those problems, a team led by Jürgen Huber of the University of Innsbruck emailed some 3300 researchers, asking whether they would review an economics study prepared for a real journal. The study had two authors, both at Chapman University: Vernon Smith, a 2002 Nobel laureate in economics who last year had more than 54,000 citations listed on Google Scholar; and Sabiou Inoua, one of Smith’s former Ph.D. students, who last year had just 42 citations. The potential peer reviewers were sent one of three descriptions of the paper: One mentioned only Smith, listing him as the corresponding author; another, only Inoua; and a third, no author.

Ultimately, 821 researchers agreed to review, the team reported last week at the International Congress on Peer Review and Scientific Publication in Chicago. (The re-

sults also appeared in a preprint posted last month on the SSRN server.) Smith’s prominence appeared to sway the responses: Of the researchers given just his name, 38.5% accepted the invitation to review; the figures were 30.7% for those given no name and 28.5% for those given just Inoua’s.

The team then took a second step to avoid bias in their own study. They focused on the 313 willing reviewers who had initially received no author’s name and randomly assigned them to review one of three manuscripts, one listing only Smith, another just Inoua, and a third with no authors.

The manuscript credited to Smith won the highest marks from reviewers, who

lauded it for including new information and conclusions supported by data. (Smith and Inoua are revising the paper, which they later posted as a preprint, for publication in a journal.) And 24% of those who reviewed the version with no authors recommended accepting it (outright or with minor revisions), more than double the share that endorsed the version credited to Inoua alone.

The stark disparity might not surprise many researchers. But it is troubling, an author of the new study told the peer-review congress. “Identical work should not be evaluated differently depending on who wrote it,” said Christian König-Kersting, a behavioral economist at Innsbruck. “Because that makes it especially hard for younger and unknown researchers to get their foot in the door in the academic process.”

The authors couldn’t rule out that discrimination based on perceptions of race or geographic origin shaped some reviewer decisions. Smith’s name is “American sounding” and he is white, König-Kersting noted, whereas Inoua is a citizen of Niger and dark skinned.

Researchers who study bias in publishing have suggested double-blind reviews—in which the identities of both authors and reviewers are masked—might reduce the Matthew effect. But that tactic might not work, König-Kersting told the congress, given that reviewers can often identify authors from a preprint or conference presentation. ■

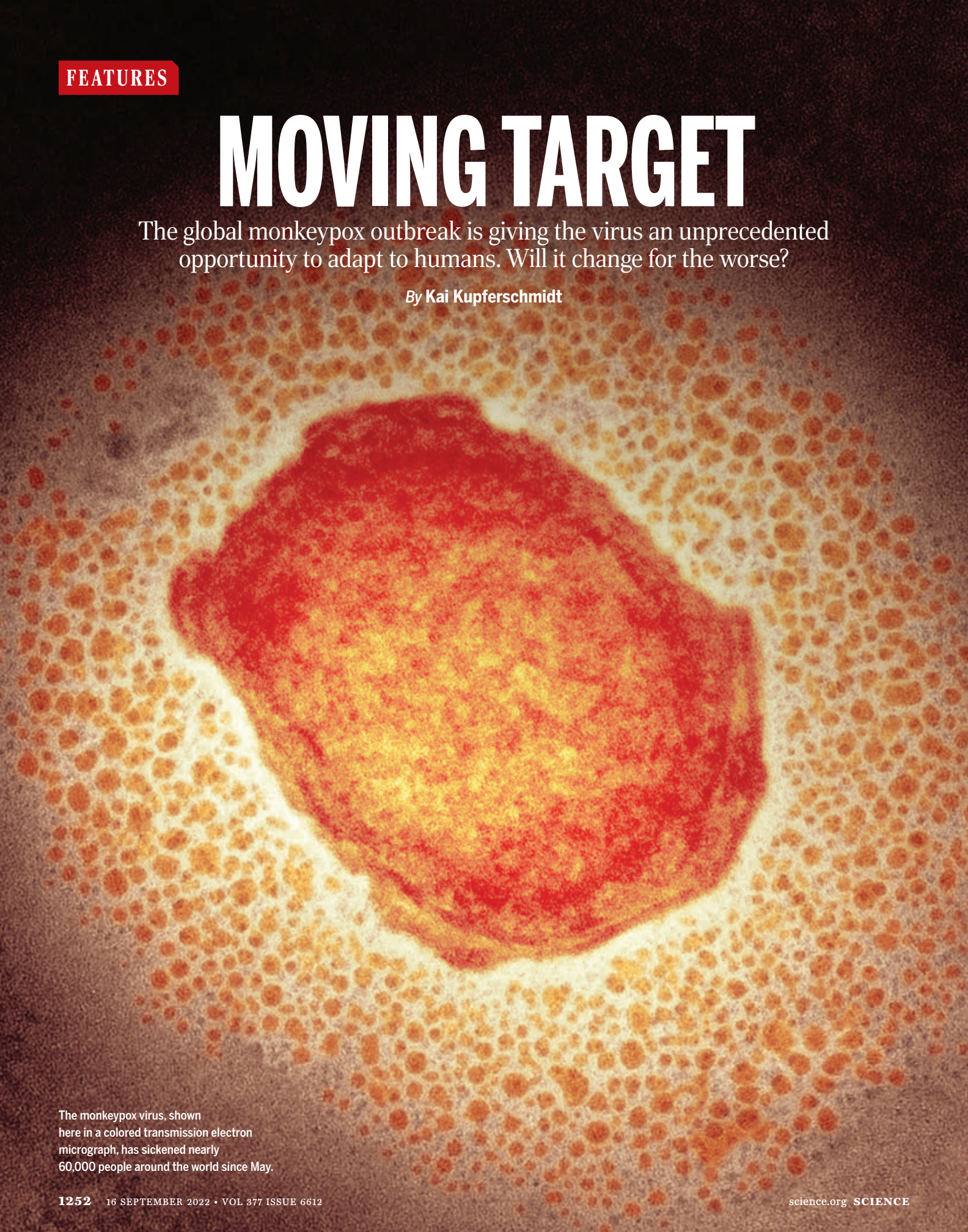
**“It is the largest ... controlled trial we have seen on publication bias.”**

**Mario Malički,**  
Stanford University

# MOVING TARGET

The global monkeypox outbreak is giving the virus an unprecedented opportunity to adapt to humans. Will it change for the worse?

By Kai Kupferschmidt



The monkeypox virus, shown here in a colored transmission electron micrograph, has sickened nearly 60,000 people around the world since May.



A few years ago, researchers scoured the remains of 1867 people who lived between 30,000 and 150 years ago for genetic traces of variola, the virus that causes smallpox. In the teeth and bones of four Northern Europeans from the Viking era, they found enough DNA to reconstruct entire variola genomes. The sequenced viruses weren't direct ancestors of the feared variola strain that was eradicated in the second half of the 20th century. But they may hold a clue to how smallpox became so deadly.

Over the span of 350 years, the Viking virus lost several genes, the researchers reported in a 2020 paper in *Science*. Researchers had seen this pattern before. The modern smallpox virus also lost several genes in the recent past, although as a result of different mutations. Seeing it twice “suggests that the loss of the genes was not an accident,” says poxvirologist Antonio Alcamí of the Severo Ochoa Center of Molecular Biology in Madrid. “It was selected for.” Alcamí thinks the losses may have made variola more virulent, resulting in its 30% mortality rate. In the past, smallpox may have been a “widespread mild disease,” he wrote in a commentary accompanying the paper.

Now, some scientists are wondering: Could something like this happen again?

Since May, a far less lethal cousin of variola, the monkeypox virus, has been spreading around the globe, giving the virus unprecedented opportunities to change and adapt to the human population. Will it

evolve to become more contagious or cause more severe disease?

Nobody knows, but recent history with SARS-CoV-2 offers a sobering lesson. After emerging in Wuhan in late 2019, that virus first spawned a series of variants that could spread much faster than their progenitors and then evolved further to evade human immunity. Its tricks surprised even some scientists who have long studied viral evolution (*Science*, 20 August 2021, p. 844). SARS-CoV-2 showed that “if a novel virus is coming into a space in which there isn't immunity, rapid adaptation can happen,” says Aris Katzourakis, an evolutionary virologist at the University of Oxford.

Monkeypox could present humanity with equally unpleasant surprises. In July, researchers in Berlin published a preprint analyzing the genome sequences of virus found in the lesions of 47 monkeypox patients. In addition to many small changes, they found one virus in which an entire gene was duplicated and four others were simply gone. The paper's last paragraph almost read like a warning: “The consequence of changes in poxvirus genes whose products are no longer required in a new host or otherwise altered context is unpredictable,” the authors said. “The [monkeypox virus] phenotype we have known for the last 64 years may not resemble near-future human” monkeypox.

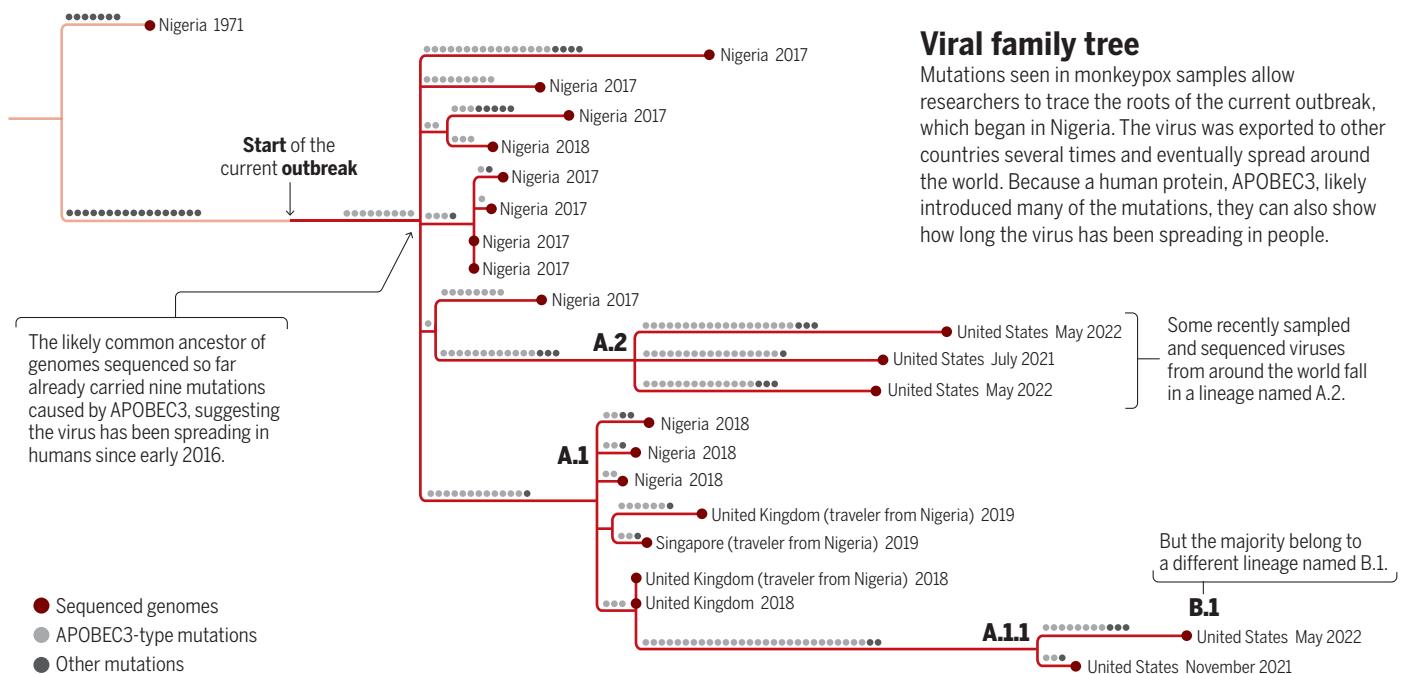
Many researchers say we shouldn't worry too much yet. Geoffrey Smith, a poxvirologist at the University of Cambridge, doubts the monkeypox virus will readily turn into a much more virulent version. Poxviruses' mas-

sive genomes are known to evolve at a sluggish pace, and they don't adapt easily to elude immunity, as SARS-CoV-2 does so masterfully. And SARS-CoV-2 is a wildly contagious respiratory pathogen that infected hundreds of millions in its first year in the human population; monkeypox is spreading mostly among men who have sex with men, and only about 60,000 cases have been reported so far, so it has much less opportunity to evolve.

That could change, however. One “bad scenario,” says Bernard Moss, a veteran poxvirus researcher at the U.S. National Institute of Allergy and Infectious Diseases, is that the virus evolves to replicate faster in humans. That would allow it to infect more people, which would in turn speed up its evolution, potentially making it still more adept at infecting people.

**FOR NOW, THE MONKEYPOX VIRUS** is not very good at infecting humans. It is a generalist that appears to thrive in a range of animal species—most of them rodents—in sub-Saharan Africa. From time to time the virus has spilled over into people, who have sometimes infected a few others. Although outbreaks have grown more frequent in recent years (see Perspective, p. 1261), they have typically been small. After each emergence the virus apparently disappeared again from the human population.

This time around is different, as monkeypox has continued to spread from person to person in a global outbreak. “We've never seen this virus with such an opportunity to adapt to humans before,” says Terry Jones, a



CREDITS: (GRAPHIC) C. BICKEL/SCIENCE; (DATA) MADE AVAILABLE ON GENBANK BY NCDC AND OTHERS; (IMAGE, OPPOSITE PAGE) AZEL APPLETON/HEALTH PROTECTION AGENCY CENTRE FOR INFECTIONS/SCIENCE SOURCE

computational biologist at Charité University Hospital in Berlin and one of the authors of the July preprint.

Reported cases are going down in many Western countries—most likely as a result of behavioral changes and vaccination—and public health officials in Europe are already talking about eliminating the virus in the region. But infections are still on the rise elsewhere in the world. In many places vaccines are unavailable, or people at risk either lack information about how to avoid infection or fear asking for it, because gay sex is criminalized.

“I don’t think [monkeypox] will cause massive numbers of infections, but it will stay there and it will be difficult to eradicate,” Alcamí says. “Decision-makers have to realize that this is not going away anytime soon,” adds Christian Drosten, a virologist at Charité and a co-author of the July preprint.

Science can’t do more than hint at how the virus might evolve as it continues to circulate. One reason is that research interest in poxviruses has dwindled after the worldwide smallpox eradication campaign ended in triumph in 1980. “I always had to start my talks by almost apologizing for working on poxviruses,” Alcamí says.

Evolutionary virologists have instead concentrated on the influenza virus, HIV, and other small viruses whose genomes consist of RNA. Poxviruses, by contrast, are made of DNA, and are much larger and more complex. With roughly 200,000 nucleotides and 200 genes, the monkeypox genome is more than 20 times the size of HIV’s. It’s not clear what many of those genes do, Moss says, let alone how they interact with each other or how changes in any of them might affect their impact on humans.

Moss has been trying for years to figure out the crucial difference between two variants of monkeypox virus: clade 2, which until recently was found only in West Africa and is now causing the global outbreak, and clade 1, believed to be much deadlier, which has caused outbreaks in the Democratic Republic of Congo for many decades. He’s found that clade 1 virus can kill a mouse at levels 1000 times lower than those needed with clade 2. To find out why, Moss and his colleagues swapped dozens of clade 2 genes, one at a time, into clade 1 virus, hoping to see it become less deadly, but with no luck so far. Now, they are planning to try the opposite, endowing clade 2 virus with genes from its deadlier relative.

One thing is clear, however: Poxviruses mutate slowly compared with RNA viruses. “Their genomes are pretty stable and don’t change quickly,” Smith says. And although poxviruses have ways of tricking the immune system, they don’t change their surface pro-

teins to escape immunity, as SARS-CoV-2 does. An infection with smallpox, if you survived it, provided immunity for life, and the vaccines remained very effective right until the end of the eradication campaign. That, too, offers some hope that monkeypox won’t transform into a bigger threat.

**RESEARCHERS AROUND THE WORLD** are now mining monkeypox genomes from recent patients to learn how the virus has evolved so far. Getting high-quality sequences is harder and more expensive than it is for SARS-CoV-2, not just because the monkeypox genome is so vast but also because crucial re-



The animal hosts of the monkeypox virus remain unknown, but many rodent species in Africa seem able to carry it, including the African pouched rat (*Cricetomys emini*, top) and the fire-footed rope squirrel (*Funisciurus pyrropus*, bottom).

regions near its ends can be full of repetitions or deletions that can trip up researchers when they assemble sequences. “Handling these genomes is more complex than the RNA viruses,” says Richard Neher, a computational biologist at the University of Basel. “It will be more important than with SARS-CoV-2 that people share their raw data.”

Still, the work is already yielding some results. When researchers compared recent genomes from the current monkeypox outbreak with older sequences, like one isolated from a traveler from Nigeria in the United Kingdom in 2019, they quickly noticed two interesting things. The genomes had more

point mutations than expected after only a few years, and many of them followed the same pattern, with the nucleotide combination guanine-arginine changing to arginine-arginine, or thymine-cytosine changing to thymine-thymine.

Those mutations are probably traces of an ongoing fight between the virus and the human immune system. A human protein called APOBEC3 acts as a cellular defense mechanism by introducing errors into the viral genome as it gets copied, and the changes spotted in the monkeypox genomes are its signature. “Clearly, it’s not sufficient to stop the virus replicating,” says molecular evolutionary biologist Andrew Rambaut of the University of Edinburgh.

In the long term, though, the mutations could make the virus less fit as they accumulate—or one of them could happen to benefit the virus. Still, “My hunch is that this is probably not going to be very important from an evolutionary point of view,” Rambaut says.

What these mutations can do is give researchers a clock to determine how long ago monkeypox began to circulate in humans. Comparing genomes from different time points suggests the virus is currently adding about six APOBEC3-related changes per year, says Áine O’Toole, an evolutionary biologist at Edinburgh. A family tree of virus genomes from the current outbreak suggests viruses circulating in Nigeria in late 2017 already carried nine APOBEC3-type mutations, which would mean the virus jumped into humans sometime in early 2016, about a year and a half before the outbreak was recognized in Nigeria (see graphic, p. 1253). The analysis also suggests the virus has been continuously circulating in humans since then.

**BUT POXVIRUSES CAN EVOLVE** in other, more drastic ways than single nucleotide changes. They “do a lot of evolutionary off-roading,” says Nels Elde, a virologist at the University of Utah who turned to monkeypox after many years of studying vaccinia, the weakened poxvirus that served as a smallpox vaccine. Elde explains that poxvirus genomes usually consist of a central region with about 100 genes that are mostly involved in creating new copies of the virus, and terminal regions with another 100 or so genes that interact with the host, for instance to counteract immune defenses.

Those terminal genes appear to be a key site of evolution. Generalist poxviruses that infect many different hosts, including monkeypox and cowpox, tend to have more genes in the terminal regions, whereas smallpox, which specializes in infecting humans, has many fewer. Most researchers believe smallpox evolved from a rodent poxvirus that



New Yorkers line up for smallpox vaccination in 1939. The eradication of smallpox, completed in 1980, caused research interest in poxviruses to dwindle.

jumped to humans. Over time, gene losses such as those seen in the Viking virus may have made it more deadly, says molecular evolutionary geneticist Hendrik Poinar of McMaster University.

“Smallpox goes from what we think is actually a very avirulent form, to repeated gene inactivation to really damn nasty until we eradicate it,” Poinar says. Based on the 2020 *Science* paper and his own work on a variola genome from a 17th century child mummy, Poinar believes this happened sometime between the fourth and the 15th century.

How the loss of genes would have made variola more virulent is not exactly clear, however. Simply having a smaller genome might make the virus more adept at replicating in human cells, says Eugene Koonin, a researcher at the U.S. National Center for Biotechnology Information. “Making the replication, say, 10% faster is a very big deal,” Koonin says. “Once it happens, this variant outgrows the competitors very, very quickly.”

The terminal genes can also evolve through another mechanism. They often get duplicated during viral replication, which can help the virus in two ways. The additional copies enable it to quickly produce much more of a needed protein, and they increase the chance that at least one copy of the gene will undergo a beneficial mutation. The “improvement” can make the other copies redundant, and they may be lost, shortening the genome. Elde, who studied the

mechanism in the vaccinia virus, calls it a “genomic accordion.”

Those changes could affect how the virus interacts with the human immune system, weakening its defenses, for example. But trying to predict the effects of specific mutations is like “shitty weather forecasting,” Elde says: “We have some patterns and some predictions we can make, but we really can’t stand solidly behind them because there’s a



Viral DNA found in Viking skeletons suggested the loss of some genes may have made the smallpox virus more virulent.

weather system that has massive variables spinning all around.”

Since they posted the preprint in July, Drosten’s lab has been studying the virus isolated from a patient in Berlin that had deleted and duplicated genes. As-yet-unpublished results are unsettling: “In cell culture it shows a clear difference, replicating a lot faster,” Drosten says. “We should not overinterpret that,” he cautions, because findings in the laboratory do not necessarily translate into an advantage for the virus in the real world. “But I find it remarkable that this virus already shows a difference in cell culture.”

If the virus had a real-world advantage but it simply did not transmit onward, then humanity may have been “just lucky,” Jones says—“this time.” He sees the current outbreak as a race between the monkeypox virus and humanity: “The virus is trying to adapt to humans and humans are trying to get rid of the virus,” he says. “Who’s going to get the upper hand? In the long term, I would put my money on the virus.”

Whatever comes next, the epidemic offers researchers an unexpected chance to watch a poxvirus evolve in real time. “We’re all kind of taking the clues, piecing it together, and hoping that this also is an opportunity to move science forward,” Elde says. “But I’m rooting for us, I’m rooting for the humans. ... I want to learn how these viruses operate, and then use that information so that we can have some control over this.” ■

### SOCIAL SCIENCE

# Weak ties, failed tries, and success

A large-scale study provides a causal test for a cornerstone of social science

By **Dashun Wang**<sup>1,2,3,4</sup> and **Brian Uzzi**<sup>2,3</sup>

**A** seminal finding in social science is that people are most likely to land high-paying jobs through their social connections rather than through advertisements or direct job applications (1). Unexpectedly, the most useful contacts are not the job seeker's strong ties—close friends or family. Rather, they are friends of a friend, or weak ties (1)—contacts least expected to be capable, or willing, to help. Although numerous studies of in-person and online social networks in various contexts have used the strength of weak ties

(SWT) to explain their findings, the theoretical foundations had yet to be put to a causal test. Now, having traced more than 20 million users on the LinkedIn social network platform, Rajkumar *et al.* report on page 1304 (2) a causal test for the SWT thesis. The data bear out the power of weak ties but raise questions about the implications of human connections for success and failure.

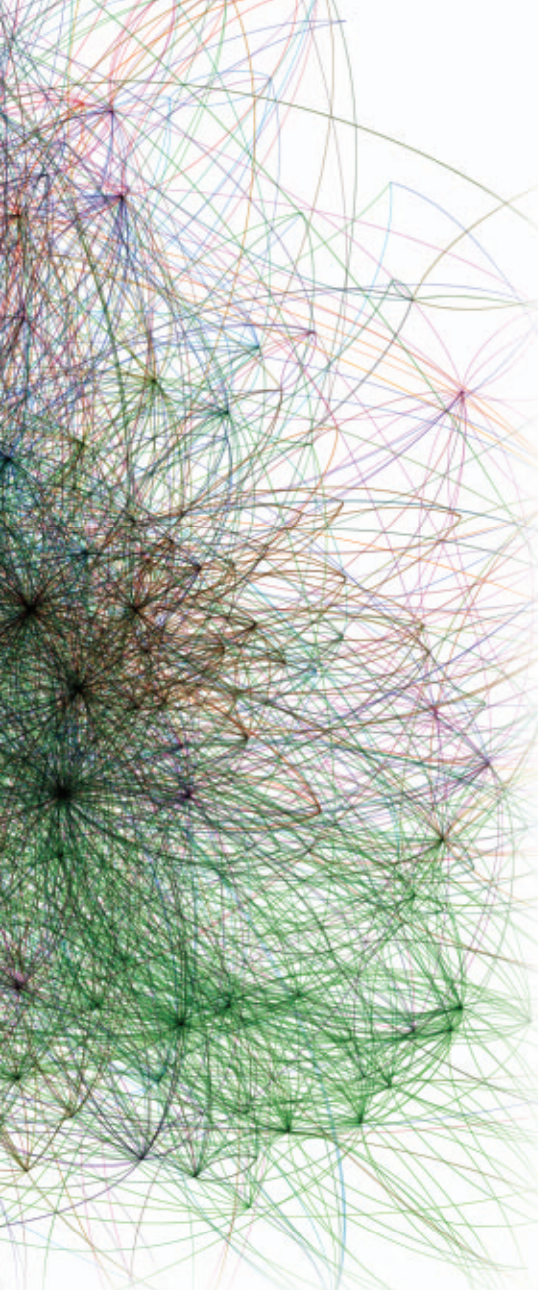
Mark Granovetter's landmark SWT publication (1) revealed much more about social networks than just their role in getting a job. It showed that different types of network contacts play different roles in shaping our lives. Strong ties tend to know the same information and to think in similar ways. By contrast, weak ties access new information because they bridge otherwise disconnected social circles (3). Particularly, over the past two decades, network science has developed rapidly, transforming our understanding of systems as diverse as the Internet, social

networks, and human cells (4). At the same time, there has been an explosion in large-scale social network data and the use of experimentation that have helped isolate how social networks drive political behavior (5), individual preferences (6), and the formation of social norms (7).

Yet, despite advances in data and computational power, there has been a persistent lack of causal understanding of the SWT theory. This highlights the many core challenges that researchers must overcome, even when armed with massive amounts of observational data. A correlation between the prevalence of weak ties in one's social network and their job outcomes does not mean that the two are causally linked.

Consider a dream experiment, where the prevalence of strong and weak ties within social networks was randomly varied to see whether these variations cause any changes in the probability of finding a job.

<sup>1</sup>Center for Science of Science and Innovation, Northwestern University, Evanston, IL, USA. <sup>2</sup>Northwestern Institute on Complex Systems, Northwestern University, Evanston, IL, USA. <sup>3</sup>Kellogg School of Management, Northwestern University, Evanston, IL, USA. <sup>4</sup>McCormick School of Engineering, Northwestern University, Evanston, IL, USA. Email: dashun.wang@northwestern.edu



Data from Rajkumar *et al.* (2) comprise all worker transitions recorded on LinkedIn. For the sake of illustration here, those data were down-sampled as follows: (i) Nodes are limited to companies with at least 10,000 employees. (ii) Edges are limited to those with at least five transitions between two companies. (iii) Companies are limited to a representative sample from the 30 largest industries. Transitions were then plotted, with colors representing industries.

Specifically, to infer causality, the authors used the random assignment of users to seven different variations of PYMK algorithms as an instrument, which varied each user's exposure to fewer or greater numbers of weak or strong ties depending on the experimental variants to which the user was assigned. They examined job outcomes by measuring both job applications and job transitions (see the illustration). They approximated tie strength between two individuals using two common measures—calculating the number of their common friends and the intensity of their interactions.

Their findings confirm Granovetter's thesis but also add further nuance. First, they found that weak ties do matter. For example, ties with just one mutual friend—i.e., very weak ties—are more likely to lead to job changes than strong ties, such as those with 25 mutual friends or more. Yet, at the same time, they also uncovered an inverted U-shaped relationship between tie strength and job outcomes. For example, compared with those very weak ties with one mutual friend, a tie with 10 mutual friends nearly doubles the probability of changing jobs. That is, moderately weak ties appear to be the most beneficial for job outcomes.

These results are fascinating for several reasons. First, amid the rise of online social networks, which has substantially altered the meaning of “friend” or “friend of a friend,” it seems that online social networks today are just as relevant in explaining economic outcomes, such as job mobility, as the offline social network studied by Granovetter some 50 years ago.

Further, although this inverted U-shaped relationship is not inconsistent with Granovetter's findings, it suggests a need for further conceptualization. That acquaintances, with whom you share few connections or experiences, are nevertheless willing to help you is not only sociologically interesting, but it also speaks to a set of social psychology findings. Research shows that people are more likely to help someone with whom they share something in common (8), even if sometimes these shared identities are random, such as sharing the same birthday. This is especially interesting considering that tie strength follows a long tail distribution (4), which means that there are a lot more

very weak ties than strong ties. However, the finding suggests that weaker social ties are not always better, which has implications for how to best manage one's social network. It suggests that on LinkedIn, your most valuable contacts for finding a better job are not the persons you are closest to or the thousands of contacts you accepted an invite from, but rather lie somewhere in between. These persons share some contacts with you that can motivate them to help and are, at the same time, distant enough to expose you to new and useful job information that your close contacts and you do not already have.

Among the many directions for future work, two broad opportunities are particularly noteworthy. First, how does the role of social networks differ for people of different genders, races, or other demographic characteristics? SWT implies that social connections are key sources of inequality in job mobility. For example, given that weak ties involve having diverse contacts outside your strong ties, groups that tend to form social networks within their enclave may have few opportunities to connect with weak ties outside their community. Hence, understanding a community's culture and constraints may hold the key to reducing inequality in the workplace. This is something that the authors could not examine because demographic information was not available.

The absence of demographic information also means that the authors could not address how job attainment through social network differs for men and women. A recent study of graduate student placement in science, technology, engineering, and mathematics (STEM) and other professional fields showed that the weak tie hypothesis appears to hold only for male students (9). All else being equal, female students competing for the same jobs seem to need both weak and strong ties to other women to get the best jobs, presumably because the strong ties conveyed employer information regarding the company's cultural orientation toward women in leadership positions. These findings echo Granovetter's initial focus on inequality and further highlight the importance of social networks in understanding inequality across the many facets of society (10).

It is also important to recognize that social network literature has disproportionately focused on how networks drive success while ignoring failures that frequently occur with individuals, teams, and organizations. For example, people rarely land their dream job through their first interview; rather, they often have to endure round after round of rejections. Research on job loss suggests that strong ties are the contacts that supported

And imagine that this experiment was conducted multiple times on the world's largest professional social network, with tens of millions of subjects in a global context. That dream just came true, thanks to a clever use of data from LinkedIn.

One key feature of social networking platforms is the so-called People You May Know (PYMK) algorithm, which recommends new connections to users. Social network companies frequently conduct experiments to tune their tie recommendation engines. As LinkedIn tried out different versions of their PYMK algorithms, it created random variations in the prevalence of weak ties in the professional networks of more than 20 million LinkedIn users over a 5-year period, during which ~2 billion new ties and 600,000 job changes were recorded. Rajkumar *et al.* harnessed these exogenous variations of weak ties and conducted retrospective analyses of these PYMK experiments by LinkedIn.

job seekers through failed tries (11). These possibilities highlight fruitful research opportunities while raising the broader question of whether insights obtained by analyzing success tell the full story of the role of failure in breeding success in the labor market and beyond.

Fortunately, the situation is improving radically, thanks to newly available large-scale datasets that record ubiquitous yet often neglected failures—as well as their successful counterparts—that span social, scientific, and technical domains (12). New research that pays specific focus to failures has begun to uncover a range of fascinating insights that challenge the way success is thought about. For example, when people experience negative shocks in their job, they tend to tap their strong ties rather than adaptively activating weak ties to obtain new information (13). And, despite the widespread evidence supporting the idea that success breeds success, failure seems to have rather powerful, offsetting effects, propelling individuals to greater long-term success (14). Combined with mathematical tools and modeling, analyzing failures—the precursors of success—could help to identify detectable early signals embedded in failures that will lead to ultimate victory or defeat (15). A systematic understanding of failure may transform our thinking around not only failure, but also success.

Although science may have succeeded in understanding how networks help us succeed, it has failed to understand how networks sustain us through failures. And that highlights a profound opportunity. Indeed, many scientists study success to learn the sources of inequality. But our failure to take failure seriously may be the reason why inequality has not yet been solved. ■

#### REFERENCES AND NOTES

1. M. S. Granovetter, *Am. J. Sociol.* **78**, 1360 (1973).
2. K. Rajkumar, G. Saint-Jacques, I. Boginov, E. Brynjolfsson, S. Aral, *Science* **377**, 1304 (2022).
3. R. S. Burt, *Am. J. Sociol.* **110**, 349 (2004).
4. A.-L. Barabási, *Network Science* (Cambridge Univ. Press, 2016).
5. R. M. Bond et al., *Nature* **489**, 295 (2012).
6. S. Aral, D. Walker, *Science* **337**, 337 (2012).
7. D. Centola, J. Becker, D. Brackbill, A. Baronchelli, *Science* **360**, 1116 (2018).
8. J. M. Burger, N. Messian, S. Patel, A. del Prado, C. Anderson, *Pers. Soc. Psychol. Bull.* **30**, 35 (2004).
9. Y. Yang, N. V. Chawla, B. Uzzi, *Proc. Natl. Acad. Sci. U.S.A.* **116**, 2033 (2019).
10. R. Chetty et al., *Nature* **608**, 108 (2022).
11. E. B. Smith, T. Menon, L. Thompson, *Organ. Sci.* **23**, 67 (2012).
12. D. Wang, A.-L. Barabási, *The Science of Science* (Cambridge Univ. Press, 2021).
13. D. M. Romero, B. Uzzi, J. Kleinberg, in *Proceedings of the 25th International Conference on World Wide Web (WWW '16)* (International World Wide Web Conferences Steering Committee, 2016).
14. Y. Wang, B. F. Jones, D. Wang, *Nat. Commun.* **10**, 4331 (2019).
15. Y. Yin, Y. Wang, J. A. Evans, D. Wang, *Nature* **575**, 190 (2019).

10.1126/science.add0692

#### WATER MANAGEMENT

# The “water machine” of Bengal

A data-driven and policy-supported strategic use of aquifers for irrigation is needed to maximize their benefits

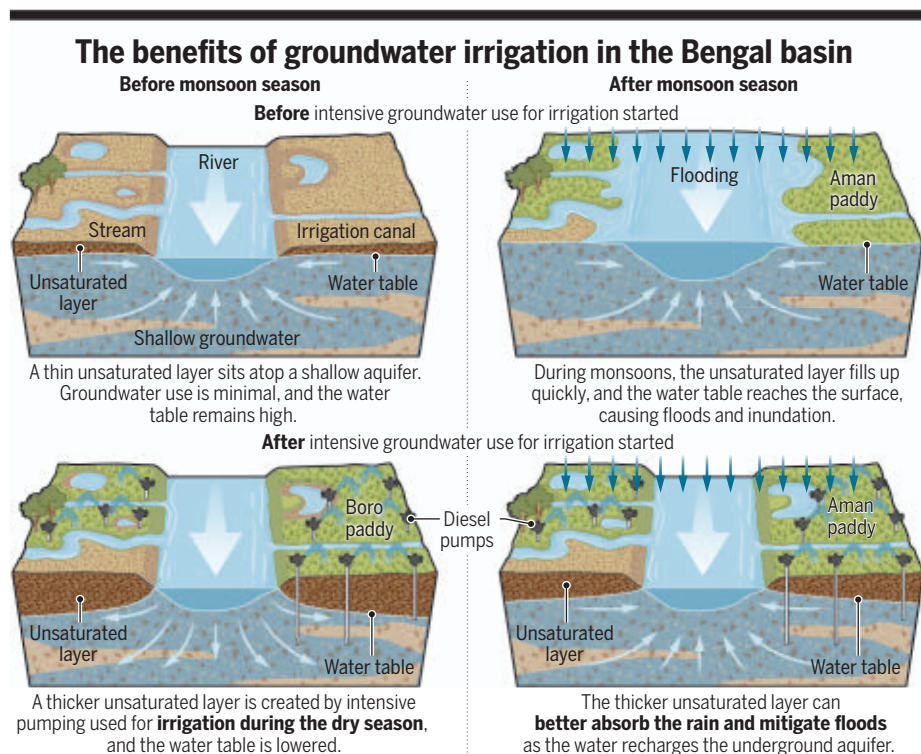
By Aditi Mukherji

For decades, millions of farmers in Bangladesh have been capturing more water than even the world's largest dams. They did so simply by irrigating intensively in the summer dry season using water from shallow wells. The ability to use groundwater to irrigate rice paddies during the dry seasons (January to May) helped Bangladesh become food self-sufficient by the 1990s, which was no small feat for one of the most densely populated countries in the world. Researchers proposed that lowering of the groundwater table as a result of intensive irrigation practices in the dry season created conditions for recharge from monsoon rains (June to September), which then replenishes the groundwater (1). On page 1315 of this issue, Shamsudduha *et al.* (2) present a quantitative analysis of this depletion-replenish process and show that this recharge has indeed been happening at a large scale, in a process they call the Bengal Water Machine (BWM).

The name of the BWM pays homage to the Ganges Water Machine, which was coined in

the 1970s. Both “water machines” describe a process in which the underground water table is lowered during dry seasons by human activities. This creates more space in the alluvial aquifer (made of loose sediments) for taking in heavy rainfall during the monsoon season. Such replenishment has the double benefit of helping farmers to grow dry-season crops and also increasing water storage capacity in underground aquifers for flood mitigation. In Bangladesh, Shamsudduha *et al.* observed an increase in annual intake, or “recharge,” after farmers started intensive irrigation from shallow wells (2011 to 2015) as compared with before (1976 to 1980). However, the authors also note that BWM is neither ubiquitous nor unlimited and can be affected by a number of factors, including local geology, land use, and year-to-year variations in rainfall.

Although Bangladesh is endowed with fertile land and a favorable climate that allows cultivation throughout the year, the country has faced food shortages throughout its history. These can be attributed to the complex colonial history of the region, but it is undeniable that Bangladesh's population density



and the region's vulnerability to cyclones and floods also played a role. After severe food shortages in the 1970s, Bangladesh embarked on a path toward agricultural intensification. Groundwater irrigation played a huge role in enabling this effort by allowing farmers to cultivate boro, a type of summer rice crop (3, 4). Affordable drilling of shallow tube wells, policy support for the import of cheap water pumps, and removal of bureaucratic control over pump installation have all contributed to a consistent increase in the area and production of boro rice (5, 6). In all, rice production increased from 9.9 million metric tons during the 1971–1972 season to 36.4 million metric tons during the 2018–2019 season. During the same period, the share of agricultural land use for boro cultivation also increased from 17.7 to 53.8%. However, more than 30 years after the removal of bureaucratic controls over pump installation, the government of Bangladesh reintroduced a pump permit system in 2019 to limit groundwater use (7). Without customizing these policies according to local aquifer and recharge conditions, the regulation may create unnecessary hurdles for farmers in search of affordable irrigation (8).

The findings of Shamsudduha *et al.* may help inform and develop region-specific guidelines for groundwater use. For example, their findings show that regions such as the Brahmaputra Basin, where the BWM seems to have the most potential, can be prioritized for groundwater use intensification. Conversely, restrictions for groundwater use can be tightened in the Ganges Basin and in Northwest Bangladesh, where the potential of the BWM has already reached its limit. This means that the BWM mechanism in those regions is already working at its maximum possible capability, with no room for additional recharge if the water tables are lowered further. In addition, regular upkeep of water bodies—including local streams, ponds, and canals—is needed to ensure that the BWM continues to function well. Using spatially explicit findings from Shamsudduha *et al.* to calibrate current groundwater use restrictions will ensure that the BWM continues to provide benefits.

The amount of energy needed to operate the water pumps must also be considered. Currently, roughly 1.3 million out of the 1.5 million water pumps in use are diesel operated, with the rest running on electricity generated from fossil fuels. In 2017 to 2018, the Bangladesh Petroleum Corporation sold 1.1 million metric tons of diesel to the agriculture sector, which ultimately accounted for 3.5 million metric tons of carbon dioxide

(CO<sub>2</sub>) being emitted, or 4.3% of the country's entire production-based CO<sub>2</sub> emissions (9). As a net importer of fossil fuel, it is in the interest of Bangladesh's energy security to develop a self-sufficient pathway to power the BWM. Replacing fossil fuel-reliant water pumps with solar-powered irrigation pumps is one such solution. The Bangladeshi government has started promoting solar-powered pumps, but advocates have demanded a faster pace in policy changes and public financing (10).

The long-term effect of climate change on the BWM is unclear. There is a lack of specificity for models of the impact of future climate change on how aquifers recharge under different conditions. There is some consensus about enhanced recharge in dry tropics because of increased precipitation (11, 12). However, future projections of recharge under climate change are lacking for humid and sub-humid tropics such as Bangladesh.

Induced recharge—such as that observed in the BWM—may also work in other aquifers with similar rainfall and geological conditions. Intensive groundwater use for irrigation in the dry season has created conditions for additional water storage in underground aquifers in parts of the Bengal Basin, with the double benefits of improving food security and flood mitigation. Similar high rainfall and alluvial aquifers also exist in the Ganga basins in eastern India and Nepal, where intensive groundwater irrigation can bring livelihood improvements, with positive cobenefits of additional induced recharge. Long-term groundwater monitoring along with policy support to farmers to make intensive use of groundwater will remain essential to unleash the benefits of BWM. ■

#### REFERENCES AND NOTES

1. R. Revelle, V. Lakshminarayana, *Science* **188**, 611 (1975).
2. M. Shamsudduha *et al.*, *Science* **377**, 1315 (2022).
3. A. U. Ahmed, R. K. Sampath, *Am. J. Agric. Econ.* **74**, 144 (1992).
4. A. R. Bell *et al.*, *Land Use Policy* **48**, 1 (2015).
5. M. Hossain, "The impact of shallow tubewells and boro rice on food security of Bangladesh," discussion paper 00917 (International Food Policy Research Institute, 2009); <https://bit.ly/3Q9g9A5>.
6. R. Salim, A. Hossain, *Appl. Econ.* **38**, 2567 (2006).
7. A. Mukherji *et al.*, "Role of groundwater in agrarian change in West Bengal and Bangladesh: A comparative analysis—Final report" (Australian Centre for International Agrarian Research, 2021); <https://bit.ly/3wJL4fv>.
8. M. S. Islam, *Austral. J. Asian Law* **21**, 47 (2021).
9. H. Ritchie *et al.*, "CO<sub>2</sub> and greenhouse gas emissions" (Our World in Data, 2020); <https://bit.ly/3RoUP15>.
10. A. Mitra *et al.*, "Solar irrigation in Bangladesh: A situation analysis report" (International Water Management Institute, 2021); <https://doi.org/10.5337/2021.216>.
11. A. Asoka *et al.*, *Geophys. Res. Lett.* **45**, 5536 (2018).
12. R. G. Taylor *et al.*, *Nat. Clim. Chang.* **3**, 374 (2012).

#### ACKNOWLEDGMENTS

The author acknowledges the Swiss Agency for Development and Cooperation for their support of the project Solar Irrigation for Agricultural Resilience organized by the International Water Management Institute. Also acknowledged are support received from Transforming Agri-Food Systems in South Asia, and Mitigate+: Research for Low-Emission Food Systems.

#### CANCER

# Replication timing and genetic instability

## Synchronized activation of DNA replication origins induces genetic instability in lymphoma

By Marcel Méchali

Chromosomal translocations are promoted by DNA double-strand breaks (DSBs) that are joined inappropriately.

They are common in cancer cells, and some are characteristic of specific tumor types. The proto-oncogene *MYC* (on chromosome 8) often undergoes chromosomal translocation into the immunoglobulin heavy chain (*IGH*) locus on chromosome 14, which initiates B cell and plasma cell neoplasms in humans, including Burkitt lymphoma (1). This translocation places *MYC* under the control of the powerful *IGH* enhancer, resulting in strong *MYC* overexpression in lymphoid cells. It has been suggested that the spatial proximity of *MYC* and *IGH* in the nucleus, determined by chromatin folding, promotes this common translocation (2). On page 1277 of this issue, Peycheva *et al.* (3) report that replication timing mediates the *IGH-MYC* translocation. Furthermore, they infer that shared replication timing arises from the physical proximity of the two loci, resulting in a shared replication hub, where the *MYC* and *IGH* replication origins are synchronously activated.

The *IGH-MYC* translocation requires two DSBs. The first one occurs at the *IGH* locus owing to the regular action of the activation-induced cytidine deaminase (AID), which causes DNA mutations that produce antibody diversity through class-switch recombination. The other DSB, which occurs close to *MYC*, results from off-target activity of AID. Efficient class-switch recombination in the *IGH* locus depends on S phase entry and requires the helicase function of the minichromosome maintenance (MCM)

complex (4), which is involved in the opening of double-stranded DNA at replication origins (points throughout the genome where replication of distinct “replication timing domains” starts). Peycheva *et al.* investigated whether the timing of DNA replication origin activation is involved in *MYC-IGH* translocation during antibody maturation in human primary splenic B cells that are activated upon AID overexpression. They confirmed that MCM depletion decreases replication origin activity at translocation hotspots and show specifically that *MYC-IGH* translocation and replication origin activity decrease at both loci. In addition, the deletion of only the *MYC* replication origin impaired the *MYC*-replication timing domain and *MYC-IGH* translocation downstream of the DSB without affecting *MYC* expression and class-switch recombination. This revealed the crucial participation of the timing of replication origin activation in the translocation process.

The *IGH* locus constitutes a topologically associating domain (TAD), where DNA sequences interact with each other (5). The authors previously proposed that the *IGH* TAD contained a cluster of synchronously firing replication origins, leading to locus compaction by chromosome looping that allowed recombination (4). To explain their new results, Peycheva *et al.* extend this idea and propose that the *IGH* locus interacts with the *MYC* locus, forming a hub through liquid-liquid phase separation. These membraneless organelles increase the density and activity of components involved in the same function. The authors observed that the proximity of the *MYC* and *IGH* territories was strongly reduced in cells lacking MCM6 or the *MYC* replication origin but was restored when a new *MYC* origin was inserted. They propose that a hub assembles among AID target genes located in close chromosome territories. This hub would favor the synchronization of *MYC* and *IGH* replication origin firing and consequently the synchronization of the recombination events needed for translocation.

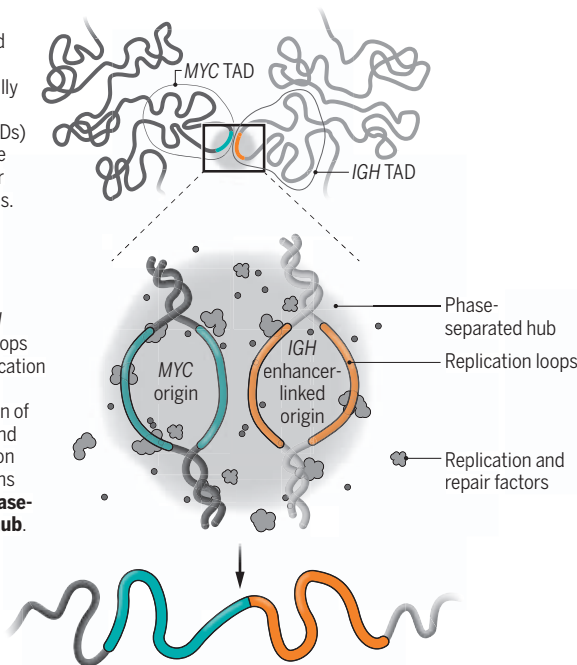
What could be the underlying mechanism? The hub concept extends the idea of replication foci (sites of DNA synthesis in the nucleus), replicon clusters (groups of replication origins that are synchronously activated), chromatin loops, and TADs.

## Translocations at replication hubs

The immunoglobulin heavy chain (*IGH*) enhancer on chromosome 14 and the *MYC* locus on chromosome 8 form translocations that are associated with lymphoma. These loci also contain DNA replication origins, and the *IGH* locus undergoes recombination in B cells during antibody maturation. These processes and the proximity of the two loci increase the opportunity for translocation.

The *MYC* and *IGH* loci are in topologically associating domains (TADs) that are close to each other in the nucleus.

*MYC* and *IGH* chromatin loops contain replication origins. The concentration of replication and recombination repair proteins creates a **phase-separated hub**.



Replication and recombination create opportunities for DNA double-strand breaks to arise in *MYC* and *IGH*, which can be joined to form **oncogenic *IGH-MYC* translocation**.

The overlap between TADs and replication timing domains (6), as well as the notable enrichment of replication origins at TAD borders (7), possibly reflects the role of DNA replication origins in forming chromatin loops. Replication foci are observed in all eukaryotic cells where components involved in DNA replication are concentrated. However, the hub proposed by Peycheva *et al.* would form between two loci located on different chromosomes (e.g., the *IGH* and *MYC* loci). Their short distance apart in the nucleus would permit this hub and the replication origins to synchronously fire at both loci. The concentration in this hub of DNA repair proteins involved in recombination at the *IGH* locus and replication initiation proteins would allow synchronous DNA DSBs and thus translocations. The branched structures formed by DNA unwinding at replication origins may also favor this model. The finding that replication initiation proteins can phase separate (8) may further substantiate this model. Moreover, it extends the idea that replication clusters from different chromosomes may interact together in a common hub (trans-hub) (see the figure).

It is not known what genetic or epigenetic elements may favor such hubs. However, some clues might come from the genetic

nature of the AID targets and DNA replication origins. It has been shown that structured substrates, such as G quadruplexes (G4) and branched DNA, are preferred AID targets in vitro (9). This observation may explain AID targeting mammalian immunoglobulin (Ig) switch regions that harbor a high density of G-repeat sequences and AID off-target activity on genes that often contain G repeats. Notably, DNA replication origin activation naturally generates branched DNA and G-repeated elements, which are preferred motifs at DNA replication origins (10–12). The *MYC* replication origin is an example of such replication origins because it contains an extended G-rich region upstream of its promoter, potentially forming G4 (13). Such G repeats link AID target sequences, Ig switch regions, and replication origins and may at least partly explain the formation of the proposed hubs. Several proteins involved in DNA replication origin recognition also recognize G4 and may participate in the hub complex

that links DNA replication origin activation and the formation of translocations. RIF1, a master regulator of the timing of DNA replication (14), also binds long stretches of G repeats and G4 structures. Therefore, it might be interesting to investigate whether such G repeats are essential to the clustering of replication origins and formation of the corresponding hubs that regulate synchronized replication origin activation. Additionally, such interchromosomal interactions that generate a hub involved in two different functions (such as activation of DNA replication origins and DNA repair functions) may favor illegitimate recombination that induces genetic instability, which may lead to tumorigenesis. ■

## REFERENCES AND NOTES

1. A. Bisso *et al.*, *Immunol. Rev.* **288**, 178 (2019).
2. J. J. Roix *et al.*, *Nat. Genet.* **34**, 287 (2003).
3. M. Peycheva *et al.*, *Science* **377**, eabj5502 (2022).
4. E.-M. Wiedemann *et al.*, *Cell Rep.* **17**, 2927 (2016).
5. L. Montefiori *et al.*, *Cell Rep.* **14**, 896 (2016).
6. B. D. Pope *et al.*, *Nature* **515**, 402 (2014).
7. I. Akerman *et al.*, *Nat. Commun.* **11**, 4826 (2020).
8. M. W. Parker *et al.*, *eLife* **8**, e48562 (2019).
9. Q. Qiao *et al.*, *Mol. Cell* **67**, 361 (2017).
10. C. Cayrou *et al.*, *Genome Res.* **21**, 1438 (2011).
11. C. Cayrou *et al.*, *Cell Cycle* **11**, 658 (2012).
12. E. Besnard *et al.*, *Nat. Struct. Mol. Biol.* **19**, 837 (2012).
13. S. E. Waltz *et al.*, *Nucleic Acids Res.* **24**, 1887 (1996).
14. S. Alaviet *et al.*, *J. Biochem.* **169**, 1 (2021).



# Monkeypox: The consequences of neglecting a disease, anywhere

A disease anywhere can spread everywhere, if neglected

By **Oyewale Tomori<sup>1</sup>** and **Dimie Ogoina<sup>2</sup>**

**M**onkeypox (MPX) is a zoonotic disease caused by the monkeypox virus (MPV), which is a double-stranded DNA virus belonging to the genus Orthopoxvirus, which includes variola virus, the cause of smallpox (1). The first human case of MPX was reported in a 9-month-old boy in the Democratic Republic of Congo (DRC) in 1970 (2), and MPX cases remained infrequent, until recently. Currently, MPX is endemic in the rainforest areas of West and Central Africa, where human MPX outbreaks often occur, especially in rural settings, owing to spillover events from animal reservoirs and occasionally from human-to-human transmission within households (3). On 6 May 2022, a new phase of MPX began when the first case of the disease, not associated with travel from Africa, was reported in the UK (4). There is now substantial human-to-human spread of MPX in nonendemic countries. What is the history of MPX and can this help inform control measures now?

Laboratory monkeys imported in 1958 from Singapore to Denmark contracted the disease now known as MPX, after exposure to other laboratory animals already housed in the Copenhagen facility (5). The source of infection of the monkeys remains a mystery. The poxvirus family is ubiquitously distributed, parasitizing a host of invertebrates and vertebrates (1). MPV is now endemic in sub-Saharan Africa, in unconfirmed animal reservoirs (6), which are likely to be rodents. With the successful eradication of smallpox, and the cessation of smallpox vaccination in 1980, over 70% of the global population is unprotected against smallpox, and through cross-immunity, to the closely related orthopoxviruses, such as MPV (6). The little-known MPX disease has since begun a slow replacement of smallpox among largely unvaccinated populations (6).

There are two distinct genetic clades of MPV (1): the Congo Basin clade (now renamed as Clade I) and the West African clade (now renamed as Clade II) (7). Additionally, Clade II consists of two subclades, IIa and IIb, with the latter primarily being the group of variants circulating in the 2022 global outbreak (7). Clade II MPV causes less severe disease in West Africa, with a less than 1% case fatality rate (CFR), whereas the Clade I MPV causes more severe disease in Central Africa, with up to a 10% CFR (1). Since the first human case was reported in 1970 in DRC, suspected or confirmed human MPX cases have been reported in other African countries (8), including Liberia and Sierra Leone (1970–1971), Cote d'Ivoire (1971), Nigeria (1971), Gabon (1987), Cameroon (1989), Central African Republic (2001), and Republic of the Congo (2003).

Outside of Africa, the US was the first country to report human MPX cases in 2003 when individuals were infected by pet prairie dogs that had contact with infected rodents imported from Ghana (6). Importations of MPV into other countries by travelers from endemic regions have also occurred between 2018 and 2022, but these did not lead to large outbreaks (6). Of the seven cases of MPX in the UK between 2018 and 2021, four were imported, two were household contacts, and one was a health care worker involved in the treatment of an imported case. There was no documented community transmission in these outbreaks (9). Importations into Israel and Singapore in 2018 and 2019, respectively, were similarly self-limiting (6).

Since 6 May 2022, human MPX has been rapidly spreading in nonendemic countries, including in Europe, the Americas, Asia, and Australia. Three African countries (Benin, Ghana, and South Africa) are also reporting cases for the first time (4, 10). MPX-associated deaths, previously limited to outbreaks in endemic countries, have now been reported since 29 July 2022 in nonendemic countries (4). Notably, all recent cases outside of the known endemic zones are due to Clade II MPV (4). This Clade II strain of MPV has diverged by 50 single-nucleotide polymorphisms (SNPs)

from the MPV that caused an outbreak in Nigeria in 2018–2019; these changes rendered the virus more transmissible (11).

Has MPX been spreading undetected, and is now established outside the known endemic zones? If so, is there a link between the 2018–2019 importations (6), from endemic countries into Europe? Detailed epidemiological studies are required in endemic countries and the emerging zones of the disease to better understand and control MPX. For example, despite more than 50 years since the first human case of MPX was reported, the animal reservoirs of the virus, mistakenly linked to monkeys, are still unknown. However, studies suggest that Gambian pouched rats, which are hunted for food, may play an important role in the transmission of the virus to humans (12). Identifying other reservoirs of MPV in different ecosystems will contribute substantially to prevention and control efforts.

Evidence suggests various aspects of the epidemiology of human MPX on the African continent have changed in the past 30 years (6, 8). Despite the poor quality of disease surveillance in the two hotspots of MPX in Africa, the number and magnitude of MPX outbreaks have been increasing in DRC and Nigeria (8, 13) (see the figure). After the initial report of two cases in 1971, and a single case in 1978, Nigeria did not report any MPX until 2017 with 88 confirmed cases (13). Since the first report of MPX in 1970, the DRC has continued to report thousands of suspected MPX cases annually from the 1980s (8, 10).

Outbreaks of MPX in DRC caused by Clade I MPV have been increasing in frequency and magnitude, with a surge in 2020, when 6257 suspected cases and 229 deaths were reported (8, 10). In 2021, 9155 suspected cases and 310 deaths were reported (10). For the first 6 months of 2022, DRC reported 1439 suspected cases with 67 deaths in endemic and new provinces (10). However, with only ~10% of suspected cases being laboratory confirmed, it is difficult to estimate the full burden of the disease. In Nigeria, where Clade II MPV circulates, an analogous situation has been reported since the resurgence of cases in 2017. Between 2017 and the end of 2021, Nigeria reported 766 suspected cases, and confirmed 288 with 9 deaths (13). Of the 357 suspected cases reported from January to 24 July 2022 in Nigeria, 133 were laboratory confirmed with three deaths (13).

There have also been recent changes in the demographics, ecological risk factors, and clinical presentation of the disease. In Nigeria and the DRC, the average age of those most affected has evolved from less than 10 years between 1970 and 2010

<sup>1</sup>African Centre of Excellence for Genomics of Infectious Diseases (ACEGID), Redeemer's University, Ede, Osun State, Nigeria. <sup>2</sup>Niger Delta University/Niger Delta University Teaching Hospital, Yenagoa, Bayelsa State, Nigeria. Email: oyewaletomori@gmail.com; oyewaletomori@run.edu.ng

to above 15 years after 2010 (6, 14). Most confirmed cases during the 2017 Nigeria outbreak lived in urban or peri-urban settings, and only ~8% of the 122 confirmed or probable cases reported contact with animals (14). There has been an expansion of human MPX beyond rainforest areas in Nigeria, with confirmed cases reported in the northern dry savannah areas (14). Although most patients infected in the 2017 Nigeria outbreak had typical features of MPX, such as fever accompanied by a skin rash, there were also various atypical clinical presentations with 12% of cases having skin rash without fever, and in two cases, genital ulcer was the first symptom (14). A few HIV-1-coinfected cases had large nodular ulcerating skin lesions (up to 10 cm in diameter) and more severe systemic illness and complications, which resulted in deaths of three people who had substantial immunosuppression (14). The detection of cases among a few married sexual partners, and the high rates of

genital ulcers, suggest a role of sexual contact in the transmission of MPX during the 2017 outbreak in Nigeria (14).

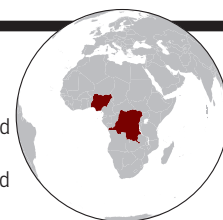
The simultaneous multicountry emergence of MPX cases in various locations outside endemic regions early in May 2022 took the world by surprise. As more cases were reported outside Africa, “global” attention ensured that action plans were rapidly put in place (primarily the release of smallpox vaccines from the global stockpile) to control the outbreak, protect cases and their contacts, and stop MPV from becoming endemic in Europe and other nonendemic countries. However, no such emergency plan has been put in place for the MPX endemic zones, where the first human MPX case was reported in DRC in 1970. Between January and July 2022, African countries have reported 2031 MPX cases and 75 deaths (CFR 3.7%). The number of MPX cases in the nonendemic countries as of 7 August 2022 is 27,439 cases, with four deaths (CFR 0.01%) (10).

This selective attention, despite the long years of inaction and absence of response to the continuous transmission of MPV in Africa over the past 30 years, highlights the glaring inequity in global health, which is also demonstrated by the inequitable availability of, and access to, COVID-19 vaccines. As MPX ravaged different communities in Africa, the world was silent. Calls for investments in field investigations during and after outbreaks, and research to generate data for a better understanding of MPX epidemiology, went unheeded, both at the national and international levels.

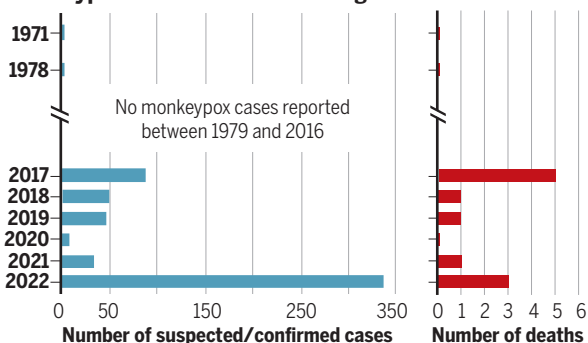
What should be done to control MPX in endemic countries and prevent it from becoming endemic in other parts of the world (if it is not already)? There is an urgent need for a collaborative effort to develop a sustainable and equitable global plan. This plan should address the identification of the natural animal hosts and reservoirs of MPV to improve understanding of the

## The changing patterns of monkeypox infections

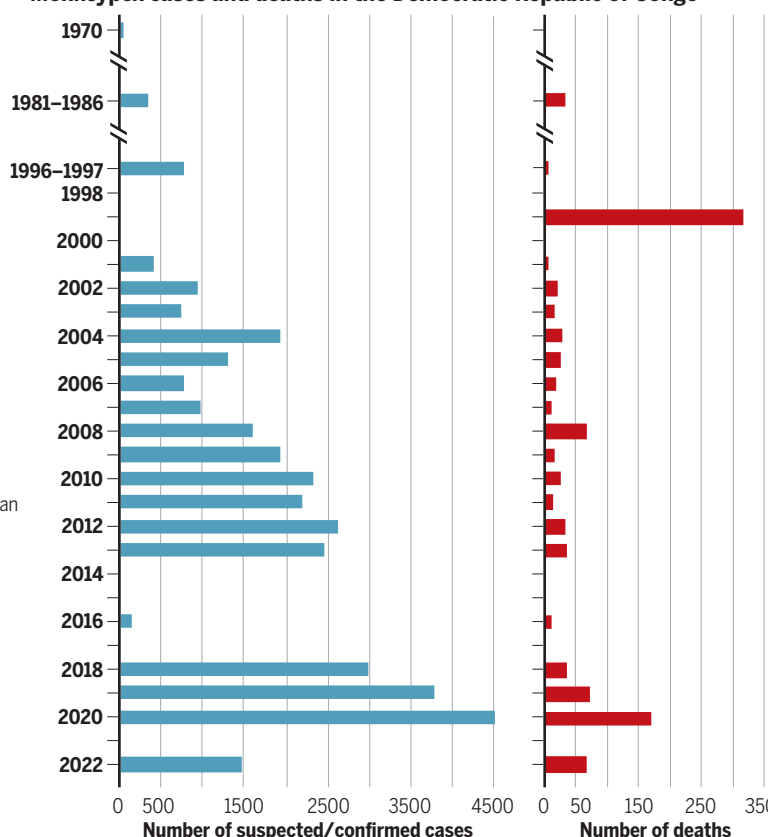
Although human monkeypox was first reported in the 1970s in Nigeria and the Democratic Republic of Congo, there were very few cases until outbreaks began in these endemic regions from around 1980. Recently, there have been larger monkeypox outbreaks—affecting more people and causing more deaths—as well as changes in the demographics of cases and clinical presentation in endemic regions. These changes preceded the emergence of monkeypox outside of endemic countries in May 2022, and within 2 months, the World Health Organization (WHO) declared monkeypox a Public Health Emergency of International Concern. Graphs are based on data to 24 July 2022 from (4, 8, 10, 13, 15).



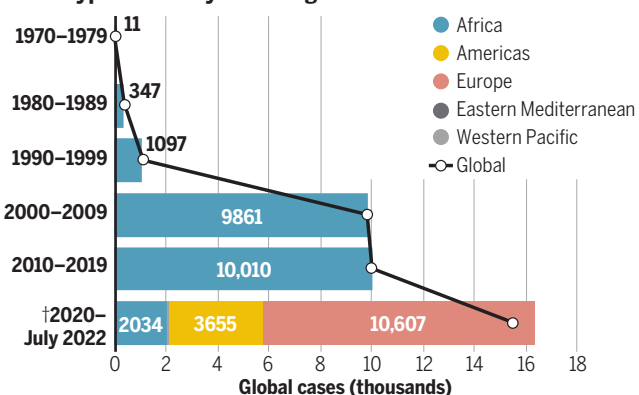
Monkeypox cases and deaths in Nigeria



Monkeypox cases and deaths in the Democratic Republic of Congo



Monkeypox cases by WHO Region: 1970–2022\*



\*Small outbreaks in nonendemic regions that were imported from Africa are not shown. †Cases for Eastern Mediterranean and Western Pacific in 2022 are 15 and 48, respectively.

transmission and epidemiology of the disease. It should also apply the One Health approach in designing field research and laboratory support that will build the requisite capacity, especially of scientists, in MPX endemic countries. The plan should include drug development and improved vaccines that are readily available and affordable, for the care of the infected and protection of the exposed. Public awareness should also be a focus of the plan, ensuring targeted education and risk communication that clarifies individual roles in preventing infection and spreading the disease.

The current global spread of MPX reminds us once again that infectious diseases know no borders and responses should protect everyone, leaving no country behind. This also requires an equitable contribution from each country and taking ownership of finding solutions to the ravages of such diseases at the national level. By applying resources responsibly, countries where these diseases are endemic can gradually move away from depending on the crumbs of equity for their disease control and response activities and contribute appropriately and effectively to national and global action that is needed to mitigate the effects of emerging infectious diseases. ■

#### REFERENCES AND NOTES

1. J. W. Barrett, G. McFadden, *Origin and Evolution of Poxviruses* (Academic Press, ed. 2, 2008), pp. 431–436.
2. I. D. Ladnyj, P. Ziegler, E. Kima, *Bull. World Health Organ.* **46**, 593 (1972).
3. P.-Y. Nguyen *et al.*, *Emerg. Infect. Dis.* **27**, 1007 (2021).
4. WHO (2022), <https://www.who.int/publications/m/item/multi-country-outbreak-of-monkeypox-external-situation-report--3--10-august-2022>.
5. P. von Magnus *et al.*, *Acta Pathol. Microbiol. Scand.* [A] **46**, 156 (1959).
6. K. Simpson *et al.*, *Vaccine* **38**, 5077 (2020).
7. WHO (2022), <https://www.who.int/news/item/12-08-2022-monkeypox-experts-give-virus-variants-new-names>.
8. E. M. Beer, V. B. Rao, *PLOS Negl. Trop. Dis.* **13**, e0007791 (2019).
9. UK Health Security Agency (2022), <https://www.gov.uk/government/publications/monkeypox-outbreak-epidemiological-overview/monkeypox-outbreak-epidemiological-overview-2-august-2022>.
10. World Health Organization, Africa Region (2022), <https://apps.who.int/iris/bitstream/handle/10665/361525/OEW32-0107082022.pdf>.
11. J. Isidro *et al.*, *Nat. Med.* **28**, 1569 (2022).
12. E. A. Falendysz *et al.*, *PLOS Negl. Trop. Dis.* **9**, e0004130 (2015).
13. Nigeria Centre for Disease Control, An Update of Monkeypox Outbreak in Nigeria July 24th, 2022 (2022).
14. D. Ogoina *et al.*, *Clin. Infect. Dis.* **71**, e210 (2020).
15. C. D. C. Africa (2022), <https://africacdc.org/news-item/multi-country-monkeypox-outbreak-declared-a-global-public-health-emergency-of-international-concern-2/>.



Maternal transmission of gut bacteria has promoted the maintenance of microbial strains that evolve with specific human populations.

#### MICROBIOLOGY

## Loyal gut microbes

Bacterial strains in the gut microbiota diversified as humans spread across the globe

By Andrew H. Moeller

The human gut harbors hundreds of species of bacteria. The most prominent species are found in people worldwide but display substantial genetic differences between human populations (1, 2). Piecing together how this strain-level diversity evolved has been a critical gap in understanding symbiosis between humans and gut bacteria. Because robust archeological and fossil records of human microbiota are lacking, lineage histories must be inferred primarily from genomic data, which have been difficult to produce in sufficient quality and quantity. On page 1328 of this issue, Suzuki *et al.* (3) report that strains within dozens of gut bacterial species diversified in parallel (codiversified) with human populations as they spread throughout Africa, Europe, and Asia, showing that these symbionts have kept fidelity to human lineages for thousands of human generations. In addition to revealing the evolution of the human microbiota, this discovery has implications for the generalizability of microbiota-based therapeutics.

When lineages engage in intimate symbioses over evolutionary time, they can codiversify, generating parallelism between the lineages' evolutionary trees. Earlier work found that codiversification between gut bacteria and humans has occurred in at least a few species. For example, the relationships

among strains within *Bifidobacterium* spp. (4) and *Helicobacter pylori* (5) have been shown to align with the dispersal of humans from Africa to other continents. However, the extent of codiversification in the gut microbiota has remained contentious (6, 7). Diet, hygiene practices, and other environmental factors are known to markedly affect the composition of the microbiota, so long-term relationships between bacteria and humans that are needed for codiversification may be rare. Generating the strain-level information required to test for codiversification has been laborious and expensive, so scaling-up such studies has not been readily achievable.

With high-throughput data and recently developed computational tools, it is now possible to assemble hundreds of bacterial genome sequences directly from the complex mixture of DNA (metagenome) present in a single sample of human stool. This new paradigm—termed “genome-resolved metagenomics”—affords new opportunities to study bacterial evolution within and between host individuals, populations, and species (8). To test for codiversification between gut bacteria and human populations, Suzuki *et al.* sequenced and assembled thousands of bacterial genomes from hundreds of women and their children living in Gabon, Cameroon, Vietnam, Germany, and the United Kingdom. Using these data, the authors compare the evolutionary trees of strains within gut bacterial species with the evolutionary tree of the humans inferred from genetic analyses of saliva samples. The results are notable: 36 of the 59 bacterial species tested displayed sig-

Department of Ecology and Evolutionary Biology, Cornell University, Ithaca, NY, USA. Email: andrew.moeller@cornell.edu

10.1126/science.add3668

nificant evidence of codiversification. Nearly all of these species, such as *Eubacterium* and *Roseburia* spp., were not previously known to have codiversified with humans. That associations between bacterial and host evolutionary trees were found for ~50% of gut bacterial species suggests that codiversification of gut microbiota with humans is the norm rather than the exception.

The widespread codiversification between gut bacteria and human populations raises questions about what mechanisms enable the fidelity of symbionts to host lineages. Codiversification is consistent with familial transmission (such as mother to child) of bacteria, but it could also occur in the absence of familial transmission if bacteria are transmitted within, but not between, host populations or social groups. There is evidence for both familial and social transmission of human microbiota (9, 10), but no studies had parsed the transmission routes that promote codiversification. Suzuki *et al.* found that many of the codiversifying strains were shared by mothers and their children more often than expected by chance. In addition, some bacterial species, such as *Prevotella copri*, displayed significant patterns of codiversification with humans within individual countries, implying specificity of these bacteria to not just human populations but also human genealogies. These findings imply that maternal transmission has promoted the maintenance of codiversifying strains within host genealogies. Thus, maternal transmission may enable some constancy over human generations to the lineages that make up the microbiota, despite profound and ongoing changes to human lifestyles and environments. It will be important for future work to assess how the prevalence of these bacteria within infants is affected by specific childbirth and maternal care practices.

Codiversification of bacteria with animal hosts has important consequences for bacterial evolution. For example, studies of insect-associated bacterial symbionts have shown that the joint evolutionary forces of mutation and random sampling (genetic drift) have eroded the genomes of symbionts (11, 12). In most bacteria, mutation is biased toward deleting DNA rather than adding it, and transmission bottlenecks between host generations cause symbionts to experience strong genetic drift more often than is typical for their free-living relatives. Over millions of years, the genomes of bacterial symbionts of diverse insects have been whittled down to core sets of essential functions. In turn, the consequent loss of biochemical repertoires needed for these symbionts to be free-living has led to the complete dependence of symbionts on their

hosts. Suzuki *et al.* find that the genomes of codiversifying bacteria of humans were consistently smaller than those of noncodiversifying relatives. This result supports the view that codiversifying bacteria within the human gut may have begun to exhibit early signs of the genomic degradation that has been repeatedly found in other animal-bacteria symbioses.

The findings of Suzuki *et al.* also suggest the exciting possibility that the close-knit associations with codiversifying gut bacteria have affected human evolution. Codiversifying host-microbe symbioses can generate divergent selection pressures on hosts, driving adaptation of host populations to the specific strains with which the hosts evolve. Even in the absence of divergent selection, certain host genetic variants whose frequencies differentiate populations may be neutral in terms of fitness in the presence of codiversified strains but harmful in their absence. If human genetic variation has been shaped by interactions with codiversifying gut bacteria, then microbiota-based therapeutics may need to consider the genealogical histories of both patients and the patients' gut bacterial strains. For example, fecal microbiota transplants (FMTs)—which have already had success in treating antibiotic-resistant *Clostridium difficile* infection—have attempted to improve outcomes by matching donors and patients according to factors such as host age, diet, and relatedness (13), but determining the specific matching criteria that maximize efficacy has been challenging (14). It will be worthwhile to explore whether efforts to restore microbiota for human health can be informed by the history of codiversification uncovered by Suzuki *et al.* Their results highlight that gut bacterial communities are not haphazard collections of bacteria but reflections of the distinct ancestries of human populations. ■

#### REFERENCES AND NOTES

1. A. Tett *et al.*, *Cell Host Microbe* **26**, 666 (2019).
2. N. Karcher *et al.*, *Genome Biol.* **21**, 138 (2020).
3. T. A. Suzuki *et al.*, *Science* **377**, 1328 (2022).
4. A. H. Moeller *et al.*, *Science* **353**, 380 (2016).
5. D. Falush *et al.*, *Proc. Natl. Acad. Sci. U.S.A.* **98**, 15056 (2001).
6. A. H. Nishida, H. Ochman, *Nat. Commun.* **12**, 5632 (2021).
7. M. Groussin *et al.*, *Cell Host Microbe* **28**, 12 (2020).
8. N. R. Garud, K. S. Pollard, *Trends Genet.* **36**, 53 (2020).
9. I. L. Brito *et al.*, *Nature* **4**, 964 (2019).
10. H. P. Browne *et al.*, *Curr. Opin. Microbiol.* **69**, 102173 (2022).
11. G. M. Bennett, N. A. Moran, *Proc. Natl. Acad. Sci. U.S.A.* **112**, 10169 (2015).
12. J. Perreau, N. A. Moran, *Nat. Rev. Genet.* **23**, 23 (2022).
13. C. Duvallet *et al.*, *PLOS ONE* **14**, e0222881 (2019).
14. S. W. Olesen *et al.*, *Nat. Rev. Gastroenterol. Hepatol.* **15**, 387 (2018).

#### ACKNOWLEDGMENTS

A.H.M. is funded by the National Institutes of Health (R35 GM138284).

#### SOLAR SYSTEM

# How Saturn got its tilt and its rings

The destruction of a hypothetical moon may help explain the origin of both

By Maryame El Moutamid

The angle between a planet's equator and its orbit plane is known as its axial tilt or obliquity. As gas giants form from the disk made of gas and dust that swirls around the host star, the gas accretion process is expected to conserve the angular momentum and force the planet to spin perpendicular to its orbital plane. However, within our own Solar System, all gas giants, except for Jupiter, have a substantial nonzero tilt. This implies that something else must have happened to these planets after they formed that caused them to tilt. On page 1285 of this issue, Wisdom *et al.* (1) describe a model that can explain the origin of Saturn's obliquity. Its tilt may have been caused by a process involving Saturn's wobbling tilt (i.e., spin-axis precession), Neptune's wobbling orbit (i.e., nodal precession), the elimination of a hypothetical satellite, and the outward migration of Titan—the largest moon of Saturn.

According to the model of Wisdom *et al.*, the rapid outward migration of Titan increased Saturn's obliquity through a process known as secular resonance. This occurs when one or more planetary bodies have one or more of their frequencies synchronized (as in "resonance"), which then leads to long-lasting perturbations for each of these frequencies (as in "secular"). In the case of Saturn's tilt, the two frequencies of each of the two bodies are Saturn's spin-axis precession and Neptune's orbital nodal precession. As Titan slowly migrated away from Saturn, the resonance between the two frequencies of Saturn and Neptune is expected to have shifted in a way that would have increased the tilt of Saturn. To verify if Saturn is currently in resonance with Neptune, it is necessary to

determine the rate of Saturn's spin-axis precession with high precision. This is challenging to obtain from direct observations, mainly because of the slow precession rate of Saturn's spin axis. The problem is made more difficult because of the complex influence coming from all the satellites of Saturn, which add noise to the observed precession rate (1–4).

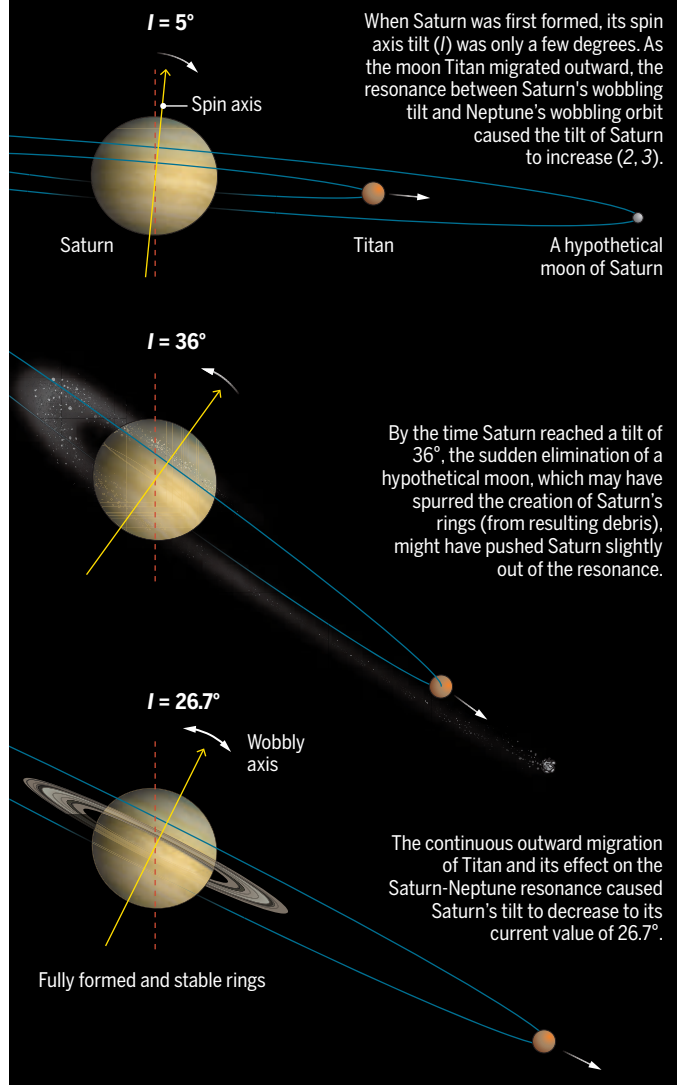
An alternative approach to direct observations is to model the spin-axis rate using a model of Saturn's interior. This method considers that the spin-axis precession of Saturn depends on its other physical parameters, such as its gravitational coefficients (which measure how a gravitational field deviates from spherical symmetry). Previous works have argued that the current knowledge about Saturn's interior is not precise enough to assess whether Saturn is currently in resonance (2, 3, 5–7).

By combining gravitational data from the Cassini mission and a refined model of Saturn's interior structure, Wisdom *et al.* deduced that Saturn is currently sitting just outside the range of what is needed for its resonance with Neptune. To solve this apparent contradiction with expectation, the authors suggest that the outward migration of Titan first caused Saturn's obliquity to increase up to 36°, before an unknown event pushed Saturn out of the resonance. Then, the still ongoing migration of Titan would make Saturn step over the resonance, decreasing its tilt this time and reducing it down to the current value of 26.7°. Titan may have subsequently shifted the resonance and decreased the tilt (see the figure). One possible candidate for the unknown event could have been the destruction or ejection of a moon from the Saturn system. The elimination of a hypothetical moon could have caused Saturn's spin axis-axis precession rate to suddenly decrease and for Saturn to have escaped its resonance with Neptune.

In proposing this model, Wisdom *et al.* touch on another hotly debated topic of Saturn—the age of its rings. Different sources have estimated their age to range from a few hundred million years old

## A lost moon, a young ring, and Saturn's tilt

Wisdom *et al.* propose a model that could explain how the current tilt of Saturn's spin axis may be linked to how the planet gained its rings from the destruction of a hypothetical moon 100 million to 200 million years ago.



(8–10) to 4.5 billion years old (11). It is difficult to reconcile the different estimates because of differences in methodology. The younger estimates are calculated using the observed microwave emission of non-icy materials from the rings and is based on the assumption that the rings' age is the same as their exposure time to micrometeoroids. By contrast, the old-age argument assumes that the rings are responsible for the formation of small and mid-sized moons, which requires the rings to be old and to have been more massive than they currently are. The old-age hypothesis also assumes the rings to have been much rockier than they are now. To explain why Saturn's rings are as icy, "old age" support-

ers have proposed processes that would remove the rocky materials from Saturn's rings but leave the ice behind (12). The debate between the young-age and old-age hypotheses is ongoing because of the lack of knowledge about the general evolution of the rings. Wisdom *et al.* insert themselves in the middle of this debate by providing a plausible mechanism for the evolutionary history of Saturn's rings—one that supports the young-age argument.

To put their claims about Saturn's tilt in more quantifiable terms, Wisdom *et al.* performed simulations that show the destruction of their hypothetical moon to be a low-probability event. They found that the mechanism for destabilizing the resonance is chaotic and can produce very different outcomes with small variations in the starting parameters. Out of their 390 simulated scenarios, only 17 produced results in which the satellite is disrupted close enough to Saturn to form the rings. This is compatible with the destruction of one of Saturn's moons being a one-time event.

Wisdom *et al.* provide a plausible mechanism for explaining Saturn's close proximity to the precession resonance with Neptune and the seemingly young age of its rings. To further corroborate these claims, future research will need to better define the polar moment of inertia of Saturn and the likelihood of similar events occurring for other planets with rings. ■

### REFERENCES AND NOTES

1. J. Wisdom *et al.*, *Science* **377**, 1285 (2022).
2. M. Saillenfest, G. Lari, G. Boué, A. Courtot, *Astron. Astrophys.* **647**, A92 (2021).
3. M. Saillenfest, G. Lari, G. Boué, *Nat. Astron.* **5**, 345 (2021).
4. R. G. French *et al.*, *Icarus* **290**, 14 (2017).
5. W. R. Ward, D. P. Hamilton, *Astron. J.* **128**, 2501 (2004).
6. G. Boué, J. Laskar, P. Kuchynka, *Astrophys. J.* **702**, L19 (2009).
7. D. Vokrouhlický, D. Nesvorný, *Astrophys. J.* **806**, 143 (2015).
8. Z. Zhang *et al.*, *Icarus* **281**, 297 (2017).
9. Z. Zhang *et al.*, *Icarus* **294**, 14 (2017).
10. L. Less *et al.*, *Science* **364**, eaat2965 (2019).
11. J. Salmon, S. Charnoz, A. Crida, A. Brahic, *Icarus* **209**, 771 (2010).
12. A. Crida, S. Charnoz, H.-W. Hsu, L. Dones, *Nat. Astron.* **3**, 967 (2019).

### ACKNOWLEDGMENTS

M.E.M. is funded by the NASA Cassini Data Analysis Program, grant 80NSSC19K0893.

10.1126/science.abq3184



Employees work on solar panels at a factory in Hai'an, Nantong, Jiangsu Province, China, on 18 April 2022.

## CLIMATE CHANGE

# Risks of decoupling from China on low-carbon technologies

For most technologies, the cure is likely worse than the disease

By Michael R. Davidson<sup>1,2</sup>, Valerie J. Karplus<sup>3</sup>, Joanna I. Lewis<sup>4</sup>, Jonas Nahm<sup>5</sup>, Alex Wang<sup>6</sup>

China plays, and will likely continue to play, an indispensable role in research, development, and demonstration (RD&D) and manufacturing of low-carbon technologies that are necessary to address climate change. For example, China's scale-up capabilities that are underpinned by manufacturing process improvements, supply chain optimization, and deep government support have contributed to substantial reductions in costs for mature technologies such as solar photovoltaics (PV) (1). However, the growing size of these economic sectors, coupled with

national security concerns over the strong dependence on China in certain critical industries, has prompted policy-makers from Washington to Brussels to ask whether to alter course. Recognizing that economic and national security risks differ across technologies and the nature of a country's integration with China, we highlight five primary risks to integration—separated into their economic and national security implications—and apply them to five leading low-carbon technologies: solar, wind, batteries, “green” steel, and carbon capture and sequestration (CCS).

Calls to decouple from China's economy would have considerable implications for the future of clean energy technology and the ability to meet climate goals. At present, China accounts for roughly three-quarters of global production capacity for lithium-ion batteries, two-thirds of production capacity for solar PV, and a sizable share of manufacturing capacity for wind turbines and their components. With most of the global clean energy deployment needed in the developing world, it is unclear how countries will meet deployment targets if they lack affordable and reliable sources of clean technology.

We focus on how US government policy affects technological development and deployment but draw lessons for other settings around the world as many nations rethink their reliance on other nations for energy security reasons, whether it be Russian gas or Chinese solar panels. Policy-makers in Europe and North America have justified decoupling with concerns about future national economic competitiveness, because domestic markets for key energy technologies (subsidized with taxpayer dollars) are now highly dependent on imports from a geostrategic competitor (2). Officials also consider the supply and trade of clean energy as a matter of national security (3). Concerns about alleged forced labor practices in China have further amplified calls for decoupling.

Given the realities of expected deepening political contests between the United States and China and the real risks of shocks to globalized supply chains, it is increasingly important to manage these risks while recognizing the benefits of integration. Across numerous technology areas, the level of integration is so great that true decoupling would be nearly impossible and potentially counterproductive to national interests. In the area of trade, coordination is essential to ensure that market mechanisms efficiently support climate goals (4).

## EVALUATING RISKS OF INTEGRATION

We focus on two broad categories of risk—economic and national security—that are germane to the integration discussion and can be assessed at the technology level. Within each, we focus on three salient, but not exhaustive, dimensions. We assess levels of risk in each category for a given technology with the two facets of risk in mind: the probability of an event as well as its impact. Our approach applies quantitative metrics where publicly available, such as the current dependence on China within supply chains (5). Because many of these risks are inherently hard to quantify, we provide in-depth case examples that combine quantitative and subjective assessments to determine component-level rankings of risk, which are aggregated to the technology level for comparison. Our approach integrates data and perspectives from industry, the financial sector, and government (see supplementary materials).

### Economic risks

**Domestic job losses.** Jobs associated with integrating production of low-carbon technologies occur primarily in three areas:

<sup>1</sup>School of Global Policy and Strategy, University of California, San Diego, La Jolla, CA, USA. <sup>2</sup>Department of Mechanical and Aerospace Engineering, University of California, San Diego, La Jolla, CA, USA. <sup>3</sup>Department of Engineering and Public Policy, Carnegie Mellon University, Pittsburgh, PA, USA. <sup>4</sup>Science, Technology and International Affairs Program, Edmund A. Walsh School of Foreign Service, Georgetown University, Washington, DC, USA. <sup>5</sup>School of Advanced International Studies, Johns Hopkins University, Washington, DC, USA. <sup>6</sup>School of Law, University of California, Los Angeles, Los Angeles, CA, USA. Email: mrdavidson@ucsd.edu

manufacturing, installation and project development, and operation and maintenance. Products that are modular, mass produced, and lightweight can more easily create manufacturing jobs far from the point of deployment, explaining the high degree of US reliance on China for low-carbon technologies such as solar PV. At the same time, mass production can lead to a high degree of automation, the largest predictor of aggregate manufacturing job losses. Compared with manufacturing jobs, installation and project development jobs, as well as operations and maintenance, are generally more localized. The job creation potential of onshoring green energy manufacturing can vary widely, with less potential where economies of scale exist. Greater potential for job gains exists when substantial work must be done on-site and customer acquisition is more time-intensive.

When technologies are developed outside of the United States, domestic projects

context of trade policy, with reports of up to \$600 billion in losses annually worldwide for US firms (8). Governments can also engage in violations of trade law such as “forced technology transfer” programs, for example, coercing joint venture partnerships in exchange for access to local markets. Although China is increasingly becoming a source of innovation, it still lags behind the United States and European Union in patent creation for key clean energy technologies (9). The true scale and scope of IPR violations is difficult to determine (10). Firms voluntarily locate in China and make IPR trade-offs, including strategic licensing, to access the large market. The ease with which Chinese firms can extract IPR from US firms, and at what cost, varies by technology. The form of IPR (e.g., patents, trade secrets) differs by technology and influences accessibility, as does the business model used (joint venture, local subsidiary, and so on).

interdependencies present systemic risks of a loss of operational control. Virtually every piece of modern energy equipment has a communication interface with some risk of attack—for example, if hidden technology “backdoors” are installed in equipment—though potential disruptions scale with the concentration of the particular assets. Taking a single solar installation offline would be far less disruptive than an attack on the infrastructure, such as the ransomware attack on Colonial Pipeline’s natural gas network in May 2021. A secondary concern, with questionable impacts on national security, is the control of data on users of the infrastructure, which motivated, for example, the blocking of Chinese electric vehicle maker BYD from selling electric buses to US municipalities in 2020.

**Dual use.** Technologies that have both military and commercial applications can be subject to export controls (on domestic firms), restrictions on investment (by foreign firms), and enhanced domestic sourcing requirements to reduce reliance on foreign suppliers. Export controls implicate a wide range of components for green technology, though the fraction of exports in these areas subject to license restrictions was less than 1% (14). Considering that some exports were not even attempted because of restrictions, this is an underestimate, but impacts likely remain small (10). The United States also places additional restrictions on technology exports to firms on the Chinese Military-Industrial Complex Companies List (or CMIC), which once contained China Three Gorges Corporation, a prominent hydropower, wind, and solar developer. Because of the challenges of identifying early-stage technologies that may eventually gain military applications as well as potential negative impacts on basic research, former US Secretary of Defense Robert Gates has advocated for a “small yard, high fence” strategy when screening technologies.

**Energy security.** Dependence on foreign sources of energy has long caused concerns about energy security, or the ability to satisfy consumer demands without rationing. Unlike dependence on imported fossil sources of energy, which require constant supply and are highly exposed to political conflict, increasing tensions with China would not affect energy availability of low-carbon technologies that have already been installed. Risks are limited to the future supply of low-carbon technologies, which are included in this analysis as supply chain disruptions. Therefore, energy security is not deemed to be at risk because of integration and is not included further in our assessments.

## Technology-specific risks of integration with China

National security risks are generally lower and more homogeneous than economic risks.

|                                  | ECONOMIC RISKS      |                                  |                          | NATIONAL SECURITY RISKS |          |
|----------------------------------|---------------------|----------------------------------|--------------------------|-------------------------|----------|
|                                  | DOMESTIC JOB LOSSES | INTELLECTUAL PROPERTY VIOLATIONS | SUPPLY CHAIN DISRUPTIONS | CRITICAL INFRASTRUCTURE | DUAL USE |
| Solar photovoltaics              | Medium              | Low                              | High                     | Low                     | Low      |
| Batteries                        | Low                 | Low                              | High                     | Low                     | Medium   |
| Wind turbine system              | Low                 | Medium                           | Low                      | Medium                  | Low      |
| Green steel                      | Low                 | Medium                           | Low                      | Low                     | Low      |
| Carbon capture and sequestration | Low                 | Medium                           | Low                      | Low                     | Low      |

may rely on overseas companies for operational expertise and technical standards, potentially limiting local job creation and creating lock-in effects that favor overseas innovators. Moreover, many low-carbon technologies have high capital costs and up-front jobs and lower recurring operations and maintenance jobs and requirements. Beyond quantity, job quality also matters: Average salaries in skill-adjacent low-carbon occupations tend to be lower compared with jobs in fossil energy (6); conversely, domestic development of other clean energy technologies, such as CCS or hydrogen production, may have the potential to generate permanent, high-paying domestic jobs (7). Decoupling is likely to affect the quantity and quality of jobs differently by sector, function, and worker skill level.

**Intellectual property violations.** The protection of intellectual property rights (IPR) is a commonly referenced concern in the

**Supply chain disruptions.** Vulnerability to disruptions in critical materials supply, whether by natural disaster or government intervention, is a key factor motivating reviews of supply chains (11). We define disruption as the inability of suppliers to deliver sufficient product to US consumers at reasonable cost. Rare earth elements are key inputs to several low-carbon technologies, and some reports indicate that China is studying the effects of restricting exports, reminiscent of an embargo placed on Japan after a territorial dispute in 2010 (12). Regional concentration of materials processing or production necessarily increases the risks of disruption. The impact hinges upon how quickly firms can resume operations after a disruption or make alternative sourcing arrangements (13).

### National security risks

**Critical infrastructure.** The electricity system is at the core of “critical infrastructures,” whose impacts on the economy and complex

## Benefits

Risks must be weighed against the benefits of integration with China. Economic benefits include economies of scale and rapidly declining costs for clean-energy technologies, for instance, because Chinese development banks have been willing to fund large-scale investments in manufacturing capacity that other financial systems have shunned. The greater availability and affordability of clean energy technologies made in China have also yielded energy security benefits, because they have allowed economies to switch to energy sources that are more insulated from the volatility of global oil and gas markets. Of course, not all technologies have yet benefitted to the same degree: Wind, solar, and batteries have displayed rapid improvement along the cost curve as a result of integration with China, whereas others, such as CCS and green steel, are less mature and not yet able to equally benefit from China's infrastructure for mass production.

In the process of commercializing and manufacturing new energy technologies, Chinese firms have also sourced materials, components, production equipment, and technology licenses through global supply chains, including from firms in the United States and Europe. Harder to estimate and likely more heterogeneous across technologies are the climate and health benefits from the greater deployment of these technologies. By increasing the availability and affordability of wind, solar, and battery technologies, integration has already led to local improvements in air quality and avoided greenhouse gas emissions.

## FIVE KEY TECHNOLOGIES

We observe heterogeneity across technologies in the economic risks of integrating with China (see the table and tables S1 to S6). For established technologies with far-flung supply chains (solar, wind, and batteries), US manufacturing is more specialized with a smaller labor force. Job losses in manufacturing are substantially outweighed by job gains in installation and development, though the quality of those jobs may depend on sector characteristics such as skills requirements and collective bargaining. IPR violations have occurred in some of these sectors (notably, wind), though the susceptibility and potential gain to Chinese

firms for IPR violations going forward are likely muted. The most salient economic risk is a supply chain disruption that affects cost and availability to US consumers due to the concentration of production activities in China across key components of the solar PV supply chain as well as materials-processing activities in upstream solar PV and battery minerals.

National security risks for all five technologies are more homogeneous and generally low, given their limited system-wide impacts on critical infrastructure. Wind turbine systems in the future may present

can selectively impose penalties or provide incentives to make it difficult to work with actors within specific countries while permitting integration with others. (iii) Open. Governments can promote free exchange of products and open commercial and scientific relationships.

We provide a framework for mapping assessed levels of risk of the five technologies to these three policy recourse strategies (see the figure). Higher economic risks indicate a need for more diversification as a means of coping with disruptions and other commercial risks. The highest economic risk may also require diversifying RD&D to develop less-mature alternative technology pathways. National security risks enhance the underlying economic drivers, leading to the need for diversification and possibly even domestic sourcing and RD&D.

Responses can lead to counterproductive outcomes if not carefully structured and if potential retaliation is not anticipated. For example, 2012 US import tariffs on Chinese solar cells and modules led Chinese authorities to levy duties against US-made polysilicon. This enabled Chinese companies to ramp up their own polysilicon capacity. At the time that the tariffs were imposed, US producers accounted for 24% of the global polysilicon market, whereas China produced very little. Today, US firms only account for 5% and China nearly 70%.

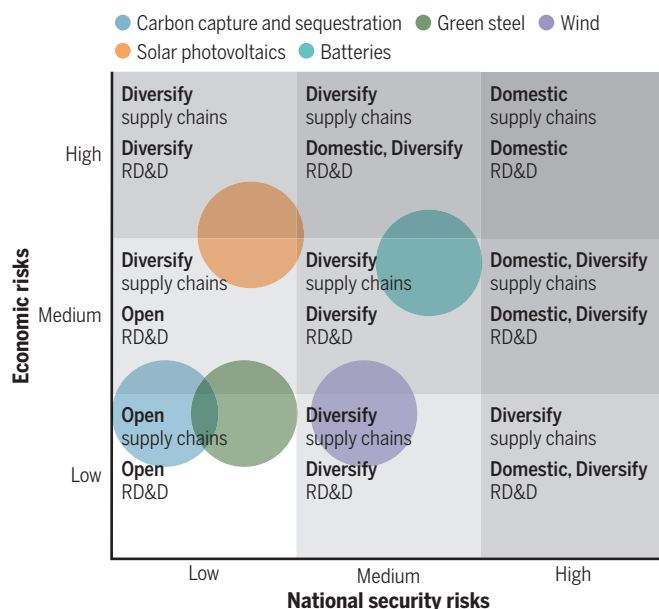
One instrument that can encourage sourcing from countries with climate-friendly production is a border carbon adjustment, which involves penalizing important products based on country of origin and assessed carbon intensity. Border carbon adjustments should align with domestic policies that similarly penalize domestic production according to carbon intensity.

## DISCUSSION

Decoupling of production means higher costs for end users but may lead to concentrated job gains, preservation of technological leadership, and decreased vulnerability to disruption. Too much decoupling will slow technology deployment and the global low-carbon transition; too little will leave major markets exposed to unpredictable geopolitical tensions over which they may have no control. For most technologies, the decoupling "cure" is likely to be worse than the integration "disease." Each technology will imply a different calculus

## Integration risks and policy recourse strategies

Policies regarding supply chains and research, development, and demonstration (RD&D) should reflect assessments of technology-specific risks.



medium-level risks due to the potential for attacks on increasingly sophisticated software that facilitates integration of wind energy onto the grid. Similarly, except for batteries that have some high-performance military applications, the risks to dual-use technology development appear minimal.

## RESPONSE AND RECOURSE

Countries have a range of policies to shape sourcing and research relationships. We identify a spectrum of three main options. (i) Domestic sourcing. Policies encourage or require government agencies, firms, and consumers to source from domestic suppliers or exclusively work with domestic entities (e.g., in RD&D). (ii) Diversification. This is an intentional approach to source and work with a larger variety of partners and/or incorporate a range of technology types; "selective diversification" policies



and a differentiated approach, based on a sound underlying logic.

Many of the strongest US firms combine domestic and international sourcing strategies. Whereas some US firms have failed to become competitive internationally, others have stronger positions because of their integration and reliance on global supply chains and, in particular, China-sourced components, such as in the wind sector. Employment in certain sectors—for example, manufacturing—may have been reduced relative to a world where the United States enforces strict supply chain localization but effects are far from unidirectional or uniform across domestic market participants. Although it may be sensible to bring some clean energy manufacturing jobs onshore to address security or resilience concerns, there may be little economic rationale to do so. More nuanced attention should be paid to both the short-run impacts of decoupling or integration on the quantity, quality, and geography of newly created installation and operation and maintenance jobs and to the long-run impacts on the ability of the United States to compete at the frontier of global clean energy innovation. To remain competitive, some US industries will need to embrace automation, thus reducing the prospective job benefits.

Some low-carbon technology component sourcing is heavily concentrated geographically, presenting both short-term and long-term risks for supply chain resilience. There are generic benefits of diversification but specific costs of decoupling, depending on the technology and time frame. The wind sector already shows high diversification, with multiple countries able to ramp up supply of most components in case of supply disruption. Conversely, the battery and solar sectors are heavily dependent on China either for finished cells or for processed materials. Long-term reorganizations of supply chains have implications for upstream jobs. If supply chain disruptions cause increases in costs and a reduced ability to deploy products, downstream jobs are also at risk.

National security risks appear to be manageable across most of the technologies studied. Instead of specific manufacturing processes, which for military applications are likely to be for higher-performance designs, the larger intersection between civilian and military clean energy technologies may be in shared upstream critical minerals, specifically in batteries. Securing diversified or domestic access to sufficient quantities of minerals, refining, and production capacity for use in a crisis could be a reasonable response to increasing integration with China. These more muted national se-

curity impacts should help focus the policy debate on the economic calculus.

For a given sector or technology, policy choices to decouple will lead to uneven distribution of risks and benefits across US producers and consumers, which will in turn influence the political feasibility of decoupling. We encourage national policymakers to consider the effects of decoupling in a given technology at the level of states, regions, companies, and consumers, with particular attention to how they affect public goods (e.g., the environment, national security) and distributed private benefits (e.g., jobs, wages), because concentrated beneficiaries are likely to organize and advocate for themselves. For example, local content subsidies in the recently passed Inflation Reduction Act and the Biden administration's decision to use the Defense Production Act to increase domestic clean energy manufacturing are steps toward decoupling that will privately benefit the companies, localities, and workers tapped to produce them. However, trade measures such as import tariffs with the same goals increase the cost of clean energy and slow deployment, imposing diffuse costs on installation and maintenance firms as well as consumers and generating more emissions.

The current clean energy landscape reflects substantial competition among suppliers and technological pathways, and the wider pool of resources to scale-up technologies has helped entrepreneurs bring innovations to market. The United States, China, and other countries should continue to encourage healthy competition and the free flow of goods, capital, and talent to accelerate cost and performance improvements. Protecting IPR is a salient tension and a key prerequisite for future technological developments.

In areas where risks are low and mutual benefits are likely to be high, there is a strong rationale for governments to facilitate supply chain and RD&D integration. In areas deemed lower risk and at earlier stages of development, active technological collaboration and demonstration projects could help accelerate important strides in, for example, green steel production and CCS. Scientific cooperation should be motivated by a clear calculus of the anticipated gains accruing to both sides weighed against how these endeavors may magnify or diffuse political conflicts (15). In cooperating, there are also benefits of diversification. The recent European Union–United States deal on green steel could provide a blueprint for using standards and border tariffs based on carbon content to create multilateral incentives for advanced technology research and deployment.

Our approach may be applicable to any national government that is eager to balance economic and security risks with the benefits of integration across clean energy activities. Firms or research organizations that face a decision to integrate with China through supply chains or collaborative research will have different sets of considerations that more heavily weight generating viable and innovative technologies with less competition and will have shorter-term metrics for success. Nevertheless, governments should consult broadly with business, labor, academia, and other stakeholders to produce policies whose incentives recognize the diverse circumstances and motivations of the actors involved and achieve their intended goals. ■

## REFERENCES AND NOTES

1. J. Nahm, *Collaborative Advantage: Forging Green Industries in the New Global Economy* (Oxford Univ. Press, 2021).
2. J. I. Lewis, *Glob. Environ. Polit.* **14**, 10 (2014).
3. The White House, "Interim national security strategic guidance," 3 March 2021.
4. R. Bowen *et al.*, "The role of trade in addressing climate change: Recommendations for policies and practices" (UC San Diego School of Global Policy and Strategy, 2021).
5. US Department of Energy (DOE), "America's strategy to secure the supply chain for a robust clean energy transition" (Technical Report 1871491, DOE, 2022).
6. G. J. Jolley, C. Khalaf, G. Michaud, A. M. Sandler, *Reg. Sci. Policy Pract.* **11**, 403 (2019).
7. R. H. Bezdek, *Renew. Energy Environ. Sustain.* **4**, 1 (2019).
8. Commission on the Theft of American Intellectual Property, "Update to the IP Commission report—The theft of American intellectual property: Reassessments of the challenge and United States policy" (The National Bureau of Asian Research, 2017).
9. International Energy Agency (IEA), "Patents and the energy transition: Global trends in clean energy technology innovation" (IEA, 2021); [https://iea.blob.core.windows.net/assets/d14427c6-2aa2-4422-9074-5a68940a5a96/Patents\\_and\\_the\\_energy\\_transition\\_-\\_keyfindings.pdf](https://iea.blob.core.windows.net/assets/d14427c6-2aa2-4422-9074-5a68940a5a96/Patents_and_the_energy_transition_-_keyfindings.pdf).
10. M. A. Cohen, P. C. Rogers, *World Trade Rev.* **20**, 238 (2021).
11. The White House, "Building resilient supply chains, revitalizing American manufacturing, and fostering broad-based growth," June 2021.
12. S. Yu, D. Sevastopulo, "China targets rare earth export curbs to hobble US defence industry," *Financial Times*, February 2021.
13. C. Freund, A. Mattoo, A. Mulabdic, M. Ruta, "Natural disasters and the reshaping of global value chains" (Policy Research Working Paper 9719, *The World Bank*, 2021).
14. J. Watts, K. Bagin, "Critical technology assessment: Impact of U.S. export controls on green technology items" (US Department of Commerce, 2010); <https://www.bis.doc.gov/index.php/documents/technology-evaluation/137-impact-of-u-s-export-controls-on-green-technology-items/file>.
15. V. J. Karplus, M. G. Morgan, D. G. Victor, *Issues Sci. Technol.* **38**, 76 (2021).

## ACKNOWLEDGMENTS

The authors would like to acknowledge members of the 21st Century China Center at the University of California, San Diego for comments on an earlier draft.

## SUPPLEMENTARY MATERIALS

[science.org/doi/10.1126/science.abq5446](https://science.org/doi/10.1126/science.abq5446)

10.1126/science.abq5446

## PHYSICS

# Whom is real science for?

Skip the metaphors—physics needn't be diluted for nonexperts to achieve real understanding

By **Adilson E. Motter**

When one says “follow the science” to a layperson, it often reads as “have faith in science.” This is because popular-level descriptions of research findings tend to abandon the language of science in favor of metaphors and analogies, which inadvertently limits the reader's connection with the corroborating body of knowledge. In *The Biggest Ideas in the Universe*, Sean Carroll shows that there is another way, arguing that the essence of physics, including its fundamental equations, can be made accessible to anyone equipped with no more than high school math.

Carroll is an accomplished science writer, a talent with few peers. He is also the author of an outstanding textbook (1), but like others before him, his previous popular science books relied on images and parallels rather than equations. His new book has the appeal of a popular science book while covering in depth much of the material that ought to be found in physics textbooks.

The key new ingredient is math, includ-

ing calculus and differential equations. The transformative insight that makes this possible is the author's awareness that the main issue with which nonexperts struggle is not in understanding equations and interpreting their implications, which is done superbly in this book, but rather in manipulating and solving them. The latter is very carefully avoided and indeed not missed in the narrative. This balance between describing the real stuff and steering clear of explicit calculations renders the book accessible yet not oversimplified.

This volume—subtitled *Space, Time, and Motion*—is the first of a trilogy, which will also include a volume on quanta and fields and one on complexity and emergence. A glimpse into the content of the upcoming volumes is possible through the supplementary materials referenced in the book, which include videos by the author on which the book series is based (2).

Carroll's presentation style is arresting and informative. He adopts a conversational tone, with ample references to historical developments, to the evolution of ideas, and to the scientists behind them. In chapters 1 to 3, for example, to discuss classical mechan-

Advanced topics, such as black holes, are made transparent without being oversimplified.

ics, he does not begin with the current understanding as established by Isaac Newton but rather with more rudimentary concepts introduced by Aristotle and others after him.

The book's discussion goes from the human scale to fundamental questions that concern different scales such as the meaning of space, time, and predictability. Chapter 5, for example, explains how individual particles would behave similarly if time moved backward, and yet the future is ostensibly different from the past for macroscopic entities like us.

Carroll's focus is on well-established results, and he reaches reasonably advanced topics, such as general relativity, gravitational waves, and black holes. He does not venture into speculative research and even comments on the accuracy (or lack thereof) of physics in some Hollywood blockbusters.

The narrative is enriched by schematic illustrations and appendices with mathematical details. In chapters 7 and 8, for example, the notion that even light may not follow a straight line in strong gravitational fields is conveyed qualitatively using simple formulae and drawings of geodesics, while a detailed quantitative description of the geometry is left for appendix B.

To what extent can this format be adapted to communicate other scientific findings without watering them down? Using math without the need to solve equations could go a long way in other areas. Calculus in particular has been the basis of numerous advances in natural science, engineering, and technology, as beautifully illustrated in Steven Strogatz's 2019 book, *Infinite Powers* (3). Thus, it is

not difficult to imagine a similarly effective use of this format, for example, for a book conceived around newsworthy applications such as the workings of electric cars, GPS, smartphones, quantum computers, drones, fusion power, and more.

*The Biggest Ideas in the Universe* brings science dissemination to a new level. In doing so, the biggest and most consequential idea in Carroll's trilogy about

well be that substantive discussions about science can ultimately be had by everyone. ■

#### REFERENCES AND NOTES

1. S. M. Carroll, *Spacetime and Geometry: An Introduction to General Relativity* (Cambridge Univ. Press, 2019).
2. <https://preposterousuniverse.com/biggestideas/videos/>
3. S. Strogatz, *Infinite Powers: How Calculus Reveals the Secrets of the Universe* (Eamon Dolan Books, 2019).

10.1126/science.add6308

The reviewer is at the Department of Physics and Astronomy, Northwestern University, Evanston, IL 60208, USA. Email: motter@northwestern.edu

## WORKFORCE

# Dos and don'ts for achieving managerial diversity

A pair of sociologists turn to data to determine how to diversify organizations' upper ranks

By Edward H. Chang

**A**fter accusations that the company had a culture biased against women, Nike made “diversity training”—instruction designed to reduce bias and discrimination while promoting positive interactions between individuals from different backgrounds—mandatory for all managers. Nike is not alone in using training to try to solve such problems; most mid- to large-sized employers in the US offer some sort of diversity training to their employees. But do practices like this actually help companies address the problems at hand?

In *Getting to Diversity*, sociologists and longtime collaborators Frank Dobbin and Alexandra Kalev examine the effects of diversity training and other diversity-related practices on organizations, using data gleaned from hundreds of companies over the past three decades. In each chapter, the authors review a set of practices ranging from training to recruitment to work-life policies and provide empirical data on whether a given tactic helps companies in-

The reviewer is at Harvard Business School, Boston, MA 02163, USA. Email: ehchang@hbs.edu

crease diversity, does nothing, or even backfires. In other words, they provide hard evidence to managers and organizations about what to do and what not to do if they are serious about increasing diversity, particularly in managerial ranks.

This is not a fluffy book. No long-winded stories of specific companies or individuals who have achieved success (i.e., “anecdotal”) are passed off as generalizable knowledge. Instead, the authors focus on empirical data that call into question the efficacy of many popular practices.

Every year, companies in the United States with at least 100 employees are required to file reports to the Equal Employment Opportunity Commission (EEOC) detailing their demographic diversity, broken down by race and gender and whether an employee is a manager or not. Using these reports along with surveys they have conducted at the same companies about their workforce practices (e.g., whether the company has instituted diversity training, whether the company has mentoring programs), the authors analyzed how various factors influenced the demographic diversity of managers over time.

In the book's first chapter, they show that diversity training that focuses on the

## Getting to Diversity: What Works and What Doesn't

Frank Dobbin  
and Alexandra Kalev  
Belknap Press, 2022. 272 pp.



legal compliance aspects of diversity (e.g., what the law requires and how companies can avoid lawsuits) is associated with decreases in demographic diversity of managers, whereas training that focuses on cultural inclusion (e.g., how managers can work across differences and cultivate cohesion) is associated with increases. To paint a more detailed picture about why various practices have these effects on managerial diversity, the authors intersperse quantitative data with interviews they have conducted with managers.

Most extant diversity research focuses only on short-term effects of training or on attitude changes documented through surveys of employees. This book focuses on long-term changes on the real-world outcome of managerial diversity. The breadth of practices the authors examine is also impressive and includes those typically associated with diversity, such as employee resource groups, as well as practices that are not specifically tied to diversity, such as whether an organization allows for self-managed teams.

There is an inherent trade-off in breadth versus depth—in order to cover so many different workplace practices, the authors necessarily limit how deeply they examine the underlying mechanisms of any specific practice. At times, I wished for more insight into why the strategies they consider have the effects they do or why some practices have positive effects for some minority groups and not others (for example, parental leave policies increase the share of white women, Black women, Latinos, and Asian men among managers, but not Latinas or Asian women). The laser-like focus on managerial diversity also means that the book has less to say about topics such as inclusion and belonging in the broader workforce. Ultimately, however, this book is essential reading for anyone who wants to learn which practices can actually improve managerial diversity in organizations. ■



Parental leave policies increase the share of managers who are Black women, find the authors.

10.1126/science.add8064

## LETTERS

Edited by Jennifer Sills

## A genomics revolution in amphibian taxonomy

Amphibians feature the highest rates of both new species discoveries and species declines among vertebrates worldwide (1). To characterize this diversity faster than it disappears, zoologists have been using molecular data to rapidly describe new frog and salamander lineages, from species to family levels (2). About a third of the approximately 8500 known amphibian species (3) were first described in 2005 or later (4). However, mainstream species description practices relying on one or a few genes are critically flawed.

The majority of taxonomic descriptions rely on a few mitochondrial or nuclear-encoding genes (known as DNA barcodes). Because the variation of a small set of genes is often poorly indicative of the true evolutionary history of populations, overreliance on DNA barcodes distorts our perception of species diversity and distributions (5). In addition, a substantial proportion of newly identified amphibians merely consist of populations of the same species separated

by geography that differ at the few genes analyzed. The ongoing trend of splitting such genetic lineages into multiple species (“phylogenetic species”) artificially increases the total number of species identified on Earth (an issue known as “taxonomic inflation”), a shortcoming that complicates conservation, social, and economic decision-making (6).

Emerging genomic data are demonstrating the risks of these practices (7). The unreliability of frequently used DNA barcodes appears to be more common than previously assumed. Any new amphibian taxon supported mostly by mitochondrial divergence could be a “ghost lineage” (i.e., not a real extant species). Furthermore, it might be affiliated to the wrong clade, and its rank as a “species” might be inappropriate. Its name might also be mistaken because the type locality (i.e., the reference population where the taxon was first described) was misidentified (7).

Because of these ambiguities, the massive number of recent amphibian species descriptions will undoubtedly require time-consuming taxonomic revisions in the near future. To limit the confusion, we call for more cautious interpretations of genetic data in testing new species hypotheses. Given their higher resolution, genomic datasets will ultimately recover any structured population as unique

genetic lineages, rendering the idea of “phylogenetic species” obsolete (8). The rise of genomics in taxonomy will inevitably require a conceptual revolution.

Christophe Dufresnes<sup>1</sup> and Daniel Jablonski<sup>2</sup>

<sup>1</sup>Laboratory for Amphibian Systematic and Evolutionary Research, College of Biology and the Environment, Nanjing Forestry University, Nanjing, China. <sup>2</sup>Department of Zoology, Comenius University in Bratislava, Bratislava, Slovakia.

\*Corresponding author.

Email: christophe.dufresnes@hotmail.fr

### REFERENCES AND NOTES

1. B. C. Scheele *et al.*, *Science* **363**, 1459 (2019).
2. J. M. Padiál *et al.*, *Front. Zool.* **7**, 16 (2010).
3. AmphibiaWeb, “Newly described species by year” (2022); <https://amphibiaweb.org/amphibian/newspecies.html>.
4. AmphibiaWeb, “Amphibian species by the numbers” (2022); <https://amphibiaweb.org/amphibian/speciesnums.html>.
5. D. Rubinoff, B. S. Holland, *Syst. Biol.* **54**, 952 (2005).
6. F. E. Zachos, *Nature* **494**, 35 (2013).
7. C. Dufresnes *et al.*, *Mol. Phylogenet. Evol.* **141**, 106615 (2019).
8. J. Sukumaran, L. L. Knowles, *Proc. Natl. Acad. Sci. U.S.A.* **114**, 1607 (2017).

10.1126/science.ade5002

## Comprehensive support for diversity in STEM

In their Policy Forum “Achieving STEM diversity: Fix the classrooms” (3 June, p. 1057), J. Handelsman *et al.* explain that past interventions have not resulted in equitable representation for students from historically excluded communities in science, technology, engineering, and mathematics (STEM). We agree that implementation of their suggested classroom changes would likely contribute to greater persistence and retention in STEM throughout college. However, fixing the classroom alone will not be sufficient. If we are to achieve a fully inclusive workforce (1, 2), we need a comprehensive approach that simultaneously and collaboratively addresses factors both within and outside the classroom (3).

Recruitment into a scientific discipline requires classroom experiences that stimulate curiosity and foster the sense that a career in the field is possible (4, 5). Once student interest is piqued, retention demands financial, mentoring, and advising support (6), all of which occur outside the classroom. Achieving positive change in workplace demographics requires increased attention to postgraduation factors. For instance, employers must reconsider where and how they advertise positions to reach diverse populations. They must also recognize that stating preferences for candidates with work or



The green toad (*Bufotes sitibundus*) has been misidentified as a result of overreliance on single-gene barcoding.

PHOTO: DANIEL JABLONSKI

internship experience (7) may deter otherwise qualified candidates from historically excluded communities, who have not had access to internships or relevant work experience, from applying. Employers also need to mitigate potential unconscious biases in the interview and hiring processes by using strategies such as standardized interview questions (8, 9).

Institutions and organizations need to dismantle barriers to equity and build a culture of inclusion through career mentoring and sponsorship programs. Equity-focused mechanisms that support vulnerable groups, opportunities that recognize their contributions, and clear paths for professional advancement are critical (10–12). An ecosystem approach that includes classroom fixes, individual support, and institutional culture change is essential for achieving enduring diversity in STEM.

**Teresa Mourad<sup>1\*</sup> and George Middendorf<sup>2</sup>**

<sup>1</sup>Ecological Society of America, Washington, DC 20036, USA. <sup>2</sup>Howard University, Washington, DC 20059, USA.

\*Corresponding author. Email: [teresa@esa.org](mailto:teresa@esa.org)

#### REFERENCES AND NOTES

1. V. Bush, "Science: The endless frontier (75th anniversary edition)" (2020); [www.nsf.gov/about/history/EndlessFrontier\\_w.pdf](http://www.nsf.gov/about/history/EndlessFrontier_w.pdf).
2. Committee on Equal Opportunities in Science and Engineering, "Broadening participation in STEM: 2013–2014 biennial report to Congress" (2014); [www.nsf.gov/od/oia/activities/ceose/reports/2013-2014-ceose-biennial-report-508.pdf](http://www.nsf.gov/od/oia/activities/ceose/reports/2013-2014-ceose-biennial-report-508.pdf).
3. T. Mourad, G. Middendorf, *Front. Ecol. Environ.* **18**, 368 (2020).
4. R. Dou, Z. Hazari, K. Dabney, G. Sonnert, P. Sadler, *Sci. Educ.* **103**, 623 (2019).
5. K. Kricorian *et al.*, *Int. J. STEM Educ.* **7**, 16 (2020).
6. S. J. Cheng *et al.*, *Bull. Ecol. Soc. Am.* **102**, e01842 (2021).
7. National Association of Colleges and Employers, "Employers prefer candidates with work experience" (2017); [www.naceweb.org/talent-acquisition/candidate-selection/employers-prefer-candidates-with-work-experience/](http://www.naceweb.org/talent-acquisition/candidate-selection/employers-prefer-candidates-with-work-experience/).
8. R. P. Chamberlain, *Strat. H.R. Rev.* **15**, 199 (2016).
9. B. Carnahan, C. Moore, "Actively addressing unconscious bias in recruiting," Harvard Business School (2020); [www.hbs.edu/recruiting/insights-and-advice/blog/post/actively-addressing-unconscious-bias-in-recruiting](http://www.hbs.edu/recruiting/insights-and-advice/blog/post/actively-addressing-unconscious-bias-in-recruiting).
10. M. Miriri, *BioScience* **70**, 237 (2020).
11. A. Chaudhury, S. Colla, *Conserv. Lett.* **14**, e12774 (2021).
12. J. Coffman, E. Rosenblum, A. D'Arcy, L. T. Love, "How clear career paths strengthen retention—and diversity," Bain and Company (2021); [www.bain.com/insights/how-clear-career-paths-strengthen-retention-and-diversity/](http://www.bain.com/insights/how-clear-career-paths-strengthen-retention-and-diversity/).

10.1126/science.add8056

## Ecological footprint of Russia's Ukraine invasion

Russia's invasion of Ukraine continues to have a devastating effect on the well-being of Ukrainians and their economy (1). The tragic human consequences will be

## In memoriam

The *Science* family mourns longtime copyeditor Jeffrey Cook, who died unexpectedly last month. Jeff joined AAAS in 1994. He was a true perfectionist and cared deeply about language, editing, and scientific communication. Thousands of *Science* papers published over the past three decades are clearer and more accurate because of Jeff's meticulous dedication to his craft. He deftly transitioned from the hardcopy era to the world of online publication. Beyond being a mainstay of the Editorial team, Jeff was an accomplished musician and multi-instrumentalist. When *Science* launched its weekly podcast in 2007, Jeff composed the theme music, which still welcomes listeners to this day. Jeff was kind, talented, and thorough. He will be missed.

compounded by the long-term ecological implications of the war, such as the contamination of soil and water by the weaponry and other pollutants, wildfires and disruptions to ecosystem structure and services, and the environmental impact of the eventual postwar rebuilding activities (2, 3). Ongoing hostilities in the vicinity of the Zaporizhzhia Nuclear Power Station (the biggest in Europe) highlight the risks of large-scale nuclear disaster (4). To prepare for Ukraine's recovery, we need to understand both the current and long-term environmental impacts of the war (2–5).

The Ukrainian government has established the Operational Headquarters of the State Environmental Inspectorate to create an inventory of war damages (6). The damage is broadly divided into several categories, including infrastructure and ecology. Infrastructure damage evaluation will benefit from on-the-ground observations, remote sensing data, and media reports (7–9). In contrast, the long-lasting detrimental effects on the environment and the resulting ecosystem damages are notoriously difficult to quantify, especially during wartime and by a resource-constrained governmental authority (10–12).

The international science community can complement the top-down, government-driven, centralized approach by Ukrainian institutions by conducting robust, decentralized, distributed research. Researchers, managers, and funding institutions can help by developing collaborative projects that focus on the ecological impacts of the war, including assessment of the costs of remediation efforts. We hope that the body of knowledge accumulated through such studies would provide a reference point for subsequent remediation plans in Ukraine as well as evidence to support postwar reparation claims to Russia. It could also provide a blueprint for wartime damage and recovery assessments in other parts of the world affected by military conflicts.

**Mark Zheleznyak<sup>1\*</sup>, Gennadii Donchyts<sup>2</sup>, Vladimir Maderich<sup>3</sup>, Iryna Dronova<sup>4</sup>, Pavel Tkalic<sup>5</sup>, Dmytro Trybushnyi<sup>6</sup>, Boris Faybishenko<sup>7</sup>, Alla Dvorzhak<sup>8</sup>**

<sup>1</sup>Institute of Environmental Radioactivity, Fukushima University, Fukushima, Japan. <sup>2</sup>Deltares, Delft, Netherlands. <sup>3</sup>Institute of Mathematical Machine and System Problems, National Academy of Science, Kyiv, Ukraine. <sup>4</sup>Department of Environmental Science, Policy and Management and Department of Landscape Architecture and Environmental Planning, University of California Berkeley, Berkeley, CA 94720, USA. <sup>5</sup>Tropical Marine Science Institute, National University of Singapore, Singapore 119222, Singapore. <sup>6</sup>Institute for Thermal Energy Technology and Safety, Karlsruhe Institute of Technology, Karlsruhe, Germany. <sup>7</sup>Energy Geosciences Division, Earth and Environmental Sciences Area, Lawrence Berkeley National Laboratory, Berkeley, CA 94720, USA. <sup>8</sup>Centre for Energy, Environment and Technology Research, Madrid, Spain.

\*Corresponding author. Email: [r702@ipc.fukushima-u.ac.jp](mailto:r702@ipc.fukushima-u.ac.jp)

The opinions expressed in the text are those of the authors and do not necessarily reflect the positions of their institutions.

#### REFERENCES AND NOTES

1. World Bank, "Europe and Central Asia Economic Update, Spring 2022: War in the Region" (2022); <https://openknowledge.worldbank.org/handle/10986/37268>.
2. P. Pereira, F. Bašić, I. Bogunovic, D. Barcelo, *Sci. Tot. Environ.* **837**, 155865 (2022).
3. D. Rawtani, G. Gupta, N. Khatri, P.K. Rao, C. Mustansar, *Sci. Tot. Environ.* **850**, 157932 (2022).
4. Z. Savitsky, *Science*, 10.1126/science.ade4199 (2022).
5. Conflict and Environment Observatory, "Ukraine conflict environmental briefing: Nuclear sites and radiation risks" (2022); <https://ceobs.org/ukraine-invasion-environmental-brief-nuclear-and-radiation-risks/>.
6. Operational Headquarters at the State Environmental Inspectorate of Ukraine (2022); <https://shtab.gov.ua/en>.
7. EcoZagroza, Ukraine Ministry of Environmental Protection and Natural Resources, "Dashboard with data on environmental threats" (2022); <https://ecozagroza.gov.ua/en>.
8. J. Riga, "Satellite images show scale of destruction in Ukrainian industrial city of Sievierodonetsk" (2022); [www.abc.net.au/news/2022-06-08/satellite-images-of-destruction-in-sieverodonetsk-ukraine/101133912](http://www.abc.net.au/news/2022-06-08/satellite-images-of-destruction-in-sieverodonetsk-ukraine/101133912).
9. K. Deininger *et al.*, "Quantifying war-induced crop losses in Ukraine in near real time to strengthen local and global food security" (Policy Research Working Paper 10123, World Bank, 2022); <https://openknowledge.worldbank.org/handle/10986/37665>.
10. R. Costanza *et al.*, *Ecosyst. Serv.* **28**, 1 (2017).
11. W. H. Desvousges, N. Gard, H. J. Michael, A. D. Chance, *Ecol. Econ.* **143**, 74 (2018).
12. A. Zagorodny, *Nature* **603**, 228 (2022).

10.1126/science.ade6869

# RESEARCH

## IN SCIENCE JOURNALS

Edited by **Michael Funk**

### REPRODUCTIVE BIOLOGY

#### Fetal macrophages to the rescue

**P**remature rupture of the amniotic sac that encloses the fetus may trigger preterm birth. Kawamura *et al.* investigated repair mechanisms in the amnion, the innermost epithelial cell layer of the amniotic sac. Macrophages were recruited to rupture sites in human and mouse amnions, which showed signs of epithelial-mesenchymal transition, a process that is critical for tissue repair. Depletion of macrophages in fetuses in pregnant mice prevented macrophage recruitment and repair of amnion ruptures. —WW *Sci. Signal.* **15**, eabi5453 (2022).

Fetal macrophages aid in repairing damage to the amniotic sac, pictured above surrounding mice embryos, by inducing developmental changes to epithelial cells.

### CRISPR

#### CRISPR keeps on giving

CRISPR RNA-guided nucleases have been the driving force behind the current revolution of genomic medicine. Hu *et al.* introduce a new member into the work force: a CRISPR RNA-guided protease dubbed Craspase. Combining cryo-electron microscopy and molecular genetics approaches, the study defines the conditions leading to the RNA-guided activation and inactivation of Craspase in vitro and in vivo and provides a thorough set of high-resolution mechanistic explanations for the observed activities. Because Craspases do not touch DNA, they could be a safe alternative to Cas

nucleases and have the potential to be used in therapeutic applications in the future. —DJ *Science*, add5064, this issue p. 1278

### ORGANIC CHEMISTRY

#### Carbon-hydrogen bonds through tunneling

Much of organic chemistry revolves around bonding carbon to atoms other than hydrogen. However, it is sometimes necessary to restore a carbon-hydrogen bond, and the methods can be surprisingly cumbersome, often involving tin reagents. Constantin *et al.* report a photoinitiated method to transform carbon-halogen and analogous carbon-heteroatom bonds into

carbon-hydrogen bonds using a cyclohexadiene derivative that undergoes aromatization. Kinetic studies support a quantum mechanical tunneling mechanism for the transfer of hydrogen atom equivalents. —JSY *Science*, abq8663, this issue, p. 1323

### SIGNAL TRANSDUCTION

#### Cholesterol sensing at the lysosome

Cholesterol is an essential cell membrane component, and cells need a way to assess cholesterol abundance and link it to signaling pathways that control cell growth. Shin *et al.* identified G protein-coupled receptor 155 as a cholesterol sensor and

renamed it lysosomal cholesterol signaling (LYCHOS). LYCHOS bound cholesterol, and depletion of LYCHOS decreased mechanistic target of rapamycin complex 1 (mTORC1) signaling, which promotes the synthesis and uptake of cholesterol in proliferating cells by interacting with mTORC1 regulatory factors. LYCHOS thus appears to integrate metabolic status and cell growth, helping to ensure the appropriate availability of cholesterol. —LBR *Science*, abg6621, this issue p. 1290

### STRUCTURAL BIOLOGY

#### Tasting bitter

Bitter, sweet, and umami tastes are transduced by G protein-coupled receptors (GPCRs). The taste receptor type 1 (TAS1R)

family has three members that combine to sense sweet and umami tastes, and a distinct type 2 family (TAS2R) facilitates the perception of bitter tastes. Xu *et al.* determined the structures of the human bitter taste receptor TAS2R46 bound to a mini-G protein containing the TAS2R46-binding site from the G protein gustducin. The structures reveal distinct features of TAS2R46 compared with other GPCRs and provide insight into how ligands such as the bitter alkaloid strychnine activate this GPCR to evoke a bitter taste. —VV

*Science*, abo1633, this issue p. 1298

## EVOLUTION

### A Devonian heart

Placoderms were some of the earliest jawed vertebrates, and transformations to their morphology inform our understanding of the world of vertebrates that came after. Trinajstić *et al.* studied three-dimensionally preserved soft tissue organs from Devonian arthrodire placoderms showing changes in the shapes of the heart, liver, and intestines associated with the evolution of the jaws and neck. Additionally, the fossils show that the lungs are absent, refuting the hypothesis that lungs are ancestral in jawed vertebrates. —SNV

*Science*, abf3289, this issue p. 1311

## QUANTUM SIMULATION

### Zooming through singularities

Singularities in the band structure of materials often have a profound influence on their properties. Like the better-known Dirac points, in which linearly dispersing bands touch, quadratic band touching points can lead to exotic effects. Brown *et al.* introduce a method for studying both types of singularities in a cold atom quantum system. In their experiment, atoms of rubidium-87 were placed in a honeycomb optical lattice and driven through the singularities along various trajectories by accelerating the

lattice potential. By measuring the band population, the researchers were able to determine the winding number of the singularities. —JS

*Science*, abm6442, this issue p. 1319

## TUMOR IMMUNOLOGY

### Metabolite boost for immunotherapy

Despite its success, immune checkpoint blockade (ICB) has largely failed in pancreatic cancer patients, but how the microbiome contributes to this failure is unclear. Mirji *et al.* used mouse pancreatic tumor modeling to establish that a metabolite produced from the gut microbiome, trimethylamine *N*-oxide (TMAO), delayed tumor growth. Treating mice with TMAO slowed tumor growth in a type I interferon-mediated manner and boosted the efficacy of ICB in mouse models. TMAO-producing gut bacteria positively correlated with survival in cancer patients, suggesting a way to improve the efficacy of ICB. —DAE

*Sci. Immunol.* 7, eabn0704 (2022).

## NANOPHOTONICS

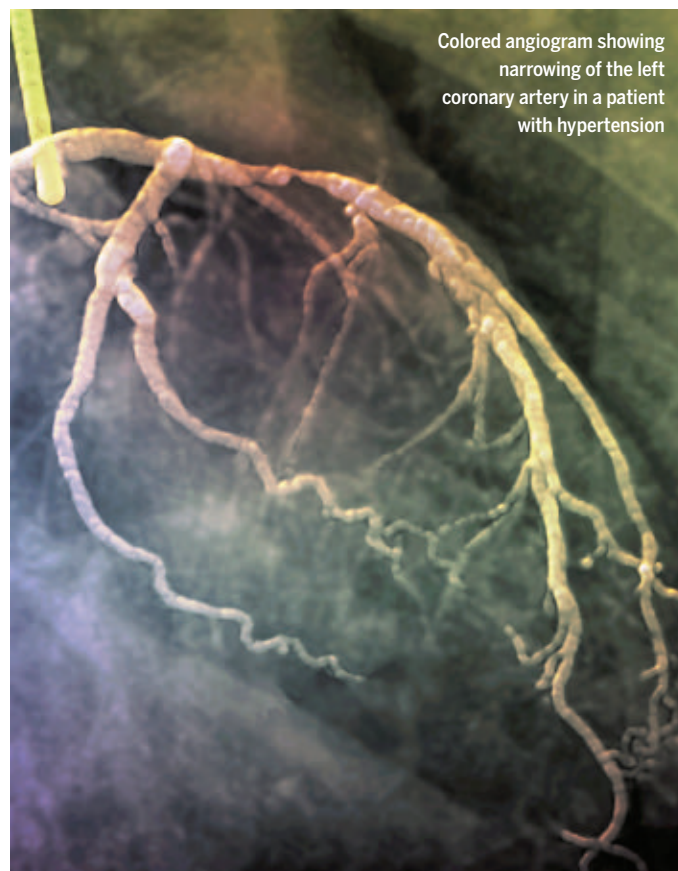
### Putting a squeeze on nanophotonics

Squeezed quantum states of light are states in which the noise in one of the quadratures is less than the standard quantum noise limit. The generation and manipulation of such states lies at the core of quantum-enhanced technologies, but such systems tend to require auxiliary bulk optical components for their preparation. Nehra *et al.* demonstrate an integrated nanophotonics platform based on lithium niobate to generate and measure squeezed states on the same optical chip. This generation and measurement of few-optical-cycle squeezed states in a nanophotonics setting should be useful for the development of scalable quantum information systems. —ISO

*Science*, abo6213, this issue p. 1333

## IN OTHER JOURNALS

Edited by **Caroline Ash**  
and **Jesse Smith**



Colored angiogram showing narrowing of the left coronary artery in a patient with hypertension

## VASCULAR DISEASE

### Hypertension through a DNA lens

**P**ulmonary arterial hypertension is a potentially life-threatening condition of high blood pressure in the lungs and the right side of the heart. It is not well understood, and existing biomarkers do not always predict patient outcomes accurately. To address this problem, Brusca *et al.* turned to analysis of cell-free DNA in the patients' blood. This approach is already used in oncology and obstetrics to detect tumor- or fetal-derived DNA. In the case of pulmonary arterial hypertension, the amount of cell-free DNA was correlated with disease severity and patient outcomes, and this DNA also showed distinctive methylation patterns that may eventually yield insights into the pathophysiology of this disease. —YN

*Circulation* 10.1161/CIRCULATIONAHA.121.056719 (2022).

## BEHAVIOR

### Sleepless and unhelpful

Helping among human beings is ubiquitous and has contributed to shaping modern civilizations. Motivations to help others span cultural norms, personality traits,

socioeconomic factors, and evolutionary forces. Moreover, an individual's decision to help another person involves brain regions linked to altruism, known as the social cognition brain network. Sleep deprivation impairs function in this



## ORGANIC CHEMISTRY

## Four rings from one

**A**lkaloid natural products often contain complex arrangements of edge-sharing rings. Chemical syntheses of these compounds from simple precursors therefore rely critically on ring-closing strategies. Kerkovius *et al.* now report a concise route to five different lupin alkaloids, inspired by their posited biosynthetic pathway, that assembles the underlying tetracyclic framework in the opening step through reaction of two equivalents of pyridine with linear glutaryl chloride. More than 160 grams of this intermediate could be prepared and then purified using simple precipitation. Simulations supported a stepwise mechanism. —JSY

*J. Am. Chem. Soc.* 10.1021/jacs.2c06584 (2022).

Complex natural alkaloids, such as the ones produced by *Sophora flavescens* (pictured), can be synthesized from simple precursors by employing a de-aromatic annulation reaction.

brain region and disrupts emotional processing; however, the question is whether sleep loss affects willingness to help. Simon *et al.* examined this possibility in three studies and found that sleep-deprived participants showed less desire to help strangers and friends, as well as less activity in the social cognition brain network, compared with better rested participants. Because sleep deprivation is modifiable, these findings highlight the importance of policy development to promote adequate sleep. —EEU

*PLoS Biol.* 10.1371/journal.pbio.3001733 (2022).

## COGNITION

## A sleeping touch improves vision

Sensory modalities such as touch and vision interact with each other, providing redundant information about the surrounding environment. During wakefulness, tactile stimuli moving in the same or opposite direction of a visual stimulus affect the perceived speed of movement. However, whether sensory interactions depend on arousal state is unknown. Onuki *et al.* examined the effects of

directional tactile stimulation during sleep on visual motion perception after waking. Similar to what happens during wakefulness, the direction of tactile stimulations during sleep affected the perception of speed of movement after the subjects woke up. The effect was associated with modulation of occipital brain oscillations recorded with scalp electrodes. These results indicate that crossmodal interaction of sensory stimuli can occur independently of the arousal state. —MM

*J. Neurosci.* 10.1523/JNEUROSCI.1512-21.2022 (2022).

## MICROBIOLOGY

## Invading microbes trip an alarm

Gut pathogens induce the secretion of ATP, which when extracellular, acts as a danger signal initiating inflammatory cascades by intestinal epithelial cells. However, what triggers ATP secretion during infection is unknown. Tadała *et al.* show that intestinal epithelial cells detect the invasion of enteric pathogens mechanically, which stimulates a proinflammatory signal. Similar signaling can

be experimentally tripped by contact with appropriately sized sterile beads. Pharmacological, genetic, and microscopy-based evidence has implicated the mechanosensitive ion channel PIEZO1 in signaling physical invasion. The extensive plasma membrane ruffling caused by invasive bacteria induces PIEZO1 opening and calcium ion influx. These events culminate in the rapid secretion of the ATP danger signal and activation of protective gene expression programs. Thus, PIEZO1 can act as an immune sensor that mechanically detects invasive bacteria. —SMH

*Cell Rep.* 40, 111173 (2022).

## SUPERCONDUCTORS

## Vibrating above a gigahertz

Nonlinear mechanical oscillators are useful for a wide range of signal processing and sensing applications. Currently, these oscillators are limited to operating in frequencies up to the megahertz range. Han *et al.* designed a nonlinear oscillator that works at gigahertz frequencies by coupling a piezoelectric oscillator to a nonlinear superconducting resonator.

The oscillation frequency of the nonlinear superconducting resonator is around 10 gigahertz but changes depending on the current going through the resonator from the piezoelectric oscillator. The ability to sense frequencies in the gigahertz range has the advantage over megahertz frequencies of being able to avoid thermal noise. —YY

*Phys. Rev. Lett.* 129, 107701 (2022).

## CELLULAR UPTAKE

## Switching sides

Large molecules cannot easily cross biological membranes, but amphipathic molecules have an advantage in that they can more easily insert into lipids. Donohoe *et al.* studied the molecule redaporfin, a metal-free porphyrin derivative decorated with bulky aryl sulfonamide groups on four sides that is being considered for use in photodynamic therapy. The four groups can either be up or down relative to the plane of the ring, leading to four isomers with different properties. The authors found that the isomer with all four groups on one side was considerably more amphipathic and thus was better able to enter cells and become more phototoxic. —MAF

*J. Am. Chem. Soc.* 144, 15252 (2022).



## ALSO IN SCIENCE JOURNALS

Edited by Michael Funk

## INFECTIOUS DISEASE

**Monkeypox: A neglected disease**

Monkeypox is a zoonotic disease that is endemic in the rainforest regions of west and central Africa. The first case arose in a child in 1970, and cases remained infrequent until the 1980s, but there have been increasing outbreaks recently that affect more people in endemic regions. The epidemiology of the disease has also changed with the emergence of human-to-human transmission. With the emergence of monkeypox outside of endemic regions since May 2022, what can we learn from monkeypox in Africa? In a Perspective, Tomori and Ogoina discuss the history of monkeypox in endemic regions, the emergence of this new phase of the disease, and what we need to understand to be able to equitably mitigate monkeypox for the benefit of everyone affected. —GKA

*Science*, add3668, this issue p. 1261

## CANCER GENETICS

**When timing is everything**

Chromosomal translocations, in which unrelated genes on different chromosomes are joined, play key roles in a number of cancers. These translocations result from DNA double-strand breaks that form during normal physiological processes, being ligated incorrectly. For example, in B cells, the normal process of antibody maturation involves DNA breaks, but sometimes aberrant fusions between antibody genes and oncogenes such as *Myc* drive the development of lymphoma and other cancers. Peycheva *et al.* discovered that DNA replication timing is key in this process (see the Perspective by Méchali). In particular, early replication of both *Myc* and its translocation partners was required for clinically important

translocations to form, which could be prevented by delaying the replication of *Myc*. —YN

*Science*, abj5502, this issue p. 1277;  
see also ade4734, p. 1259

## GAS GIANT PLANETS

**How did Saturn get its rings?**

Saturn's rings are about 100 million years old, but it is unclear how they could have formed so recently. Wisdom *et al.* propose that the Saturn system previously contained an additional moon, the orbit of which was perturbed by the orbital migration of Titan, Saturn's largest moon (see the Perspective by El Moutamid). The authors used numerical simulations to show that the perturbation would have eventually destabilized the system, scattering the additional moon. If it came too close to Saturn, the moon would have been ripped apart by tidal forces, forming the rings. The scenario explains several otherwise puzzling properties of Saturn's tilt and the orbits of its other moons and is consistent with the measured age and mass of the rings. —KTS

*Science*, abn1234, this issue p. 1285;  
see also abq3184, p. 1264

## SOCIAL NETWORKS

**The influence of weak associations**

The strength of weak ties is an influential social-scientific theory that stresses the importance of weak associations (e.g., acquaintance versus close friendship) in influencing the transmission of information through social networks. However, causal tests of this paradoxical theory have proved difficult. Rajkumar *et al.* addressed this issue using multiple large-scale, randomized experiments conducted on LinkedIn's "People You May Know" algorithm, which

recommends connections to users (see the Perspective by Wang and Uzzi). The experiments showed that weak ties increase job transmissions, but only to a point, after which there are diminishing marginal returns to tie weakness. The authors show that the weakest ties had the greatest impact on job mobility, whereas the strongest ties had the least. Together, these results help to resolve the apparent "paradox of weak ties" and provide evidence of the strength of the weak ties theory. —AMS

*Science*, abl4476, this issue p. 1304;  
see also add0692, p. 1256

## GROUNDWATER

**Recharge!**

In many dryland areas, irrigated agriculture depends on groundwater, and food cultivation can be disrupted if too much is withdrawn. Rainfall replenishes groundwater, but how much can be captured and through what mechanisms? Shamsudduha *et al.* calculated the magnitude of seasonal freshwater underground storage capture in the Bengal Basin of Bangladesh over the past 40 years (see the Perspective by Mukherji). They found that monsoon rainfall has recharged 75 to 90 cubic kilometers of water over that time, a volume equivalent to twice the reservoir capacity of the Three Gorges Dam. —HJS

*Science*, abm4730, this issue p. 1315;  
see also ade0393, p. 1258

## MICROBIOME

**Intimate traveling companions**

Most human populations have a similar range of microbial species living within their guts but show diversity among strains. Some microbial lineages are known to have speciated alongside hominids, but we do not know whether that is the

case for modern humans. Suzuki *et al.* noted that the global distribution of some human gut microbial strains mirrors historical human migration patterns out of Africa (see the Perspective by Moeller). Paired phylogenies for humans and their respective microbiomes from Gabon, Vietnam, and Germany revealed that 59 bacterial strains and one archaeal strain have evolutionary histories in parallel with human phylogenies, indicating co-diversification. These organisms appear to have acquired traits, such as oxygen intolerance and reduced genomes, that indicate host dependency. —CA

*Science*, abm7759, this issue p. 1328;  
see also ade2879, p. 1263

## WOUND HEALING

**Understanding anti-biofilm activity**

Bacterial biofilms pose a therapeutic challenge to managing chronic wounds and contribute to antimicrobial resistance. Powell *et al.* investigated the structure/activity relationships of epoxy-tigliane compounds derived from the bluishwood tree with respect to their role in wound healing. The compounds interacted with the cell wall of bacteria but showed variable permeabilization in Gram-negative versus Gram-positive cultures. The compounds disrupted established biofilms by interacting with the extracellular polymeric substance matrix, activated immune cells to induce reactive oxygen species, and promoted wound healing in infected thermal injuries in calves when applied topically. In chronic wounds in diabetic mice, the semisynthetic compound EBC-1013 upregulated host-defense peptides, altered cytokine expression, activated immune cells, and led to greater wound closure. These results help to uncover the mechanism by which epoxy-tiglianes

promote wound healing and support the further development of EBC-1013. —CC

*Sci. Transl. Med.* **14**, eabn3758 (2022).

**CELL BIOLOGY****Guidance of amoeboid cell migration**

Amoeboid migration is activated by many cell types in confined, nonadhesive environments. However, the interplay between intrinsic and extrinsic cues guiding such cell migration in vivo remains incompletely understood. Li *et al.* investigated the migration of fruit fly primordial germ cells (PGCs) during guided developmental homing in vivo. They found that PGCs navigate using an amoeboid migration mode that is protrusion independent and driven by global cortical actin flow. This mechanism remains active when PGCs are isolated in culture, whereas it is regulated by interactions with AMP-dependent protein kinase and the guanine exchange factor RhoGEF2 for directed migration in vivo. The authors speculate that similar RhoGEF2-dependent mechanisms may also broadly drive amoeboid cell migration in development, adult homeostasis, and disease. —A.-H.M.-B.

*Sci. Adv.* 10.1126/sciadv.abo0323 (2022).

## RESEARCH ARTICLE SUMMARY

## CANCER GENETICS

## DNA replication timing directly regulates the frequency of oncogenic chromosomal translocations

Mihaela Peycheva, Tobias Neumann, Daniel Malzl, Mariia Nazarova, Ursula E. Schoeberl, Rushad Pavri\*

**INTRODUCTION:** Chromosomal translocations involving proto-oncogenes are a common feature of cancers and can drive tumorigenesis by deregulating gene expression. Translocations form through the ligation of DNA double-strand breaks (DSBs) created on two chromosomes. However, although the sources of DSBs are numerous, we know little about the pathways and mechanisms that link DSB formation to DSB ligation.

**RATIONALE:** In antigen-activated B lymphocytes, deleterious translocations arise during the physiological process of antibody maturation, during which rapidly proliferating B cells diversify the antibody repertoire by mutating and rearranging the immunoglobulin (Ig) genes. These cells express the mutator enzyme activation-induced deaminase (AID) and gen-

erate DSBs at Ig genes through the processing of AID-induced mismatches by DNA repair pathways. However, AID also mutates proto-oncogenes, notably *MYC* and *BCL6*, leading to DSBs in these genes, and deleterious translocations between them and Ig loci that are typical of most mature B cell cancers such as Burkitt lymphoma and diffuse large B cell lymphoma. Here, we aimed to understand the mechanisms driving AID-dependent translocations.

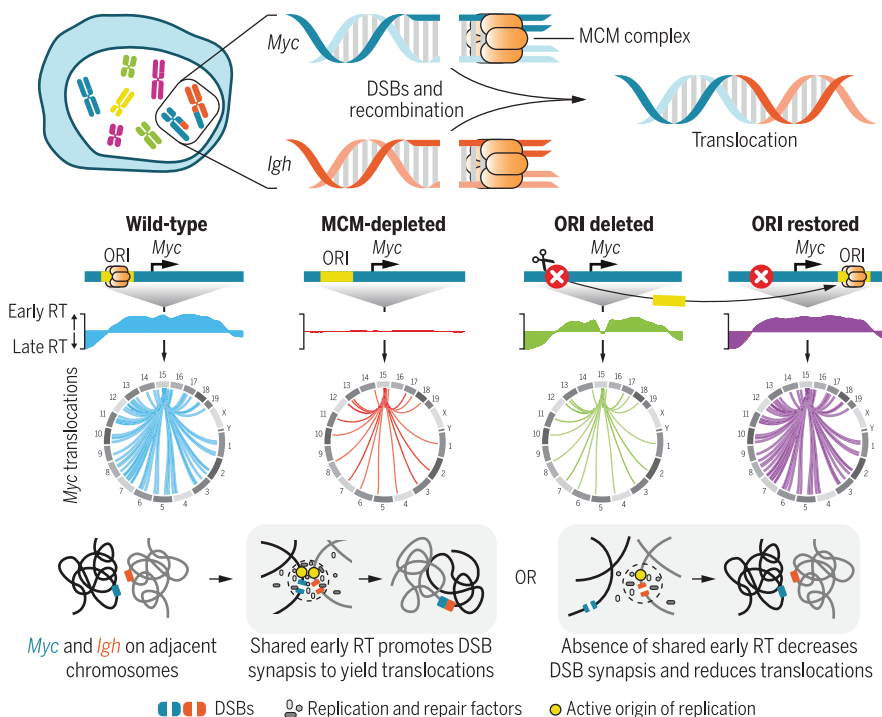
**RESULTS:** In activated murine B cells, AID-dependent *Myc* translocations were globally decreased upon reducing the levels of the minichromosome maintenance (MCM) complex, a replicative helicase. This was accompanied by decreased activity of origins of replication at *Myc*, *Igh*, and other AID

target genes without affecting gene expression or AID-induced mutation. These results pointed to a link between DNA replication and AID-dependent translocations downstream of mutagenesis.

Deletion of the promoter-proximal origin of replication at *Myc* (*Myc*<sup>ΔORI</sup>) majorly decreased *Myc-Igh* translocations as well as AID-dependent *Myc* translocations globally without affecting mutation frequency or transcription of *Myc*. Moreover, the translocation defect in *Myc*<sup>ΔORI</sup> or MCM-depleted cells was not rescued by an exogenous DSB introduced at supraphysiological frequency at *Myc* by the endonuclease Cas9. These results suggest that replication origin activity at *Myc* regulates a critical step in translocation biogenesis downstream of DSB formation and independent of DSB frequency.

DNA replication origin activity influences replication timing (RT), which has been correlated with translocations in cancer. RT analysis showed that AID target genes were normally early replicating. MCM depletion led to the global deregulation of the RT program, resulting in the absence of distinct early and late replication domains. In *Myc*<sup>ΔORI</sup> cells, a localized early-to-late RT switch was observed at *Myc*, creating a new, 60-kb late-RT domain centered at *Myc*. Reinserting the *Myc* origin of replication deleted in *Myc*<sup>ΔORI</sup> cells downstream of *Myc* (*Myc*<sup>ΔORI rest</sup>) restored early RT at *Myc* and, most importantly, globally rescued *Myc* translocations to wild-type levels. The perturbation of RT in any of the above experimental conditions was not associated with changes in global chromatin architecture. Finally, genomic interaction frequency of *Myc* and *Igh* was decreased in *Myc*<sup>ΔORI</sup> and MCM-depleted cells but restored in *Myc*<sup>ΔORI rest</sup> cells, suggesting that changes in RT influence the proximity of translocation partner loci.

**CONCLUSION:** Shared early RT of partner loci is important for AID-mediated translocations and regulates a step after DSB formation and before DSB ligation. We propose that the early origins of replication on neighboring chromosomes can occasionally congregate and fire synchronously. This can trigger translocation by bringing origin-proximal DSBs into physical proximity. We found that changes in RT also reduced leukemia-associated *AFF4-MLL1* and lymphoma-associated *BCL6-IGH* translocations in human cells, implicating RT generally in the biogenesis of tumorigenic translocations. ■



**RT regulates translocation biogenesis.** Translocations between DSBs in Ig genes and proto-oncogenes such as *Myc* arise during antibody maturation. Translocations and early RT at *Myc* are impaired by reducing replication origin (ORI) activity (MCM depletion) and ORI deletion but are rescued upon ORI restoration. We propose that neighboring early-replicating origins may occasionally congregate and fire synchronously, facilitating synapsis of origin-proximal DSBs and translocation.

The list of author affiliations is available in the full article online.

\*Corresponding author. Email: rushad.pavri@imp.ac.at  
Cite this article as M. Peycheva et al. *Science* 377, eabj5502 (2022). DOI: 10.1126/science.abj5502

**S** READ THE FULL ARTICLE AT  
<https://doi.org/10.1126/science.abj5502>

## RESEARCH ARTICLE

## CANCER GENETICS

## DNA replication timing directly regulates the frequency of oncogenic chromosomal translocations

Mihaela Psycheva<sup>1</sup>, Tobias Neumann<sup>1,2†</sup>, Daniel Malz<sup>1</sup>, Mariia Nazarova<sup>1</sup>, Ursula E. Schoeberl<sup>1</sup>, Rushad Pavri<sup>1\*</sup>

Chromosomal translocations result from the joining of DNA double-strand breaks (DSBs) and frequently cause cancer. However, the steps linking DSB formation to DSB ligation remain undeciphered. We report that DNA replication timing (RT) directly regulates lymphomagenic *Myc* translocations during antibody maturation in B cells downstream of DSBs and independently of DSB frequency. Depletion of minichromosome maintenance complexes alters replication origin activity, decreases translocations, and deregulates global RT. Ablating a single origin at *Myc* causes an early-to-late RT switch, loss of translocations, and reduced proximity with the immunoglobulin heavy chain (*Igh*) gene, its major translocation partner. These phenotypes were reversed by restoring early RT. Disruption of early RT also reduced tumorigenic translocations in human leukemic cells. Thus, RT constitutes a general mechanism in translocation biogenesis linking DSB formation to DSB ligation.

In antigen-activated B lymphocytes, deleterious translocations arise during the physiological process of antibody maturation, when B cells diversify their antibody repertoire through somatic hypermutation and isotype class-switch recombination at the immunoglobulin (Ig) genes (1–6). Antibody maturation involves double-strand break (DSB) formation at Ig genes induced by the mutagenic action of activation-induced deaminase (AID) in a transcription-dependent manner (7–10). Therefore, antibody maturation is inextricably linked to genome instability because AID also targets major transcribed proto-oncogenes in B cells, such as *MYC* and *BCL6*, resulting in DSBs and translocations between these genes and the Ig loci, an event that deregulates their expression and triggers tumorigenesis (11–18). *MYC* and Ig translocations are frequently observed in major mature B cell cancers, including diffuse large B cell lymphoma, multiple myeloma, and, most markedly, in Burkitt lymphoma, where *MYC*-Ig translocations are seen in all tumors and are proposed to be the primary drivers of tumorigenesis (19–21). These translocations have been recapitulated, not only in mouse tumor models (22–24), but also, most pertinently, in primary B cells (25–29) and the murine B lymphoma line CH12 upon AID overexpression (30, 31). This makes the latter systems well suited for addressing the mechanisms of translocation biogenesis. In this study, we retrovirally expressed AID fused to the estrogen receptor ligand-binding domain (AIDER) (32)

in CH12 cells (33) or used primary splenic B cells expressing AIDER from the *Rosa26* locus (23) and added 4-hydroxy tamoxifen (4-HT) to trigger the nuclear import of AIDER.

## Results

The MCM complex is required for oncogenic *Myc-Igh* translocations

It has been shown that reduced levels of the minichromosome maintenance (MCM) complex, a hexameric replicative helicase, in mice can lead to cancer resulting from increased replicative stress-mediated genome instability (34, 35). Therefore, we reasoned that MCM complexes may play a protective role in B cells during AID-mediated translocation genesis, which occurs in B cells undergoing massive antigen-mediated proliferation with very short cell cycles (6 to 8 hours) (36). We depleted MCM6 with a short hairpin RNA (shRNA) (hereafter called shMcm6) in activated CH12 cells and in activated primary splenic B cells. Under these conditions, shMcm6 cells expressed ~20% of MCM6 protein compared with control cells (shLacZ) (fig. S1A), were proliferative (fig. S1B), and showed normal DNA synthesis (fig. S1C). The normal growth and viability of MCM-depleted cells is consistent with several previous reports in a variety of cell types (37–41). In our previous study, we showed that shMcm6 cells did not undergo detectable DNA damage, as measured by the Comet assay, nor did they have altered levels of the DSB response proteins  $\gamma$ H2AX, 53BP1, and RPA at the Ig heavy chain (*Igh*) gene locus in activated B cells (42). RNA sequencing (RNA-seq) showed that *Mcm6* RNA, but not other MCM subunits, was strongly down-regulated in shMcm6 cells (Fig. 1A; fig. S1, D and E; and table S1). By contrast, mass spectrometry from nuclear extracts revealed decreased protein expression of MCM6

(~3.5-fold), as well as other MCM complex subunits (Fig. 1B, fig. S1F, and table S2). Thus, the MCM complex was destabilized at the protein level when MCM6 protein was limiting. We did not detect loss of other DNA replication factors or DNA repair factors either at the RNA level or the protein level (Fig. 1, A and B). Gene ontology analysis also revealed no enrichment of pathways linked to DNA replication or the DNA damage response (fig. S1G and table S1). In addition, shMcm6 cells did not show major changes in RNA or protein expression of AID, the *Myc* and *Igh* genes (fig. S1, E and F), or AID translocation hotspot genes (Fig. 1A).

Translocations between *Myc* and the *Igh* locus in AIDER-expressing shLacZ and shMcm6 cells were quantified using a previously established nested polymerase chain reaction (PCR) assay (29) (fig. S1H). Contrary to our expectation, we observed a significant decrease in *Myc-Igh* translocation frequency in shMcm6 CH12 cells relative to the shLacZ control ( $P = 0.00021$ ; Fig. 1, C and D). Moreover, these translocations were almost completely abrogated when wild-type (WT) cells were arrested at the G<sub>1</sub>/S phase boundary with the DNA polymerase inhibitor aphidicolin (Fig. 1E). *Myc-Igh* translocations were also significantly reduced in shMcm6 primary activated splenic B cells ( $P = 0.0032$ ; Fig. 1, F and G). We conclude that MCM depletion in activated B cells suppresses AID-mediated *Myc-Igh* translocations. Moreover, this function of the MCM complex was exerted downstream of AID targeting, as determined by the normal rates of AID-mediated mutation at *Myc* and *Igh* in shMcm6 cells (fig. S1, I and J). In sum, these results reveal a role of the MCM complex in promoting AID-dependent translocations.

Myc-Igh translocation frequency correlates with the activity of origins of replication at *Myc* and *Igh*

The loading of MCM complexes to origins of replication licenses these origins for activation by replication firing factors during the S phase (43). The normal cycling of shMcm6 cells (42) implied that the act of DNA replication was unlikely to be a causal factor in driving *Myc-Igh* translocations. Rather, we hypothesized that MCM depletion would reduce the licensing of origins and thereby decrease origin activation frequencies at AID target genes. Therefore, we performed short nascent strand sequencing (SNS-seq) in CH12 cells to measure the relative enrichment of nascent leading strands at origins of replication (44, 45) (fig. S2A). In effect, replication initiation sites identified by SNS-seq enrichments reflect the relative firing frequency of the underlying replication origins in the population. Two independent SNS-seq experiments were performed in CH12 cells, each with two replicates (fig. S2B). Only replication initiation sites that reproducibly fell within initiation zones were retained to obtain

<sup>1</sup>Research Institute of Molecular Pathology (IMP), Vienna Biocenter, 1030 Vienna, Austria. <sup>2</sup>Vienna BioCenter PhD Program, Doctoral School of the University of Vienna and Medical University of Vienna, Vienna Biocenter, 1030 Vienna, Austria.

\*Corresponding author. Email: rushad.pavri@imp.ac.at

†Present address: Quantro Therapeutics, Vienna Biocenter, 1030 Vienna, Austria.

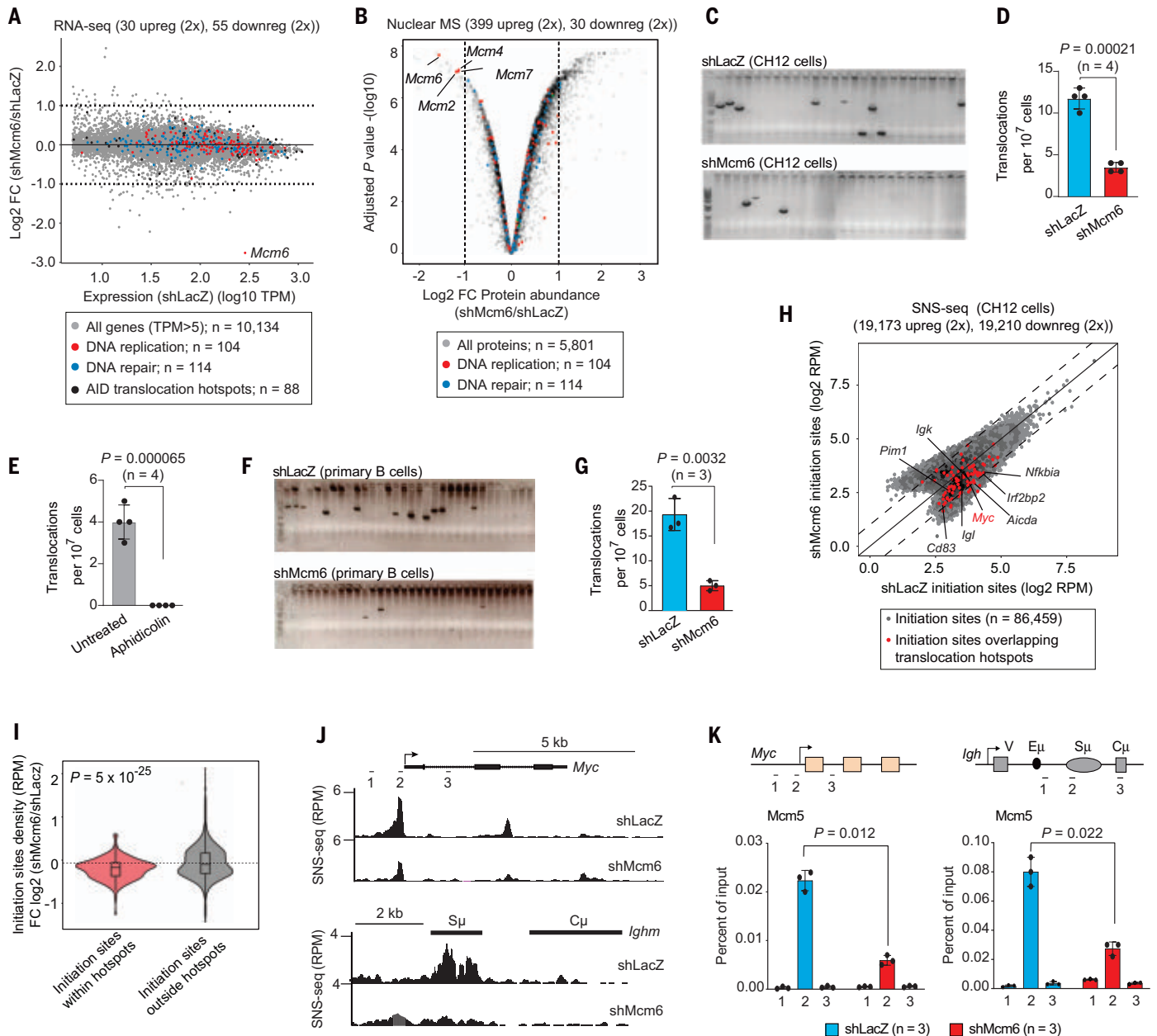


**Fig. 1. AID-dependent *Myc-Igh* translocation frequency correlates with the frequency of replication origin activity at *Myc* and *Igh*.** (A) RNA-seq analysis in shLacZ and shMcm6 CH12 cells (averaged from triplicate experiments) and represented as the FC (shMcm6/shLacZ) against RNA expression in shLacZ cells calculated as transcripts per million (TPM). Dots represent mRNAs with TPM > 5, the cutoff for expressed genes. The dotted lines demarcate twofold up-regulated ( $\log_2$  FC > 1) or twofold down-regulated ( $\log_2$  FC < -1) RNAs. Red, blue, and black dots represent DNA replication genes, DNA repair genes, and AID translocation hotspots, respectively. The location of *Mcm6* RNA is indicated. (B) Nuclear mass spectrometric analysis from shLacZ and shMcm6 CH12 cells represented as a volcano plot of FC (shMcm6/shLacZ) against the adjusted *P* value. The dotted lines demarcate twofold up-regulated ( $\log_2$  FC > 1) or twofold down-regulated ( $\log_2$  FC < -1) proteins. (C) Representative agarose gel revealing translocation PCR products from the genomic DNA of activated CH12 cells expressing AIDER and infected with lentiviruses expressing shRNAs against LacZ (shLacZ) or *Mcm6* (shMcm6). 4-HT was added at the time of activation to induce nuclear import of AIDER. (D) Quantitation of translocations after Sanger sequencing of PCR products. The data represent four independent experiments. (E) *Myc-Igh* translocation assay as above in WT activated

CH12 cells expressing AIDER treated with aphidicolin (1  $\mu$ M) for 48 hours. (F) Translocation PCR assay from primary activated splenic B cells expressing AIDER from the *Rosa26* locus infected with retroviruses expressing shLacZ or shMcm6 and treated with 4-HT. (G) Quantification from three independent translocation PCR experiments in primary splenic B cells. (H) SNS-seq analysis in shLacZ and shMcm6 CH12 cells. Each dot represents a replication initiation site identified through peak calling and overlapping with initiation zones (see also fig. S2C). Red dots are replication initiation sites overlapping AID-dependent translocation hotspots (table S1). Initiation site density is calculated as reads per million (RPM). The dotted lines indicate twofold change on either side of the diagonal. ( $\log_2$  FC = 1 or -1) (I) Violin plots based on data from (H) showing the enrichment of replication initiation sites within AID translocation hotspots compared with initiation sites outside of AID translocation hotspots. (J) UCSC browser snapshots of SNS-seq profiles at *Myc* (top) and *Igh* (bottom) from shLacZ and shMcm6 cells. Amplicons 1 to 3 are those used for chromatin immunoprecipitation (ChIP)-qPCR in (K). (K) ChIP-qPCR for Mcm5 occupancy at *Myc* (left) and *Igh* (right) in shLacZ and shMcm6 CH12 cells. The location of amplicons 1 to 3 is indicated in the top panel. Data represent three independent experiments. All *P* values were determined by unpaired Student's *t* test.

a confident and rigorous set of initiation sites for further analysis (fig. S2, C and D).

We observed an altered replication origin landscape in shMcm6 cells marked by several up-regulated and down-regulated replication initiation sites relative to shLacZ cells (Fig. 1H). By overlapping initiation sites with selected chromatin marks and genomic compartments (obtained from Hi-C analysis), we observed that down-regulated initiation sites were located mostly in active chromatin within A compartments, whereas up-regulated initiation sites overlapped largely with histone H3 trimethylated at lysine 9 (H3K9me3)-rich constitutive heterochromatin within B compartments (fig. S2, E and F). Using a statistical permutation test, we found that AID-dependent translocation hotspots overlap with replication initiation sites significantly more often than a null distribution of randomly placed translocation hotspots and initiation sites ( $P = 0.0029$ ; fig. S3A). Initiation sites overlapping AID-dependent translocation hotspots were significantly down-regulated in shMcm6 cells ( $P = 5 \times 10^{-25}$ ; Fig. 1, H and I). Thus, AID-dependent translocation hotspots are enriched in MCM-sensitive replication initiation zones.

At *Myc*, we observed a strong origin of replication just upstream of the promoter that was down-regulated in shMcm6 cells (Fig. 1J, top panel). SNS-quantitative PCR (SNS-qPCR) analysis confirmed this decrease in origin activity in CH12 cells, as well as in primary B shMcm6 cells (fig. S3B). At *Igh*, SNSs were enriched within the switch recombination sequences, and these origins were down-regulated in shMcm6 cells (Fig. 1J, bottom panel). We confirmed the loss of origin activity at *Igh* with SNS-qPCR in both CH12 and primary B shMcm6 cells (fig. S3C). As an alternative approach to detect initiation sites, we pulsed cells with bromodeoxyuridine (BrdU), isolated the SNS-containing fraction, and enriched the BrdU-labeled DNA with immunoprecipitation using an anti-BrdU antibody (fig. S3D) (46). qPCR analysis at *Igh* and *Myc* revealed that, similar to our observation in the SNS-seq and SNS-qPCR experiments, there was a decrease of origin activity upon MCM complex depletion (fig. S3, E and F, compare with Fig. 1, J and K). Finally, at both *Myc* and *Igh*, the decrease in origin activity correlated with significantly reduced MCM complex occupancy, which is indicative of decreased origin licensing ( $P = 0.012$  for *Myc* and  $P = 0.022$  for *Igh*; Fig. 1K). We conclude that the frequency of *Myc-Igh* translocation correlates with the frequency of replication origin licensing and origin activity at *Myc* and *Igh*.

#### Replication origin activity at *Myc* directly regulates *Myc-Igh* translocation frequency

To determine whether the observed correlation between translocation frequency and replication origin activity reflects a direct, causal re-

lationship between these processes, we deleted the promoter-proximal origin of replication at *Myc* in CH12 cells, spanning 800 base pairs (bp), with CRISPR editing (Fig. 2A, top panel, and fig. S4A). We hypothesized that if replication origin activity were causal for translocation genesis, then deletion of the origin of replication would impair translocation frequency independently of *Myc* transcription and AID-mediated mutagenesis. The deletion did not overlap the core promoter, as determined by the occupancy of TATA box-binding protein (TBP) and transcription factor IIB (TFIIB), core components of the transcription preinitiation complex (Fig. 2A). In addition, the deletion did not overlap with the major transcription initiation sites identified by precision run-on sequencing for capped transcripts (PRO-cap) (47), which maps the location and orientation of capped transcription initiation sites associated with actively engaged RNA polymerase II (Fig. 2A).

Two independent deletion clones, c13 and c23, were chosen for analysis and are hereafter called *Myc* origin-deleted *Myc*<sup>AORI</sup> c13 and *Myc*<sup>AORI</sup> c23, respectively (fig. S4B). Genotyping confirmed that all three *Myc* alleles were targeted (fig. S4C). Both clones were viable and neither suffered from proliferation defects (fig. S4D). RNA-seq revealed no major changes in the expression of AID target genes or the DNA replication and repair genes (fig. S4E). *Myc* itself was expressed at similar levels in both *Myc*<sup>AORI</sup> clones (fig. S4F). Class-switch recombination was robust in both *Myc*<sup>AORI</sup> lines, indicating that transcription-coupled mutagenesis, DSB formation, DNA repair, and nonhomologous end-joining pathways, all of which are essential for class-switch recombination and translocations, were fully functional in these clones (fig. S4, G and H). Furthermore, AID-mediated mutation frequencies at *Myc* in *Myc*<sup>AORI</sup> cells were comparable to those in WT cells, implying that AID targeting was unaffected by the loss of replication origin activity (fig. S4I). Therefore, the minor gene expression differences observed between the two *Myc*<sup>AORI</sup> lines are likely due to their different clonal origins and have no discernible impact on major physiological processes in these cells.

SNS-qPCR analysis confirmed the loss of origin activity at the deleted region in *Myc*<sup>AORI</sup> cells (Fig. 2A, bottom panel bar graph). However, *Myc*<sup>AORI</sup> cells also showed a decrease in the activity of the intragenic origin of replication, mimicking the results from shMcm6 cells, in which this intragenic origin was also down-regulated (compare SNS-seq tracks with the SNS-qPCR bar graphs in Fig. 2A). Therefore, the replication origin landscape at the *Myc*<sup>AORI</sup> allele resembled that of *Myc* in shMcm6 cells. *Myc-Igh* translocation frequency was severely reduced in *Myc*<sup>AORI</sup> cells relative to WT cells (Fig. 2, B and C). We conclude that

replication origin activity at *Myc* has a direct and profound effect on the genesis of *Myc-Igh* translocations downstream of AID-mediated mutagenesis.

#### DNA replication origin activity regulates a distinct step in translocation genesis downstream of DSB formation and independently of DSB frequency

Given that AID targeting was unaffected in *Myc*<sup>AORI</sup> cells (fig. S4I), we investigated whether DSB formation, the next obligatory step for translocations, was affected. Because of the low mutation rate coupled with the low density of AID hotspot motifs at non-*Ig* AID targets such as *Myc*, DSBs occur rarely and are challenging to detect. However, we reasoned that if DSB formation were indeed limiting in *Myc*<sup>AORI</sup> cells, then a potent exogenous DSB within the translocation hotspot should rescue the *Myc-Igh* translocation rate. Therefore, we transfected AIDER-expressing *Myc*<sup>AORI</sup> cells with Cas9 and a small guide RNA (sgRNA) targeting the first intron of *Myc*, a region that lies within the known translocation hotspot (30). Cas9/sgRNA-transfected WT and *Myc*<sup>AORI</sup> cells were sorted and analyzed for *Myc-Igh* translocations (Fig. 2D). We detected virtually no increase in *Myc-Igh* translocation frequency in *Myc* sgRNA-expressing *Myc*<sup>AORI</sup> cells relative to cells with a control sgRNA (Fig. 2E). This was not due to inefficient Cas9 activity because 70 to 80% of WT and *Myc*<sup>AORI</sup> cells harbored indels at the Cas9 cleavage site (Fig. 2F). This result also ruled out the possibility that such translocations are driven by the random interactions of neighboring chromatin fibers harboring DSBs. Therefore, we conclude that the *Myc* origin regulates translocation frequency downstream of DSBs. Moreover, because the frequency of the Cas9-induced DSB is orders of magnitude greater than that of a physiological AID-induced DSB, we conclude that the *Myc* origin regulates translocation genesis completely independently of DSB frequency.

To determine whether other AID-dependent translocations are also affected in *Myc*<sup>AORI</sup> cells, we performed a modified version of linear amplification-mediated high-throughput genome-wide translocation sequencing (LAM-HTGTS) (48), which uses an exogenously introduced bait DSB to identify associated prey translocations by locus-specific enrichment and deep sequencing. A high-frequency bait DSB was introduced in *Myc* with Cas9 and a *Myc*-specific sgRNA (30). This procedure inherently bypassed the AID-dependent DSB formation step at *Myc*, thereby allowing us to determine, on a genome-wide scale, whether decreased replication origin activity at *Myc* (*Myc*<sup>AORI</sup> cells) or AID target genes generally (shMcm6 cells) regulated *Myc* translocation genesis upstream or downstream of DSB formation.

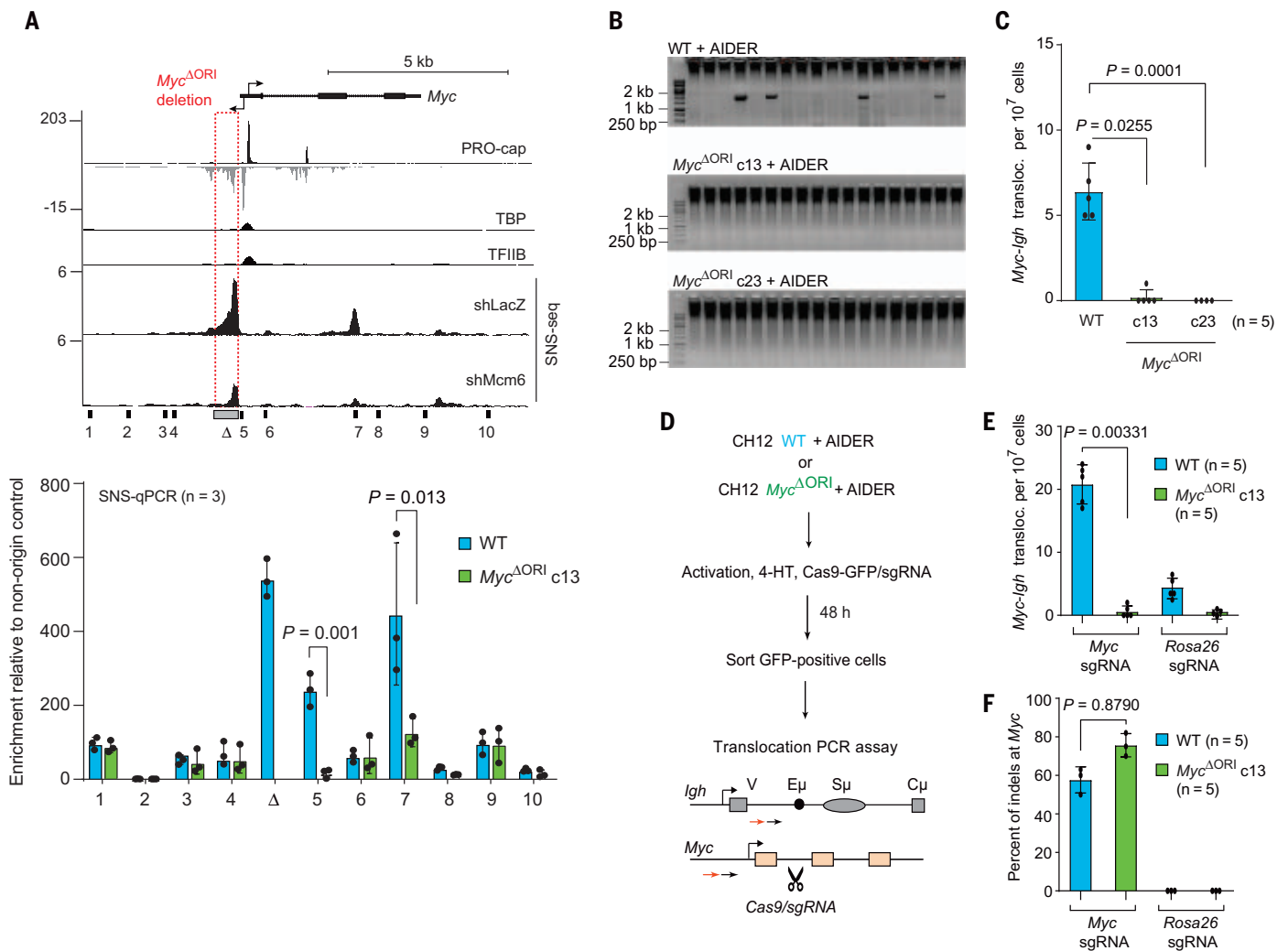


**Fig. 2. Deletion of a single origin of replication at *Myc* strongly decreases *Myc-Igh* translocation rate downstream of DSBs and independently of DSB frequency.** (A) Top panel: Snapshot of the *Myc* locus showing the SNS-seq profiles in shLacZ and shMcm6 cells. Also shown are CH12 (WT) tracks of PRO-cap (indicating capped transcription initiation sites) and TBP and TFIIIB (both indicating the core promoter). The origin targeted for CRISPR-mediated deletion is boxed in red and lies upstream of both the core promoter and the major antisense initiation site. Bottom panel: SNS-qPCR at the *Myc* locus in WT and *Myc*<sup>ΔORI</sup> clone 13 (c13) cells. Amplicons for qPCR are shown in the top panel below the SNS-seq snapshot. Enrichments are calculated relative to a non-origin control. (B) Representative agarose gel of a *Myc-Igh* translocation PCR assay in WT, *Myc*<sup>ΔORI</sup> c13, and *Myc*<sup>ΔORI</sup> c23 cells

We performed LAM-HTGTS in AIDER-expressing WT, *Myc*<sup>ΔORI</sup> c13 (Fig. 3A), and *Myc*<sup>ΔORI</sup> c23 (Fig. 3B) cells, as well as in shLacZ and shMcm6 cells (Fig. 3C). In this system, the DSB at *Myc* is generated primarily by Cas9, whereas AIDER is required to ensure high rates of physiological DSBs at other AID target genes. Three independent LAM-HTGTS experiments were conducted, and libraries were sequenced with the MinIon flow cell (Oxford Nanopore Technologies), which detects translocation breakpoints at single-nucleotide res-

olution by spanning the entire site with long reads. Raw translocations involving the *Myc* DSB were seen in all conditions, indicating that translocation genesis was not impaired per se in these cells (fig. S4, J to L). The numbers and distribution of translocation junctions at *Myc* were similar in all conditions, indicating that Cas9 cleavage and DSB processing occurred at comparable efficiencies in these cells (fig. S5, A to F).

From these data, we defined 88 high-confidence AID-dependent hotspots on the

basis of the density of translocations, consistency between replicates, and several quality criteria (table S3). Decreased translocation frequency was observed at virtually all AID-dependent hotspots in shMcm6 cells and both *Myc*<sup>ΔORI</sup> lines, as seen from the circos plots showing the fold changes (FCs) in translocations (Fig. 3, A to C) and scatter plots of translocation hotspot densities (Fig. 3, D to F).

The transcribed *Igh* genes (*Ighm*, *Igha*, and *Igh2b*) were the strongest hotspots in WT and

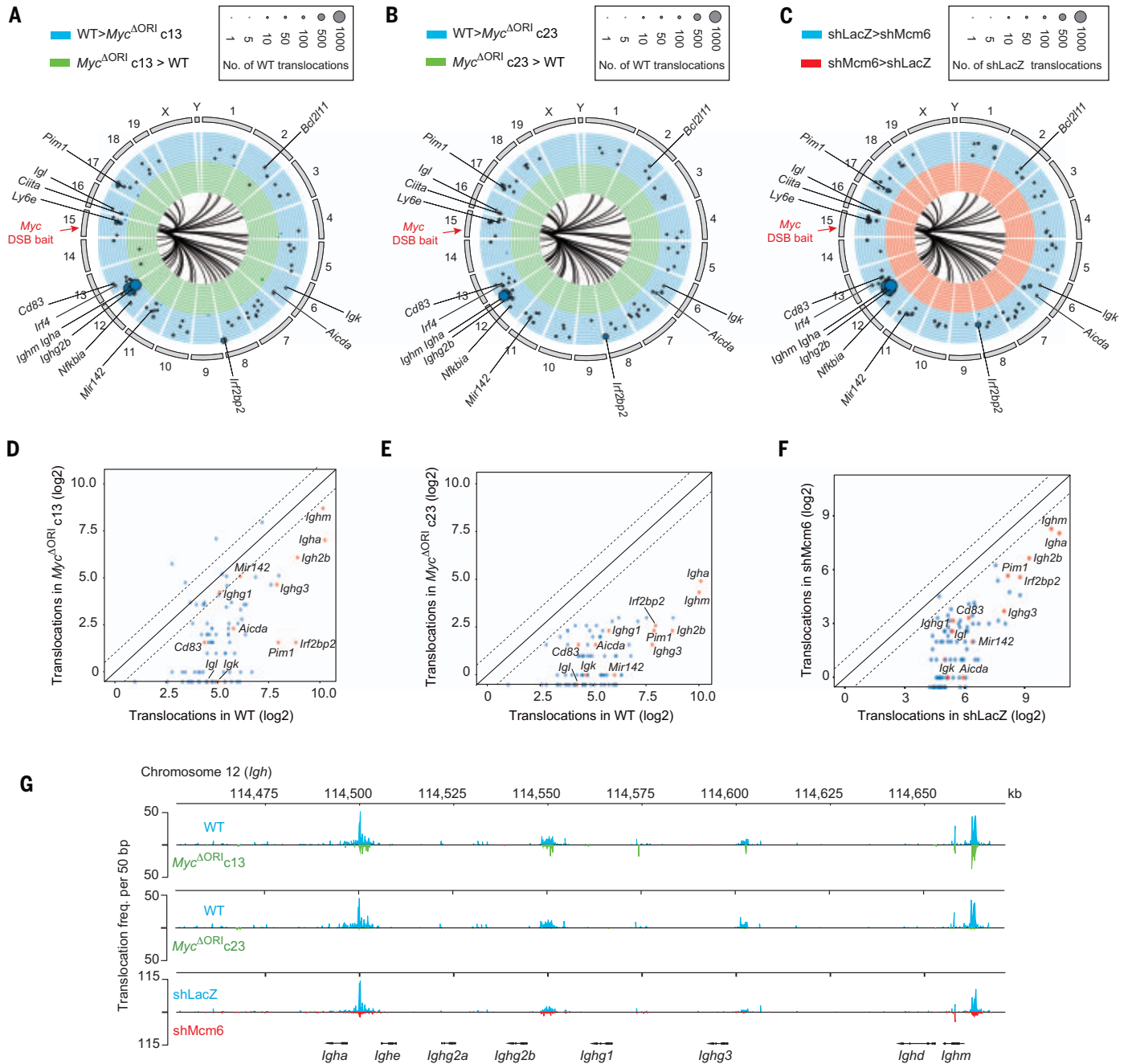


**Fig. 3. AID-dependent translocations are globally reduced in *Myc*<sup>AORI</sup> and shMcm6 cells.** (A to C) Circos plots displaying AID-dependent translocations obtained from LAM-HTGTS in *Myc*<sup>AORI</sup> c13 versus WT cells (A), *Myc*<sup>AORI</sup> c23 versus WT cells (B), and shMcm6 versus shLacZ cells (C). The location of the Cas9-induced *Myc* bait DSB is indicated in red text. Each arc radiating from *Myc* indicates an AID-dependent *Myc* translocation hotspot to the indicated chromosome. The plots show the FC of translocations: log<sub>2</sub> WT/*Myc*<sup>AORI</sup> in (A) and (B) and log<sub>2</sub> shMcm6/shLacZ in (C) in the following manner. Each plot is divided into concentric circles ranging from lowest FC (log<sub>2</sub> FC = -7, innermost circle) to highest FC (log<sub>2</sub> FC = 7, outermost circle), with the middle circle (the border between the two colors) indicating no change (log<sub>2</sub> FC = 0). Each dot on the plot represents a hotspot, and the dot size correlates with the raw numbers of translocations within that hotspot in WT cells, as shown in the key above each plot. Thus, for example, the *Igh* locus has the largest dot size in (A) to (C), indicating that it is the most frequent translocation partner of *Myc* in WT and shLacZ cells, as

expected. Dots in the blue portion of the plots in (A) to (C) represent hotspots where translocation frequency is reduced in *Myc*<sup>AORI</sup> or shMcm6 cells, and dots in the green [(A) and (B)] and red (C) portion represent hotspots with increased translocation frequency in *Myc*<sup>AORI</sup> and shMcm6 cells, respectively. The fact that the dots are located mostly in the blue portions of the plots in (A) to (C) indicates that translocation frequency is reduced at nearly all hotspots in *Myc*<sup>AORI</sup> and shMcm6 cells. Selected AID translocation hotspots found recurrently in many studies are highlighted. (D to F) Scatter dot plots showing the quantification of translocation frequency in *Myc*<sup>AORI</sup> c13 versus WT cells (D), *Myc*<sup>AORI</sup> c23 versus WT cells (E), and shMcm6 versus shLacZ cells (F). Selected hotspots [same as in (A) to (C)] are indicated as red dots. The dotted lines indicate twofold change (log<sub>2</sub> FC = 1 or -1) on either side of the diagonal. (G) Snapshot of *Myc* translocations to the *Igh* locus in the indicated conditions. The location of the various *Igh* constant region genes is indicated at the bottom. *Ighm*, *Igh2b*, and *Igha* are transcribed in these cells and thus harbor most of the translocations.



shLacZ cells, as expected given that they are the prime targets of AID in activated CH12 cells (Fig. 3, A to F). Moreover, translocations to all of these genes were strongly reduced in all conditions (Fig. 3, A to G). In addition, WT and shLacZ cells harbored several known and recurrent AID-dependent hotspots, including *Igh* and *Igl* (encoding the  $Ig\kappa$  and  $Ig\lambda$  antibody light chains, respectively), *Cd83*, *Pim1*, *Mir142*, and *Aicda* (Fig. 3, A to F, and fig. S6, A to C) (26, 27, 30, 49).

We conclude that replication origin activity at *Myc* directly regulates genome-wide AID-dependent translocation frequency at a step downstream of DSB formation and independently of DSB frequency. Moreover, we infer that the defect in AID-dependent translocations in shMcm6 cells arises due to decreased local origin activity at *Myc* and other AID target genes (Fig. 1, F to I) because the translocation phenotype of *Myc*<sup>AORI</sup> cells, where replication origin activity is locally decreased at *Myc*, is virtually identical to that of shMcm6 cells, where replication origin activity of AID targets is globally decreased.

#### DNA RT is locally perturbed at *Myc* in *Myc*<sup>AORI</sup> cells and globally abrogated in shMcm6 cells

Having established that local replication origin activity at *Myc* has a direct role in the genesis of *Myc* translocations, we investigated the underlying mechanism. Replication origin activation has been proposed to occur in clusters or hubs, in which neighboring origins in three-dimensional space are colocalized and fire synchronously (50, 51). Because this event involves the spatial proximity of replication origins, we hypothesized that shared replication timing (RT) of neighboring origins in AID target genes would also lead to the colocalization of DSBs in the vicinity of these origins. This hypothesis predicts that: (i) AID target genes have similar RT in WT cells, (ii) shMcm6 cells have altered RT of at least the AID target genes, (iii) the *Myc*<sup>AORI</sup> alleles have an altered RT compared with the WT *Myc* alleles, and (iv) *Myc-Igh* physical proximity is decreased in *Myc*<sup>AORI</sup> cells.

To measure RT, we performed Repli-seq in shMcm6 and *Myc*<sup>AORI</sup> cells. Repli-seq involves pulse-labeling of S phase cells through incorporation of BrdU into replicating DNA followed by isolation of early and late S-phase cells, genomic DNA extraction, enrichment of BrdU-labeled DNA, and quantification of enriched DNA with deep sequencing (fig. S7, A and B) (52, 53). WT and shLacZ cells showed distinct and largely nonoverlapping early and late domains (Fig. 4, A and B). RT was displayed as a log<sub>2</sub> early/late ratio (log<sub>2</sub> E/L), where early and late domains are demarcated by positive and negative values, respectively (Fig. 4, A and B). This was also visualized in metaplots showing a wide separation be-

tween early and late replication domains in WT and shLacZ cells (Fig. 4C). *Myc*<sup>AORI</sup> cells showed similar profiles to WT, although the metaplots revealed a slight shift in the early RT peak relative to WT cells (Fig. 4C), which we infer to be due to clonal variation between the *Myc*<sup>AORI</sup> and the parental WT cells. Thus, we conclude that *Myc*<sup>AORI</sup> cells do not undergo global changes in RT.

In shMcm6 cells, however, a substantial loss of all early and late domains was observed (note the raw early and late tracks in Fig. 4A). This resulted in log<sub>2</sub> early/late values close to zero manifesting as a severely flattened RT profile across the length of all chromosomes (Fig. 4, A to C). Thus, shMcm6 cells appear to undergo temporally uncoordinated replication in which any origin is capable of firing at any time in the S phase. This complete deregulation of the RT program reveals that the endogenous levels of MCM complexes are critical for establishing normal RT. These findings also demonstrate that changes in origin activity directly and profoundly affect RT.

AID-dependent translocation hotspots (Fig. 3) had a highly positive log<sub>2</sub> early/late ratio in WT and shLacZ cells, indicating that they were mostly early replicating (Fig. 4C). This profile was unchanged in *Myc*<sup>AORI</sup> cells, indicating that these cells retained early replication of AID targets (Fig. 4C). By contrast, in shMcm6 cells, these hotspots had log<sub>2</sub> early/late ratios close to zero, similar to the average genomic profile, indicating that AID targets, like the rest of the early-replicating genome, had lost their early RT potential in shMcm6 cells and now replicated in an uncoordinated manner throughout the S phase (Fig. 4C).

In contrast to the unchanged RT of other AID targets in *Myc*<sup>AORI</sup> cells, the RT profile at *Myc* in *Myc*<sup>AORI</sup> cells was markedly altered. *Myc* is located within an ~1.8-Mb early-replicating domain (Fig. 4D, top panel). At the *Myc*<sup>AORI</sup> allele, a new ~250 kb domain was created that was characterized by a continuous decrease in early RT relative to the WT allele, with the middle ~60-kb portion, which harbors *Myc*, exhibiting late replication (Fig. 4D, bottom panel zoomed-in view). The switch in RT at *Myc* was confirmed by Repli-qPCR analysis (fig. S7C). These data suggested that this new replication domain was passively replicated by replication forks originating from neighboring early RT domains in *Myc*<sup>AORI</sup> cells.

We conclude, first, that the activity of the origin of replication at *Myc* is essential to establish early RT, and, second, based on the results from shMcm6 cells, that the activity of origins of replication can have a profound impact on global RT. Thus, early RT of AID hotspots is tightly linked to the loss of translocations in both shMcm6 cells and *Myc*<sup>AORI</sup> cells.

#### Changes in RT are not associated with altered genome architecture

RT is strongly correlated with genome compartmentalization, namely, active A and silent B compartments typically replicate early and late, respectively (54). The fact that compartmentalization and RT are established concurrently after exit from mitosis has led to the proposal that these two features may be mechanistically linked (51). Given these observations, we performed Hi-C (55) to determine whether the changes in RT were accompanied by alteration in genome organization. Hi-C analysis showed that neither shMcm6 nor *Myc*<sup>AORI</sup> cells underwent major global changes in compartmentalization or topologically associating domain (TAD) integrity (Fig. 4, E and F, and fig. S7, D and E). Moreover, we detected no discernible topological changes at *Myc* in shMcm6 (Fig. 4G) or *Myc*<sup>AORI</sup> cells (Fig. 4H) or other AID target genes (fig. S7, F to K). The new, ~60-kb late RT domain at *Myc* in *Myc*<sup>AORI</sup> cells spanned approximately equally across either side of the TAD border, which is located ~6 kb upstream of *Myc* (Fig. 4H, bottom panel zoom), suggesting that the TAD boundary did not interfere with the establishment of the new late replication domain. In sum, our data show, first, that RT and genome compartmentalization are independent processes, and, second, that the decrease in AID-dependent translocations is not associated with gross alterations in locus architecture. Therefore, we conclude that the decrease of AID-dependent translocations is exclusively linked to the loss of early RT at *Myc* in *Myc*<sup>AORI</sup> cells and at AID targets globally in shMcm6 cells.

#### Re-establishing origin activity and early RT at *Myc* in *Myc*<sup>AORI</sup> cells restores normal *Myc-Igh* translocation frequency

The above results strongly suggested that altered RT was a key factor underlying the decrease in translocations in shMcm6 and *Myc*<sup>AORI</sup> cells. This led us to hypothesize that restoring RT at the *Myc*<sup>AORI</sup> allele would be sufficient to rescue *Myc* translocation frequency. Therefore, we generated a new cell line in which the deleted 800-bp *Myc* origin of replication was inserted into the intergenic space ~14 kb downstream of the *Myc*<sup>AORI</sup> allele (Fig. 5A and fig. S8, A to C), a region that lies well within the 60-kb late-replicating region created in *Myc*<sup>AORI</sup> cells (Fig. 4D). These clones, called *Myc*<sup>AORI rest c2</sup> and *Myc*<sup>AORI rest c13</sup>, were viable and proliferative, showed normal *Myc* expression (fig. S8D), and underwent efficient class-switch recombination (fig. S8, E and F). SNS-qPCR analysis showed that the *Myc* origin was active in its new location, implying that it could function autonomously, at least within the same RT domain (fig. S8G). Repli-seq (Fig. 5B) and Repli-qPCR (fig. S8H)

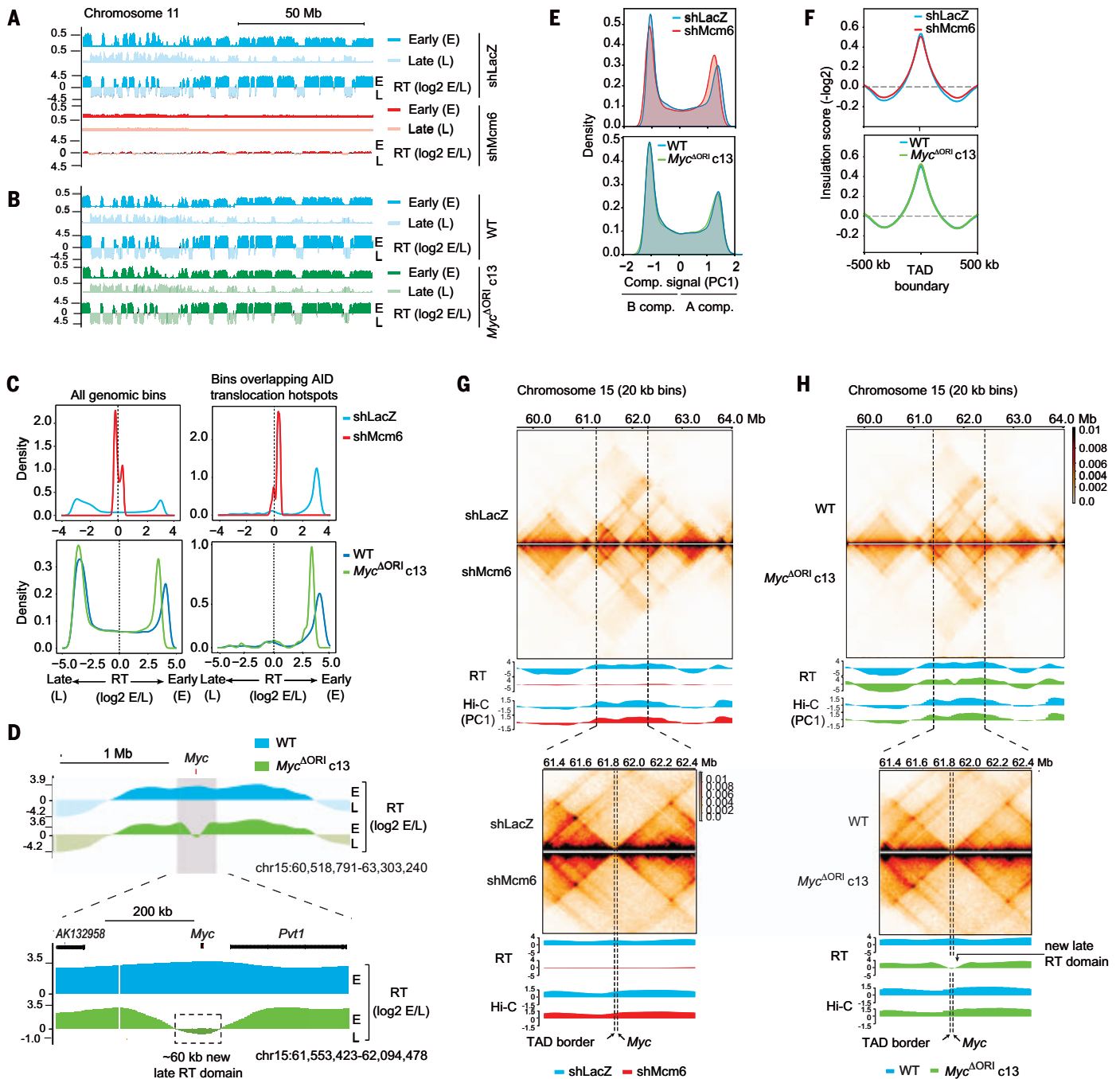
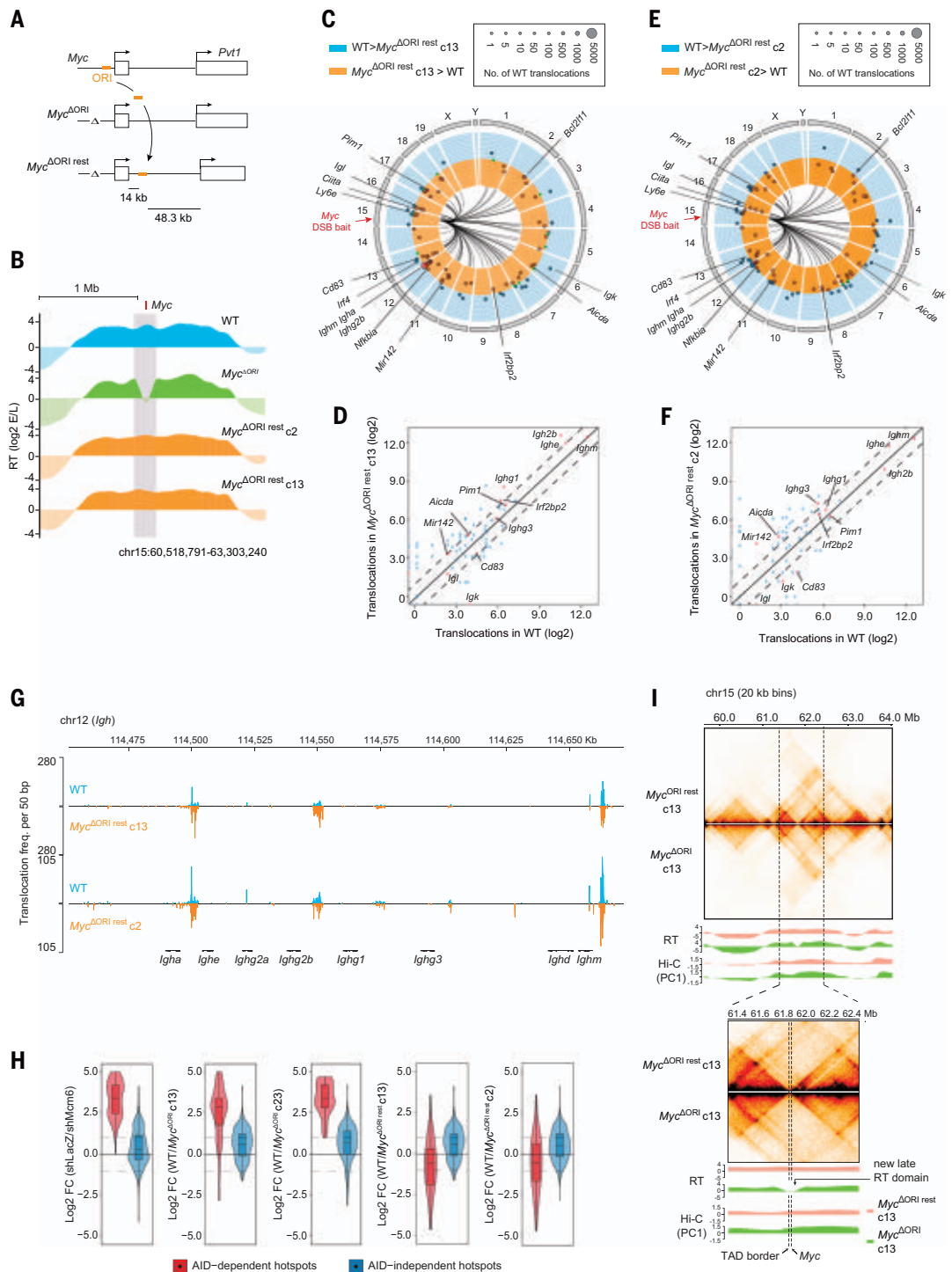


**Fig. 4. RT is globally disrupted in shMcm6 cells and locally at *Myc* in *Myc<sup>AOR1</sup>* cells.** (A) Snapshot of the whole chromosome 11 showing the individual early (E) and late (L) Repli-seq tracks followed by the RT ( $\log_2 E/L$  ratio) tracks for shLacZ and shMcm6 where positive and negative values reflect early and late RT, respectively. (B) Snapshot of chromosome 11 showing E, L, and RT tracks from WT and *Myc<sup>AOR1</sup> c13* cells. (C) Repli-seq-derived metaplots showing the RT profiles ( $\log_2 E/L$  ratio) upon *Mcm6* depletion (top) and in *Myc<sup>AOR1</sup> c13* cells (bottom). The left plots show composite genome-wide profiles, and the right plots show profiles of only AID-dependent translocation hotspots identified from LAM-HTGTS in Fig. 3. (D) RT tracks at the *Myc* locus in WT and *Myc<sup>AOR1</sup> c13* cells showing the large, 1.8-Mb early-replicating domain in WT cells (top) and a magnified view (bottom) highlighting the new, ~60-kb late RT domain created in *Myc<sup>AOR1</sup> c13* cells (boxed). (E) Histogram of Hi-C genome compartmentalization quantified as

the first principal component (PC1) from the Hi-C matrix, where positive and negative values reflect the A and B compartments, respectively. (F) Average insulation score around the boundaries of 553 TADs (400 to 900 kb) computed from a 10-kb Knight-Ruiz (KR)-normalized contact matrix. (G) Hi-C matrices at *Myc* plotted at 20-kb resolution in shLacZ and shMcm6 cells showing an ~5-Mb region with several TADs (top) and a magnified, ~1-Mb region (bottom) showing two TADs with *Myc* lying in the right TAD ~6 kb from the TAD border. Below each matrix are the Repli-seq RT tracks and genome compartmentalization tracks (Hi-C PC1). Note how the PC1 profile is unchanged in shMcm6 cells, whereas RT is strongly attenuated. (H) Hi-C matrices at *Myc* plotted at 20-kb resolution from WT and *Myc<sup>AOR1</sup> c13* cells and displayed as in (G). Note how the shift to late RT at *Myc* is not accompanied by a change in compartmentalization. Note also that TAD integrity is intact and that the new RT domain created in *Myc<sup>AOR1</sup> c13* cells spans well across the TAD border.

### Fig. 5. Early RT at *Myc* is essential for translocation genesis.

(A) Schematic showing the strategy to restore RT at *Myc* in *Myc*<sup>ΔORI</sup> cells. The 800-bp origin sequence (orange bar) deleted in *Myc*<sup>ΔORI</sup> cells (Fig. 2A) was reinserted 14 kb downstream of *Myc* in *Myc*<sup>ΔORI rest</sup> cells, and this allele is referred to as *Myc*<sup>ΔORI rest</sup>. (B) Snapshot of the RT domains at *Myc* in WT, *Myc*<sup>ΔORI</sup>, and two clones (c2 and c13) of *Myc*<sup>ΔORI rest</sup> cells. Note the complete restoration of early RT at the *Myc*<sup>ΔORI rest</sup> allele compared with *Myc*<sup>ΔORI</sup>. (C to F) LAM-HTGTS analysis of *Myc* translocations in *Myc*<sup>ΔORI rest</sup> c13 [(C) and (D)] and c2 [(E) and (F)] cells. Circos plots [(C) and (E)] and corresponding scatter plots [(D) and (F)] were generated as in Fig. 3A. (G) Snapshot of the *Igh* locus showing the distribution of *Myc* translocations in *Myc*<sup>ΔORI rest</sup> c2 and c13 cells compared with WT cells. (H) FC violin plots of translocations obtained from the LAM-HTGTS results. Hotspots were stratified as AID dependent and AID independent. (I) Hi-C analysis at the *Myc* TAD from *Myc*<sup>ΔORI rest</sup> c13 and the parental *Myc*<sup>ΔORI</sup> cells. The bottom matrix shows a magnified view of the boxed portion in the top matrix. The Repli-seq RT and Hi-C PC1 profiles are shown below the matrices.



showed that early RT was fully restored at the *Myc*<sup>ΔORI rest</sup> allele in *Myc*<sup>ΔORI rest</sup> cells. RT metaplots revealed a clear separation of early and late domains genome wide in *Myc*<sup>ΔORI rest</sup> cells, indicative of a normal RT program, although clone-specific differences were evident (fig. S8, I and J).

LAM-HTGTS showed that *Myc* translocations in both *Myc*<sup>ΔORI rest</sup> clones (c2 and c13) were restored to levels comparable to WT cells

(Fig. 5, C to F, with examples in Fig. 5G and fig. S9, A and B). In *Myc*<sup>ΔORI rest</sup> cells, translocation breakpoints at *Myc* were similar in number and distribution relative to WT and *Myc*<sup>ΔORI</sup> cells (fig. S5, C to F). By quantifying the global changes in *Myc* translocations, we confirmed that translocations in *Myc*<sup>ΔORI</sup> cells were restored to WT levels in *Myc*<sup>ΔORI rest</sup> cells (Fig. 5H). This rescue of *Myc* translocations in *Myc*<sup>ΔORI rest</sup> cells provided additional confir-

mation that the parental *Myc*<sup>ΔORI</sup> lines were not deficient in factors required for translocation, but rather only lacked early RT at *Myc*.

Next, we investigated whether changes in RT at *Myc* selectively affected AID-dependent translocations or affected *Myc* translocations generally. Therefore, we extracted 794 AID-independent *Myc* translocation hotspots, that is, hotspots observed in the absence of AIDER expression and B cell activation, and compared

them with AID-dependent translocations. Whereas AID-dependent hotspots were predominantly seen in early-replicating, transcribed regions, AID-independent hotspots were roughly equally distributed between early and late RT domains (fig. S9C) and between transcribed and silent chromatin (fig. S9D). The frequency of AID-independent *Myc* translocations was essentially unchanged in shMcm6 cells, *Myc*<sup>AORI</sup> cells, and *Myc*<sup>AORI rest</sup> cells (Fig. 5H). Thus, early RT of *Myc* is required specifically for the genesis of AID-dependent *Myc* translocations.

Finally, Hi-C analysis in *Myc*<sup>AORI rest</sup> cells did not reveal any discernible changes in chromatin architecture at *Myc* relative to the parental *Myc*<sup>AORI</sup> cells, implying that the TAD architecture was not affected by the loss of the *Myc* origin or its relocation within the *Myc* TAD (Fig. 5I, compare with Fig. 4H). We conclude that the restoration of early RT at *Myc* in *Myc*<sup>AORI rest</sup> cells is sufficient to rescue the defect in AID-dependent *Myc* translocations in the parental *Myc*<sup>AORI</sup> cells. These results provide further evidence that RT does not grossly influence locus architecture. Altogether, we show that the loss of *Myc* translocations in *Myc*<sup>AORI</sup> cells is due to the loss of origin activity and early RT at *Myc*, thus establishing RT as a critical and distinct step in translocation genesis that directly links DSB formation to DSB ligation.

#### Altered RT at *Myc* does not affect other AID-dependent translocations

Because *Myc*<sup>AORI</sup> cells suffer from loss of early RT exclusively at *Myc*, we investigated whether this local switch in RT also affects other AID-dependent translocations. We performed LAM-HTGTS using a bait in *Irf2bp2*, a major translocation partner of AID (Fig. 3, A to C). Analysis of translocation breakpoints at *Irf2bp2* showed similar numbers and distributions around the Cas9 cleavage site (fig. S10, A to D). We hypothesized that AID-dependent *Irf2bp2* translocations would be decreased genome wide upon MCM depletion, when RT is globally disrupted, but not in *Myc*<sup>AORI</sup> or *Myc*<sup>AORI rest</sup> cells. Indeed, a global decrease in AID-dependent *Irf2bp2* translocations was observed in shMcm6 cells, whereas in *Myc*<sup>AORI</sup> cells, *Irf2bp2* translocations were either unchanged or slightly increased relative to WT cells (fig. S11, A to D, and fig. S12, A and B). Closer inspection showed that translocations at normally stronger hotspots (such as all of the *Igh* genes, *Igk*, and *Igl*) were not affected in *Myc*<sup>AORI</sup> cells; however, at normally weaker hotspots, an increase in translocations was observed in *Myc*<sup>AORI</sup> cells (fig. S11D). We suspect that this was caused by clonal differences influencing the results at weak hotspots that harbor few translocations and where fluctuations result in larger FCs. In *Myc*<sup>AORI rest</sup>

cells, *Irf2bp2* translocations were comparable to WT cells (fig. S11, E and F, and fig. S12C).

Quantifying and comparing the results from the *Irf2bp2* bait with the *Myc* counterpart, we found that only MCM knockdown globally affected *Irf2bp2* translocations (fig. S11G, compare with Fig. 5H). *Irf2bp2*-*Myc* translocations were decreased in *Myc*<sup>AORI</sup> cells and restored in *Myc*<sup>AORI rest</sup> cells (fig. S11H). By contrast, *Irf2bp2*-*Igh* translocations were not decreased in *Myc*<sup>AORI</sup> or *Myc*<sup>AORI rest</sup> cells (fig. S11I). We conclude that MCM complex levels regulate AID-dependent *Myc* and *Irf2bp2* translocations genome wide, whereas the loss of AID-dependent translocations in *Myc*<sup>AORI</sup> cells is specific to *Myc* translocations.

#### *Myc*-*Igh* nuclear proximity is RT dependent

Translocations can only occur when partner loci are in physical proximity within the nucleus. AID target genes, including *Myc* and *Igh*, have been found to colocalize in B cell nuclei (56–58). On the basis of our hypothesis that shared RT of *Myc* and *Igh* drives their proximity and results in the colocalization of DSBs, we investigated whether the loss of early RT at *Myc* reduces its proximity to the *Igh* locus. Because chromosomal territories vary from cell to cell, such physical contacts between any pair of loci are expected to be extremely infrequent, making their detection and statistical evaluation from Hi-C data very challenging. Therefore, we performed chromosome conformation capture with qPCR (3C-qPCR) using TaqMan probes (Fig. 6A) to investigate *Myc*-*Igh* nuclear proximity. Interactions between *Myc* and *Igh* were observed in WT and shLacZ cells (Fig. 6, B and C). PCR products were sequenced to confirm the presence of the expected 3C ligation product containing a HindIII site (fig. S13A). *Myc*-*Igh* interaction frequency was significantly reduced in shMcm6 cells ( $P = 0.028$ ) and *Myc*<sup>AORI</sup> cells ( $P = 0.016$ ) (Fig. 6, B and C) and was restored to WT levels in *Myc*<sup>AORI rest</sup> cells (Fig. 6C).

As a control, we also investigated the known interaction of *Myc* with its superenhancer located ~190 kb downstream within the *Pvt1* gene, an interaction not easily resolvable by Hi-C. *Myc*-*Pvt1* interactions were unchanged in shMcm6, *Myc*<sup>AORI</sup>, and *Myc*<sup>AORI rest</sup> cells (Fig. 6, B and C), which is consistent with the normal levels of *Myc* transcripts observed in all of these conditions. This finding also indicates that intra-TAD *cis*-regulatory contacts of *Myc* are not influenced by changes in RT and supports the notion from Hi-C analyses that there are no gross changes in TAD architecture when the normal RT program is disrupted.

We conclude that the proximity of *Myc* and *Igh* in the nucleus is RT dependent, and that the loss of *Myc*-*Igh* translocations in shMcm6 and in *Myc*<sup>AORI</sup> cells is due to impaired *Myc*-*Igh* colocalization.

#### AF4-MLL1 and BCL6-IGH translocation frequency correlates with early RT

To expand on the role of early RT in translocation genesis in other systems, we focused on two well-studied tumorigenic translocations, the leukemia-associated *AF4*-*MLL1* translocation in human leukemic K562 cells and the B lymphoma-associated *BCL6*-*IGH* translocation in the human B lymphoma cell line Ramos. In both cases, we generated translocations using Cas9 and gene-specific sgRNAs and quantified translocations with digital-droplet PCR (ddPCR) (Fig. 6D, fig. S13B, and table S4). *AF4*-*MLL1* translocations were readily detected and confirmed by Sanger sequencing (fig. S13C). Translocations were strongly reduced upon depletion of *MCM6* with two different shRNAs, shMCM6\_1 and shMCM6\_2 (Fig. 6, E and F, and fig. S13D). We confirmed that *MCM6* depletion did not alter the expression of *AF4* and *MLL1* but did strongly reduce *MCM6* expression, as expected (Fig. 6G). Moreover, *MCM6* depletion did not lead to defects in cell proliferation (fig. S13E), whereas cell cycle analysis revealed a slight block in the G<sub>2</sub>/M phase, likely due to G<sub>2</sub>/M checkpoint activation (fig. S13, F and G). The percentage of indels at the Cas9 cleavage site in both *AF4* and *MLL1* was comparable between the shRenilla control and shMCM6 cells, implying that Cas9 cleavage activity was similarly efficient in both conditions (fig. S13H). Repli-qPCR analysis showed that both *AF4* and *MLL1* are normally early-replicating, in agreement with analysis of Repli-seq data in K562 cells obtained from a previous study (54) (Fig. 6H and fig. S13I). *MCM6* depletion led to a slightly delayed RT of *MLL1*, but to a complete switch of RT at *AF4* from early to late replication (Fig. 6H). *MCM6* depletion also impaired RT of two conserved early-replicating loci (*HBB* and *BMP1*), but not late-replicating loci (*NETO1* and *ZFP42*) (Fig. 6H) (52).

As an alternative means of perturbing RT without depleting MCM complexes, we treated K562 cells with aphidicolin (fig. S13, J and K). Similar to our findings with *Myc*-*Igh* translocations in CH12 cells (Fig. 1E), we observed decreased *AF4*-*MLL1* translocations (Fig. 6, I and J). This was accompanied by a switch from early to late replication at *AF4* (Fig. 6K) but no changes in *AF4* or *MLL1* gene expression (fig. S13L). Aphidicolin also disrupted early and late RT of conserved early- and late-replicating genes (Fig. 6K), consistent with its ability to cause global changes in RT (59). We conclude that *AF4*-*MLL1* translocations correlate with the shared early RT of *AF4* and *MLL1* in K562 cells. This provides further evidence that disrupting synchronized early RT of partner loci results in a loss of translocations.

In Ramos cells, *BCL6*-*IGH* translocations induced by Cas9 were readily detected (fig. S14, A and B). In these cells, *MCM6* depletion

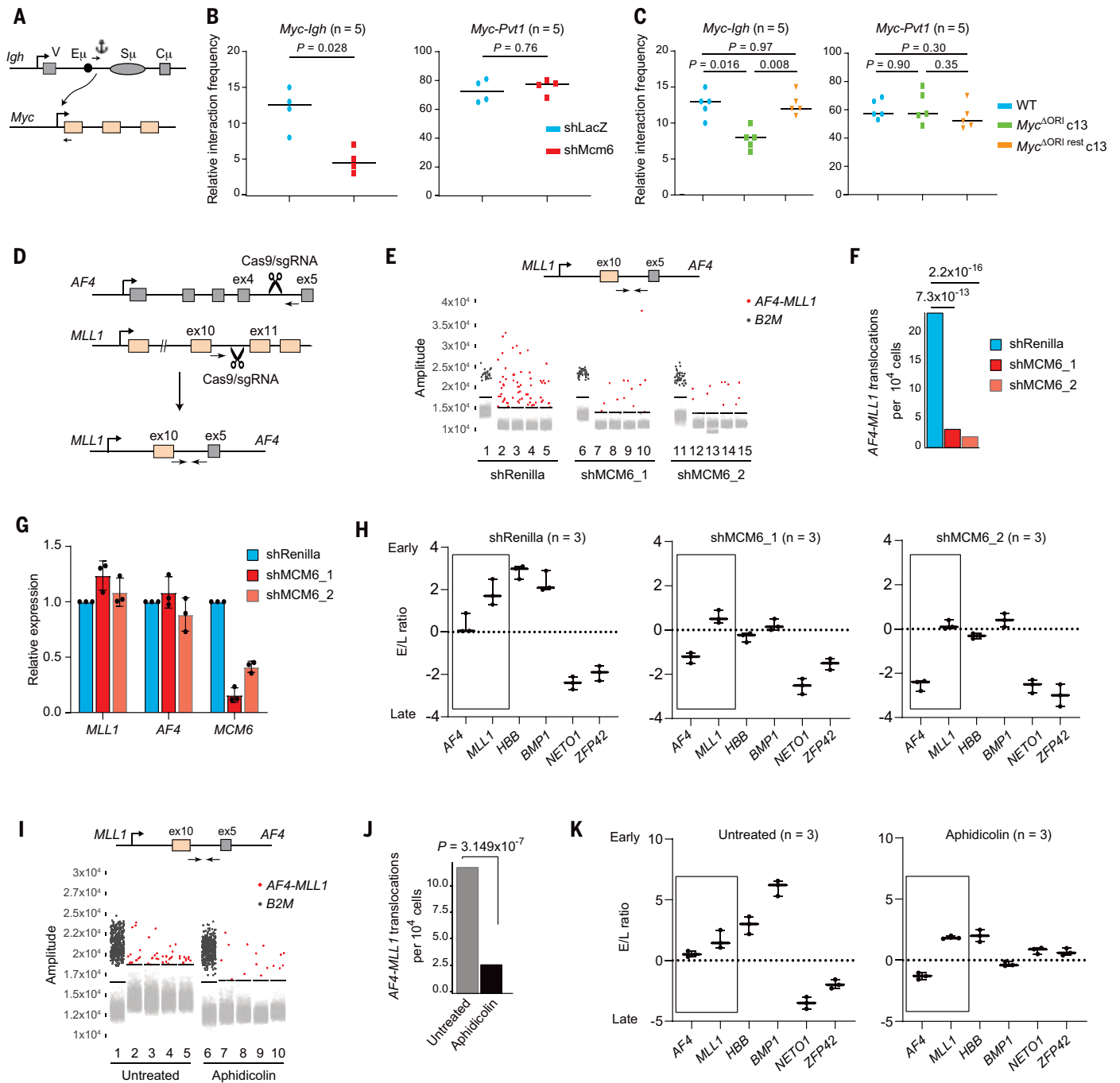


**Fig. 6. *Myc-Igh* proximity is RT dependent, and cancer-associated translocations in human cells correlate with shared early RT of partner loci.**

(A) Diagram showing the *Myc-Igh* interaction being probed by chromosome conformation capture (3C)-qPCR. (B) 3C-qPCR analysis of *Myc-Igh* (left) and *Myc-Pvt1* (right) interaction frequency in shLacZ and shMcm6 cells from four independent experiments. Statistical analyses were performed with the unpaired Student's *t* test. (C) 3C-qPCR analysis for *Myc-Igh* (left) and *Myc-Pvt1* (right) interaction in WT, *Myc*<sup>ΔORI</sup>, and *Myc*<sup>ΔORI rest c13</sup> cells. (D) Diagram illustrating the sgRNA cleavage sites in *AF4* and *MLL1* and the resulting *AF4-MLL1* translocation in K562 cells. The location of PCR primers is indicated. (E) Analysis of *AF4-MLL1* translocations by ddPCR in shRenilla and shMCM6 cells. Two shRNAs against *MCM6* were used: shMCM6\_1 and shMCM6\_2. The results shown are from one of three independent experiments. Five reactions were performed for the translocation event (lanes 2 to 5 for shRenilla, lanes 7 to 10 for shMCM6\_1, and

lanes 12 to 15 for shMCM6\_2), and one reaction was performed for the reference, *B2M* (lanes 1, 6, and 11), which was used to determine the amount of total DNA from which the total number of cells is calculated (see the materials and methods). Fluorescence-negative droplets are indicated in gray, and the amplitude threshold separating the negative from the positive events is indicated by black lines. Each red dot is a fluorescence-positive translocation PCR product, each black dot is a fluorescence-positive *B2M* PCR product, and each gray dot is a PCR reaction without a product. The amplitude (y axis) measures the fluorescence intensity of each droplet. (F) Quantification of the ddPCR results from three independent experiments as described in the materials and methods. Statistical analyses were performed with Fisher's exact test. (G) Reverse transcription qPCR analysis of *AF4*, *MLL1*, and *MCM6* expression in K562 cells in shRenilla and shMCM6 cells. *HBB* and *BMP1* are conserved, early-replicating genes, and *NETO1* and *ZFP42* are conserved,

late-replicating genes. Data are from three independent experiments.

**(H)** Repli-qPCR analysis from three independent experiments to measure RT at *AF4* and *MLL1* after shMcm6 knockdown in K562 cells. **(I)** *AF4-MLL1* translocation ddPCR analysis as described above in (E) in untreated and aphidicolin-treated K562 cells. The results from one of three independent experiments are shown. Five reactions were performed for the translocation

was inefficient, and we did not detect changes in RT or *BCL6-IGH* translocation frequency. However, treatment of Ramos cells with aphidicolin led to a significant loss of *BCL6-IGH* translocations ( $P = 5.3 \times 10^{-6}$ ; fig. S14, A to D) accompanied by delayed RT of both partner loci, especially *BCL6*, which switched from early to late replication (fig. S14F). As in K562 cells, aphidicolin also affected RT of conserved early- and late-replicating genes in Ramos cells (fig. S14F). No changes in nascent transcription were observed at either partner gene (fig. S14G).

Taken together, these results reveal that synchronized early RT of translocation partner loci contributes to the genesis of not only AID-dependent translocations in murine B cells, but also tumorigenic translocations in human B cells and human non-B cells, establishing RT-driven translocation genesis as a general mechanism for driving translocation biogenesis across cell types and species.

## Discussion

Our results show that early RT directly regulates the genesis of AID-dependent *Myc* translocations downstream of DSB formation and suggest that shared RT drives the physical proximity of translocation partner loci. How might shared early RT drive translocation genesis? In the context of gene regulation, recent *in vivo* imaging studies suggest that contacts between enhancers and promoters form through multivalent interactions between transcription factors and cofactors, resulting in phase-separated transcription hubs consisting of a high concentration of proteins required for optimal gene activation (60, 67). Although such hubs have not been reported during replication *in vivo*, ORC, Cdc6, and Cdt1, essential components of the prereplication complex, were shown to form phase-separated condensates *in vitro* that could efficiently recruit MCM complexes (62). On the basis of these studies, we suggest that in cells in which AID target genes are located in neighboring chromosome territories, the activation of early replication origins may occasionally occur synchronously through the congregation of neighboring origins, perhaps forming a phase-separated hub, the stability of which may be further reinforced by the presence of DNA repair proteins (putative replication-repair hub; fig. S15) (62). Such a process would bring DSBs located near the origins into temporal and physical proximity and promote translocation (fig. S15). Therefore, if origins

in partner loci are not activated synchronously (such as in *Myc*<sup>AORI</sup> cells or shMcm6 cells), then origin congregation would be inefficient such that DSBs (even when introduced at high frequency through Cas9) interact less often, resulting in fewer translocations (fig. S15). The residual translocations seen in *Myc*<sup>AORI</sup> cells and shMcm6 cells may occur through random interactions of *trans* DSBs between neighboring TADs and reflect the baseline frequency of translocation. Because AID-dependent DSBs are ligated through nonhomologous end-joining DNA repair pathways, which are inefficient as cells progress into the S phase, DSB ligation would need to occur in the early S phase, coinciding with the RT of AID target loci. In our system, early RT at *Myc* is linked to the activation of the *Myc* origin of replication. Thus, we cannot rule out that the initiation of replication also plays a role in translocation biogenesis in addition to early replication of the locus.

In summary, we describe a step in translocation genesis regulated by the activity of early replication origins and early RT that we propose promotes DSB synopsis and thereby physically links DSB formation to DSB ligation. Translocation breakpoints in several cancers have been correlated with early RT and transcriptional activity (63–66), but whether early RT is causal for translocation genesis was unknown. In particular, early RT was correlated with *trans* translocations and late RT with *cis* translocations in solid tumors, namely prostate and breast tumors (65). This suggests that the principle of RT-mediated translocation genesis that we propose for B lymphoma- and leukemia-associated translocations would apply to both nonsolid and solid tumors. On the basis of the observations that replication origin activity is higher in transcribed, early-replicating regions than in silent, late-replicating regions (44, 45, 67–71), we propose that having more licensed origins in the genomic neighborhood increases the probability of active replication origins congregating in *trans*— and thus of *trans* translocation. Because such a scenario is more likely between neighboring, early-replicating A compartments, which have more licensed origins, the likelihood of *trans* translocations is higher in these regions. Conversely, late-replicating heterochromatin domains have fewer licensed origins that will be less likely to congregate in *trans*, and so DSBs here will be more likely to recombine in *cis*.

event (lanes 2 to 5 for untreated samples and lanes 7 to 10 for aphidicolin-treated samples), and one reaction was performed for the reference, B2M (lanes 1 and 6). **(J)** Quantification of the ddPCR results as in (F). Statistical analyses were performed with Fisher's exact test. **(K)** Repli-qPCR analysis as in (H) from three independent experiments in untreated and aphidicolin-treated K562 cells.

We anticipate that our findings could provide the conceptual and experimental framework needed for a deeper exploration of the role of RT in different cancer contexts and for the development of targeted therapeutic interventions aimed at mitigating oncogenic translocations. It is plausible that altering RT without affecting genome architecture or gene expression could be a viable means of decreasing the incidence of deleterious translocations. A deeper understanding of the pathways regulating RT is therefore necessary to yield candidate factors that, when inhibited, could reduce the frequency of tumorigenic translocations.

## Methods summary

A full description of the methods can be found in the supplementary materials (72). This includes descriptions of the generation of new cell lines, viral infections, RNA-seq, proteomics, SNS-seq, Repli-seq, Hi-C, LAM-HTGTs, and statistical tests and bioinformatics analyses.

## REFERENCES AND NOTES

- J. Chaudhuri, F. W. Alt, Class-switch recombination: Interplay of transcription, DNA deamination and DNA repair. *Nat. Rev. Immunol.* **4**, 541–552 (2004). doi: 10.1038/nri1395; pmid: 15229473
- S. P. Methot, J. M. Di Noia, Molecular mechanisms of somatic hypermutation and class switch recombination. *Adv. Immunol.* **133**, 37–87 (2017). doi: 10.1016/bs.ai.2016.11.002; pmid: 28215280
- R. Casellas *et al.*, Mutations, kataegis and translocations in B cells: Understanding AID promiscuous activity. *Nat. Rev. Immunol.* **16**, 164–176 (2016). doi: 10.1038/nri.2016.2; pmid: 26898111
- C. Keim, D. Kazadi, G. Rothschild, U. Basu, Regulation of AID, the B-cell genome mutator. *Genes Dev.* **27**, 1–17 (2013). doi: 10.1101/gad.200014.112; pmid: 23307864
- R. Pavri, M. C. Nussenzweig, AID targeting in antibody diversity. *Adv. Immunol.* **110**, 1–26 (2011). doi: 10.1016/B978-0-12-387663-8.00005-3; pmid: 21762814
- J. Stavnezer, C. E. Schrader, IgH chain class switch recombination: Mechanism and regulation. *J. Immunol.* **193**, 5370–5378 (2014). doi: 10.4049/jimmunol.1401849; pmid: 25411432
- M. Muramatsu *et al.*, Class switch recombination and hypermutation require activation-induced cytidine deaminase (AID), a potential RNA editing enzyme. *Cell* **102**, 553–563 (2000). doi: 10.1016/S0092-8674(00)00078-7; pmid: 11007474
- P. Revy *et al.*, Activation-induced cytidine deaminase (AID) deficiency causes the autosomal recessive form of the Hyper-IgM syndrome (HIGM2). *Cell* **102**, 565–575 (2000). doi: 10.1016/S0092-8674(00)00079-9; pmid: 11007475
- S. K. Petersen-Mahrt, R. S. Harris, M. S. Neuberger, AID mutates *E. coli* suggesting a DNA deamination mechanism for antibody diversification. *Nature* **418**, 99–104 (2002). doi: 10.1038/nature00862; pmid: 12097915
- A. R. Ramiro, P. Stavropoulos, M. Jankovic, M. C. Nussenzweig, Transcription enhances AID-mediated cytidine deamination by exposing single-stranded DNA on the nontemplate strand. *Nat. Immunol.* **4**, 452–456 (2003). doi: 10.1038/nri920; pmid: 12692548

11. L. Pasqualucci *et al.*, AID is required for germinal center-derived lymphomagenesis. *Nat. Genet.* **40**, 108–112 (2008). doi: 10.1038/ng.2007.35; pmid: 18066064
12. L. Pasqualucci, A. Neri, L. Baldini, R. Dalla-Favera, A. Migliozza, BCL-6 mutations are associated with immunoglobulin variable heavy chain mutations in B-cell chronic lymphocytic leukemia. *Cancer Res.* **60**, 5644–5648 (2000). pmid: 11059755
13. L. Pasqualucci *et al.*, Hypermutation of multiple proto-oncogenes in B-cell diffuse large-cell lymphoma. *Nature* **412**, 341–346 (2001). doi: 10.1038/35085588; pmid: 11460166
14. R. Dalla-Favera, S. Martinotti, R. C. Gallo, J. Erikson, C. M. Croce, Translocation and rearrangements of the c-myc oncogene locus in human undifferentiated B-cell lymphomas. *Science* **219**, 963–967 (1983). doi: 10.1126/science.6401867; pmid: 6401867
15. P. H. Hamlyn, T. H. Rabbitts, Translocation joins c-myc and immunoglobulin gamma 1 genes in a Burkitt lymphoma revealing a third exon in the c-myc oncogene. *Nature* **304**, 135–139 (1983). doi: 10.1038/304135a0; pmid: 6306472
16. T. H. Rabbitts, A. Forster, P. Hamlyn, R. Baer, Effect of somatic mutation within translocated c-myc genes in Burkitt's lymphoma. *Nature* **309**, 592–597 (1984). doi: 10.1038/309592a0; pmid: 6547209
17. H. M. Shen, A. Peters, B. Baron, X. Zhu, U. Storb, Mutation of BCL-6 gene in normal B cells by the process of somatic hypermutation of Ig genes. *Science* **280**, 1750–1752 (1998). doi: 10.1126/science.280.5370.1750; pmid: 9624052
18. M. Liu *et al.*, Two levels of protection for the B cell genome during somatic hypermutation. *Nature* **451**, 841–845 (2008). doi: 10.1038/nature06547; pmid: 18273020
19. K. Basso, R. Dalla-Favera, Germinal centres and B cell lymphomagenesis. *Nat. Rev. Immunol.* **15**, 172–184 (2015). doi: 10.1038/nri3814; pmid: 25712152
20. D. F. Robbiani, M. C. Nussenzweig, Chromosome translocation, B cell lymphoma, and activation-induced cytidine deaminase. *Annu. Rev. Pathol.* **8**, 79–103 (2013). doi: 10.1146/annurev-pathol-020712-164004; pmid: 22974238
21. M. Gostissa, F. W. Alt, R. Chiarle, Mechanisms that promote and suppress chromosomal translocations in lymphocytes. *Annu. Rev. Immunol.* **29**, 319–350 (2011). doi: 10.1146/annurev-immunol-031210-101329; pmid: 21219174
22. D. F. Robbiani *et al.*, AID produces DNA double-strand breaks in non-Ig genes and mature B cell lymphomas with reciprocal chromosome translocations. *Mol. Cell* **36**, 631–641 (2009). doi: 10.1016/j.molcel.2009.11.007; pmid: 19941823
23. D. F. Robbiani *et al.*, Plasmodium infection promotes genomic instability and AID-dependent B cell lymphoma. *Cell* **162**, 727–737 (2015). doi: 10.1016/j.cell.2015.07.019; pmid: 26276629
24. M. Jankovic *et al.*, 53BP1 alters the landscape of DNA rearrangements and suppresses AID-induced B cell lymphoma. *Mol. Cell* **49**, 623–631 (2013). doi: 10.1016/j.molcel.2012.11.029; pmid: 23290917
25. D. F. Robbiani *et al.*, AID is required for the chromosomal breaks in c-myc that lead to c-myc/IgH translocations. *Cell* **135**, 1028–1038 (2008). doi: 10.1016/j.cell.2008.09.062; pmid: 19070574
26. I. A. Klein *et al.*, Translocation-capture sequencing reveals the extent and nature of chromosomal rearrangements in B lymphocytes. *Cell* **147**, 95–106 (2011). doi: 10.1016/j.cell.2011.07.048; pmid: 21962510
27. R. Chiarle *et al.*, Genome-wide translocation sequencing reveals mechanisms of chromosome breaks and rearrangements in B cells. *Cell* **147**, 107–119 (2011). doi: 10.1016/j.cell.2011.07.049; pmid: 21962511
28. A. R. Ramiro *et al.*, Role of genomic instability and p53 in AID-induced c-myc-IgH translocations. *Nature* **440**, 105–109 (2006). doi: 10.1038/nature04495; pmid: 16400328
29. A. R. Ramiro *et al.*, AID is required for c-myc/IgH chromosome translocations in vivo. *Cell* **118**, 431–438 (2004). doi: 10.1016/j.cell.2004.08.006; pmid: 15315756
30. R. A. Panchakshari *et al.*, DNA double-strand break response factors influence end-joining features of IgH class switch and general translocation junctions. *Proc. Natl. Acad. Sci. U.S.A.* **115**, 762–767 (2018). doi: 10.1073/pnas.1719988115; pmid: 29311308
31. T. Doi *et al.*, The C-terminal region of activation-induced cytidine deaminase is responsible for a recombination function other than DNA cleavage in class switch recombination. *Proc. Natl. Acad. Sci. U.S.A.* **106**, 2758–2763 (2009). doi: 10.1073/pnas.0813253106; pmid: 19202055
32. T. Doi, K. Kinoshita, M. Ikegawa, M. Muramatsu, T. Honjo, De novo protein synthesis is required for the activation-induced cytidine deaminase function in class-switch recombination. *Proc. Natl. Acad. Sci. U.S.A.* **100**, 2634–2638 (2003). doi: 10.1073/pnas.0437710100; pmid: 12591955
33. R. Pavri *et al.*, Activation-induced cytidine deaminase targets DNA at sites of RNA polymerase II stalling by interaction with Spt5. *Cell* **143**, 122–133 (2010). doi: 10.1016/j.cell.2010.09.017; pmid: 20887897
34. C. H. Chuang, M. D. Wallace, C. Abratte, T. Southard, J. C. Schimenti, Incremental genetic perturbations to MCM2-7 expression and subcellular distribution reveal exquisite sensitivity of mice to DNA replication stress. *PLOS Genet.* **6**, e1001110 (2010). doi: 10.1371/journal.pgen.1001110; pmid: 20838603
35. N. Shima *et al.*, A viable allele of Mcm4 causes chromosome instability and mammary adenocarcinomas in mice. *Nat. Genet.* **39**, 93–98 (2007). doi: 10.1038/ng1936; pmid: 17143284
36. G. D. Victoria, M. C. Nussenzweig, Germinal centers. *Annu. Rev. Immunol.* **30**, 429–457 (2012). doi: 10.1146/annurev-immunol-020711-075032; pmid: 22224772
37. X. Q. Ge, D. A. Jackson, J. J. Blow, Dormant origins licensed by excess Mcm2-7 are required for human cells to survive replicative stress. *Genes Dev.* **21**, 3331–3341 (2007). doi: 10.1101/gad.457807; pmid: 18079179
38. M. E. Hubbi, W. Luo, J. H. Baek, G. L. Semenza, MCM proteins are negative regulators of hypoxia-inducible factor 1. *Mol. Cell* **42**, 700–712 (2011). doi: 10.1016/j.molcel.2011.03.029; pmid: 21658608
39. A. Ibarra, E. Schwob, J. Méndez, Excess MCM proteins protect human cells from replicative stress by licensing backup origins of replication. *Proc. Natl. Acad. Sci. U.S.A.* **105**, 8956–8961 (2008). doi: 10.1073/pnas.0803978105; pmid: 18579778
40. D. Kunnev *et al.*, DNA damage response and tumorigenesis in Mcm2-deficient mice. *Oncogene* **29**, 3630–3638 (2010). doi: 10.1038/onc.2010.125; pmid: 20440269
41. A. M. Woodward *et al.*, Excess Mcm2-7 license dormant origins of replication that can be used under conditions of replicative stress. *J. Cell Biol.* **173**, 673–683 (2006). doi: 10.1083/jcb.200602108; pmid: 16754955
42. E. M. Wiedemann, M. Peycheva, R. Pavri, DNA replication origins in immunoglobulin switch regions regulate class switch recombination in an R-loop-dependent manner. *Cell Rep.* **17**, 2927–2942 (2016). doi: 10.1016/j.celrep.2016.11.041; pmid: 27974207
43. M. L. Bochman, A. Schwacha, The Mcm complex: Unwinding the mechanism of a replicative helicase. *Microbiol. Mol. Biol. Rev.* **73**, 652–683 (2009). doi: 10.1128/MMBR.00019-09; pmid: 19946136
44. R. Lombrana *et al.*, High-resolution analysis of DNA synthesis start sites and nucleosome architecture at efficient mammalian replication origins. *EMBO J.* **32**, 2631–2644 (2013). doi: 10.1038/emboj.2013.195; pmid: 23995398
45. C. Cayrou *et al.*, Genome-scale analysis of metazoan replication origins reveals their organization in specific but flexible sites defined by conserved features. *Genome Res.* **21**, 1438–1449 (2011). doi: 10.1101/gr.121830.111; pmid: 21750104
46. H. Fu *et al.*, Mapping replication origin sequences in eukaryotic chromosomes. *Curr. Protoc. Cell Biol.* **65**, 201–17, 17 (2014). doi: 10.1002/0471143030.cb2220s65; pmid: 25447077
47. D. B. Mahat *et al.*, Base-pair-resolution genome-wide mapping of active RNA polymerases using precision nuclear run-on (PRO-seq). *Nat. Protoc.* **11**, 1455–1476 (2016). doi: 10.1038/nprot.2016.086; pmid: 27442863
48. J. Hu *et al.*, Detecting DNA double-stranded breaks in mammalian genomes by linear amplification-mediated high-throughput genome-wide translocation sequencing. *Nat. Protoc.* **11**, 853–871 (2016). doi: 10.1038/nprot.2016.043; pmid: 27031497
49. E. Pefanis *et al.*, Noncoding RNA transcription targets AID to divergently transcribed loci in B cells. *Nature* **514**, 389–393 (2014). doi: 10.1038/nature13580; pmid: 25119026
50. M. Fragkos, O. Ganier, P. Coulombe, M. Méchali, DNA replication origin activation in space and time. *Nat. Rev. Mol. Cell Biol.* **16**, 360–374 (2015). doi: 10.1038/nrm4002; pmid: 25999062
51. C. Marchal, J. Sima, D. M. Gilbert, Control of DNA replication timing in the 3D genome. *Nat. Rev. Mol. Cell Biol.* **20**, 721–737 (2019). doi: 10.1038/s41580-019-0162-y; pmid: 31477886
52. T. Ryba, D. Battaglia, B. D. Pope, I. Hiratani, D. M. Gilbert, Genome-scale analysis of replication timing: From bench to bioinformatics. *Nat. Protoc.* **6**, 870–895 (2011). doi: 10.1038/nprot.2011.328; pmid: 21637205
53. C. Marchal *et al.*, Genome-wide analysis of replication timing by next-generation sequencing with E/L Repli-seq. *Nat. Protoc.* **13**, 819–839 (2018). doi: 10.1038/nprot.2017.148; pmid: 29599440
54. B. D. Pope *et al.*, Topologically associating domains are stable units of replication-timing regulation. *Nature* **515**, 402–405 (2014). doi: 10.1038/nature13986; pmid: 25409831
55. S. S. Rao *et al.*, A 3D map of the human genome at kilobase resolution reveals principles of chromatin looping. *Cell* **159**, 1665–1680 (2014). doi: 10.1016/j.cell.2014.11.021; pmid: 25497547
56. P. P. Rocha *et al.*, Close proximity to Igh is a contributing factor to AID-mediated translocations. *Mol. Cell* **47**, 873–885 (2012). doi: 10.1016/j.molcel.2012.06.036; pmid: 22864115
57. C. S. Osborne *et al.*, Myc dynamically and preferentially relocates to a transcription factory occupied by Igh. *PLOS Biol.* **5**, e192 (2007). doi: 10.1371/journal.pbio.0050192; pmid: 17622196
58. J. J. Roix, P. G. McQueen, P. J. Munson, L. A. Parada, T. Misteli, Spatial proximity of translocation-prone gene loci in human lymphomas. *Nat. Genet.* **34**, 287–291 (2003). doi: 10.1038/ng1177; pmid: 12808455
59. L. Courtot *et al.*, Low replicative stress triggers cell-type specific inheritable advanced replication timing. *Int. J. Mol. Sci.* **22**, 4959 (2021). doi: 10.3390/ijms22094959; pmid: 34066960
60. S. Chong *et al.*, Imaging dynamic and selective low-complexity domain interactions that control gene transcription. *Science* **361**, eaar2555 (2018). doi: 10.1126/science.aar2555; pmid: 29930090
61. S. Chong *et al.*, Tuning levels of low-complexity domain interactions to modulate endogenous oncogenic transcription. *Mol. Cell* **82**, 2084–2097.e5 (2022). doi: 10.1016/j.molcel.2022.04.007; pmid: 35483357
62. M. W. Parker *et al.*, A new class of disordered elements controls DNA replication through initiator self-assembly. *eLife* **8**, e48562 (2019). doi: 10.7554/eLife.48562; pmid: 31560342
63. I. Janoueix-Lerosey *et al.*, Preferential occurrence of chromosome breakpoints within early replicating regions in neuroblastoma. *Cell Cycle* **4**, 1842–1846 (2005). doi: 10.4161/cc.4.12.2257; pmid: 16294040
64. M. Shugay, I. Ortiz de Mendivil, J. L. Vizmanos, F. J. Novo, Genomic hallmarks of genes involved in chromosomal translocations in hematological cancer. *PLOS Comput. Biol.* **8**, e1002797 (2012). doi: 10.1371/journal.pcbi.1002797; pmid: 23236267
65. Q. Du *et al.*, Replication timing and epigenome remodelling are associated with the nature of chromosomal rearrangements in cancer. *Nat. Commun.* **10**, 416 (2019). doi: 10.1038/s41467-019-08302-1; pmid: 30679435
66. J. Sima, D. M. Gilbert, Complex correlations: Replication timing and mutational landscapes during cancer and genome evolution. *Curr. Opin. Genet. Dev.* **25**, 93–100 (2014). doi: 10.1016/j.cde.2013.11.022; pmid: 24598232
67. I. Akerman *et al.*, A predictable conserved DNA base composition signature defines human core DNA replication origins. *Nat. Commun.* **11**, 4826 (2020). doi: 10.1038/s41467-020-18527-0; pmid: 32958757
68. C. Cayrou *et al.*, The chromatin environment shapes DNA replication origin organization and defines origin classes. *Genome Res.* **25**, 1873–1885 (2015). doi: 10.1101/gr.192799.115; pmid: 26560631
69. J. C. Cadoret *et al.*, Genome-wide studies highlight indirect links between human replication origins and gene regulation. *Proc. Natl. Acad. Sci. U.S.A.* **105**, 15837–15842 (2008). doi: 10.1073/pnas.0805208105; pmid: 18838675
70. F. Comoglio *et al.*, High-resolution profiling of Drosophila replication start sites reveals a DNA shape and chromatin signature of metazoan origins. *Cell Rep.* **11**, 821–834 (2015). doi: 10.1016/j.celrep.2015.03.070; pmid: 25921534
71. E. Besnard *et al.*, Unraveling cell type-specific and reprogrammable human replication origin signatures associated with G-quadruplex consensus motifs. *Nat. Struct. Mol. Biol.* **19**, 837–844 (2012). doi: 10.1038/nsmb.2339; pmid: 22751019
72. See the supplementary materials and methods.

## ACKNOWLEDGMENTS

We thank the Vienna Biocenter Core Facilities (VBCF) for next-generation sequencing and recombinant Cre protein and sgRNA synthesis; the IMP/IMBA core facilities, especially the animal house for maintenance of mice, bio-optics for flow cytometry support, molecular biology service for Sanger sequencing, and proteomics service for mass spectrometry; P. Reschender (Oxford Nanopore Technologies), D. Handler (IMBA), and L. Leidecker (IMP) for valuable input on setting up the MiniON platform and supply of essential reagents;

A. Goloborodko (IMBA) and R. Stocsits (IMP) for advice on Hi-C data analysis; J. Zuber (IMP), M. Fellner (IMP), and M. Hinterndorfer (IMP) for providing K562-iCas9 cells, plasmids for shRNA cloning, and shRNA sequences for human MCM6; and M. Busslinger (IMP), A. Stark (IMP), D. Gerlich (IMBA), C. Plaschka (IMP), and I. Patten for critical reading of the manuscript. **Funding:** This work was funded by Boehringer Ingelheim, the Austrian Industrial Research Promotion Agency (headquarter grant FFG-834223), and the Austrian Science Fund (grant FWF P 29163-B26 to R.P.). **Author contributions:** M.P. designed and performed translocation assays, ddPCR, SNS-seq, SNS-qPCR, RNA-seq, LAM-HTGTS, Repli-qPCR, Repli-seq, and Hi-C; generated and characterized all cell lines; and analyzed the data. T.N. performed bioinformatic analyses of SNS-seq, RNA-seq, LAM-HTGTS, Repli-seq, ddPCR, and Hi-C. D.M. performed bioinformatic analyses of SNS-seq and Hi-C. T.N. and D.M. together established the bioinformatic workflows used in this study available at <https://github.com/pavrilab>. M.N. prepared material for nuclear mass spectrometry. U.S. performed PRO-cap. R.P. conceived and supervised the

project; performed ChIP-qPCR, SNS-qPCR, 3C-qPCR, and translocation assays; and analyzed data. R.P., T.N., and M.P. wrote the manuscript. **Competing interests:** The authors declare no competing interests. **Data and materials availability:** All next-generation sequencing data in this study have been deposited in the Gene Expression Omnibus (GEO) under accession number GSE161822. The established data-processing workflows for the main next-generation sequencing datasets produced in this study, along with data analysis scripts, are available centrally at <https://github.com/pavrilab>, with stable version releases provided on Zenodo as listed in the supplementary materials. The quantitative proteomics and mass spectrometry data have been deposited to the ProteomeXchange Consortium PRIDE repository under accession number PXD034446. Transgenic cell lines and plasmids generated in this study are available from the corresponding author under a material transfer agreement with the IMP Research Institute of Molecular Pathology. **License information:** Copyright © 2022 the authors, some rights reserved; exclusive licensee American

Association for the Advancement of Science. No claim to original US government works. <https://www.science.org/about/science-licenses-journal-article-reuse>

#### SUPPLEMENTARY MATERIALS

[science.org/doi/10.1126/science.abj5502](https://doi.org/10.1126/science.abj5502)

Materials and Methods

Figs. S1 to S15

Tables S1 to S8

References (73–118)

MDAR Reproducibility Checklist

Submitted 24 May 2021; resubmitted 11 June 2022

Accepted 5 August 2022

10.1126/science.abj5502





Where  
Science  
Gets  
Social.

[AAAS.ORG/COMMUNITY](https://aaas.org/community)



AAAS' Member Community is a one-stop destination for scientists and STEM enthusiasts alike. It's "Where Science Gets Social": a community where facts matter, ideas are big and there's always a reason to come hang out, share, discuss and explore.

Member  
**COMMUNITY**  
AAAS

AMERICAN ASSOCIATION FOR THE ADVANCEMENT OF SCIENCE

## RESEARCH ARTICLES

## CRISPR

## Caspase is a CRISPR RNA-guided, RNA-activated protease

Chunyi Hu<sup>1†</sup>, Sam P. B. van Beljouw<sup>2,3†</sup>, Ki Hyun Nam<sup>4</sup>, Gabriel Schuler<sup>1</sup>, Fran Ding<sup>1</sup>, Yanru Cui<sup>1</sup>, Alicia Rodríguez-Molina<sup>2,3</sup>, Anna C. Haagsma<sup>2,3</sup>, Menno Valk<sup>2,3</sup>, Martin Pabst<sup>5</sup>, Stan J. J. Brouns<sup>2,3\*</sup>, Ailong Ke<sup>1\*</sup>

The CRISPR-Cas type III-E RNA-targeting effector complex gRAMP/Cas7-11 is associated with a caspase-like protein (TPR-CHAT/Csx29) to form Craspase (CRISPR-guided caspase). Here, we use cryo-electron microscopy snapshots of Craspase to explain its target RNA cleavage and protease activation mechanisms. Target-guide pairing extending into the 5' region of the guide RNA displaces a gating loop in gRAMP, which triggers an extensive conformational relay that allosterically aligns the protease catalytic dyad and opens an amino acid side-chain-binding pocket. We further define Csx30 as the endogenous protein substrate that is site-specifically proteolyzed by RNA-activated Craspase. This protease activity is switched off by target RNA cleavage by gRAMP and is not activated by RNA targets containing a matching protospacer flanking sequence. We thus conclude that Craspase is a target RNA-activated protease with self-regulatory capacity.

It has become clear that RNA-guided DNA/RNA degradation is not the sole mechanism for CRISPR-Cas to confer immunity against foreign genetic elements in prokaryotes (1–5). Type III CRISPR-Cas systems in particular present a plethora of alternative mechanisms, including RNA-guided secondary messenger production and signaling (6, 7), to activate a range of immune responses (e.g., collateral RNA damage) (6–8). Type III CRISPR-Cas effectors are typically assembled from multiple protein subunits to enable CRISPR RNA (crRNA) binding and target RNA cleavage, DNA cleavage, and secondary messenger synthesis (9, 10). Type III-E is a recently identified atypical type III system. It encodes a large polypeptide (gRAMP) as a fusion of four Cas7-like domains, one Cas11-like domain, and a big insertion domain (BID), but lacks Cas10, the signature component of a canonical type III system that is required for secondary messenger production (5). Subsequent studies demonstrated that the gRAMP ribonucleoprotein (RNP) complex is capable of RNA-guided RNA cleavage at two specific sites (11, 12) that are six nucleotides apart (11). Unlike the type VI CRISPR-Cas effector Cas13, gRAMP does not cause collateral RNA cleavage and has no cytotoxicity in eukaryotic cells (12).

In type III-E loci, gRAMP frequently associates with TPR-CHAT, a caspase-like protein with N-terminal tetratricopeptide repeats (TPRs) (5). Caspases are a family of cysteine proteases controlling programmed cell death pathways in eukaryotes (13). Cleavage of gasdermin by caspases, for example, triggers membrane pore formation to cause cell death (14, 15). An equivalent programmed cell death pathway was recently discovered in prokaryotes, where TPR-CHAT was shown to cleave bacterial gasdermin to induce cellular suicide (2). In type III-E systems, TPR-CHAT and gRAMP physically interact to form an effector complex named Craspase, for CRISPR-guided caspase (11). This observation raised the possibility that Craspase may function as a crRNA-guided protease to prevent the spread of phage infection through a suicide mechanism. However, it remains unknown how Craspase is structurally organized, whether TPR-CHAT in Craspase is a protease, and whether its activity is regulated by RNA (16, 17).

## gRAMP structures in resting, RNA-bound, and postcleavage states

To gain insights into the RNA-guided target RNA cleavage mechanisms inside gRAMP, we reconstituted *Candidatus* “Scalindua brodae”-gRAMP (*Sb*-gRAMP) (11) and determined its cryo-electron microscopy (cryo-EM) structures in different functional states (Fig. 1A and fig. S1). Consistent with previous results (11), *Sb*-gRAMP bound to the complementary RNA target with better than 25 nM affinity and cleaved it at two distinct locations: after the third nucleotide (site 1) and after the ninth nucleotide (site 2) (fig. S1, A to C). Single-particle three-dimensional (3D) reconstruction produced *Sb*-gRAMP RNP in

four different functional states: a 3.81-Å structure of the *apo* (resting) state, a 3.65-Å structure of the nonmatching protospacer flanking sequence (PFS) target-bound state, a 3.76-Å structure of the matching PFS target-bound state, and a 3.62-Å structure of the postcleavage state (Fig. 1, B to E, figs. S2 to S4, and table S1).

The overall architecture of *Sb*-gRAMP is similar to that of *Desulfonema ishimotonii* Cas7-11 (*Di*-Cas7-11), recently reported in the target-bound form (18). The two structures in the same functional state superimpose with a root mean square deviation of 1.1 Å for Ca atoms, excluding the BID domain, which is less conserved and poorly resolved in the EM density (fig. S5). *Sb*-gRAMP also shares some degree of similarity with the canonical type III-A effector Csm (10, 19–21) in overall architecture, guide RNA display, and target RNA-binding mode (fig. S6). The *Sb*-gRAMP backbone consists of four nonidentical Cas7 domains fused together (Cas7.1 - Cas7.4) instead of the three identical Cas7 subunits in Csm (fig. S6). A Zn knuckle is present in each of the four Cas7 domains, which appears to be a shared hallmark among type III effectors (fig. S7A). Csm further contains one copy of Csm4 for 5'-handle recognition, two copies of Csm2 as part of the backbone, and one copy of Csm5 for continued guide-target pairing. By contrast, *Sb*-gRAMP is streamlined: Its Cas7.1 has been repurposed for 5'-handle recognition, the single-copy Cas11 domain has been repurposed for target cleavage, and a structurally distinct BID replaces Csm5 (fig. S6, A to H). On the guide RNA side, the ordered 18-nucleotide (nt) 5' handle of the crRNA in *Sb*-gRAMP is twice as long as in other class I CRISPR-Cas systems (Fig. 2, A and B). Most of the handle residues are bound by Cas7.1 and shielded on the top by the linker from Cas11 to Cas7.2 and the Zn knuckle in Cas7.2 (fig. S6, S7, B and C). Mutagenesis of the Zn-knuckle structure or sequence-specific contacts to the 5' handle abolished the in vivo RNA silencing activity of *Sb*-gRAMP, presumably through disruption of RNP assembly (fig. S8). Unexpectedly, *Sb*-gRAMP differs from *Di*-Cas7-11 in crRNA biogenesis. In *Di*-Cas7-11, there is an endoribonuclease center in Cas7.1 for crRNA processing, whereas the equivalent residues in *Sb*-gRAMP are noncatalytic (Fig. 2, C and D) (18). This structural difference explains the observation that the crRNA 5' handle in *Sb*-gRAMP is 3 nt longer. We speculate that *Sb*-gRAMP may rely on certain host nucleases for crRNA biogenesis.

The last two handle nucleotides (5'-A-2 and C-1-3') are base-pairing competent because they are displayed like a guide (Fig. 2A and fig. S6, H to G). Type I, III, and IV effectors display the crRNA spacer (guide region) in 6-nt segments, with the sixth nucleotide pinned down by the thumb loop of Cas7; the target is

<sup>1</sup>Department of Molecular Biology and Genetics, Cornell University, Ithaca, NY 14853, USA. <sup>2</sup>Department of Bionanoscience, Delft University of Technology, 2629 HZ Delft, Netherlands. <sup>3</sup>Kavli Institute of Nanoscience, 2629 HZ Delft, Netherlands. <sup>4</sup>Department of Life Sciences, Pohang University of Science and Technology, Pohang, Gyeongbuk 37673, Republic of Korea. <sup>5</sup>Department of Environmental Biotechnology, Delft University of Technology, 2629 HZ Delft, Netherlands.

\*Corresponding author. Email: ailong.ke@cornell.edu (A.K.); stanbrouns@gmail.com (S.J.J.B.)

†These authors contributed equally to this work.

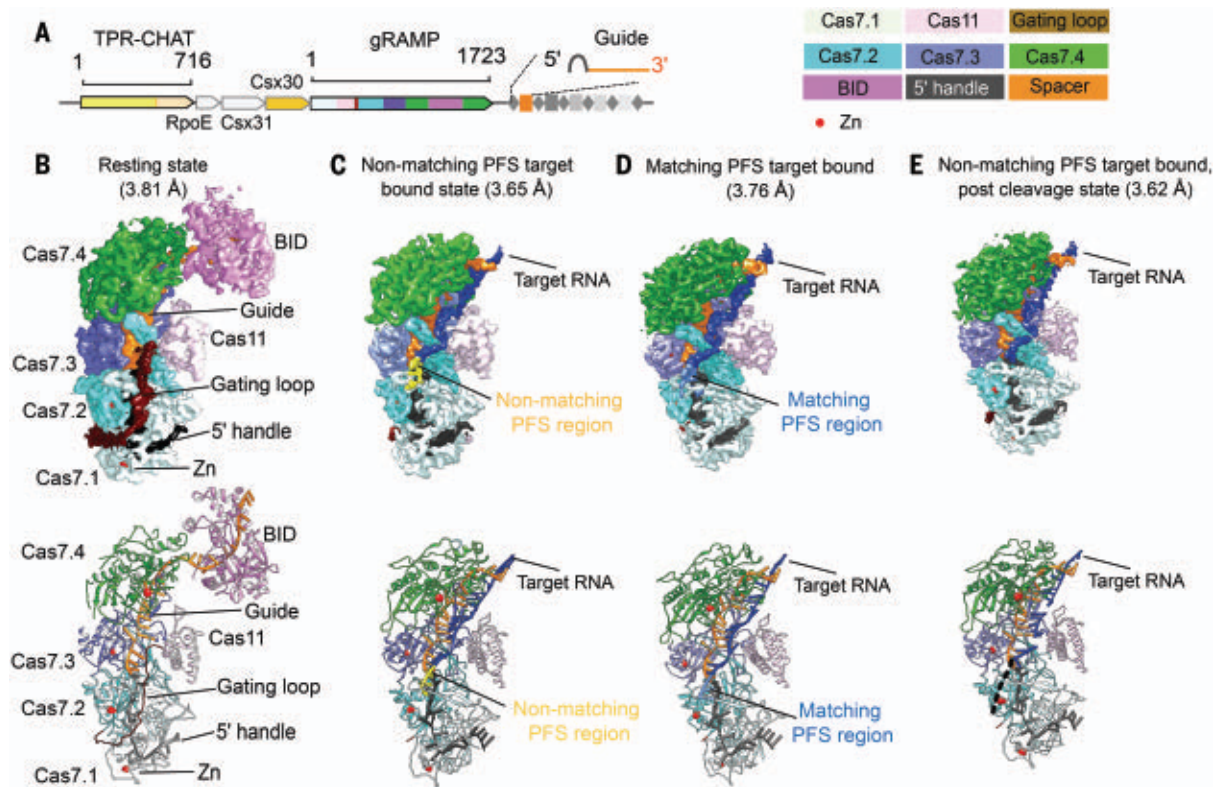


**Fig. 1. Structural snapshots of *Sb*-gRAMP RNP in different functional states.** (A) Type III-E operon in *Ca. S. brodae*. (B to E) Snapshots of *Sb*-gRAMP at resting state (B), nonmatching PFS RNA-bound state (C), matching PFS RNA-bound state (D), and nonmatching PFS RNA postcleavage state with  $MgCl_2$  (E). Top images are cryo-EM densities and bottom images are structural models.

thus recognized in 5-nt segments with the sixth nucleotide unspecified. *Sb*-gRAMP contains major exceptions. The first 5-nt segment contains the last two nucleotides of the 5' handle and the first three nucleotides of the spacer, a scenario only observed in type III-E (18) (Fig. 2, A and E, and fig. S6, H to G). The third segment deviates from the normal again, because an unconventional knotted protein loop from Cas7.4 divides the displayed bases to a 3-nt block and a 6-nt block. The two blocks are divided by a single-peptide crossover rather than by a  $\beta$ -hairpin thumb, so no nucleotide is pinned underneath and the base pairing in the third segment is not interrupted. The following crRNA nucleotides are displayed by the dynamic BID domain (amino acids 1031 to 1385), which is only resolved to low resolution and therefore docked with an AlphaFold-predicted model (22) (Fig. 1B).

#### Off-targeting prevention and RNA cleavage mechanisms in *Sb*-gRAMP

By capturing three additional functional states, we achieved the temporal resolution to interpret the target recognition and cleavage mechanisms by *Sb*-gRAMP. We found that the long linker from Cas11 to Cas7.2 (G375 to E412, here named the gating loop) has acquired important functions for RNase regulation (Fig. 3, A and B,

and fig. S9). Its N-terminal portion (G375 to G397) senses RNA substrate binding and controls RNase activities. In the resting state, the gating loop blocks the first segment of the guide RNA and the nearby site 1 cleavage center. This conformation is incompatible with target-guide pairing at the first segment, and the gating loop has to be displaced to enable cleavage at site 1 (Fig. 3A). We therefore envision that the target-guide pairing initiates from the third and second segments and propagates into the first segment (fig. S9), as observed for other type III systems (23). In follow-up experiments, we found that *Sb*-gRAMP's RNase activity was optimal against a target with 18-nt complementarity from the 5' end of the spacer portion: 12-nt or shorter complementarity abolished cleavage and 24-nt or longer complementarity attenuated cleavage (fig. S10). This suggests that at least some base pairing along all three segments of the guide RNA, displayed by Cas7.2 to Cas7.4, is required for efficient RNA cleavage. By contrast, additional base pairing with crRNA at the BID is not required or may even be counterproductive (fig. S10). This is consistent with the previous observation that the 3' end of the crRNA in the endogenous *Sb*-gRAMP is often as short as 20 nt (11), and that the BID is dispensable for Cas7-II activity in human cells (18).

*Sb*-gRAMP was further incubated with two kinds of RNA targets with PFS that was either matching (complementary) or nonmatching with the 5' handle in the crRNA, because complementarity in this region may be indicative of a self-target (i.e., antisense transcript from the CRISPR locus) and thus may lead to alternative structural configurations in *Sb*-gRAMP. However, our structures reveal that regardless of the PFS status, RNA binding induces the same set of conformational changes in *Sb*-gRAMP. Where the guide nucleotides are pinned down by the Cas7 thumbs, the corresponding target nucleotides (fourth and tenth) flip outward. Rotation of the backbone orients their 2'-OH toward the previous phosphate, forming the so-called "in-line" conformation that is necessary for RNA cleavage. For target RNA with a matching PFS, the first segment consists of five base pairs, starting from the last two nucleotides of the 5' handle and ending with the third nucleotide in the spacer portion (Fig. 2E). The rest of the PFS is not traceable in the EM map. For target RNA with a nonmatching PFS, only three base pairs are found between the target RNA and the spacer portion of the guide. Although the first two nucleotides of the PFS do not form hydrogen bonds with the two 5'-handle residues on the opposite side, they remain stacked to complete

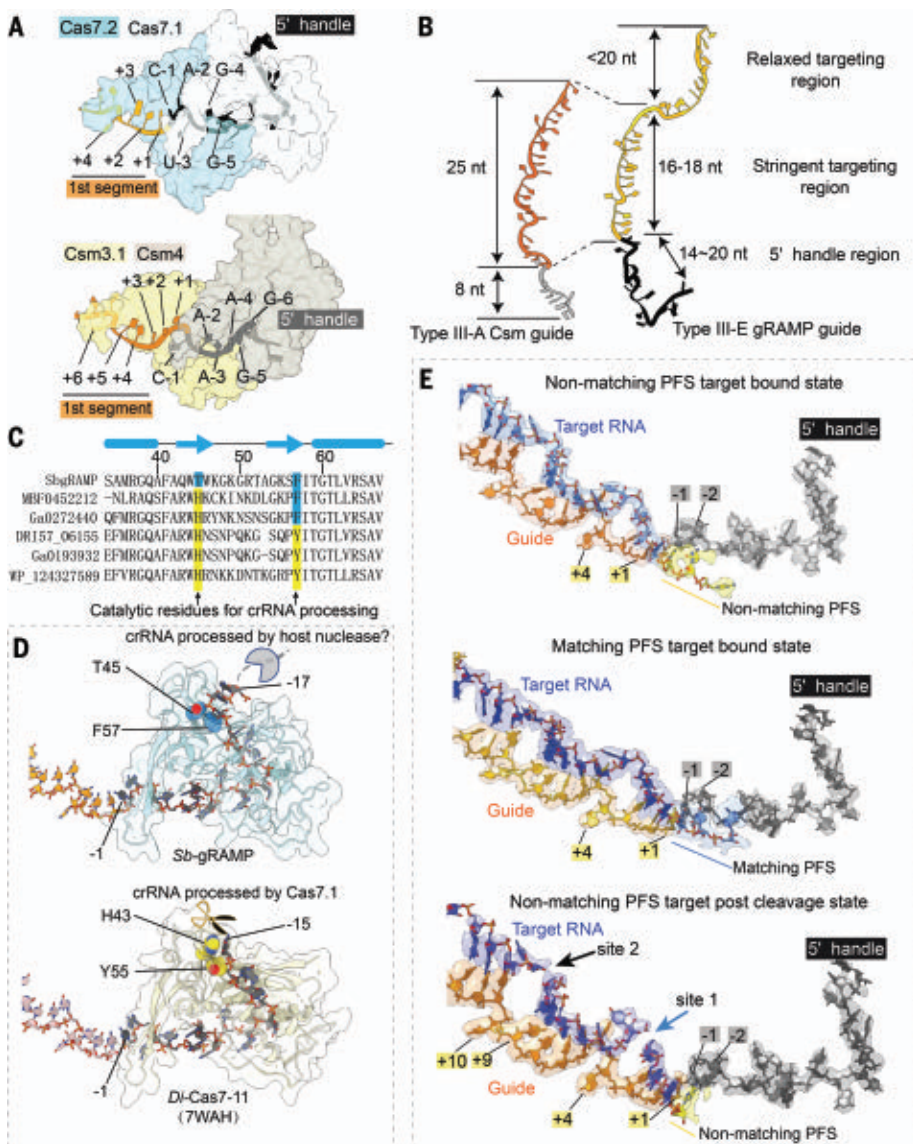


**Fig. 2. crRNA accommodation and target RNA recognition mechanisms by *Sb*-gRAMP.** (A and B) Accommodation of the crRNA 5' handle (A) and spacer region (B) in type III-E *Sb*-gRAMP and type III-A Csm. (C and D) Primary sequence (C) and 3D structural alignment (D) at the pre-crRNA cleavage center. Catalytic residues in *Di*-Cas7-11 are shown in yellow; equivalent residues in *Sb*-gRAMP are shown in blue. (E) Extracted cryo-EM density from nonmatching PFS RNA (top), matching PFS RNA (middle), and nonmatching PFS RNA postcleavage state (bottom).

the first target-guide segment (Fig. 2E). In both PFS-matched and -nonmatched conditions, the impinging gating loop in *Sb*-gRAMP is pushed away from the first segment and becomes entirely disordered (Fig. 3A). Concurrently, the cleavage center at site 1 is exposed and further enhanced by a hinge motion in Cas11 (Fig. 3C and fig. S11A), which aligns catalytic residues among Cas11 and Cas7.2. It should be noted that stacking from the additional 2-nt PFS is not a prerequisite to activate *Sb*-gRAMP, because RNA substrates lacking nucleotides in the PFS region were found to be cleaved efficiently (11, 18). To validate these structural findings, we replaced the tip of the gating loop

with a flexible linker to evaluate its importance in target RNA recognition (fig. S9, D and E). Wild-type *Sb*-gRAMP did not bind or cleave RNA that only base-pairs with the first 9 nt of the crRNA spacer. By contrast, the gating loop mutant bound this target RNA efficiently and subsequently cleaved it (Fig. 3D). These experiments suggest that the gating loop plays a pivotal role in preventing off-targeting. Overall, our RNA-bound *Sb*-gRAMP structures support a mechanistic model in which the resting *Sb*-gRAMP exists in an autoinhibited state to avoid sequence-nonspecific RNA binding and cleavage. Target RNA is validated through crRNA pairing in a directional fashion from

the 3' to the 5' region of the guide. Upon completion of target binding, movement of the gating loop initiates a chain of allosteric events to switch on the RNase centers in gRAMP (Fig. 3E and movie S1).

We further attempted to interpret the cleavage mechanism by comparing the pre- and postcleavage states (Figs. 1 and 3, F and G). EM densities suggest that the RNA substrate was cleaved after the third and ninth nucleotides (site 1 and site 2, respectively) (Fig. 2E), which is consistent with previous reports (11, 18). Because cleavage is metal dependent, we identified multiple candidate residues around the cleavage sites that may contribute to metal coordination (generally acidic residues), proton shuttling (generally polar residues), and transition state stabilization (generally positively charged residues) (Fig. 3, F and G). In subsequent mutagenesis testing (fig. S11, B to D), RNA cleavage at site 1 was abolished by alanine substitutions of D547 in Cas7.2 and of R294, D298, Y367, and K371 in Cas11 (Fig. 3H). Because site 1 is assembled from residues in both Cas11 and Cas7.2, it may only become active after target binding-induced hinge motion in Cas11. Cleavage at site 2 was abolished by Cas7.3 mutations D698A (11) and D806A, but not by Cas11 mutations R323A and H328A (Fig. 3H). An allosteric effect was noticed: Site 1-disruptive mutations D547A and D298A impaired site 2 cleavage as well, and site 2 mutation H328A impaired site 1 cleavage instead. These mutants appeared to weaken or alter the RNA-binding mode of *Sb*-gRAMP, as revealed by electrophoretic mobility shift assay (Fig. 3H and fig. S11C). *Sb*-gRAMP containing the double mutations R294A/D698A or D547/D806A was efficient in RNA binding but completely inactive in RNA cleavage (fig. S11C). Such dead-gRAMP variants could be useful in RNA editing, tagging, or tracing applications.

### Caspase architecture and component interfaces

To gain mechanistic insights into how the putative RNA-guided protease system may work, we reconstituted Caspase in its *apo* state, the matching PFS-containing RNA target-bound state, and the nonmatching PFS-containing target-bound state, and generated their corresponding cryo-EM structures at 3.7, 2.6, and 2.7 Å resolutions, respectively (fig. S12 to S14). The TPR-CHAT-binding surface is on top of the buried crRNA 5' handle in *Sb*-gRAMP, architecturally similar to where the cOA synthetase (Csm1/Cas10) binds in canonical type III-A effector complexes (Fig. 4, A and B; fig. S15A; and movie S2). TPR-CHAT consists of an N-terminal TPR domain (amino acids 1 to 323), a dynamic midregion (amino acids 324 to 399), and a C-terminal cysteine protease from the caspase family (amino acids 400 to 717). The domain arrangement of TPR-CHAT resembles that of separase (24, 25), an essential eukaryotic

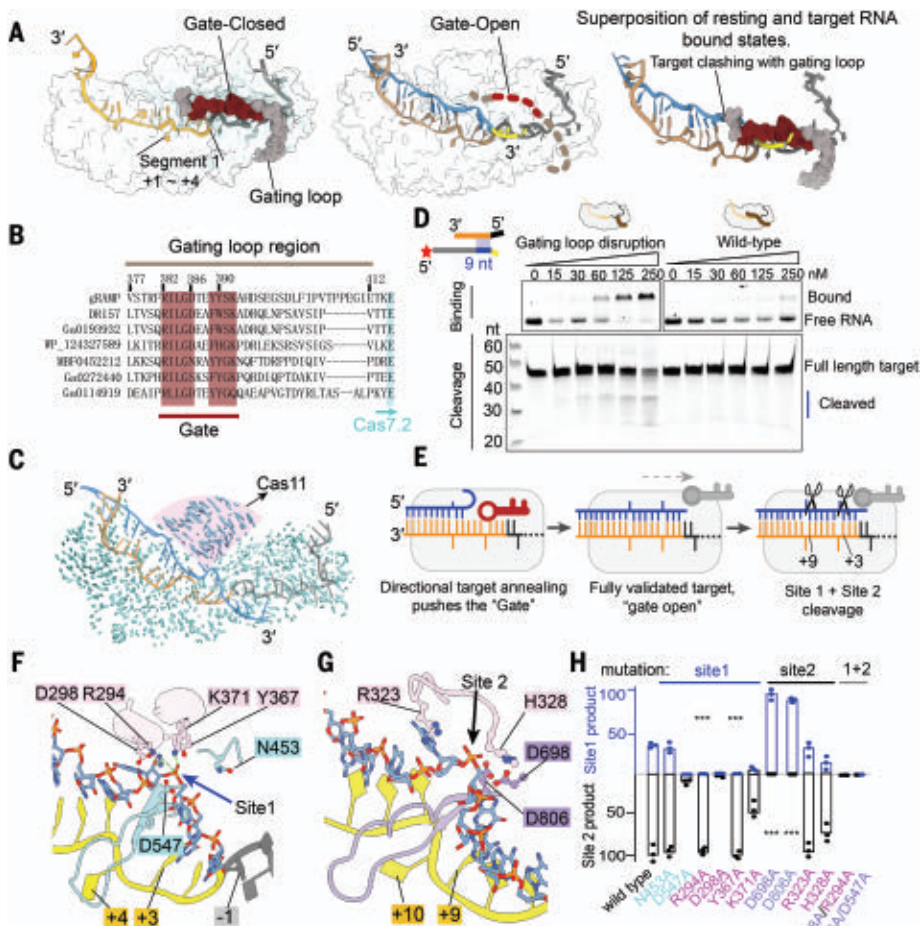


**Fig. 3. Target validation and cleavage mechanisms by *Sb*-gRAMP RNP.** (A) Models depicting the gate-closed structure in resting state (left) and the gate-open structure in the target RNA-bound state (middle). Superposition is shown in the right panel. (B) Sequence alignment at the gating loop region. Conserved residues are highlighted in burgundy. (C) Structural comparison of the resting and nonmatching PFS RNA-bound states. Vector length is proportional to residue movement distance. Hinge motion in Cas11 is pronounced. (D) Electrophoretic mobility shift assay (top) and urea-polyacrylamide gel electrophoresis (bottom) to evaluate the impact of gating loop disruption on the binding and cleavage of partially matching RNA targets. (E) Mechanistic model depicting the essential role of the gating loop in target validation. (F) Structural basis for site 1 cleavage. (G) Structural basis for site 2 cleavage. (H) Impact of site 1 (in blue) and site 2 (in black) mutations on target RNA cleavage efficiency.

protein that cleaves cohesin rings to allow chromosome segregation (fig. S15, B to D). Like separase, the CHAT domain contains an N-terminal pseudocaspase domain, a long dimeric coiled-coil midinsertion, and a C-terminal active-protease domain (24, 25). Although structurally distinct, the two caspase domains pack in a similar fashion as the eukaryotic caspase dimers (26). In TPR-CHAT, the  $\beta$ -sheet structure in the pseudocaspase domain interacts with the TPR domain, and the midregion serves as the sole anchoring point of CHAT onto *Sb*-gRAMP. The TPR repeats belong to the so-called solenoid domains, which are assembled from repeating structural units and often mediate protein-protein or protein-ligand interactions (27). The seven TPR repeats in TPR-CHAT pack side by

side to form a C-shaped architecture, with the seventh TPR repeat packing against the  $\beta$  sheet of the globular CHAT domain. TPR-CHAT adopts the rough shape of a padlock, with TPR being the shackle and CHAT the body (fig. S15B). In the Craspase structure without target RNA (*apo*-Craspase), the shackle of the padlock captures a long “switch helix” (amino acids 338 to 362) in the middle. The switch helix is captured by the molecular contacts from the inward-facing loops in the TPR repeats. When wedged in the shackle, the switch helix pins down a loop-helix-loop structure underneath (amino acids 324 to 337). Together, they mediate an extensive set of molecular contacts to multiple regions inside the padlock (fig. S15B), including contacts to the tips of

two long  $\beta$  hairpins (sensor hairpins) that further extend all the way to the protease center in CHAT (fig. S15E).

An  $\sim 75 \times 35 \text{ \AA}^2$  area of the Cas7.1 surface in *Sb*-gRAMP is buried by TPR-CHAT (Fig. 4, C and D). However, the actual physical contacts between TPR-CHAT and *Sb*-gRAMP are limited to two surface patches 50  $\text{\AA}$  apart. On the TPR side, a hydrophobic patch in the first and second TPR repeats makes hydrophobic and main-chain hydrogen bond contacts to a portion of the gating loop (F381, I383, and L384) and a nearby Cas7.2 loop (L450 and V451) (Fig. 4C). A more extensive and mostly hydrophobic interface is found between one of the coiled-coil helices in the CHAT domain (amino acids 434 to 450) and two regions of *Sb*-gRAMP, namely the C-terminal portion of the gating loop (amino acids 396 to 403) and the Zn knuckle of Cas7.2 (Fig. 4D). In particular, Y450 and L499 of CHAT insert into a hydrophobic pocket on the *Sb*-gRAMP surface, promoting shape complementarity at the interface. The interaction between gRAMP and TPR-CHAT was completely disrupted by Y75A and F103A mutations in the TPR interface and severely impaired by A445R and L449A/Y450A mutations in the CHAT interface (Fig. 4E). An important observation is that the gating loop of *Sb*-gRAMP, which plays a pivotal role in regulating the RNase activity of *Sb*-gRAMP through conformational changes, is sandwiched between *Sb*-gRAMP and TPR-CHAT (fig. S16A). Whereas the entire gating loop becomes unstructured in the RNA-bound *Sb*-gRAMP structure, only the tip of it is rearranged in the RNA-bound Craspase (Fig. 3A and fig. S17). Given this conformational restriction, we speculated that the energetic barrier for RNase activation may be higher in Craspase compared with *Sb*-gRAMP. Indeed, RNA binding was consistently weaker at different temperatures, and the cleavage was slower in Craspase compared with *Sb*-gRAMP (Fig. 4F and fig. S16, B and C).

### RNA-guided protease activation mechanism in Craspase

When Craspase is in the resting state, the catalytic dyad in the TPR-CHAT protease center, Cys627 and His585, are 6.6  $\text{\AA}$  apart (fig. S18). Because this exceeds the hydrogen-bonding distance by a large margin, C627 could not be deprotonated by H585 and thus could not initiate the nucleophilic attack on the peptide substrate. Our structure therefore suggests that TPR-CHAT in the *apo*-Craspase is an inactive protease. When Craspase is bound to a target RNA with a matching PFS (Fig. 5A), a perfectly base-paired first segment is formed between the guide and target. Constrained by the base pairing from the first two PFS residues to the guide, the remaining PFS nucleotides point toward the bottom of TPR. Although their densities are difficult to model, possible phosphate

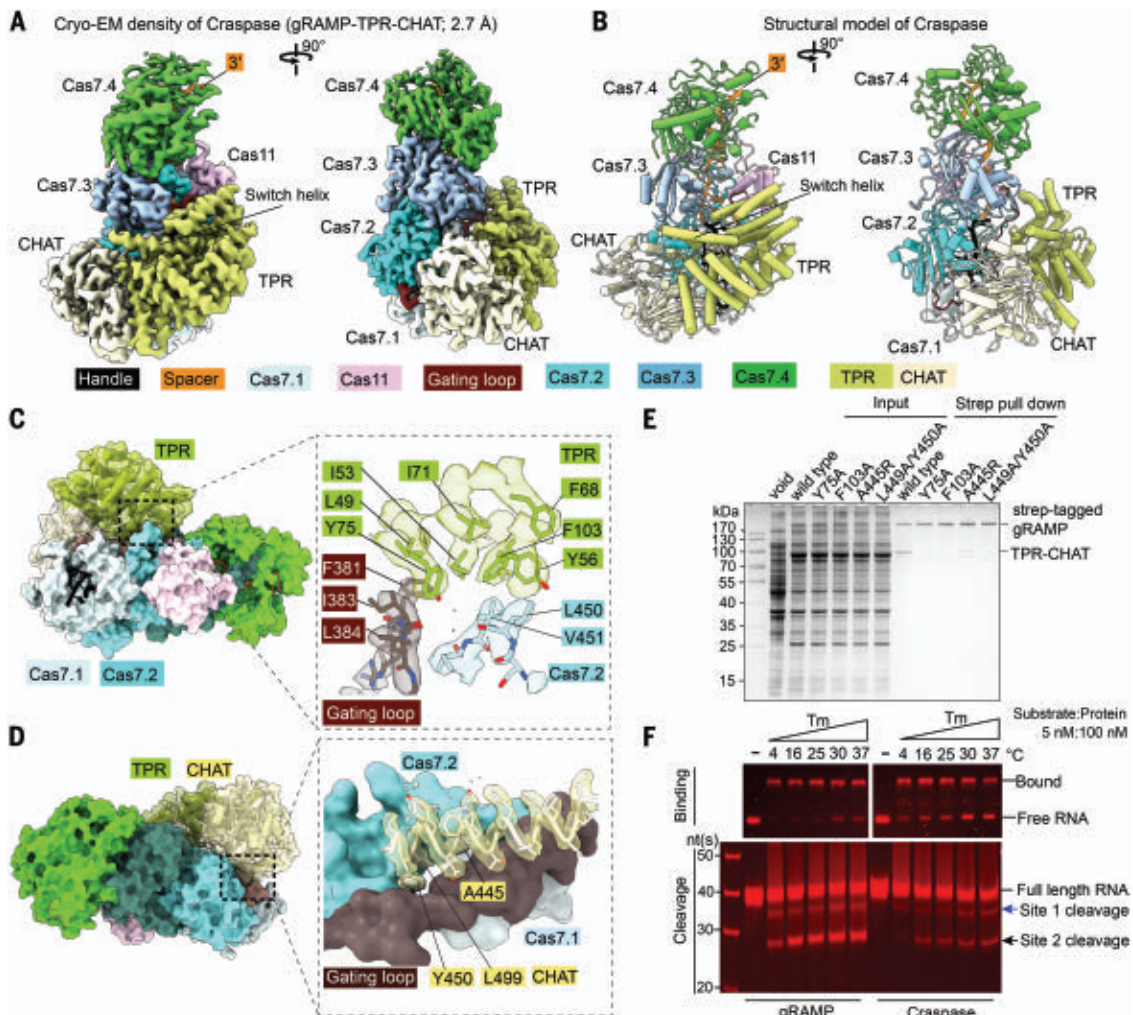


**Fig. 4. Structural basis for Craspase assembly.** (A) 2.7-Å cryo-EM density and (B) structural model of Craspase (gRAMP-TPR-CHAT). (C) Location and enlarged view of the molecular contacts between gRAMP and TPR. Interface residues and corresponding cryo-EM densities are shown. (D) Location and enlarged view of the molecular contacts between gRAMP and CHAT.

(E) Strep-tag affinity purifications quantifying the impact of interface mutations on Craspase complex formation. (F) Electrophoretic mobility shift assay (top) and urea-polyacrylamide gel electrophoresis (bottom) to quantify activity differences in RNA binding and cleavage by gRAMP and Craspase.

densities suggest that the PFS travels underneath TPR (Fig. 5C and movies S3 to S5). This path may have perturbed the conformational dynamics of the sensing  $\beta$  hairpin in CHAT because its tip that may contact PFS becomes disordered. This coincides with a backbone twitch at the protease center, on the opposite end of the sensing hairpin (amino acids 626 to 631) (Fig. 5D). C627 and H585 reside on the two strands of the sensing hairpin. The allosteric change shortens their distance from 6.6 to 5.2 Å (fig. S18B). This distance, however, is still too far to allow H585-mediated C627 deprotonation. Moreover, the nearby side-chain-binding pocket found in the *apo* structure is closed after the structural rearrangement (Fig. 5D). Therefore, the matching PFS RNA-bound Craspase is not expected to be proteolytically active either.

A greater set of conformational changes take place when RNA target containing a non-

matching PFS is bound by Craspase (Fig. 5B). Lacking sequence complementarity to the first 2 nt of PFS, the base pairing in the first guide-target segment is incomplete and the gating loop is only partially dislodged (fig. S17). Although the first nucleotide of PFS forms a partially frayed A•C pair, the rest of PFS pivots toward the surface of the TPR (Fig. 5C). The switch helix is dislodged from the shackle of the padlock, possibly due to clashes with the nonmatching PFS. This helix and the preceding loop-helix-loop connection rotates 90° and packs against CHAT as a coiled-coil structure (Fig. 5D and fig. S19). The sensor hairpin undergoes a larger set of long-range allosteric alterations. Consequently, C627 and H585 become oriented within the hydrogen-bonding distance (3.3 Å) (Fig. 5D), and a hydrophobic pocket opens nearby (fig. S18C). The entire CHAT domain further undergoes a rigid-body move-

ment. As the result, the cleft between *Sb*-gRAMP and TPR-CHAT widens, which may enable the peptide substrate to access binding surfaces (Fig. 5D).

On the basis of the observed structural features in the protease center, we designed candidate peptides to probe for potential RNA-guided peptidase activity in Craspase. We noticed that one designed peptide showed Craspase-dependent cleavage in thin-layer chromatography assays (Fig. 5E and fig. S20, A and B). Consistent with our mechanistic predictions, the activity was stronger in the presence of a nonmatching PFS RNA substrate than a matching PFS substrate (Fig. 5E). This peptide could also be cleaved by Craspase in the context of an interdomain protein linker, and the cleavage was stimulated by non-PFS target RNA (fig. S20, C to F). Mass spectrometry revealed that the cleavage took place after a leucine residue

(fig. S21). Judging by the fact that only one of the two leucine residues in the peptide was selectively cleaved (Fig. 5F) and that the cleavage activity was low and only partially RNA dependent, Craspase clearly specifies additional sequences nearby.

The above mechanistic analysis defines how RNA-guided RNA recognition regulates the protease activity of Craspase (Fig. 5G). Sequence complementarity in the target RNA is a prerequisite that is indirectly read out from the gating loop movement. A NOT logic gate is also in place to avoid activation by a self-RNA. Craspase is only activated when both conditions are true. The structural feature performing the logic calculation is the switch helix: Its movement triggers a stepwise conformational relay that allosterically unlocks the TPR-CHAT padlock and switches on the protease activity (Fig. 5H).

### Craspase proteolytically cleaves Csx30 in an RNA-dependent manner

Type III-E *loci* encode three other well-conserved proteins: the putative sigma-factor RpoE and two proteins of unknown function denoted Csx30 and Csx31 (5, 11, 12). Because a protease and its target are often co-localized in the genome (2, 8), we tested Craspase protease activity against these proteins in co-expression experiments (Fig. 6A). Full-length Csx30 was strongly reduced in the presence of target-bound Craspase, whereas full-length RpoE and Csx31 levels were unaffected (Fig. 6B). This effect was alleviated when Craspase carried inactivated cysteine-histidine residues (H585A and C627A) (Fig. 6B), suggesting that Craspase has proteolytic activity against Csx30. This observation was confirmed in vitro, where purified Craspase processes Csx30 into two distinct fragments (Fig. 6C and table S2), demonstrating that Csx30 is a natural protein target of Craspase. Mutational analysis of the amino acids encompassing the cleavage site showed that L407 in Csx30 is important for Craspase activity (tables S3 and S4 and fig. S22, A and B). Cleavage by Craspase after a leucine residue is consistent with mass spectrometry (fig. S22A) and the peptide cleavage experiments (Fig. 5, E and F). Corroborating the structural insights, proteolytic digestion could only be observed in the presence of target RNA with nonmatching PFS, whereas no cleavage fragments accumulated with nontarget RNA or target RNA with matching PFS (Fig. 6, C and D). Because Craspase cleaves bound RNA only under bivalent cation conditions (11), we reasoned that the peptidase in target-bound Craspase would stay active in the absence of magnesium ions. We indeed observed a marked increase in Csx30 processing under magnesium-poor conditions compared with magnesium-rich conditions (Fig. 6E), suggesting that target RNA cleavage switches off the peptidase. This is further supported by the finding that

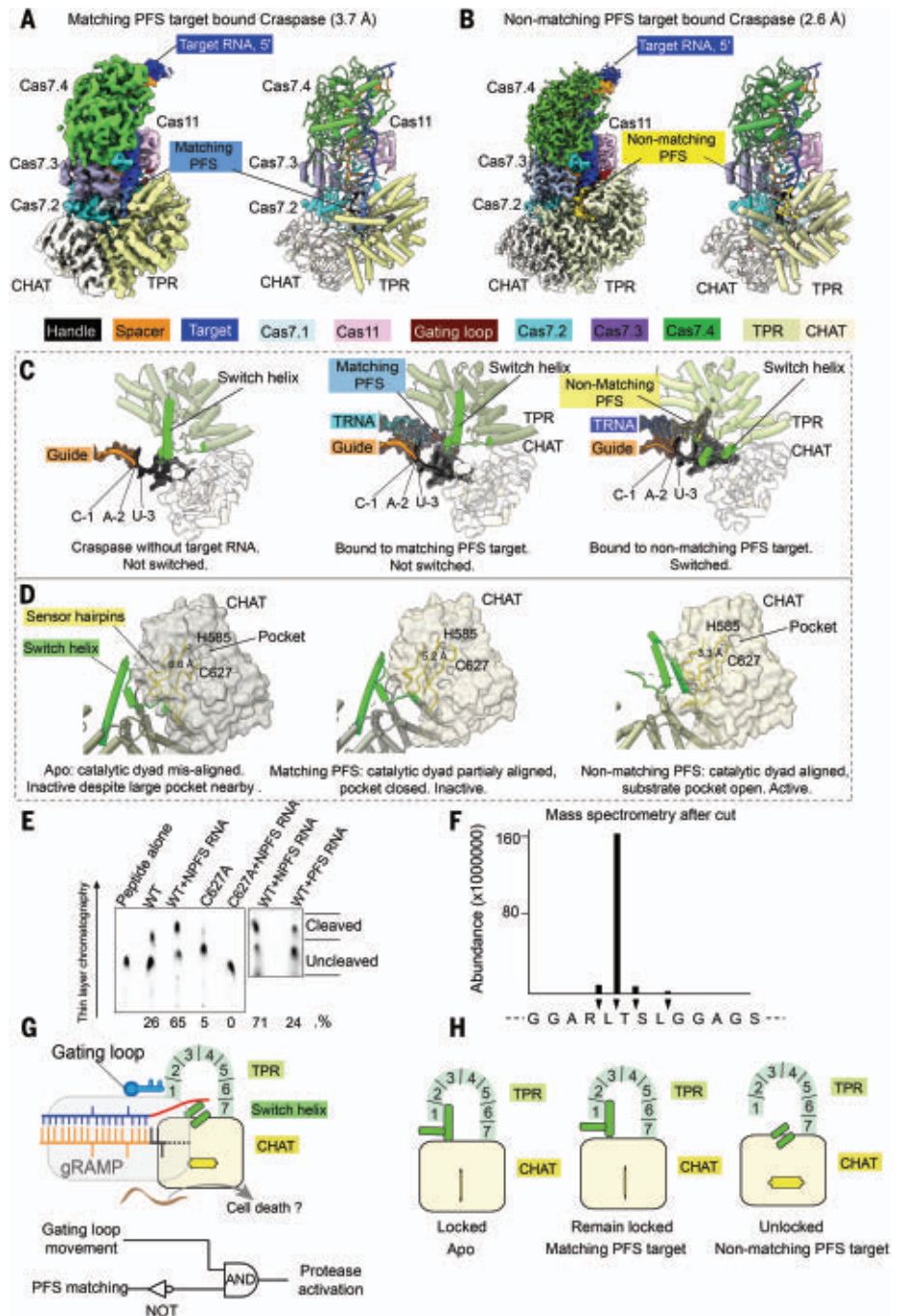


**Fig. 5. Structural basis for Craspase protease activation.** (A) 3.7-Å cryo-EM density (left) and structural model (right) of matching PFS RNA-bound Craspase. (B) 2.6-Å cryo-EM density (left) and structural model (right) of nonmatching PFS RNA-bound Craspase. (C) Close-up views of the switch helix in the resting state (left), the matching PFS RNA-bound state (middle), and the nonmatching PFS RNA-bound state (right). The switch helix is highlighted in green, and the density of crRNA and target RNA (TRNA) are shown in mesh. (D) Conformation of the switch helix and sensor hairpin in three states. Changing status in the catalytic dyad and the nearby side-chain-binding pocket in CHAT (gray surface) are highlighted. (E) TLC-based peptide cleavage assay by Craspase. (F) Cleavage site mapping by mass spectrometry. Cleavage percentages are quantified. (G) Top: model depicting nonmatching PFS RNA-induced Craspase activation. Bottom: Logic gate diagram illustrating the protease activation mechanism. (H) Model depicting TPR-CHAT status in the apo state, the matching PFS RNA-bound state, and the nonmatching PFS RNA-bound state.

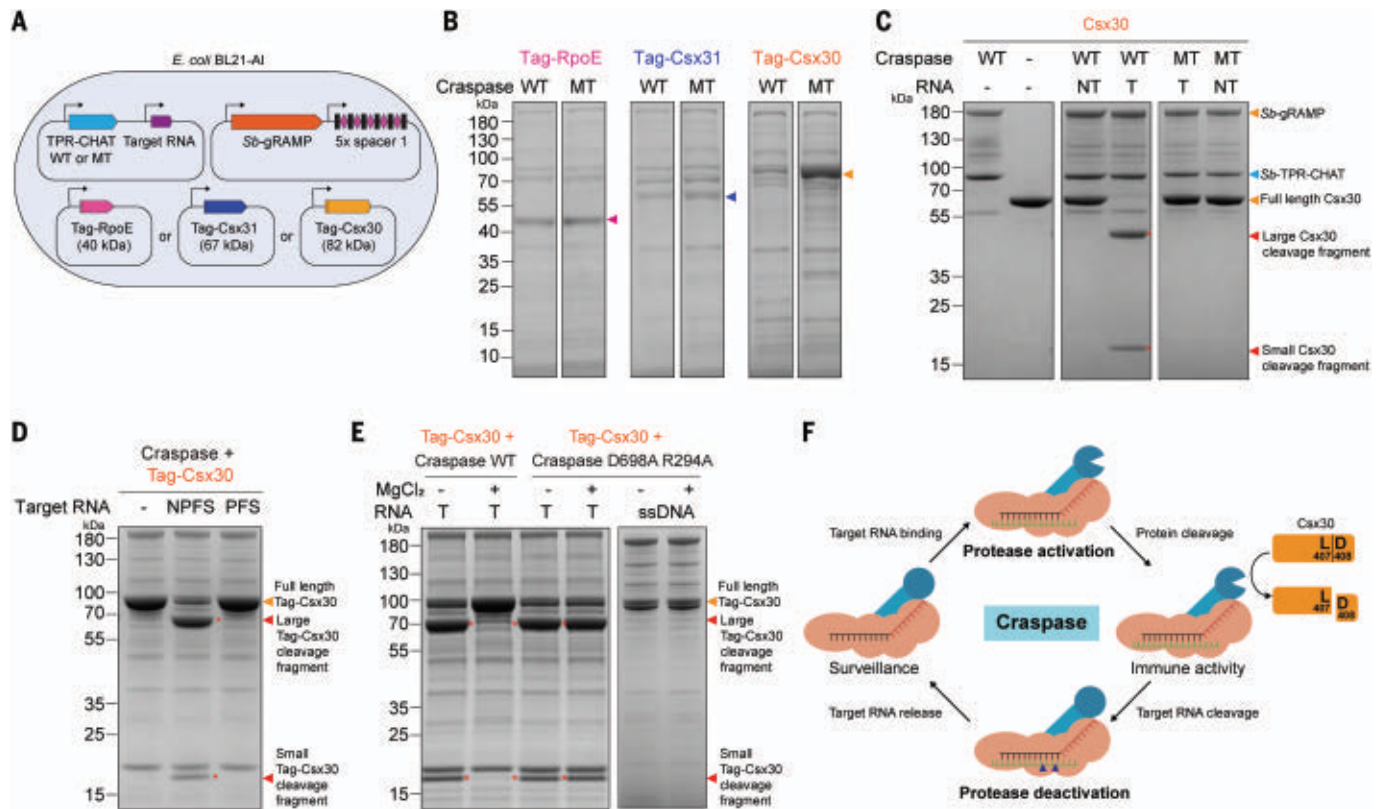


**Fig. 6. Craspase proteolytically cleaves Csx30 in an RNA-dependent manner.** (A) Genetic context for RpoE, Csx31, and Csx30 co-expression with Craspase wild-type (WT) or mutant (MT; H585A C627A) and a target RNA in *E. coli* BL21-AI. (B) Protein gel showing the eluted protein content from streptavidin purifications of Tag-RpoE, Tag-Csx31, and Tag-Csx30 after co-expression with either Craspase WT or Craspase MT (H585A C627A). Colored arrows indicate the expected size for the full-length protein. (C) Protein gels after Craspase WT or Craspase MT (H585A C627A) incubation with Csx30 in the presence of target RNA or nontarget RNA. Protein cleavage products are

indicated with a red asterisk. (D) Protein gel after Craspase WT incubation with target RNA containing either a nonmatching PFS (NPFS) or matching PFS. (E) Left: protein gel after incubation of Tag-Csx30 with RNA and Craspase target WT or Craspase D698A R294A, with or without prior incubation with MgCl<sub>2</sub>. Right: protein gel after incubation of Tag-Csx30 with single-stranded target DNA and Craspase D698A R294A. (F) Model for Craspase functionality. Once unbound Craspase has bound a target RNA, the peptidase activity is activated. This results in proteolytic cleavage of Csx30 between L407 and D408. Upon target RNA cleavage by Craspase, the peptidase activity is shut off.

the peptidase activity of a nuclease-dead variant of Craspase is not impaired in the presence of magnesium ions (Fig. 6E), rendering Craspase R294A D698A a “stay-on” variant. Binding of a complementary single-stranded DNA that is not cleaved by Craspase (11, 12) does not activate the peptidase (Fig. 6E). These findings combined support a model (Fig. 6F) in which the peptidase activity of Craspase is switched on upon target RNA binding to cleave Csx30 after L407, separating a large N-terminal fragment of ~47 kDa from a small C-terminal fragment of ~19 kDa. Because of the low sequence and structural similarity to known proteins, a prediction of the function of the two protein fragments cannot be made with confidence (fig. S22C). However, on the basis of analogous defense systems, processed Csx30 fragments likely enable an immune response, possibly by eliciting toxicity to the native host cell. Craspase then self-regulates through target RNA cleavage to switch the peptidase off, thereby timing the duration of the immune re-

sponse and possibly recycling the Craspase complex to bind new target RNAs.

### Discussion

A new frontier in CRISPR-Cas biology has emerged, in which the RNA-guided effectors control physiological responses using mechanisms other than nucleic acid degradation. Here, we define how the Craspase protease is allosterically activated by target RNA recognition and inactivated by target RNA cleavage to cleave the native substrate Csx30 in a binary fashion. We tuned its dynamic response range using mechanism-inspired mutants, which will pave the way for biotechnological and therapeutic applications. Our observations suggest the possibility that the cleavage sequence in the native protein substrate is read out in the context of the 3D structure, which is also the case for the molecular recognition of gasdermins by eukaryotic caspases (26, 28). We await follow-up studies revealing the missing recognition codes in substrate recognition and cleavage.

Despite the large structural distinctions, our studies revealed that type III-E systems share fundamental mechanistic similarities with canonical CRISPR-Cas type III systems. Analogous to Cas10 activation in other type III effectors, Craspase only turns on the protease activity in response to nonself RNA targets; it does not differentiate self and nonself RNA targets at the RNA cleavage level. This, combined with the observation that Craspase switches off protease activity upon target RNA cleavage, suggests that the protease activity may only be desired temporarily in the cell, which points to a possible ominous consequence of turning on the Craspase pathway. Does Csx30 proteolysis lead to cell dormancy or possibly programmed cell death? Because of the lack of homology to known proteins, it is difficult to infer the physiological function of Csx30 with confidence. On the basis of the AlphaFold-predicted structure (22), we speculate that proteolysis may relieve a physical sequestration or trigger a conformational change in Csx30, converting



it to the active form (fig. S22, C and D). An analogous scenario was described for bacterial gasdermin, which only induced its anti-viral effect after site-specific cleavage by TPR-CHAT (2). The potential involvement of the other Craspase-associated proteins, RpoE and Csx31, needs to be assessed in future experiments. However, unraveling the biological details is complicated by the difficulty of working with the native host, *Ca. S. brodae* (29). Alternative model organisms may be needed for future functional studies. On the application side, the fact that the Craspase peptidase is only active in the presence of a specific RNA species renders it useful for both in vivo (e.g., gene expression profiling) and in vitro (e.g., RNA diagnostics) biotechnological applications. This represents a major expansion of the range of biomolecular engineering possibilities of CRISPR-Cas effectors.

#### REFERENCES AND NOTES

1. S. Doron *et al.*, *Science* **359**, eaar4120 (2018).
2. A. G. Johnson *et al.*, *Science* **375**, 221–225 (2022).
3. S. A. Shah *et al.*, *RNA Biol.* **16**, 530–542 (2019).
4. K. S. Makarova *et al.*, *Nucleic Acids Res.* **48**, 8828–8847 (2020).
5. K. S. Makarova *et al.*, *Nat. Rev. Microbiol.* **18**, 67–83 (2020).
6. M. Kazlauskienė, G. Kostiuik, Č. Venclovas, G. Tamulaitis, V. Siksnys, *Science* **357**, 605–609 (2017).
7. O. Niewoehner *et al.*, *Nature* **548**, 543–548 (2017).
8. C. Rouillon *et al.*, *SAVED by a toxin: Structure and function of the CRISPR Lon protease*. bioRxiv, 2021.2012.2006.471393 (2021).
9. R. Molina, N. Sofos, G. Montoya, *Curr. Opin. Struct. Biol.* **65**, 119–129 (2020).
10. L. You *et al.*, *Cell* **176**, 239–253.e16 (2019).
11. S. P. B. van Beljouw *et al.*, *Science* **373**, 1349–1353 (2021).
12. A. Özcan *et al.*, *Nature* **597**, 720–725 (2021).
13. Y. Shi, *Cell* **117**, 855–858 (2004).
14. J. Ding *et al.*, *Nature* **535**, 111–116 (2016).
15. J. Shi *et al.*, *Nature* **526**, 660–665 (2015).
16. M. L. Hochstrasser, J. K. Nuñez, *Nat. Microbiol.* **6**, 1481–1482 (2021).
17. R. J. Catchpole, M. P. Terns, *Mol. Cell* **81**, 4354–4356 (2021).
18. K. Kato *et al.*, *Cell* **185**, 2324–2337.e16 (2022).
19. N. Jia *et al.*, *Mol. Cell* **73**, 264–277.e5 (2019).
20. M. Guo *et al.*, *Cell Res.* **29**, 305–312 (2019).
21. S. Sridhara *et al.*, *Commun. Biol.* **5**, 279 (2022).
22. J. Jumper *et al.*, *Nature* **596**, 583–589 (2021).
23. J. A. Steens *et al.*, *Nat. Commun.* **12**, 5033 (2021).
24. Z. Lin, X. Luo, H. Yu, *Nature* **532**, 131–134 (2016).
25. A. Boland *et al.*, *Nat. Struct. Mol. Biol.* **24**, 414–418 (2017).
26. Z. Liu *et al.*, *Immunity* **53**, 106–114.e5 (2020).
27. G. L. Blatch, M. Lässle, *BioEssays* **21**, 932–939 (1999).
28. K. Wang *et al.*, *Cell* **180**, 941–955.e20 (2020).
29. T. Awata *et al.*, *Appl. Environ. Microbiol.* **79**, 4145–4148 (2013).

#### ACKNOWLEDGMENTS

We thank E. Tan for the critical reading of the manuscript. **Funding:** This work was supported by the National Institutes of Health (grant GM118174 to A.K.); the Department of Defense through the National Defense Science & Engineering Graduate Fellowship Program (G.S.); the National Science Foundation (MRSEC program grant DMR-1719875 to the Cornell Center for Materials Research Shared Facilities); the Department of Energy Office of Biological and Environmental Research (grant KP1607011 to the Laboratory for BioMolecular Structure); the Netherlands Organisation for Scientific Research (NWO VICI grant VI.C.182.027 to S.J.J.B.); the European Research Council (ERC) Consolidator Grants under the European Union's Horizon 2020 Research and Innovation Program (grant 101003229 to S.J.J.B.). **Author contributions:** Conceptualization: A.K., C.H., S.J.J.B., S.P.B.v.B.; Funding acquisition: A.K., S.J.J.B.; Investigation: C.H., G.S., K.H.N., F.D., Y.C., A.K., S.J.J.B., S.P.B.v.B., A.C.H., A.R.-M., M.P., M.V.; Methodology: C.H., G.S., K.H.N., F.D., Y.C., A.K., S.J.J.B., S.P.B.v.B., A.C.H., A.R.-M., M.P.; Project administration: A.K., S.J.J.B.; Supervision: A.K., S.J.J.B.; Visualization: C.H., A.K.; Writing – original draft: A.K.,

C.H., G.S., S.J.J.B., S.P.B.v.B.; Writing – review and editing: A.K., C.H., G.S., S.J.J.B., S.P.B.v.B. **Competing interests:** S.P.B.v.B. and S.J.J.B. are inventors on patent application N2028346 and PCT/NL2022/050296 submitted by Delft University of Technology that covers uses of gRAMP and Craspase. A provisional patent application related to this research has been filed by Cornell University. The remaining authors declare no competing interests. **Data and materials availability:** The resting-gRAMP coordinates and cryo-EM density map have been deposited in the Protein Data Bank (PDB:8D97) and the Electron Microscopy Data Bank (EMD-27257); gRAMP/nonmatching PFS RNA-bound (PDB:8D8N, EMD-27252); gRAMP/matching PFS RNA-bound (PDB:8D9E, EMD-27259); gRAMP/nonmatching PFS RNA postcleavage state (PDB:8D8I, EMD-27263); Craspase complex (PDB:8D8F, EMD-27260); Craspase/matching PFS RNA complex (PDB:8D8H, EMD-27262); Craspase/nonmatching PFS RNA complex (PDB:8D8G, EMD-27261). Plasmids used in this study are available upon request. **License information:** Copyright © 2022 the authors, some rights reserved;

exclusive licensee American Association for the Advancement of Science. No claim to original US government works. <https://www.science.org/about/science-licenses-journal-article-reuse>

#### SUPPLEMENTARY MATERIALS

[science.org/doi/10.1126/science.add5064](https://science.org/doi/10.1126/science.add5064)  
Materials and Methods  
Figs. S1 to S22  
Tables S1 to S5  
References (30–36)  
Movies S1 to S7  
MDAR Reproducibility Checklist

Submitted 15 June 2022; accepted 16 August 2022  
Published online 25 August 2022  
10.1126/science.add5064

## GAS GIANT PLANETS

# Loss of a satellite could explain Saturn's obliquity and young rings

Jack Wisdom<sup>1\*</sup>, Rola Dbouk<sup>1</sup>, Burkhard Militzer<sup>2,3</sup>, William B. Hubbard<sup>4</sup>, Francis Nimmo<sup>5</sup>, Brynna G. Downey<sup>5</sup>, Richard G. French<sup>6</sup>

The origin of Saturn's ~26.7° obliquity and ~100-million-year-old rings is unknown. The observed rapid outward migration of Saturn's largest satellite, Titan, could have raised Saturn's obliquity through a spin-orbit precession resonance with Neptune. We use Cassini data to refine estimates of Saturn's moment of inertia, finding that it is just outside the range required for the resonance. We propose that Saturn previously had an additional satellite, which we name Chrysalis, that caused Saturn's obliquity to increase through the Neptune resonance. Destabilization of Chrysalis's orbit ~100 million years ago can then explain the proximity of the system to the resonance and the formation of the rings through a grazing encounter with Saturn.

Saturn's obliquity, the angle between its equator and the plane of its orbit around the Sun, is too large to have arisen during Saturn's formation from a protoplanetary disk or from a large impact (1). Saturn's rings appear to be only ~100 million years (Myr) old, based on the estimated strength of satellite ring torques (2) and the estimated rate of darkening of the ice-rich material (3, 4). However, the lack of a suitable mechanism to explain such young rings has led some to question the young age (5).

The precession frequency of Saturn's spin axis (the rate at which the axis rotates about the vertical) is close to the precession frequency of Neptune's orbit (6). This raises the possibility that the obliquity resulted from a resonance between these two frequencies. Resonances between the precession of the spin axis of a

body and the precession of its orbit occur elsewhere in the Solar System. The spin axis of the Moon and the orbit of the Moon precess at the same rate (7, 8). Spin-orbit precession resonances also arise if the precession frequency of a spin axis is close to a frequency component in the precession of its orbit. Mars has a chaotic obliquity due to a resonance between the precession of its spin axis and a chaotically varying component in its orbit precession associated with the precession of Venus (9, 10). The obliquity of the Moon, locked in the precession resonance, depends on the rate of mutual precession of the orbit and spin axis. The Moon's obliquity was different in the past because the rate of orbit precession depends on the distance to Earth and the Moon is tidally evolving outward from Earth. There were times when the obliquity of the Moon was large (11).

If the large obliquity of Saturn is the result of a spin-orbit resonance between the precession of Saturn's spin axis and the precession of the orbit of Neptune, how would this have come about? One proposal is that the precession frequency of Neptune's orbit could have changed as the distribution of protoplanetary mass changed during planet formation (1). An alternative proposal relies upon the observed

<sup>1</sup>Department of Earth, Atmospheric, and Planetary Sciences, Massachusetts Institute of Technology, Cambridge, MA 02139, USA. <sup>2</sup>Department of Astronomy, University of California, Berkeley, CA 94720, USA. <sup>3</sup>Department of Earth and Planetary Science, University of California, Berkeley, CA 94720, USA. <sup>4</sup>Lunar and Planetary Laboratory, University of Arizona, Tucson, AZ 85721-0092, USA. <sup>5</sup>Department of Earth and Planetary Sciences, University of California, Santa Cruz, CA 95064, USA. <sup>6</sup>Department of Astronomy, Wellesley College, Wellesley, MA 02481, USA.  
**\*Corresponding author. Email: wisdom@mit.edu**

rapid migration of Saturn's largest satellite, Titan (*I2–I4*). The precession frequency of Saturn is modified by the presence of its satellites, which are locked to orbit in the equatorial plane of Saturn. Because of this lock, the Sun's gravitational pull on the satellites contributes to the torque that precesses Saturn. The precession of Saturn is dominated by these solar torques on Titan, which are proportional to the square of the distance of Titan from Saturn (*I1*), so as Titan migrates outward, the precession frequency increases. This could have caused the precession frequency of the Saturn system to become resonant with the precession of Neptune (*I2*). We define a resonance angle  $\sigma$  to be the longitude of Saturn's equator minus the longitude of the descending node of Neptune's orbit (*I0*). While in the Neptune resonance, this angle oscillates about zero. If the migration of Titan was slow, compared with the period of oscillation in the precession resonance, the obliquity of Saturn could have risen as Titan migrated (*I3*).

Both of these scenarios require the moment of inertia of Saturn to be in a certain range and predict that the system is currently in this spin-orbit precession resonance. Previous determinations of the moment of inertia had too high an uncertainty to draw definitive conclusions (*I, I2*).

### Moment of inertia of Saturn

The exterior gravity field of Saturn, as determined using the Cassini spacecraft (*4*), provides tight constraints on models of the planet's interior structure. We constructed interior models using four different sets of assumptions. For a range of rotation periods, the corresponding moments of inertia are shown in Fig. 1 in terms of the normalized angular momentum: the product of the moment of inertia and the rotation rate, normalized by  $MR_e^2 \sqrt{GM/R_e^3}$ , where  $G$  is the gravitational constant,  $M$  is the mass of Saturn, and  $R_e$  is its fiducial equatorial radius, taken to be 60,268 km (*15*).

We combine an equation of state for hydrogen-helium mixtures (*16*) with assumptions about Saturn's interior composition. We assume that the interior of Saturn is differentially rotating on cylinders, chosen to match cloud tracking observations. We use the concentric Maclaurin spheroid (CMS) method (*17, 18*) to construct models that match (fig. S1) the gravitational moments from  $J_2$  to  $J_{12}$  (*4*). The  $J_s$  are dimensionless coefficients in the expansion of the exterior gravity field. Normalized angular momentum values are shown in Fig. 1 and listed in table S1.

To estimate how much the computed moment of inertia depends on the assumptions, we used three additional approaches to construct models of the interior of Saturn. These models only match the gravitational moments  $J_2$ ,  $J_4$ , and  $J_6$  without invoking differential rotation.

The first approach uses the consistent level curve method (*19*), with polynomial equations

of state that relate pressure and density. The order of the polynomial is increased until the values of  $J_2$  to  $J_6$  can be reproduced. The second approach uses the CMS method as before but introduces a single discontinuity in the density to match  $J_2$  to  $J_6$  without differential rotation. The third method introduces more flexibility by representing Saturn's interior with four constant-density spheroids. Their densities and thicknesses are adjusted until the observed moments up to  $J_6$  can be matched with CMS calculations. The resulting spread of model predictions is indicated in Fig. 1 and fig. S2. Results for a larger number of spheroids are shown in fig. S3. We find consistent results from all models that match  $J_2$ ,  $J_4$ , and  $J_6$  while assuming uniform rotation. The angular momentum depends only on the assumed rotation rate and the observed gravitational moments.

Models that assume uniform rotation do not match the high-order gravitational moments ( $J_8$  to  $J_{12}$ ). The observed large magnitudes of the high-order moments are indicative of differential rotation (*4, 20*). However, the inclusion of differential rotation lowers the implied angular momentum by only  $\sim 0.5\%$  (Fig. 1).

The resulting moments of inertia are in close agreement with one another, indicating that they are tightly constrained by the gravitational moments and insensitive to the assumed composition and equation of state. The values of  $J_2$  and  $J_4$  alone provide sufficient constraints on the planet's angular momentum to show that Saturn is slightly out of resonance with Neptune (see supplementary text). Models without differential rotation provide an upper bound on the angular momen-

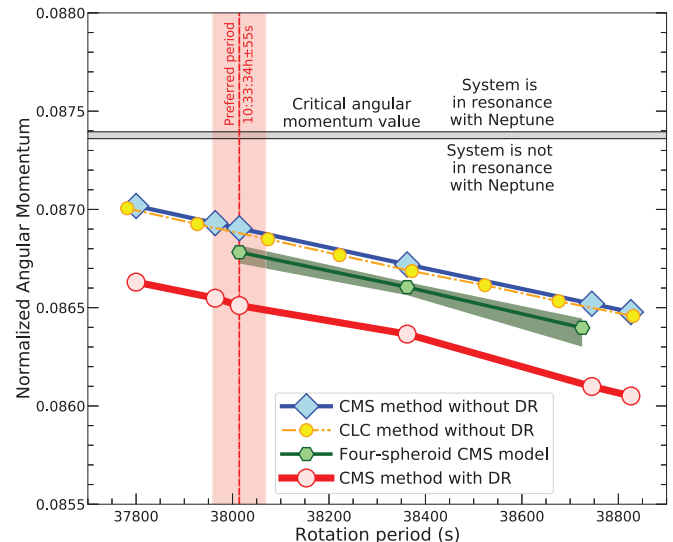
tum, whereas including differential rotation (to match the higher-order gravitational moments) reduces the angular momentum slightly (Fig. 1 and fig. S4) (see supplementary text).

### Numerical integrations of the satellite system

We used numerical integration to investigate the dynamical evolution of the Saturn satellite system. These integrations include Saturn, modeled as a rigid body; the gravitational moments of Saturn from  $J_2$  to  $J_6$ ; the major satellites of Saturn from Mimas to Iapetus; the Sun; and the other three outer planets. The system is fully coupled: The gravitational moments affect the motion of the satellites as well as the rotation of Saturn. Some of our integrations included tidal evolution, specified by the rate of change of Titan's semimajor axis; for simplicity, we ignore the tidal evolution of the other satellites (*21*).

We used direct numerical integration to determine the range of moments of inertia of Saturn for which the system is in the spin-orbit precession resonance. Numerical integration avoids the need to analytically estimate a host of small effects (*21*). We refer to the lower bound of this range as the critical value. We performed a series of forward and backward 50-million-year integrations to determine the critical moment of inertia. These integrations did not include tidal friction and excluded the tiny satellite Hyperion. The results are also shown in Fig. 1, in terms of the normalized angular momentum. We find that the system is outside, but close to, the resonance region for all model assumptions and rotation periods. If we adopt a rotation period of 10:33:34 hours,

**Fig. 1. Saturn's normalized angular momentum as a function of rotation period.** The red curve and circles represent results for models using physical equations of state with differential rotation (DR), matched to the even gravitational moments up to  $J_{12}$ . The other three models assume uniform rotation and only match  $J_2$ ,  $J_4$ , and  $J_6$ . The results of the consistent level curve method (yellow dash-dotted curve and circles) and the CMS method (blue curve and diamonds) are consistent with each other



and close to the more approximate four-spheroid CMS results (green curve and hexagons). The green-shaded region indicates the range of results for an ensemble of four-spheroid CMS models that each match the gravitational moments. The vertical red line and band indicate the rotation period (and uncertainty) estimated from the measured flattening of Saturn. The horizontal gray band (between 0.087360 and 0.087399) indicates the critical value to be in the precession resonance. All models fall below the critical value, so the system is near, but not in, the spin-orbit precession resonance. Numeric values are listed in table S1.

derived by matching Saturn’s flattening (15, 18), the predicted angular momenta are between 0.5 and 1.0% below the critical value.

The critical angular momentum to be in resonance corresponds to a dimensionless polar moment of inertia of 0.2201. The estimated value, with differential rotation, for a rotation period of 10:33:34 hours is  $0.2182^{+0.0006}_{-0.0003}$ , which is about 1% below the critical value. Previous work (12), though more approximate, found that for Saturn to have had an initial obliquity less than  $10^\circ$ , the moment of inertia must be in the range 0.224 to 0.237, and for Saturn to be oscillating in the resonance, it must be between 0.22 and 0.24, a 10% range.

Small changes in the system parameters can make large changes in the rate of precession. For example, changing the semimajor axis of Saturn by only 5% changes the rate of precession by 15% (Eq. 1). Similarly, making small changes in the mass or position of Uranus or Neptune can also make large changes in the precession frequency of Neptune. So, the system being only 1.0% away from the resonance suggests that the Neptune resonance has played a role in the recent history of the Saturn system.

The rapid migration of Titan rules out scenarios that depend on the Neptune resonance in the early Solar System (12). If the Neptune resonance played a role in the development of the obliquity of Saturn, it rules out other proposed early Solar System explanations (22, 23). We propose that the obliquity of Saturn arose because the system was previously trapped in the Neptune resonance as Titan migrated outward but escaped from the resonance recently enough to still be near the resonance.

**Resonance model**

We construct a simple model that captures many aspects of the dynamics of the spin-orbit precession resonance with Neptune (21). This model can be used to interpret the results of the full numerical simulations.

A parameter in this model is the precession constant. Averaging over the orbital time scale, an oblate planet with satellites orbiting the Sun in a fixed circular orbit has a rate of regression of the spin axis of  $\alpha \cos(\epsilon)$ , where  $\alpha$  is the precession constant and  $\epsilon$  is the obliquity of the spin axis to the fixed orbit normal. The precession constant is (11, 13)

$$\alpha = \frac{3}{2} n \frac{J_2 + q}{\omega \lambda + l} \tag{1}$$

where  $n$  is the orbital frequency;  $\omega$  is the rotation rate;  $J_2$  is the second gravitational moment;  $\lambda = C/(MR_e^2)$  is the dimensionless polar moment of inertia, where  $C$  is the moment of inertia; and

$$q = \frac{1}{2} \sum_j \frac{m_j a_j^2}{M R_e^2} \frac{\sin[2(\epsilon - i_j^l)]}{\sin(2\epsilon)}$$

**Fig. 2. Saturn evolu-**

**tion. (A and B)** Obliquity of Saturn  $I$  (A), and the resonance angle  $\sigma$  (B), as a function of time  $t$ . The obliquity is with respect to the invariable plane, the plane perpendicular to the total angular momentum of the Solar System. The blue curve is a full numerical simulation, with  $da_{\text{Titan}}/dt = 13.75 \text{ cm year}^{-1}$ , where  $a_{\text{Titan}}$  is the semimajor axis of Titan. The gray curve is the resonance model. At recent times, it coincides with the blue curve. The red curve is the resonance model with Chrysalis. Chrysalis has an instability around 160 Myr before present and is removed from the system.

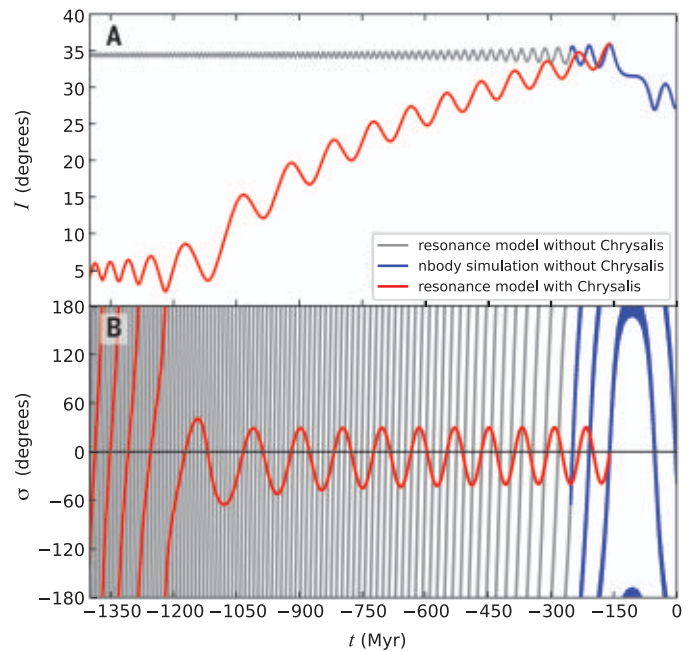
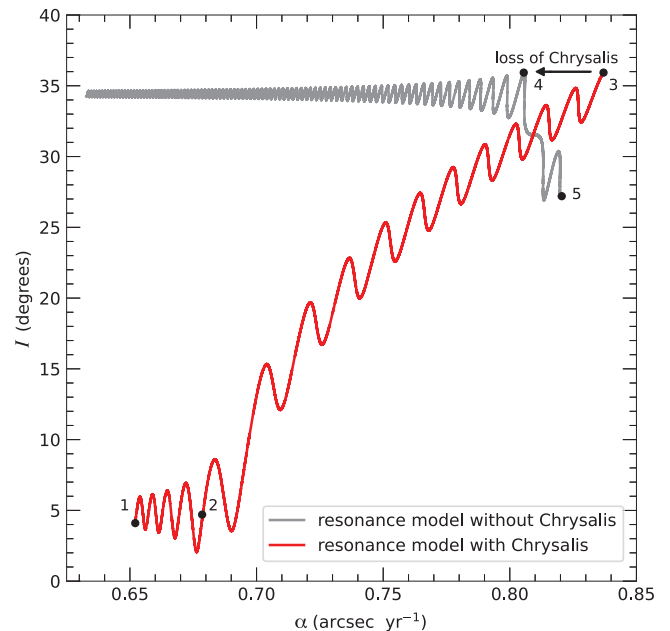


**Fig. 3. Evolution as a function of precession constant.**

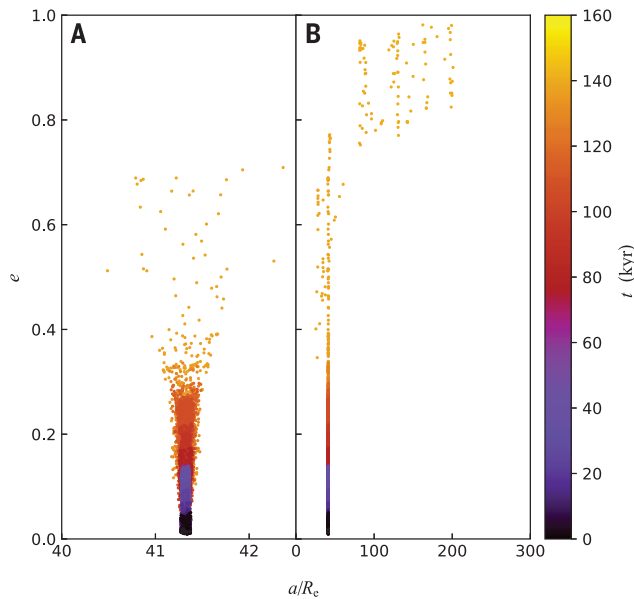
The system starts outside the Neptune resonance at point 1. As Titan migrates, the precession constant increases, and the system enters the resonance at point 2. With continued evolution, the obliquity of Saturn increases. At point 3, Chrysalis experiences an instability and has a close encounter with Saturn, forming the rings. The precession constant suddenly decreases to point 4. Further evolution, without Chrysalis, carries the system to point 5, at the present.



equator plane, whereas for a distant satellite, it coincides with the plane of the orbit of the planet about the Sun. The magnitude of  $i_j^l$  depends on the planetary oblateness and obliquity and the semimajor axes involved.

Equation 2 shows that the contribution from each satellite to  $q$ , the factor that is added to  $J_2$ , is proportional to the product of the mass of the satellite and the square of its distance from the planet. The contribution of Titan to the precession constant dominates the contribution from  $J_2$ , and this contribution increases as Titan migrates outward.

**Fig. 4. Eccentricity of Chrysalis as a function of its semimajor axis, in an example simulation. (A and B)** The early evolution in the chaotic zone is visible in (A). In (B), the chaotic phase shown in (A) appears as a spike on the left; the semimajor axis ( $a$ ) and eccentricity ( $e$ ) increase because of scattering encounters with Titan and Iapetus. Time, in thousand years (kyr), is indicated by the color bar. The trajectory is sampled every 500 years.



### Resonance escape mechanisms

We next consider how the Saturn system could have escaped the resonance with Neptune. We identify two possibilities: First, the satellites' contribution to the precession of Saturn could have changed because of changes in their orbits (Eq. 2). This might have happened by the passage of the system through an orbital resonance involving the satellites. Second, the system could have escaped the Neptune resonance if a satellite was ejected from the system or collided with Saturn (removing a term in the sum in Eq. 2). A close encounter of a satellite with Saturn could have produced the debris that has evolved into the rings.

We investigated the first possibility through direct integration of the system using the full numerical model. We find that two principal orbital resonances are encountered (see supplementary text), which have been previously studied (25, 26). We carried out integrations of the full system backward in time for ~200 Myr, with the Saturn moment of inertia that was determined with differential rotation and with various rates of tidal evolution that are consistent with the measured rate of evolution of Titan (21). These integrations confirm that the Saturn system is currently not in the Neptune resonance.

In no case did we find changes in the satellite orbits that were sufficiently large to allow the system to escape the Neptune resonance. Figure 2 shows an example numerical integration. The evolution coincides with the resonance model over the full span of the integration, indicating that passage through these orbital resonances cannot take the system out of the Neptune resonance. The comparison also illustrates that no other, previously unknown, strong orbital resonance was encountered.

### Instability of an additional satellite

The second possibility is that there was previously an additional satellite in the Saturn system and that this satellite suffered some orbital instability that led to either its escape or its collision with Saturn. With the loss of the hypothetical satellite, Chrysalis, the precession rate would have suddenly changed, allowing the system to escape the Neptune resonance. By requiring that the system evolved to the present configuration, we place constraints on when this could have occurred.

While in the Neptune resonance, the resonance angle  $\sigma$  oscillates about zero. Because  $\sigma$  does not change when a satellite is lost, Chrysalis could only have been lost when  $\sigma$  was close to zero in the simulations of the full system, backward in time from the present, without Chrysalis.

We have determined that the moment of inertia of Saturn is a little too small for the system to be in the Neptune resonance today, or the precession constant is a little too high. In the past, as Titan was closer to Saturn, the precession constant was smaller (Eq. 2). Therefore, there was a moment in the past when the system crossed the resonance. Figure 2 shows that this happens in the example simulation at about 100 Myr before present, where the motion of  $\sigma$  reverses direction. Figure 3 shows the evolution in terms of the precession constant. The loss of Chrysalis connects the evolution with Chrysalis to the evolution without Chrysalis. The system evolves into the resonance, then to higher obliquity as the precession constant changes because of the migration of Titan, at which point Chrysalis could have been lost, causing the precession constant to suddenly decrease. The subsequent evolution passes through the resonance to the currently observed Saturn system.

In this example simulation, the most recent time that Chrysalis could have been lost is about 160 Myr before present. In the full suite of simulations that vary the rate of tidal evolution of Titan, we find that the loss of Chrysalis could have occurred roughly 100 to 200 Myr before present. The combination of evolution in the Neptune resonance, followed by recent loss of Chrysalis, accounts for both the present-day obliquity of Saturn and the system's proximity to the Neptune resonance.

To explore the possibility that Chrysalis's orbit was destabilized, we integrated the full system with Chrysalis placed between Titan and Iapetus. As Titan migrates in the simulations, the Titan-Chrysalis pair encounters orbital resonances. We focused our exploration on the 3:1 mean-motion resonance (at which the orbital period of Chrysalis is approximately three times the orbital period of Titan), because this is the first strong resonance that would have been encountered as Titan migrated outward. The mass of Chrysalis must be chosen so that the precession constant has the required change. For the 3:1 resonance, the mass of Chrysalis must be approximately equal to the mass of Iapetus, though the value depends on when the 3:1 resonance is encountered, which in turn depends on the rate of tidal evolution of Titan. In these simulations, we set the tidal evolution rate for Titan to be  $13.75 \text{ cm year}^{-1}$  and the mass of Chrysalis to equal the mass of Iapetus. The initial conditions are taken from the backward simulation shown in Fig. 2.

We carried out integrations with Titan's orbital semimajor axis initially smaller than is required to be in the 3:1 resonance with Chrysalis. As Titan migrates outward, the system reaches the resonance, the behavior becomes chaotic, and the orbital eccentricity of Chrysalis rapidly increases, leading to close encounters with the other satellites (fig. S5).

### Exploration of an unstable system

We explored the expected outcomes of this scenario by simulating the system starting in the chaotic zone of the 3:1 Titan-Chrysalis resonance. We studied 390 cases, started with slightly different initial conditions (21). These integrations included Hyperion because Chrysalis repeatedly crosses its orbit. The present obliquity of Saturn could be explained if Chrysalis was either lost by ejection on a hyperbolic orbit or broken up during a grazing encounter with Saturn, with most of the material eventually hitting Saturn. In the latter case, a breakup of the satellite could explain the age of Saturn's rings.

The evolution of Chrysalis follows a typical pattern. In the first stage, the eccentricity and semimajor axis explore the chaotic zone and migrate to larger eccentricity. This stage is illustrated for an example simulation in Fig. 4A. This is followed by numerous close encounters with both Titan and Iapetus. The

number of encounters varies but is typically of the order of a few tens. These encounters lead to an increase in the semimajor axis and eccentricity of Chrysalis. This stage is illustrated in Fig. 4B. Eventually, Chrysalis either has a close encounter with Saturn, is ejected from the satellite system, or has a collision with Titan, Hyperion, or Iapetus. For the simulation in Fig. 4, Chrysalis has a grazing encounter with Saturn at a distance of  $1.9R_e$ , close enough to undergo tidal disruption followed by formation of a ring (27).

Of our 390 simulations, there were 90 cases in which Hyperion was left with an orbit that was within  $1.5R_e$  of its present orbit. Of these, there were 19 cases in which Chrysalis became hyperbolic (21%) and 17 Saturn grazers (18%) (the distance became smaller than  $2.5R_e$  from Saturn; see supplementary text). Both of these cases would allow the system to escape the Neptune resonance (39%); those with Saturn grazers could make the rings. Hyperion's orbit is modified somewhat, so we cannot determine where it originated before Chrysalis was scattered. In 8 of the 17 grazing cases (47%), Hyperion was left librating in the Titan-Hyperion 4:3 mean motion resonance, as observed today (28).

The simulated Chrysalis has multiple encounters with Titan and Iapetus, so we expect that their orbits were modified. Titan's orbital eccentricity is of particular interest, because its relatively large value of 0.0288 has been considered a puzzle (29). In these integrations, we set the initial eccentricity of Titan to be zero; at the time of the encounter of Chrysalis with Saturn, we find that the eccentricity of Titan ranges from 0.004 to 0.055, with a mean of 0.026 and standard deviation of 0.015 (Fig. 5). The scattering of Chrysalis off of Titan leads to an orbital eccentricity of Titan similar to the current value.

We conclude that the loss of the hypothetical satellite Chrysalis can explain the obliquity of Saturn, the young age of its rings, and the eccentricity of Titan. The increased eccentricity and concomitant tidal heating (proportional to the square of the eccentricity) of Titan might also explain the presence of short-lived methane in its atmosphere (30).

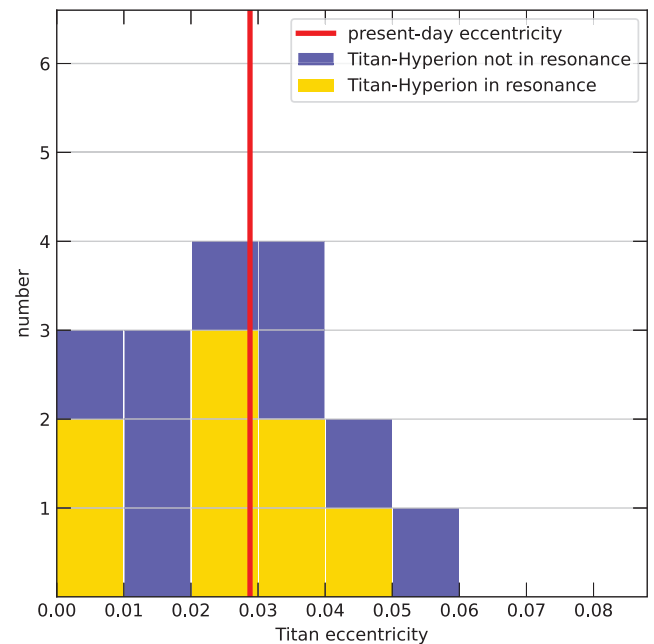
### Formation of Saturn's rings

A close encounter of Chrysalis with Saturn would have caused Chrysalis to break apart. If we assume that Chrysalis was predominantly made of water ice, like Iapetus, then this debris could have developed into Saturn's rings (27). Previous simulations of the formation of the rings from a disrupted cometary body, similar to the mass we assume for Chrysalis, indicate that it provides enough mass to produce the present-day rings (31).

The required timing of the loss of Chrysalis coincides with the estimated age of the rings.

**Fig. 5. Histogram of the eccentricity of Titan at the moment when Chrysalis experiences a grazing encounter with Saturn.**

Yellow (blue) bars indicate simulations in which Titan and Hyperion are (are not) left in a 4:3 mean motion resonance, in which we find Hyperion today. The vertical red line indicates the current eccentricity of Titan.



In our scenario, the ring age is anchored to a measured quantity, the rate of Titan's orbital expansion (14).

We propose that Saturn once had an additional satellite, Chrysalis; that the system was previously in the spin-orbit precession resonance with Neptune; that Saturn's obliquity increased as the precession rate changed because of the migration of Titan; that it escaped the precession resonance because of an instability of the orbit of Chrysalis; and that a close encounter of this hypothesized satellite with Saturn led to the formation of its rings.

### REFERENCES AND NOTES

- W. R. Ward, D. P. Hamilton, *Astrophys. J.* **128**, 2501–2509 (2004).
- P. Goldreich, S. Tremaine, *Annu. Rev. Astron. Astrophys.* **20**, 249–283 (1982).
- Z. Zhang *et al.*, *Icarus* **294**, 14–42 (2017).
- L. Less *et al.*, *Science* **364**, eaat2965 (2019).
- A. Crida, S. Charnoz, H.-W. Hsu, L. Dones, *Nat. Astron.* **3**, 967–970 (2019).
- A. W. Harris, W. R. Ward, *Annu. Rev. Earth Planet. Sci.* **10**, 61–108 (1982).
- G. Cassini, *Traite de L'origine ede Progres de L'Astronomie* (Paris, 1693).
- S. J. Peale, *Astron. J.* **74**, 483–489 (1969).
- J. Laskar, P. Robutel, *Nature* **361**, 608–612 (1993).
- J. Touma, J. Wisdom, *Science* **259**, 1294–1297 (1993).
- W. R. Ward, *Science* **189**, 377–379 (1975).
- M. Saillenfest, G. Lari, G. Boué, *Nat. Astron.* **5**, 345–349 (2021).
- M. Saillenfest, G. Lari, G. Boué, A. Courtot, *Astron. Astrophys.* **647**, A92 (2021).
- V. Lainey *et al.*, *Nat. Astron.* **4**, 1053–1058 (2020).
- G. F. Lindal, D. N. Sweetnam, V. R. Eshleman, *Astron. J.* **90**, 1136–1146 (1985).
- B. Militzer, W. B. Hubbard, *Astrophys. J.* **774**, 148 (2013).
- W. B. Hubbard, *Astrophys. J.* **768**, 43 (2013).
- B. Militzer, S. Wahl, W. B. Hubbard, *Astrophys. J.* **879**, 78 (2019).
- J. Wisdom, W. B. Hubbard, *Icarus* **267**, 315–322 (2016).
- W. B. Hubbard, *Icarus* **137**, 357–359 (1999).
- Materials and methods are provided in the supplementary materials.
- S. Tremaine, *Icarus* **89**, 85–92 (1991).
- R. Brasser, M. H. Lee, *Astron. J.* **150**, 157 (2015).
- S. Tremaine, J. Touma, F. Namouni, *Astron. J.* **137**, 3706–3717 (2009).

- W. Polycarpe *et al.*, *Astron. Astrophys.* **619**, A133 (2018).
- M. Čuk, L. Dones, D. Nesvorný, K. J. Walsh, *Mon. Not. R. Astron. Soc.* **481**, 5411–5421 (2018).
- L. Dones, *Icarus* **92**, 194–203 (1991).
- A. T. Sinclair, *Mon. Not. R. Astron. Soc.* **160**, 169–187 (1972).
- C. Sagan, S. F. Dermott, *Nature* **300**, 731–733 (1982).
- G. Tobie, J. I. Lunine, C. Sotin, *Nature* **440**, 61–64 (2006).
- R. Hyodo, S. Charnoz, K. Ohtsuki, H. Genda, *Icarus* **282**, 195–213 (2017).
- J. Wisdom *et al.*, SaturnObliquityRings, Harvard Dataverse Repository (2022); <https://doi.org/10.7910/DVN/RJZXGW>.
- J. Wisdom, NbodySatellites, Zenodo (2022); <https://doi.org/10.5281/zenodo.6960630>.

### ACKNOWLEDGMENTS

We thank J. Touma, S. Tremaine, and T. Perron for carefully reading the manuscript. C. Hill provided computing time on the MIT Engaging Cluster. **Funding:** Support for this work was provided by NASA's SSW program (J.W., F.N., and R.D.), NASA's extended Juno mission (W.B.H. and B.M.), the National Nuclear Security Administration (B.M.), NASA's CDAP program (R.G.F.), and the NSF Graduate Research Fellowships Program (B.D.). **Author contributions:** J.W. and F.N. designed the overall research; J.W. noticed that Titan's migration could lead to capture in the Neptune resonance; B.M., W.B.H., and J.W. developed interior models; J.W. wrote the satellite evolution software; R.D. developed the resonance model; J.W. suggested that an extra satellite might have been resonantly destabilized and form the rings; R.D. identified the conditions for escape; and J.W. and R.D. carried out the simulations and analysis. F.N. and B.G.D. provided input throughout. R.G.F. validated the numerical model of Saturn's pole. **Competing interests:** The authors declare no competing interests. **Data and materials availability:** All data and software have been deposited in Harvard Dataverse (32). The satellite evolution code is also available on Zenodo (33). **License information:** Copyright © 2022 the authors, some rights reserved; exclusive licensee American Association for the Advancement of Science. No claim to original US government works. <https://www.science.org/about/science-licenses-journal-article-reuse>

### SUPPLEMENTARY MATERIALS

[science.org/doi/10.1126/science.abn1234](https://science.org/doi/10.1126/science.abn1234)  
Materials and Methods  
Supplementary Text  
Figs. S1 to S5  
Table S1  
References (34–51)

Submitted 4 November 2021; accepted 12 August 2022  
10.1126/science.abn1234

## SIGNAL TRANSDUCTION

## Lysosomal GPCR-like protein LYCHOS signals cholesterol sufficiency to mTORC1

Hijai R. Shin<sup>1,2</sup>, Y. Rose Citron<sup>1,2,†</sup>, Lei Wang<sup>3,†,‡</sup>, Laura Tribouillard<sup>4</sup>, Claire S. Goul<sup>1,2</sup>, Robin Stipp<sup>1,2</sup>, Yusuke Sugawara<sup>5</sup>, Aakriti Jain<sup>1,2</sup>, Nolwenn Samson<sup>4</sup>, Chun-Yan Lim<sup>1,2</sup>, Oliver B. Davis<sup>1,2</sup>, David Castaneda-Carpio<sup>1,2</sup>, Mingxing Qian<sup>6</sup>, Daniel K. Nomura<sup>1,7</sup>, Rushika M. Perera<sup>8</sup>, Eunyoung Park<sup>1</sup>, Douglas F. Covey<sup>9,10</sup>, Mathieu Laplante<sup>4</sup>, Alex S. Evers<sup>3,9,10</sup>, Roberto Zoncu<sup>1,2\*</sup>

Lysosomes coordinate cellular metabolism and growth upon sensing of essential nutrients, including cholesterol. Through bioinformatic analysis of lysosomal proteomes, we identified lysosomal cholesterol signaling (LYCHOS, previously annotated as G protein–coupled receptor 155), a multidomain transmembrane protein that enables cholesterol-dependent activation of the master growth regulator, the protein kinase mechanistic target of rapamycin complex 1 (mTORC1). Cholesterol bound to the amino-terminal permease-like region of LYCHOS, and mutating this site impaired mTORC1 activation. At high cholesterol concentrations, LYCHOS bound to the GATOR1 complex, a guanosine triphosphatase (GTPase)–activating protein for the Rag GTPases, through a conserved cytoplasm-facing loop. By sequestering GATOR1, LYCHOS promotes cholesterol- and Rag-dependent recruitment of mTORC1 to lysosomes. Thus, LYCHOS functions in a lysosomal pathway for cholesterol sensing and couples cholesterol concentrations to mTORC1-dependent anabolic signaling.

Cholesterol, an essential building block for membrane biogenesis, is also a signaling molecule that regulates embryonic development and numerous physiological processes by acting either as a ligand or as a precursor for oxysterols and steroid hormones. Aberrant amounts and activity of cholesterol are associated with pathological conditions such as obesity, atherosclerosis, infertility, and cancer, making its accurate sensing essential (1, 2). For example, dedicated machinery on the endoplasmic reticulum (ER) senses local cholesterol concentrations and, in response, fine-tunes the rate of cholesterol synthesis and uptake (3, 4).

In actively proliferating cells, including cancer cells, the phosphatidylinositol 3-kinase (PI3K)–AKT–mechanistic target of rapamycin complex 1 (mTORC1) pathway stimulates both de novo cholesterol synthesis and uptake to

meet the increased demand for both cholesterol itself and its growth-promoting biosynthetic intermediates (5–7). However, where in the cell and how cholesterol abundance is signaled to growth-regulating pathways are not well understood.

The lysosome is a key nutrient-sensing center for the cell (6). At the lysosome, the master growth regulator protein kinase, mTORC1, integrates many environmental signals, including nutrients, growth factors, energy, oxygen and stress and, in response, triggers downstream anabolic programs that increase cell mass (8). When intracellular concentrations of nutrients, including cholesterol, are increased, mTORC1 localizes to the lysosomal membrane, where it contacts the small guanosine triphosphatase (GTPase) Rheb, which activates mTORC1 kinase function (8–10). Conversely, when nutrient abundance is low, mTORC1 relocalizes to the cytosol, where it remains inactive until nutrient concentrations are restored.

Multiple proteins control the nutrient-dependent localization of mTORC1 to the lysosome. The Rag GTPases are heterodimers composed of either RagA or RagB in complex with either RagC or RagD (11, 12). A key event when nutrients are plentiful is the loading of RagA or B with GTP, which enables it to physically bind to mTORC1 and anchor it to the lysosomal membrane (8, 13, 14). In turn, the nucleotide state of RagA or B is controlled by other lysosome-associated proteins. The GATOR1 complex is a dedicated GTPase-activating protein (GAP) for RagA. When nutrient concentrations are low, GATOR1 triggers GTP hydrolysis on RagA, thereby promoting the inactive state of the Rag GTPase complex that leads to cytoplasmic relocaliza-

tion and inactivation of mTORC1 (15, 16). This negative regulatory activity of GATOR1 is countered by the amino acids leucine, arginine, and methionine, through dedicated sensors that inhibit the GAP activity of GATOR1 either directly or via a second complex known as GATOR2 (8). Whether cholesterol regulates the GAP activity of GATOR1 toward RagA is unknown but, consistent with this possibility, genetic inactivation of GATOR1 renders mTORC1 constitutively active even if cholesterol concentrations are low (17).

In cells and in vitro, cholesterol on the lysosomal limiting membrane directly participates in the recruitment and activation of mTORC1. This cholesterol pool is highly regulated: The sterol carrier, oxysterol binding protein (OSBP), localizes at ER–lysosome membrane contact sites, where it transfers cholesterol from the ER to the lysosome to enable mTORC1 activation (1, 6, 17). Conversely, the cholesterol transporter Niemann–Pick C1 (NPC1) promotes export of cholesterol from the lysosomal surface, thereby inhibiting mTORC1 signaling (10, 17).

How cholesterol interacts with the mTORC1-scaffolding machinery is not well understood. Various cholesterol pools coexist at the lysosomal membrane, one derived from low-density lipoprotein (LDL), another deposited across membrane contact sites (17). Moreover, the concentration of cholesterol likely varies across different regions of the lysosomal membrane and as a function of metabolic states (18). Thus, like sensing of amino acids, cholesterol sensing may rely on multiple cholesterol-sensing factors with distinct localization, affinity for the sterol ligand, and upstream regulatory mechanisms. One important player is the lysosomal transmembrane protein, SLC38A9 (19, 20), which participates in cholesterol-dependent activation of mTORC1 through conserved sterol-interacting motifs within its transmembrane domains (10). However, SLC38A9 primarily relays arginine abundance to mTORC1, whereas a dedicated sensor for cholesterol remains to be identified.

More generally, it is likely that the lysosome has as yet undiscovered nutrient sensors that could regulate cellular metabolism through mTORC1-dependent or independent pathways. Identifying putative nutrient sensors can be challenging, because they generally have weak interactions with their cognate metabolites and have diverse domain composition and topologies (21). Building on recent advances in immunoprecipitation and proteomic profiling of lysosomes combined with a robust bioinformatic pipeline that identifies and prioritizes putative signaling proteins, we identified GPR155, which we rename lysosomal cholesterol sensing (LYCHOS) protein, as a candidate lysosomal cholesterol sensor that controls signaling functions of this organelle.

<sup>1</sup>Department of Molecular and Cell Biology, University of California at Berkeley, Berkeley, CA 94720, USA. <sup>2</sup>Innovative Genomics Initiative at the University of California, Berkeley, Berkeley, CA 94720, USA. <sup>3</sup>Department of Anesthesiology, Washington University School of Medicine, St. Louis, MO 63110, USA. <sup>4</sup>Centre de recherche sur le cancer de l'Université Laval, Université Laval, Québec, QC G1R 3S3, Canada. <sup>5</sup>Department of Anesthesiology and Pain Medicine, Juntendo University School of Medicine, Tokyo 113-8421, Japan. <sup>6</sup>Department of Developmental Biology, Washington University School of Medicine, St. Louis, MO 63110, USA. <sup>7</sup>Department of Nutritional Sciences and Toxicology, University of California at Berkeley, Berkeley, CA 94720, USA. <sup>8</sup>Department of Anatomy, University of California San Francisco, San Francisco, CA 94143, USA. <sup>9</sup>Department of Developmental Biology and Biochemistry, Washington University School of Medicine, St. Louis, MO 63110, USA. <sup>10</sup>The Taylor Family Institute for Innovative Psychiatric Research, Washington University School of Medicine, St. Louis, MO 63110, USA.

\*Corresponding author. Email: rzoncu@berkeley.edu

†These authors contributed equally to this work.

‡Present address: Department of Anesthesiology, Union Hospital, Tongji Medical College, Huazhong University of Science and Technology, Wuhan, Hubei 430022, China.

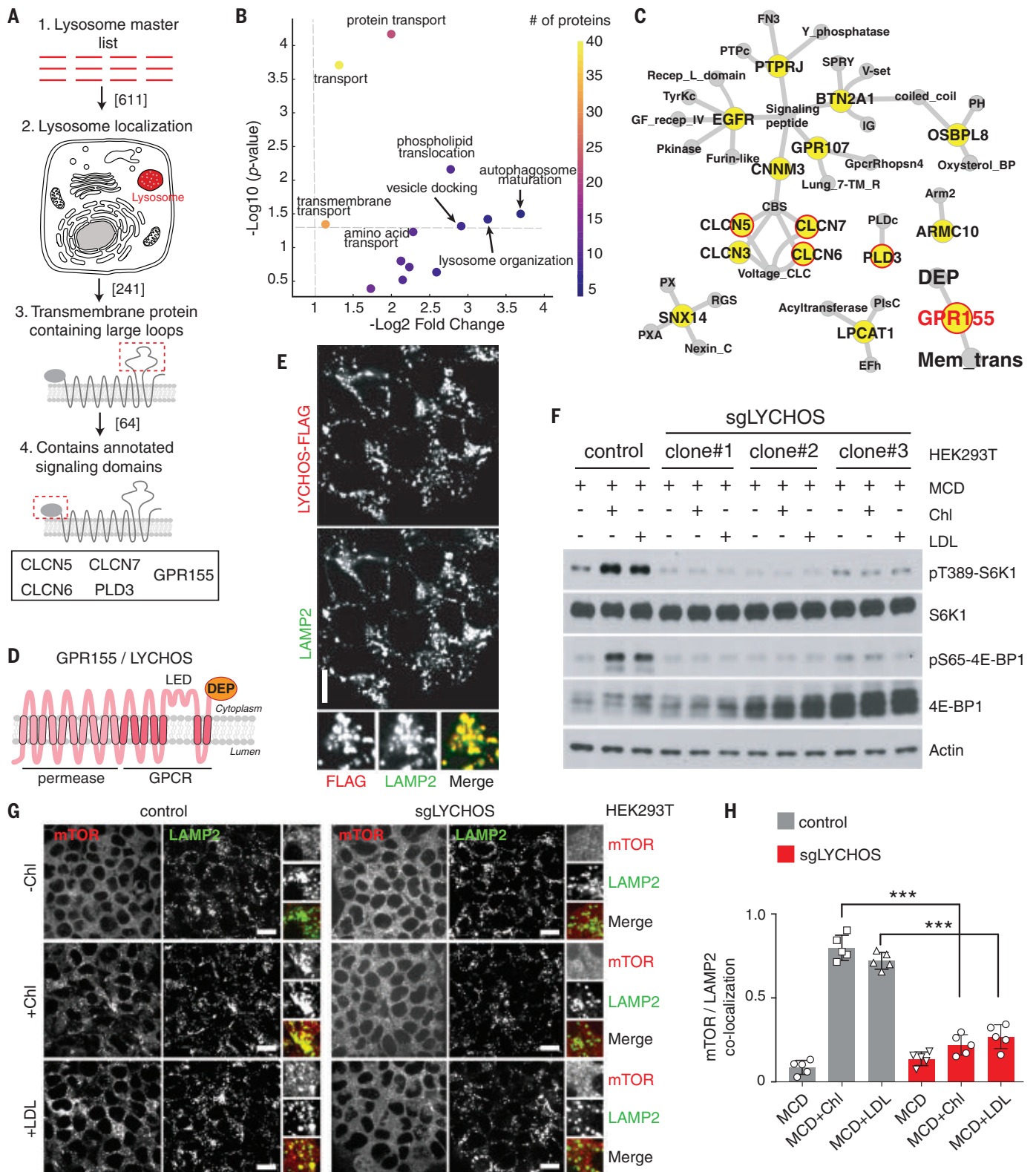


**Fig. 1. Lysosomal transmembrane protein LYCHOS is required for cholesterol-mediated mTORC1 activation.** (A) Summary chart of the workflow for the identification of lysosomal transmembrane signaling proteins.

(B) Volcano plots of “biological process” GO terms enriched in lysosome-resident transmembrane proteins relative to all transmembrane proteins.

(C) Network representation of lysosome-associated transmembrane proteins

with large loops (yellow). Gray nodes show annotated signaling domains. Predicted lysosome-resident transmembrane proteins are circled in red. (D) Schematic of the predicted GPR155/LYCHOS topology and domain organization.

(E) LYCHOS is a lysosomal protein. HEK-293T cells stably expressing LYCHOS-FLAG were fixed and stained with antibodies targeting FLAG and LAMP2. Scale bar, 10  $\mu$ m. (F) LYCHOS is required for mTORC1 activation by cholesterol.

Control HEK-293T cells or LYCHOS-deleted cells (sgLYCHOS) were depleted of sterols by using methyl- $\beta$ -cyclodextrin (MCD, 0.75% w/v) for 2 hours, followed by refeeding for 2 hours with 50  $\mu$ M cholesterol (Chl) in complex with 0.1% MCD or with 50  $\mu$ g/ml LDL. Cell lysates were blotted with the indicated antibodies. **(G)** LYCHOS is required for cholesterol-dependent mTORC1 recruitment to lysosomes. LYCHOS-deleted HEK293T cells were subjected to

cholesterol depletion and restimulation, followed by immunofluorescence of endogenous mTOR and LAMP2. Representative images are shown. Scale bars, 10  $\mu$ m. **(H)** Quantification of colocalization of mTOR with LAMP2-positive lysosomes in the indicated genotypes and conditions. Data are means  $\pm$  SD. Statistical analysis was performed using analysis of variance with Dunnett's multiple comparison test; \*\*\* $p$  < 0.001.

### LYCHOS is required for cholesterol-mediated mTORC1 activation

To identify candidate nutrient-sensing factors that reside at the lysosome, we devised a bioinformatic method to analyze a 611-protein “master list” that combines published and unpublished lysosomal proteomic datasets (17, 22–24) (Fig. 1A and fig. S1A and table S1). Gene ontology (GO) analysis of this list showed the expected enrichment of biological processes associated with the lysosome (fig. S1B).

From this, we selected proteins that satisfied all the following criteria: (i) transmembrane topology, commonly found in metabolite receptors and “transceptors” (21); (ii) presence of relatively large loops that could facilitate interaction with cytoplasmic effectors; (iii) presence of structural domains and architecture associated with signal transduction; and (iv) absence of reported localization to other membrane compartments, which may indicate pleiotropic roles (Fig. 1A). Consistent with the role of the lysosome in releasing the products of macromolecular breakdown to the cytosol, the 127 lysosome-specific transmembrane proteins were highly enriched for metabolite transport and translocation compared to the 5208 transmembrane proteins annotated in UniProt (Fig. 1B and fig. S1, C and D).

Five transmembrane proteins satisfied all of the above criteria: chloride voltage-gated channel (CLCN) 5, 6, and 7; phospholipase D family member 3 (PLD3); and G protein-coupled receptor 155 (GPR155) (Fig. 1C). Of these, GPR155 (also known as DEP domain containing 3) stood out because of its topological features, consisting of a 10-transmembrane (TM) domain N-terminal portion with similarity to solute carriers (SLCs); a 7-TM central portion with similarity to class B GPCRs (25), which contains a large (118 amino acid) insertion between TM helices 15 and 16; and a C-terminal region containing a Dishevelled, Egl-10, and Pleckstrin (DEP) domain. On the basis of UniProt and AlphaFold predictions, we predict a 17-TM topology for GPR155 (Fig. 1D and fig. S1E).

We confirmed the lysosomal localization of GPR155 by immunoblotting of immunoprecipitated lysosomal samples with an antibody to the endogenous protein (fig. S2A). Moreover, double immunofluorescence of endogenous lysosomal-associated membrane protein 2 (LAMP2) and FLAG-labeled GPR155, stably expressed in human embryonic kidney (HEK)-293T cells, showed that GPR155 specifically

localized to lysosomes, with no detectable signal in vesicular structures that lack LAMP2, in the Golgi, or in the plasma membrane (Fig. 1E and fig. S2, B and C). Through immunostaining with antibodies directed against the TM15-16 loop and the DEP domain under semipermeabilized conditions, we experimentally verified that both domains face the cytoplasm, not the lysosomal lumen (fig. S2, D and E). For reasons described below, we hereafter refer to GPR155 as lysosomal cholesterol signaling protein (LYCHOS), and its TM15-16 loop as the LYCHOS effector domain (LED).

Because the domain architecture of LYCHOS is consistent with a signaling function, we tested whether LYCHOS regulated mTORC1 activation. Depletion of LYCHOS by CRISPR-Cas9 or shRNA in HEK-293T cells decreased mTORC1 signaling under full nutrient conditions, as shown by loss of phosphorylation of canonical substrates p70 S6-kinase 1 (S6K1) and 4E-binding protein 1 (4E-BP1) (11, 12) (fig. S3, A and B). Conversely, transient overexpression of LYCHOS boosted phosphorylation of mTORC1 substrates in a dose-dependent manner (fig. S3C).

Consistent with decreased mTORC1 signaling, LYCHOS depletion resulted in significant suppression of cell proliferation, which was rescued by reconstituting LYCHOS-deleted cells with LYCHOS wild type (WT) (fig. S3, D and E). Moreover, RNA sequencing (RNAseq) analysis of LYCHOS-depleted cells showed a decreased expression of several genes involved in glycolysis, the pentose phosphate pathway, and lipid biosynthesis—a gene signature similar to that observed upon pharmacological mTORC1 inhibition (5) (fig. S3, F to H). These gene expression changes were completely reversed by reexpressing a short hairpin RNA (shRNA)-resistant isoform of LYCHOS (fig. S3H).

A bioinformatic query of the 611-gene lysosomal master list in the NIH Gene Expression Omnibus (GEO) Profiles database identified LYCHOS as one of eight lysosomal genes that have decreased expression upon fasting in liver, muscle, and adipose tissue of mice (fig. S4, A and B, and table S2). We confirmed these *in silico* results by quantitative polymerase chain reaction (qPCR) from livers of mice subjected to 6 hours and 24 hours of fasting, which showed a time-dependent decrease in *Lychos* expression (fig. S4C). Conversely *Npc1*, a negative regulator of cholesterol-dependent mTORC1 activation (10, 17), was 1 of 14 lyso-

somal genes with increased expression in fasting animals (fig. S4D).

We tested whether LYCHOS enables mTORC1 activation by specific nutrient stimuli. In LYCHOS knockout (KO) cells, mTORC1 activation by acute starvation-refeeding with amino acids (fig. S5A) or glucose (fig. S5B) was unperturbed. By contrast, LYCHOS was required for mTORC1 stimulation by cholesterol, delivered to cells in complex with methyl-beta cyclodextrin (MCD), or in LDL particles, following its depletion with MCD plus the cholesterol synthesis inhibitor, mevastatin (10, 17) (Fig. 1F and fig. S5, C and D).

Like amino acids and glucose, cholesterol induces mTORC1 relocalization from the cytosol to the lysosomal membrane (8, 10, 17). In LYCHOS KO cells, mTORC1 failed to localize to lysosomes upon stimulation with either MCD:cholesterol or LDL (Fig. 1, G and H, and fig. S5, E and F). By contrast, LYCHOS deletion did not affect lysosomal localization of the Rag GTPases or their membrane anchor, the Ragulator/LAMTOR complex (fig. S5, G to J). Thus, LYCHOS appears to be required for cholesterol-dependent activation of the mTORC1 lysosomal scaffolding complex, not for its physical integrity.

### LYCHOS binds to cholesterol through its N-terminal domain

The presence of both an N-terminal permease-like domain and two signaling modules (GPCR-like and DEP) indicates that LYCHOS may be either a cholesterol transporter or an effector. Lipidomic analysis of immuno-isolated lysosomes from control cells and cells lacking LYCHOS did not reveal a significant difference in total lysosomal cholesterol content following loss of LYCHOS (fig. S6, A and B).

We also ablated LYCHOS in cells lacking NPC1, loss of which causes cholesterol to accumulate both within the lysosomal lumen and on the limiting membrane (17, 26, 27). The two pools were visualized, respectively, with filipin and with mCherry-D4H, a recombinant, fluorescently tagged cholesterol probe based on the fourth domain of *Clostridium perfringens* theta-toxin (17, 28, 29). Depleting LYCHOS in cells lacking NPC1 did not reveal notable changes in the filipin or mCherry-D4H signal, whereas inactivating OSBP, which transfers cholesterol from the ER to the lysosomal limiting membrane, ablated mCherry-D4H but not filipin staining in cells lacking NPC1 (fig. S6, C to E).



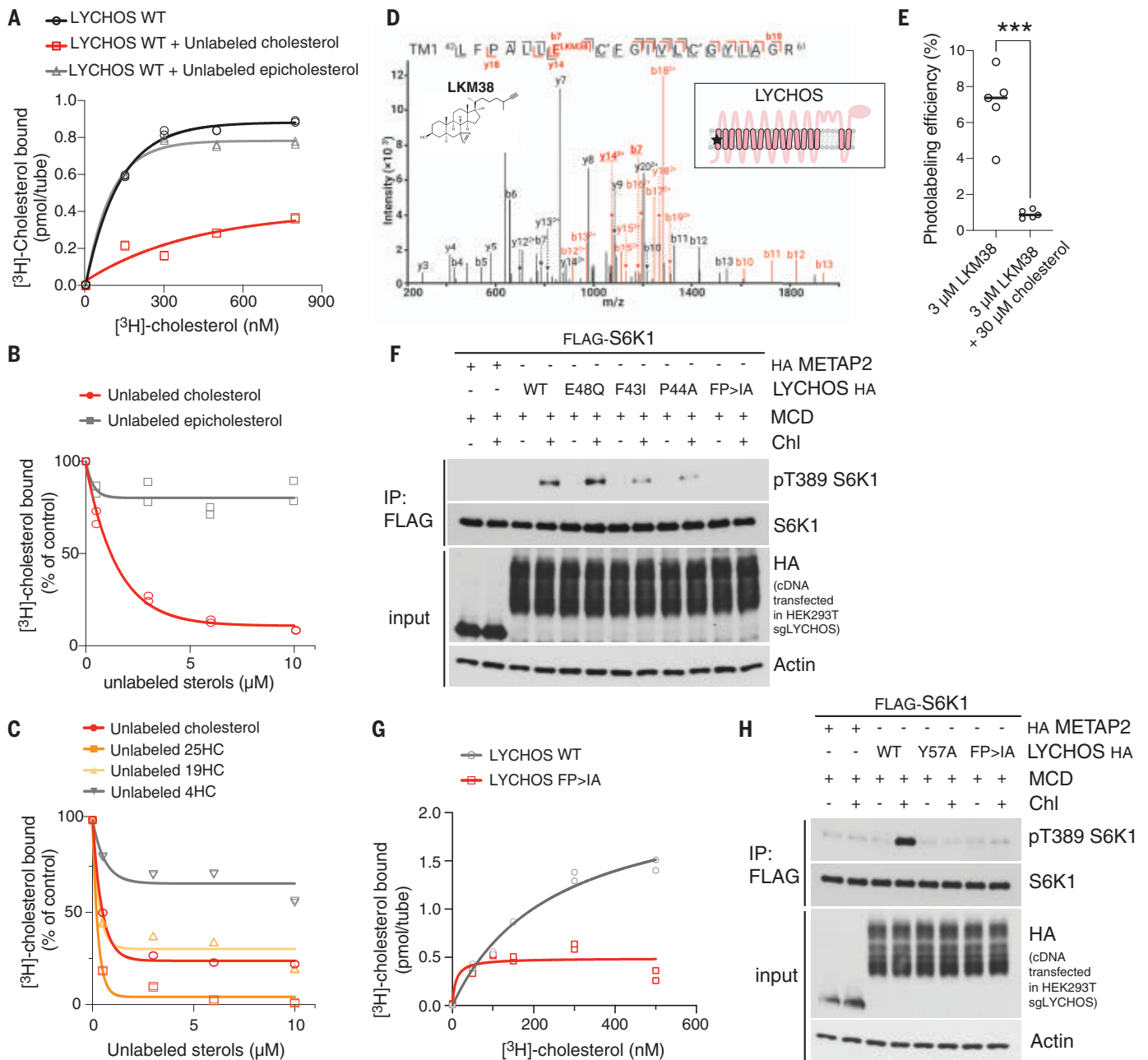


**Fig. 2. Cholesterol binding at the N-terminal region of LYCHOS is essential for mTORC1 activation.**

(A) [<sup>3</sup>H]-cholesterol binding to LYCHOS WT. Purified LYCHOS (150 ng) was incubated with the indicated concentration of [<sup>3</sup>H]-cholesterol, in the presence or absence of 10 μM cold cholesterol or epicholesterol. Bound [<sup>3</sup>H]-cholesterol was measured by scintillation counting. The assay was performed in duplicate and each data point is shown. (B and C) Competitive binding of unlabeled sterols to LYCHOS. LYCHOS (150 ng) was incubated with 500 nM [<sup>3</sup>H]-cholesterol along with increasing concentrations of the indicated unlabeled sterol. Bound [<sup>3</sup>H]-cholesterol was measured by scintillation counting. The assay was performed in duplicate and each data point is shown. (D) Collision-induced dissociation (CID) product ion spectrum of the TM1 tryptic peptide photolabeled with 3 μM LKM38. TM1 peptide [mass to charge ratio (*m/z*) = 934.53, *z* = 3] is photolabeled by LKM38 at E48. Red and black indicate product ions that do or do not contain LKM38 adduct, respectively. The C\* indicates that the cysteine is alkylated by *N*-ethylmaleimide. The inset schematic of LYCHOS in the panel indicates the approximate location of the residues labeled by LKM38 (black star). The numerical data are included in table S3. TM, transmembrane helix. (E) Photolabeling efficiency of recombinant LYCHOS by LKM38

in the absence or presence of excess unlabeled cholesterol. Data are mean ± SD of 5 replicates. Statistical analysis was performed using student *t* test; \*\*\**p* < 0.001. (F) LYCHOS TM1 is required for cholesterol-mediated mTORC1 activation. HEK293T/sgLYCHOS cells were transfected with FLAG-S6K1 along with hemagglutinin (HA)-tagged METAP2 (negative control), LYCHOS WT, and TM1 mutants. Cells were cholesterol starved, or starved and restimulated as indicated in the presence of 50 μM mevalonate and mevastatin, followed by FLAG immunoprecipitation (IP) and immunoblotting for the phosphorylation state and levels of the indicated proteins. (G) [<sup>3</sup>H]-cholesterol binding to LYCHOS WT and LYCHOS FP→IA mutant. Purified LYCHOS (150 ng) was incubated with the indicated concentration of [<sup>3</sup>H]-cholesterol, and bound radioactive cholesterol was measured by scintillation counting. The assay was performed in duplicate and each data point is shown. (H) LYCHOS TM1 mutants FP→IA and Y57A blunt cholesterol-mediated mTORC1 activation. HEK293T/sgLYCHOS cells were transfected with FLAG-S6K1 along with HA-METAP2 (negative control) or LYCHOS WT, Y57A, or FP→IA-HA and analyzed as in (F). Abbreviations for the amino acid residues are as follows: A, Ala; C, Cys; D, Asp; E, Glu; F, Phe; G, Gly; H, His; I, Ile; K, Lys; L, Leu; M, Met; N, Asn; P, Pro; Q, Gln; R, Arg; S, Ser; T, Thr; V, Val; W, Trp; and Y, Tyr.

Loss of NPC1, and the resulting cholesterol accumulation on the lysosomal membrane renders mTORC1 constitutively and aberrantly active (10, 17, 30). Depleting LYCHOS from cells lacking NPC1 completely suppressed constitutive mTORC1 signaling (fig. S6F). Thus, LYCHOS does not control the concentrations of lysosomal cholesterol but is required for lysosomal cholesterol to activate mTORC1.

To determine whether LYCHOS directly binds to cholesterol, we expressed LYCHOS recombinantly, verified its purity (fig. S7, A and B), and incubated it with increasing concentrations of [<sup>3</sup>H]-cholesterol under detergent conditions that preserve protein stability (fig. S7C). LYCHOS exhibited saturable binding to [<sup>3</sup>H]-cholesterol with an apparent dissociation constant ( $K_d$ ) between 100 and 200 nM, which was competed by unlabeled cholesterol but not by its 3-OH epimer, epicholesterol (Fig. 2, A and B, and table S3). Cholesterol appeared to bind to LYCHOS in a stereo-specific manner, because binding of [<sup>3</sup>H]-cholesterol was competed by 25- and 19-hydroxycholesterol but not by 4 $\beta$ -hydroxycholesterol, indicating that binding is sensitive to modifications in specific positions of the cholesterol structure (Fig. 2C and table S3).

To map the site(s) of cholesterol binding, we labeled recombinantly expressed LYCHOS in vitro with photo-crosslinkable cholesterol analogs that combine an ultra violet-activated diazirine group to create a peptide-steroid adduct, and with an alkyne group for identification of the labeled site via copper-catalyzed cycloaddition and mass spectrometry (10, 31). Bulk photolabeling of LYCHOS was competed by excess cholesterol or cholesterol hemisuccinate, indicative of a specific binding reaction (fig. S8, A and B). Mass spectrometry profiling of peptide adducts with the analog LKM38, which bears the photoreactive diazirine group in ring 2, identified two sites of labeling, one corresponding to transmembrane helix 1 (TM1) in the permease-like N-terminal region (<sup>42</sup>LFPALLECFGIVLVCYGIAGR<sup>61</sup>), the second in the DEP domain (<sup>809</sup>LVQGGVIQ-HITNEYEFRDEYLFYR<sup>832</sup>) (Fig. 2D, fig. S8C, and tables S4 and S5). Both labeling sites were competed by excess free cholesterol (Fig. 2E and fig. S8, D and E). Moreover, the TM1 site was independently labeled by a second cholesterol analog, KK231, which bears the photoreactive diazirine group in the aliphatic tail (fig. S8F and table S6).

To determine whether the TM1 or DEP represent a cholesterol-binding regulatory site for mTORC1 activation, we reconstituted LYCHOS-deleted cells with isoforms lacking the TM1-containing permease-like domain, the DEP domain, or the LED. All three modified proteins were expressed in amounts comparable to those of the full-length protein and localized to the lysosome (fig. S9, A to C).

However, whereas deleting the DEP had no effect on cholesterol-dependent mTORC1 activation, removing the permease-like domain completely abolished it (fig. S9C). Removing the LED also ablated cholesterol-dependent mTORC1 activation; however, recombinantly expressed LED, held in a loop configuration by a leucine zipper, did not show appreciable binding to [<sup>3</sup>H]-cholesterol (fig. S9D). Thus, we further pursued TM1 as a cholesterol-dependent regulatory site.

Aromatic amino acids are often found in cholesterol-binding pockets (27, 32, 33). The TM1 domain has two conserved aromatic residues, Phe<sup>43</sup> and Tyr<sup>57</sup>, located near the sites of adduct formation by LKM38 and KK231 (Glu<sup>48</sup> and Cys<sup>55</sup>, respectively) (Fig. 2D and fig. S8F). In LYCHOS-deleted cells reconstituted with a Phe<sup>43</sup>→Ile mutant, cholesterol-dependent mTORC1 activation was blunted (Fig. 2F). Nearby Pro<sup>44</sup> may help establish the conformation of the cholesterol-binding pocket. Consistent with this possibility, binding of [<sup>3</sup>H]-cholesterol to the F43I-P44A double mutant LYCHOS was nearly abolished, and this double mutant had a stronger mTORC1 activation defect than either the F3I or P44A single mutants (Fig. 2, F and G). By contrast, mutating Glu<sup>48</sup> to Gln had no effect on mTORC1 signaling, indicating that this residue, which is labeled by the photoreactive diazirine of LKM38, is not involved in binding to native cholesterol (Fig. 2F). Finally, mutating the second aromatic residue, Tyr<sup>57</sup> to Ala also blunted cholesterol-dependent mTORC1 activation (Fig. 2H). All of these mutants localized correctly to lysosomes and were expressed at near-identical amounts (Fig. 2, F and H, and fig. S9E).

#### LYCHOS promotes mTORC1 signaling via cholesterol-regulated interaction with GATOR1

To delineate the mechanisms by which LYCHOS communicates cholesterol abundance to mTORC1, we used proximity biotinylation coupled with proteomics (34). We C-terminally fused LYCHOS to the TurboID biotin ligase (LYCHOS-TiD, which correctly localized to lysosomes, fig. S10A), along with NPC1-TiD as a control.

Although our lysosomal “master list” includes several trimeric G proteins known to transduce signals downstream of canonical GPCRs (table S1), none scored as LYCHOS interactors in TiD experiments (table S7) or by coimmunoprecipitation (co-IP) (fig. S10, B and C). Instead, LYCHOS-TiD specifically biotinylated the GATOR1 subunits NPRL2, NPRL3, and DEPDC5, and the SZT2 subunit of the GATOR1-associated KPTN, ITFG2, C12orf66, and SZT2-containing regulator of mTORC1 (KICSTOR) complex (35) (Fig. 3, A and B, and table S7). Confirming the proximity biotinylation results, endogenous LYCHOS, tagged

with a triple FLAG epitope by CRISPR-Cas9, bound to endogenous NPRL2 and NPRL3 in pull-down experiments, albeit to a smaller extent than DEPDC5 (also endogenously tagged with FLAG) (fig. S10D). No binding of LYCHOS to the KICSTOR subunit KPTN was observed, indicating that LYCHOS primarily interacts with GATOR1, not KICSTOR (fig. S10D).

We tested whether cholesterol controls the LYCHOS-GATOR1 interaction. In co-IP experiments, LYCHOS-FLAG bound more GATOR1 subunits when isolated from cells treated with cholesterol, than from cholesterol-depleted cells (Fig. 3C). By contrast, cholesterol did not affect the interaction of DEPDC5 with its partner GATOR1 subunits (Fig. 3C). Also, amino acids had no effect on the LYCHOS-GATOR1 interaction (fig. S10E).

Stimulation of LYCHOS-GATOR1 interaction by cholesterol was dose dependent, with a median effective concentration ( $EC_{50}$ ) of 31.5  $\mu$ M that matched that of cholesterol-induced activation of mTORC1 signaling (fig. S11, A and B). Based on measurements of lysosomal lipid content by lyso-IP and mass spectrometry, this value corresponded to a 33% molar ratio of cholesterol to phospholipids, although what fraction of this cholesterol is unbound by sphingomyelin and accessible by LYCHOS is unknown (36) (fig. S11C).

These data suggest that LYCHOS promotes mTORC1 signaling by interacting with and inhibiting GATOR1. Consistent with this hypothesis, deleting the essential GATOR1 subunit NPRL3 resulted in constitutively active mTORC1 signaling regardless of cholesterol abundance or LYCHOS deletion (Fig. 3D). Further supporting LYCHOS action through the GATOR1-Rag GTPase axis, stable expression of the GTP-locked RagB<sup>Q99L</sup> mutant, which is refractory to GATOR1-mediated inhibition (15, 16), induced constitutive mTORC1 signaling that bypassed loss of LYCHOS (fig. S11D).

SLC38A9 is also required for cholesterol-dependent activation of mTORC1 (10). However, SLC38A9-dependent and LYCHOS-dependent signaling are mechanistically distinct. SLC38A9 binds to the Rag GTPases and Ragulator complex, but not to GATOR1, whereas LYCHOS binds to GATOR1 but not Rag GTPases or Ragulator (fig. S12, A and B). Treatment of cells with cholesterol weakens SLC38A9 interaction with the Rag GTPases, likely because RagA becomes GTP-loaded in cells with high cholesterol concentrations (10, 19, 37). However, in LYCHOS-deleted cells, the SLC38A9-Rag GTPase interaction became unresponsive to cholesterol (Fig. 3E). On the contrary, cholesterol-dependent strengthening of the LYCHOS-GATOR1 interaction occurred irrespective of SLC38A9 status (Fig. 3F). Thus, through its interaction with GATOR1, LYCHOS

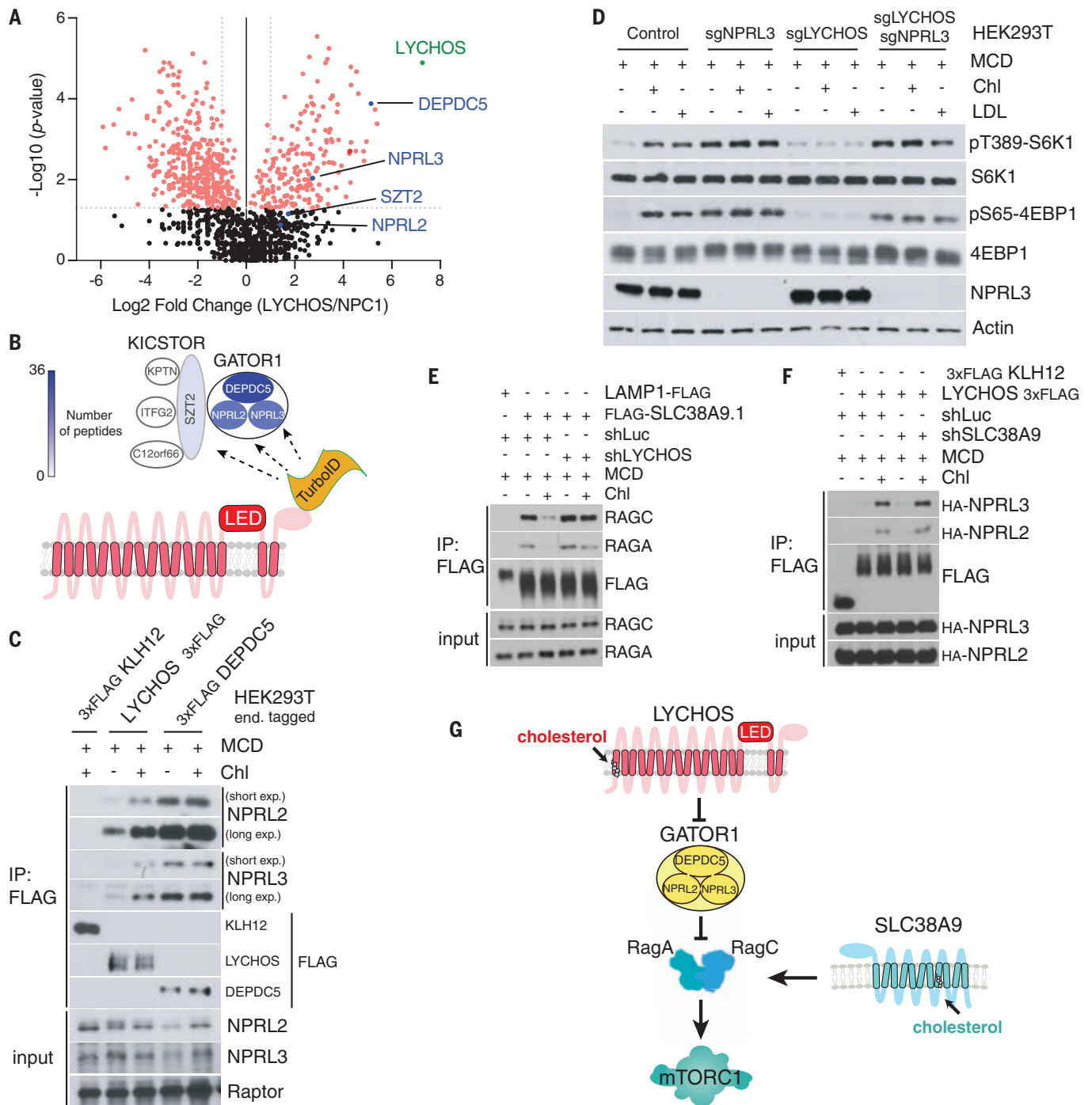


**Fig. 3. LYCHOS promotes mTORC1 signaling via cholesterol-regulated interaction with GATOR1.** (A) TurboID-based proximity labeling combined with liquid chromatography–mass spectrometry identified GATOR1 complex components (DEPDC5, NPRL2, and NPRL3) as interactors of LYCHOS. Volcano plot of the ratio of LYCHOS-FLAG-TurboID (LYCHOS) to NPC1-FLAG-TurboID (NPC1) is shown. Proteins with statistically significant ( $p \geq 0.05$ , two-tailed unpaired  $t$  test) with fold change LYCHOS/NPC1  $\geq 2$  are displayed as red circles. (B) Cartoon summarizing the TurboID proteomic analysis in (A). GATOR1 and KICSTOR subunits are color-coded according to their peptide counts. (C) Cholesterol strengthens the LYCHOS-GATOR1 interaction. HEK-293T cells bearing endogenously 3xFLAG-tagged KLH12, LYCHOS, and DEPDC5 were depleted of sterols then refed with 50  $\mu\text{M}$  cholesterol, followed by FLAG immunoprecipitation and immunoblotting for the indicated proteins.

(D) LYCHOS regulates cholesterol-dependent mTORC1 signaling via GATOR1. HEK-293T cells lacking GATOR1 (sgNPRL3), LYCHOS (sgLYCHOS), or both (sgNPRL3/sgLYCHOS) were cholesterol starved, or starved and refed with 50  $\mu\text{M}$  cholesterol or 50  $\mu\text{g/ml}$  LDL, followed by immunoblotting for the indicated proteins. (E) LYCHOS functions upstream of RagA GTP loading. HEK-293T cells stably expressing LAMP1-FLAG or FLAG-SLC38A9.1 were infected with shRNA targeting luciferase or LYCHOS for FLAG immunoprecipitation to assess SLC38A9.1-RAG A/C interaction. (F) SLC38A9.1 functions downstream of RagA GTP loading. SLC38A9.1 was knocked down in cells edited with 3xFLAG tags at the endogenous KLH12 and LYCHOS genes, respectively, followed by FLAG immunoprecipitation and immunoblotting for the indicated proteins. (G) LYCHOS and SLC38A9 mediate distinct cholesterol-sensing pathways, converging on mTORC1.

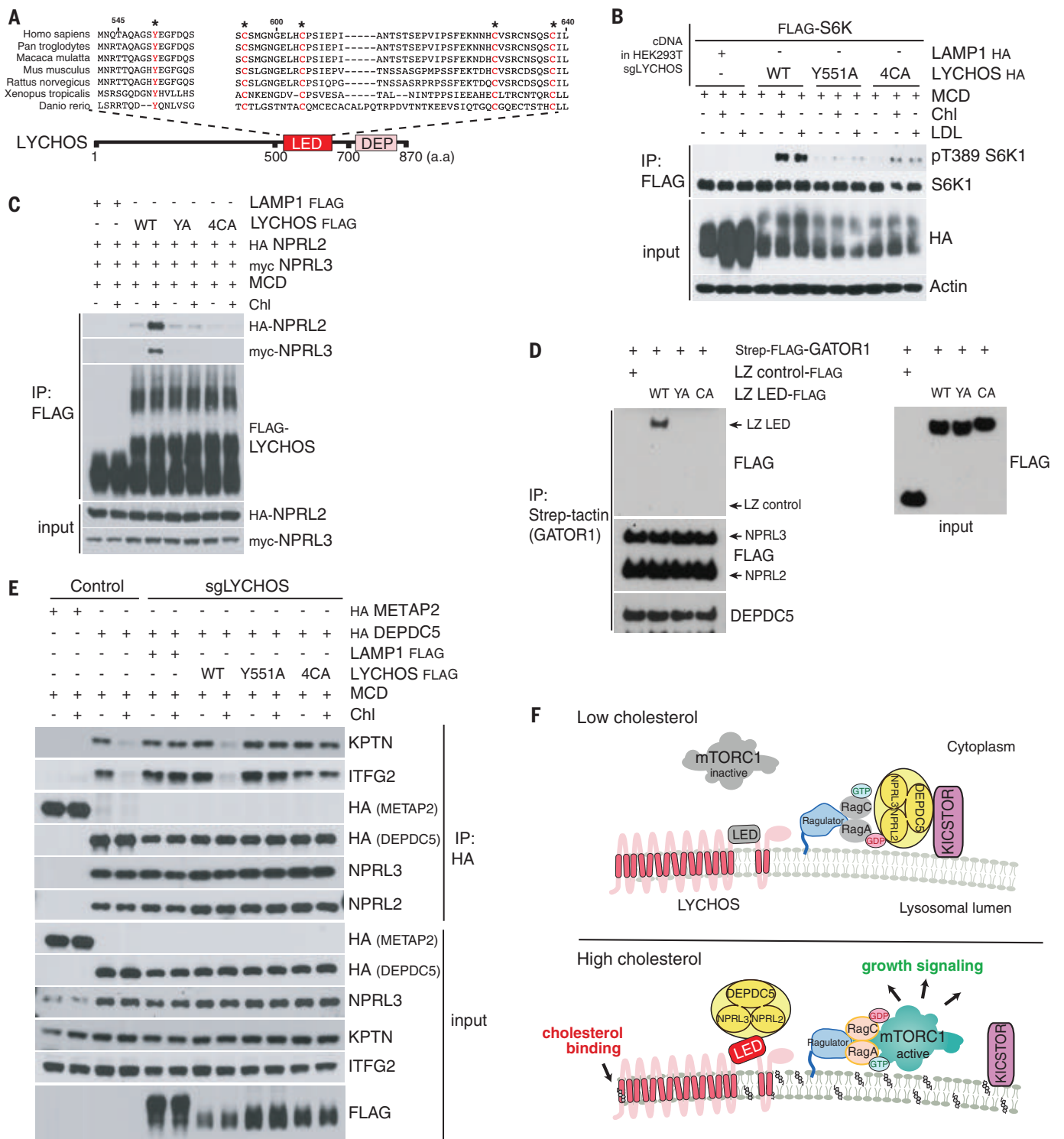


**Fig. 4. Cholesterol disrupts the GATOR1-KICSTOR interaction via the LYCHOS LED.** (A) Sequence alignment of LYCHOS LED domain. Highly conserved residues selected for mutagenesis are highlighted in red. (B) HEK-293T/sgLYCHOS cells were transfected with FLAG-S6K1 along with LAMP1-HA (negative control) or LYCHOS WT, Y551A, or 4CA-HA, followed by FLAG immunoprecipitation and immunoblotting for the phosphorylation state and levels of the indicated proteins. (C) LYCHOS LED mutations disrupt cholesterol-dependent LYCHOS interaction with GATOR1. HEK-293T/sgLYCHOS

cells were reconstituted with the indicated WT and LED-mutant LYCHOS constructs along with GATOR1. FLAG immunoprecipitates were analyzed by immunoblotting. (D) LYCHOS LED is sufficient for GATOR1 interaction: in vitro binding assay between purified GATOR1 and recombinant WT or mutant LYCHOS LED fused to a leucine zipper (LZ). LZ alone was used as negative control. (E) In high cholesterol, LYCHOS disrupts the GATOR1-KICSTOR interaction via its LED. Control HEK-293T cells, or HEK-293T/sgLYCHOS cells reconstituted with the indicated WT and mutant FLAG-LYCHOS constructs, and

coexpressing HA-METAP2 or HA-DEPDC5 as indicated, were cholesterol starved, or starved and restimulated, followed by HA immunoprecipitation. Lysates were analyzed by immunoblotting. (F) Molecular mechanisms of LYCHOS-dependent regulation of cholesterol-mTORC1 signaling. Under low cholesterol, stable GATOR1-KICSTOR complex promotes GATOR1-dependent

GTP hydrolysis of RagA/B, which maintains mTORC1 inactive in the cytosol. In high cholesterol, a conformational change in the LED stimulates LYCHOS interaction with GATOR1 while displacing KICSTOR, thus favoring the GTP-loaded state of RagA/B that leads to lysosomal recruitment and activation of mTORC1.

functions at a step upstream of GTP loading of RagA, whereas SLC38A9 functions downstream of it (Fig. 3G). Whereas deleting the GATOR1 subunit NPRL3 fully rescued loss of LYCHOS, depleting SLC38A9 in NPRL3-deleted cells blunted cholesterol-dependent mTORC1 activation, further supporting the function of LYCHOS and SLC38A9 on distinct but converging pathways (fig. S12C).

### Cholesterol disrupts the GATOR1-KICSTOR interaction through the LYCHOS LED

Because of our previous results indicating that the LED does not bind to cholesterol but is nonetheless required for cholesterol-dependent mTORC1 activation, we tested whether the LED might function in binding to GATOR1. Consistent with this possibility, deleting the LED abolished cholesterol-dependent interaction between LYCHOS and the GATOR1 subunits NPRL2 and NPRL3 (fig. S13A).

We sought to identify conserved amino acids within the LED that are essential for LYCHOS-GATOR1 interaction and mTORC1 activation. The LED contains a cluster of highly conserved Cys residues (Fig. 4A). Cys-rich motifs participate in signal transduction by promoting protein-protein as well as protein-lipid interactions (38). Mutating four of the conserved cysteines to alanine (C<sup>592</sup>→A, C<sup>604</sup>→A, C<sup>629</sup>→A, C<sup>638</sup>→A, collectively termed 4CA) abolished the ability of LYCHOS to support cholesterol-mediated mTORC1 activation, although the 4CA mutant of LYCHOS was expressed in amounts comparable to that of the WT protein and had normal lysosomal localization (Fig. 4B and fig. S13B). We also tested Tyr<sup>551</sup>, which is conserved from human to zebrafish (Fig. 4A). Similar to the 4-cysteine cluster, Tyr<sup>551</sup> also appeared to be essential for LYCHOS signaling activity, because a LYCHOS<sup>Y551A</sup> mutant failed to restore cholesterol-dependent mTORC1 activation in LYCHOS-deleted cells (Fig. 4B).

In contrast to WT LYCHOS, and consistent with their inability to support cholesterol-dependent mTORC1 activation, the Y551A and 4CA LED mutants showed barely detectable interaction with GATOR1 subunits NPRL2 and NPRL3, which was not strengthened by treating cells with cholesterol (Fig. 4C). Consistent with the LED as the GATOR1-interacting domain in LYCHOS, recombinantly expressed WT LED, held in a loop configuration with a leucine zipper, was sufficient for binding to GATOR1, whereas the interaction was abolished by the Y551A and 4CA mutations (Fig. 4D).

To gain mechanistic insight into how the cholesterol-regulated LYCHOS-GATOR1 interaction promotes mTORC1 signaling, we tested whether the LED can inhibit the RagA-GAP activity of GATOR1. However, neither recombinantly expressed LED nor full-length LYCHOS affected GATOR1-dependent GTP-to-GDP conversion on RagA, when added in molar excess to GATOR1 *in vitro* (39) (fig. S13, C to E). Based on lack of direct inhibition of GATOR1 GAP activity, and given that LYCHOS displayed a weak interaction with the KICSTOR subunit SZT2 in proximity biotinylation experiments, we considered the alternative possibility that LYCHOS may regulate the association between GATOR1 and the KICSTOR complex, which is essential for the GAP activity of GATOR1 toward RagA or B in cells (35).

Under full nutrient conditions, the interaction between the GATOR1 subunit DEPDC5 and the KICSTOR subunit KPTN was strengthened in LYCHOS-depleted cells compared to that in LYCHOS WT cells, suggesting that LYCHOS inhibits GATOR1-KICSTOR binding (fig. S14, A and B). Cholesterol inhibited the GATOR1-KICSTOR interaction in a LYCHOS-dependent manner. In LYCHOS WT cells depleted of cholesterol, DEPDC5 interacted with the KICSTOR subunits KPTN and ITFG2, whereas cholesterol refeeding inhibited this interaction (Fig. 4E). By contrast, in cells lacking LYCHOS, DEPDC5 and KICSTOR interacted strongly both in the absence and presence of cholesterol (Fig. 4E). Reexpression of WT LYCHOS restored cholesterol-dependent inhibition of GATOR1-KICSTOR binding, whereas both the 4CA and Y551A LED mutants (expressed at comparable or higher amounts than WT) failed to do so (Fig. 4E). Consistent with a key role for the LED in regulating GATOR1-KICSTOR binding, recombinantly expressed WT LED was sufficient to disrupt a preformed GATOR1-KICSTOR complex *in vitro* in a dose-dependent manner. By contrast, the Y551 and 4CA mutants, added in amounts equal to that of the WT, were largely ineffective (fig. S14, C and D). Unlike cholesterol, neither amino acids nor glucose stimulation affected the strength of GATOR1-KICSTOR binding (fig. S14E), further supporting a specific role of LYCHOS-dependent GATOR1-KICSTOR modulation for cholesterol sensing upstream of mTORC1.

Collectively, these results support a model in which, upon binding of cholesterol to the permease-like region of LYCHOS, the LED engages GATOR1, antagonizes its interaction

with KICSTOR, and thus interferes with the ability of GATOR1 to act as a GAP for RagA/B. Conversely, when cholesterol concentrations are low, LYCHOS is unable to perturb the KICSTOR-GATOR1 complex, favoring GATOR1-dependent GTP hydrolysis on RagA/B and leading to inhibition of mTORC1 signaling (Fig. 4F). Consistent with this model, deleting the essential KICSTOR subunit KPTN completely bypassed loss of LYCHOS, as did GATOR1 inactivation (fig. S14F).

### Discussion

We identified LYCHOS as a component of a lysosome-based pathway that transduces cholesterol levels into activation of mTORC1 signaling. Unlike SLC38A9, which also participates in regulation of mTORC1 by cholesterol (as well as arginine) (10, 19, 20), LYCHOS does not directly interact with the Rag GTPases but rather regulates their nucleotide state through cholesterol-dependent interaction with GATOR1 (Fig. 4F). Thus, LYCHOS functions in a manner analogous to amino acid sensors that modulate the GAP activity of GATOR1, either directly (e.g., SAMTOR) or via the GATOR2 complex (e.g., Sestrin, CASTOR) (8).

Despite its GPCR-like core, LYCHOS appears not to function like a classical GPCR. The specific localization of LYCHOS at the lysosomal membrane makes it unlikely that this protein senses extracellular ligands. Based on our mapping of a cholesterol-binding site to TM1 within the permease-like domain, we propose that cholesterol within the lysosomal membrane is in fact the main ligand for LYCHOS.

Cholesterol binding to TM1 may initiate a reorientation of specific helices within LYCHOS that enables the interaction of the LED with GATOR1. The LED is located in a position analogous to the intracellular loop 3 (ICL3) in canonical GPCRs, but is larger (~110 residues) compared to ICL3 in most GPCRs (25 to 50 residues) (40). Rather than binding to a trimeric G protein as canonical ICL3s do, the LYCHOS LED appears to directly bind to GATOR1 and disrupt its interaction with KICSTOR, thereby inhibiting the RagA-GAP function of GATOR1.

The identification of a GPCR-like protein as a putative cholesterol sensor upstream of mTORC1 suggests intriguing parallels with the Hedgehog (Hh) pathway. In the Hh pathway, the Smoothed GPCR protein binds to cholesterol (and hydroxysterols) and, in response, triggers a signaling cascade that culminates in activation of transcriptional programs for

differentiation and morphogenesis (41–46). The Hh pathway also includes Patched, a NPC1-related protein that moves cholesterol away from Smo to block its activation, a similar function to that of NPC1 in inhibiting cholesterol-dependent mTORC1 activation (10, 47–49).

Regulation of LYCHOS expression by fasting or feeding points to how cholesterol-mTORC1 signaling may be integrated with the metabolic state of the organism. Higher LYCHOS levels in fed states may promote cholesterol-dependent mTORC1 signaling when metabolic building blocks are abundant, a possibility consistent with the LYCHOS-dependent anabolic gene signature that we identified (5, 6). Conversely, during starvation, simultaneous decreased expression of LYCHOS and increased expression of NPC1 may help shut down cholesterol-mTORC1 signaling, thus favoring conservation of cellular resources.

## REFERENCES AND NOTES

- J. Luo, H. Yang, B.-L. Song, *Nat. Rev. Mol. Cell Biol.* **21**, 225–245 (2020).
- R. Riscail, N. Skuli, M. C. Simon, *Mol. Cell* **76**, 220–231 (2019).
- A. Radhakrishnan, J. L. Goldstein, J. G. McDonald, M. S. Brown, *Cell Metab.* **8**, 512–521 (2008).
- R. Yan et al., *Science* **371**, eabb2224 (2021).
- K. Düvel et al., *Mol. Cell* **39**, 171–183 (2010).
- H. R. Shin, R. Zoncu, *Dev. Cell* **54**, 226–238 (2020).
- X.-Y. Lu et al., *Nature* **588**, 479–484 (2020).
- G. Y. Liu, D. M. Sabatini, *Nat. Rev. Mol. Cell Biol.* **21**, 183–203 (2020).
- Y. Sancak et al., *Cell* **141**, 290–303 (2010).
- B. M. Castellano et al., *Science* **355**, 1306–1311 (2017).
- Y. Sancak et al., *Science* **320**, 1496–1501 (2008).
- E. Kim, P. Goraksha-Hicks, L. Li, T. P. Neufeld, K.-L. Guan, *Nat. Cell Biol.* **10**, 935–945 (2008).
- K. B. Rogala et al., *Science* **366**, 468–475 (2019).
- M. Anandapadamanaban et al., *Science* **366**, 203–210 (2019).
- L. Bar-Peled et al., *Science* **340**, 1100–1106 (2013).
- N. Panchaud, M.-P. Péli-Gulli, C. De Virgilio, *Sci. Signal.* **6**, ra42 (2013).
- C.-Y. Lim et al., *Nat. Cell Biol.* **21**, 1206–1218 (2019).
- A. Toulmay, W. A. Prinz, *J. Cell Biol.* **202**, 35–44 (2013).
- S. Wang et al., *Science* **347**, 188–194 (2015).
- M. Rebsamen et al., *Nature* **519**, 477–481 (2015).
- L. Chantranupong, R. L. Wolfson, D. M. Sabatini, *Cell* **161**, 67–83 (2015).
- G. A. Wyant et al., *Science* **360**, 751–758 (2018).
- B. Schröder et al., *Traffic* **8**, 1676–1686 (2007).
- A. Chapel et al., *Mol. Cell. Proteomics* **12**, 1572–1588 (2013).
- D. K. Vassiliatis et al., *Proc. Natl. Acad. Sci. U.S.A.* **100**, 4903–4908 (2003).
- P. Saha et al., *eLife* **9**, e57089 (2020).
- H. J. Kwon et al., *Cell* **137**, 1213–1224 (2009).
- M. Maekawa, G. D. Fairn, *J. Cell Sci.* **128**, 1422–1433 (2015).
- J. Li, P. L. Lee, S. R. Pfeffer, *Methods Mol. Biol.* **1583**, 85–95 (2017).
- O. B. Davis et al., *Dev. Cell* **56**, 260–276.e7 (2021).
- M. M. Budelier et al., *J. Biol. Chem.* **292**, 9294–9304 (2017).
- A. N. Bukiya, A. M. Dopico, *J. Lipid Res.* **58**, 1044–1054 (2017).
- M. A. Hanson et al., *Structure* **16**, 897–905 (2008).
- K. F. Cho et al., *Nat. Protoc.* **15**, 3971–3999 (2020).
- R. L. Wolfson et al., *Nature* **543**, 438–442 (2017).
- A. Das, M. S. Brown, D. D. Anderson, J. L. Goldstein, A. Radhakrishnan, *eLife* **3**, e02882 (2014).
- S. A. Fromm, R. E. Lawrence, J. H. Hurley, *Nat. Struct. Mol. Biol.* **27**, 1017–1023 (2020).
- P. Huang et al., *Cell* **174**, 312–324.e16 (2018).
- R. E. Lawrence et al., *Science* **366**, 971–977 (2019).
- B. K. Kobilka et al., *Science* **240**, 1310–1316 (1988).
- M. K. Cooper et al., *Nat. Genet.* **33**, 508–513 (2003).
- P. Huang et al., *Cell* **166**, 1176–1187.e14 (2016).
- I. Deshpande et al., *Nature* **571**, 284–288 (2019).

- X. Qi et al., *Nature* **571**, 279–283 (2019).
- X. Xiao et al., *Mol. Cell* **66**, 154–162.e10 (2017).
- X. Qi, L. Friedberg, R. De Bose-Boyd, T. Long, X. Li, *Nat. Chem. Biol.* **16**, 1368–1375 (2020).
- H. Qian et al., *Cell* **182**, 98–111.e18 (2020).
- X. Qi, P. Schmiege, E. Coutavas, X. Li, *Science* **362**, eaas8843 (2018).
- Y. Zhang et al., *Cell* **175**, 1352–1364.e14 (2018).

## ACKNOWLEDGMENTS

We thank R. Irannejad, J. Thorner, and all the members of the Zoncu lab for critical reading of the manuscript. We thank M. Rape for providing endogenously tagged 3xFLAG KHL12 HEK293T cells, R. Irannejad for the Gi/Gs/Gq cDNA constructs, the Stroud lab for the anti-GFP nanobody Sepharose, and T. Wu in the Gestwicki lab for assistance with the DSF experiment. **Funding:** This work was supported by NIH R01GM127763, a University of Notre Dame/APMRF grant, an Edward Mallinckrodt Jr. Foundation Scholar Award to R.Z., a 2019 AACR-Amgen Fellowship in Clinical/Translational Cancer Research (19-40-11-SHIN) and a 2021 AFTD-Holloway postdoctoral fellowship (2021-002) to H.R.S., NIH R01MH110550, NIH R01HL067773 to D.F.C., NIH R01GM108799 to A.S.E., and 1P50MH122379 to D.F.C. and A.S.E. **Author contributions:** H.R.S. and R.Z. conceptualized the study. H.R.S. designed and performed experiments with assistance from Y.R.C., R.S., C.S.G., A.J., C.-Y.L., O.B.D., and D.C.-C. L.W. performed the photolabeling and site identification by mass spectrometry. L.T. and C.S.G. performed the bioinformatic analysis. L.T. and N.S. performed the mouse experiments. A.J. and D.K.N. performed the lipidomic mass-spectrometry experiments. H.R.S. and R.Z. wrote the manuscript, and all authors contributed corrections and comments. **Competing interests:** R.Z. is a cofounder of,

stockholder in, and scientific adviser for Frontier Medicines Corp., and a scientific adviser for Nine Square Therapeutics and Apertor Pharmaceuticals. D.K.N. is a cofounder of, shareholder in, and adviser for Frontier Medicines and Vicinitas Therapeutics. D.K.N. is also on the scientific advisory board of The Mark Foundation for Cancer Research, Photys Therapeutics, and Apertor Pharmaceuticals and is a consultant for MPM Capital and Droia Ventures. The other authors declare that they have no competing interests. **Data and materials availability:** The RNA-sequencing data discussed in this manuscript and performed in this study are deposited in the NCBI Gene Expression Omnibus (NCBI-GEO) with accession nos. GSE46495 and GSE196384, respectively. All other data are available in the main text or the supplementary materials. **License information:** Copyright © 2022 the authors, some rights reserved; exclusive licensee American Association for the Advancement of Science. No claim to original US government works. <https://www.science.org/about/science-licenses-journal-article-reuse>

## SUPPLEMENTARY MATERIALS

[science.org/doi/10.1126/science.abg6621](https://science.org/doi/10.1126/science.abg6621)  
Materials and Methods  
Figs. S1 to S14  
Tables S1 to S7  
References (50–63)  
MDAR Reproducibility Checklist

Submitted 24 January 2021; resubmitted 12 February 2022

Accepted 11 August 2022

Published online 25 August 2022

10.1126/science.abg6621

## STRUCTURAL BIOLOGY

# Structural basis for strychnine activation of human bitter taste receptor TAS2R46

Weixiu Xu<sup>1,2</sup>, Lijie Wu<sup>1</sup>, Shenhui Liu<sup>1,2</sup>, Xiao Liu<sup>1,2</sup>, Xiaoling Cao<sup>1,2</sup>, Cui Zhou<sup>1,2</sup>, Jinyi Zhang<sup>1,2</sup>, You Fu<sup>1,2</sup>, Yu Guo<sup>1</sup>, Yiran Wu<sup>1</sup>, Qiwen Tan<sup>1</sup>, Ling Wang<sup>1</sup>, Junlin Liu<sup>1</sup>, Longquan Jiang<sup>1,2</sup>, Zhongbo Fan<sup>1,2</sup>, Yuan Pei<sup>1</sup>, Jingyi Yu<sup>3</sup>, Jianjun Cheng<sup>1,2</sup>, Suwen Zhao<sup>1,2</sup>, Xiaojiang Hao<sup>4</sup>, Zhi-Jie Liu<sup>1,2\*</sup>, Tian Hua<sup>1,2\*</sup>

Taste sensing is a sophisticated chemosensory process, and bitter taste perception is mediated by type 2 taste receptors (TAS2Rs), or class T G protein-coupled receptors. Understanding the detailed molecular mechanisms behind taste sensation is hindered by a lack of experimental receptor structures. Here, we report the cryo-electron microscopy structures of human TAS2R46 complexed with chimeric mini-G protein gustducin, in both strychnine-bound and apo forms. Several features of TAS2R46 are disclosed, including distinct receptor structures that compare with known GPCRs, a new “toggle switch,” activation-related motifs, and precoupling with mini-G protein gustducin. Furthermore, the dynamic extracellular and more-static intracellular parts of TAS2R46 suggest possible diverse ligand-recognition and activation processes. This study provides a basis for further exploration of other bitter taste receptors and their therapeutic applications.

The taste sensory system helps us to avoid the ingestion of harmful substances (1–3). Taste perception is initiated by the physical interaction of tastants with the receptors located on the surface of taste receptor cells on the tongue and palate (1). In humans, tastants evoke five taste sensations: sweet, bitter, salty, sour, and umami. Among the five taste modalities, ion channels transduce sour (4) and salty (5) signals, whereas bitter, sweet, and umami tastes are mediated by G protein-coupled receptors (GPCRs) (6–9). The type 1 taste receptor (TAS1R) family, classified

as class C GPCRs, includes three members: TAS1R1, TAS1R2, and TAS1R3, which combine to form heterodimers that sense sweet (TAS1R2+TAS1R3) and umami (TAS1R1+TAS1R3)

<sup>1</sup>Human Institute, ShanghaiTech University, Shanghai 201210, China. <sup>2</sup>School of Life Science and Technology, ShanghaiTech University, Shanghai 201210, China. <sup>3</sup>School of Information Science and Technology, ShanghaiTech University, Shanghai 201210, China. <sup>4</sup>State Key Laboratory of Phytochemistry and Plant Resource in West China, Kunming Institute of Botany, Chinese Academy of Sciences, Kunming 650210, China.

\*Corresponding author. Email: liuzhj@shanghaitech.edu.cn (Z.-J.L.); huatian@shanghaitech.edu.cn (T.H.)

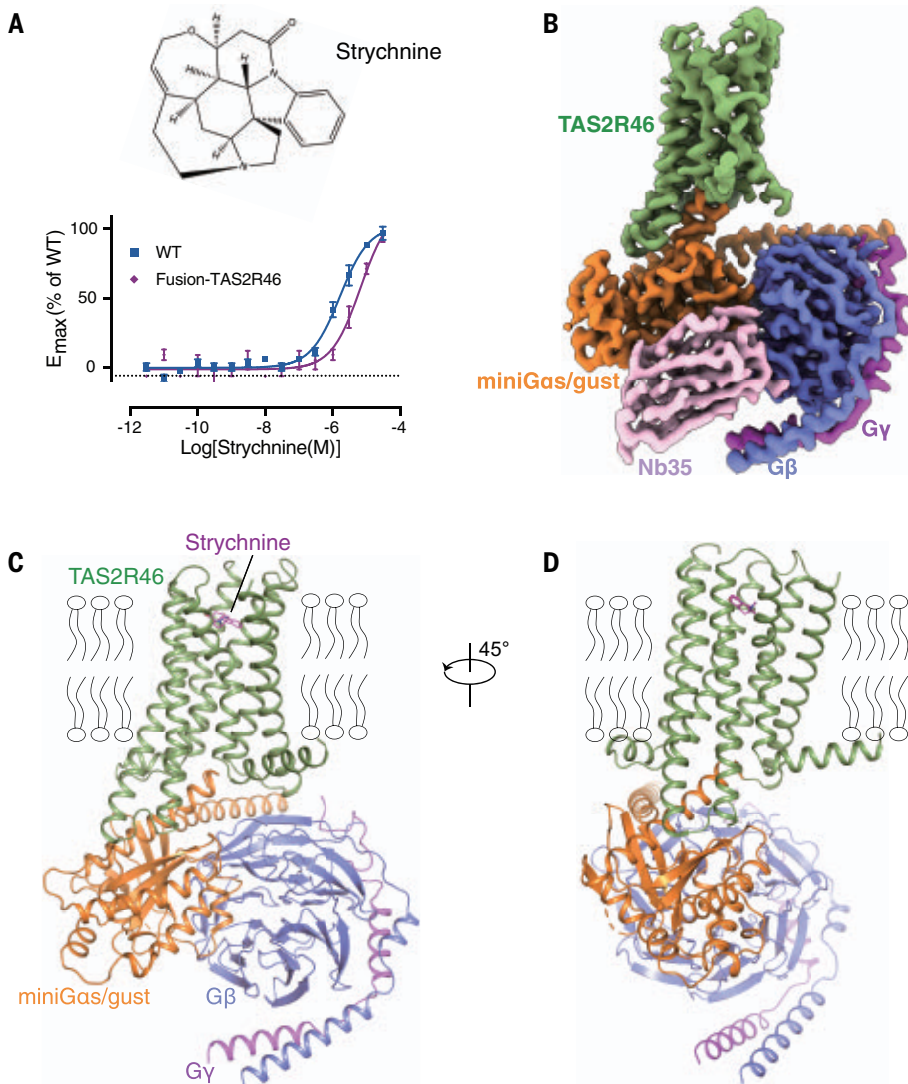


**Fig. 1. Cryo-EM structure of the strychnine-TAS2R46-miniG<sub>s</sub>/gust complex.** (A) Strychnine is an agonist of TAS2R46 in the fluorescence imaging plate reader (FLIPR) Ca<sup>2+</sup> assay. Data are means ± SEM of three biological replicates. (B) Cryo-EM density map of the strychnine-TAS2R46-miniG<sub>s</sub>/gust complex. (C and D) Cartoon representation of the strychnine-TAS2R46-miniG<sub>s</sub>/gust complex structure from two viewpoints, with strychnine shown as magenta sticks.

tastes (9–14). However, a distinct group of type 2 taste receptors (TAS2Rs) is responsible for bitter taste perception (15–17). Despite their structural diversity, TAS1Rs and TAS2Rs share a common signaling G protein pathway, which activates the heterotrimeric G protein gustducin (18–20).

TAS2Rs display low sequence identity (<20%) with other GPCRs and are classified as a separate class T GPCR subfamily (21). TAS2Rs recognize thousands of different bitter molecules, which have diverse scaffolds, shapes, and molecular weights (22). In humans, there are only ~25 TAS2Rs to cover this broad chemosensory space. Therefore, some TAS2Rs, such as TAS2R46, TAS2R14, and TAS2R10 (23), can be activated by multiple tastants (24). Other receptor subtypes, by contrast, are

more ligand selective. Furthermore, the TAS2Rs are distributed not only in the oral cavity but also in extraoral tissues, including the upper and lower airways, gut, adipose tissue, brain, heart, and immune cells (25, 26). These ectopic bitter taste receptors are involved in a variety of physiological processes and are associated with different diseases (27, 28). For example, TAS2R46 and TAS2R38 are expressed on the motile cilia of human airway epithelial cells and are implicated as putative targets for asthma treatment (25, 29).

Owing to their association with many diseases, TAS2Rs represent promising targets for pharmacological interventions. However, no experimental structures have yet been determined for any taste receptors, which are key for understanding signal transduction and

related drug discovery. Here, we report the cryo-electron microscopy (cryo-EM) structures of TAS2R46 in complex with chimeric mini-G protein gustducin, in a potent neurotoxin strychnine-bound form, and in the apo form. In combination with previous computational modeling and mutagenesis studies (22, 30–32), the structures reveal molecular features of class T GPCRs, which is the last structureless class of GPCRs, contributing to a deeper understanding of the biology behind bitter taste perception and signaling.

## Results

### Structures of TAS2R46-miniG<sub>s</sub>/gust complexes in different states

Strychnine is a toxic bitter alkaloid that activates the TAS2R46-mediated G protein gustducin (G<sub>gust</sub>) signaling pathway (33) (Fig. 1A). It is extracted from the seeds of *Strychnos nux-vomica* and is used as a herb in traditional Chinese medicine to treat ailments such as dyspepsia and pain (34). We set out to determine the structure of human TAS2R46 in complex with strychnine and G<sub>gust</sub> using cryo-EM (see materials and methods). To overcome the low surface expression and tendency to oligomerize of TAS2R (35), protein endoglucanase H [Protein Data Bank (PDB) ID 2CIT] was fused into the N terminus of wild-type (WT) TAS2R46 with an optimized linker between the fusion protein and receptor (fig. S1). Strychnine potency is comparable for the modified construct and WT receptor, with median effective concentration (EC<sub>50</sub>) values of 6.6 and 1.6 μM, respectively (Fig. 1A). To constitute the complex, we initially attempted to coexpress the modified TAS2R46 with heterometric G protein G<sub>α<sub>gust</sub>β<sub>1</sub>γ<sub>2</sub></sub> or G<sub>α<sub>gust</sub>β<sub>3</sub>γ<sub>13</sub></sub>. However, both G<sub>gust</sub> and TAS2R46-G<sub>gust</sub> were unstable. We used the NanoBiT tethering strategy (36) to stabilize the complex and also generated the chimeric G protein miniG<sub>s</sub>/gust where the α5 helix of miniG<sub>s</sub> was replaced with the α5 helix of G<sub>α<sub>gust</sub>β<sub>3</sub>γ<sub>13</sub></sub> with the aim being to achieve a stable G protein that maintains binding to TAS2R46. This gave a strychnine-TAS2R46-miniG<sub>s</sub>/gust complex with improved homogeneity and stability (fig. S2, A and B), and we determined the complex structure at a resolution of 3.01 Å (Fig. 1B; fig. S2, C to G; and table S1).

The resulting high-quality density map allowed accurate model building of the TAS2R46, strychnine, and miniG<sub>s</sub>/gust trimer complex (fig. S3). TAS2R46 adopts a seven-transmembrane (7TM) bundle topology, like GPCR structures in other families, yet some of its helices and loops have distinct folding features (Figs. 1, C and D, and 2A).

### Structure comparison of TAS2R46 with other GPCRs

We compared the structure of TAS2R46 as a representative of class T GPCRs with published

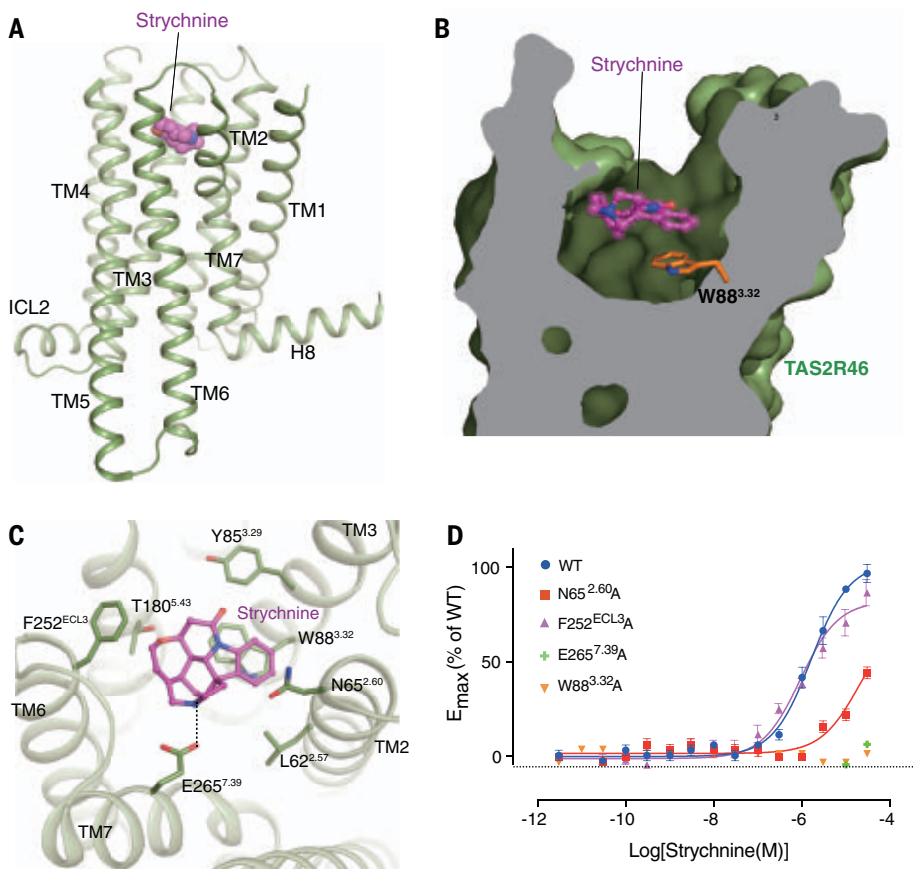


**Fig. 2. Architecture of TAS2R46 and the strychnine binding pocket.** (A) Side view of the 7TM bundle of the strychnine-TAS2R46 complex. H, helix. (B) Vertical cross section of the strychnine binding pocket in TAS2R46. The side chain of W88<sup>3.32</sup> is shown as orange sticks. (C) Binding pocket of strychnine from the extracellular view. Key residues of TAS2R46 that interact with strychnine are shown as sticks. Hydrogen bonds are shown as black dashed lines. (D) Alanine substitution of TAS2R46 residues that interact with strychnine reduced its potency. Data are means  $\pm$  SEM of three biological replicates.  $E_{max}$ , maximal efficacy.

human GPCR-G protein complex structures (fig. S4), which are grouped into six different classes (table S2): class A (34 structures), class B1 (14 structures), class B2 (1 structure), class C (8 structures), and class F (2 structures). We used the template modeling (TM)-score (37) and root mean square deviation (RMSD) to assess the fold and geometrical similarities between structures. The calculation was carried out to compare 7TM  $\alpha$  atoms both between all structures in each class and between TAS2R46 and all other GPCRs (fig. S5; see materials and methods). The results show that TAS2R46 has a distinct three-dimensional structure. Based on the average TM-score and RMSD values of TAS2R46 and different classes of GPCRs, TAS2R46 is most similar to class F GPCRs with the highest average TM-score of 0.80 or class A GPCRs with smallest average RMSD value of 3.53 Å. However, TAS2R46's most similar receptor in terms of RMSD (3.35 Å) is the active-state cannabinoid receptor 1 (PDB ID 6KPG) (38) or, based on TM-score (0.81),

the active-state CXC chemokine receptor 2 (PDB ID 6LFO) (39).

TAS2R46 exhibits several distinct features compared with other GPCR-G protein structures, including a different structural arrangement of TM3-TM4-TM5 (Fig. 2A and figs. S4 and S6, A and B). Here, the extracellular part of TM5 packs close to TM3, but the extracellular proximal region (after residue N176<sup>5.39</sup>, where N is Asn) moves outward and becomes disordered with weak EM density. We note that residue N176<sup>5.39</sup> was reported to be glycosylated and important for receptor function (40). Meanwhile, the extracellular part of TM4 moves away from TM3 and TM5. This results in a pocket formed by TM3-TM4-TM5 near the membrane bilayer (fig. S6A). Extracellular loop 2 (ECL2) displays consistently weak density, reflecting its flexible nature. Notably, TM7 shows a sharp “kink” in the middle of the helix at P272<sup>7.46</sup> (P, proline), where the intracellular part bends toward the core of the 7TM bundle and the extracellular part

swings outward, leading to a large ligand binding cavity that often appears in peptide- or protein-bound GPCRs (Fig. 2A and fig. S6A). The EM density is clear for intracellular loop 2 (ICL2) (fig. S3), which forms a short helix and orients parallel to the membrane surface in TAS2R46 instead of forming a loop and participating in the interaction with the G protein, as observed in other GPCR-G protein complex structures (Fig. 2A and figs. S4 and S6B).

#### Strychnine binding mode in TAS2R46

TAS2R46 is a bitter taste receptor that responds to a broad spectrum of bitter substances, but strychnine is the most potent agonist identified so far (31, 33, 41). The orthosteric binding pocket resembles a wide-open funnel that is formed by residues from TM2, TM3, TM5, and TM7 (Fig. 2, B and C). We observed a “baseball cap”-shaped EM density in the orthosteric binding pocket, which is similar to that in the strychnine-glycine receptor (GlyR) structure (fig. S3) (42, 43). We placed strychnine into that piece of EM density and identified that W88<sup>3.32</sup> and E265<sup>7.39</sup> (W, Trp; E, Glu) are involved in the direct coordination of strychnine, which is also consistent with previously reported mutagenesis data (31, 44). In detail, the side chain of W88<sup>3.32</sup> from TM3 sticks into the middle of the pocket at one-third the height of the orthosteric funnel (Fig. 2B), and its horizontally placed indole ring functions as a landing platform for the strychnine molecule and establishes a  $\pi$ - $\pi$  interaction with strychnine's benzene ring (Fig. 2C). Sequence alignment shows that W3.32 is highly conserved among TAS2Rs (fig. S7), and a mutagenesis assay showed that W88<sup>3.32</sup>A (W88<sup>3.32</sup>→Ala) abolished strychnine activity, confirming its important role in ligand binding (Fig. 2D). Additionally, E265<sup>7.39</sup> makes a hydrogen bond with the tertiary amine of strychnine (Fig. 2C), which is largely protonated at physiological pH ( $pK_a = 8.26$ , where  $K_a$  is the acid dissociation constant). Concordantly, the mutation E265<sup>7.39</sup>A also diminishes strychnine activity (Fig. 2D).

#### Structure of TAS2R46-miniG<sub>s/gust</sub> complex in the apo state

During the EM data processing of complex samples with strychnine, two different particle components were identified. The major one yielded the strychnine-TAS2R46-miniG<sub>s/gust</sub> complex discussed earlier. The other particle component was solved at a nominal resolution of 3.08 Å (fig. S2 and table S1). This structure is similar to strychnine-TAS2R46-miniG<sub>s/gust</sub> in terms of overall architecture and miniG<sub>s/gust</sub> coupling; however, the EM density for strychnine is absent, and this structure is named as ligand-free TAS2R46-miniG<sub>s/gust</sub> (figs. S2 and S6, C and D). To verify that TAS2R46 could be coupled by miniG<sub>s/gust</sub> without strychnine,



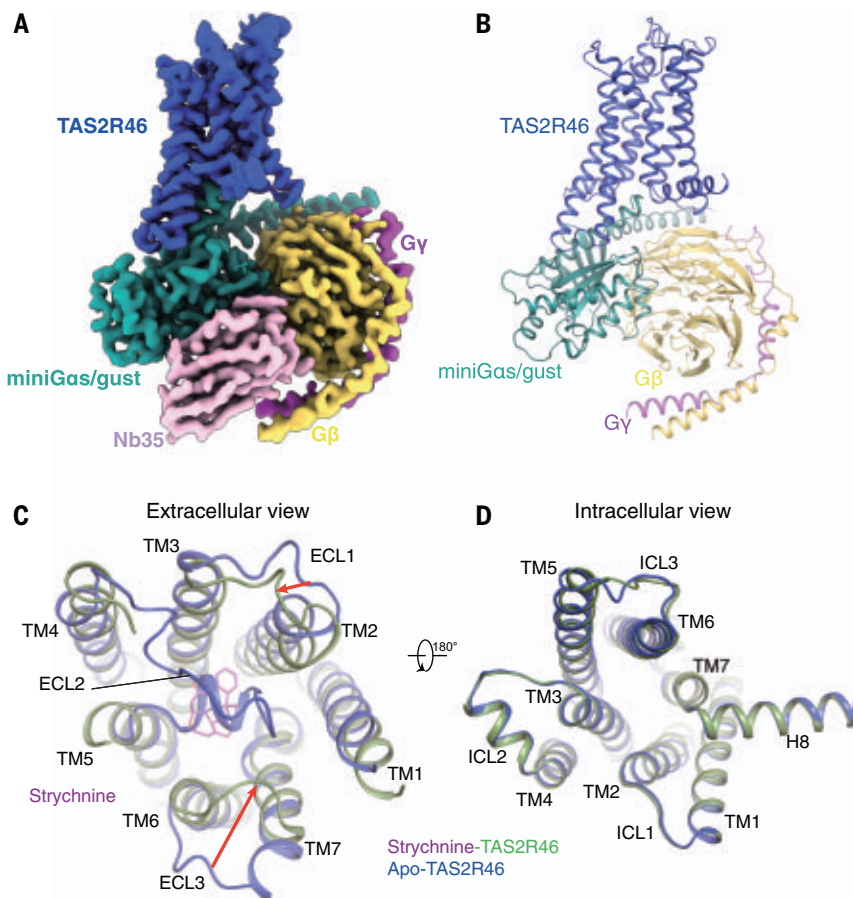


**Fig. 3. Cryo-EM structure of the apo-TAS2R46-miniG<sub>s/gust</sub> complex.** (A) Cryo-EM density map of the apo-TAS2R46-miniG<sub>s/gust</sub> complex. (B) Cartoon representation of the apo-TAS2R46-miniG<sub>s/gust</sub> complex structure. (C and D) Extracellular (C) and intracellular (D) views of the comparison of the strychnine-bound (green) and apo (blue) TAS2R46 structures. The conformational changes are indicated with red arrows.

TAS2R46 and miniG<sub>s/gust</sub> were constituted without adding any agonists. Subsequently, the cryo-EM structure of the apo-TAS2R46-miniG<sub>s/gust</sub> complex was obtained at a nominal resolution of 3.01 Å (Fig. 3, A and B; fig. S8; and table S1). Interestingly, this apo TAS2R46 is indeed coupled with miniG<sub>s/gust</sub> and is almost identical to the ligand-free structure discussed earlier.

The overall structure of the apo-TAS2R46-miniG<sub>s/gust</sub> complex (the separately determined structure) is, for the most part, similar to the strychnine-bound TAS2R46-miniG<sub>s/gust</sub> complex structure, with a RMSD of 0.89 Å for 7TM  $\alpha$  atoms (fig. S9A). When the structures of the two states are superimposed, the intracellular parts of 7TMs align well, but the extracellular portions are more divergent (Fig. 3, C and D). The biggest structure difference occurs at ECL2 (Fig. 3C). In the strychnine-TAS2R46-miniG<sub>s/gust</sub> structure, most of ECL2 is assumed to be disordered owing to the missing EM density. However, in the apo-TAS2R46-miniG<sub>s/gust</sub> structure, the disordered ECL2 makes a sharp turn at residue N176<sup>5,39</sup> and folds into a short helix that occupies the orthosteric binding

pocket and partially overlaps with the strychnine position in the superimposed structures (Fig. 3C, fig. S9B, and movie S1). Meanwhile, the extracellular proximal regions of TM1 and TM5 bend into the 7TM core in the apo state structure (Fig. 3C). However, ECL1 and ECL3 move outward about 6.7 Å (A74<sup>ECL1</sup>) and 13.5 Å (E256<sup>ECL3</sup>), respectively, leaving a more opened extracellular region compared with that in strychnine-TAS2R46-miniG<sub>s/gust</sub> (Fig. 3C). We performed intramolecular fluorescent arsenical hairpin bioluminescence energy transfer (FLAsH-BRET) experiments (45) to monitor the strychnine-induced conformational changes in the extracellular region (fig. S9, C to F). The results showed that the binding of strychnine indeed caused the outward movement of ECL2 away from the N terminus in a concentration-dependent manner (fig. S9F).

#### Activation of TAS2R46

The apo and strychnine-bound structures enable us to investigate the activation process of TAS2R46 (Fig. 4A and movie S1). In addition to the converged movements of extracellular

helices and loops, strychnine binding also induces a side chain flip of W88<sup>3,32</sup>, which transforms the side chain from double conformations in the apo state to a single conformation in the strychnine-bound state (fig. S9B). The activation-related conserved toggle switch W<sup>6,48</sup> found in class A GPCRs is absent in TAS2Rs. The 6.48 residue was assigned to C238<sup>6,48</sup> (C, Cys) in GPCRdb (21). However, structural superimposition with solved active class A GPCRs, such as the most fold-similar active-state structure CXCR2 (PDB ID 6LFO), suggests that the corresponding residue to position 6.48 is Y241<sup>6,51</sup> (hereafter named Y241<sup>6,48T</sup>; Y, Try) in TAS2R46 (Fig. 4C). Concordantly, Y241<sup>6,48T</sup> shows a large conformational change between the apo and strychnine-bound states, where the side chain of Y241<sup>6,48T</sup> rotates about 90° from pointing outward to pointing into the core of the transmembrane bundle (Fig. 4B and movie S1). Thus Y241<sup>6,48T</sup> may play the “toggle switch” role for TAS2R46 activation (Fig. 4, B and C). Consistently, the Y241<sup>6,48T</sup>A mutation abolishes strychnine activity (Fig. 4F). However, in our structure, the rotation of Y241<sup>6,48T</sup> does not induce the large outward movement of TM6 that is observed in class A GPCRs. An interaction network around Y241<sup>6,48T</sup> stabilizes the active-state conformation in the strychnine-bound TAS2R46 structure (Fig. 4D). First, TM5, TM6, and TM7 are tethered by hydrophobic and  $\pi$ - $\pi$  stacking interactions mediated by residues F188<sup>5,51</sup>, Y241<sup>6,48T</sup>, and Y271<sup>7,45</sup> (F, Phe) (Fig. 4D). In addition, R55<sup>2,50</sup> (R, Arg) points into the 7TM core, and the mutation R55<sup>2,50</sup>A impairs strychnine-induced TAS2R46 activation (Fig. 4D). Residues forming the “triad core” (F188<sup>5,51</sup>, Y241<sup>6,48T</sup>, and Y271<sup>7,45</sup>) and R2.50 are relatively conserved among bitter taste receptors (fig. S9G), suggesting that they may play a general role in stabilizing the active state of TAS2Rs. Also, the P272<sup>7,46</sup>-induced kink shifts Y271<sup>7,45</sup> into the proximity of the “triad core” and provides the flexibility for TM7 to yield space for the rotation of Y241<sup>6,48T</sup> (Fig. 4D), which may aid ligand binding and receptor activation. Residue Y<sup>6,48T</sup> in TAS2R46 is not highly conserved among TAS2Rs, implying that diverse activation mechanisms may exist in other bitter taste receptors or with other ligands (30).

TAS2Rs lack other conserved activation-related motifs, such as N<sup>7,49</sup>p<sup>7,50</sup>XXY<sup>7,53</sup> and D<sup>3,49</sup>R<sup>3,50</sup>V<sup>3,51</sup> motifs (where D is Asp and X is any residue), in class A GPCRs (15, 46). The N<sup>7,49</sup>p<sup>7,50</sup>XXY<sup>7,53</sup> corresponding motif is HP<sup>7,50</sup>FIL in TAS2R46, and H275<sup>7,49</sup>, I278<sup>7,52</sup>, and L279<sup>7,53</sup> form hydrophobic interactions with residues A99<sup>3,43</sup>, L102<sup>3,46</sup>, L237<sup>6,47</sup>, and F234<sup>6,44</sup> in the strychnine-bound TAS2R46 structure (H, His; I, Ile; L, Leu) (Fig. 4E). This hydrophobic core mediates the packing of TM3, TM6, and TM7, which is different from the interaction network observed in class A GPCRs. In the apo

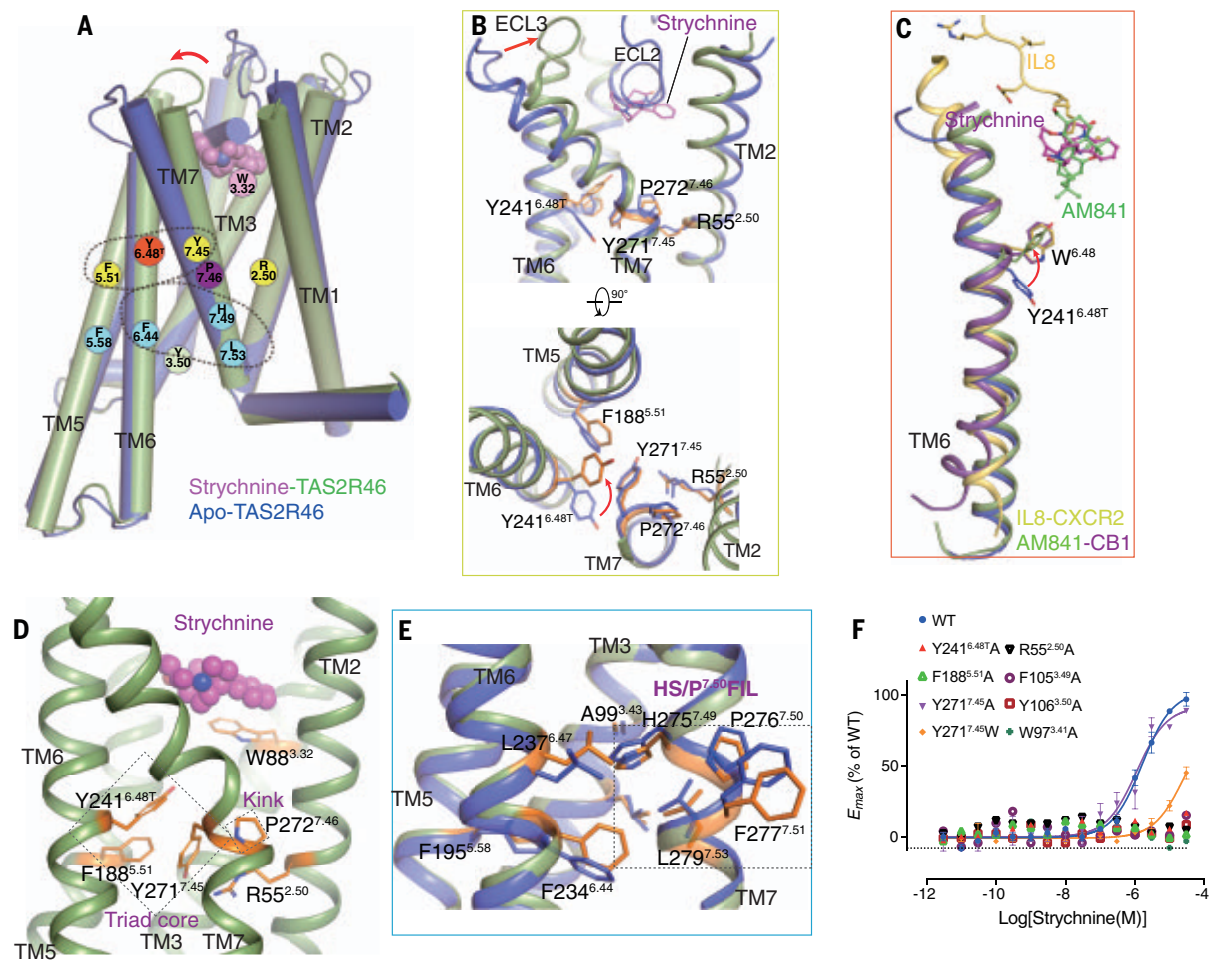


**Fig. 4. The activation features of TAS2R46.** (A) Schematic summarizing the key translational and rotational movements that contribute to the activation of TAS2R46. (B) The conformational changes of the extracellular region and key residues between apo-TAS2R46 and strychnine-bound TAS2R46. (C) Superimposition of the strychnine-bound TAS2R46, apo-TAS2R46, monomer IL8-CXCR2-G<sub>i1</sub>, and AM841-CB1-G<sub>i1</sub> structures aligned at the W6.48 position in class A GPCRs. (D) Detailed interactions of residues that stabilize the conformation

of the TM2-TM3-TM5-TM6-TM7 core in the strychnine-bound TAS2R46 structure. (E) The detailed interactions around the HS/P<sup>7.50</sup>FIL motif in the strychnine-bound and apo-TAS2R46 structures. S, Ser. (F) The effects of mutations in TM helix tethering residues on strychnine-induced Ca<sup>2+</sup> mobilization. Data are means ± SEM of three biological replicates. The side chains of key residues are shown as orange and blue sticks in the strychnine-bound and apo-TAS2R46 structures, respectively.

state, these hydrophobic interactions are weakened owing to the side chain shift of residue F234<sup>6.44</sup> (Fig. 4E). In class A GPCR activation, structural rearrangement of the D<sup>3.49</sup>R<sup>3.50</sup>Y<sup>3.51</sup> motif usually unleashes TM6 from TM3 to accommodate G protein coupling. In strychnine-bound TAS2R46, the corresponding residues are F<sup>3.49</sup>Y<sup>3.50</sup>L<sup>3.51</sup>, and this motif is relatively conserved in TAS2Rs (fig. S9I and movie S2) (30). Our results are consistent with the involvement of this region in G protein binding—Y106<sup>3.50</sup> forms a hydrogen bond with the carbonyl oxygen of residue C351 from the G<sub>α</sub><sup>gust</sup> α5 helix, and the mutation F105<sup>3.49</sup>A or Y106<sup>3.50</sup>A impairs the activation of TAS2R46 by strychnine (Fig. 4F). We note that the extent of activation may be influenced by the chimeric G protein and stabilization of the receptor. However, the preassociation of TAS2R46 with gustducin without agonist binding might be indicative of

flexibility of the receptor that is required for binding and rapid activation by many ligands (47). In our BRET assay, addition of strychnine decreased bioluminescence resonance energy transfer between labeled TAS2R46 and WT gustducin heterotrimers (fig. S10D), further confirming the precoupling state of TAS2R46 with gustducin.

Additionally, W97<sup>3.41</sup> in TM3 is the sole strictly conserved residue in all TAS2Rs (fig. S9G). Its side chain points into the cavity between TM4 and TM5 and is sandwiched by P136<sup>4.51</sup> and P187<sup>5.50</sup> in TAS2R46 (fig. S9H). The mutation of W97<sup>3.41</sup>A abolishes the activity of strychnine on TAS2R46 (Fig. 4F), suggesting that W3.41 stabilizes the interface of TM4-TM3-TM5. Interestingly, the mutation to tryptophan at position 3.41 has also been frequently used to stabilize the conformation of class A GPCRs (48).

#### TAS2R46 and miniG<sub>s/gust</sub> interaction interface in the strychnine-bound state

Gustducin is closely related both to transducins (20) and to the G<sub>T10</sub> class, based on the phylogenetic tree of G protein α subunits. The structure of the strychnine-TAS2R46-miniG<sub>s/gust</sub> complex reveals several distinct features of the α5 helix–gustducin engagement to TAS2R46's cytoplasmic cavity that are mainly contributed by TM3, TM5, and TM6 (Fig. 5 and fig. S10, A and B). More specifically, the α5 helix of miniG<sub>s/gust</sub> forms hydrophobic and polar interactions, as well as hydrogen bonds, with the cytoplasmic cavity (Fig. 5C). Whereas the intracellular loops, especially ICL2, are often involved in receptor–G protein interactions in other GPCR complex structures, the intracellular loops here have almost no direct interaction with the miniG<sub>s/gust</sub> trimer in the strychnine-TAS2R46-miniG<sub>s/gust</sub> complex

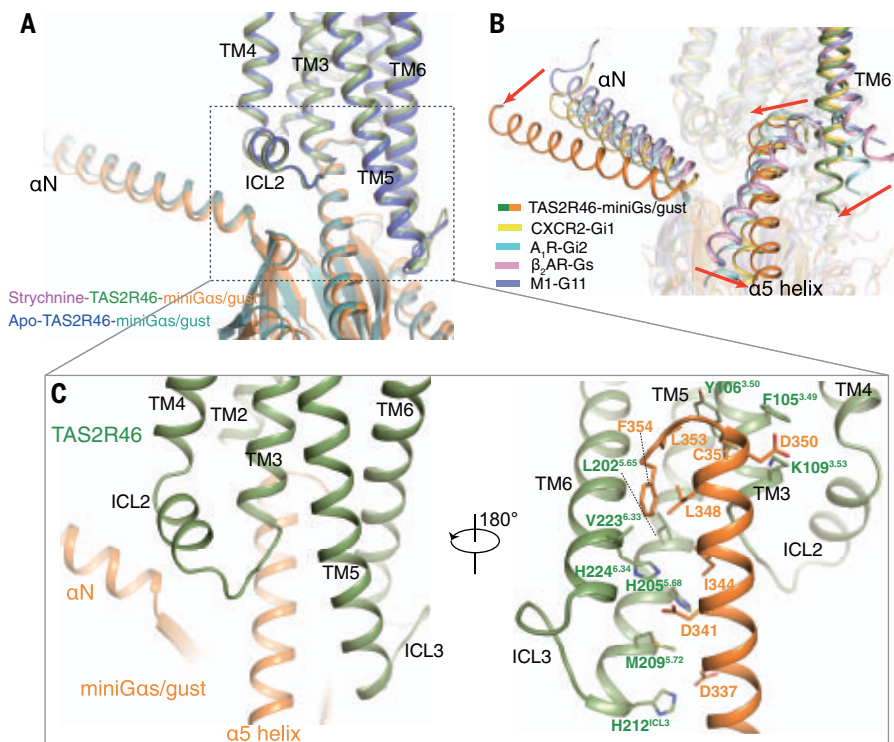


**Fig. 5. General features of miniG<sub>s/gust</sub> coupling to TAS2R46.** (A) The coupling mode of miniG<sub>s/gust</sub> with TAS2R46 in the strychnine-bound and apo-TAS2R46-miniG<sub>s/gust</sub> complex structures. (B) Structural comparison of the strychnine-TAS2R46-miniG<sub>s/gust</sub> complex with CXCR2-Gi1 (yellow), A<sub>1</sub>R-Gi2 (cyan), β<sub>2</sub>AR-Gs (pink), and M1-G11 (bluish purple) complexes when aligned with the receptor. The differences in TM6 of the receptor and the α5 and αN helices of the G protein are indicated by red arrows. (C) Detailed interactions of TAS2R46 with the α5 helix of miniG<sub>s/gust</sub> in the strychnine-bound TAS2R46-miniG<sub>s/gust</sub> complex structure.

(fig. S10F). Rather, ICL2 takes an unusual conformation where part of it forms a short helix that lies parallel to the cytoplasmic cell membrane (Fig. 5A). By contrast, TM5 and TM6 are more extended into the cytosol, and residues H205<sup>5,68</sup> and H224<sup>6,34</sup> establish hydrogen bonds with D341 of the α5 helix of miniG<sub>s/gust</sub> (Fig. 5C). The mutation H205<sup>5,68</sup>A or H224<sup>6,34</sup>A impairs the activity of strychnine on TAS2R46 in the functional assay (fig. S10C). The end of the α5 helix of miniG<sub>s/gust</sub> inserts into the receptor core, and residues L353 and C351 form hydrophobic interactions with F105<sup>3,49</sup> and Y106<sup>3,50</sup> from the cytoplasmic proximal region of TM3 (Fig. 5C). Additionally, K109<sup>3,53</sup> (K, Lys) forms a hydrogen bond with D350 of the α5 helix in miniG<sub>s/gust</sub>, which stabilizes the receptor–G protein interaction (Fig. 5C). K3.53 is highly conserved in TAS2Rs, suggesting a general role in G<sub>α</sub> coupling.

When comparing TAS2R46 with class A GPCRs in complex with different G protein subtypes (i.e., CXCR2-G<sub>i1</sub>, A<sub>1</sub>R-G<sub>i2</sub>, β<sub>2</sub>AR-G<sub>s</sub>, and M1-G<sub>11</sub>) or GPCR–G protein complexes in other classes (i.e., GPR97-G<sub>o</sub>, FZD7-miniG<sub>s</sub>, and GLP1R-G<sub>s</sub>), major differences occur in the relative positions and orientations of the α5 and αN helices of the G<sub>α</sub> subunits, as well

as the corresponding position shifts of TM6 and intracellular loops (Fig. 5B and fig. S10, F to I). TAS2R46's TM6 has a smaller outswing angle, a shallower α5 helix insertion of miniG<sub>s/gust</sub> and a more-tilted α5 helix, which is, interestingly, more similar to that of the CXCR2-G<sub>i</sub> complex structure (Fig. 5B and fig. S10, E and F). Of note, the potential impact of the chimeric G protein warrants further investigation with WT gustducin.

#### Bitter substance recognition by TAS2R46

The ligand recognition pattern of TAS2R46 was further explored through molecular docking studies. A list of 68 bitter molecules was retrieved from BitterDB (22, 30, 33) for molecular docking, and the representative binding poses were analyzed. In agreement with the strychnine-bound TAS2R46 structure and previous molecular simulation studies (32), W88<sup>3,32</sup> and E265<sup>7,39</sup> play the most critical roles in the recognition and coordination of these molecules. Very similar to strychnine, binding poses of the therapeutic drugs quinine, berberine, and chlorpheniramine are stabilized by π–π stacking interactions between an aromatic moiety in their structures and W88<sup>3,32</sup>, as well as a salt bridge interaction between a positively

charged nitrogen and E265<sup>7,39</sup> (fig. S11, A and B). The combination of an aromatic moiety and a positively charged nitrogen may allow many clinical drugs (49) to be recognized by TAS2R46, which explains the saying “good medicine tastes bitter” from ancient Chinese wisdom (27). For the bitter substances that do not contain an aromatic ring or a positively charged nitrogen, most feature a lactone substructure (22, 33), in which the carbonyl group forms a hydrogen bond with the NH group of W88<sup>3,32</sup> and a distant hydroxyl group forms another hydrogen bond with the carboxyl group of E265<sup>7,39</sup> (fig. S11, A, C, and D). Together with previous modeling and bioinformatic works (23, 30, 33, 50), these findings provide clues for the understanding of broad-spectrum ligand recognition of TAS2R46, which may help to identify or design other chemical entities for bitter taste receptors.

#### Conclusion

Our structures disclose the roles of W88<sup>3,32</sup> and E265<sup>7,39</sup> in strychnine binding and identify features involved in the transition from the apo state to the strychnine-bound state. We suggest that Y241<sup>6,48T</sup> acts as the “toggle switch” for receptor activation. The dynamic ECL2 may play a role in diverse ligand binding (32) and receptor activation. Finally, our structure and functional assay highlight that apo TAS2R46 is precoupled by miniG<sub>s/gust</sub>; such “preassociated” complexes have also been described in other GPCRs (47). Precoupling might facilitate a rapid response by the receptor when potentially toxic bitter molecules are detected.

#### REFERENCES AND NOTES

- D. A. Yarmolinsky, C. S. Zuker, N. J. Ryba, *Cell* **139**, 234–244 (2009).
- K. Scott, *Neuron* **48**, 455–464 (2005).
- F. Bermúdez-Rattoni, *Nat. Rev. Neurosci.* **5**, 209–217 (2004).
- Y. H. Tu et al., *Science* **359**, 1047–1050 (2018).
- J. Chandrashekar et al., *Nature* **464**, 297–301 (2010).
- G. T. Wong, K. S. Gannon, R. F. Margolskee, *Nature* **381**, 796–800 (1996).
- N. Chaudhari, A. M. Landin, S. D. Roper, *Nat. Neurosci.* **3**, 113–119 (2000).
- J. Chandrashekar, M. A. Hoon, N. J. Ryba, C. S. Zuker, *Nature* **444**, 288–294 (2006).
- G. Nelson et al., *Nature* **416**, 199–202 (2002).
- G. Nelson et al., *Cell* **106**, 381–390 (2001).
- G. Q. Zhao et al., *Cell* **115**, 255–266 (2003).
- M. Max et al., *Nat. Genet.* **28**, 58–63 (2001).
- J. P. Montmayeur, S. D. Liberles, H. Matsunami, L. B. Buck, *Nat. Neurosci.* **4**, 492–498 (2001).
- X. Li et al., *Proc. Natl. Acad. Sci. U.S.A.* **99**, 4692–4696 (2002).
- E. Adler et al., *Cell* **100**, 693–702 (2000).
- J. Chandrashekar et al., *Cell* **100**, 703–711 (2000).
- H. Matsunami, J. P. Montmayeur, L. B. Buck, *Nature* **404**, 601–604 (2000).
- Y. Zhang et al., *Cell* **112**, 293–301 (2003).
- L. Huang et al., *Nat. Neurosci.* **2**, 1055–1062 (1999).
- S. K. McLaughlin, P. J. McKinnon, R. F. Margolskee, *Nature* **357**, 563–569 (1992).
- A. J. Kooistra et al., *Nucleic Acids Res.* **49**, D335–D343 (2021).
- A. Dagan-Wiener et al., *Nucleic Acids Res.* **47**, D1179–D1185 (2019).
- M. Behrens, W. Meyerhof, *J. Agric. Food Chem.* **66**, 2204–2213 (2018).

24. W. Meyerhof *et al.*, *Chem. Senses* **35**, 157–170 (2010).
25. S. J. Lee, I. Depoortere, H. Hatt, *Nat. Rev. Drug Discov.* **18**, 116–138 (2019).
26. S. S. Calvo, J. M. Egan, *Nat. Rev. Endocrinol.* **11**, 213–227 (2015).
27. P. Lu, C. H. Zhang, L. M. Lifshitz, R. ZhuGe, *J. Gen. Physiol.* **149**, 181–197 (2017).
28. F. A. Shaik *et al.*, *Int. J. Biochem. Cell Biol.* **77**, 197–204 (2016).
29. A. S. Shah, Y. Ben-Shahar, T. O. Moninger, J. N. Kline, M. J. Welsh, *Science* **325**, 1131–1134 (2009).
30. J. Topin *et al.*, *Cell. Mol. Life Sci.* **78**, 7605–7615 (2021).
31. A. Brockhoff, M. Behrens, M. Y. Niv, W. Meyerhof, *Proc. Natl. Acad. Sci. U.S.A.* **107**, 11110–11115 (2010).
32. M. Sandal *et al.*, *J. Chem. Theory Comput.* **11**, 4439–4449 (2015).
33. A. Brockhoff, M. Behrens, A. Massarotti, G. Appendino, W. Meyerhof, *J. Agric. Food Chem.* **55**, 6236–6243 (2007).
34. R. Guo *et al.*, *Am. J. Chin. Med.* **46**, 1–23 (2018).
35. C. Kuhn, B. Bufe, C. Batram, W. Meyerhof, *Chem. Senses* **35**, 395–406 (2010).
36. J. Duan *et al.*, *Nat. Commun.* **11**, 4121 (2020).
37. Y. Zhang, J. Skolnick, *Proteins* **57**, 702–710 (2004).
38. T. Hua *et al.*, *Cell* **180**, 655–665.e18 (2020).
39. K. Liu *et al.*, *Nature* **585**, 135–140 (2020).
40. C. Reichling, W. Meyerhof, M. Behrens, *J. Neurochem.* **106**, 1138–1148 (2008).
41. S. Born, A. Levit, M. Y. Niv, W. Meyerhof, M. Behrens, *J. Neurosci.* **33**, 201–213 (2013).
42. X. Huang, H. Chen, K. Michelsen, S. Schneider, P. L. Shaffer, *Nature* **526**, 277–280 (2015).
43. J. Du, W. Lü, S. Wu, Y. Cheng, E. Gouaux, *Nature* **526**, 224–229 (2015).
44. A. N. Pronin, H. Tang, J. Connor, W. Keung, *Chem. Senses* **29**, 583–593 (2004).
45. Y. Q. Ping *et al.*, *Nature* **589**, 620–626 (2021).
46. F. Fierro *et al.*, *Front. Mol. Biosci.* **4**, 63 (2017).
47. W. Jiang *et al.*, *Proc. Natl. Acad. Sci. U.S.A.* **117**, 30755–30762 (2020).
48. C. B. Roth, M. A. Hanson, R. C. Stevens, *J. Mol. Biol.* **376**, 1305–1319 (2008).
49. E. Vitaku, D. T. Smith, J. T. Njardarson, *J. Med. Chem.* **57**, 10257–10274 (2014).
50. A. Dagan-Wiener *et al.*, *Sci. Rep.* **7**, 12074 (2017).

#### ACKNOWLEDGMENTS

The cryo-EM data were collected at the Bio-Electron Microscopy Facility, ShanghaiTech University, with the assistance of Q.-Q. Sun, Z.-H. Zhang, and other staff members. We also thank the staff members of the Assay, Cell Expression, Cloning, and Purification Core Facilities of the iHuman Institute for their support. **Funding:** This work was supported by the CAS Strategic Priority Research Program XDB37030104 (Z.-J.L.), the National Science Fund for Distinguished Young Scholars 32022038 (T.H.), the National Natural Science Foundation of China grants 31930060 (Z.-J.L.) and 31870744 (T.H.), the National Key Research and Development Program of China grant 2018YFA0507000 (T.H.), and the Shanghai Rising-Star Program 20QA1406500 (T.H.). **Author contributions:** W.X. designed the expression constructs, purified the protein complexes, prepared the final samples for cryo-EM data collection, and participated in figure and manuscript preparation. L.Wu performed the EM data processing and structure determination. S.L. and Y.G. performed structure comparison analyses and molecular docking and prepared related figures. X.L., Q.T., and L.Wa. performed the functional assays. X.C. performed the BRET assays. C.Z. assisted with construct optimization. J.L., L.J., and Z.F. expressed proteins. J.Z. assisted with the cryo-EM sample preparation. Y.F. assisted with cryo-EM data processing and movie preparation. Y.P. and J.Y. assisted with cryo-EM data processing. J.C. assisted with the docking poses analysis. Y.W. and S.Z. assisted with the strychnine binding pose analysis. X.H. performed strychnine analog synthesis. Z.-J.L. and T.H. managed and supervised the overall project, analyzed the structures, and wrote the manuscript. **Competing interests:** The authors declare no competing interests. **Data and materials availability:** Coordinates and structures factors have been deposited in the Protein Data Bank for strychnine-TAS2R46-miniG<sub>s/gust</sub> (PDB ID 7XP6, EMD-33366), ligand-free TAS2R46-miniG<sub>s/gust</sub> (PDB ID 7XP5, EMD-33365), and apo-TAS2R46-miniG<sub>s/gust</sub> (PDB ID 7XP4, EMD-33364). **License information:** Copyright © 2022 the authors, some rights reserved; exclusive licensee American Association for the Advancement of Science. No claim to original

US government works. <https://www.science.org/about/science-licenses-journal-article-reuse>

#### SUPPLEMENTARY MATERIALS

science.org/doi/10.1126/science.abo1633  
Materials and Methods  
Figs. S1 to S11  
Tables S1 to S3

References (51–79)  
MDAR Reproducibility Checklist  
Movies S1 and S2

Submitted 18 January 2022; accepted 16 August 2022  
10.1126/science.abo1633

## REPORTS

### SOCIAL NETWORKS

# A causal test of the strength of weak ties

Karthik Rajkumar<sup>1</sup>, Guillaume Saint-Jacques<sup>1</sup>, Iavor Bojinov<sup>2</sup>, Erik Brynjolfsson<sup>3,4</sup>, Sinan Aral<sup>5\*</sup>

The authors analyzed data from multiple large-scale randomized experiments on LinkedIn's People You May Know algorithm, which recommends new connections to LinkedIn members, to test the extent to which weak ties increased job mobility in the world's largest professional social network. The experiments randomly varied the prevalence of weak ties in the networks of over 20 million people over a 5-year period, during which 2 billion new ties and 600,000 new jobs were created. The results provided experimental causal evidence supporting the strength of weak ties and suggested three revisions to the theory. First, the strength of weak ties was nonlinear. Statistical analysis found an inverted U-shaped relationship between tie strength and job transmission such that weaker ties increased job transmission but only to a point, after which there were diminishing marginal returns to tie weakness. Second, weak ties measured by interaction intensity and the number of mutual connections displayed varying effects. Moderately weak ties (measured by mutual connections) and the weakest ties (measured by interaction intensity) created the most job mobility. Third, the strength of weak ties varied by industry. Whereas weak ties increased job mobility in more digital industries, strong ties increased job mobility in less digital industries.

The Strength of Weak Ties (1) is one of the most influential social theories of the past century, underpinning networked theories of information diffusion (2, 3), social contagion (4, 5), social movements (6), industry structure (7), influence maximization (8), and human cooperation (9, 10). It argues that infrequent, arms-length relationships, known as “weak ties,” provide more new employment opportunities (11), promotions and greater wage increases (12), creativity (13), innovation (14, 15), productivity (16), and performance (17) because they deliver more novel information than strong ties. Weak ties are thought to provide access to diverse, novel information because they connect us to disparate and diverse parts of the human social network (18–24). In addition to productivity, performance, innovation, and other benefits, weak ties are thought to be specifically well suited to deliver new employment opportunities because they provide novel labor market information, making job mobility a centerpiece of the original weak tie theory.

Recent large-scale correlational investigations of the weak tie hypothesis, however, have uncovered a seeming “paradox of weak ties,” suggesting that strong ties are more valuable than weak ties in generating job transmissions (25, 26). Though these are the largest, most direct empirical examinations of the weak tie hypothesis to date, because the work is not experimental the authors rightfully acknowledge that their results “may not be the true causal effect of tie strength on the probability of a sequential job.” More generally, two empirical challenges have prevented robust causal tests of the weak tie theory to date: First, a lack of large-scale data linking human social networks to job transmission makes measurement of the relationship between weak ties and labor market outcomes difficult. Second, network ties and labor market outcomes are endogenous, making the causal link between weak ties and job placement elusive. Individuals' labor market outcomes are likely to be determined by and to simultaneously determine their social networks. The evolution of social networks and job trajectories are also likely correlated with unobserved factors such as effort, ability, and sociability, which confound empirical identification of the link between weak ties and jobs.

We address these two empirical challenges and provide an experimental causal test of

<sup>1</sup>LinkedIn Corporation, 700 E Middlefield Rd, Mountain View, CA 94043, USA. <sup>2</sup>Harvard Business School, Soldiers Field, Boston, MA 02163, USA. <sup>3</sup>Stanford University, 353 Jean Stanford Way, Stanford, CA 94305, USA. <sup>4</sup>National Bureau of Economic Research, 1050 Massachusetts Ave., Cambridge, MA 02138, USA. <sup>5</sup>Massachusetts Institute of Technology, MIT Sloan School of Management, 100 Main St., Cambridge, MA 02142, USA. \*Corresponding author. Email: [sinan@mit.edu](mailto:sinan@mit.edu)

the weak tie theory with data from multiple large-scale randomized experiments on LinkedIn, the world's largest professional social network. The experiments randomly varied the prevalence of strong and weak ties in the professional networks of over 20 million LinkedIn members by adjusting the platform's People You May Know (PYMK) algorithm, which recommends new connections to members (Fig. 1A illustrates the experimental design). LinkedIn's PYMK algorithm is an ensemble machine learning model comprising the following: (i) a model for estimating the propensity of an ego (i.e., a focal member) to send a connection invite to an alter (i.e., a member the focal member is not currently connected with), (ii) a model estimating the alter's propensity to accept an invite from the ego, (iii) a model estimating the engagement between the ego and alter once connected and (iv) weights on each of these models for relative importance. The experiments tuned these components, introduced new data sources, and relied on the number of mutual connections between the ego and a potential tie recommendation as one of the most important features of the ensemble model to randomly vary weak and strong tie recommendations. We performed a retrospective analysis of the randomization created by the PYMK experiments conducted by LinkedIn between 2015 and 2019 in two waves.

The first wave examined a global experiment conducted in 2015 that had over 4 million experimental subjects and created over 19 million new connections. We collected edge-level observations of tie strength and job transmission outcomes for each tie created during this experiment. We then analyzed a larger second wave of node-level PYMK experiments that took place worldwide in 2019. The second wave spanned every continent and US state, had more than 16 million experimental subjects, created ~2 billion new connections and recorded more than 70 million job applications that led to 600,000 new jobs during the experimental period (Fig. 1, B and C). The data were collected both at the node level (in 2019), where each observation corresponds to a unique LinkedIn member, and at the edge level (in 2015), where each observation corresponds to a unique tie between two LinkedIn members (see Fig. 1A for a description of how we compiled the edge- and node-level datasets).

We analyzed labor market mobility by measuring both job applications and job transmissions. Job applications are simply the number of jobs LinkedIn members applied to on the platform in the three months after an experiment. In accordance with the literature (25, 26), we consider a job transmission to have occurred when three criteria are satisfied: First, user *A* reports working at company *c* at date  $D_1$ . Second, user *B* reports working at that same company *c* at a later date  $D_2$ , with  $D_2$  and

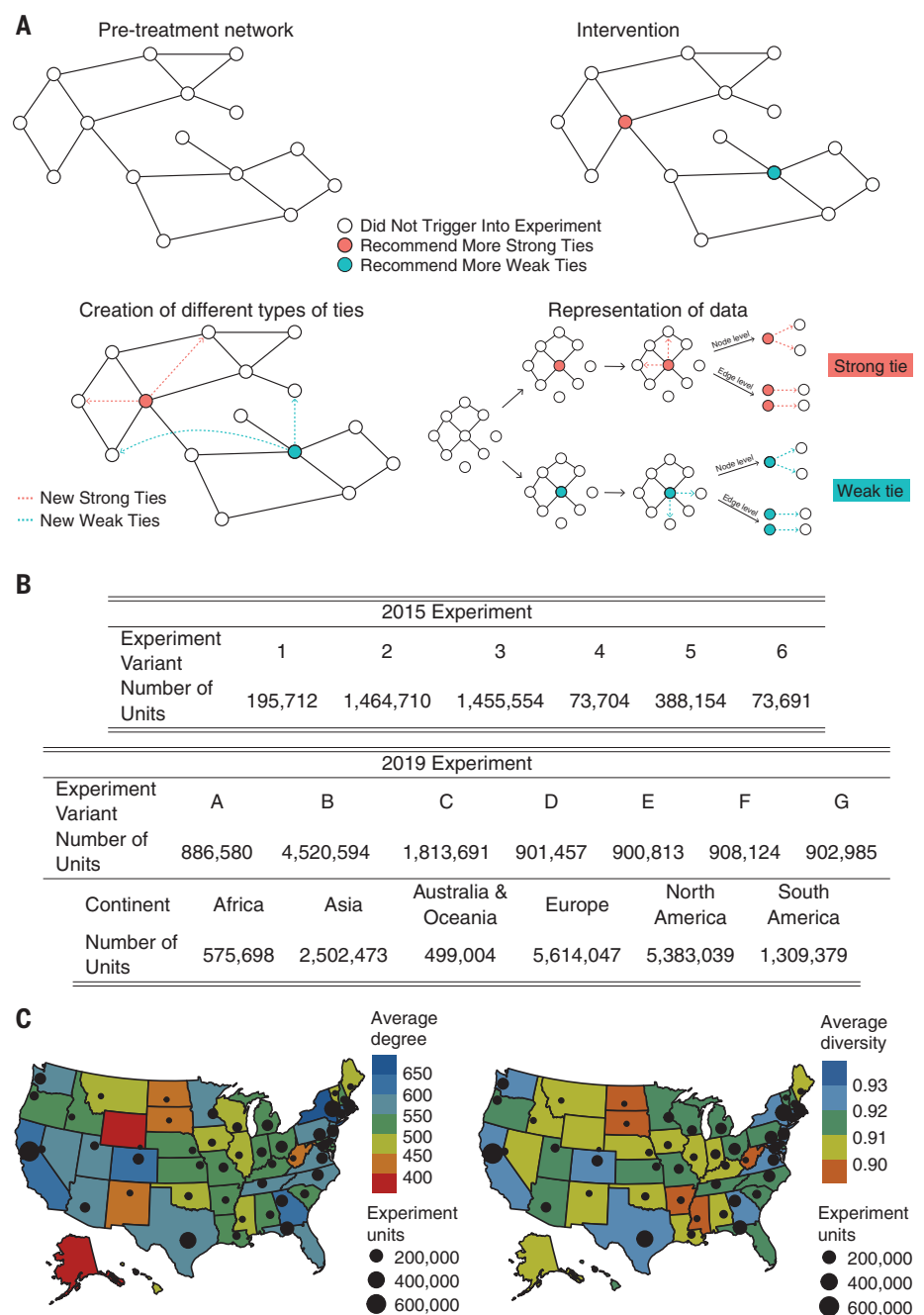


**Fig. 1. Experiment design and summary statistics.** (A) describes the experimental design and representation of the resultant data in node- and edge-level analyses; (B) displays the number of experimental units in the 2015 and 2019 experiments by continent and experimental variant (98.8% of the 2015 data was from the U.S.); and (C) displays the average degree, network diversity (formally defined in the SM), and number of experimental units by U.S. state in our 2019 experiments.

$D_1$  being at least one year apart. Third, user *A* and user *B* were friends on the social network at least one full year before  $D_2$ . In the weak tie literature, when these three criteria are met, a tie is considered a “sequential job” tie, which represents the state of the art in measuring relational job mobility.

We measured tie strength by its two leading indicators: the intensity of the interaction

between two people and the number of mutual connections they had in common. We measured interaction intensity by counting the number of interactions LinkedIn members had with one another through bilateral messaging. We measured mutual friendship by counting the number of friends any two connected individuals had in common when their tie was created. Structural tie strength, based on mutual

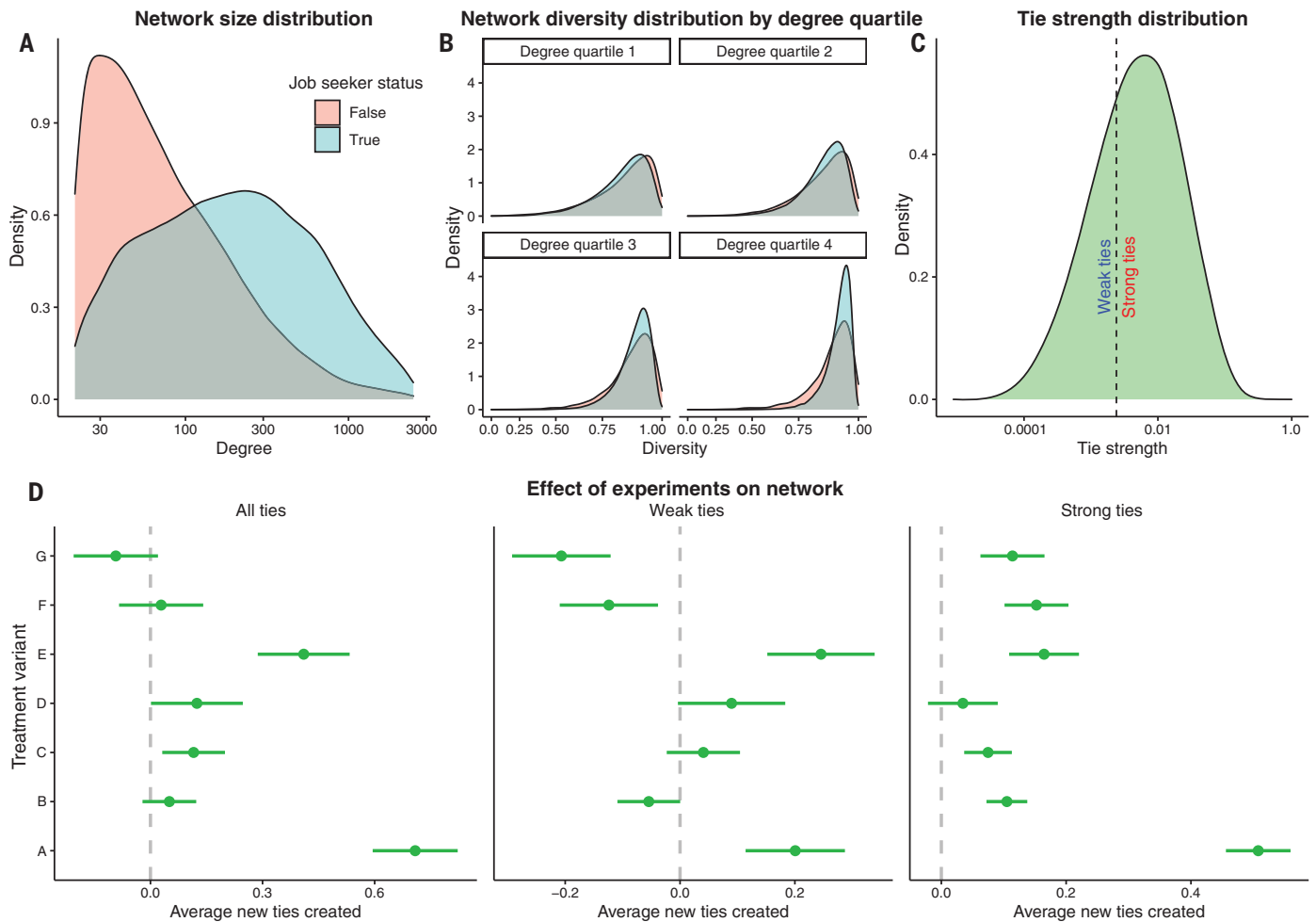


**Fig. 2. Network statistics and first stage effects of experimental treatments.** (A) displays the node-level degree distributions of job seekers and non-job seekers whereas (B) displays the corresponding distribution of network diversity by job seeker status by quartiles of members' degrees to distinguish diversity and network size, in which job seekers are members who applied for a job in the three months before an experiment; (C) displays the edge-level structural tie strength distribution of all ties created during the 2019

experiments, in which the cutoff for determining weak or strong ties is the median of structural tie strength in the LinkedIn network before the experiments; and (D) displays the "first stage" effects of the experimental treatments on how many new ties are created by members. The point estimates and standard error bars report the number of new ties created and their relative split between strong and weak ties by members assigned to different treatment variants compared to a control variant.

friendship, was then defined bidirectionally as follows:

$$StructuralTieStrength_{ij} = \frac{M_{ij}}{D_i + D_j - M_{ij} - 2}$$

where  $i$  and  $j$  are LinkedIn members,  $M_{ij}$  is the number of mutual connections between them, and  $D_i$  and  $D_j$  are the total number of direct connections of members  $i$  and  $j$ , respectively. Network diversity is defined as  $1 - C_i$ , where  $C_i$  is the local clustering coefficient (formally defined in the SM).

Because tie strength changes in response to one's own friending behavior and the friending behavior of one's connections, we measured structural tie strength pretreatment and examined the causal effect of adding a new connection whose pretreatment tie strength

was either strong or weak depending on whether it was above or below the median of the pre-treatment tie strength distribution (Fig. 2C). Interaction intensity is observed once a new tie is created. We therefore measured interaction intensity during the experimental period after ties were formed. Job seekers have more connections (greater degree) (Fig. 2A) and greater network diversity at higher degrees (Fig. 2B). But because these network variables are endogenously determined in observational data, random variation in LinkedIn members networks is necessary for a robust causal assessment of the relationship between weak ties and job mobility.

We estimated the causal effects of strong and weak ties on job mobility with an instrumental variables (IV) approach (27–29). The IV

framework disentangles endogeneity by using random variation created by exogenous treatment assignments as a shock to endogenous counts of newly created weak and strong ties to estimate their causal effect on job mobility. We estimated these effects in a two-stage least squares (2SLS) specification, using the random assignment of members to weak- or strong-tie experimental variants as instruments for identifying the effect of adding weak or strong ties on job applications and job transmissions.

We conducted both node-level and edge-level analyses of the relationship between tie strength and job mobility. Node-level analyses estimated the effect of the number of weak or strong ties created by the experiments on job applications and job mobility. Though the node-level analysis estimates how assignments

to weak- or strong-tie-inducing experimental treatments created changes in job mobility, it obfuscates which weak or strong ties led to job transmission. We therefore also conducted edge-level analyses to estimate the marginal effect of adding strong or weak ties to members' networks on their subsequent job mobility.

The first stage regressions estimated the effects of assignments to different experimental treatment variants on the creation of weak and strong ties in LinkedIn members' professional networks. The results of these first stage regressions, shown in Fig. 2D, demonstrate the random variation created by our experiments by displaying the effects of the experimental treatment variants on the creation of weak and strong ties between members in the LinkedIn network. As the figure shows, some treatment variants caused members to form more weak ties (e.g., variants A and E), whereas others caused members to form fewer weak ties (e.g., variants F and G). The different variants also caused members to create more ties (e.g., variants A, C, and E), fewer ties (e.g., variant G), or approximately the same number of ties (e.g., variants B, D, and F), allowing us to distinguish the causal effect of tie strength on job outcomes from the causal effects of the number of new ties created.

The second stage regressions estimated the effect of weak and strong ties on job mobility. The fitted values estimated in the first stage captured only those changes in the number of new weak or strong ties caused by our experiments. In the second stage only the variation in the creation of new weak or strong ties caused by our exogenous treatment assignments was used to estimate the effects of weak or strong ties on job applications and job transmissions. In this way the IV approach enabled causal inference by excluding (i) the effects of job mobility on the formation of weak and strong ties, (ii) the effects of strategic network formation behaviors that precede job mobility, and (iii) variation created by observable and unobservable confounding factors that can affect both network formation and job mobility, from estimates of the effects of weak and strong ties on labor market behaviors and outcomes.

For our approach to provide valid causal inference, the treatment assignment to a PYMK algorithm variant should be a valid instrument for the number of weak and strong ties created by experimental subjects and thus should satisfy four assumptions (27). First, the independence assumption, which requires that the instrument was randomly assigned, was satisfied as the LinkedIn experimentation platform used a Bernoulli design to randomly assign all users to different treatment arms. Second, the exclusion restriction, which requires that the instrument did not affect the outcome through any channels except the

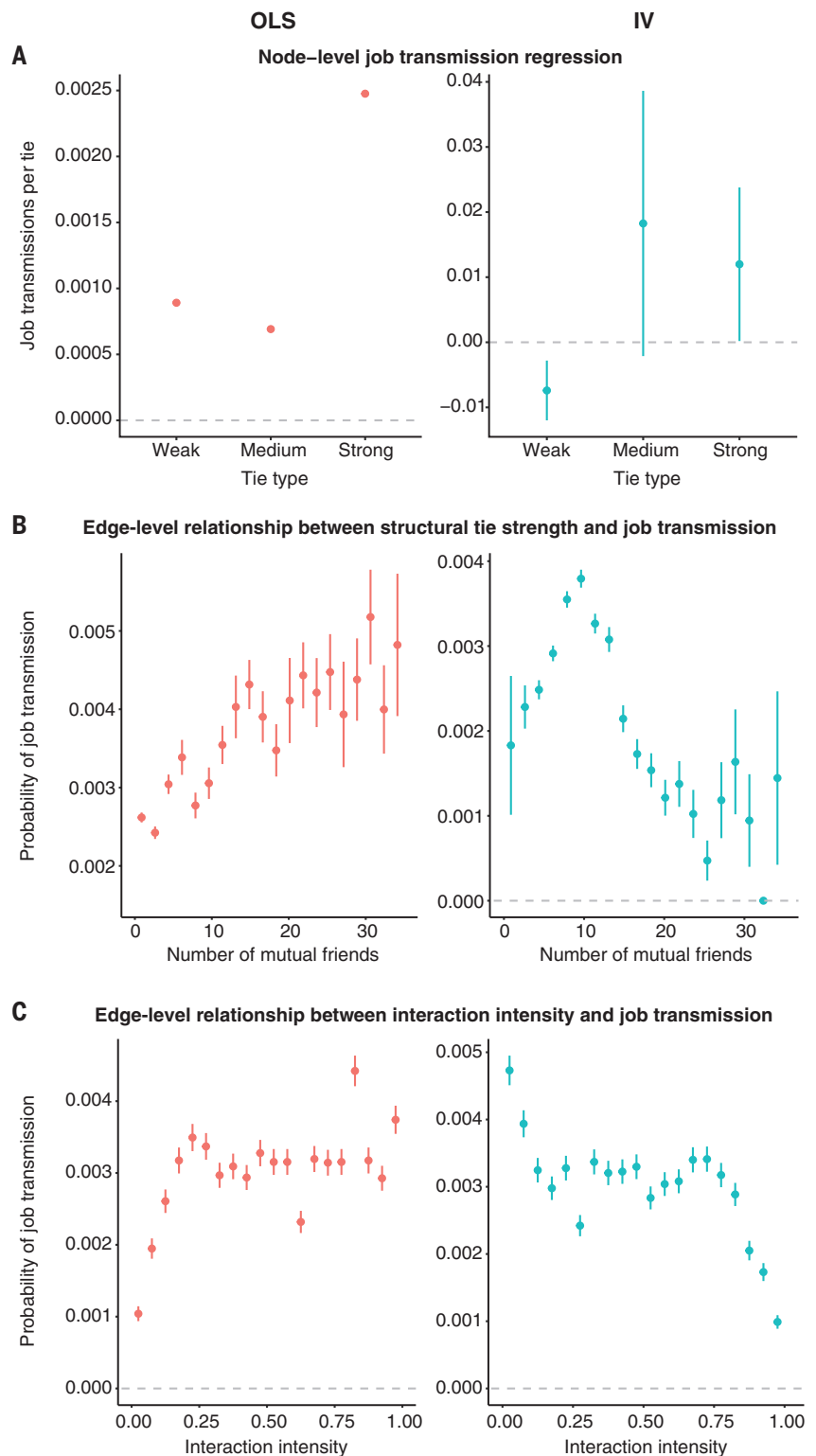


**Fig. 3. The causal effect of tie strength on job mobility.** The figure displays the estimated effects of tie strength on job transmissions at the node and edge levels. In each panel the left column displays the results of the OLS analysis whereas the right column displays the experimental IV results from first wave experiments conducted in 2015. (A) displays the effect of weak, medium, and strong ties (defined by terciles of mutual friends) on job transmissions aggregated to the node level; (B) displays the effects of structural tie strength based on the number of mutual friends on job transmissions at the edge level whereas (C) displays the effects of tie strength based on interaction intensity on job transmissions at the edge level.

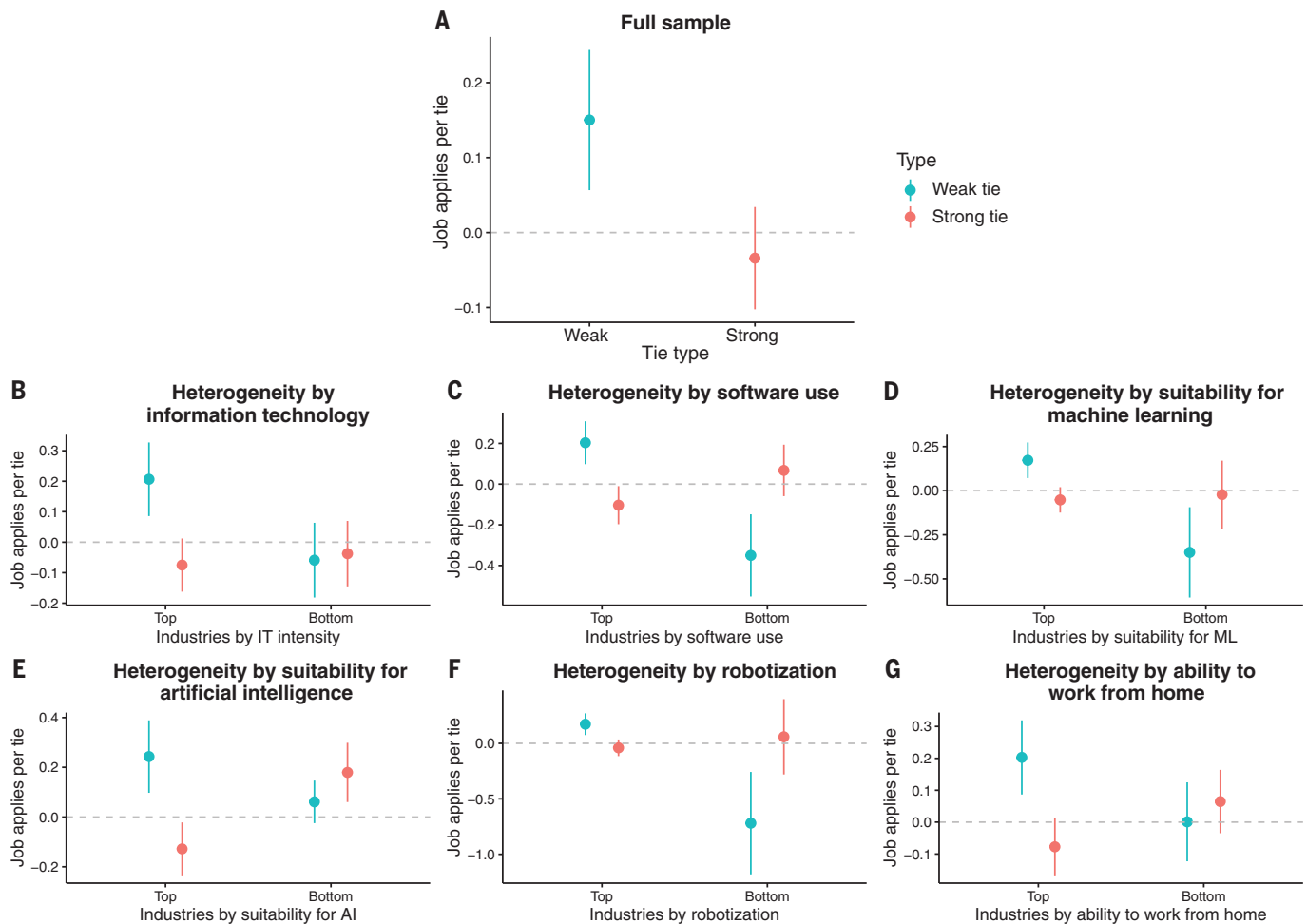


**Fig. 4. Heterogeneous causal effects by industry.** (A) displays experimental IV analysis of the effects of weak and strong ties on job applications at the node level in the full sample. The rest of the panels display experimental IV analysis of the heterogeneous effects of weak and strong ties on job applications

at the node level to jobs in industries in the top and bottom half of the industry distributions of (B) IT intensity; (C) software intensity; (D) suitability for machine learning; (E) suitability for artificial intelligence; (F) degree of robotization; and (G) suitability for remote work.

treatment channel, held because the experiments uniquely altered tie recommendations without altering any other algorithm related to job outcomes such as job recommendations or job search rankings. It also had no effect on how members interacted or shared social information with each other (e.g., messages, posts, comments, likes, and shares), other than through the new connections formed as a result of the experiments (see Section C.3 and table S24 in the SM). Third, the monotonicity assumption, precluding the existence of “defiers”—egos that initiated more weak tie connections when assigned to an algorithm that promoted strong ties—was satisfied by the design of the PYMK algorithm, which assigned suggested treatment connections to ranks that were much more likely to be clicked on and initiated. This assumption was also satisfied by the strong suggestive evidence that these assignments worked to create the desired behaviors observed in the new con-

nection outcomes for each treatment variant (Fig. 2D). Fourth, the relevance assumption, which requires that the instrument had an effect on the treatment, was satisfied by the varying numbers of weak, strong, and total ties created by the different treatment arms shown in Fig. 2 (see Section C.3 of the SM for an in-depth discussion of these assumptions and their verification). To estimate the bias in correlational analyses of the weak tie hypothesis, we also specified and estimated standard ordinary least squares (OLS) regressions assessing the correspondence between tie strength and job mobility.

Our main results are summarized in Fig. 3. The first column in each panel displays results from OLS estimation whereas the second column displays results from the experimental instrumental variables (IV) analysis. Dots represent point estimates of the effects and bars represent standard errors. Figure 3A displays the results of our OLS and experimental esti-

mates of the effect of weak and strong ties on job transmissions at the node level. Although the OLS analysis replicated previous findings of an apparent paradox of weak ties in which strong ties were more strongly correlated with job transmissions, the experimental IV analysis reversed this result and suggested a non-linear relationship between tie strength and job transmission in which medium strength ties were the most effective in generating job mobility. As the statistical power of the node-level analysis was not sufficient to confirm individual differences between the effects of strong, medium, and weak ties in our experiments, we also analyzed these relationships at the more granular edge level.

Figure 3B displays the results of our OLS and experimental estimates of the effect of the strength of a newly added tie, measured by the number of mutual connections between LinkedIn members before treatment, on the probability of a job transmission between them after



treatment at the edge level. Although the OLS estimates again replicated previous correlational research demonstrating the paradox of weak ties and showed that strong ties were more strongly correlated with an increased probability of a job transmission through the tie, the experimental IV results mirrored the node-level experimental results and revealed a more nuanced correspondence—namely that there was an inverted U-shaped relationship between tie strength and the likelihood of a job transmission. At low levels of mutual friendship adding new ties with more mutual friends caused the probability of a job transmission to go up. However, adding ties with more than ten friends in common reduced the probability of a job transmission.

Figure 3C displays the results of our OLS and experimental estimates of the effect of the strength of a newly added tie, measured by the interaction intensity between LinkedIn members and on the probability of a job transmission between them, again at the edge level. Although the OLS estimates showed that stronger ties were correlated with an increased probability of job transmission the experimental IV results revealed the opposite—the stronger the newly added ties the less likely they were to lead to a job transmission. This relationship was also nonlinear. The weakest ties with the least interaction intensity increased the likelihood of a job transmission the most whereas the strongest ties with the greatest interaction intensity increased the likelihood of a job transmission the least; further, the relationship between interaction intensity and job transmission was approximately flat for the middle quartiles of the interaction intensity distribution.

Three major conclusions emerged from our main results: First, experimental analysis helped resolve the apparent paradox of weak ties in multiple large-scale experiments of job mobility in the world's largest professional social network. Although the correlational analysis supported the seeming importance of strong ties for job mobility, the experimental analyses—conducted over multiple sample populations, numerous years, and in all geographic regions of the world—confirmed that relatively weaker ties increased the likelihood of job mobility the most.

Second, our experiments uncovered a consistent nonlinearity in the relationship between tie strength and job mobility. In contrast to the increasing likelihood of job transmission associated with greater tie strength in correlational analyses, our experiments showed that when considering structural tie strength based on the number of mutual friends between contacts, an inverted U-shaped relationship exists between tie strength and job mobility—with moderately weak ties increasing job mobility the most and the strongest ties increasing

job mobility the least. When considering tie strength based on interaction intensity, in a direct reversal of the correlational evidence, the experimental analysis showed that the weakest ties had the greatest impact on job mobility whereas the strongest ties had the least.

Third, whereas node-level analyses measured the impact of experimental variation in the number of weak or strong ties in one's network on job transmission, our edge-level analysis enabled an assessment of the marginal effects of adding strong or weak ties. The results showed that adding new moderately structurally diverse ties with weak interaction intensity created the greatest marginal increases in the likelihood of job transmissions.

Prior research also suggests that weak and strong ties have different effects across different industries (22). We therefore examined the heterogeneity in the impact of strong and weak ties on job mobility across industry sectors. Although the second wave experimental sample was sufficiently powered to examine this heterogeneity, experiments conducted in this wave in 2019 do not leave sufficient time to examine impacts on longer-term job transmission outcomes. Therefore we limited our analysis of these heterogeneous effects to job applications, which are estimable in the short term.

We classified the industries in which LinkedIn members applied for jobs on the basis of the demand for particular skills listed for those jobs and the counts of occupations in different industries calculated from Burning Glass Technologies (BGT) data and other sources (see supplementary material for details). The industry classifications were created by measuring the weighted skill demands of all job postings within an industry listed in the BGT data and the counts of an industry's hiring for different occupations listed in the job postings of that industry. Based on these metrics, we developed scores that measured each industry's information technology (IT) intensity, software intensity, suitability for machine learning, suitability for artificial intelligence, degree of robotization, and suitability for remote work using known indices for these metrics in the labor economics literature (30–32). We then measured the degree to which experimental variation in the acquisition of new strong or weak ties led to increases or decreases in job applications to industries of these types.

Results of our IV analysis showed that, in the full sample, adding weak ties led to more job applications overall (Fig. 4A), which provides evidence of the mechanism linking weak ties to job transmissions. As members acquired more weak ties through the PYMK algorithm experiments they applied to more jobs and experienced considerably greater job mobility. The heterogeneous treatment effects also reflect a clear trend toward weak ties creating

greater job mobility in more digital sectors of the economy. The results showed that weak ties resulted in more job applications than strong ties to industries with greater IT (Fig. 4B) and software intensity (Fig. 4C), as well as industries more suitable for machine learning (Fig. 4D), artificial intelligence (Fig. 4E) and remote work (Fig. 4G), along with those that have experienced a greater degree of robotization (Fig. 4F). By contrast, adding strong ties caused more job applications to industries that relied less on software (Fig. 4C) and were less automated by robots (Fig. 4F).

Although our work presents the first large-scale, longitudinal, experimental evidence on the causal effects of strong and weak ties on job mobility in a global sample and across multiple industries, it is not without limitations. First, although PYMK experiments provided a robust channel through which to introduce experimental variation into the evolution of human social networks, we could not compel LinkedIn users to take these recommendations. Therefore a degree of self selection exists in who acted on the connection recommendations. For this reason we analyzed our experiments as having an “intent to treat” and compared the population assigned to weak-tie experimental variants to those assigned to strong-tie experimental variants and control groups (for raw intent to treat point estimates, see table S14). Although this approach controls for any bias from self selection, it circumscribes the populations to which our results generalize. Although there were some observable differences between members who took PYMK recommendations on LinkedIn and those who did not, most did, making our results broadly generalizable to the LinkedIn population. However, unsurprisingly, exposure depended on use of the platform and viewing the PYMK recommendations. As we report in the SM, LinkedIn members exposed to our treatments were slightly younger and more active job seekers, clarifying the population to which our results reliably generalize.

Second, LinkedIn is a professional social network and may be different than other online social networks such as Facebook or offline social relationships such as those originally studied by Granovetter. However we do know that certain characteristics such as network clustering, for example, are similar across Facebook, LinkedIn, and Twitter (see SM Section F.2). Furthermore, our OLS results closely mirrored the results of very large global studies of networks and job mobility on Facebook, which suggests that similar processes are occurring in both networks. There are some differences between the population of workers on LinkedIn and those in the US, European, and broader global economies. For example, LinkedIn skews more heavily toward workers in finance, information and professional services, high technology industries, and construction

and manufacturing, and less toward wholesale and retail trade work than the US workforce (see SM Section F.2 for a comparison of LinkedIn profiles with the US and EU workforces). However, LinkedIn is also the world's largest professional social network and one of the largest websites for job listings. Many people rely on LinkedIn to find work so this network may be even more representative of how networks affect job mobility in the larger labor market than, for example, friendship networks or the Facebook network.

Third, any networked experiment must pay close attention to the possibility of statistical interference, in which one unit's treatment assignment affects another unit's outcome, the ignorability of which is known as the stable unit treatment value assumption (33). To minimize such interference we only tracked the edges that each member initiated through PYMK recommendations. Nevertheless, there were still three possible channels through which interference could have occurred in our setting. First, interference could have emerged if an ego's treatment assignment affected their alters through changes in ego's behaviors that were visible to the alters. LinkedIn facilitates some social actions that might have been seen by a member's alters including posting on the news feed, commenting on a post, or sending private messages. However, none of these behaviors were considerably affected by the various treatments, making this channel of interference unlikely to affect our results (see table S24). A second interference channel could have arisen if member  $i$  intended to connect with member  $j$  but, because of member  $j$ 's treatment assignment,  $j$  initiated a connection request before  $i$  had a chance to send one. If accepted, such ties would be attributed to ego  $j$  in our analysis. To account for this possibility we verified that the treatments did not affect the number of connection requests received by members in different treatment arms, allowing us to conclude that any effect from receiving connection requests was small and balanced across treatments and therefore negligible (see table S25). Third, interference could have occurred if new ties generated by members as a result of treatment changed the composition of other members' PYMK recommendation lists. Fortunately, LinkedIn's membership is large enough to ensure a sufficient inventory of new ties to replenish any removed ties with comparable individuals, ensuring that the composition of the potential ties was consistent throughout the experiment. Furthermore, PYMK inputs did not change often enough for new connections to immediately change the types of algorithmic recommendations any member saw, ensuring the experiments' stability. This minimized the risk that connection behaviors instantaneously updated the algorithms and thus changed the types of recommendations other members saw.

For more details on the interference assumption, please see SM Section C.2.

Despite these limitations, our analysis of several large-scale experiments on the world's largest professional social network demonstrated that weak ties create job mobility. In contrast to recent large-scale correlational evidence of a paradox of weak ties, we found that moderately weak ties with low interaction intensity—measured by the number of mutual friends between two people—increased job applications and job transmissions the most, whereas strong ties—measured by both the number of mutual friends and interaction intensity—increased job applications and job transmissions the least. We also found an inverted U-shaped relationship between structural tie strength and job transmissions and a nonmonotonically decreasing correspondence between interaction intensity and job transmissions, demonstrating a consistent nonlinearity in the relationship between tie strength and job mobility, as well as heterogeneity in the impact of weak ties on job applications across industries with varying degrees of digitization. The industry analysis showed that weak ties caused more job applications to high-tech industries, broadly speaking, whereas strong ties caused more job applications to low-tech industries. Together, these results provide some of the first large-scale experimental evidence of the strength of weak ties and suggest the need to revise the theory to incorporate the nonlinear effects of tie strength on job transmissions, differences between the effects of structural tie strength and tie strength measured by interaction intensity, and differences between the effects of weak and strong ties on job mobility across industries.

#### REFERENCES AND NOTES

- M. S. Granovetter, *Am. J. Sociol.* **78**, 1360–1380 (1973).
- E. Bakshy, I. Rosenn, C. Marlow, L. Adamic, The role of social networks in information diffusion, in *Proceedings of the 21st International Conference on World Wide Web* (2012), pp. 519–528.
- P. S. Park, J. E. Blumenstock, M. W. Macy, *Science* **362**, 1410–1413 (2018).
- J. Ugander, L. Backstrom, C. Marlow, J. Kleinberg, *Proc. Natl. Acad. Sci. U.S.A.* **109**, 5962–5966 (2012).
- D. Centola, *Science* **329**, 1194–1197 (2010).
- D. Centola, M. Macy, *Am. J. Sociol.* **113**, 702–734 (2007).
- G. Walker, B. Kogut, W. Shan, *Organ. Sci.* **8**, 109–125 (1997).
- D. Kempe, J. Kleinberg, É. Tardos, Maximizing the spread of influence through a social network, in *Proceedings of the Ninth ACM SIGKDD International Conference on Knowledge Discovery and Data Mining* (2003), pp. 137–146.
- D. G. Rand, S. Arbesman, N. A. Christakis, *Proc. Natl. Acad. Sci. U.S.A.* **108**, 19193–19198 (2011).
- C. L. Apicella, F. W. Marlowe, J. H. Fowler, N. A. Christakis, *Nature* **481**, 497–501 (2012).
- J. D. Montgomery, *Am. Econ. Rev.* **81**, 1408–1418 (1991).
- J. M. Podolny, J. N. Baron, *Am. Sociol. Rev.* **62**, 673–693 (1997).
- R. S. Burt, *Am. J. Sociol.* **110**, 349–399 (2004).
- S. Rodan, C. Galunic, *Strateg. Manage. J.* **25**, 541–562 (2004).
- A. Hargadon, R. I. Sutton, *Adm. Sci. Q.* **42**, 716–749 (1997).

- R. Reagans, E. W. Zuckerman, *Organ. Sci.* **12**, 502–517 (2001).
- N. Eagle, M. Macy, R. Claxton, *Science* **328**, 1029–1031 (2010).
- R. S. Burt, *Structural holes* (Harvard Univ. Press, 1992).
- B. Uzzi, *Am. Sociol. Rev.* **61**, 674–698 (1996).
- D. Lazer, A. Friedman, *Adm. Sci. Q.* **52**, 667–694 (2007).
- M. McPherson, L. Smith-Lovin, J. M. Cook, *Annu. Rev. Sociol.* **27**, 415–444 (2001).
- S. Aral, M. Van Alstyne, *Am. J. Sociol.* **117**, 90–171 (2011).
- D. J. Watts, S. H. Strogatz, *Nature* **393**, 440–442 (1998).
- A.-L. Barabási, R. Albert, *Science* **286**, 509–512 (1999).
- L. K. Gee, J. Jones, M. Burke, *J. Labor Econ.* **35**, 485–518 (2017).
- L. K. Gee, J. J. Jones, C. J. Fariss, M. Burke, J. H. Fowler, *J. Econ. Behav. Organ.* **133**, 362–372 (2017).
- J. D. Angrist, G. W. Imbens, D. B. Rubin, *J. Am. Stat. Assoc.* **91**, 444–455 (1996).
- J. D. Angrist, A. B. Krueger, *J. Econ. Perspect.* **15**, 69–85 (2001).
- J. D. Angrist, J.-S. Pischke, *Mostly Harmless Econometrics* (Princeton Univ. Press, 2008).
- E. Brynjolfsson, T. Mitchell, D. Rock, *AEA Pap. Proc.* **108**, 43–47 (2018).
- M. Webb, The Impact of Artificial Intelligence on the Labor Market (Stanford University, 2020); [https://www.michaelwebb.co/webb\\_ai.pdf](https://www.michaelwebb.co/webb_ai.pdf)
- J. I. Dingel, B. Neiman, *J. Public Econ.* **189**, 104235 (2020).
- D. B. Rubin, *J. Am. Stat. Assoc.* **75**, 591–593 (1980).
- K. Rajkumar, rajkumarkarthik/weak\_ties\_data\_and\_code: Replication files for A Causal Test of the Strength of Weak Ties, Version v1.0.1, Zenodo (2022); <https://zenodo.org/record/6533898#.YwkcWnbMl2w>.

#### ACKNOWLEDGMENTS

We thank D. Eckles and participants of the MIT Conference on Digital Experimentation, the Workshop on Information Systems Economics, and the HBS Junior Faculty Research Seminar for their helpful comments on earlier drafts of this manuscript. We also thank the MIT Initiative on the Digital Economy and the Stanford Digital Economy Lab for their intellectual support, as well as M. Garlinghouse, I. Perisic, Y. Xu, and P. Ahammad at LinkedIn for intellectual and organizational support and data access. The study was approved by the MIT Institutional Review Board (IRB Protocols E-3347 and E-2755). **Funding:** The authors received no external financial support for the research and publication of this work. **Author contributions:** Conceptualization: G.S.-J., E.B., and S.A.; Methodology: K.R., G.S.-J., I.B., and S.A.; Data curation, software, and formal analysis: K.R. and G.S.-J.; Investigation: K.R., G.S.-J., I.B., E.B., and S.A.; Writing: K.R., I.B., E.B., and S.A.; Visualization: K.R., I.B., E.B., and S.A.; Project administration and resources: K.R., G.S.-J., E.B., and S.A.; Supervision: G.S.-J., I.B., E.B., and S.A.; Validation: K.R. and G.S.-J. **Competing interests:** K.R. and G.S.-J. are or were employees of LinkedIn and hold a significant financial interest in Microsoft Corporation. All other authors declare no competing interests. **Data and materials availability:** All original analysis code, aggregated data and annotated code sufficient to replicate all correlational regressions are available here: (34). Individual-level data supporting this study are not publicly available due to user privacy and other legal restrictions. Researchers seeking replication should submit a request to [mailto:reg\\_data@linkedin.com](mailto:reg_data@linkedin.com) clearly stating the work that you would like to reproduce and the names and organizational affiliations of the researchers. LinkedIn reviews all such requests but will grant access at its sole discretion. **License information:** Copyright © 2022 the authors, some rights reserved; exclusive licensee American Association for the Advancement of Science. No claim to original US government works. <https://www.sciencemag.org/about/science-licenses-journal-article-reuse>

#### SUPPLEMENTARY MATERIALS

[science.org/doi/10.1126/science.abl4476](https://science.org/doi/10.1126/science.abl4476)

Materials and Methods

Fig. S1

Tables S1 to S28

References (35–52)

MDAR Reproducibility Checklist

Submitted 19 July 2021; accepted 20 July 2022

10.1126/science.abl4476

## EVOLUTION

# Exceptional preservation of organs in Devonian placoderms from the Gogo lagerstätte

Kate Trinajstić<sup>1,2\*</sup>, John A. Long<sup>3,4</sup>, Sophie Sanchez<sup>5,6</sup>, Catherine A. Boisvert<sup>1</sup>, Daniel Snitting<sup>5</sup>, Paul Tafforeau<sup>6</sup>, Vincent Dupret<sup>5</sup>, Alice M. Clement<sup>3</sup>, Peter D. Currie<sup>7</sup>, Brett Roelofs<sup>1</sup>, Joseph J. Beviitt<sup>8</sup>, Michael S. Y. Lee<sup>3,9</sup>, Per E. Ahlberg<sup>5</sup>

The origin and early diversification of jawed vertebrates involved major changes to skeletal and soft anatomy. Skeletal transformations can be examined directly by studying fossil stem gnathostomes; however, preservation of soft anatomy is rare. We describe the only known example of a three-dimensionally mineralized heart, thick-walled stomach, and bilobed liver from arthrodire placoderms, stem gnathostomes from the Late Devonian Gogo Formation in Western Australia. The application of synchrotron and neutron microtomography to this material shows evidence of a flat S-shaped heart, which is well separated from the liver and other abdominal organs, and the absence of lungs. Arthrodires thus show the earliest phylogenetic evidence for repositioning of the gnathostome heart associated with the evolution of the complex neck region in jawed vertebrates.

**T**he Gogo lagerstätte shows exceptional three-dimensional bone and muscle preservation within placoderms (1–3), a paraphyletic taxon of stem gnathostomes (4, 5). Preservation occurred through bacterially mediated authigenic mineralization under conditions of photic zone euxinia [(6) and supplementary text]. The discovery that this process also preserved internal organs in arthrodires reveals a virtually unknown aspect of vertebrate evolution. Early gnathostome internal organs are unknown outside of digestive tract infills (7–9) and blood vessel impressions in the antiarch placoderm *Bothriolepis* (8–10). Using propagation phase contrast synchrotron x-ray microtomography (PPC-SRμCT) and neutron tomography, arthrodire organs can be visualized in three dimensions and distinguished from bones and mineral matrix (Fig. 1, A to E, and fig. S1). Internal viscera are preserved in approximate life position, although they have undergone postmortem shrinkage (figs. S2 and S3 and supplementary text). All organs have been recovered from multiple specimens (supplementary materials), but no single specimen shows a full complement, which is consistent with decay experiments (11).

An asymmetrical structure comprising a small dorsal chamber, a larger ventral pyramid-shaped chamber, and an anterior tube-like extension lies at the back of the pharyngeal cavity in a ventral midline position (Fig. 1 and movie S1). It is not a cavity infilling because empty space borders the external surfaces (Fig. 1, A to D). It is interpreted as a heart because of its orthotopic position, S-shaped configuration, two chambers, and an outflow tract. The anterior tubular structure is interpreted as the conus arteriosus, which is anterior to the ventricle with the atrium dorsolateral to the ventricle (Fig. 1, H to J, and fig. S4). Unlike in *Rhacolepis* (12), the sinus venosus or conal valves cannot be distinguished. There is no evidence of the cartilaginous or ossified pericardial capsule present in lampreys and osteostracans (13). Fanning out from the heart are a nexus of anteroposteriorly oriented, linear structures, rounded in cross section (movie S2), which are interpreted as the median ventral aorta with associated vessels (Fig. 1, F and G, and fig. S4, K and L).

Posterior to the body wall, occupying a ventral position and extending to the midpoint of the posterior ventrolateral plate, are two distally tapering lozenge-shaped structures (Fig. 2, A to C, and fig. S5). A broad anterior margin is preserved, evidently natural, and transverse to the long axis of the body. The bilobed nature of the structure, its size, and its ventral position in the anterior part of the abdomen indicate that this is the liver. The left lobe is approximately three-fourths the size of the right (Fig. 2C). The lobes were likely medially joined in life, as they are separated by a gap of less than 1 mm in WAM 95.1.1 (fig. S6A). The lobes of the liver from the Famennian shark *Ferromurum oukherbouchi* have been similarly separated postmortem (14).

A conicospiral tubular structure (Fig. 2, A, G, and H, and figs. S11 and S7, A to C) extends along the axis of the body to the level of the pelvic girdle. The spiral arrangement, extension through the abdominal region, and comparable morphology to the spiral intestine of *Bothriolepis* (7) confirms it as the spiral intestine. The posterior portion of the intestine widens, and isolated parts of the arthropod *Montecaris gogoensis* (15) have been identified within (fig. S8). The ventral position at the terminal end of the intestine, posterior to the posterior ventrolateral plates, and the presence of digested contents confirm that this is the rectum.

Anterior to the intestine, a rectangular sack-like structure lies slightly right of the midline resting directly on the liver (Fig. 2A). The ventral wall is ruptured, likely due to the gases from decomposition (Fig. 2I), but the thick anterodorsal wall and anterior margin are preserved (Fig. 2, I to L). Tomography reveals the walls of this structure to be smooth externally but rugose internally (Fig. 2, D and E). The rugose internal surface is exposed in the acid-prepared specimen WAM 95.1.1 (Fig. 2F). On the basis of its position dorsal to the liver, its rugose internal surface, and its smooth external surface, the structure is identified as the stomach. An identical structure has been recovered from a similar position within *Rhacolepis* sp. (16).

Lungs or a swim bladder are present in most extant osteichthyans but absent in all chondrichthyans (13). Chondrichthyans use a large oily liver as a buoyancy organ (supplementary text). This suggests that lungs are an osteichthyan autapomorphy, but the alleged presence of lungs in the antiarch placoderm *Bothriolepis* (7–9) has been used to argue that lungs are a jawed vertebrate innovation subsequently lost in chondrichthyans. Extant sarcopterygians (including tetrapods) and the lung-breathing actinopterygians (17) demonstrate that lungs, if present, should lie ventrolateral to the stomach. However, no remnants of lung-like structures can be observed in this region, although this might reflect poor preservation potential of lung tissue. The phylogenetic position of antiarchs in the gnathostome stem group is usually considered stemward to arthrodires (4) (Fig. 3 and figs. S9 and S10) but has also been proposed to be crownward (5). If lungs are indeed absent in arthrodires but present in antiarchs, this would be more consistent with the heterodox crownward position of antiarchs. However, the morphology of the supposed “lungs” in *Bothriolepis* (9) is incompatible with the functionally necessary presence of a narrow anterior trachea in the lungs of osteichthyans. The recognition of a postbranchial lamina in antiarchs [Yunnanolepididae (18)] and here in *Bothriolepis* (fig. S11 and supplementary text) supports

<sup>1</sup>School of Molecular and Life Sciences, Curtin University, Bentley, WA 6102, Australia. <sup>2</sup>Western Australian Museum, Welshpool, WA 6106, Australia. <sup>3</sup>College of Science and Engineering, Flinders University, Adelaide, SA 5001, Australia. <sup>4</sup>Museum Victoria, Melbourne, VIC 3001, Australia. <sup>5</sup>Department of Organismal Biology, Evolutionary Biology Center, Uppsala University, 75236 Uppsala, Sweden. <sup>6</sup>European Synchrotron Radiation Facility, 38000 Grenoble, France. <sup>7</sup>Australian Regenerative Medicine Institute and EMBL Australia, Monash University, Clayton, VIC 3800, Australia. <sup>8</sup>Australian Nuclear Science and Technology Organisation (ANSTO), Lucas Heights, NSW 2234, Australia. <sup>9</sup>Earth Sciences Section, South Australian Museum, Adelaide, SA 5000, Australia.

\*Corresponding author. Email: k.trinajstic@curtin.edu.au

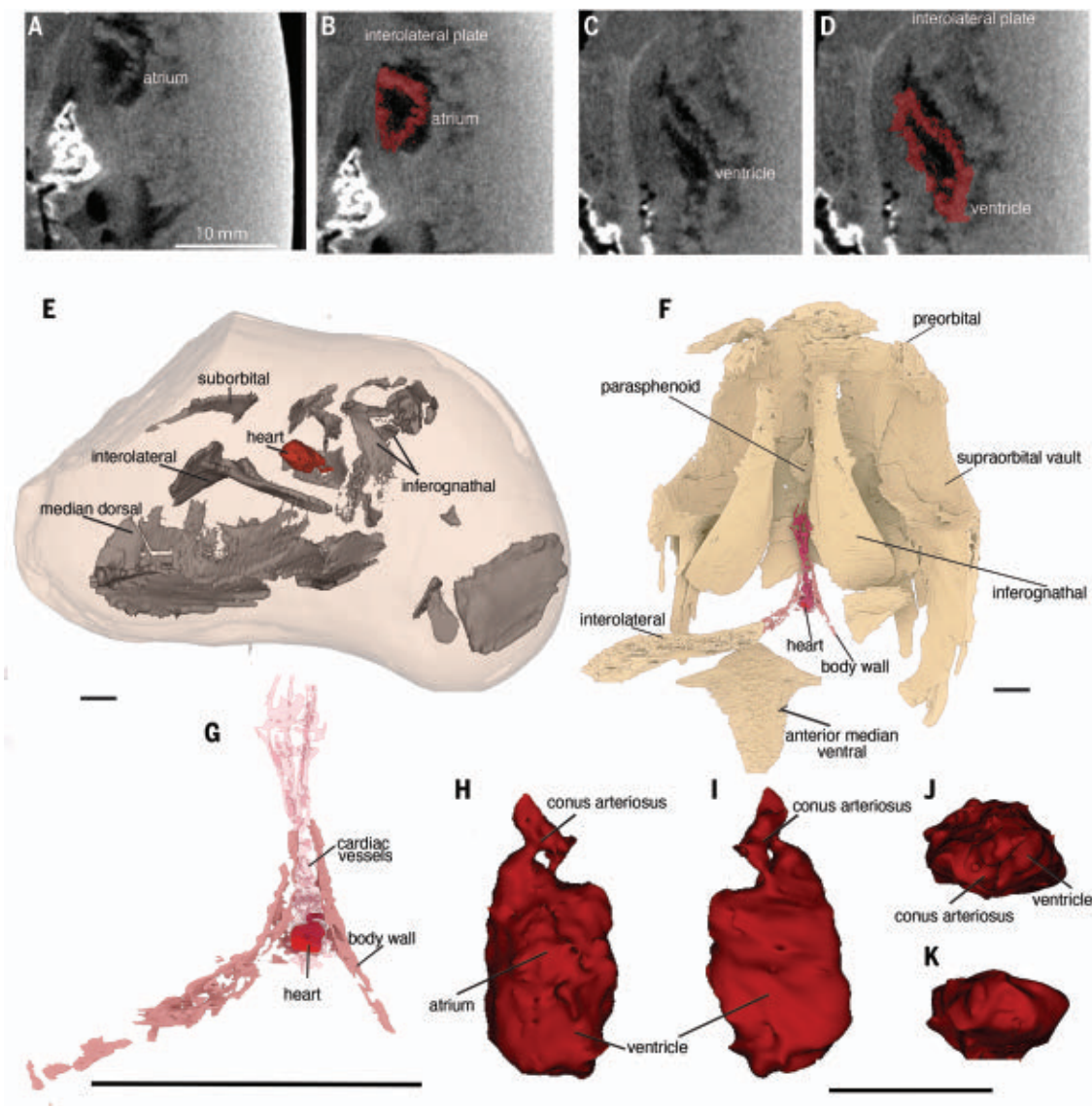


**Fig. 1. The morphology of the cardiac region in arthrodires.** (A to D) The heart modeled from NT $\mu$ CT WAM 2020.2.1, showing the atrium (A), atrium colored red (B), ventricle (C), and ventricle colored red (D). (E) Carbonate nodule showing the relationship of the heart to the dermal plates. (F and G) Pericardial region modeled from PPC-SR $\mu$ CT MV

P230859 with the dermal plates modeled (F) and showing the heart and cardiac vessels only (G). (H to K) The heart showing detail of the conus arteriosus, atrium, and ventricle modeled from NT $\mu$ CT of WAM 2020.2.1 in dorsal (H), ventral (I), anterior (J), and posterior (K) view. Scale bars, 1 cm.

the notion that the paired bilobed organ in *Bothriolepis* occupied the identical position to the liver in arthrodires (Fig. 3). Therefore, we conclude that this structure is the liver, and that both antiarchs and arthrodires lack evidence of lungs. This implies a single origin of lungs, above both these stem taxa, and potentially as late as in the Osteichthyes (Fig. 3).

Our fossil data also provide evidence for a dorsal shift of the heart atrium and the repositioning of the heart anterior to the caudal wall of the branchial chamber (Fig. 3 and sup-

plementary text). In jawless fishes, the atrium and ventricle are lateral to each other (19) and the heart is posterior to the branchial field (Fig. 3). In chondrichthyans and fish-like osteichthyans, the atrium is dorsal to the ventricle, the heart is level (anteroposteriorly) with the branchial chamber, the bones of the shoulder girdle are close to the branchial arches, and the hypobranchial and cucullaris muscles connect these bones to the skull, resulting in narrow neck (20). In antiarchs, the heart is posterior to the branchial lamina (Fig. 3) and the nuchal gap separating the

dorsal head and trunk armor is absent (fig. S11E), as is the cucullaris muscle (8, 20, 21). Arthrodires possess an anteriorly positioned heart underneath the branchial arches, nuchal gap, and cucullaris muscles (2) (Fig. 4). These traits show that arthrodires share the crown gnathostome morphology to the exclusion of antiarchs and thus support the conventional arrangement of a paraphyletic Placodermi with arthrodires more crownward than antiarchs (Fig. 3). Recent studies in extant gnathostomes have shown that the progenitor cells of the hypobranchial and

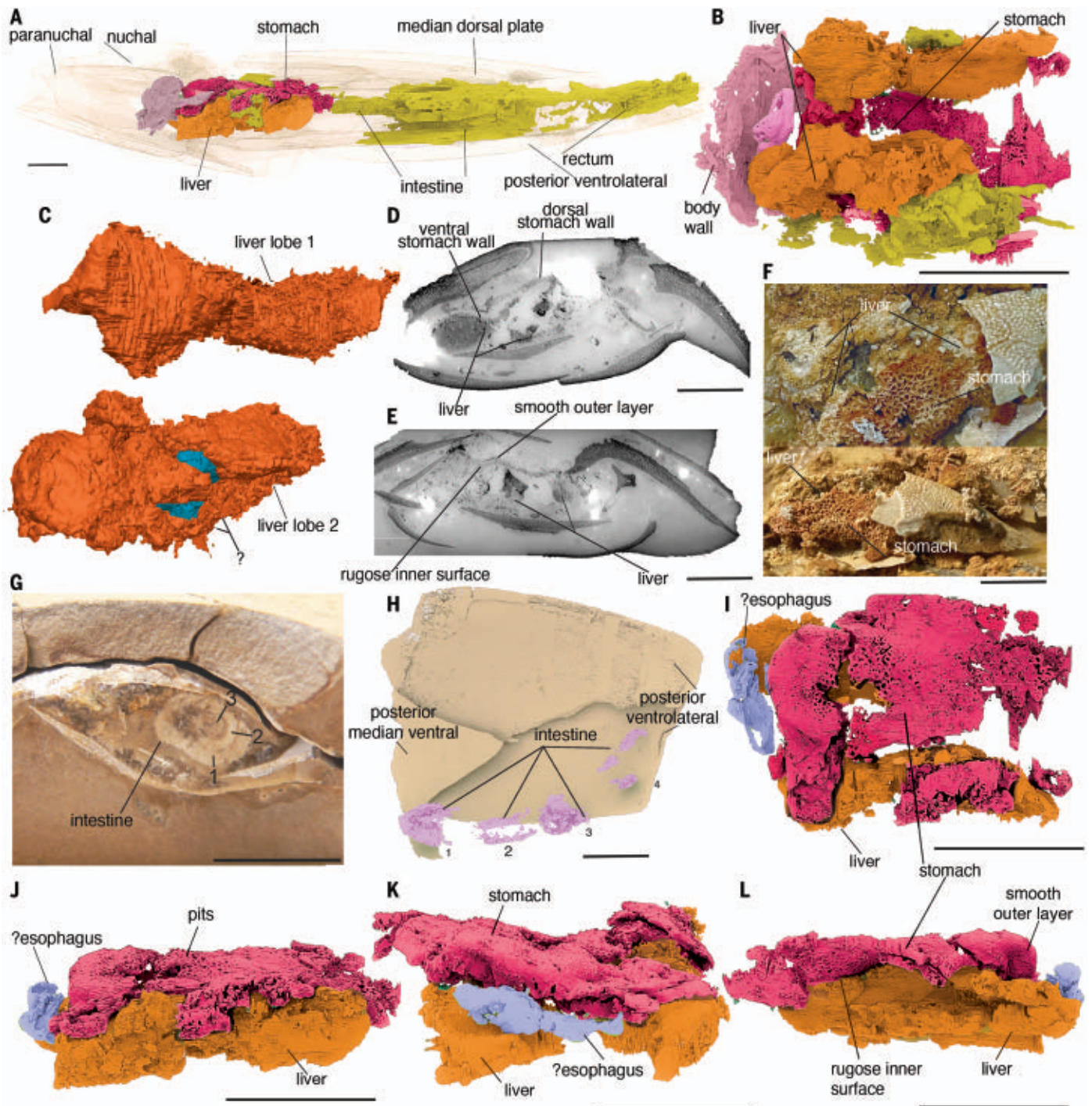


**Fig. 2. The abdominal viscera preserved in arthropods.** (A) The position of the abdominal organs in relation to the dermal plates modeled from PPC-SR $\mu$ CT MV P230859 (lateral view). (B) Three-dimensional model from MV P230859 showing the liver and stomach. (C) Liver in dorsal view. (D) Anterior tomographic slice of the liver and stomach (MV P230859). (E) Posterior tomographic slice. (F) Ventral

stomach wall and liver (WAM 95.1.1). (G) Spiral valves of the intestine (WAM 09.4.1), transverse view. (H) Dorsal view modeled from PPC-SR $\mu$ CT WAM 09.4.1. Numbers 1 to 4 indicate the layers of the spiral valve from outer (1) to inner (4). (I to L) Morphology of the liver and stomach modeled from PPC-SR $\mu$ CT MV P230859 in dorsal (I), lateral (J), anterior (K), and ventrolateral (L) view. Scale bars, 1 cm.

cuticularis muscles are shared by the cardiac muscle (22) and that the shifting of the head-trunk interface and elongation of the neck is driven by gain of function of the newly duplicated *Tbx5* gene [(23) and sup-

plementary text]. Our fossil data support the hypothesis that the anterior repositioning of the heart and development of the neck are not restricted to crown gnathostomes but were both present in the lineage leading to

arthropods and crown gnathostomes. Notably, they are absent in antiarchs.

Together with the previously described musculature (J), the three-dimensionally preserved organs make the Gogo arthropods the most

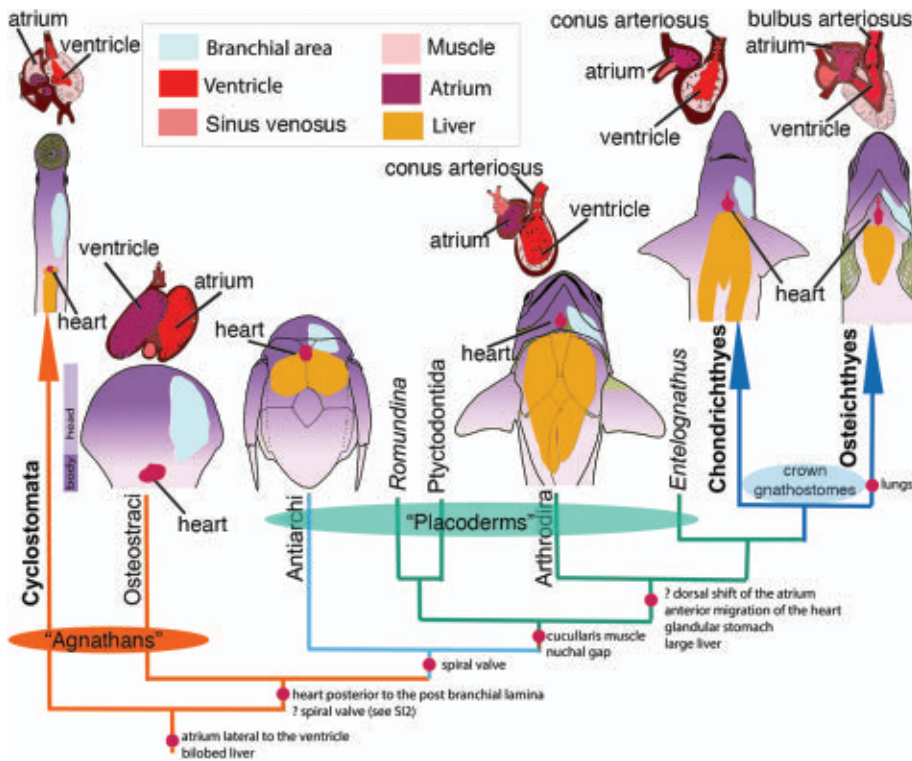


**Fig. 3. A phylogenetic framework of the lower vertebrates.** The proposed sequence of evolution for organs preserved within arthrodirans is indicated [simplified from fig. S14 and adapted from figure 1 of (1)].

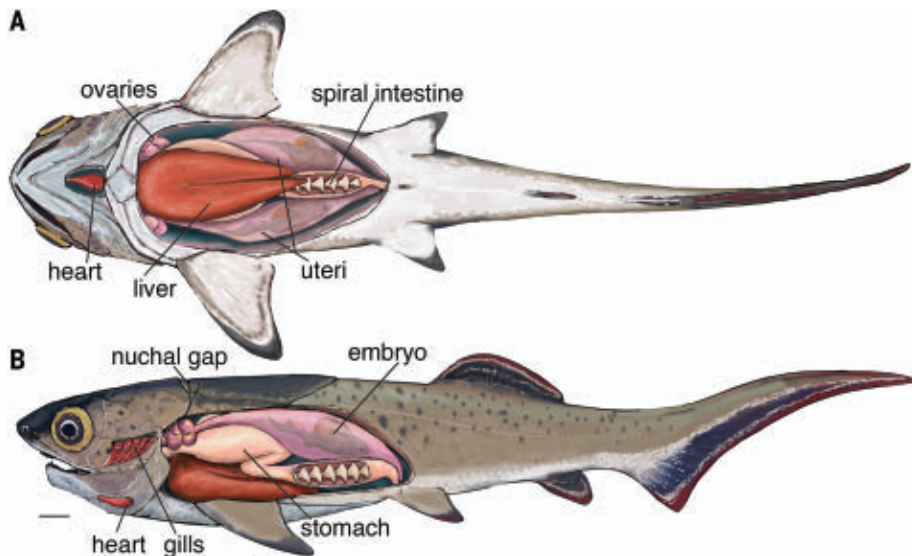


**Fig. 4. Reconstruction of arthrodiran internal anatomy.** (A) Lateral view; (B) ventral view. The reconstruction is based on preserved organs recovered from WAM 2020.2.1 and MV P230859 and embryos recovered from P50934. Scale bar, 1 cm.

fully understood of all jawed stem gnathostomes, help to resolve conflicting phylogenies for early fish, and can validate evolutionary transition hypotheses generated by extant developmental models (20, 22, 23). They provide a unique window on jawed vertebrate evolution just before the origin of the crown

group and the assembly of the gnathostome body plan.

**REFERENCES AND NOTES**

1. K. Trinajstić *et al.*, *Science* **341**, 160–164 (2013).
2. K. Trinajstić, C. Marshall, J. Long, K. Bifield, *Biol. Lett.* **3**, 197–200 (2007).

3. J. A. Long, K. Trinajstić, *Annu. Rev. Earth Planet. Sci.* **38**, 255–279 (2010).
4. B. King, T. Qiao, M. S. Y. Lee, M. Zhu, J. A. Long, *Syst. Biol.* **66**, 499–516 (2017).
5. Y. A. Zhu *et al.*, *Curr. Biol.* **31**, 1112–1118.e4 (2021).
6. I. Melendez *et al.*, *Geology* **41**, 123–126 (2013).
7. R. H. Denison, *J. Paleontol.* **15**, 553–561 (1941).
8. M. Arsenaault, S. Desbiens, P. Janvier, J. Kerr, in *Recent Advances in the Origin and Early Radiation of Vertebrates*, G. Arratia, M. V. H. Wilson, R. Cloutier, Eds. (Pfeil, Munich, 2004), pp. 439–445.
9. P. Janvier, S. Desbiens, J. A. Willett, *J. Vertebr. Paleontol.* **27**, 709–710 (2007).
10. D. Goujet, *C. R. Palevol* **10**, 323–329 (2011).
11. S. E. Gabbott, R. S. Sansom, M. A. Purnell, *Palaeontology* **64**, 789–803 (2021).
12. L. Maldanis *et al.*, *eLife* **5**, e14698 (2016).
13. P. Janvier, *Early Vertebrates* (Oxford Univ. Press, 1996).
14. L. Frey, M. I. Coates, K. Tietjen, M. Rücklin, C. Klug, *Commun. Biol.* **3**, 681 (2020).
15. D. E. G. Briggs, W. I. Rolfe, P. D. Butler, J. J. Liston, J. K. Ingham, *J. Syst. Palaeontology* **9**, 399–424 (2011).
16. P. R. Wilby, D. M. Martill, *Hist. Biol.* **6**, 25–36 (1992).
17. N. Tatsumi *et al.*, *Sci. Rep.* **6**, 30580 (2016).
18. Y. Wang, M. Zhu, *PeerJ* **6**, e4808 (2018).
19. P. Janvier, L. R. Percy, I. C. Potter, *J. Zool.* **223**, 567–576 (1991).
20. N. Adachi, J. Pascual-Anaya, T. Hirai, S. Higuchi, S. Kuratani, *Zool. Lett.* **4**, 1–3 (2018).
21. R. Ericsson, R. Knight, Z. Johanson, *J. Anat.* **222**, 67–78 (2013).
22. E. Heude *et al.*, *eLife* **7**, e40179 (2018).
23. H. Higashiyama *et al.*, *J. Morphol.* **277**, 1146–1158 (2016).

**ACKNOWLEDGMENTS**

We acknowledge the Goonyandi people, the traditional owners on whose land the fossils were collected. We thank the Western Australian Museum and Museum of Victoria for assistance with curation and access to collections. **Funding:** Supported by Australian Research Council grants DP1092870 and ARC-DP140104161 (J.A.L., K.T.), DP1096002 (C.A.B., P.D.C.), ARC-DP110101127 (K.T.), and ARC-DP200103219 (P.D.C., K.T.); European Research Council Advanced Investigator grant 233111 (P.E.A., V.D., S.S.); the Knut and Alice Wallenberg Foundation (P.E.A.); European Synchrotron proposal EC-203 (P.E.A., S.S., K.T.); and Australian Neutron proposal P5203 (A.M.C., J.A.L., K.T.). **Author contributions:** Conceptualization: K.T., J.A.L., P.E.A. Methodology: All authors. Investigation: K.T., J.A.L., S.S., V.D., P.D.C., P.E.A. Visualization: S.S., C.A.B., P.T., D.S., V.D., A.M.C., J.J.B. Funding acquisition: K.T., J.A.L., S.S., A.M.C., P.D.C., P.E.A. Project administration: K.T., C.A.B. Writing: All authors. **Competing interests:** The authors declare no competing interests. **Data and materials availability:** All fossils are accessioned in public collections and, upon curator approval, are available for study by qualified researchers. All (other) data needed to evaluate the conclusions of the paper are presented in the paper or the supplementary materials. Raw CT scans of fossils scanned at ESRF are deposited in the ESRF database (<http://paleo.esrf.eu/>). Neutron scan data is available in the paleontological microtomographic database MorphoSource at [www.morphosource.org/concern/media/000381874?locale=en](http://www.morphosource.org/concern/media/000381874?locale=en). **License information:** Copyright © 2022 the authors, some rights reserved; exclusive licensee American Association for the Advancement of Science. No claim to original US government works. [www.science.org/about/science-licenses-journal-article-reuse](http://www.science.org/about/science-licenses-journal-article-reuse)

**SUPPLEMENTARY MATERIALS**

[science.org/doi/10.1126/science.abf3289](http://science.org/doi/10.1126/science.abf3289)  
 Provenance Statement  
 Materials and Methods  
 Supplementary Text  
 Figs. S1 to S14  
 References (24–64)  
 Movies S1 and S2  
 Data S1 to S4

Submitted 20 January 2021; resubmitted 9 January 2022  
 Accepted 16 August 2022  
[10.1126/science.abf3289](http://10.1126/science.abf3289)

## GROUNDWATER

# The Bengal Water Machine: Quantified freshwater capture in Bangladesh

Mohammad Shamsudduha<sup>1,2\*</sup>, Richard G. Taylor<sup>3</sup>, Md Izazul Haq<sup>3,4</sup>, Sara Nowreen<sup>5</sup>, Anwar Zahid<sup>6</sup>, Kazi Matin Uddin Ahmed<sup>7</sup>

Global food security depends on the sustainability of irrigated agriculture. Rising groundwater withdrawals from seasonally humid, alluvial plains across tropical Asia have enabled dry-season rice cultivation. This groundwater pumpage increases available subsurface storage that under favorable conditions amplifies groundwater replenishment during the subsequent monsoon. We empirically quantified this nature-based solution to seasonal freshwater storage capture described as the “Bengal Water Machine,” revealing its potential and limitations. On the basis of a million piezometric observations from 465 monitoring wells, we show that the collective operation of ~16 million smallholder farmers in the Bengal Basin of Bangladesh from 1988 to 2018 has induced cumulative freshwater capture that volumetrically (75 to 90 cubic kilometers) is equivalent to twice the reservoir capacity of the Three Gorges Dam.

The intensification of agricultural production enabled by irrigation over the past half century has contributed unquestionably to improved global food security (1). Over the past half century, global groundwater withdrawals for irrigation have risen substantially to ~950 km<sup>3</sup>/year in 2010 (2) owing in part to their resilience to climate variability and change (3).

Groundwater depletion has, however, been observed in association with intensively irrigated, large-scale farming in dryland areas such as the North China Plain, California Central Valley, and southern High Plains of the United States (4–6) and threatens global food security (7).

In the Indo-Gangetic Basin, groundwater depletion has recently been observed to arise from high pumping rates for irrigation but is largely restricted to semiarid regions of northern India and Pakistan (8).

Under Asia’s Green Revolution, use of shallow groundwater by smallholder farmers continues to occur from large alluvial aquifers within seasonally humid river basins such as the Ganges-Brahmaputra, Red River, and Mekong (9) so that Asian farmers now account for 90% of the world’s rice production (10). These river basins are characterized by strong seasonal imbalances in rainfall and river discharge associated with the Asian monsoon. In the Bengal Basin of Bangladesh (Fig. 1), for example, 80% of the annual discharge of the Rivers

Ganges, Brahmaputra, and Meghna occurs between July and October (11); wet-season (May to October) and dry-season (November to April) rainfall represents 90 and 10%, respectively, of the annual total rainfall (12).

Conventional approaches to the storage of seasonal river discharge use dams (13), yet the low-lying relief of densely populated alluvial plains challenges the implementation of such infrastructure. In 1975, Revelle and Lakshminarayana (14) proposed an alternative solution to freshwater storage in the River Ganges Basin in which incremental increases

in dry-season groundwater pumpage for irrigation near river channels lower groundwater levels and enhance leakage under gravity of river flow during the subsequent monsoon. Dubbed the “Ganges Water Machine,” this intervention seeks to increase the capture and storage of seasonal freshwater surpluses while mitigating the monsoonal flood risk. We extended the concept of freshwater capture of monsoonal flows beyond perennial rivers to include a range of surface waters (such as ponds, canals, and seasonal rivers), diffuse recharge through enhanced local drainage, and irrigation return flows (supplementary text, section S3) in the Bengal Basin. We describe this broader set of recharge pathways induced by dry-season groundwater pumping as the “Bengal Water Machine” (BWM). Evidence of its operation in the Bengal Basin of Bangladesh has been noted previously where amplification of seasonal groundwater recharge occurs as a consequence of dry-season groundwater-fed irrigation for rice cultivation (15, 16).

We quantified the magnitude of freshwater captured (in excess to predevelopment recharge) by the BWM from 1988 to 2018 through the collective operation of ~16 million smallholder farmers pumping shallow (well depth <100 m below ground level) groundwater for dry-season irrigation in the Bengal Basin of Bangladesh. This empirical analysis used a million weekly piezometric observations from 465 monitoring sites with time series that ranged from 24 to 54 years (median = 43 years) in duration.

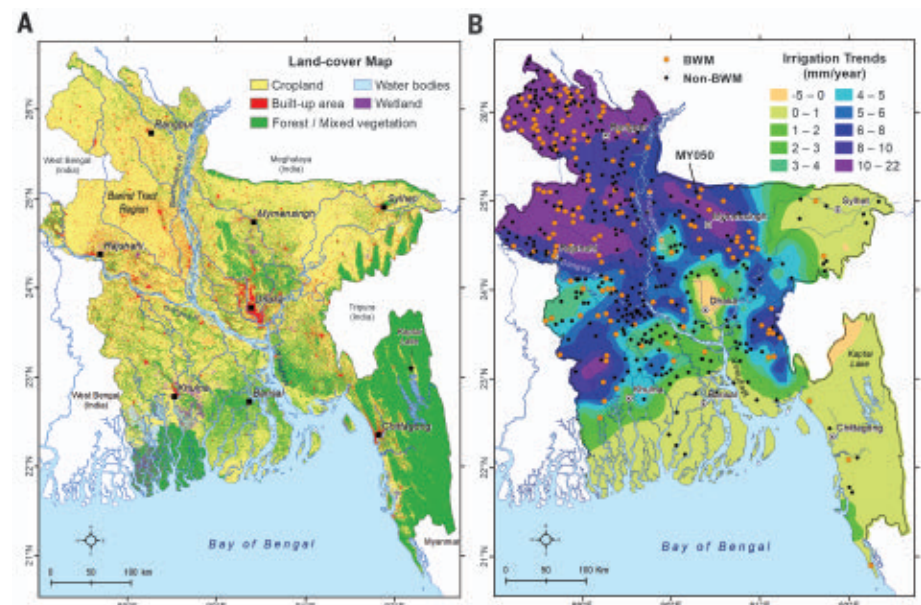


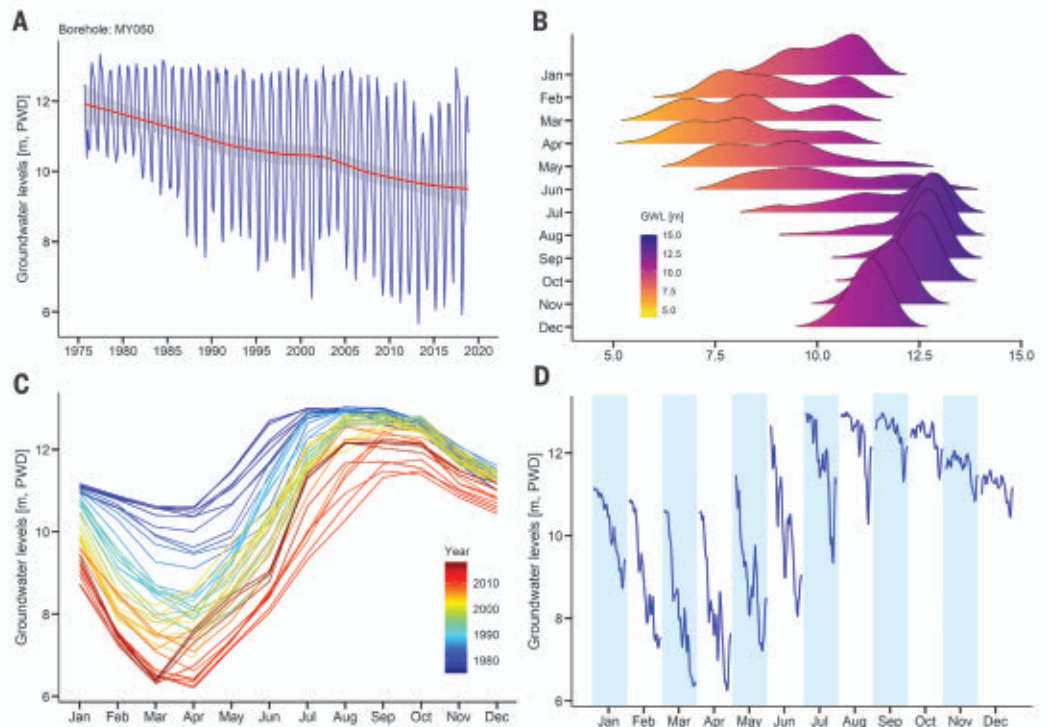
**Fig. 1. Maps of land-cover and groundwater-fed irrigation trends in Bangladesh.** (A) High-resolution (100 m) land-cover map from global land classification datasets, published by Copernicus Global Land Service (27). Highlighted is the Barind Tract region in the northwest of Bangladesh, where groundwater irrigation dominates. (B) Mapped trends (1985 to 2019) in groundwater-fed irrigation for dry-season crop cultivation in Bangladesh (supplementary text, section S1.2) and locations of 465 boreholes plotted in orange (BWM) and black (non-BWM) solid circles.

<sup>1</sup>Institute for Risk and Disaster Reduction, University College London, London, UK. <sup>2</sup>Department of Geography, University of Sussex, Brighton, UK. <sup>3</sup>Department of Geography, University College London, London, UK. <sup>4</sup>Department of Disaster Science and Climate Resilience, University of Dhaka, Dhaka, Bangladesh. <sup>5</sup>Institute of Water and Flood Management, Bangladesh University of Engineering and Technology, Dhaka, Bangladesh. <sup>6</sup>Ground Water Hydrology Circle, Bangladesh Water Development Board, Dhaka, Bangladesh. <sup>7</sup>Department of Geology, University of Dhaka, Dhaka, Bangladesh.

\*Corresponding author. Email: m.shamsudduha@ucl.ac.uk

**Fig. 2. Observed groundwater levels at borehole MY050 in north central Bangladesh.** MY050 location is shown in Fig. 1B.

(A) Monthly groundwater levels relative to the Public Works Datum (PWD) from September 1975 to November 2018, with a nonlinear trend line (red) as Loess smooth fit and uncertainty envelop (gray shading) around the trend line. (B) Probability density function showing variability in groundwater levels for each month from January to December. The x axis indicates groundwater levels. (C) Line plot showing monthly groundwater levels observed in each year. (D) Observations of groundwater levels in each month of the year from 1975 to 2018 (for example, groundwater levels in January from 1975 to 2018).



Previous estimations of freshwater capture in the River Ganges Basin have been hypothetical and based on modeled scenarios (17, 18). Furthermore, our empirical analysis allowed us to report where and when the BWM has operated, which reveals both the potential and limitations of this strategy of freshwater capture.

Bangladesh occupies nearly three-quarters of the Bengal Basin (Fig. 1A) and is dominated (~50%) by cropland cover, of which 80% is irrigated with groundwater (15). Dry-season groundwater-fed irrigation of Boro rice (19) has transformed much of Bangladesh's single-crop rain-fed floodplains into highly productive double-cropping and, in places, triple-cropping lands, which makes it the world's fourth-highest producer of rice (10). This transformation in groundwater use accelerated in the mid-1990s after droughts in 1992 and 1994 (fig. S1). Groundwater withdrawals for irrigation are highest in the Barind area in the northwest (Fig. 1B), which is known as the "bread basket" of Bangladesh (20).

Quantification of freshwater capture by the BWM (additions to groundwater storage) derives from long-term, in situ observations of groundwater levels. We selected 465 multidecadal piezometric records (Fig. 1B and supplementary text, section S1) from a dense network of nearly 1250 monitoring stations (21) on the basis of their duration and continuity. The method for quantifying the BWM involved the following steps (supplementary text, section S2): (i) identification through cluster

analysis and visual inspection of groundwater-level time series exhibiting BWM, which is characterized unambiguously by an increasing amplitude in seasonal oscillations over time (Fig. 2); (ii) calculation of annual net recharge by using the water-table fluctuation method (15), which is based on the annual amplitude (difference between 5th and 95th percentile values) of groundwater-level change; (iii) subtraction of mean annual recharge for the baseline ( $j$ th year) during the predevelopment period ( $R_{\text{predev}}$ ), which is identified objectively as the period of consistent seasonal oscillations before the induction of groundwater recharge by pumping, from computed net recharge over the BWM period ( $R_{\text{netBWM}}$ ); (iv) sum of annual ( $i$ th year) recharge induced by pumping for each groundwater-level time-series records exhibiting BWM ( $R_{\text{BWM}}$ ) (Eq. 1); and (v) computation and mapping of cumulative groundwater storage captured by BWM from the product of  $R_{\text{BWM}}$  and the interpolated grid-cell area.

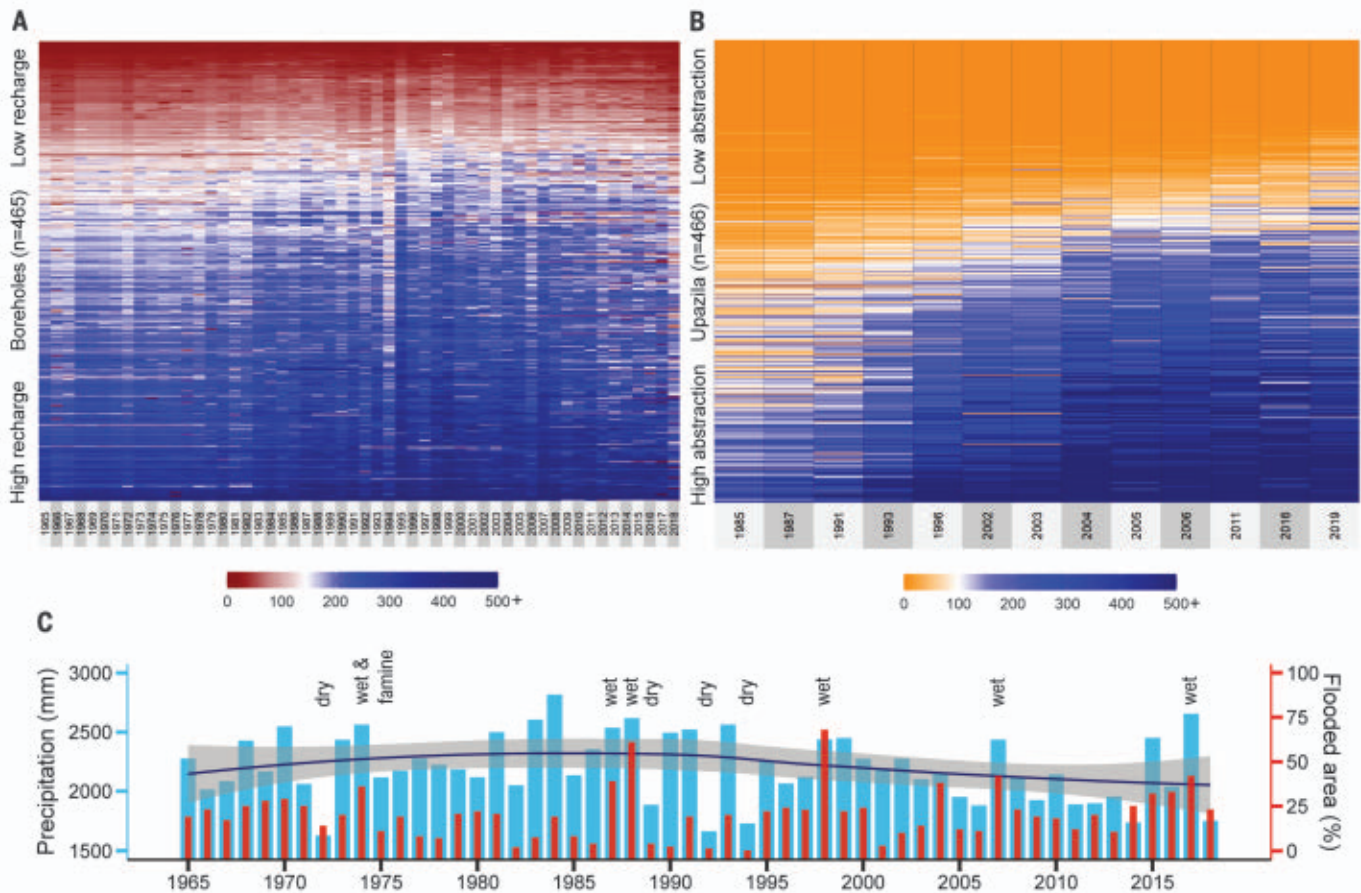
$$R_{\text{BWM}} = \sum_{i=(1,2,\dots,n)}^n \left[ R_{\text{netBWM}}^i - \frac{1}{m = \sum (1, 2, \dots, j)} R_{\text{predev}}^j \right] \quad (1)$$

Figure 2 depicts the impact of the operation of the BWM in piezometric records at a site in the Old Brahmaputra floodplains of north-central Bangladesh (Fig. 1B). A rising amplitude in seasonal oscillations of groundwater levels starting in the early 1980s reflects not only the

consequences of steady increases in shallow groundwater withdrawals for irrigation but also induced recharge associated with the BWM (Fig. 2A). The groundwater level at the end of the dry season in April is relatively constant (mean = 10.5 m) before the onset of groundwater-fed irrigation (1976 to 1981) but then decreases incrementally by >4 m to the period of 2013 to 2018. Variability in monthly groundwater levels is amplified most, especially toward the end of the dry season (February to May) with the continued irrigation of Boro rice (Fig. 2B). Incremental decreases in groundwater levels and their intra-annual recovery through induced recharge are amplified over the time series (Fig. 2C). Furthermore, there is evidence of a recent (after 2010) shift to an earlier start from April to March in the recharge period (Fig. 2C) that is also indicated by positive deflections over the observation period (1975 to 2018) for individual months (Fig. 2D).

Across the Bengal Basin of Bangladesh, groundwater-level dynamics reflecting the BWM are observed at 153 sites (fig. S2), which amount to approximately one-third of the 465 analyzed piezometric records (Fig. 1B). These sites are primarily located in northwestern, north-central, and southwestern Bangladesh, where increasing trends (1985 to 2019) in groundwater-fed irrigation are highest. By contrast, very few BWM sites are identified in southeastern and northeastern (such as Sylhet) regions of Bangladesh, where rising trends in irrigation are lowest in areas outside of the alluvial plain, and coastal regions, where





**Fig. 3. Comparison of estimated groundwater recharge and abstraction for irrigation across Bangladesh.** (A) Heatmap showing estimated recharge at 465 boreholes in Bangladesh (1965 to 2017). Missing recharge values for boreholes were infilled by using the random forest algorithm only for visualization purposes. (B) Heatmap showing estimated abstraction at 466 Upazilas (subdistrict) from

irrigation surveys at available years between 1985 and 2019. (C) Bar plots of (blue) annual rainfall in Bangladesh from 1965 to 2018 (mean = 2211 mm) from Climatic Research Unit (CRU TS4.05) dataset and (red) flooded area in Bangladesh. Exceptional dry or wet conditions are noted; the blue line denotes local regression using Loess, and gray shading delimits the 95% confidence interval of fitted nonlinear trends.

the salinity of shallow groundwater restricts its use. Within areas of intensive irrigation, piezometric records that do not reflect the BWM can occur in close proximity to BWM sites. This observation points to other factors that control the operation of the BWM, including principally surface geology (fig. S3), which enables or inhibits transmission of induced recharge (supplementary text, section S3) (15, 22, 23). Furthermore, proximity to surface drainage (fig. S4) of monsoonal floodwaters (such as rivers, ponds, canals, and oxbow lakes) can enhance the magnitude of recharge through induced surface water (fig. S5) leakage (16, 23).

Annual groundwater recharge computed from piezometric records at 465 sites throughout the Bengal Basin of Bangladesh shows a generalized increase from 1965 to 2017 (Fig. 3A), notably between the predevelopment (mean period 1976 to 1980) and recent (mean period 2011 to 2015) recharge (fig. S6). This rise in recharge corresponds to increasing volumes of abstracted groundwater for irrigation re-

corded over available years between 1985 and 2019 (Fig. 3B). Use of shallow groundwater for irrigation began in 1975 to 1976 in Bangladesh and rose steadily to a peak of nearly 1.5 million shallow wells (fig. S1) recorded between 2011 and 2015 (24). In the two most recent years for which records are available (2017 to 2019), a ~10% decline in shallow wells used for irrigation has been recorded and attributed to groundwater depletion (25) where freshwater withdrawals exceed seasonal capture through BWM. Furthermore, a reduction in the availability of piezometric time series in the database continuing to 2017 ( $n = 430$  time series) and 2018 ( $n = 374$ ) may also explain the reduction in annual recharge computed in 2018 (Fig. 3A). The influence of interannual variability in rainfall and flooded land area in the Bengal Basin (Fig. 3C) on annual groundwater recharge (Fig. 3A) is visible in both comparatively dry years (such as 1972, 1992, and 1994) and distinctly wet years (such as 1984, 1988, 1991, 1993, 1998, 1999, and 2007).

The large increase in groundwater recharge, which is most pronounced in relatively dry northwestern region of Bangladesh (fig. S6) since the mid-1990s, occurred over a period when the overall trend in annual rainfall was marginally in decline.

Groundwater recharge induced by the BWM (Eq. 1,  $R_{\text{netBWM}}$ ) represents contributions to freshwater capture enabled by irrigation abstraction by smallholder farmers. Geospatial maps (Fig. 4, A and B) show that freshwater capture and the likelihood of occurrence (fig. S7) through the BWM have taken place primarily in northwestern and north central areas of the Bengal Basin in Bangladesh, where increasing trends in (Fig. 1B) and magnitudes of (fig. S8) groundwater-fed irrigation are highest. Variations in computed freshwater capture presented in Fig. 4, A and B, depict uncertainty in this computation as a function of differences in applied geostatistical methods and representations of aquifer storage coefficients (supplementary text, section S2.2, and

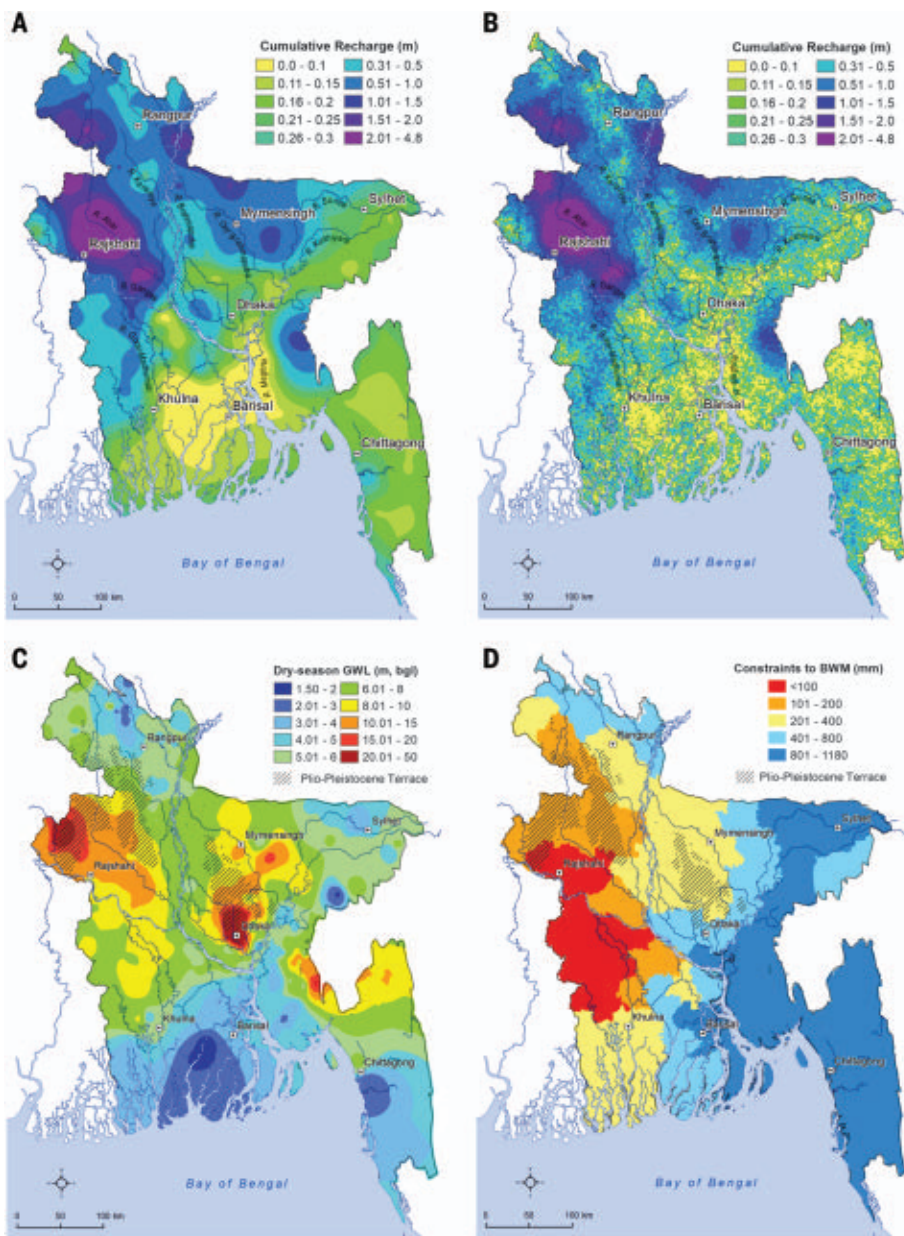


**Fig. 4. Uncertainty in the estimation of freshwater capture from 1988 to 2018 through the BWM and identified constraints to BWM operation.** (A and B) Cumulative induced recharge (meters) mapped at the national scale by using (A) ordinary kriging interpolation and (B) conditional sequential Gaussian simulation methods. (C) Depth to dry-season groundwater levels [meters below ground level (bgl)] in 2015. (D) Difference between potential (23) and long-term (1985 to 2015) mean groundwater recharge.

table S3). Notwithstanding these uncertainties, areas along the River Atrai north of Rajshahi, for example, consistently have the highest computed freshwater capture despite having the lowest mean rainfall (<1500 mm) (fig. S9) in Bangladesh. Total freshwater capture computed across the Bengal Basin of Bangladesh from 1988 to 2018 ranges from 75 to 90 km<sup>3</sup> of water (Fig. 4, A and B, and supplementary text, section S2.3), a volume that amounts to approximately twice the reservoir capacity of large dams such as the Three Gorges Dam

(~39 km<sup>3</sup>) in China and Hoover Dam (~37 km<sup>3</sup>) in the United States (26).

Important limitations to the operation of the BWM are evident from compiled hydrographs (for example, figs. S10 to S12), which reveal locations where induced monsoonal recharge is insufficient to fully replenish groundwater abstracted during the dry season. For example, areas with a surface geology of low permeability (fig. S3) restrict the BWM and coincide with dry-season groundwater levels >8 m below ground (Fig. 4C) that render groundwater inac-

cessible to households reliant on shallow wells. Furthermore, the Barind region and Ganges floodplain in western Bangladesh (Fig. 4D), where observed groundwater recharge approaches or exceeds potential recharge—the latter governed by rainfall, surface geology, and flood extent (23)—are most at risk of realizing the limits of increased freshwater capture through the BWM. Consequently, opportunities to expand operation of the BWM in Bangladesh are now largely restricted to the River Brahmaputra floodplains (Fig. 4, C and D). Induced groundwater recharge is shown from basin-scale statistical analyses (22) to flush mobile arsenic from shallow groundwater.

Our analysis shows how the collective action of millions of smallholder farmers abstracting shallow groundwater to irrigate a dry-season rice crop in a tropical alluvial plain has achieved freshwater capture that rivals the world's largest dams. In doing so, we confirm the vision of this nature-based solution to seasonal freshwater capture, following a broader set of pathways than first proposed in *Science* in 1975 (14), while noting its limitations. Because alluvial plains in the seasonally humid tropics cover an area of nearly 4 million km<sup>2</sup> (fig. S13), there is scope to scale up operation of the BWM to improve the sustainability of irrigated food production globally. Evidence from the Bengal Basin, the most intensely monitored alluvial plain in the world, highlights the pivotal role played by surface geology (fig. S3) in enabling the transmission of induced recharge (15, 16, 22). Improved planning of irrigated agriculture that explicitly recognizes operation of the BWM in seasonally inundated alluvial plains can optimize freshwater capture and minimize groundwater depletion where this capture is insufficient to sustain groundwater-fed irrigation. Of strategic importance is the demonstrated resilience of this conjunctive use of groundwater and surface water to hydrological extremes that are amplified by climate change.

#### REFERENCES AND NOTES

1. L. Rosa, D. D. Chiarelli, M. C. Rulli, J. Dell'Angelo, P. D'Odorico, *Sci. Adv.* **6**, eaaz6031 (2020).
2. Y. Wada, D. Wisser, M. F. P. Bierkens, *Earth Syst. Dyn.* **5**, 15–40 (2014).
3. R. G. Taylor et al., *Nat. Clim. Chang.* **3**, 322–329 (2013).
4. M. Rodell et al., *Nature* **557**, 651–659 (2018).
5. B. R. Scanlon et al., *Proc. Natl. Acad. Sci. U.S.A.* **109**, 9320–9325 (2012).
6. W. Feng et al., *Water Resour. Res.* **49**, 2110–2118 (2013).
7. C. Dalin, Y. Wada, T. Kastner, M. J. Puma, *Nature* **543**, 700–704 (2017).
8. A. M. MacDonald et al., *Nat. Geosci.* **9**, 762–766 (2016).
9. P. Schneider, F. Asch, *J. Agron. Crop Sci.* **206**, 491–503 (2020).
10. N. Bandumula, *Proc. Natl. Acad. Sci., India, Sect. B Biol. Sci.* **88**, 1323–1328 (2017).
11. G. Rasul, *Int. J. River Basin Manage.* **13**, 387–400 (2015).
12. S. J. Ahammed, E.-S. Chung, S. Shahid, *Sustainability (Basel)* **10**, 819 (2018).
13. D. Grey, C. W. Sadoff, *Water Policy* **9**, 545–571 (2007).

14. R. Revelle, V. Lakshminarayana, *Science* **188**, 611–616 (1975).
15. M. Shamsudduha, R. G. Taylor, K. M. Ahmed, A. Zahid, *Hydrogeol. J.* **19**, 901–916 (2011).
16. S. Nowreen *et al.*, *Hydrogeol. J.* **28**, 2917–2932 (2020).
17. M. R. Khan, C. I. Voss, W. Yu, H. A. Michael, *Water Resour. Manage.* **28**, 1235–1250 (2014).
18. U. A. Amarasinghe, L. Muthuwatta, L. Surinaidu, S. Anand, S. K. Jain, *Hydro. Earth Syst. Sci.* **20**, 1085–1101 (2016).
19. Boro is the dry-season irrigated rice crop planted from December to early February and harvested between April and June. In 2018 to 2019, Boro rice accounted for 54% of the total production of rice in Bangladesh.
20. K. Alam, *Agric. Water Manage.* **148**, 196–206 (2015).
21. M. Shamsudduha, R. E. Chandler, R. G. Taylor, K. M. Ahmed, *Hydro. Earth Syst. Sci.* **13**, 2373–2385 (2009).
22. M. Shamsudduha, R. G. Taylor, R. E. Chandler, *Water Resour. Res.* **51**, 685–703 (2015).
23. British Geological Survey (BGS) and Bangladesh Department of Public Health Engineering (DPHE), “Arsenic contamination of groundwater in Bangladesh,” D. G. Kinneburgh, P. L. Smedley, Eds. (British Geological Survey Technical Report WC/00/19, Keyworth, 2001).
24. Bangladesh Agricultural Development Corporation (BADC), “Survey report on irrigation equipment and irrigated area for the 2018-19 Boro rice season” (BADC, 2020).
25. K. M. Ahmed, in *Global Groundwater*, A. Mukherjee, B. R. Scanlon, A. Aureli, S. Langan, H. Guo, A. A. McKenzie, Eds. (Elsevier, 2021), pp. 425–438.
26. Estimated reservoir capacities derive from the UN Food and Agricultural Organization geo-referenced database on dams: <https://www.fao.org/aquastat/en/databases/dams>.
27. M. Buchhorn *et al.*, *Remote Sens.* **12**, 1044 (2020).

#### ACKNOWLEDGMENTS

We thank the Bangladesh Water Development Board (BWDB) and the Bangladesh Agricultural Development Corporation (BADC) for providing groundwater-level and irrigation datasets, respectively. We thank P. Ravenscroft and M. M. Rahman for providing a subset of irrigation data. **Funding:** R.G.T. and M.S. acknowledge support from DFID (UK government) under grant GA/11F/099/S2, “Groundwater resources in the Indo-Gangetic Basin: Resilience to climate change and pumping.” S.N., M.I.H., and R.G.T. acknowledge support of a Commonwealth Split-Site Scholarship (BDCN-2014-4), Commonwealth Scholarship (BDCS-2017-60), and The Royal Society–Leverhulme Trust Senior Fellowship (ref. LT170004), respectively. **Author contributions:** M.S. and R.G.T. conceived and designed the work. M.I.H. collated the groundwater-level monitoring data; M.S. quality-controlled, processed, and analyzed groundwater-level and irrigation abstraction data and produced all the figures. R.G.T. and M.S. wrote the manuscript, with inputs from S.N., A.Z., M.I.H., and K.M.U.A.; M.S. and R.G.T. wrote the supplementary materials. **Competing interests:** The authors declare no competing interests. **Data and materials availability:** We secured groundwater-level monitoring data from the BWDB and dry-season irrigation well information from the BADC; the latter was used to estimate groundwater abstraction. Original weekly monitored groundwater-level time-series data can be obtained from the BWDB (<http://www.hydrology.bwdb.gov.bd/index.php>) by making an “online data request” and payment. Processed monthly time-series data used in this paper along with codes written in R programming language can be made available upon request to the corresponding author for the purpose of reproducing or extending the analysis and creating visual illustrations. BWDB piezometric location coordinates and site-specific information as well as estimates of groundwater storage are provided in the supplementary materials. Groundwater-fed irrigation data that were estimated in this study by using dry-season well information from annual reports published by the BADC are also available in the supplementary materials. **License information:** Copyright © 2022 the authors, some rights reserved; exclusive licensee American Association for the Advancement of Science. No claim to original US government works. <https://www.science.org/about/science-licenses-journal-article-reuse>

#### SUPPLEMENTARY MATERIALS

[science.org/doi/10.1126/science.abm4730](https://science.org/doi/10.1126/science.abm4730)  
Materials and Methods  
Supplementary Text  
Figs. S1 to S23  
Tables S1 to S4  
References (28–60)

Submitted 20 September 2021; accepted 20 July 2022  
10.1126/science.abm4730

## QUANTUM SIMULATION

# Direct geometric probe of singularities in band structure

Charles D. Brown<sup>1,2,4\*</sup>, Shao-Wen Chang<sup>1,2</sup>, Malte N. Schwarz<sup>1,2</sup>, Tsz-Him Leung<sup>1,2</sup>, Vladyslav Kozii<sup>1,3,5</sup>, Alexander Avdoshkin<sup>1</sup>, Joel E. Moore<sup>1,3</sup>, Dan Stamper-Kurn<sup>1,2,3\*</sup>

A quantum system’s energy landscape may have points where multiple energy surfaces are degenerate and that exhibit singular geometry of the wave function manifold, with major consequences for the system’s properties. Ultracold atoms in optical lattices have been used to indirectly characterize such points in the band structure. We measured the non-Abelian transformation produced by transport directly through the singularities. We accelerated atoms along a quasi-momentum trajectory that enters, turns, and then exits the singularities at linear and quadratic band-touching points of a honeycomb lattice. Measurements after transport identified the topological winding numbers of these singularities to be 1 and 2, respectively. Our work introduces a distinct method for probing singularities that enables the study of non-Dirac singularities in ultracold-atom quantum simulators.

Energy surfaces are used to describe the structure and dynamics of quantum systems whose Hamiltonians contain one or more continuous parameters. Notable examples include band structure, which describes the motion of single particles within a crystal as a function of their quasi-momentum, and the potential energy surfaces that describe molecules as a function of their nuclear coordinates. Each point on an energy surface corresponds to an eigenenergy and an eigenstate of the physical system. Although the energies themselves are highly important for explaining material (*I*, 2) and chemical (*3–6*) properties, so too are the local geometry and global topology of the eigenstate manifolds.

The geometry of an eigenstate manifold can be revealed through transport of a quantum state along a smooth path of parameters that define the system’s Hamiltonian. This transport is generally nonholonomic, meaning that the state generated by transport from an initial to a final point depends on the path along which the system was transported. Such transport has been explored mainly in the two limiting cases in which the energy spectrum of a system is either largely gapped (*7*, *8*) or entirely gapless (*9*) along a closed loop in parameter space. In the former limit, the state-space geometry generates a Berry phase; in the latter, the nonholonomy generalizes to a Wilson loop operator that describes a path-dependent rotation within the degenerate subspace. In terms of  $|u_{\mathbf{q}}^m\rangle$ , the cell-periodic part of the Bloch wave function that

describes a single particle, both types of dynamics derive from the Berry connection matrix,  $A_{\mathbf{q}}^{mm} \equiv i\langle u_{\mathbf{q}}^m | \partial_{\mathbf{q}} | u_{\mathbf{q}}^m \rangle$ , which expresses the local geometry of state space. Focusing on the case of band structure, *n* and *m* are band indices, and  $\mathbf{q}$  is the quasi-momentum. In the gapped limit, the Berry phase is determined solely by one (Abelian) diagonal element of this matrix; in the gapless limit, off-diagonal elements enter, leading to non-Abelian state rotations (*10*).

In this work, we explored the nonholonomy of transport through a state space containing singular points of degeneracy. One example of such points, which we probed experimentally, is the Dirac points of degeneracy between the  $n = 1$  and  $n = 2$  bands of the two-dimensional honeycomb lattice, lying at the  $\mathbf{K}$  and  $\mathbf{K}'$  points of the Brillouin zone (Fig. 1). Away from these points, the energy gap between the touching bands grows linearly with quasi-momentum. The singular state geometry around each linear band-touching point (LBTP) has profound implications for the material properties of graphene—for example, related to Klein tunneling of electrons through potential barriers (*11*) and the appearance of a half-integer quantum Hall effect (*12*). The Dirac point of the honeycomb lattice has been explored also in ultracold-atom experiments (*13*), including interferometric measurements of the Berry phase produced along trajectories that circle the Dirac point (*14*) and direct mapping of the Bloch-state structure across the Brillouin zone (*15–17*).

Crystalline materials may also host a singular quadratic band-touching point (QBTP), about which the energy gap between two bands grows quadratically with quasi-momentum. As before, the QBTP can profoundly affect material properties. For example, the singular QBTP is predicted to produce an anomalous Landau-level spectrum (*18*). Interactions can destabilize a QBTP, leading to topologically protected edge states, nematic phases,

<sup>1</sup>Department of Physics, University of California, Berkeley, Berkeley, CA 94720, USA. <sup>2</sup>Challenge Institute for Quantum Computation, University of California, Berkeley, Berkeley, CA 94720, USA. <sup>3</sup>Materials Sciences Division, Lawrence Berkeley National Laboratory, Berkeley, CA 94720, USA. <sup>4</sup>Department of Physics, Yale University, New Haven, CT 06520, USA.

<sup>5</sup>Department of Physics, Carnegie Mellon University, Pittsburgh, PA 15213, USA.

\*Corresponding author. Email: [charles.d.brown@yale.edu](mailto:charles.d.brown@yale.edu) (C.D.B.); [dmsk@berkeley.edu](mailto:dmsk@berkeley.edu) (D.S.-K.)

and both quantum anomalous Hall and spin phases (19–22). The role of QBTPs is being investigated intensely in both untwisted and twisted bilayer graphene (23–27). Despite their importance, QBTPs have remained unexplored in ultracold-atom systems.

Using ultracold atoms within an optical lattice, we demonstrated that transport of a quantum state through a singular band-touching point leads to a non-Abelian, coherent state rotation between bands, with the rotation depending on the relative orientation of path tangents entering and exiting the singular point. Further, we have shown that this dependence characterizes and distinguishes the Bloch-state geometry surrounding linear and quadratic band-touching singularities.

First, we considered the *s*-orbital LBTP of a two-dimensional honeycomb optical lattice (Fig. 1). To probe this Dirac point, we prepared an optically trapped <sup>87</sup>Rb Bose-Einstein condensate and then slowly ramped up an overlain static honeycomb lattice, placing the atoms initially at the  $\Gamma$ -point of the  $n = 1$  band. Next, we applied a fictitious force to the gas by accelerating the optical lattice potential to a velocity  $\mathbf{v}_{\text{lat}}(t)$ . Although the atoms remained at zero quasi-momentum in the laboratory frame, they evolved to nonzero velocity  $\mathbf{v} = \hbar\mathbf{q}/m = -\mathbf{v}_{\text{lat}}$  in the lattice frame, where  $\hbar$  is Planck's constant  $h$  divided by  $2\pi$ ,  $\mathbf{q}$  is the lattice-frame quasi-momentum, and  $m$  is the atomic mass.

To demonstrate the nonholonomy generated by the LBTP, we accelerated the atoms on a trajectory that proceeded at constant acceleration from  $\Gamma$  to  $\mathbf{K}$  (at quasi-momentum  $\mathbf{q}_{\mathbf{K}}$ ) and then at a different constant acceleration to 24 distinct points on a circle lying at a distance of  $0.4\|\mathbf{q}_{\mathbf{K}}\|$  from the  $\mathbf{K}$ -point. The turning angle between the rays entering and leaving the  $\mathbf{K}$ -point, as defined in Fig. 2A, was varied in equal steps over  $\theta \in [0, 2\pi]$ . We then performed “band mapping” by smoothly ramping off the lattice potential at the fixed final quasi-momentum—that is, with the lattice at a constant final laboratory-frame velocity. This ramp maps the population in each band onto a distinct momentum state. Measuring this momentum distribution quantified band populations in the moving lattice.

Transport along paths passing through the singular LBTP led to interband transitions that varied with the turning angle (Figs. 2, C and D). For trajectories that entered the singularity and then reversed onto themselves ( $\theta = 0$ ), the population remained nearly entirely in the initial  $n = 1$  band. For trajectories that continued with constant tangent through the singularity ( $\theta = \pi$ ), the atoms underwent a near complete transition to the upper  $n = 2$  bands [seen also in (28)]. Over the full range of  $\theta$ , each population underwent one cycle of oscillation.

### Fig. 1. Experimental scheme.

(A) Illustration of an optical honeycomb lattice with two sites (“A” and “B”) in the unit cell, formed by overlapping three  $\lambda = 1064$ -nm wavelength light beams (red arrows). Offsetting the optical frequencies of two lattice beams by  $\delta\omega_{1,2}(t)$  accelerates the lattice and drives lattice-trapped atoms through a trajectory in quasi-momentum. (B) The  $n = \{1, 2, 3, 4\}$  Brillouin zones of the honeycomb lattice are shown in green, blue, pink, and purple, respectively. (C) The band structure of the honeycomb lattice (plotted with potential depth of  $20 \text{ kHz} \times h$ ) exhibits an LBTP in the *s*-orbital band manifold at  $\mathbf{q} = \mathbf{K}$  and a QBTP in the *p*-orbital band manifold at  $\mathbf{q} = \Gamma$ .

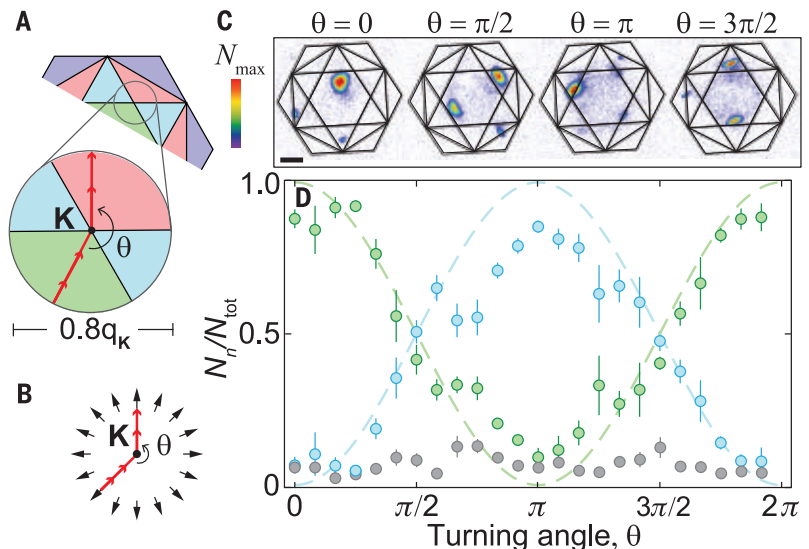
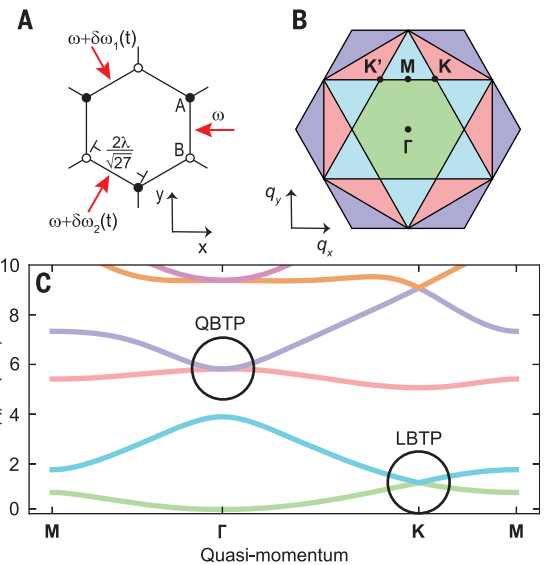


**Fig. 2. Non-Abelian state rotations around a Dirac point.** (A) Enlarged view of Brillouin zone map. Atoms are loaded into the state  $n = 1$ ,  $\mathbf{q} = \Gamma$  in the lattice and transported (trajectory indicated with red arrows) at constant accelerations from  $\Gamma \rightarrow \mathbf{K}$  and then from  $\mathbf{K}$  to a final point lying on a circle of diameter  $0.8\|\mathbf{q}_{\mathbf{K}}\|$  centered at the Dirac point. In this particular experiment, the atoms evolve between the  $n = 1$  and  $n = 2$  bands. The colors of the Brillouin zones do not indicate the state of the atomic wave packet along the trajectory. Rather, the color scheme is used to interpret the band index of atoms after a band-mapping measurement. (B) Bloch states near the Dirac point are described as pseudo-spin-1/2 states in a pseudo-magnetic field (black arrows) that points radially outward from, and wraps once around, the Dirac point. (C) Band-mapping images at the final quasi-momentum, with overlain Brillouin zone maps, show that the band populations vary with turning angle  $\theta$ . A third, short-length, and adiabatic translation step ensures that band mapping does not occur near a Brillouin zone boundary so that there is no ambiguity in the band index of atoms [(31), section 3]. Scale bar, 0.1 mm. (D) Fractional band populations  $N_n/N_{\text{total}}$  ( $n = 1$ , green;  $n = 2$ , blue; sum of other bands, gray) versus  $\theta$ . Means and standard mean errors are determined from seven repeated measurements. The green and blue dashed lines indicate a  $\cos^2(\theta/2)$  and  $\sin^2(\theta/2)$  dependence, respectively.

The unit-cell wave function of the  $n = 1$  and  $n = 2$  Bloch states near the Dirac point can be represented as a pseudo-spin-1/2 vector, with *s*-orbital Wannier states at the lattice sites A and B representing the up- and down-spin

basis states. In this basis, the Bloch states are eigenstates of the Hamiltonian  $H_{\text{LBTP}} = -\mathbf{B}(\mathbf{q}) \cdot \boldsymbol{\sigma}$ , where  $\mathbf{B}(\mathbf{q})$  is a pseudo-magnetic field that lies in the transverse pseudo-spin plane, and  $\boldsymbol{\sigma}$  is the vector of Pauli matrices.  $\mathbf{B}(\mathbf{q})$

has a magnitude  $B = \hbar v_g \|\mathbf{q} - \mathbf{q}_K\|$  that varies linearly with distance from the singularity and has an orientation (in the proper gauge) that is radially outward from  $\mathbf{K}$  (Fig. 2B). Here,  $v_g$  is the group velocity near the Dirac point. The  $2\pi$  rotation of  $\mathbf{B}(\mathbf{q})$  about the Dirac point is responsible for the  $\pi$ -valued Berry phase of trajectories that encircle the Dirac point (14).

This pseudo-spin model explains our observations. The atomic pseudo-spin entering the Dirac point along a ray experiences a pseudo-magnetic field whose orientation  $\mathbf{n}$  remains constant and whose magnitude smoothly tunes to zero. Under this field, the initial-state pseudo-spin remains aligned along  $\mathbf{n}$ . Departing the Dirac point, the pseudo-spin experiences a magnetic field along a new orientation  $\mathbf{m}$ , with  $\mathbf{n} \cdot \mathbf{m} = \cos\theta$ , and a magnitude increasing linearly with time. The pseudo-spin is thus placed in a superposition of eigenstates, with population  $\cos^2(\theta/2)$  in the  $\mathbf{m}$ -oriented pseudo-spin eigenstate ( $n = 1$  bands) and  $\sin^2(\theta/2)$  in the orthogonal state ( $n = 2$  bands). This simple prediction is in good agreement with our data (Fig. 2D), with residual differences accounted by numerical simulations (fig. S6) of the dynamics of noninteracting atoms over the finite duration of our experimental stages (29).

We found that passage through the Dirac point produces a phase-coherent superposition of band states. Such coherence was demonstrated by allowing the atoms to evolve at the final point of the trajectory for a variable time before measuring populations in a basis different from the local energy eigenbasis. Temporal oscillations in these measurements, with a frequency matching the calculated gap between the  $n = 1$  and  $n = 2$  bands, demonstrate the coherence of the atomic state after transport (fig. S3).

The energy-time uncertainty relation places a bound on how finely the singular point can be located by our method. We considered a trajectory where the acceleration has magnitude  $a$  near the singularity. The system spends a time  $\delta t \sim (\hbar/ma)\delta q$  within  $\delta q$  of the singularity; the energy gap has magnitude  $\delta E \sim \hbar v_g \delta q$  in that vicinity. Setting  $(\delta t)(\delta E) \sim \hbar$  establishes that the band structure is effectively gapless within a quasi-momentum distance of  $\delta q = R \sim \sqrt{mah}/v_g$  of the singularity. That is, the nonholonomy generated by the singular point should be observed also for finite time trajectories that pass within the effective radius,  $R$ , of the singularity.

We measured  $R$  by driving the atoms along a family of trajectories (Fig. 3A) that connect between the initial  $\Gamma$ -point to a final  $\Gamma$ -point that is one reciprocal lattice vector away, and by performing band-mapping measurements at the final point. These trajectories cross the boundary between the first and second Brillouin zones at nine equally spaced points along the  $\mathbf{K}' - \mathbf{M} - \mathbf{K}$  line. As shown in Fig. 3B for various traversal times  $\tau$ , we observed that

trajectories that pass directly through either Dirac point yield a band population distribution that is independent of  $\tau$ , with  $\sim 3/4$  of the atoms transferring to the upper band. By contrast, for traversal times that are longer and for paths that veer farther from the Dirac points, the transition between bands is increasingly suppressed, demonstrating that  $R$  decreases with decreasing  $a$  (increasing  $\tau$ ). At first glance, the experiment of Fig. 3 is analogous to Majorana losses. The study presented in Fig. 3 is quite close to Majorana's description (30) and to the picture of the "Majorana hole" that appears in a spherical quadrupole magnetic trap. How-

ever, a difference between our experiment and magnetic traps is that in traps, the spin flips that occur because of transport through the state geometry of the system lead to loss, whereas in our experiment, they led to transitions between trapped bands of the lattice.

The singularity at an LBTP can be characterized by two different experimental methods: either by Berry phase measurements along trajectories that encircle the singularity (14), or as shown here, through state rotations produced along trajectories that pass through the singularity. These two methods are related but non-equivalent. Berry phase measurements measure

### Fig. 3. Effective size of a Dirac singularity.

(A) Illustration of quasi-momentum trajectories over which the atoms are transported for the measurements in (B). Each trajectory connects two different  $\Gamma$ -points but traverses one of nine equally spaced points along the  $\mathbf{K}' - \mathbf{M} - \mathbf{K}$  line. (B) Fractional  $n = 1$  band population plotted, for different trajectory traversal times  $\tau$ , against the trajectory midpoints from (A). Means and standard mean errors are generated from three to five repeated measurements. (C) An effective radius  $R$  (plotted normalized by  $\hbar k = \hbar/\lambda$ ) is defined for each  $\tau$  by the distance along the  $\mathbf{K}' - \mathbf{M} - \mathbf{K}$  line for which the threshold  $N_1/N_{\text{total}} = 0.5$  is fulfilled.  $R$  diminishes with larger  $\tau$ .

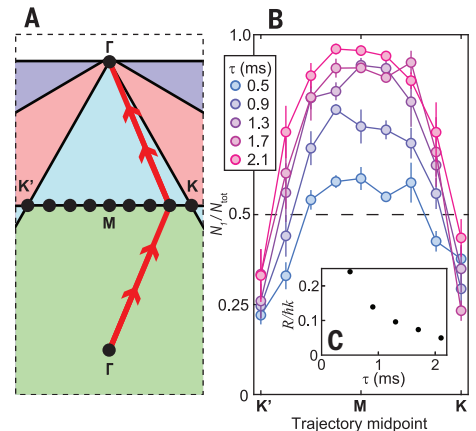
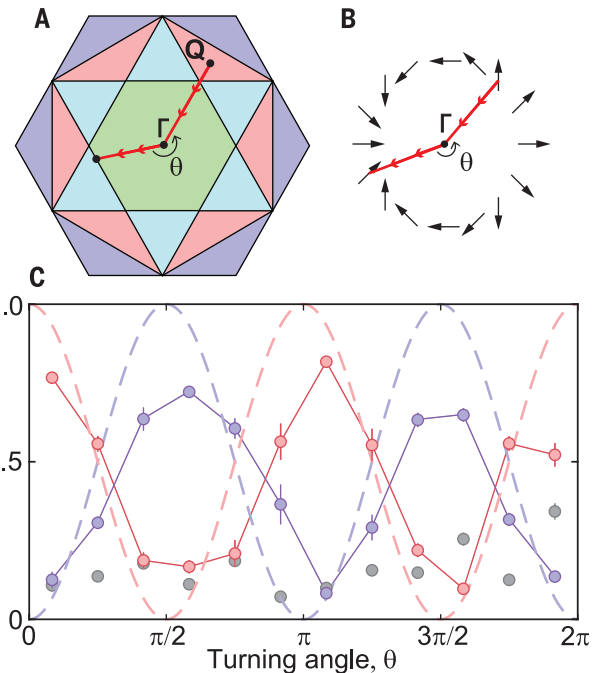


### Fig. 4. Non-Abelian state rotations around a QBTP.

(A) Atoms are prepared in the  $n = 3$  bands at  $\mathbf{Q}$ , transported (along red arrows) to the QBTP at  $\Gamma$ , and then transported to a final quasi-momentum for band mapping. In this particular experiment, the atoms evolve between the  $n = 3$  and  $n = 4$  bands. The colors of the Brillouin zones do not indicate the state of the atomic wave packet along the trajectory. Rather, the color scheme is used to interpret the band index of atoms after a band-mapping measurement. (B) The pseudo-magnetic field (black arrows) describing the Bloch state geometry wraps twice in orientation for one revolution around the QBTP. (C) A plot of normalized band population as a function of  $\theta$ , collected by analyzing band-mapping data (fig. S2). Red circles indicate the  $n = 3$  bands; purple circles indicate the  $n = 4$  band; and gray circles indicate bands with  $n \neq 3, 4$ . Mean and standard mean errors are determined from seven repeated measurements. The dashed pink and purple lines indicate a  $\cos^2(\theta)$  and  $\sin^2(\theta)$  dependence, respectively. Our numerical simulations suggest that the data does not reach unity oscillation amplitude owing to nonadiabaticity in the band-mapping procedure (fig. S6).



the integrated Berry flux, which is determined from a diagonal element of the Berry connection matrix  $A_{\mathbf{q}}^m$ . A  $\pi$ -valued flux was found pinned to the singular point. By contrast, the non-Abelian state rotations detected in our method derived directly from the off-diagonal elements  $A_{\mathbf{q}}^{nm}$ , with  $n = 1$  and  $m = 2$  being the two crossing bands (31). Further, different from Berry phase measurements, our method can be regarded as measuring the Hilbert-Schmidt quantum distance  $d^2(\mathbf{q}, \mathbf{q}') = 1 - |\langle u_{\mathbf{q}'}^1 | u_{\mathbf{q}}^1 \rangle|^2$  (32, 33), with  $\mathbf{q}$  identified as a point along the input path into, and  $\mathbf{q}'$  as a point along the exit path from, the singularity. The oscillation of the  $n = 1$  band population as a function of the turning angle reveals the quantum distance to undergo one complete oscillation between zero and unity on a contour encircling the LBTP.

The distinction between these two methods is notable in the case of a QBTP. Similar to the LBTP, a singular QBTP also carries concentrated Berry flux that is restricted, assuming time reversal and  $C_6$  symmetry, to be 0 or  $\pm 2\pi$  (20). However, these values of Berry phase are undetectable with interference measurements. By contrast, our method uncovers the characteristic nonholonomy of the singular QBTP and the concomitant modulation of the quantum distance around the singular point.

For a singular QBTP, the geometric structure of Bloch states of the two intersecting bands at the vicinity of the singularity can again be described as those of a pseudo-spin in a pseudo-magnetic field. Different from the LBTP, in this work the pseudo-magnetic field, lying in the transverse pseudo-spin plane, has a magnitude that increases quadratically with distance to the singularity and has an orientation that wraps by an angle of  $4\pi$  along a path encircling the singularity (Fig. 4B).

We probed this geometric structure at the QBTP that occurs at  $\Gamma$  between the  $n = 3$  and  $n = 4$  bands of the honeycomb lattice. For this, we first loaded the Bose-Einstein condensate into the  $n = 3$  bands of the lattice by means of “inverse band mapping.” In previous work (34), such loading into excited bands was realized with moving atoms in a static lattice; in this study, we realized similar state-preparation with static atoms loaded into a moving lattice. Specifically, we gradually increased the depth of a honeycomb lattice moving with velocity  $\mathbf{v}_{\mathbf{Q}}$  that is located within the third Brillouin zone in the extended zone scheme (Fig. 4A). Then, we accelerated atoms (in the lattice frame) at constant acceleration along the path  $\mathbf{Q} \rightarrow \Gamma$ , into the QBTP, and then turning by an angle  $\theta$ , accelerated the atoms at a different constant acceleration out of the QBTP and to the edge of the Brillouin zone. Final points were chosen as ones where populations in the  $n = 3$  and  $n = 4$  bands were easily distinguished with band mapping.

We observed a nonholonomy at the QBTP that was distinct from that observed at the LBTP. Specifically, we observed two cycles of oscillation in the final band populations over the interval  $\theta \in [0, 2\pi]$ . This behavior is explained well by the pseudo-spin representation of the singular QBTP. Different from the LBTP, pseudo-magnetic-field orientations along the incoming ( $\mathbf{n}$ ) and outgoing ( $\mathbf{m}$ ) paths were related as  $\mathbf{n} \cdot \mathbf{m} = \cos^2\theta$ . The nonholonomy of the QBTP produced populations of  $\cos^2(\theta)$  and  $\sin^2(\theta)$  in the  $n = 3$  (initial) and  $n = 4$  bands, respectively.

The amplitude of the observed oscillation is lower than suggested by this simple theory; again, we ascribe this difference to dynamical effects of our finite-duration acceleration and band-mapping stages. Nevertheless, the periodicity of the oscillations, combined with the known time reversal and  $C_6$  symmetry of our lattice, unambiguously determined the topological winding number around the QBTP to be well defined and equal to 2 (31).

We have demonstrated transport of a quantum system through singular band-touching points with different topological winding numbers. We observed non-Abelian, coherent state rotation between bands. The dependence of this rotation on the relative orientation of path tangents entering and exiting the singular point unambiguously measured the winding number.

Our method of probing band structure could be applied to gain insight on other band structure singularities and on interaction effects. It would be interesting to study higher-order singular band-touching points, between more than two bands. We deliberately minimized interaction effects in these experiments, but in future work, it will be interesting to observe potential interaction-induced instabilities of Dirac points, QBTPs, or other band-touching points. The path-dependent non-Abelian nonholonomy observed in this work may also pertain to chemical systems, in which potential energy surfaces are endowed similarly with conical intersections (3–6), suggesting a potential route for quantum state control in optically driven molecules.

#### REFERENCES AND NOTES

- D. Xiao, M.-C. Chang, Q. Niu, *Rev. Mod. Phys.* **82**, 1959–2007 (2010).
- A. Bansil, H. Lin, T. Das, *Rev. Mod. Phys.* **88**, 021004 (2016).
- D. R. Yarkony, *J. Phys. Chem. A* **105**, 6277–6293 (2001).
- G. A. Worth, L. S. Cederbaum, *Annu. Rev. Phys. Chem.* **55**, 127–158 (2004).
- W. Domcke, D. R. Yarkony, *Annu. Rev. Phys. Chem.* **63**, 325–352 (2012).
- M. S. Schuurman, A. Stolow, *Annu. Rev. Phys. Chem.* **69**, 427–450 (2018).
- B. Simon, *Phys. Rev. Lett.* **51**, 2167–2170 (1983).
- M. V. Berry, *Proc. R. Soc. London Ser. A* **392**, 45–57 (1984).
- F. Wilczek, A. Zee, *Phys. Rev. Lett.* **52**, 2111–2114 (1984).
- A. Bohm, A. Mostafazadeh, H. Koizumi, Q. Niu, J. Zwanziger, *The Geometric Phase in Quantum Systems* (Springer, 2003).
- M. I. Katsnelson, K. S. Novoselov, A. K. Geim, *Nat. Phys.* **2**, 620–625 (2006).
- Y. Zhang, Y.-W. Tan, H. L. Stormer, P. Kim, *Nature* **438**, 201–204 (2005).
- L. Tarruell, D. Greif, T. Uehlinger, G. Jotzu, T. Esslinger, *Nature* **483**, 302–305 (2012).
- L. Duca et al., *Science* **347**, 288–292 (2015).
- M. Tarnowski et al., *Phys. Rev. Lett.* **118**, 240403 (2017).
- T. Li et al., *Science* **352**, 1094–1097 (2016).
- N. Fläschner et al., *Science* **352**, 1091–1094 (2016).
- J.-W. Rhim, K. Kim, B.-J. Yang, *Nature* **584**, 59–63 (2020).
- K. Sun, E. Fradkin, *Phys. Rev. B Condens. Matter Mater. Phys.* **78**, 245122 (2008).
- K. Sun, H. Yao, E. Fradkin, S. A. Kivelson, *Phys. Rev. Lett.* **103**, 046811 (2009).
- J. M. Murray, O. Vafek, *Phys. Rev. B Condens. Matter Mater. Phys.* **89**, 201110 (2014).
- J. Shah, S. Mukerjee, *Phys. Rev. B* **103**, 195118 (2021).
- E. McCann, V. I. Fal'ko, *Phys. Rev. Lett.* **96**, 086805 (2006).
- E. McCann, M. Koshino, *Rep. Prog. Phys.* **76**, 056503 (2013).
- S. Pujari, T. C. Lang, G. Murthy, R. K. Kaul, *Phys. Rev. Lett.* **117**, 086404 (2016).
- K. Hejazi, C. Liu, L. Balents, *Phys. Rev. B* **100**, 035115 (2019).
- K. Hejazi, C. Liu, H. Shapourian, X. Chen, L. Balents, *Phys. Rev. B* **99**, 035111 (2019).
- G. Jotzu et al., *Nature* **515**, 237–240 (2014).
- The maximum duration of our experiment was limited by the observed decay of atoms from the excited-energy Bloch states populated during lattice acceleration.
- E. Majorana, *Nuovo Cim.* **9**, 43–50 (1932).
- Materials and methods are available as supplementary materials.
- J. P. Provost, G. Vallee, *Commun. Math. Phys.* **76**, 289–301 (1980).
- Y. Hwang, J. Jung, J.-W. Rhim, B.-J. Yang, *Phys. Rev. B* **103**, L241102 (2021).
- T.-H. Leung et al., *Phys. Rev. Lett.* **125**, 133001 (2020).
- C. D. Brown et al., Dataset for direct geometric probe of singularities in band structure. Zenodo (2022).

#### ACKNOWLEDGMENTS

We thank E. Altman, M. Zaletel, N. Read, and J. Harris for early insights into this work. **Funding:** We acknowledge support from the NSF QLCI program through grant OMA-2016245 and also NSF grant PHY-1806362, and from the ARO through the MURI program (grant W911NF-17-1-0323). C.D.B. acknowledges support from the National Academies of Science, Engineering, and Medicine Ford Postdoctoral Fellowship program. V.K. and J.E.M. were supported by the Quantum Materials program at LBNL, funded by the US Department of Energy under contract DE-AC02-05CH11231. A.A. and J.E.M. acknowledge support from the NSF under grant DMR-1918065 and from a Kavli ENSI fellowship. J.E.M. acknowledges support from a Simons Investigatorship. **Author contributions:** All authors contributed substantially to the work presented in this manuscript. C.D.B., S.-W.C., M.N.S. and T.-H.L. acquired the data and maintained the experimental apparatus. C.D.B., S.-W.C., and M.N.S. analyzed the data. C.D.B. prepared the manuscript. M.N.S., A.A., and V.K. performed the numerical calculations. A.A. and V.K. performed supporting theory calculations. J.E.M. and D.S.-K. supervised the study. All authors worked on the interpretation of the data and contributed to the final manuscript. **Competing interests:** The authors declare no competing interests. **Data and materials availability:** The data and the codes used for both data analysis and theory curve generation are available at Zenodo (35). **License information:** Copyright © 2022 the authors, some rights reserved; exclusive licensee American Association for the Advancement of Science. No claim to original US government works. <https://www.science.org/about/science-licenses-journal-article-reuse>

#### SUPPLEMENTARY MATERIALS

[science.org/doi/10.1126/science.abm6442](https://science.org/doi/10.1126/science.abm6442)  
Materials and Methods  
Supplementary Text  
Figs. S1 to S7  
References (36–41)

Submitted 4 October 2021; accepted 28 July 2022  
10.1126/science.abm6442

## ORGANIC CHEMISTRY

## Halogen-atom and group transfer reactivity enabled by hydrogen tunneling

Timothée Constantin<sup>1†</sup>, Bartosz Górski<sup>1†</sup>, Michael J. Tilby<sup>1†</sup>, Saloua Chelli<sup>2</sup>, Fabio Juliá<sup>1</sup>, Josep Llaveria<sup>3</sup>, Kevin J. Gillen<sup>4</sup>, Hendrik Zipse<sup>5</sup>, Sami Lakhdar<sup>2\*</sup>, Daniele Leonori<sup>6\*</sup>

The generation of carbon radicals by halogen-atom and group transfer reactions is generally achieved using tin and silicon reagents that maximize the interplay of enthalpic (thermodynamic) and polar (kinetic) effects. In this work, we demonstrate a distinct reactivity mode enabled by quantum mechanical tunneling that uses the cyclohexadiene derivative  $\gamma$ -terpinene as the abstractor under mild photochemical conditions. This protocol activates alkyl and aryl halides as well as several alcohol and thiol derivatives. Experimental and computational studies unveiled a noncanonical pathway whereby a cyclohexadienyl radical undergoes concerted aromatization and halogen-atom or group abstraction through the reactivity of an effective H atom. This activation mechanism is seemingly thermodynamically and kinetically unfavorable but is rendered feasible through quantum tunneling.

Carbon radicals are integral reactive species for the synthesis of numerous organic compounds (1–4). Among the methods for their generation, strategies based on halogen-atom and group transfer chemistry are advantageous for their use of halides and alcohol or thiol derivatives that are commercially available or otherwise easy to access (5–9).

Halogen-atom transfer processes follow three general reactivity principles (Fig. 1A): (i) They rely on a collinear arrangement among the three atoms involved in the process (i.e., C, X, and Y) to achieve maximum orbital overlap between the abstracting radical (Y•) singly occupied molecular orbital (SOMO) and the carbon-halogen antibonding orbital ( $\sigma^*$ ). (ii) The Y-halogen bond needs to be stronger than the original carbon-halogen bond in the reactant so that the process is thermodynamically favorable (exergonic;  $\Delta G^\circ < 0$ , where  $\Delta G^\circ$  is Gibbs free energy; enthalpic effect). (iii) Rapid kinetics ensue from the interplay of polar effects at the transition state that lower the barriers by charge transfer. Considering the natural polarization of carbon-halogen bonds (10), nucleophilic radicals are ideally suited to stabilize emerging positive character and therefore accelerate the abstraction. Species like tin and silicon radicals maximize both enthalpic and polar effects and are thus routinely used for radical

generation despite their toxicity, cost, and waste management issues (9, 11–13).

We report a distinct approach for halogen-atom transfer that does not adhere to any of these three features. This noncanonical process exploits the reactivity of cyclohexadienyl radicals that enable, through concerted aromatization-abstraction events, the use of formal hydrogen atoms (H•) as the abstracting species. This process relies on a collinear arrangement of four atoms in the transition state, and its feasibility is enabled by quantum mechanical tunneling rather than thermodynamic (enthalpic) or kinetic (polar) considerations. The mechanistic blueprint is not limited to the activation of organic halides but likewise enables the generation of carbon radicals from alcohol and thiol derivatives, which suggests that quantum tunneling is also operating in group transfer chemistry.

The development of this alternative strategy for carbon radical generation started with the analysis of the key thermodynamic and polar features controlling halogen-atom transfer. This led us to speculate that a hydrogen atom, H•, might be a suitable reagent to perform these reactions. This mechanistic hypothesis was based on the evidence that H-halogen bonds are stronger than standard C-halogen bonds and that they immediately dissociate in weakly basic media (14). This combination should make the overall radical abstraction exothermic. Furthermore, the H atom should polarize the transition state through the emergence of proton-like character, thus aiding charge transfer stabilization. A computational comparison of halogen-atom transfer reactions on Cy-Br **1** mediated by  $\text{Me}_3\text{Sn}^\bullet$ ,  $\text{Me}_3\text{Si}^\bullet$ , and H• demonstrated that all three abstractions are highly exothermic but that the one mediated by H• faces the smallest kinetic barrier (Fig. 1A) (15). Although these results would support this mode for halogen abstraction, its implementation is clearly hampered by the

lack of methods for generating naked H• in synthetic settings.

In approaching this challenge, we turned our attention to the concept of proaromaticity, which has been extensively applied to the generation of silicon radicals (Fig. 1B) (16–20). This strategy requires the preparation of bespoke  $\text{Me}_3\text{Si}$ -containing cyclohexadiene derivatives (e.g., **2**) that are activated by H-atom transfer (HAT) at the bis-allylic methylenic position. This event generates the cyclohexadienyl radical **3** that, through a thermodynamically favorable aromatization process, ejects  $\text{Me}_3\text{Si}^\bullet$ . This species can then be used in many types of radical chain propagations based on halogen-atom as well as group transfer chemistry. Our initial mechanistic plan sought synthetic conditions to translate this reactivity blueprint to simple cyclohexadiene radical **4•** as a gateway to generate and implement H• reactivity in synthetic radical chemistry.

To experimentally validate this hypothesis, we looked at dehalogenation reactions, which are heavily exploited by the pharmaceutical sector but still require a large excess of difficult-to-handle tin and silicon reagents with azobisisobutyronitrile (AIBN) at often high temperatures (>100°C). We demonstrated that the cyclohexadiene derivative  $\gamma$ -terpinene, a feedstock derived from the essential oil of *Melaleuca alternifolia*, led to the quantitative debromination of **5** (to give **17**) under mild photoredox conditions using the organic dye 4CzIPN as the photocatalyst (5 mol %) and NaCl or  $\text{NaN}_3$  as an additive (10 mol %) in acetonitrile solvent under blue light-emitting diode (LED) irradiation. The supplementary materials discuss the identification of other reaction conditions of similar efficiency based on the use of diarylketones photocatalysts, which demonstrates that this  $\gamma$ -terpinene-mediated debromination can be adapted to manifolds outside the realm of photoredox catalysis (fig. S19 and table S8). Additionally, the replacement of  $\gamma$ -terpinene by other proaromatic agents, such as simple 1,4-cyclohexadiene, provided similar experimental results, in line with our working hypothesis (fig. S3 and table S2). In terms of substrate scope, this reactivity was extended to the activation and dehalogenation of the corresponding C-4 iodide (**6**) and, notably, chloride (**7**). Deactivated and electron-rich aryl halides were also competent substrates, as demonstrated by the high-yielding dehalogenation of **8** to **10** (to give **18**), which presumably proceeds through the formation of an aryl radical. Compounds **7** and **10** exemplify a class of highly sought-after precursors for application in radical chemistry that are still difficult to engage in methods based on both single-electron transfer (SET) and halogen-atom transfer reactivity (21–26).

<sup>1</sup>Department of Chemistry, University of Manchester, Manchester M13 9PL, UK. <sup>2</sup>CNRS/Université Toulouse III – Paul Sabatier, Laboratoire Hétérochimie Fondamentale et Appliquée, LHFA UMR 5069, 31062 Toulouse Cedex 09, France. <sup>3</sup>Global Discovery Chemistry, Therapeutics Discovery, Janssen Research & Development, Janssen-Cilag S.A., 45007 Toledo, Spain. <sup>4</sup>LifeArc, Accelerator Building, Open Innovation Campus, Stevenage SG1 2FX, UK. <sup>5</sup>Department Chemie, LMU München, D-81377 München, Germany. <sup>6</sup>Institute of Organic Chemistry, RWTH Aachen University, 52056 Aachen, Germany.

\*Corresponding author. Email: sami.lakhdar@univ-tlse3.fr (S.L.); daniele.leonori@rwth-aachen.de (D.L.)

†These authors contributed equally to this work.

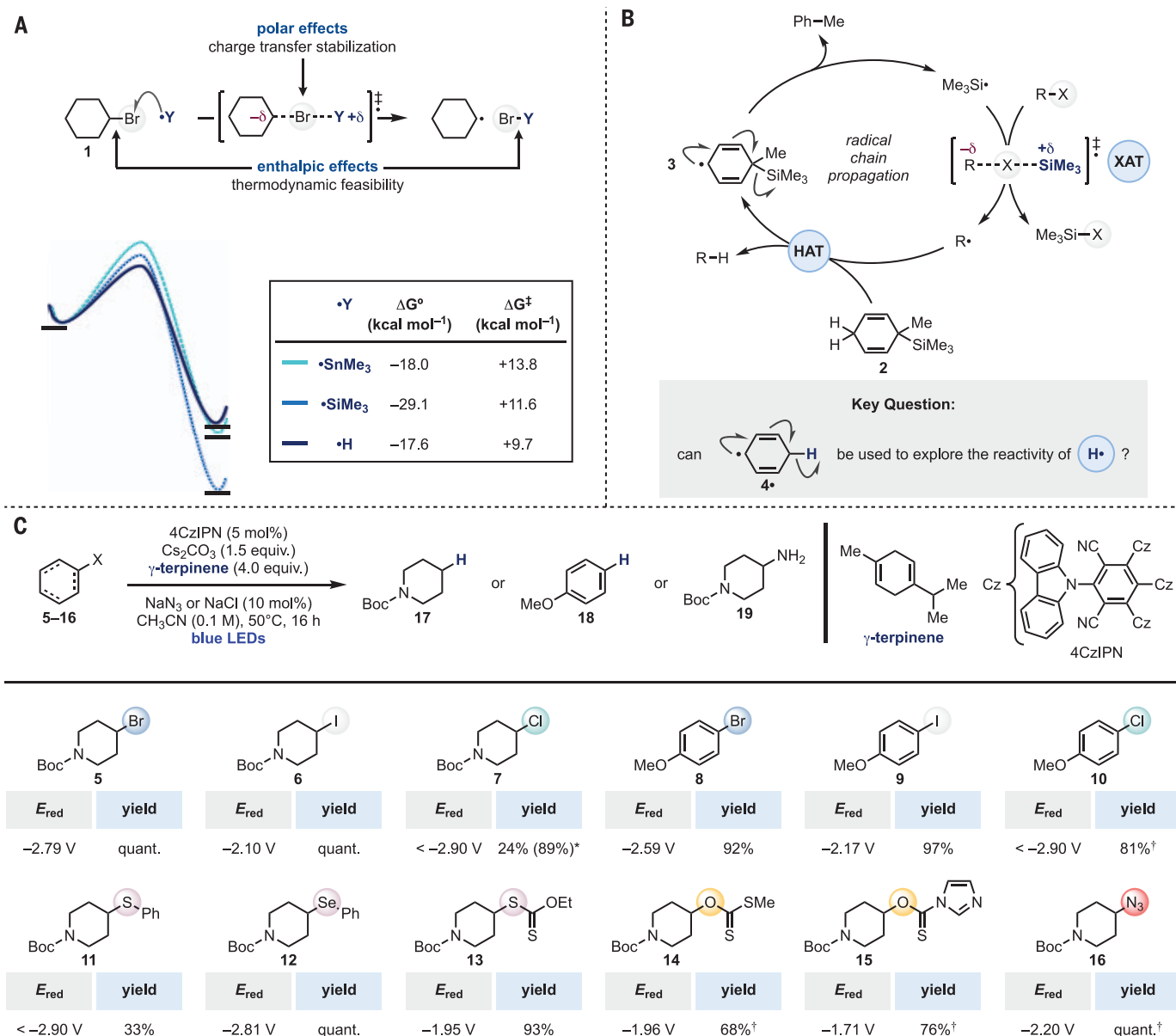


**Fig. 1. A**  $\gamma$ -terpinene-mediated radical generation by halogen-atom and group transfer. **(A)** General mechanism for halogen-atom transfer reactions and computational studies on three model bromine-atom abstractions [density functional theory (DFT) method: (u)M06-2X/def2-TZVP-SMD(MeCN) in kilocalories per mole, where Gibbs free energies are based on the individual reactants and products]. **(B)** Si-containing proaromatic cyclohexadienyl radicals

that generate silicon radicals by fragmentation. XAT, halogen-atom transfer. **(C)** Development of a general strategy for halogen-atom and group transfer chemistry using  $\gamma$ -terpinene as the formal H• donor. Yields are isolated. Boc, *tert*-butoxycarbonyl; Ph, phenyl; equiv., equivalents; quant., quantitative. \*Yield obtained using Ir(ppy)<sub>3</sub> as the photocatalyst. †See the supplementary materials for minor deviation from the standard reaction conditions.

This  $\gamma$ -terpinene-based strategy is not limited to the activation of organic halides, and we successfully translated it into group transfer settings. This enabled the defunctionalization of C-4 sulphide (**11**), selenide (**12**), xanthate (**13**), and alcohol derivatives (**14** and **15**) in moderate to excellent yields (to give **17**). Alkyl azide **16** was also readily engaged, providing access to the corresponding primary amine **19** and thus offering a transition metal-free option to standard hydrogenation conditions.

Taken together, these results demonstrate that this mild  $\gamma$ -terpinene-mediated reactivity engages the whole spectrum of substrates classically activated by tin and silicon radical chemistry while bypassing SET activation and therefore the requirement for strong reductants. These features should make it a useful tool for carbon radical generation, so we conducted an extensive scope investigation with the aim of benchmarking its utility in synthetic settings. Numerous functionalized alkyl and aryl halides **20** to **59** were susceptible to

this reaction, leading to generally high yields of the corresponding reduced products (Fig. 2, A to C). The reactivity spanned a broad class of unactivated alkyl derivatives (primary, secondary, and tertiary) and was compatible with commonly encountered organic functionalities, including free and protected alcohols and amines, acetal, ester, lactone, lactam, aldehyde, and ketone as well as HAT-labile benzylic, allylic, and  $\alpha$ -heteroatom centers. Although most of the scope exploration was conducted on a 0.1-mmol scale, these reactions



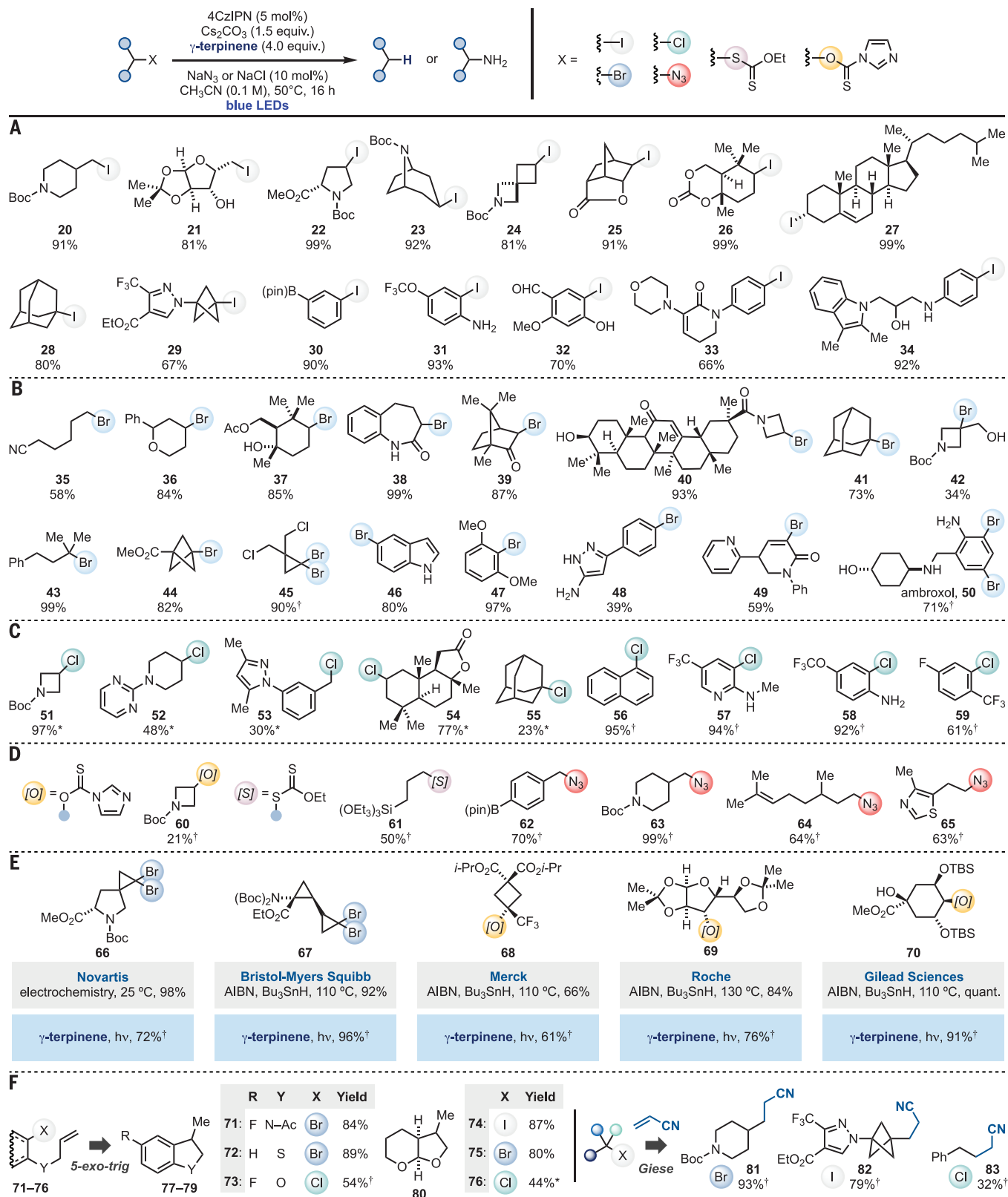


**Fig. 2. Extended substrate scope.** (A to D) Alkyl and aryl iodides (A), alkyl and aryl bromides (B), alkyl and aryl chlorides (C), and alcohol and thiol derivatives and alkyl azides (D). (E) Application of the reactivity to industrially relevant defunction-

alizations (27–29). (F) Application to other modes of radical reactivity. Yields are isolated. \*Yield obtained using Ir(ppy)<sub>3</sub> as the photocatalyst. †See the supplementary materials for minor deviation from the standard reaction conditions.

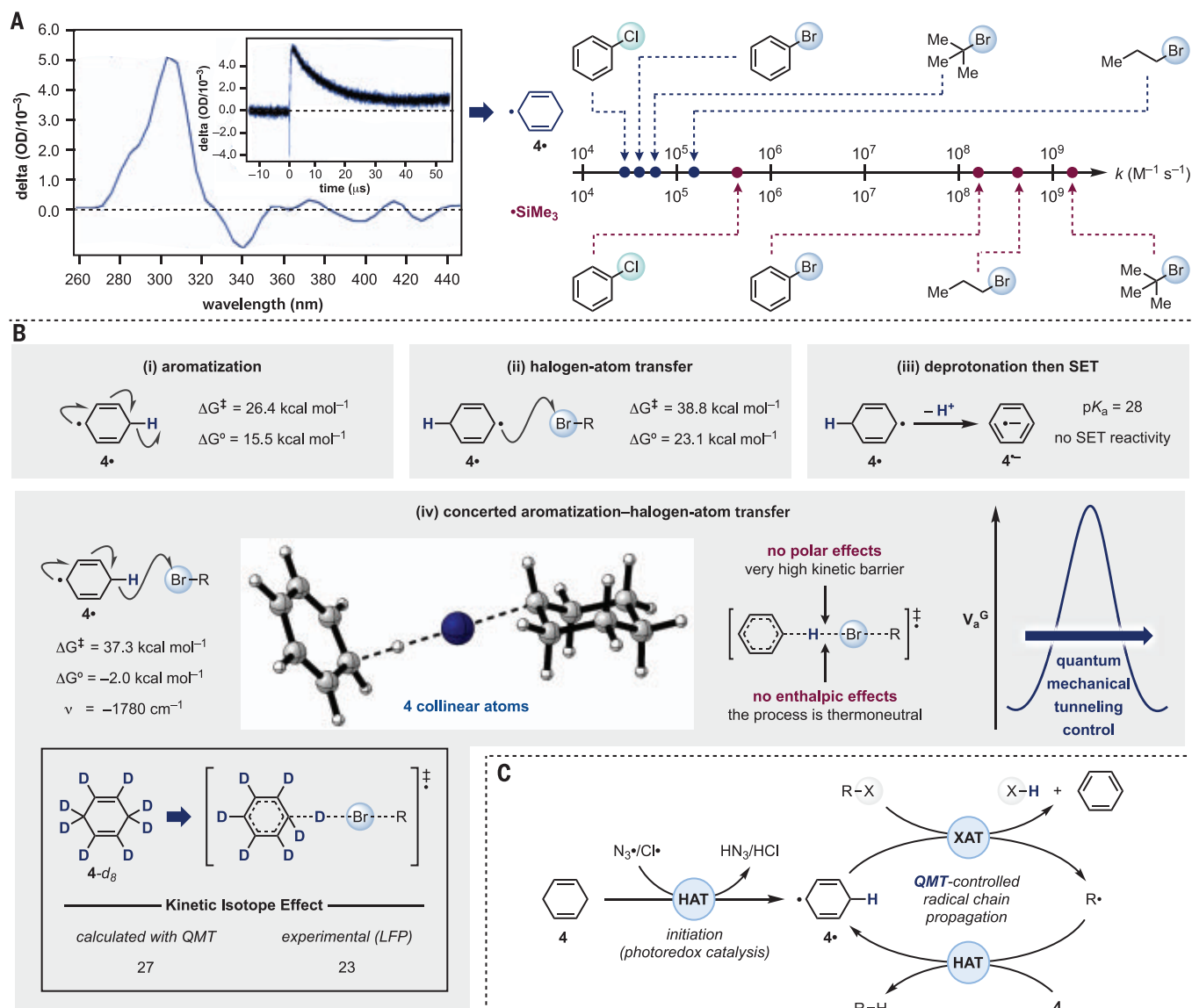


**Fig. 3. Mechanistic studies.** (A) Laser flash photolysis studies monitoring the decay of the cyclohexadienyl radical. OD, optical density. (B) Outline of possible mechanistic scenarios leading to quantum tunneling-controlled concerted aromatization-halogen-atom transfer [DFT method: (u)M06-2X/def2-TZVP-SMD

(MeCN) in kilocalories per mole, where Gibbs free energies are based on the individual reactants and products]. QMT, quantum mechanical tunneling; LFP, laser flash photolysis. (C) Proposed quantum tunneling-enabled radical chain propagations.

can be translated to a larger scale in similar yields and efficiencies through the use of photochemical flow reactors (figs. S15 and S16) (15). In exploring the aryl halide scope, we mostly focused on substrates containing strongly electron-donating substituents that challenge the implementation of SET-based approaches; several privileged N-heterocycles; and groups that can act as a handle for cross-coupling reactivity, such as pinacol boronic ester. All of these derivatives worked well, giving the desired products in high yields. Synthetic applications in group transfer and reduction chemistry were demonstrated on alcohol and thiol derivatives (**60** and **61**) as well as several alkyl azides, giving the corresponding primary amines (**62** to **65**) (Fig. 2D).

As mentioned above, radical defunctionalization processes are often encountered in the pharmaceutical literature for the preparation of high-value bioactive compounds. Substrates **66** to **70** exemplify some of these processes, which are generally performed through the use of toxic tin or silicon reagents at high temperature (Fig. 2E) (27–29). Our  $\gamma$ -terpinene-based protocol proved applicable to these targets, thus offering, in similar chemical yields, milder and more sustainable conditions with a volatile aromatic by-product in place of tin or silicon waste. As a further demonstration of the general utility of this method, we explored the use of alkyl and aryl halides in other modes (Fig. 2F), such as reductive 5-*exo-trig* cyclizations (**71** to **73** to give **77** to **79**, and

**74** to **76** to give **80**) and Giese additions (**81** to **83**).

We next turned our attention to the underlying reaction mechanism. First, we performed control experiments to verify that  $\gamma$ -terpinene and light are essential to observe reactivity; furthermore, different bases, initiators, and photocatalysts can all be used (tables S1, S3, and S5 to S7) (15). We then monitored the generation and reactivity of the cyclohexadienyl radical **4•** ( $\lambda_{\text{max}} = 315 \text{ nm}$ , where  $\lambda_{\text{max}}$  is the wavelength of maximum absorption) by laser-flash photolysis measurements (30–33), irradiating cyclohexadiene at  $h\nu = 355 \text{ nm}$  (where  $h$  is Planck's constant and  $\nu$  is the photon frequency) in the presence of (*t*-BuO)<sub>2</sub> and several alkyl and aryl halides (Fig. 3A). Notably,

all of these experiments resulted in the decay of **4•** with similar bimolecular rate constants ( $k_2$ ), all clustered around  $10^5 \text{ M}^{-1} \text{ s}^{-1}$  (15). This kinetic outcome contrasts with the large difference in rates measured for the decays of silicon radicals in the presence of similar quenchers, which are generally faster and highly dependent on the bond dissociation energy (BDE) of the carbon-halogen bond, thus spanning over three orders of magnitude (34, 35). We initially attributed this noncanonical outcome to a rate-limiting aromatization, followed by a faster halogen abstraction from **H•**. However, computational analysis of this reaction profile demonstrated the generation of naked **H•** to be energetically uphill of  $>15 \text{ kcal mol}^{-1}$  with a high kinetic barrier that would not be compatible with the fast reactivity observed under our synthetic experiments (Fig. 3B, part i) (15).

These findings pointed to a distinct mechanistic pathway operating under these reaction conditions. We ruled out bromine-atom transfer (and also group transfer) taking place from **4•** because this process is highly endergonic ( $\Delta G^\circ = 23.1 \text{ kcal mol}^{-1}$ ) and kinetically unfavorable ( $\Delta G^\ddagger = 38.8 \text{ kcal mol}^{-1}$ , where  $\Delta G^\ddagger$  is Gibbs energy of activation) (Fig. 3B, part ii) (15): The halogen abstraction would generate a bis-allylic carbon-bromine bond that is weaker than the bond in the starting material while offering minimal charge transfer stabilization. A deprotonation of **4•** to the corresponding phenyl radical anion **4<sup>-•</sup>** followed by SET (36, 37) activation of the substrates was also excluded on the basis of calculated high acid dissociation constant  $\text{p}K_a = 28$  [dimethyl sulfoxide (DMSO)] for the methylenic proton in **4•** (predicted to increase in the experimentally relevant solvent  $\text{CH}_3\text{CN}$ ) (Fig. 3B, part iii) (15). Furthermore, attempts to translate the  $\gamma$ -terpinene reactivity to substrates that are easy to reduce but that cannot undergo atom or group transfer chemistry led to no reactivity, thereby ruling out the involvement of SET (table S13 and fig. S30) (15).

We then revisited our initial hypothesis and considered a hybrid mechanism, where the aromatization and the **H•**-mediated halogen abstraction are linked and occur simultaneously (Fig. 3B, part iv). Such a mechanistic option represents a noncanonical avenue in halogen-atom and group transfer chemistry because it would feature the collinear arrangement of four atoms instead of three in the transition state. Our calculations demonstrated that by linking the aromatization to the halogen transfer, the bromine abstraction between **4•** and **1** is typically close to thermoneutral ( $\Delta G^\circ = -2.0 \text{ kcal mol}^{-1}$ ) but still characterized by a significantly high kinetic barrier ( $\Delta G^\ddagger = 37.3 \text{ kcal mol}^{-1}$ ), which should thwart reactivity. However, the very large imaginary frequency observed ( $\nu = -1780 \text{ cm}^{-1}$ )

implied a barrier with a very narrow width (15, 38–40). Under these circumstances, a light particle, like an H atom, is not strictly required to have enough kinetic energy to overcome the transition state height but can penetrate the potential energy barrier through quantum mechanical tunneling (41–45). To validate this mechanistic scenario, we measured the kinetic isotope effect (KIE) because unusually large values are strong indicators for the involvement of quantum tunneling in chemical reactions. Our calculations of fully deuterated cyclohexadienyl radical **4-*d*<sub>8</sub>** in the model bromine abstraction process predicted a KIE = 6 on the basis of standard transition state theory. Crucially, when corrected with the incorporation of small curvature tunneling (SCT) (46), a KIE = 27 was obtained. We therefore prepared the fully deuterated cyclohexadiene and repeated the flash-laser photolysis kinetic studies with **1**, resulting in a large measured KIE = 23, which agrees with our calculations. Furthermore, we repeated the kinetic measurements for the photolysis of cyclohexadiene in the presence of **1** at a lower temperature ( $T = -15^\circ\text{C}$ ) and observed an almost identical bimolecular decay rate ( $k_2 = 4.14 \times 10^5 \text{ M}^{-1} \text{ s}^{-1}$  at  $T = 20^\circ\text{C}$  versus  $2.92 \times 10^5 \text{ M}^{-1} \text{ s}^{-1}$  at  $T = -15^\circ\text{C}$ ) (table S16) (15). Because quantum mechanical tunneling does not follow the traditional rules of chemical kinetics (47), the insensitivity of reaction rates to the temperature is additional evidence for its involvement. Overall, we propose this  $\gamma$ -terpinene-based process to be based on a photoredox-initiated radical chain propagation (Fig. 3C). The SET oxidation of NaCl or  $\text{NaN}_3$  additives is used to access the corresponding  $\text{Cl}^\bullet$  or  $\text{N}_3^\bullet$ . These species would initiate the radical propagation by generating the cyclohexadienyl radical **4•** through fast and favorable H-atom abstraction with cyclohexadiene [or  $\gamma$ -terpinene (48)]. Quantum mechanical tunneling-enabled aromatization-halogen-atom transfer would convert, through the reactivity of a formal H atom, the various starting materials into the corresponding alkyl and aryl radicals. These species can re-initiate the chain by HAT on **4** (49) (or  $\gamma$ -terpinene) or engage first in other types of reactivity (i.e., cyclization or Giese addition). Computational analysis for the reaction profile of the various halogen-atom and group transfer processes realized in Fig. 1C on other types of alkyl and aryl derivatives resulted in similar reaction parameters and barrier features (table S10). Collectively, these results support quantum mechanical tunneling as an important component for the whole class of radical generations.

Our current understanding of halogen-atom and group transfer chemistry is based around the consideration of enthalpic and polar effects. The results presented here demonstrate

that transition state theory is not the only framework to approach these reactions and that quantum tunneling can be leveraged to enable otherwise elusive types of reactivity. We hope that this blueprint for carbon radical generation might stimulate the development of further alternative strategies that challenge thermodynamic and kinetic control.

## REFERENCES AND NOTES

- S. P. Pitre, N. A. Weires, L. E. Overman, *J. Am. Chem. Soc.* **141**, 2800–2813 (2019).
- S. Crespi, M. Fagnoni, *Chem. Rev.* **120**, 9790–9833 (2020).
- M. Yan, J. C. Lo, J. T. Edwards, P. S. Baran, *J. Am. Chem. Soc.* **138**, 12692–12714 (2016).
- M. P. Plesniak, H.-M. Huang, D. J. Procter, *Nat. Rev. Chem.* **1**, 0077 (2017).
- F. Dénès, C. H. Schiesser, P. Renaud, *Chem. Soc. Rev.* **42**, 7900–7942 (2013).
- S. Z. Zard, *Org. Lett.* **19**, 1257–1269 (2017).
- J. Wu, R. M. Bär, L. Guo, A. Noble, V. K. Aggarwal, *Angew. Chem. Int. Ed.* **58**, 18830–18834 (2019).
- F. Juliá, T. Constantin, D. Leonori, *Chem. Rev.* **122**, 2292–2352 (2022).
- C. Chatgililoglu, C. Ferreri, Y. Landais, V. I. Timokhin, *Chem. Rev.* **118**, 6516–6572 (2018).
- R. H. Krech, D. L. McFadden, *J. Am. Chem. Soc.* **99**, 8402–8405 (1977).
- P. A. Baguley, J. C. Walton, *Angew. Chem. Int. Ed.* **37**, 3072–3082 (1998).
- C. Le, T. Q. Chen, T. Liang, P. Zhang, D. W. C. MacMillan, *Science* **360**, 1010–1014 (2018).
- W. P. Neumann, *Synthesis* **1987**, 665–683 (1987).
- Y.-R. Luo, *Comprehensive Handbook of Chemical Bond Energies* (CRC Press, ed. 1, 2007).
- See the supplementary materials for more information.
- A. Bhunia, A. Studer, *Chem. Rev.* **20**, 2060–2100 (2021).
- G. Birmore, J. C. Walton, L. Cardellini, *J. Chem. Soc. Chem. Commun.* **1995**, 27–28 (1995).
- A. Studer, S. Amrein, *Angew. Chem. Int. Ed.* **39**, 3080–3082 (2000).
- A. Studer, S. Amrein, F. Schlieh, T. Schulte, J. C. Walton, *J. Am. Chem. Soc.* **125**, 5726–5733 (2003).
- J. C. Walton, A. Studer, *Acc. Chem. Res.* **38**, 794–802 (2005).
- N. G. W. Cowper, C. P. Chernowsky, O. P. Williams, Z. K. Wickens, *J. Am. Chem. Soc.* **142**, 2093–2099 (2020).
- H. A. Sakai, W. Liu, C. C. Le, D. W. C. MacMillan, *J. Am. Chem. Soc.* **142**, 11691–11697 (2020).
- I. Ghosh, T. Ghosh, J. I. Bardagi, B. König, *Science* **346**, 725–728 (2014).
- C. M. Hendy, G. C. Smith, Z. Xu, T. Lian, N. T. Jui, *J. Am. Chem. Soc.* **143**, 8987–8992 (2021).
- T. Q. Chen, D. W. C. MacMillan, *Angew. Chem. Int. Ed.* **58**, 14584–14588 (2019).
- I. A. MacKenzie et al., *Nature* **580**, 76–80 (2020).
- Z. J. Song et al., *Org. Process Res. Dev.* **25**, 82–88 (2021).
- I. S. Young, Y. Qiu, M. J. Smith, M. B. Hay, W. W. Doubleday, *Org. Process Res. Dev.* **20**, 2108–2115 (2016).
- C. Gütz, M. Bänziger, C. Bucher, T. R. Galvão, S. R. Waldvogel, *Org. Process Res. Dev.* **19**, 1428–1433 (2015).
- K. U. Ingold, J. Luszyk, J. C. Scaiano, *J. Am. Chem. Soc.* **106**, 343–348 (1984).
- M. Salamone, G. A. DiLabio, M. Bietti, *J. Am. Chem. Soc.* **133**, 16625–16634 (2011).
- J. W. Taylor et al., *J. Phys. Chem. A* **108**, 7193–7203 (2004).
- A. Effio, D. Griller, K. U. Ingold, J. C. Scaiano, S. J. Sheng, *J. Am. Chem. Soc.* **102**, 6063–6068 (1980).
- M. Ballestri et al., *J. Org. Chem.* **56**, 678–683 (1991).
- C. Chatgililoglu, *Acc. Chem. Res.* **25**, 188–194 (1992).
- A. Studer, D. P. Curran, *Angew. Chem. Int. Ed.* **50**, 5018–5022 (2011).
- C. P. Andrieux, J. Pinson, *J. Am. Chem. Soc.* **125**, 14801–14806 (2003).
- A. Nandi, Z. Alassad, A. Milo, S. Kozuch, *ACS Catal.* **11**, 14836–14841 (2021).
- D. Ley, D. Gerbig, P. R. Schreiner, *Org. Biomol. Chem.* **10**, 3781–3790 (2012).
- P. R. Schreiner et al., *Science* **332**, 1300–1303 (2011).
- P. R. Schreiner, *Trends Chem.* **2**, 980–989 (2020).
- E. M. Greer, K. Won, A. Greer, C. Doubleday, *Tetrahedron* **72**, 7357–7373 (2016).
- P. R. Schreiner, *J. Am. Chem. Soc.* **139**, 15276–15283 (2017).

44. J. Meisner, J. Kästner, *Angew. Chem. Int. Ed.* **55**, 5400–5413 (2016).
45. J. Ho *et al.*, *J. Org. Chem.* **78**, 6677–6687 (2013).
46. R. T. Skodje, D. G. Truhlar, B. C. Garrett, *J. Phys. Chem.* **85**, 3019–3023 (1981).
47. S. H. Bae *et al.*, *J. Am. Chem. Soc.* **141**, 7675–7679 (2019).
48. B. Schweitzer-Chaput, M. A. Horwitz, E. de Pedro Beato, P. Melchiorre, *Nat. Chem.* **11**, 129–135 (2019).
49. M. Newcomb, S. U. Park, *J. Am. Chem. Soc.* **108**, 4132–4134 (1986).

## ACKNOWLEDGMENTS

**Funding:** D.L. thanks EPSRC for a fellowship (EP/P004997/1), the European Research Council for a research grant (758427), and the Leverhulme Trust for additional support (Philip Leverhulme

Prize). S.L. thanks CNRS and ANR (PhotoFlat N°220424) for financial support. N. S. Sheikh is kindly acknowledged for initial calculations. **Author contributions:** T.C., B.G., M.J.T., F.J., H.Z., S.L., and D.L. designed the project. T.C. and B.G. performed the synthetic experiments. M.J.T. and H.Z. performed the computational studies. S.C. performed the laser flash photolysis experiments. K.J.G. performed the scale-up optimization in flow. All authors analyzed the results and were involved in the mechanistic understanding of the process. **Competing interests:** The authors declare no competing interests. **Data and materials availability:** All data are available in the main text or the supplementary materials. **License information:** Copyright © 2022 the authors, some rights reserved; exclusive licensee American Association for the Advancement of Science. No claim to original US

government works. <https://www.science.org/about/science-licenses-journal-article-reuse>

## SUPPLEMENTARY MATERIALS

[science.org/doi/10.1126/science.abq8663](https://science.org/doi/10.1126/science.abq8663)  
Materials and Methods  
Figs. S1 to S35  
Tables S1 to S34  
NMR Spectra  
References (50–170)  
Data S1

Submitted 5 May 2022; accepted 10 August 2022  
10.1126/science.abq8663

## MICROBIOME

## Codiversification of gut microbiota with humans

Taichi A. Suzuki<sup>1†</sup>, J. Liam Fitzstevens<sup>1†</sup>, Victor T. Schmidt<sup>1</sup>, Hagay Enav<sup>1</sup>, Kelsey E. Huus<sup>1</sup>, Mirabeau Mbon Ngwese<sup>1</sup>, Anne Griebshammer<sup>2</sup>, Anne Pfeleiderer<sup>3</sup>, Bayode R. Adegbite<sup>3,4</sup>, Jeannot F. Zinsou<sup>3,4</sup>, Meral Esen<sup>3,5,6</sup>, Thirumalaisamy P. Velavan<sup>3,7</sup>, Ayola A. Adegnika<sup>3,4,5,8</sup>, Le Huu Song<sup>7,9</sup>, Timothy D. Spector<sup>10</sup>, Amanda L. Muehlbauer<sup>11</sup>, Nina Marchi<sup>12</sup>, Hyena Kang<sup>13</sup>, Lisa Maier<sup>2,6</sup>, Ran Blekhan<sup>14</sup>, Laure Ségurel<sup>12,15</sup>, GwangPyo Ko<sup>13</sup>, Nicholas D. Youngblut<sup>1</sup>, Peter Kreamsner<sup>3,4,5,6</sup>, Ruth E. Ley<sup>16\*</sup>

The gut microbiomes of human populations worldwide have many core microbial species in common. However, within a species, some strains can show remarkable population specificity. The question is whether such specificity arises from a shared evolutionary history (codiversification) between humans and their microbes. To test for codiversification of host and microbiota, we analyzed paired gut metagenomes and human genomes for 1225 individuals in Europe, Asia, and Africa, including mothers and their children. Between and within countries, a parallel evolutionary history was evident for humans and their gut microbes. Moreover, species displaying the strongest codiversification independently evolved traits characteristic of host dependency, including reduced genomes and oxygen and temperature sensitivity. These findings all point to the importance of understanding the potential role of population-specific microbial strains in microbiome-mediated disease phenotypes.

**A**cross populations, humans share many of the same bacterial and archaeal species in their gut microbiomes (1–3). Within these cosmopolitan species, different strains can dominate in different populations (4–7). Strain variation can arise in several ways, from the uptake of new strains to their in situ evolution (8). When strains and their hosts evolve in parallel, they codiversify, and as a result, their phylogenies are congruent. Codiversification provides opportunities to develop intimate host-microbial relationships across multiple generations (9).

Previous work showed that a small subset of gut bacterial lineages speciated with hominid ancestors (10), but whether such patterns of codiversification extended within host species, and specifically within humans, remained to be demonstrated. There are reasons not to expect to see codiversification with humans: Our diets have changed with time, our populations have expanded across the world, and modern lifestyles may have blurred any signals (11). The identification of species that codiversified with humans has important implications for understanding how humans evolved with their microbiomes and how strains within species may interact with specific host populations (12).

Several human gut microbes are thought to have followed patterns of human migration out of Africa. A notable example is the stomach-dwelling bacterium *Helicobacter pylori*, the causative agent of gastritis and stomach cancer. Cultured isolates of *H. pylori* show spatial patterns of strain diversity consistent with human migration patterns (13). A few prevalent gut microbial species, including *Prevotella copri*, are also thought to have tracked human migration, given how patterns of metagenome-derived strain variation mapped onto continents (4–6). Strain distributions that map onto human migration patterns are suggestive of codiversification, as geographic origins tend to reflect human genetic origins, especially at the continental level (14, 15). But on finer geographic and population scales, such as within countries, the assumption that geography can stand in for genotype weakens (15). A host phylogeny is required to directly test for codiversification by comparison to microbial phylogenies. Such comparative phylogenetic analyses would also allow microbial taxa to be ranked by the degree of cophylogeny they display.

Given the paucity in the public domain of matched human genotype and gut metagenome

datasets required for testing for codiversification, especially for undersampled regions (16), we generated new paired datasets from individuals that we sampled in Gabon, Vietnam, and Germany. We also leveraged existing datasets for subjects from Cameroon, the Republic of Korea (South Korea), and the UK by generating fecal metagenomes and/or host genotype data (17–20) (Fig. 1A and table S1). In addition, we collected fecal metagenomes from children whose mothers were study participants in Gabon, Vietnam, and Germany (Fig. 1A and table S2). Altogether, our combined dataset of 839 adults and 386 children allowed us to assess codiversification between humans and gut microbial species shared across and within populations.

Using 20,506 single-nucleotide polymorphisms, we created a maximum likelihood phylogeny to represent the genetic relatedness of the human subjects. As expected, humans clustered into three robust major groups matching their geographic origins (21), where individuals from Asia and Europe formed sister clades nested within individuals from Africa (Fig. 1B). We selected bacterial and archaeal species present in the guts of ≥100 adults with ≥10 individuals per major human group and ≥1 individual per country (see methods

<sup>1</sup>Department of Microbiome Science, Max Planck Institute for Biology, Tübingen, Germany. <sup>2</sup>Interfaculty Institute of Microbiology and Infection Medicine, University of Tübingen, Tübingen, Germany. <sup>3</sup>Institute for Tropical Medicine, University of Tübingen, Tübingen, Germany. <sup>4</sup>Centre de Recherches Médicales de Lambaréné, Lambaréné, Gabon. <sup>5</sup>German Center for Infection Research, Tübingen, Germany. <sup>6</sup>Cluster of Excellence EXC 2124 Controlling Microbes to Fight Infections, University of Tübingen, Tübingen, Germany. <sup>7</sup>Vietnamese German Center for Medical Research, Hanoi, Vietnam. <sup>8</sup>Fondation pour la Recherche Scientifique, Cotonou, Bénin. <sup>9</sup>108 Military Central Hospital, Hanoi, Vietnam. <sup>10</sup>Department of Twin Research and Genetic Epidemiology, King's College London, London, UK. <sup>11</sup>Department of Ecology, Evolution, and Behavior, University of Minnesota, Minneapolis, MN, USA. <sup>12</sup>Eco-anthropologie, Muséum National d'Histoire Naturelle, CNRS, Université de Paris, Paris, France. <sup>13</sup>Department of Environmental Health Sciences, Graduate School of Public Health, Seoul National University, Seoul, Republic of Korea. <sup>14</sup>Department of Genetics, Cell Biology, and Development, University of Minnesota, Minneapolis, MN, USA. <sup>15</sup>Laboratoire de Biométrie et Biologie Evolutive, CNRS, Université Lyon 1, Villeurbanne, France.

\*Corresponding author. Email: rley@tuebingen.mpg.de

†These authors contributed equally to this work.

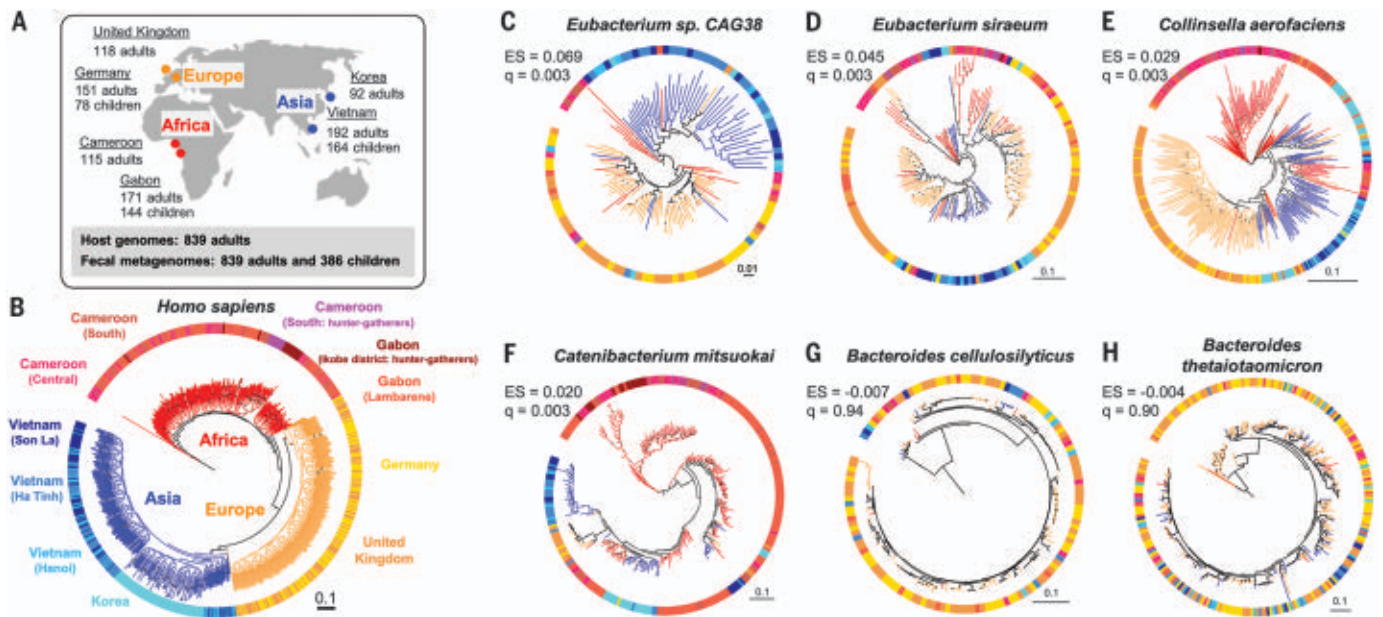


**Fig. 1. The human phylogeny and selected bacterial phylogenies.** (A) Sampling locations and sizes. (B) A maximum likelihood phylogeny of human subjects based on 20,506 single-nucleotide polymorphisms. Tree branch colors indicate continental origins. Outer strip colors indicate finer geographic locations, and labels refer to sampling locations. (C to H) Maximum likelihood phylogenies for

six bacterial species based on species-specific marker genes. PACo effect size (ES) and  $q$  values ( $q$ ) are shown. Bootstrap values >50% are plotted on branches, and all phylogenies are rooted at the midpoint. Colors of branches and outer strips correspond to sampling locations shown in (B). The scale bars show substitutions per site for all phylogenies.

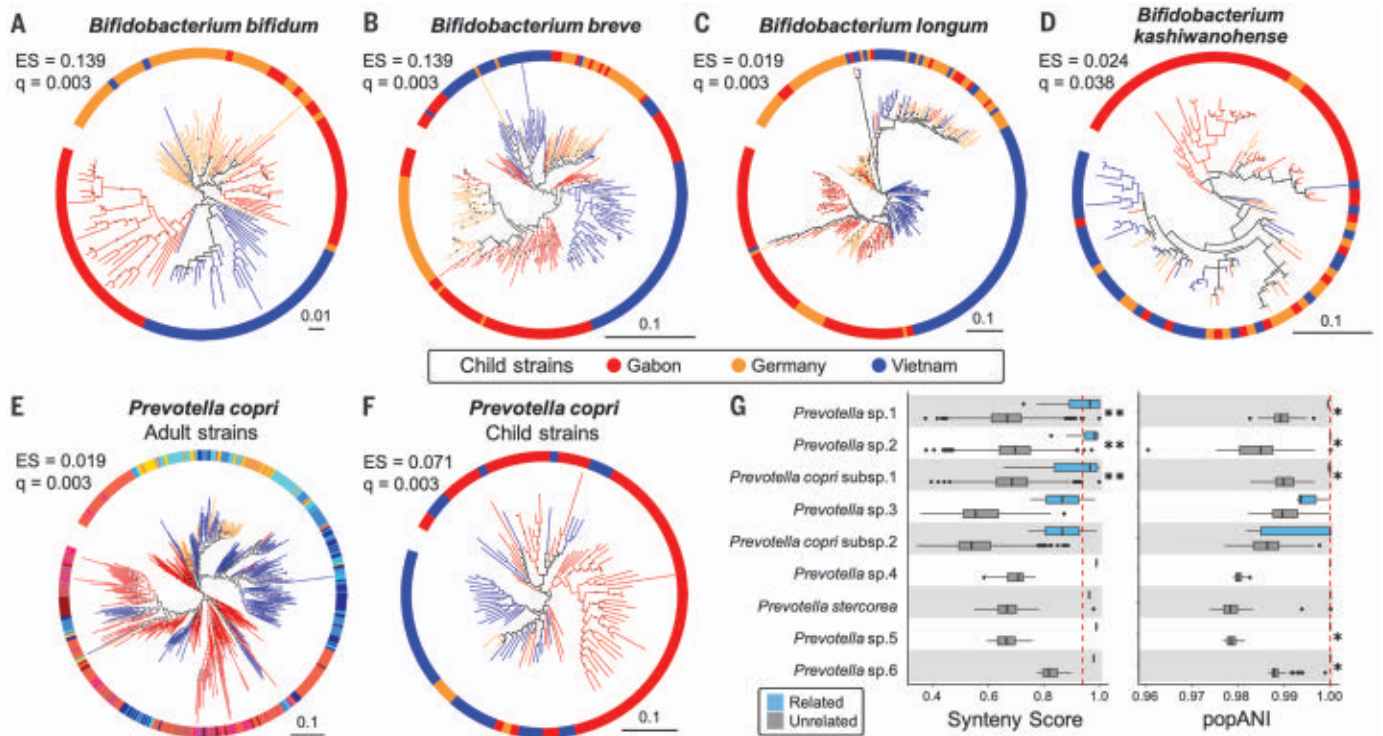


**Fig. 2. Bacterial phylogenies derived from children's microbiomes and strain sharing with their mothers.** (A to D) Four species of *Bifidobacterium* show evidence of cophylogeny based on mothers' genotypes. (E) Phylogeny of *P. copri* strains in adults and (F) in children. The colors in (E) correspond to those in Fig. 1B. Bootstrap values  $\geq 50\%$  are shown as black dots on branches, and the phylogenies are rooted at the midpoint. The scales show substitutions per site. (G) *Prevotella* strain sharing between mothers and their own children ("related,"

blue boxplots) compared with sharing between women and unrelated children ("unrelated," gray boxplots). (Left) Strain comparisons using SynTracker (39). (Right) Strain comparisons using inStrain (40). Dashed red lines indicate the thresholds for strain sharing events [0.96 for synteny; 0.99999 for popANI (population-level average nucleotide identity)]. \* $P < 0.05$  and \*\* $P < 5 \times 10^{-5}$  using Wilcoxon-Mann-Whitney test. Codiversification test results for all 20 common child taxa are reported in table S11.

in the supplementary materials and table S3). We then created phylogenies for the resulting 59 species using two methods: (i) species-specific marker genes with StrainPhlan3 (7) and (ii) metagenome-assembled genomes (MAGs) using PhyloPhlAn (22). MAG-based trees were obtained for 33 of 59 taxa in adults.

Among the 59 taxa assessed for codiversification, 36 taxa have phylogenies that are more similar to the human host phylogeny than to a permuted host phylogeny [ $q < 0.05$ , PACo positive effect size (ES); see methods]. *Eubacterium* species showed the largest ES

( $q < 0.003$ ; Fig. 1, C and D, and table S4). Similar results were obtained using two other methods, Parafit (23) and Phytools (24) (tables S4 and S5). Seven species that showed significant codiversification across all three tests included *Collinsella aerofaciens* (Fig. 1E), *Catenibacterium mitsuokai* (Fig. 1F), *Eubacterium rectale*, and *P. copri* (table S4). In contrast, *Bacteroides*, *Alistipes*, and *Parabacteroides* species generally showed the least evidence of cophylogeny (Fig. 1, G and H, and table S4). Results were robust to sample size (tables S6 and S7 and fig. S1) and to bootstrap

support for 36 to 50% of taxa (tables S4 and S8). Overall, species within the Firmicutes phylum showed more evidence of cophylogeny (Wilcoxon rank sum test,  $P = 7.6 \times 10^{-6}$ ) than others, and Bacteroidetes species showed least (Wilcoxon rank sum test,  $P = 1.5 \times 10^{-6}$ ).

We also searched for a codiversification signal within each country. For a subset of taxa, we observed codiversification in multiple countries independently (table S9). Within-country tests included fewer individuals, so the codiversification signal tended to be weaker. Overall, 20 of 59 taxa showed positive ES with uncorrected  $P < 0.05$  in at least one country, but only one taxon remained significant after false discovery rate (FDR) correction: *P. copri* within Gabon ( $q = 0.042$ ; table S9). Notably, three species (*P. copri*, *Coprococcus eutactus*, and *E. rectale*) had uncorrected  $P < 0.05$  in three countries independently (table S9). These within-country results indicate that codiversification is robust to hosts living in a shared environment and suggest that codiversification is not driven by continental-scale processes alone.

We sampled the gut metagenomes of children (average age = 7.4 months) of the genotyped participants in Gabon, Vietnam, and Germany. Using the mothers' genotypes allowed us an unprecedented opportunity to test for codiversification of the child gut microbiome. Among the 20 most prevalent child taxa tested (table S10), nine showed evidence of codiversification ( $q < 0.05$ ) (table S11). All four *Bifidobacterium* species tested showed significant PACo ES ( $q < 0.05$ ) (Fig. 2, A to D, and table S11). According to MAG-based phylogenies, *Bifidobacterium longum* showed the strongest evidence of codiversification in children (table S12). The signals of codiversification for several taxa also extended within countries in children in Gabon and Germany, but not in Vietnam (table S11). These results show that microbes common to the gut in early childhood have also codiversified with humans.

There is little overlap in species composition between adult and child microbiomes; nevertheless, of the overlapping 12 species detected, *P. copri* (Fig. 2, E and F) and *Blautia weizlerae* showed evidence of codiversification in both adults ( $q < 0.01$ ; table S4) and children ( $q < 0.01$ ; table S11). In addition, we observed that mothers and their children share the same strains of *P. copri* (Fig. 2G and fig. S2). For mother-child pairs, strain sharing is often interpreted as vertical transmission, but acquisition of strains from a shared environment cannot be excluded (8). Indeed, our data also support strain sharing between community members: Within sampling locations in Gabon and Vietnam, we observed instances of the same strains in the microbiomes of mothers and unrelated children

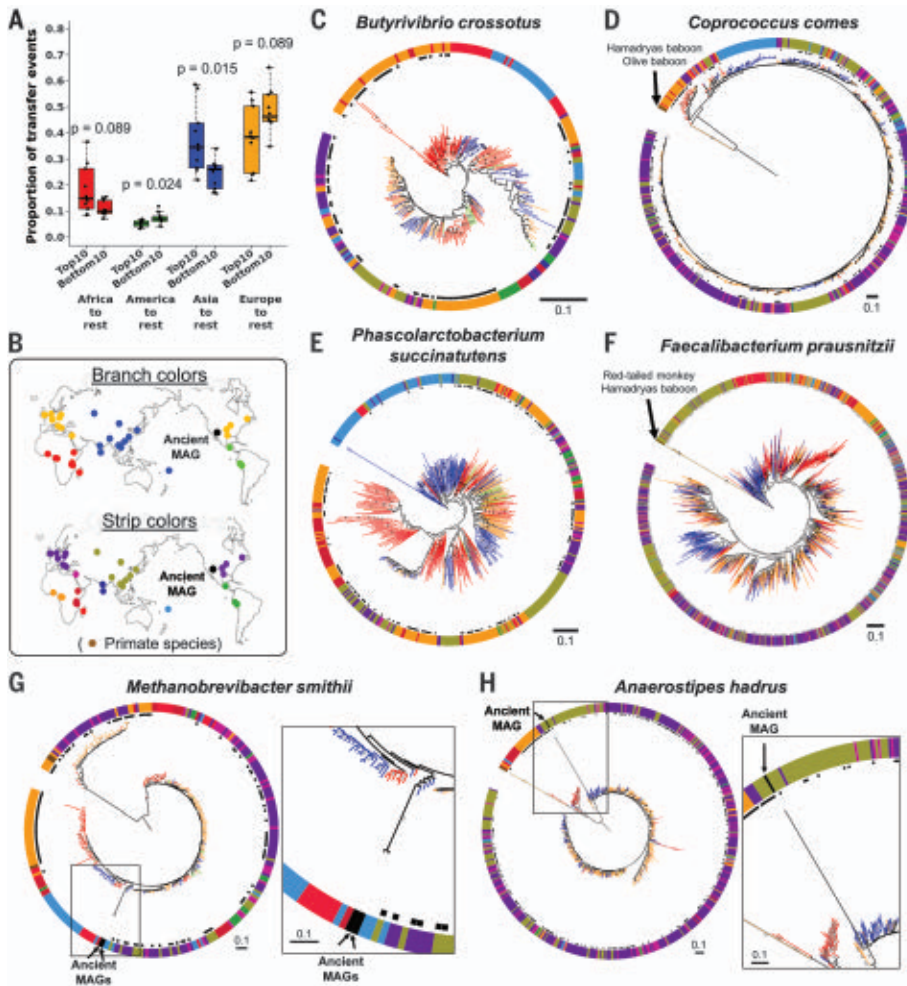


**Fig. 3. Strain transfer events and microbial phylogenies including data from public metagenomes.**

(A) Results from stochastic character mapping on microbial phylogenies including six countries from this study and public metagenomes. The boxplots compare the occurrence of transfer events between sampling regions between the top 10 and bottom 10 taxa identified by PACo ES.  $P$  values are based on the Wilcoxon rank sum test. (B) Sampling locations and color keys correspond to the panels that follow. The colors of the branches and outer color strip indicate the estimated host genetic structure based on sampling locations (21). Black dots next to the color strip indicate samples from the original six countries. Example phylogenies: (C) *Butyrivibrio crossotus*, where African strains are basal; (D) *Coprococcus comes*, where primate strains are basal, followed by African strains; (E) *Phascolarctobacterium succinatutens*, where Asian strains are basal; (F) *Faecalibacterium prausnitzii*, where strains from primates are basal, followed by strains from Asia. (G and H) Examples of microbial phylogenies with ancient MAGs recovered from paleofeces of Native Americans. Bootstrap values  $\geq 50\%$  are shown on branches. All trees were rooted at the midpoint. The scale bars show substitutions per site.

(fig. S2 and tables S13 and S14). Strain sharing is known among families and socially engaging individuals in the human species (25) and other social animal species (26, 27). Although vertical transmission from parents to offspring over long time periods can result in patterns of codiversification, strain transmission between related individuals in the same communities may also contribute to these patterns (28).

Modern humans emerged in Africa before colonizing the rest of the world (29). Microbial species that migrated with their human hosts may also show signatures of out-of-Africa patterns, and, indeed, some bacterial species exhibit such patterns (4–6). To test for an African origin for the species tested here for cophylogeny, we quantified the number and direction of strain transfer events by applying stochastic character mapping. Consistent with out-of-Africa migration events, when the 10 most highly and 10 least highly ranked taxa (by PACo ES) were compared, the top 10 had significantly greater proportions of transfer events from Africa to the rest of the regions compared with the bottom 10 (Wilcoxon rank sum test,  $P = 0.029$ ) (fig. S3). Because this analysis does not require host genotype data, we added data from 1219 public fecal metagenomes derived from other human populations and from wild primates (tables S15 and S16). Trends were the same with the expanded dataset (Wilcoxon rank sum test,  $P = 0.089$ ) (Fig. 3, A to D, and fig. S4). Additionally, the top taxa also showed significantly more transfer events from Asia to other regions (Fig. 3, A, E, and F) and fewer transfer events from America to other regions (Fig. 3A). Our results underscore the fact that each species has its own story. Caveats include inaccurate assumptions of host genetic origin based on sampling locations, or a complex history of strain transmission events among different human populations. As expected from codiversification patterns observed in some bacterial families with hominids (10), for the top taxa, primate strains tend to be basal in relation to all human strains (Fig. 3, D and F). In contrast, taxa with least evidence of cophylogeny had primate strains nested within human strains (fig. S5).

Our inference of strain transfer events is based on present-day strains, yet ancient DNA analysis can provide a snapshot directly from the past. We added high-quality ancient MAGs recovered from 1000- to 2000-year-old paleofeces of Native North American tribes (30) to the phylogenies of five gut microbial species (Fig. 3, G and H, and fig. S6). Consistent with the known migration history of the Americas (31), the ancient MAGs were most closely related to strains from modern East Asians, with high bootstrap values for species with significant codiversification (*Methanobrevibacter smithii*

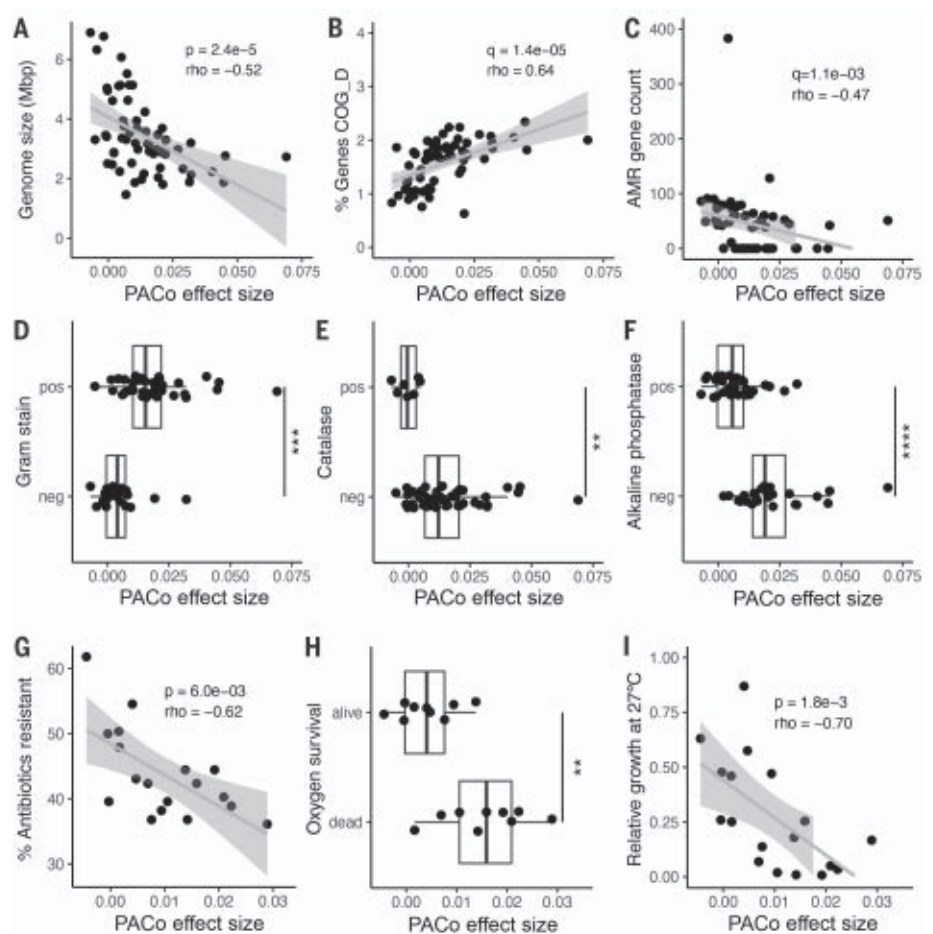


**Fig. 4. Genomic and functional features correlated with codiversification.** PACo effect size correlated with: (A) Median genome size per species. (B) Percentage of total genes in the genome annotated to COG D for cell cycle and replication. (C) Number of antimicrobial resistance (AMR) markers annotated per genome. (D) Predicted Gram stain per species. (E) Predicted catalase activity per species. (F) Predicted alkaline phosphatase activity. (G) Percentage of antibiotics to which the species was resistant in vitro in a panel of 144 common antimicrobials. (H) Survival in vitro after 48 hours of  $O_2$  exposure for a subset of culturable species. (I) Relative growth of each species in vitro at  $27^\circ\text{C}$  compared with  $37^\circ\text{C}$ . (A) to (F):  $n = 59$  species; (G) to (I):  $n = 18$  species. Statistical significance was determined by Spearman's correlation [(A) to (C), (G), and (I)] or by Wilcoxon rank sum test [(D) to (F) and (H)]. Exploratory analyses were corrected using FDR across all gene categories and predicted traits [q value; (B) to (F)]. pos, positive for the given trait; neg, negative for the given trait. \*\* $P < 0.01$ , \*\*\* $P < 0.001$ , \*\*\*\* $P < 0.0001$ . Exact  $P$  values are reported in table S18.

and *Anaerostipes hadrus*; Fig. 3, G and H); this was not the case for taxa that did not show significant codiversification (fig. S6).

We hypothesized that species that codiversified with their hosts are better adapted to the host environment than those that did not. Therefore, we predicted codiversified species (high PACo ES) to be enriched in features characteristic of host adaptation, including genome reduction, enrichment in AT content and essential functions, and depletion of non-essential functions (32). To test for these traits genomically, we collected publicly available genome sequences for the 59 species (table S17). As expected, the degree of codiversification was inversely correlated to genome size

(Fig. 4A) and positively correlated with genomic AT content (fig. S7A). The relationship with genome size, but not with AT content, remained significant after correcting for phylogenetic relatedness (see methods), indicating that genome size reduction arose independently in codiversified taxa.

To further explore the genomic signatures of codiversification, we tested for differences in 67 genomic features, including 23 functional categories [clusters of orthologous groups (COGs)], in addition to pseudogenes, antibiotic resistance markers, plasmid markers, and 41 traits predicted from genomic content (see methods and table S18). Overall, ES correlated with 24 of 67 genomic features (FDR-adjusted

$P < 0.05$ ), and five retained significance after correction for phylogenetic relatedness (table S18). A random forest model including these genomic characteristics accurately predicted ES (PACo  $q < 0.01$ ), with a mean area under the curve of  $0.83 \pm 0.22$  (SD) across a fivefold cross-validation.

PACo ES was significantly correlated with the proportion of the genome dedicated to essential functions such as replication, transcription, and translation (Fig. 4B, fig. S7B, and table S18). In contrast, greater ES was associated with fewer pseudogenes (fig. S7C) and antibiotic resistance markers Fig. 4C, and a smaller proportion of the genome dedicated for nonessential functions, such as secretion and cell wall biogenesis (fig. S7D and table S18). Gram-positive species were enriched for higher ES overall (Fig. 4D). A number of predicted traits related to environmental survival, including oxygen sensitivity (Fig. 4E), inorganic phosphate scavenging (Fig. 4F), and the use of diverse energy sources (fig. S7, E to I, and table S18), were reduced on average in species with high ES.

To directly test the functions predicted from genome-based observations, we assessed in vitro phenotypes of a representative set of 18 culturable species (see methods and table S19). Consistent with the reduction in antibiotic resistance markers, codiversified species exhibited significantly reduced antibiotic resistance in a previously published drug screen of 144 antimicrobial compounds (Fig. 4G) (33). Consistent with the predicted loss of catalase activity, species with higher ES were significantly more likely to die upon exposure to atmospheric oxygen (Fig. 4H). Increased temperature sensitivity has been associated with coevolved insect symbionts and is expected in gut microbes that enjoy a temperature-stable niche (34). Accordingly, we observed that ES was significantly correlated with poor relative growth at below-host temperature (27°C) (Fig. 4I). All in vitro phenotypic associations retained significance after correction for phylogenetic relatedness, even in cases where the corresponding genomic prediction did not (table S18).

Taken together, the features that associate with cophylogeny are highly reminiscent of those commonly seen in host-associated microbes (35–37) and coevolved insect symbionts (32). Patterns of host-microbial codiversification alone do not necessarily imply interactions or adaptations between hosts and microbes (9, 28). However, together with the observed functional attributes, such as smaller genomes and oxygen and temperature sensitivity, codiversified species likely evolved host dependency.

By expanding metagenome collections into poorly characterized populations, and pairing metagenome and host genomic data obtained from the same individuals, we have identified

common members of the human gut microbiota that have independently codiversified with human populations. These codiversified species have repeatedly and independently acquired traits that suggest limited survival capabilities outside of the host (2, 28, 35). Loss of an environmental reservoir can facilitate dependence on resources produced by other gut microbes and/or the host and lead to reduced genome size (35–37). The selection pressure on efficient host-to-host transmission could result in strain sharing between related individuals, or those living in proximity, such as we observed in our populations. Many of the traits characteristic of codiversified species likely adapted to the niche of the animal gut (not necessarily human), and whether humans reciprocally adapted to these microbial species or strains remains to be investigated. The list of codiversified species provides a starting point to investigate host-microbial coevolution in humans (12).

The list of human health conditions linked to the microbiome ranges from malnutrition to allergies and cardiovascular disease. The incidence of these diseases is population specific, and the diversity of microbiomes is also population specific. Several of the species that codiversified with humans, such as *P. copri* (4), *E. rectale* (5), and *B. longum* (38), are known to vary in their functional capacity according to population. An awareness of differences in gut microbial strains between populations has already led to the notion that probiotics for treating malnutrition should be locally sourced (38). The microbiome is a therapeutic target for personalized medicine, and our results underscore the importance of a population-specific approach to microbiome-based therapies.

#### REFERENCES AND NOTES

- V. K. Gupta, S. Paul, C. Dutta, *Front. Microbiol.* **8**, 1162 (2017).
- P. I. Costea et al., *Mol. Syst. Biol.* **13**, 960 (2017).
- E. Pasolli et al., *Cell* **176**, 649–662.e20 (2019).
- A. Tett et al., *Cell Host Microbe* **26**, 666–679.e7 (2019).
- N. Karcher et al., *Genome Biol.* **21**, 138 (2020).
- B. D. Merrill et al., *bioRxiv* 2022.03.30.486478 [Preprint] (2022). <https://doi.org/10.1101/2022.03.30.486478>.
- D. T. Truong, A. Tett, E. Pasolli, C. Huttenhower, N. Segata, *Genome Res.* **27**, 626–638 (2017).
- H. Enav, F. Bäckhed, R. E. Ley, *Cell Host Microbe* **30**, 627–638 (2022).
- N. A. Moran, D. B. Sloan, *PLOS Biol.* **13**, e1002311 (2015).
- A. H. Moeller et al., *Science* **353**, 380–382 (2016).
- A. H. Nishida, H. Ochman, *Nat. Commun.* **12**, 5632 (2021).
- T. A. Suzuki, R. E. Ley, *Science* **370**, eaaz6827 (2020).
- D. Falush et al., *Proc. Natl. Acad. Sci. U.S.A.* **98**, 15056–15061 (2001).
- J. Novembre et al., *Nature* **456**, 98–101 (2008).
- N. A. Rosenberg et al., *Science* **298**, 2381–2385 (2002).
- R. J. Abdill, E. M. Adamowicz, R. Blekhan, *PLOS Biol.* **20**, e3001536 (2022).
- A. Lokmer et al., *PLOS ONE* **14**, e0211139 (2019).
- G. Even et al., *Front. Cell. Infect. Microbiol.* **11**, 533528 (2021).
- M. Y. Lim et al., *Gut* **66**, 1031–1038 (2017).
- H. Xie et al., *Cell Syst.* **3**, 572–584.e3 (2016).
- P. Duda, Jan Zrzavý, *Sci. Rep.* **6**, 29890 (2016).
- F. Asnicar et al., *Nat. Commun.* **11**, 2500 (2020).
- P. Legendre, Y. Desjeux, E. Bazin, *Syst. Biol.* **51**, 217–234 (2002).
- L. J. Revell, *Methods Ecol. Evol.* **3**, 217–223 (2012).
- I. L. Brito et al., *Nat. Microbiol.* **4**, 964–971 (2019).

- J. Jung et al., *eLife* **4**, e05224 (2015).
- A. H. A. H. Moeller et al., *Sci. Adv.* **2**, e1500997–e1500997 (2016).
- M. Groussin, F. Mazel, E. J. Alm, *Cell Host Microbe* **28**, 12–22 (2020).
- R. Nielsen et al., *Nature* **541**, 302–310 (2017).
- M. C. Wibowo et al., *Nature* **594**, 234–239 (2021).
- T. Goebel, M. R. Waters, D. H. O'Rourke, *Science* **319**, 1497–1502 (2008).
- J. P. McCutcheon, N. A. Moran, *Nat. Rev. Microbiol.* **10**, 13–26 (2011).
- L. Maier et al., *Nature* **555**, 623–628 (2018).
- K. E. Huus, R. E. Ley, *mSystems* **6**, e0070721 (2021).
- H. P. Browne et al., *Genome Biol.* **22**, 204 (2021).
- S. Nayfach, Z. J. Shi, R. Seshadri, K. S. Pollard, N. C. Kyrpides, *Nature* **568**, 505–510 (2019).
- S. A. Frese et al., *PLOS Genet.* **7**, e1001314 (2011).
- M. J. Barratt et al., *Sci. Transl. Med.* **14**, eabk1107 (2022).
- H. Enav, R. E. Ley, *bioRxiv* 2021.10.06.463341 [Preprint] (2021). <https://doi.org/10.1101/2021.10.06.463341>.
- M. R. Olm et al., *Nat. Biotechnol.* **39**, 727–736 (2021).
- T. A. Suzuki, L. Fitzstevens, K. Huus, N. Youngblut, leylabmpi/codiversification: Zenodo release, version 1.0.1, Zenodo (2022); <https://doi.org/10.5281/zenodo.6947454>.
- T. A. Suzuki, J. L. Fitzstevens, N. D. Youngblut, R. E. Ley, Phylogenies related to "Codiversification of gut microbiota with humans," *Dryad* (2022); <https://doi.org/10.5061/dryad.qrf6q5k2>.

#### ACKNOWLEDGMENTS

We thank T. H. Nguyen, E. Cosgrove, A. Clark, A. Kostic, M. Taylor, Native American tribe officers (M. Bremer, J. Aguilar, J. Charlie, R. Williams, B. Lewis, S. Anton, A. Garcia-Lewis, and B. Bernstein), S. Dausser and members of the Department of Microbiome Science, and four anonymous reviewers. **Funding:** This work was supported by the Max Planck Society, T.D.S. was funded by the Wellcome Trust, Medical Research Council, European Union, Chronic Disease Research Foundation, Zoe Global Ltd., the National Institute for Health Research-funded BioResource, and the Clinical Research Facility and Biomedical Research Centre based at Guy's and St Thomas' NHS Foundation Trust in partnership with King's College London. L.S. was supported by an Agence Nationale de la Recherche grant (MICROREGAL, ANR-15-CE02-0003). R.B. was supported by NIH grant R35-GM128716.

**Author contributions:** Writing – original draft, Conceptualization, Methodology, and Visualization: T.A.S., J.L.F., H.E., K.E.H., N.D.Y., and R.E.L. Software, Validation, and Formal analysis: T.A.S., J.L.F., H.E., K.E.H., and N.D.Y. Investigation: T.A.S., J.L.F., V.T.S., K.E.H., M.M.N., A.G., A.P., B.R.A., J.F.Z., A.L.M., N.M., H.K., L.M., R.B., L.S., G.K., N.D.Y., and R.E.L. Resources: J.L.F., V.T.S., A.P., B.R.A., J.F.Z., M.E., T.P.V., A.A.A., L.H.S., T.D.S., A.L.M., N.M., H.K., L.M., R.B., L.S., G.K., N.D.Y., P.K., and R.E.L. Data curation: T.A.S., J.L.F., V.T.S., K.E.H., M.M.N., A.L.M., N.M., H.K., R.B., L.S., and N.D.Y. Project administration: T.A.S., J.L.F., V.T.S., L.M., R.B., L.S., G.K., and R.E.L. Supervision: L.M., R.B., L.S., G.K., N.D.Y., P.K., and R.E.L. Funding acquisition: T.D.S., L.M., R.B., L.S., G.K., and R.E.L.

**Competing interests:** G.K. is the founder and a board member of KoBioLabs, Inc. T.D.S. is a cofounder of ZOE Ltd., a personalized nutrition company. **Data and materials availability:** All data used in this study are free to access. The raw sequence data and MAGs are available from the European Nucleotide Archive under the study accession numbers PRJEB40256, PRJEB9584, PRJEB32731, PRJEB27005, PRJEB30834, and PRJEB46788. All sample metadata used in this study are provided in the supplementary materials. The code used in data analysis is outlined on Zenodo (42), and phylogenies and alignments are available in Dryad (42). **License information:** Copyright © 2022 the authors, some rights reserved; exclusive licensee American Association for the Advancement of Science. No claim to original US government works. <https://www.science.org/about/science-licenses-journal-article-reuse>

#### SUPPLEMENTARY MATERIALS

[science.org/doi/10.1126/science.abm7759](https://science.org/doi/10.1126/science.abm7759)

Materials and Methods

Supplemental Results

Figs. S1 to S7

Tables S1 to S19

References (43–80)

MDAR Reproducibility Checklist

Submitted 12 October 2021; accepted 10 August 2022  
10.1126/science.abm7759



## NANOPHOTONICS

## Few-cycle vacuum squeezing in nanophotonics

Rajveer Nehra<sup>1†</sup>, Ryoto Sekine<sup>1†</sup>, Luis Ledezma<sup>1,2</sup>, Qiushi Guo<sup>1</sup>,  
Robert M. Gray<sup>1</sup>, Arkadev Roy<sup>1</sup>, Alireza Marandi<sup>1\*</sup>

One of the most fundamental quantum states of light is the squeezed vacuum, in which noise in one of the quadratures is less than the standard quantum noise limit. In nanophotonics, it remains challenging to generate, manipulate, and measure such a quantum state with the performance required for a wide range of scalable quantum information systems. Here, we report the development of a lithium niobate-based nanophotonic platform to demonstrate the generation and all-optical measurement of squeezed states on the same chip. The generated squeezed states span more than 25 terahertz of bandwidth supporting just a few optical cycles. The measured 4.9 decibels of squeezing surpass the requirements for a wide range of quantum information systems, demonstrating a practical path toward scalable ultrafast quantum nanophotonics.

Quantum information processing offers great promise for computation, secure communication, metrology, and sensing. Many physical platforms such as nuclear spins, superconducting circuits, photonics, trapped ions, quantum dots, and neutral atoms have widely been explored in the pursuit to build quantum information processors (1). Among these, photonics stands out because of its potential for scalability, room-temperature logical operations, and ease of encoding quantum information in both discrete and continuous variables (2).

In continuous-variable (CV) quantum photonics, information is encoded in continuous amplitude and phase values of the quantized electromagnetic field. The single-mode and multimode squeezed states are widely used for various applications, including quantum-enhanced interferometry such as in the Laser Interferometer Gravitational-Wave Observatory (3), microscopy (4), and quantum teleportation (5). Moreover, highly entangled CV quantum states, that is, cluster states (6–8), serve as a universal resource for one-way quantum computation.

Typically, such high-quality CV states are generated from a single- or two-mode squeezed vacuum produced using quadratic [ $\chi^{(2)}$ ] parametric processes either in bulk crystals or waveguides with large (~10 to 100  $\mu\text{m}^2$ ) mode areas (6–10). Although such experiments using bulky discrete components have been successful in demonstrating small- and medium-scale quantum circuits, it is desirable to achieve CV quantum states with comparable qualities in nanophotonics to enable large-scale integrated quantum circuits.

In nanophotonics, silicon nitride (SiN) and silica platforms have been used for many quantum photonic experiments, such as entangled photon-pair generation, squeezing, error correction, and small-scale Gaussian boson sampling (11–13). However, their inherently weak cubic [ $\chi^{(3)}$ ] nonlinearity typically necessitates using high-quality factor resonators, which imposes limitations on accessible squeezing levels and bandwidths. Despite advances, the measured squeezing levels have so far remained around 2 dB in nanophotonics (see supplementary materials, section 8).

On the other hand, the measurements in CV quantum systems have typically relied on balanced homodyne detection using highly efficient and low-noise photodetectors, which are limited to bandwidths in the mega- to gigahertz range (14). Moreover, in nanophotonics, the loss associated with transferring the microscopic quantum states from a tightly confined mode to a photodetector has imposed barriers in the measurement capabilities of such states (15–17). A potential solution for these measurement challenges lies in all-optical measurement schemes based on a noiseless phase-sensitive amplifier with sufficiently large gain (18–21) that can eliminate the bandwidth limitations of homodyne detection and the sensitivity to detection losses. However, achieving such large gains (>30 dB) over broad optical bandwidths is challenging in nanophotonics with cubic nonlinearity (22). Such an all-optical measurement allows one to exploit the entire optical bandwidth of quantum fields and thereby paves a practical path toward ultrafast all-optical CV quantum information processors using time- and frequency-multiplexed schemes (6–8).

Recently, lithium niobate (LN) nanophotonics has opened promising avenues in optical communication, sensing, and computation owing to its extraordinary optical, electrical, and acoustic properties (23). A combination of subwavelength confinement of the optical mode, strong  $\chi^{(2)}$  nonlinearity, high-fidelity

quasi-phase-matching by periodic poling, and dispersion engineering for longer interaction lengths has enabled devices outperforming the traditional LN devices (24–26).

In this work, we used a nanophotonic circuit in LN to experimentally demonstrate the generation and all-optical measurement of an ultra-short-pulse squeezed vacuum as the building block of scalable CV quantum nanophotonics. Our circuit combines two dispersion-engineered phase-sensitive optical parametric amplifiers (OPAs) (24) (Fig. 1). The first OPA generates a microscopic squeezed vacuum, which is then amplified with a high-gain OPA to macroscopic levels within the same nanophotonic chip. The resulting macroscopic field carries information about the microscopic squeezed state, which can be measured with a high tolerance to loss.

The phase-space distributions for the vacuum (black circle) and the phase-quadrature squeezed vacuum (filled ellipse) are shown in Fig. 1A. The measurement OPA selects a certain quadrature of the microscopic squeezed field and amplifies it to macroscopic levels, in principle without adding any noise. In Fig. 1, B and C, the phase-space distributions (filled ellipses) corresponding to amplified anti-squeezed and amplified squeezed quadratures are shown for two particular pump phases of the measurement OPA,  $\phi_{\text{pump}2}$ . We set  $\phi_{\text{pump}1} = 0$  and use it as the phase reference for pump 2.

In the case of Fig. 1B with  $\phi_{\text{pump}2} = 0$ , the anti-squeezed quadrature (Q) is amplified while the orthogonal phase quadrature (P) is deamplified such that the output field is dominated entirely by the Q quadrature, and the P quadrature can be considered negligible. In such a high-gain amplification regime, the total average photon number (power) of the output field is  $\langle \hat{N}_+ \rangle \propto \langle \hat{Q}_{\text{sq-amp}}^2 \rangle \approx \mathcal{O}(10^5)$ , where  $\langle \hat{N}_+ \rangle$  and  $\langle \hat{Q}_{\text{sq-amp}}^2 \rangle$  denote the photon number and quadrature operators, respectively, for the amplified anti-squeezed quadrature. Likewise, by changing the pump phase of the measurement OPA to  $\phi_{\text{pump}2} = \pi$ , the original squeezed quadrature is amplified to achieve  $\langle \hat{N}_- \rangle \propto \langle \hat{P}_{\text{sq-amp}}^2 \rangle \approx \mathcal{O}(10^3)$ , where  $\langle \hat{N}_- \rangle$  and  $\langle \hat{P}_{\text{sq-amp}}^2 \rangle$  represent the photon number and quadrature operators, respectively, for the amplified squeezed quadrature (Fig. 1C). As a result, the macroscopic output of the measurement OPA provides a direct all-optical measurement for the quadrature variances of the microscopic squeezed state. Likewise, we determine the quadrature variances of the microscopic vacuum state by measuring the average photon number of the macroscopic amplified vacuum state when the squeezer OPA pump 1 is blocked. The phase-space distributions of the amplified vacuum are represented as the black ellipses in Fig. 1, B and C, corresponding to  $\phi_{\text{pump}2} = 0$  and

<sup>1</sup>Department of Electrical Engineering, California Institute of Technology, Pasadena, CA 91125, USA. <sup>2</sup>Jet Propulsion Laboratory, California Institute of Technology, Pasadena, CA 91109, USA.

\*Corresponding author. Email: marandi@caltech.edu (A.M.); rnehra@caltech.edu (R.N.)

†These authors contributed equally to this work.

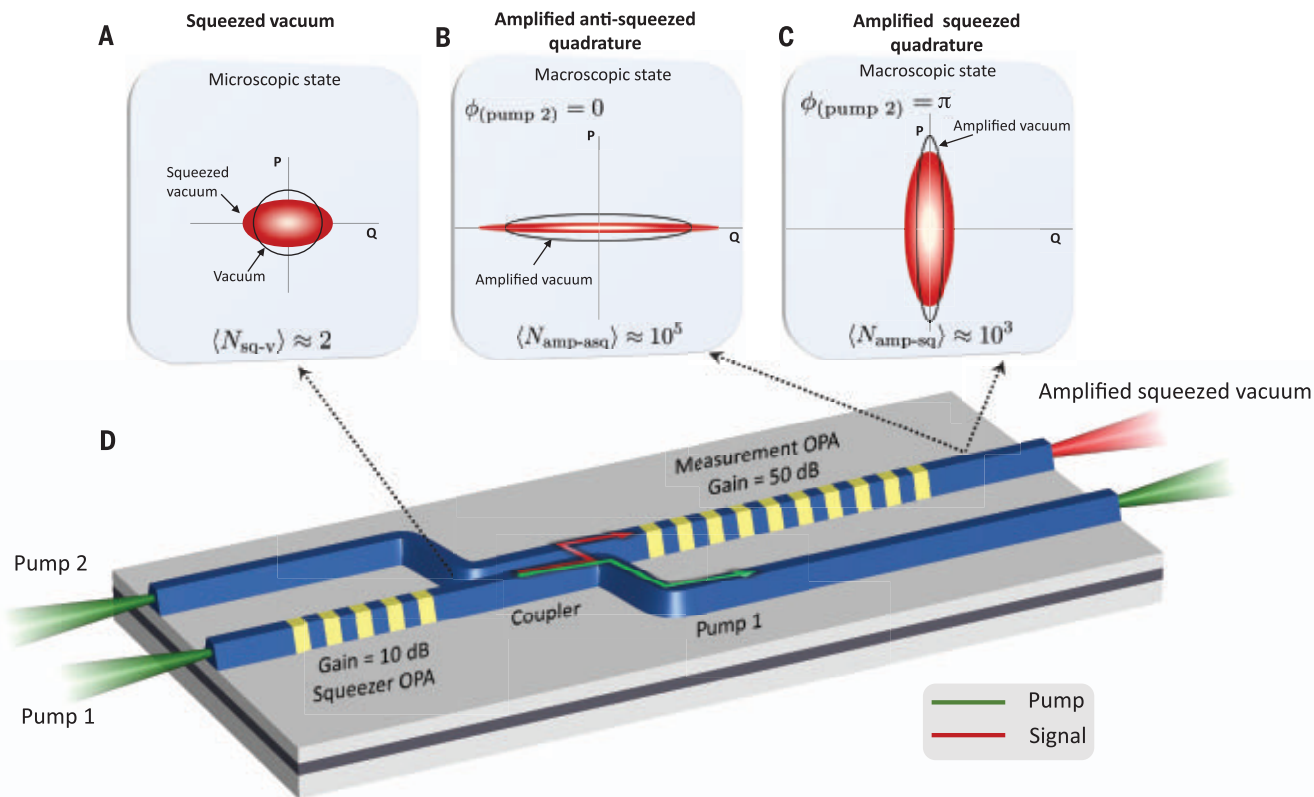


**Fig. 1. Illustration of the generation of a squeezed vacuum and its all-optical measurement in nanophotonics.** Phase-space distributions (filled ellipses) of (A) phase-quadrature squeezed vacuum, and its amplification in the (B) anti-squeezed and (C) squeezed quadratures. The black circle in (A) represents the microscopic vacuum state, and black ellipses in (B) and (C) correspond to the macroscopic vacuum state amplified in Q and P quadratures, respectively. (D) Sketch of our nanophotonic device consisting of the squeezer OPA, tapered adiabatic coupler, and measurement OPA. When pumped, the squeezer OPA generates a

squeezed vacuum state, which is selectively coupled into an adjacent waveguide. It is subsequently amplified by the measurement OPA to macroscopic power levels. The measurement OPA amplifies the quadrature under measurement to sufficiently above the vacuum noise, thereby making the measurement insensitive to losses due to off-chip coupling and imperfect detection. For (A), (B), and (C), we consider 10 dB of squeezing with mean photon number  $\langle N_{sq-v} \rangle \approx 2$ , and a 50 dB phase-sensitive gain in the measurement OPA, thereby amplifying the few-photon squeezed state to a macroscopic power level.

$\phi_{pump2} = \pi$ , respectively. The anti-squeezing ( $S_+$ ) and squeezing ( $S_-$ ) can then be determined as  $S_{\pm}[\text{dB}] = 10\log_{10}[\langle \hat{N}_{\pm} \rangle / \langle \hat{N}_{v_{\pm}} \rangle]$ , where  $\langle \hat{N}_{v_{\pm}} \rangle \propto \langle \hat{Q}_{v-amp}^2 \rangle$  and  $\langle \hat{N}_{v_{\pm}} \rangle \propto \langle \hat{P}_{v-amp}^2 \rangle$  denote the average photon number of the vacuum state amplified in the amplitude and phase quadratures, respectively (Fig. 1, B and C).

In the ideal case, the squeezing (anti-squeezing) can be determined as

$$S_{\pm}[\text{dB}] = 10\log_{10} \left[ \frac{\sinh^2(r_2 \pm r_1)}{\sinh^2 r_2} \right] \quad (1)$$

where  $r_1$  and  $r_2$  are the gain parameters for the squeezer and measurement OPAs, respectively. Sufficient gain (>33 dB for ~11 dB of squeezer OPA gain; supplementary materials, section 5) in the measurement OPA allows a direct measurement of the phase-squeezed vacuum generated in the squeezer OPA. Crucially, the high-gain measurement OPA makes our measurement tolerant to off-chip coupling

losses and photodetection inefficiencies as high as ~7 dB (supplementary materials, section 4).

In experiments, the squeezer (low-gain) and measurement (high-gain) OPAs of our circuit are periodically poled with lengths of 2.5 and 5.0 mm, respectively. The output of the squeezer OPA (microscopic squeezed vacuum) is coupled to the measurement OPA through a directional coupler. To make our directional coupler broadband and less susceptible to fabrication imperfections, we used an adiabatic design where both of the waveguides are tapered, while keeping the gap constant throughout the coupler length. The coupler directs the squeezed vacuum to the adjacent waveguide toward the measurement OPA and keeps the residual pump of the squeezer OPA in the original waveguide (Fig. 1D). The fabricated adiabatic coupler causes ~30% loss for the squeezed vacuum and leaks ~20% of the squeezer pump to the measurement OPA. Our numerical simulations suggest that the coupling perform-

ance of the adiabatic coupler can be improved to >98% for the squeezed signal and <5% for the squeezer pump with proper calibration of fabrication steps, which will lead to better measurement qualities (supplementary materials, section 4).

In our simplified experimental setup (Fig. 2A) the squeezer and measurement OPAs are pumped by a mode-locked laser (Menlo Systems Orange A) generating ~75-fs-long nearly transform-limited pulses at a 250-MHz repetition rate. The relative phase between pump 1 (squeezer OPA) and pump 2 (measurement OPA) pulses is modulated by a piezoelectric transducer (PZT) on the pump 2 arm. At the output of the nanophotonic chip, the amplified squeezed signal and measurement OPA pump are first separated using a dichroic mirror and then are detected by two different optical spectrum analyzers (OSAs; see supplementary materials, section 1). In Fig. 2A, we show (i) a false-colored scanning electron microscope (SEM) image of our nanophotonic

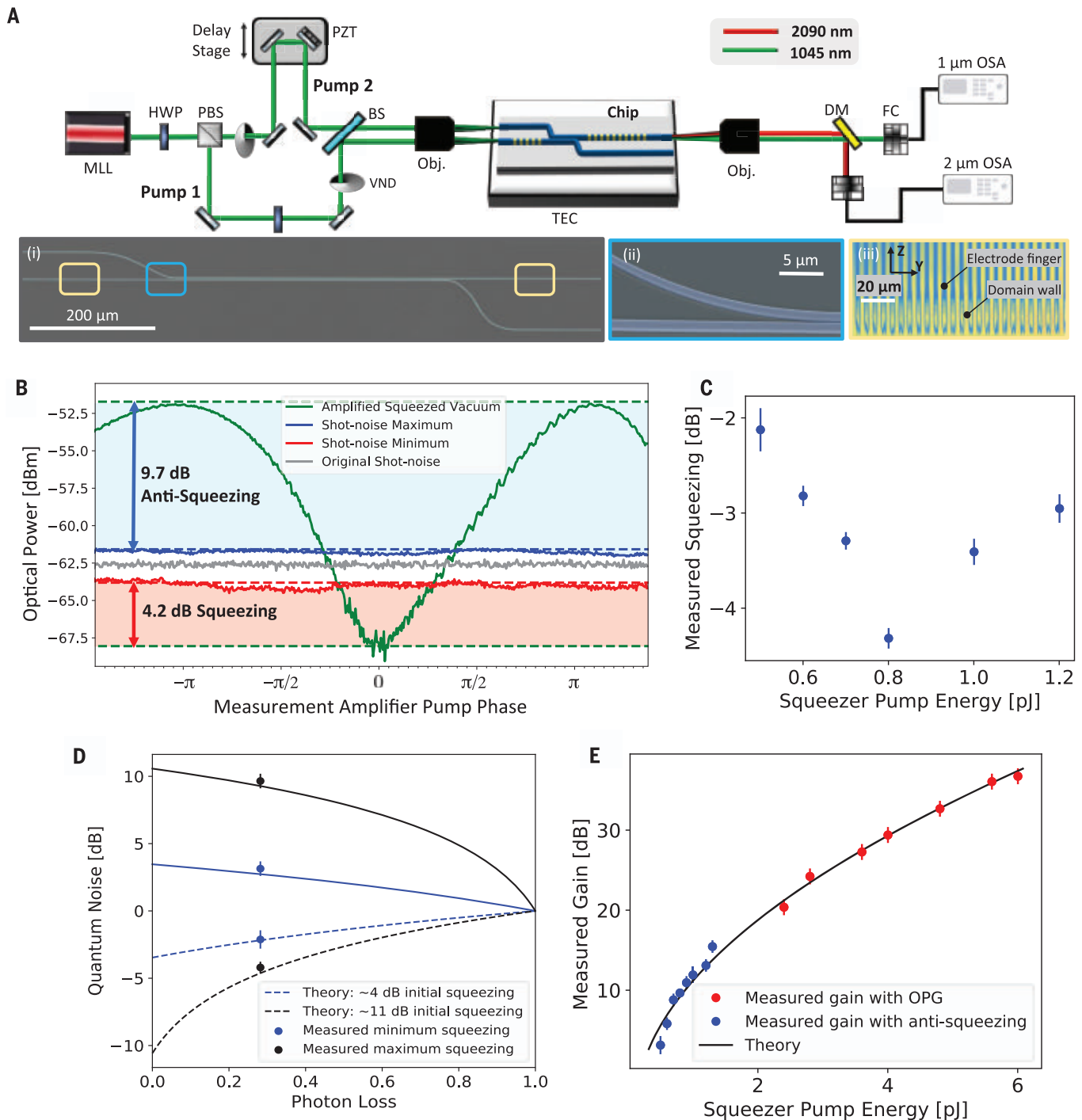


**Fig. 2. Generation and measurement of squeezed light in the LN nanophotonic chip.** (A) Experimental setup. A mode-locked laser (MLL) is used to pump the squeezer (pump 1) and measurement (pump 2) OPAs. At the output of the nanophotonic chip, the amplified squeezed signal (red) and residual pump 2 (green) are separated using a dichroic mirror (DM) and measured by two different OSAs. Bottom row shows the following: (i) a false-colored SEM image of our nanophotonic circuit, (ii) a zoomed-in SEM image of the coupler region, and (iii) a false-colored second harmonic microscope image of the periodically poled region before etching the waveguides. (B) Squeezing measurement by an OSA in the zero-span mode at 2090 nm. (C) The squeezing measured at

2090 nm for several values of pump 1 while keeping pump 2 constant. (D) Loss analysis of the squeezing measurements. The solid (dashed) curves show the degradation of anti-squeezing (squeezing) as the photon loss increases, and the solid data points correspond to measured values of minimum and maximum squeezing. (E) The squeezer gain dependence on the energy of pump 1. Blue points are measured from anti-squeezing, and red points are directly obtained from optical parametric generation (OPG) measurements. Error bars are obtained from the statistics of the measurements. PBS, polarized beam splitter; BS, beam splitter; HWP, half-wave plate; Obj., reflective objective; VND, variable neutral-density filter; FC, fiber coupler; TEC, thermoelectric cooler.

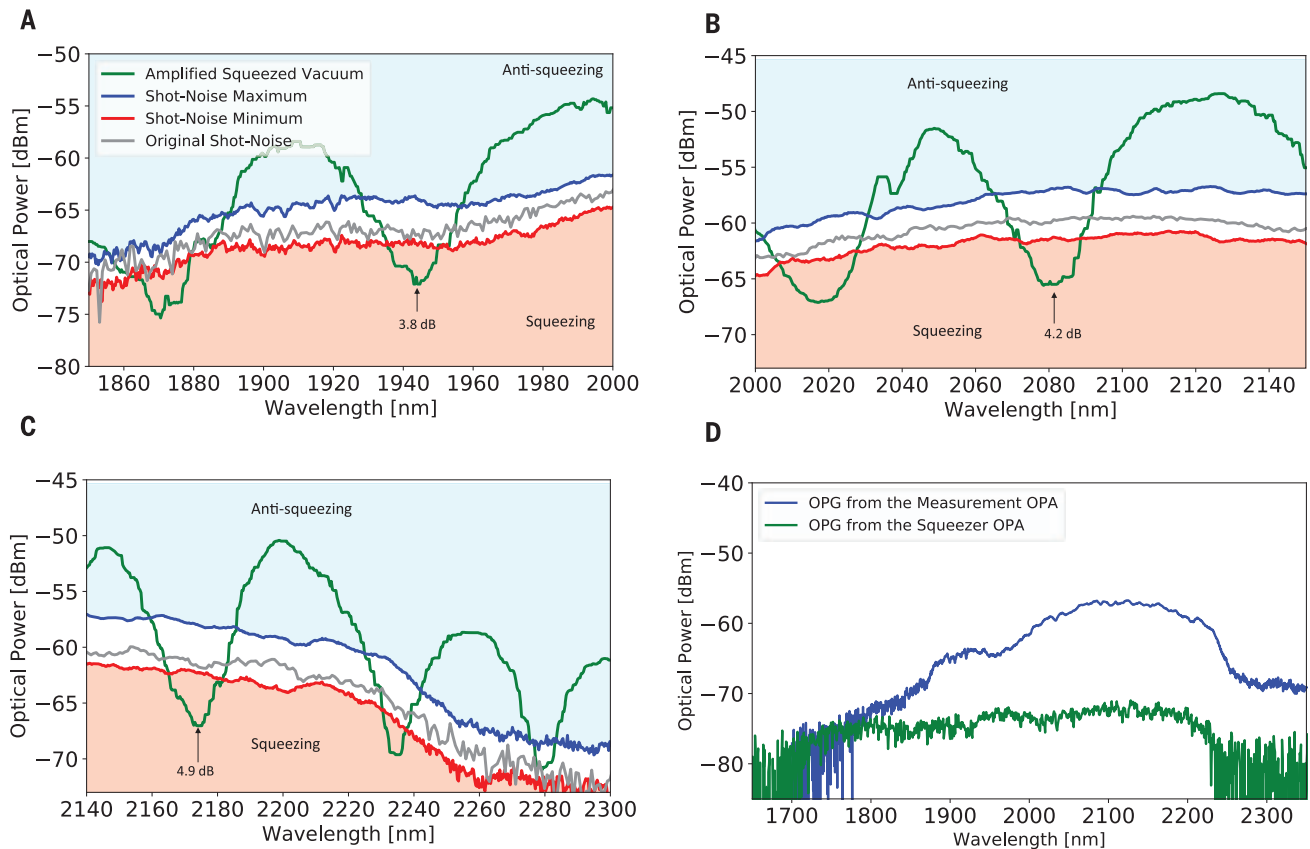


**Fig. 3. Broadband squeezing measurements.** (A to C) Three measurements over different selected bandwidths of the OSA when the PZT is modulated with a 300 mHz ramp signal. The shot noise traces (blue, gray, and red) were acquired with pump 1 blocked. (D) Optical parametric generation from the squeezer OPA (green) and measurement amplifier OPA (blue). Both traces are acquired at  $\sim 6$  pJ of pulse energy.

circuit, (ii) a zoomed-in SEM image of the coupler region, and (iii) a false-colored second harmonic microscope image of the periodically poled region before etching the waveguides.

Figure 2B shows an example measurement of our squeezed state. The green trace shows the output signal of the measurement OPA using an OSA in a zero-span mode at 2090 nm while keeping both pump 1 and pump 2 on and modulating the PZT by a 1-Hz ramp signal. To accurately measure the squeezing, we need to eliminate the effect of residual interference of the two pumps at the output of the measurement. We achieve this by determining the maximum and minimum of this residual interference and then calibrating our amplified shot-noise levels by subsequently varying the power of pump 2 to these maximum and minimum pump powers while blocking pump 1. These two levels of pump 2 result in a “shot-noise maximum” and “shot-noise minimum,” as shown in Fig. 2B, while the “original shot-noise” corresponds to the pump 2 level during the squeezing measurement. Hence, in the squeezing measurement, the shaded area below (above) the shot-noise minimum (shot-noise maximum) corresponds

to squeezing (anti-squeezing) at the input of the high-gain OPA. We measured a squeezing and anti-squeezing level of  $4.2 \pm 0.2$  dB and  $9.7 \pm 0.1$  dB, respectively, with 0.8 pJ of squeezer OPA pump energy. A detailed discussion on our shot-noise calibration measurements can be found in section 2 of the supplementary materials.

We further characterize the dependence of squeezing at 2090 nm on the pump power while keeping pump 2 constant and performing the shot-noise calibration for each power level as shown in Fig. 2C. As we increase the pump power in the squeezer OPA, the level of measured squeezing increases at first. However, above 0.8 pJ of pump pulse energy, we observe that further increasing the squeezer pump decreases the level of measured squeezing. The degradation of measured squeezing at high pump powers may be due to the existence of a small phase noise and relative chirp between pump 1 and pump 2, which can mix the loss-degraded squeezed quadrature with the relatively large anti-squeezed quadrature (27). Additionally, parasitic nonlinear effects such as the photorefractive effect and nonlinear absorption mechanisms in

the waveguide can also account for the degradation of squeezing at higher pump powers.

Figure 2D shows how squeezing levels degrade in the presence of photon loss ( $1 - \eta$ ). Analytically,  $S_{\pm}^{\eta}[\text{dB}] = 10\log[(1 - \eta) + \eta e^{\pm 2r_1}]$ , where  $(1 - \eta)$  determines the loss experienced by the microscopic squeezed signal and  $r_1$  is the squeezing parameter characterizing nonlinear interaction strength (supplementary materials, section 5). The solid dots in Fig. 2C are the experimental data points for the minimum and maximum amount of measured squeezing at 2090 nm. From these measurements, we estimate the total loss  $L = 1 - \eta \approx 0.3$  experienced by the microscopic squeezed signal before being fully amplified by the measurement OPA. The estimated total loss is mostly dominated by the coupling efficiency of the adiabatic coupler, which we measured using an auxiliary signal centered at 2090 nm (supplementary materials, section 4). From the squeezing and anti-squeezing measurements in Fig. 2D, our inferred squeezing after correcting for losses is  $10.48 \pm 0.87$  dB with a pump energy of  $< 1$  pJ. This paves the way for fault-tolerant CV quantum processors in LN nanophotonics, as 10.5 dB of squeezing is sufficient for many

architectures, including recent proposals with Gottesman-Kitaev-Preskill qubit encodings (28).

Figure 2E depicts the gain in the squeezer OPA as a function of pump 1 pulse energy. The gain for lower pump energies (<2.4 pJ) is determined from the anti-squeezing measurements, whereas for higher pump energies (>2.4 pJ), we obtain the gain from a direct measurement of average photon number (supplementary materials, section 4). When there is no input seed into the measurement OPA, the average number of photons in the high parametric gain regime ( $\langle \bar{N} \rangle \sim G/4$ ) allows us to estimate the gain. The solid curve is the fit that includes the overall detection efficiency (including off-chip coupling losses and imperfect detection after the measurement OPA) and the nonlinear strength as fitting parameters. From the fit, we extract the overall detection efficiency of  $\eta_{\text{overall}}^{\text{off-chip}} \sim 0.20$  (supplementary materials, section 5). This level of linear loss puts an upper limit of <1 dB to the measurable squeezing for a standard balanced homodyne detection. This is not a limiting factor for our all-optical squeezing measurements, because of the noiseless amplification by the measurement OPA. Note that such lossy measurements are even more detrimental for highly squeezed states, as they are extremely sensitive to losses. This can be seen in Fig. 2D, where ~11 dB of initial squeezing degrades by ~10 dB in the presence of the detection losses of  $L_{\text{overall}}^{\text{off-chip}} = 1 - \eta_{\text{overall}}^{\text{off-chip}} = 0.80$ . However, our all-optical measurement is not affected by  $L_{\text{overall}}^{\text{off-chip}}$  losses owing to the amplification by the measurement OPA and allows us to measure the squeezing levels as high as 4.9 dB. Thus, our current measured squeezing is mostly limited by the coupling loss associated with the on-chip adiabatic coupler, which can reach with near unity coupling efficiencies through better calibration of fabrication steps, as suggested by our numerical simulations (supplementary materials, section 4).

Figure 3, A to C, shows the measured squeezing over a broad bandwidth. The amplified shot-noise is calibrated, using the same method as discussed earlier, over the entire spectrum. Green traces correspond to measurements by the OSA over three different spectral windows when the PZT is modulated by a slow ramp signal at 300 mHz. Squeezing is present over the entire spectrum, with a slight spectral dependence. The measured squeezing is  $3.8 \pm 0.4$  dB around 1950 nm,  $4.2 \pm 0.2$  dB around 2090 nm, and

$4.9 \pm 0.2$  dB around 2200 nm. The slight spectral dependence is attributed to the wavelength dependence of the coupling efficiency of our adiabatic coupler (supplementary materials, section 4). We measured the squeezing bandwidth to be 25.1 THz. The bandwidth is expected to increase to 36.4 THz, as confirmed by the optical parametric generation (OPG) from the squeezer OPA in Fig. 3D. The measured squeezing bandwidth is mostly limited by the slight mismatch of measurement OPA gain in the wings of the spectrum, as evident from its OPG signal. Because of this difference in the gain spectrum, the measurement OPA does not amplify the squeezed vacuum over its entire generation bandwidth to macroscopic levels, leading to a reduced measured squeezing bandwidth. These measurements indicate that our generated squeezed state can occupy a record-level time window of about four optical cycles (supplementary materials, section 3). This temporal window can be shortened further by engineering the dispersion and quasi-phase matching (29) and may lead to opportunities for studying quantum fields in the extremely short-pulse regime (30). Our demonstrated squeezing bandwidth allows the definition of few-optical-cycle temporal bins in time-multiplexed CV quantum information processors (6, 7). As a result, such ultra-short time bins can be defined in a dense manner for which centimeter-scale on-chip delay lines can be used for large-scale cluster states on a chip.

We have demonstrated few-cycle vacuum squeezing and its all-optical measurements in the LN nanophotonic platform. Our on-chip all-optical loss-tolerant broadband measurements through high-gain phase-sensitive amplification enabled squeezing measurements over more than 25 THz of bandwidth while providing measurement purification against the detection losses as high as  $L_{\text{overall}}^{\text{off-chip}} \sim 7$  dB. Combined with the recent advances such as high-speed electro-optic modulators and integrated single-photon detectors (23), we envision that our results may enable scalable ultrafast all-optical quantum information processors in LN nanophotonic platform.

#### REFERENCES AND NOTES

1. T. D. Ladd *et al.*, *Nature* **464**, 45–53 (2010).
2. J. L. O'Brien, A. Furusawa, J. Vučković, *Nat. Photonics* **3**, 687–695 (2009).
3. H. Yu *et al.*, *Nature* **583**, 43–47 (2020).
4. C. A. Casacio *et al.*, *Nature* **594**, 201–206 (2021).
5. A. Furusawa *et al.*, *Science* **282**, 706–709 (1998).
6. W. Asavanant *et al.*, *Science* **366**, 373–376 (2019).

7. M. V. Larsen, X. Guo, C. R. Breum, J. S. Neergaard-Nielsen, U. L. Andersen, *Science* **366**, 369–372 (2019).
8. M. Chen, N. C. Menicucci, O. Pfister, *Phys. Rev. Lett.* **112**, 120505 (2014).
9. G. Kanter *et al.*, *Opt. Express* **10**, 177–182 (2002).
10. J. Roslund, R. M. De Araujo, S. Jiang, C. Fabre, N. Treps, *Nat. Photonics* **8**, 109–112 (2014).
11. V. D. Vaidya *et al.*, *Sci. Adv.* **6**, eaba9186 (2020).
12. C. Vignier *et al.*, *Nat. Phys.* **17**, 1137–1143 (2021).
13. J. M. Arrazola *et al.*, *Nature* **591**, 54–60 (2021).
14. J. F. Tasker *et al.*, *Nat. Photonics* **15**, 11–15 (2021).
15. U. A. Javid *et al.*, *Phys. Rev. Lett.* **127**, 183601 (2021).
16. P.-K. Chen, I. Briggs, S. Hou, L. Fan, *Opt. Lett.* **47**, 1506–1509 (2022).
17. D. Peace *et al.*, arXiv:2204.05694 [quant-ph] (2022).
18. C. M. Caves, *Phys. Rev. D* **26**, 1817–1839 (1982).
19. Y. Shaked *et al.*, *Nat. Commun.* **9**, 609 (2018).
20. N. Takahashi *et al.*, *Opt. Express* **28**, 34916–34926 (2020).
21. G. Frascella, S. Agne, F. Y. Khalili, M. V. Chekhova, *NPJ Quantum Inf.* **7**, 72 (2021).
22. Z. Ye *et al.*, *Sci. Adv.* **7**, eabi8150 (2021).
23. D. Zhu *et al.*, *Adv. Opt. Photonics* **13**, 242 (2021).
24. L. Ledezma *et al.*, *Optica* **9**, 303 (2022).
25. M. Jankowski *et al.*, *Optica* **7**, 40 (2020).
26. Y. Hu *et al.*, *Nature* **599**, 587–593 (2021).
27. M. J. Werner, M. G. Raymer, M. Beck, P. D. Drummond, *Phys. Rev. A* **52**, 4202–4213 (1995).
28. J. E. Bourassa *et al.*, *Quantum* **5**, 392 (2021).
29. D. Horoshko, M. Kolobov, *Phys. Rev. A* **88**, 033806 (2013).
30. M. Kizmann *et al.*, *Nat. Phys.* **15**, 960–966 (2019).
31. R. Nehra, Few-cycle vacuum squeezing in nanophotonics, Figshare (2022); <https://doi.org/10.6084/m9.figshare.20100140.v1>.

#### ACKNOWLEDGMENTS

The device nanofabrication was performed at the Kavli Nanoscience Institute (KNI) at Caltech. The authors thank NTT Research for financial and technical support. The authors thank C. González-Arciniegas and O. Pfister for fruitful discussions. **Funding:** The authors gratefully acknowledge support from ARO grant W911NF-18-1-0285, NSF grants 1846273 and 1918549, AFOSR award FA9550-20-1-0040, and NASA/JPL. This project was funded in part by the President's and Director's Research and Development Fund of Caltech and JPL. **Author contributions:** R.N. and A.M. conceived of the idea and designed the experiments; R.N. designed the devices with assistance from L.L. and Q.G.; R.S. fabricated the devices and L.L. performed the periodic poling; R.N. carried out the experiments with assistance from R.S., R.M.G., Q.G., and A.R.; R.N. performed the theoretical and numerical analysis with contributions from L.L.; R.N. and A.M. wrote the manuscript with input from all other authors; and A.M. supervised the project. **Competing interests:** R.N., A.M., R.S., and L.L. are inventors on a provisional patent application (63/299,762) by the California Institute of Technology based on the work presented here. **Data and materials availability:** All other data needed to evaluate the conclusions in the paper are present in the paper or the supplementary materials. The data files supporting the plots in the main text are available at Figshare (31). **License information:** Copyright © 2022 the authors, some rights reserved; exclusive licensee American Association for the Advancement of Science. No claim to original US government works. <https://www.science.org/about/science-licenses-journal-article-reuse>

#### SUPPLEMENTARY MATERIALS

[science.org/doi/10.1126/science.abo6213](https://science.org/doi/10.1126/science.abo6213)

Materials and Methods

Figs. S1 to S13

Table S1

References (32–50)

Submitted 15 February 2022; accepted 8 August 2022  
10.1126/science.abo6213



Frontiers of Science

# Gordon Research Conferences

January – April 2023 Preliminary Programs  
Apply now at: [www.grc.org](http://www.grc.org)

Discussion leaders are noted in bold italics.

## Alcohol-Induced End Organ Diseases + GFS

MAR 26-31, 2023 FOUR POINTS SHERATON / HOLIDAY INN EXPRESS, VENTURA, CA

CHAIRS: Elizabeth Kovacs and Gavin Arteel

VICE CHAIRS: Patricia Molina and Carol Casey

- **Keynote Session: Alcohol: A Systemic Toxin** *Hidekazu Tsukamoto*, George Koob, Paul Kubus
- **Alcohol and Neuro-Inflammation** *Fulton Crews*, Kimberly Nixon, Joanne Weinberg, Leon Coleman, Paige Anton
- **Alcohol, the GI Barrier and Gut-Peripheral Organ Axes** *Bin Gao*, Bernd Schnabl, Gyongyi Szabo, Radhakrishna (RK) Rao, Irina Kirpich
- **Alcohol and Severe Injury** *M. Katherine Jung*, Mashkoor Choudhry, Nicholas Gilpin, Borna Rejla, Craig Coopersmith
- **Alcohol, Cancer Risk and Outcome** *Robert Schwabe*, Jurgen Rehm, Mary Beth Terry, Benita McVicker, Raul Torres
- **Early Detection and Intervention for End Organ Damage** *Vijay Shah*, Lorenzo Leggio, Jay Luther, Jessica Mellinger, Stephen Pandol
- **Alcohol and Comorbidities** *Laura Nagy*, Pal Pacher, Abigail Cannon, Erin Lowery, Adam Kim
- **Alcohol, Inflamm-Aging and Senescence Across the Aging Spectrum** *Andras Orosz*, Falk Lohoff, Heather Francis, Ilhem Messaoudi
- **Informatic Advances in Alcohol-Induced End-Organ Diseases** *Vasilis Vasiliou*, Christina Mair, Majid Afshar, Takis Benos, Kathleen McTigue
- **The GRC Power Hour™** *Rebecca McCullough*

## Antimicrobial Peptides

+ GFS

JAN 15-20, 2023 RENAISSANCE TUSCANY IL CIOCCO, LUCCA (BARGA), ITALY

CHAIRS: Neelofar Mookherjee and Marilyn Anderson

VICE CHAIRS: Gerard Wong and Delphine Destoumieux-Garzon

- **Keynote Session: Perspective From COVID-19** *Annelise Barron*, Pieter Hiemstra, Maren Von Köckritz-Blickwede
- **Antimicrobial Functions and Mechanisms** *Marc Devocelle*, Donald Davidson, Octavio Franco, Paula Gomes
- **Antimicrobial Functions and One Health** *Jennifer Payne*, Henk Haagsman, Eduardo Cobo
- **Interplay and Influence of Microbiome** *Nita Salzman*, Richard Gallo, Elizabeth Kovacs, Michael Howitt, Tatsuya Dokoshi
- **Sex-Related Differences in Expression and Functions of Peptides** *Molly Ingersoll*, Catherine Greene, Cliona O'Farrelly
- **Immunobiology: Mechanisms and Functions** *Anne van der Does*, Emily Gwyer Findlay, Charles Bevin, Henrik Bringmann, Lisa Ryan
- **Impact of Environmental Exposures and Pollution** *Gill Diamond*, Aurélie Tasiemski, Chris Carlsen
- **Discovery to Commercialization** *Robert Hancock*, Nicole Van Der Weerden, Evan Haney, David Craik, Aaron Weinberg, Glenn King
- **Peptide Formulation and Delivery** *Cesar de la Fuente*, Annelise Barron, Suzana Straus
- **The GRC Power Hour™** *Julia Dorin*

## Cardiac Arrhythmia Mechanisms

+ GFS

FEB 26 - MAR 3, 2023 GRAND GALVEZ, GALVESTON, TX

CHAIRS: David Christini and Ursula Ravens

VICE CHAIRS: Crystal Ripplinger and Edward Vigmond

- **Keynote Session: Emerging Concepts in Computational and Experimental Arrhythmia Research** *Gary Mirams*, Isabelle Deschenes, Igor Efimov, Blanca Rodriguez
- **Sinoatrial Nodal Arrhythmias** *Alex Quinn*, Vadim Fedorov, Céline Fiset, Yael Yaniv
- **Autonomic Control of the Heart** *Crystal Ripplinger*, Neil Herring, Marmar Vaseghi, Annika Winbo
- **Arrhythmias of the Young and Old** *Dobromir Dobrev*, Eleonora Grandi, Claudia Moreno, Uli Schotten, Jennifer Silva
- **Methodologies in Computational Model Rigor and Data Frame Working for Arrhythmia Research and Therapy** *Mary Maleckar*, Richard Gray, David Slotwiner

- **Cardiac Imaging in the Electrophysiology Laboratory** *Patrick Boyle*, Nazem Akoum, Sabine Ernst, Steven Niederer, Elaine Wan
- **Late-Breaking Topics: Implications of COVID for Cardiac Electrophysiology and Arrhythmia** *Enaam Chleilat*
- **Ionic Underpinnings of Arrhythmogenesis** *Trine Krogh-Madsen*, Al George, Thomas Hund, W. Jonathan Lederer, Katharine Dibb
- **High Throughput Analysis and Screening** *Edward Vigmond*, Gil Bub, Teun De Boer, Emilia Entcheva
- **The GRC Power Hour™** *Crystal Ripplinger*

## Carotenoids

+ GFS

JAN 8-13, 2023 VENTURA BEACH MARRIOTT, VENTURA, CA

CHAIR: Loredana Quadro

VICE CHAIR: Salim Al-Babili

- **Keynote Session: Carotenoids: From Plants to Mammals** *Eleanore Wurtzel*, John Landrum, Johannes Von Lintig, Claudia Vickers, Volker Wendisch
- **Biosynthesis and Enzymology** *Joseph Hirschberg*, Li Li, Manuel Rodriguez-Concepcion, Philip Kiser
- **Vision and Pigmentation** *Matthew Toomey*, Paul Bernstein, John Nolan
- **Apocarotenoids and Signaling** *Alexandra Dickinson*, Giovanni Giuliano, Christopher Cazzonelli
- **Carotenoids and Photosynthesis** *Krishna Niyogi*, Roberto Bassi, Barbara Demmig-Adams
- **Biofortification and Biotechnology** *James Dale*, Antonio Melendez-Martinez, Sherry Tanumihardjo
- **Retinoids and Apocarotenoids Metabolism** *Jessica Cooperstone*, Alexander R. Moise, Claudia Stange
- **Carotenoids and Health** *Xiang-Dong Wang*, John Erdman, Ji-Young Lee
- **Carotenoids and Microorganisms** *Gerhard Sandmann*, Carmen Limon, Martin Lohr
- **The GRC Power Hour™** *Eugenia Poliakov*

## Cartilage Biology and Pathology

+ GFS

MAR 19-24, 2023 RENAISSANCE TUSCANY IL CIOCCO, LUCCA (BARGA), ITALY

CHAIRS: Farshid Guilak and Frank Zaucke

VICE CHAIRS: Rosa Serra and Gerjo Van Osch

- **Cartilage Development and Regeneration** *Terence Capellini*, Deneen Wellik, Christine Hartmann
- **Epigenetics and Non-Coding RNAs** *Louise Reynard*, Yolande Ramos, Audrey McAlinden, S. Amanda Ali, Eleftheria Zeggini
- **Extracellular Matrix** *Antonio Rossi*, Bent Brachvogel, Sarah Calve, Francis Berenbaum
- **Mechanobiology** *Tamara Alliston*, Andrew Pitsillides, Angus Wann, Niamh Nowlan, Ronald June
- **Biomechanics and Bioengineering** *Corey Neu*, Gerard Ateshian, Suzanne Maher, Markus Wimmer
- **Stem Cells and Tissue Engineering** *Brian Johnstone*, Rhima Coleman, Jos Malda, Solvig Diederichs, Denis Evseenko
- **Osteoarthritis** *Anne-Marie Malfait*, Francesco Dell'Accio, Jang-Shoo Chun, Mohit Kapoor
- **Rare Diseases, Disease Modeling and Aging** *Uwe Kornak*, Brian Diekmann, Shireen Lamande, Christopher Little, Katarzyna Pirog
- **Cartilaginous and Joint Tissues** *Susanne Graessel*, Devina Purnessur (Walter), Martin Englund, Carla Scanzello
- **The GRC Power Hour™** *Sarah Snelling, Rosa Serra, Gerjo Van Osch*

## Cell Biology of Megakaryocytes and Platelets

+ GFS

MAR 5-10, 2023 RENAISSANCE TUSCANY IL CIOCCO, LUCCA (BARGA), ITALY

CHAIRS: Elizabeth Gardiner and Alessandro Balduini

VICE CHAIRS: Yotis Senis and Renhao Li

- **Keynote Session: Platelets and Megakaryocytes** *Martine Jandrot-Perrus*, Hana Raslova, Bernhard Nieswandt
- **Platelets Under Duress** *Michele Lambert*, Milka Koupenova, Ilaria Canobbio, Mark Looney, Sophie Susen, Keith Neeves

- **Inside Platelets** *Debra Newman*, John Hwa, Wolfgang Bergmeier, Patricia Maguire
- **The Manufacturing Plant** *James Bussell*, Koji Eto, Cedric Ghevaert, Beth Psaila
- **Imaging and New Technology Evaluating Platelet and Megakaryocyte Function** *Luigi De Marco*, Anna Waterhouse, Craig Jenne, Hervé Falet
- **Mechanisms of Platelet Production** *Karina Yazdanbakhsh*, Kellie Machlus, Maegan Capitano, Ian Hitchcock, Antonija Begonja, Mattia Frontini
- **Retraining and Constraining Platelets and Megakaryocytes** *Paula Heller*, Alexandra Mazharian, Matthew Rondina, Ute Modlich
- **The Nature of the Clot** *Samantha Montague*, Alastair Poole, Katsue Suzuki-Inoue, Pierre Mangin, Leo Nicolai, Nicola Mutch
- **Extending GWAS Data to Functional Outcomes** *Katya Ravid*, Kathleen Freson, Neil Morgan, Jose Maria Bastida
- **The GRC Power Hour™** *Hervé Falet, Antonija Begonja*

## Chemical and Biological Defense

+ GFS

MAR 19-24, 2023 FOUR POINTS SHERATON / HOLIDAY INN EXPRESS, VENTURA, CA

CHAIRS: Catherine Branda and Thomas Blake

VICE CHAIRS: Charles Thompson and Katherine Delavaris

- **Keynote Session: Artificial Intelligence and Other Emerging Technologies for a New Era of Chemical and Biological Defense** *Catharine Bosio*, Brandi Vann, Lee Cronin, Jennifer Nuzzo
- **Artificial Intelligence and the Modernization of Chemical Synthesis** *Connor Coley*, Francesca Grisoni, Luke Rogers, Dobrila Rudnicki, Timothy Cernak
- **Acute Lung Injuries and Acute Respiratory Distress Syndrome in Chemical and Biological Exposures** *Livia Veress*, Jehan Alladina, Satya Achanta, Bradford Smith, Matthew McGraw
- **Harnessing Physiological Data for Chemical and Biological Exposure Warning** *Christopher Kiley*, Sarah Goodchild, Sara Mariani, Seila Selimovic, Kajal Claypool
- **Blood Brain Barrier Function, Compromise and Protection** *Henry VanBrocklin*, John Gerdes, Kurt Zinn, Michelle James, Mark Bolding, David Scott
- **Biomaterials for Chemical and Biological Defense** *Monica Serban*, Brad Pindzola, Benedetto Marelli, Caterina Lamuta, Joachim Veit
- **Countering Antimicrobial Resistance** *Mark Albrecht*, Sean Brady, Timothy Lu, Angela Coulliette-Salmond
- **Applications of Synthetic Biology for Chemical and Biological Defense** *Malin Young*, Gigi Gronvall, Christopher Voigt, Chris Oehmen, George Korch
- **Science and Technological Challenges for Digital Biosecurity** *Corey Hudson*, Peter Carr, Sterling Sawaya, Lisa Simirenko, Emilie Purvine
- **The GRC Power Hour™** *Brandi Vann*

## Chemical Reactions at Surfaces

+ GFS

FEB 12-17, 2023 RENAISSANCE TUSCANY IL CIOCCO, LUCCA (BARGA), ITALY

CHAIR: Manos Mavrikakis

VICE CHAIR: Edvin Lundgren

- **Theoretical Insights on Surface Chemistries at Single Metal Centers** *Karollina Honkala*, Gianfranco Pacchioni, Laura Gagliardi
- **Reactions on Metal Oxides** *Charles Campbell*, Zdenek Dohnalek, Unni Olsbye, Alexis Bell
- **Theoretical Insights on Reactions Taking Place at Extended Surfaces** *Axel Gross*, Joachim Sauer, Nuria Lopez
- **Surface Chemistry on 2D Materials** *Jason Weaver*, Christof Wöll, Stefano Agnoli, Baoxia Mi
- **Reactions at Electrified Interfaces: Electrocatalysis** *Enrique Herrero*, Vojislav Stamenkovic, Beatriz Roldan Cuenya
- **Reactions at Electrified Interfaces: Batteries** *Edvin Lundgren*, Bruce Dunn, Ying Shirley Meng, Hector Abruna
- **Surface Chemistry on Emerging Materials** *Andrew Gellman*, Federico Rosei, Xiaohui Qiu
- **Advanced Characterization: Microscopy and Spectroscopy** *Christian Kisielowski*, Peng Chen, Miaofang Chi, Stig Helveg

- In-Situ Characterization Methods *Alec Wodtke*, Anders Nilsson, Miquel Salmeron
- The GRC Power Hour™ *Liney Arnadóttir*

## Chloroplast Biotechnology



MAR 26-31, 2023 VENTURA BEACH MARRIOTT, VENTURA, CA

CHAIR: Ian Small

VICE CHAIR: Klaas Van Wijk

- Evolution and Diversity of Plastid Genomes *Pamela Soltis*, Eva Nowack, Susann Wicke
- Engineering Organelle Genomes *Pal Maliga*, Juan Pablo Giraldo, Scott Lenaghan
- Controlling Plastid Gene Expression *Joerg Nickelsen*, Sujith Puthiyaveetil, Alice Barkan, Mareike Schallenberg-Ruedinger
- Production of Biopolymers *Jihong Liu Clarke*, Jiang Zhang, Anil Day
- Engineering Light Reactions *Eva-Mari Aro*, Marcel Dann, Michael Jones
- Engineering Carbon Fixation *Maureen Hanson*, Gilles Peltier, Spencer Whitney
- Engineering Plastid Metabolism *Alison Smith*, Ralph Bock, Hiroshi Maeda
- Plastids as Biosensors *Patricia Leon-Mejia*, Katayoon Dehesh, Francesco Licausi, Shilo Rosenwasser, Toru Hisabori
- SynBio of Photosynthetic Organisms *Barry Pogson*, Saul Purton, Jim Haseloff
- The GRC Power Hour™ *Patricia Leon-Mejia*

## Cilia, Mucus and Mucociliary Interactions



FEB 19-24, 2023 RENAISSANCE TUSCANY IL CIOCCO, LUCCA (BARGA), ITALY

CHAIRS: Brian Button and Martin Blum

VICE CHAIRS: Katharina Ribbeck and Pleasantine Mill

- Keynote Session: Prospects and Themes in Mucociliary Biology *Matthias Salathe*, *Mary Porter*, Susan Dutcher, Christopher Evans, Steven Brody
- Genetic and Molecular Understanding of Mucociliary Disorders *Hannah Mitchison*, *Max Seibold*, Peter Jackson, Kenichi Okuda, Julia Wallmeier, John Fahy
- Systems Biology *Sudipto Roy*, *Jean-Luc Desseyn*, Sophie Darch, Virginie Hamel, Silvia Kreda, Wallace Marshall
- Mucin and Cilia Biophysics *David Hill*, *Julien Vermot*, Zeynep Ökten, Elisabeth Nystrom, Kirsty Wan, Michael Rubinstein
- Structure and Function *Laura Campbell*, *Girish Mali*, Daniela Nicastro, Deborah Fass, Katerina Toropova
- Signaling and Host Defense *Anna Ermund*, *Dominic Norris*, Julia Duerr, Hiroshi Hamada, Corey Stevens, Shialouh Yuan
- Regulation and Function *Nathalie Jurisch-Yaksj*, *Corinne Kliment*, Luke Bonser, Dagmar Wachten, John Dickinson
- Disease Modeling *Nam Soo Joo*, *Brian Mitchell*, Mustafa Khokha, John Engelhardt, Rebecca Burdine, Susan Birket
- Technologies to Study Cilia, Mucus and Mucociliary Interactions *Alessandra Livraghi-Butrico*, *Benedicte Durand*, Jessica Kramer, Raman Das, David Stoltz
- The GRC Power Hour™ *Alessandra Livraghi-Butrico*, *Girish Mali*

## Complex Active and Adaptive Material Systems



JAN 29 - FEB 3, 2023 VENTURA BEACH MARRIOTT, VENTURA, CA

CHAIR: Nicholas Abbott

VICE CHAIR: Tyler Shendruk

- Living Material Systems *Kathleen Stebe*, Margaret Gardel, Oleg Lavrentovich
- Lessons From Natural Systems *Maria Santore*, Rebecca Schulman, Sujit Datta, Isabella Guido
- Dynamic Covalent Chemistry *Todd Emrick*, Stuart Rowan
- Information Processing in Materials *Richard Vaia*, Brenda Rubenstein, Suyi Li, Todd Murphey
- Active Materials and Soft Robots *Elliot Hawkes*, Metin Sitti, Michael Tolley, Robert Shepherd
- Responsive and Adaptive Matter *Joerg Lahann*, Timothy White, Christian Santangelo, Nathan Gianneschi
- Early-Career Investigator Presentations *Arnold Mathijssen*
- Dissipation in Open Material Systems *Tyler Shendruk*, Lauren Zarzar, Daniel Schwartz, Evelyn Tang
- Autonomous and Reconfigurable Material Systems *Anna Balazs*, Barbara Mazzolai, Orin Velev
- The GRC Power Hour™ *Kathleen Stebe*

## Dendrites: Molecules, Structure and Function



MAR 26-31, 2023 RENAISSANCE TUSCANY IL CIOCCO, LUCCA (BARGA), ITALY

CHAIRS: Ely Nedivi and Matthew Larkum

VICE CHAIRS: Bartlett Mel and Judit Makara

- Keynote Session: Cross-Cutting Themes in Dendrites Research *Kristen Harris*, Hollis Cline, Jackie Schiller, Yota Poirazi
- Dendrites in Development *Christian Lohmann*, Beatriz Rico, Ania Majewska, Maya Shelly
- Dendritic Integration and Local Computations *Mark Harnett*, Kwabena Boahen, Marla Feller, Idan Segev

- Synaptic and Dendritic Plasticity Mechanisms *Nelson Spruston*, Karen Zito, Michael Hausser, Attila Losonczy
- Local Protein Dynamics in Dendrites *Yasunori Hayashi*, Erin Schuman, Emily Osterweil, Tatjana Tchumatchenko
- Dendritic Role in Higher Brain Function *Christine Grienberger*, Inbal Goshen, Antoine Adamantidis, Michael Higley
- Dendritic Wiring Programs *Tara Keck*, *Linda Van Aelst*, Wei-Chung Allen Lee, Julijana Gjorgjieva, Liqun Luo
- Synaptic Organization *Ryohei Yasuda*, Cécile Charrier, Katrin Willig, Pablo Castillo
- Specificity of Axonal Inputs to Dendrites *Lucy Palmer*, Ivo Spiegel, Jeff Lichtman, Arthur Konnerth
- The GRC Power Hour™ *Corette Wierenga*

## Directed Cell Migration



JAN 8-13, 2023 GRAND GALVEZ, GALVESTON, TX

CHAIR: Michael Sixt

VICE CHAIR: Sally Horne-Badovinac

- Keynote Session: Organization of Motile Systems on the Organismic and Molecular Scale *Peter Friedl*, Iain Couzin, Rong Li
- Cell Shape and Force Transmission *Peter Devreotes*, Dyche Mullins, Anna Akhmanova, Holger Knaut
- Collective Cell Migration *Denise Montell*, Nir Gov, Daniel Cohen, Benoit Ladoux
- Evolution of Cell Motility *Robert Insall*, Lillian Fritz-Laylin, Laurent Nguyen
- Pathfinding and Navigation *Milka Sarris*, Peter Devreotes, Johanna Ivaska, Denise Montell
- Inflammation and Regeneration *Orion Weiner*, Ana-Maria Lennon-Dumenil, Milka Sarris, Andres Hidalgo
- Pathophysiology and Malignancy *David Sherwood*, Peter Friedl, Danijela Matic Vignjevic, Kandice Tanner
- Polarity and Directional Guidance *Dyche Mullins*, Orion Weiner, Marino Arroyo
- Cell-Tissue Crosstalk *Johanna Ivaska*, Robert Insall, Fanny Jaulin, David Sherwood
- The GRC Power Hour™ *Ana-Maria Lennon-Dumenil*

## Fibronectin, Integrins and Related Molecules



FEB 5-10, 2023 VENTURA BEACH MARRIOTT, VENTURA, CA

CHAIRS: Ambra Pozzi and Jim Norman

VICE CHAIRS: Sara Wickstrom and Guy Tanentzapf

- Keynote Session: Mechanobiology From Molecules to Cells *Mark Ginsberg*, Michael Sheetz, Alexander Bershadsky, Erik Sahai
- Using Integrin Structure to Devise Therapeutic Interventions *Bernhard Wehrle-Haller*, Tina Izard, M. Amin Arnaout, William Degradó
- Imaging Dynamics of Cell-ECM Interaction and Signaling *Guy Tanentzapf*, Gaudenz Danuser, Celeste Nelson, Thomas Lecuit
- Tools and Approaches to Study Mechanotransduction *Andres Garcia*, Brent Hoffman, Guillaume Charras, Gregory Alushin, Chloe Feral
- Membrane and Receptor Trafficking *Sara Wickstrom*, Johanna Ivaska, Robert Coffey, Giorgio Scita
- Matrix Receptors in Fibrosis and Disease *David Wasserman*, Alexandra Naba, Roy Zent, Ashani Weeraratna, Rachel Lennon
- Matrix Receptors in Host-Tumor Interaction *Ellen Van Obberghen-Schilling*, Kairbaan Hodivala-Dilke, Philippe Chavrier, Janine Erler, Stephen Nishimura
- Cell-ECM Receptors in Cancer Cell Migration and Invasion *Corinne Albiges-Rizo*, Laura Machesky, David Schlaepfer, Maddy Parsons, Stephen Weiss
- Keynote Session: Fibronectin From Structure to Function *Thomas Barker*, Jean Schwarzbauer, Martin Schwartz
- The GRC Power Hour™ *Sara Wickstrom*

## Functional Genomics of Human Brain Development and Disease



APR 2-7, 2023 VENTURA BEACH MARRIOTT, VENTURA, CA

CHAIRS: Kristen Brennand and Alex Shcheglovitov

VICE CHAIR: Elisabeth Binder

- Keynote Session: Translating Genetic and Tissue Engineering Insights to Medicine *Rudolf Jaenisch*, Arnold Kriegstein, Cecilia Cotta-Ramusino
- Early Human Brain Development *Juergen Knoblich*, Magdalena Zernicka-Goetz, Sergiu Pasca, Flora Vaccarino
- Functional Genomics of Neurodevelopmental Disorders *Flora Vaccarino*, Laura Huckins, Steve McCarroll, Michael Talkowski, Danielle Posthuma
- Technological Advances: Functional Genomics *Rong Fan*, Jonathan Gootenberg, Andrew Anzalone, Michelle Chen
- Stem Cells and Neuropsychiatric Disorders *Danielle Posthuma*, Thomas Sudhof, Giorgia Quadrato
- Technological Advances: Physiological Relevance *Fred Gage*, Guo-li Ming, Mathew Blurton-Jones, Pierre Vanderhaeghen
- Stem Cells and Neurodegenerative Disorders *Sally Temple*, Celeste Karch, Hemali Phatnani
- Improved Cellular Diversity and Aging In Vitro *Kristin Baldwin*, Andrew Yoo, Jerome Mertens, Nan Yang
- CRISPR Screening *Martin Kampmann*, Xin Jin, John Doench, Rong Fan
- The GRC Power Hour™ *Randolph Ashton*

## Gaseous Ions: Structures, Energetics and Reactions



FEB 19-24, 2023 VENTURA BEACH MARRIOTT, VENTURA, CA

CHAIR: Mary Rodgers

VICE CHAIR: Richard O'Hair

- Advances in Instrumentation and Emerging Mass Spectrometry Applications *Daniel Austin*, Thomas Rizzo, Martin Jarrold
- Organic and Peptide Ion Chemistry *Benjamin Bythell*, Stephen Blanksby, Jeehuin Lee, Ivan Chu, Michael Van Stipdonk
- Electronic Spectroscopy of Ions *Ricardo Metz*, Christopher Johnson, Caroline Dessert
- Ion-Photon Interactions: Photochemistry, Photodissociation and Photoionization *Frantisek Turecek*, Gavin Reid, Jennifer Brodbelt, Andras Bodi, Martin Beyer
- Ions in Space and for Space Applications *Amanda Patrick*, Benjamin Prince, Steven Chamberau
- Gaseous Biomolecules and Biomolecular Assemblies *Elyssia Gallagher*, Kathrin Breuker, Anne Zehnacker-Rentien, Anouk Rijs, Rebecca Jockusch
- Vibrational Spectroscopy of Ions *Jongcheol Seo*, Gert von Helden, Barbara Chiavarino
- Catalysis and Reaction Intermediates *Mathias Schaefer*, Jana Rothova, Leah Dodson, Knut Asmis, Jack Beauchamp
- Keynote Session: Gas-Phase Ion Thermochemistry *Theresa Watson*, Peter Armentrout
- The GRC Power Hour™ *Elyssia Gallagher*, *Amanda Patrick*

## Glial Biology: Functional Interactions Among Glia and Neurons



MAR 5-10, 2023 VENTURA BEACH MARRIOTT, VENTURA, CA

CHAIR: Marc Freeman

VICE CHAIR: Cagla Eroglu

- Glial Interactions with Axons and Synapses *Shane Liddelow*, *Dwight Bergles*, Kelly Monk, Michelle Monje, Beth Stevens
- Glial Interactions in Circuit Formation *Beth Stevens*, *Sarah Kucenas*, Nicola Allen, Won-Suk Chung, Quan Yuan, Benjamin Deneen, Gek Ming Sia
- CNS Interactions with the Periphery Through Glia *Staci Bilbo*, Sarah Kucenas, Chenghua Gu, Richard Daneman, Maria Lehtinen, Brian MacVicar
- Ensheatment and Myelination of Axons *Anusha Mishra*, *Megan Corty*, David Lyons, Ragnhildur Thóra Kárádóttir, Laura Feltri, Jonah Chan
- Glial Functions in Disease Pathology *Harald Sontheimer*, *Wendy Xin*, Soyon Hong, Long-Jun Wu, Hui Zong
- Myeloid Cells in the Brain *Jennifer Shih*, Jaime Grutzendler, Dorothy Schafer, Harald Sontheimer
- Control of Neuronal Environment by Glia *Kevin Guttenplan*, Klaus-Armin Nave, Stefanie Schirmeyer, Anusha Mishra
- Glial Regulation of Neural Activity and Connectivity *Nicola Allen*, Lindsay De Biase, Rosa Chiara Paolicelli, Eunji Cheong, Nathalie Rouach, Vilaiwan Fernandes
- Glial Regulation of Complex Disorders *Kelly Monk*, *Klaus-Armin Nave*, *Harald Sontheimer*, Elena Blanco-Suarez, Mayssa Mokalled, Gaia Novarino
- The GRC Power Hour™ *Marc Freeman*, *Cagla Eroglu*

## Glycobiology



MAR 12-17, 2023 FOUR POINTS SHERATON / HOLIDAY INN EXPRESS, VENTURA, CA

CHAIRS: Vlad Panin and Kyoko Aoki-Kinoshita

VICE CHAIRS: Daniel Kolarich and Anne Imberty

- Keynote Session: Biological Functions of Major Glycosylation Pathways in Animals *Michael Tiermeyer*, Jeffrey Esko, Gerald Hart
- Glycoconjugate Biosynthesis, Trafficking and Signaling *Susan Bellis*, Nancy Dahms, Satoshi Goto, Shoko Nishihara
- Pathomechanisms of Glycosylation Disorders *Hudson Freeze*, Tadashi Suzuki
- Cell Communities, Pathogens and Viruses *Richard Cummings*, Tamara Doering, Eric Martens, Mohamed Abdel-Mohsen
- Glycoimmunology *Karin Hoffmeister*, Richard Cummings, James Paulson
- Evolution, Development and Neural Functions *Robert Haltiwanger*, Ajit Varki, Hiroshi Nakato
- Glycans in Pathobiology *Pamela Stanley*, Michael Demetriou, Richard Drake
- Glycoinformatics and Emerging Technologies for Glycoscience *Kelley Moremen*, Nicholas Scott, Stacy Malaker, Atsushi Kuno
- Multitude of Glycan Structures and Glycosylation Pathways *Gerald Hart*, Sriram Neelamegham, Henrik Clausen
- The GRC Power Hour™ *Nancy Dahms*, *Stacy Malaker*

## IGF and Insulin System in Physiology and Disease



MAR 12-17, 2023 VENTURA BEACH MARRIOTT, VENTURA, CA

CHAIRS: Wendie Cohick and Victor Han

VICE CHAIRS: Valentine Macaulay and Shoshana Yakar

- Keynote Session: Cellular Senescence and Aging: The Path to Translation *Robert Baxter*, James Kirkland, Phyllis Dennerly
- Early Life Origins of Health and Disease *Stephen Matthews*, Rebecca Simmons, David Hill, Miguel Constanica, Myriam Hemberger
- Tissue Homeostasis and Regeneration: Stem Cells and Cell Plasticity *Terri Wood*, Cuming Duan, Malgorzata Borowiak, Jason Mills, Friedrich Metzger

- **The Role of IGF and Insulin in Nutrient Sensing Related to Lifespan and Disease** *Jeff Holly*, Marc Tatar, Ruben Pio, Matthew Piper
- **IGF and Insulin System in Aging and Aging-Related Diseases** *Briony Forbes*, Derek Huffman, Richard Cubbon
- **Structure and Activation Mechanisms of Insulin, IGF and Hybrid Receptors: Recent Advances From Cryo-EM** *Pierre De Meyts*, Xiaochen Bai, Gerd Schluckebier, Únal Coskun, Nicholas Kirk
- **The IGF and Insulin Axis and Cancer** *Derek Leroith*, Rosemary O'Connor, Claire Perks, Emily Gallagher
- **Targeting the IGF and Insulin Axis in the Clinic** *Shoshana Yakar*, Douglas Yee, Joseph Ludwig, Guido Kroemer, Terry Smith
- **Keynote Session: New Methodologies to Advance IGF and Insulin Research** *Shin-Ichiro Takahashi*, Pnina Brodt, Klaus Kaestner
- **The GRC Power Hour™** *Elisabeth Barton*

## Immunology of Fungal Infections

**JAN 22-27, 2023** GRAND GALVEZ, GALVESTON, TX

**CHAIRS:** Jatin Vyas and Ilse Jacobsen

**VICE CHAIRS:** Tobias Hohl and Salomé LeibundGut-Landmann

- **Keynote Session: Signaling and Stress Response to Fungal Pathogens** *Sarah Gaffen*, Anita Sil, Michail Lionakis
- **Fungi and Co-Infections** *Amy Hise*, Joshua Obar, Ilan Schwartz, Priitha Sen
- **Early-Career Investigator Presentations** *Floyd Wormley, Carol Munro*, Antonia Akoumianaki, Mark Gresnigt, Neta Shlezinger, Liliane Mukaremera, Althea Campuzano
- **Therapeutic Strategies: From Vaccines to Immunotherapies** *Eric Pearlman, Karen Wozniak*, John Galgiani, Neil Gow
- **Fungi in Oncologic and Immune-Mediated Diseases** *Suzanne Noble*, Petra Bacher, Iliyan Iliev
- **From Bench to Bedside: Translating Fungal Immunity to Patients** *Michael Mansour, Anne Puel*, Jay Kolls, Thomas Lehmbacher, Don Sheppard
- **Immunogenetics and Fungal Immunity** *Carolina Coelho, Mihai Netea*, Agostinho Carvalho, Kevin Fuller
- **Innate Immunity in Fungal Infections** *Mairi Noveri, Robert Wheeler*, Stuart Levitz, Michael Lorenz, Jeniel Nett, Lena Heung
- **Effector Pathways in Fungal Immunity: Contributions of the Adaptive Immune Response** *Michal Olszewski, Salomé LeibundGut-Landmann*, Chiung-Yu Hung, Manish Butte
- **The GRC Power Hour™** *Heather Conti, Teresa Zelante*

## Inorganic Reaction Mechanisms

**MAR 5-10, 2023** GRAND GALVEZ, GALVESTON, TX

**CHAIR:** Jennifer Love

**VICE CHAIR:** Elon Ison

- **Bioinorganic Chemistry** *Elon Ison*, Wonwo Nam, Eva Nichols
- **First Row Metals** *Ethan Crumlin*, Hosea Nelson, Robert Gilliard, Renee Sifri
- **Ligand Non-Innocence: Redox Active/M-L Cooperativity** *Tianing Diao*, Kersha Clark, Karen Goldberg
- **Polymers and Materials** *Derek Wasylenko*, Aaron Sattler, Parisa Mehrkhodavandi, Michael Reynolds, David Steelman
- **Computational Chemistry** *Laurent Maron*, Sharon Hammes-Schiffer, Stuart Macgregor
- **Alternative Energy, Energy Conversion and Electrocatalysis** *Michael Pegis*, James Mayer, Gwendolyn Bailey, Shannon Stahl, Ba Tran
- **f-Block Chemistry** *James Blakemore*, Suzanne Bart, Andrew Gaunt
- **In Situ and New Methods** *Warren Piers*, Nicholas Ball, Karsten Meyer, Marcus Drover, Michael Whittlesey
- **Keynote Session: Active Sites and Mechanistic Probes Related to Catalytic Alkene Polymerization** *Patrick Holland*, Clark Landis
- **The GRC Power Hour™** *Lucie Nurdin, Marcus Drover*

## Mammalian DNA Repair

**FEB 5-10, 2023** FOUR POINTS SHERATON / HOLIDAY INN EXPRESS, VENTURA, CA

**CHAIR:** Patricia Opreko

**VICE CHAIR:** Roger Greenberg

- **Keynote Session: Frontiers in DNA Repair** *Karlene Cimprich*, Tanya Paull, K.J. Patel
- **Repair in Telomeres and Repetitive Sequences** *Hilda Pickett*, Titta de Lange, Eros Lazzarini Denchi, Puck Knipscheer, Evi Soutoglou
- **Single Molecule Approaches in DNA Repair** *Orlando Schärer*, Bennett Van Houten, Eric Greene, Wei Yang
- **CRISPR and Chromosome Break Repair** *Titia de Lange*, Britt Adamson, Lee Zou, Alberto Ciccia, Kara Bernstein
- **Replication Induced DNA Damage** *Evi Soutoglou*, David Cortez, Sharon Cantor, Helle Ulrich
- **Advances in Excision Repair** *Bret Freudenthal*, Orlando Schärer, Sheila David, Bret Freudenthal, Guo-Min Li, Nima Mosammapparast
- **DNA Damage, Repair and Immune Signaling** *Alberto Ciccia*, Joann Sweasy, Andrew Jackson, Karlene Cimprich
- **Targeting DNA Repair in Therapeutics** *Lee Zou*, Hilda Pickett, Simon Boulton, Christopher Bakkenist, Michal Zimmermann, Ralph Scully
- **DNA Damage in Aging and Disease** *Sharon Cantor*, Andre Nussenzweig, Laura Niedernhofer, Grant Stewart, Keith Caldecott
- **The GRC Power Hour™** *Sharon Cantor, Wei Yang*

## Mesophotic Coral Reef Ecosystems

**FEB 19-24, 2023** FOUR POINTS SHERATON / HOLIDAY INN EXPRESS, VENTURA, CA

**CHAIR:** Marc Slattery

**VICE CHAIRS:** Tyler Smith and Heather Spalding

- **Keynote Session: Trophic Ecology** *Sonia Rowley*, Michael Lesser, Benjamin Mueller
- **Biodiversity and Zonation** *Clark Sherman*, Heather Fullerton, Anthony Montgomery, Richard Pyle
- **Primary Producers** *Gal Eyal*, Alison Sherwood, Matthew Edwards
- **Connectivity and Modeling** *Frederic Sinniger*, Claire Paris-Limouzy, Robert Toonen, Erin Easton
- **Connectivity and Reproduction** *Daniel Holstein*, Jack Laverick, Rick Nemeth
- **Disturbances** *Joshua Voss*, Luiz Rocha, Or Ben-Zvi, Marilyn Brandt
- **Ecophysiology** *Peter Etnoyer*, Daniel Wangpraseurt, Jackie Padilla-Gamino
- **Climate Change** *Gretchen Goodbody-Gringley*, Tali Mass, Laëtitia Hédoüin, Carlo Cerrano
- **Conservation** *Marjorie Reaka*, Lucy Woodall, Randy Kosaki
- **The GRC Power Hour™** *Heather Spalding*

## Metabolomics and Human Health

**MAR 12-17, 2023** RENAISSANCE TUSCANY IL CIOCCO, LUCCA (BARGA), ITALY

**CHAIRS:** Steven Gross and Lorraine Brennan

**VICE CHAIRS:** Susan Sumner and Warwick Dunn

- **The Oncometabolite 2-Hydroxyglutarate: Genetic Versus Non-Genetic Sources in Cancers** *Warwick Dunn*, Craig Thompson
- **The Microbiome and Human Metabolome** *Gary Siuzdak*, Rima Kaddurah-Daouk, Sofia Forslund, Matej Oresic, Dirk Haller
- **Immunometabolism** *Thomas Hankemeier*, Luke O'Neill, Ron Heeren
- **Metabolome Nutrition and Precision Health** *Susan Sumner*, Elaine Holmes, Soumeiya Bekri
- **Capturing the Spatial Organization of Metabolism** *Richard Caprioli*, Per Andren, Ingela Lanekoff, Shawn Davidson
- **Biohacking Metabolism for Prolonged Lifespan and Healthspan** *Rima Kaddurah-Daouk, Elaine Holmes*, Johan Auwerx, Norbert Perrimon, Christopher Mason
- **Multomics to Assess Disease and Health Status** *Karsten Suhre*, Wiebke Art, Vassilios Fanos, Julian Griffin, Jingyuan Fu
- **Advances in Metabolomics Technologies** *David Wishart*, Gary Siuzdak, Christian Metallo, Claire O'Donovan
- **Harnessing Metabolic Individuality for Studying Health and Disease** *Matej Oresic*, Eileen White, Karsten Suhre
- **The GRC Power Hour™** *Susan Sumner, Warwick Dunn*

## Metals in Biology

**JAN 22-27, 2023** FOUR POINTS SHERATON / HOLIDAY INN EXPRESS, VENTURA, CA

**CHAIR:** Kara Bren

**VICE CHAIR:** Stephen Ragsdale

- **Metal Ions in Biological Sensing and Signaling** *Caryn Outten*, Christopher Chang, Emily Weinert, Marie Heffern
- **Structural Biology of Metallobiomolecules** *Sarah Bowman*, Nozomi Ando, Edward Snell, Stefano Ciarli, Jennifer Bridwell-Rabb, Flora Meillere
- **Biological Catalyst Design and Evolution** *Ambika Bhagi-Damodarani*, Rudi Fasan, Anabella Vancich, Giovanna Ghirlanda
- **Metallofactor Dynamics, Modification and Regulation** *R. David Britt*, Alejandro Vila, Joseph Cotruvo, Jr., Lucia Banci, Nick Le Brun, Daniel Suess
- **Controlling and Measuring Biological Electron Flow** *Ekaterrina Pletneva*, David Beratan, Carolyn (Cara) Lubner, Sean Elliott
- **Metals, Microbes, the Environment and Sustainability** *John Magyar*, Reza Ghiladi, Kelly Chacon, Ricardo Louro, Gemma Reguera, Nikhil Malvankar
- **Metallochemistry of the Global Elemental Cycles** *Kyle Lancaster*, Eric Hegg, Yvain Nicolet, Sharon Burgmayer
- **Understanding and Mimicking Biomolecular Strong Bond Activation** *Jenny Yang*, David Goldberg, Louise Berben, Yunho Lee, Smaranda Marinescu
- **Intersections of Materials and Bioinorganic Chemistry** *Alison Butler*, Gordana Dukovic, Woon Ju Song, Akif Tezcan
- **The GRC Power Hour™** *Lisa Olshansky*

## Micro and Nanoscale Phase Change Phenomena

**JAN 8-13, 2023** RENAISSANCE TUSCANY IL CIOCCO, LUCCA (BARGA), ITALY

**CHAIRS:** Vladimir Ajaev and Van Carey

**VICE CHAIR:** Nenad Miljkovic

- **Heat Transfer Enhancement with Nanoporous Membranes** *Shankar Narayan, Renkun Chen*, Chuanhua Duan, Ryan Enright
- **Micro and Nanoengineered Surfaces for Heat Transfer** *Damena Agonafer, Neelesh Patankar*, Kripa Varanasi, Patricia Weisensee, Shuhuai Yao
- **Icing Physics on Micro and Nanoengineered Surfaces** *Hadi Ghasemi, Sushant Anand*, Jonathan Boreyko, Thomas Schutzius
- **Evaporation Near Contact Lines** *Joel Plawsky, Pirouz Kavehpour*, Ali Beskok, Daniel Orejon, Pierre Colinet
- **Next-Generation Metrology Techniques** *Jonathan Maier, Li Shi*, Matteo Bucci, Amy Marconnet
- **Pulsating and Oscillating Heat Pipes, Vapor Chambers** *Hongbin Ma*, Sameer Khandekar, Vadim Nikolayev

• **Machine Learning, AI and Virtual Reality for Phase Change**

- *Chirag Kharangate*, Yoonjin Won, Vinod Srinivasan
- **Additive Manufacturing** *Jim Yao Ho*, William King, Xiaoping Qian, Xiaoxing Xia
- **Phase Change Materials** *Jason Woods, Allison Mahvi*, Patrick Shamberger, Neera Jain
- **The GRC Power Hour™** *Patricia Weisensee*

## Mitochondria in Health and Disease

**FEB 5-10, 2023** RENAISSANCE TUSCANY IL CIOCCO, LUCCA (BARGA), ITALY

**CHAIRS:** Atan Gross and Nika Danial

**VICE CHAIRS:** Giovanni Manfredi and Janine Santos

- **Mitochondrial Energy Metabolism and Redox Regulation** *Paolo Bernardi*, Bruce Spiegelman, Anu Suomalainen, Julien Prudent
- **Mitochondrial Genome Maintenance and Editing** *Janine Santos*, Samantha Lewis, Bill Copeland, Carlos Moraes
- **Mitochondrial Protein Biogenesis** *Agnieszka Chacinska*, Cole Haynes, Thomas Becker
- **Proteostasis** *Giovanni Manfredi*, Thomas Langer, Erika Holzbaur, Cynthia McMurray
- **Interorganellar Crosstalk** *Heidi McBride*, Meng Wang, Luca Scorrano, Jodi Nunnari
- **Iron Trafficking and Metabolism** *Roland Lill*, Heidi McBride, Hélène Puccio, Adam Hughes
- **Mitochondrial Carrier Proteins and Transporters** *Jean-Claude Martinou*, Edmund Kunji, Gyorgy Hajnoczky, Jared Rutter
- **Mitochondria in Senescence and Aging** *Anu Suomalainen*, Gerald Shadel
- **Mitochondria and Metabolic Regulation** *Orian Shirihai*, Navdeep Chandel, Evanna Mills
- **The GRC Power Hour™** *Jodi Nunnari*

## Multi-Drug Efflux Systems

**MAR 26-31, 2023** GRAND GALVEZ, GALVESTON, TX

**CHAIRS:** Ina Urbatsch and Satoshi Murakami

**VICE CHAIRS:** Lauren Aleksunes and Hendrik van Veen

- **Keynote Session: Paths to Discovery of Better Drugs, and Integrated Approaches to Predict their Efficacy** *Suresh Ambudkar*, Helen Zgurskaya, Jashvanti (Jash) Unadkat
- **Molecular Determinants of Drug-Binding and Drug Translocation Pathways in Multidrug Efflux Systems** *Karl Kuchler, Vassily Bavro*, Qinghai Zhang, Lutz Schmitt, Paolo Ruggerone, Osamu Nureki, Megan O'Mara
- **Genomics, Proteomics and Transcriptomics of Drug Resistance Across Diseases** *Beth McCormick*, William Shafer, Michael Gottesman, Ian Paulsen
- **Efflux Transporters in Reproduction: From Physiology to Barriers** *Nathan Cherrington*, Lynae Brayboy, Zhicheng Dou, Silvina Perez Martinez
- **Host-Pathogen Interactions and Multidrug Efflux in Acute and Chronic Cystic Fibrosis Lung Infections** *Herbert Schweizer*, John Hunt, Patrick Thibodeau
- **New Roads Leading to Old Destinations: Therapeutic Targeting of Multidrug Transporters** *Vadivel Ganapathy*, Jean Michel Bolla, Olga Lomovskaya
- **Efflux Pumps in Global Health During a Pandemic** *Lauren Aleksunes*, Balazs Sarkadi, Miguel Viveiros, Lalita Ramakrishnan
- **New Biochemical/Physical, and Computational Methods to Elucidate Structure-Function Relationships and Transport Mechanisms** *Hendrik van Veen*, Hassane Mchaourab, Arne Moeller, Maria-Elena Zoghbi
- **Disruption of Efflux Transporters: Novel Mechanisms of Regulation** *John Schuetz*, Jessica Blair, Ronald Cannon, Bjoern Bauer
- **The GRC Power Hour™** *Deanna Kroetz, William Shafer*

## Nanomaterials for Applications in Energy Technology

**FEB 26 - MAR 3, 2023** VENTURA BEACH MARRIOTT, VENTURA, CA

**CHAIR:** Matthew McDowell

**VICE CHAIR:** Yury Gogotsi

- **Keynote Session: Nanoscale Materials for Energy** *William Chueh*, M. Stanley Whittingham, Harry Atwater
- **Interaction of Materials with Light** *Joseph Luther*, Delia Milliron, André Taylor, Juan-Pablo Correa-Baena
- **Synthesis of Nanoscale Materials for Energy** *Lorenzo Mangolini*, Yu Huang, Maksym Kovalenko
- **Materials for Batteries** *Betar Gallant*, Linda Nazar, Ying Shirley Meng, Gene Berdichevsky
- **Materials Chemistry for Energy Storage** *Paul Braun*, Serena Cusssen, Kimberly See
- **Fuels, Catalysis and Photocatalysis** *Matteo Cargnello*, Karthik Manthiram, Francesca Maria Toma, Jennifer Dionne
- **2D Materials for Energy** *Abdoulaye Djire*, Manish Chhowalla, Valeria Nicolosi
- **Modeling, Data Analytics, and Machine Learning for Energy Materials** *De-en Jiang*, Prineha Narang, Maria Chan, Shyue Ping Ong
- **Energy Storage: Materials and Mechanisms** *Candace Chan*, Ekaterina Pomerantseva, Huolin Xin
- **The GRC Power Hour™** *Kimberly See*



## Neural Crest and Cranial Placodes



FEB 26 - MAR 3, 2023 RENAISSANCE TUSCANY IL CIOCCO, LUCCA (BARGA), ITALY

CHAIR: Paul Trainor

VICE CHAIR: Lisa Taneyhill

- **Systems Biology of Sensory Organs** *Sally Moody, Clare Baker, Linda Barlow*
- **EMT, Matrix Interactions and Forces** *M. Angela Nieto, Eric Theveneau, Guojun Sheng*
- **Single and Collective Cell Migration Dynamics** *Roberto Mayor, Paul Kulesa, Frances Lefcort*
- **Neural Crest Cell and Placode Interactions** *Andrea Streit, Marie Breaud, Paolo Forni*
- **Development and Morphogenesis** *Jean-Pierre Saint-Jeannet, Susan Wray, Kristen Kwan*
- **Evolution, Patterning and Differentiation** *Thomas Schilling, Andrew Groves, Tanya Whitfield*
- **Neurocristopathies and Sensory System Disorders** *Marianne Bronner, H. Joseph Yost, Hideki Enomoto*
- **Stem Cells and Multipotency** *Mai Har Sham, Robert Kelsch, Julia Ganz*
- **Neural Crest Cells in Cancer** *Lukas Sommer, Ankur Saxena, Valerie Castellani*
- **The GRC Power Hour™** *Paul Trainor, Lisa Taneyhill*

## Neuroimmune Communication in Health and Disease



JAN 22-27, 2023 VENTURA BEACH MARRIOTT, VENTURA, CA

CHAIR: Robyn Klein

VICE CHAIRS: Isaac Chiu and Frauke Zipp

- **Keynote Session: Co-Evolution of the Nervous and Immune Systems** *Carla Shatz, Thomas Bosch, Irene Salinas, Mario De Bono, Javier Irazoqui*
- **Drivers of Brain and CNS Lymphatics** *Katerina Akassoglou, Zsuzsanna Fabry, Berislav Zlokovic, Chenghua Gu, Jonathan Kipnis*
- **Micro- and Macrogliia in Neurologic Disease** *Beth Stevens, Benjamin Deneen, Cagla Eroglu, Adam Denes, Anne Schaefer, Dorothy Schafer*
- **Microbial Crosstalk with the Nervous System in Health and Disease** *Dorian McGavern, Elaine Hsiao, Adriano Aguzzi, Francesca Odoardi*
- **Neurological Effects of COVID-19** *Marco Colonna, Stanley Perlman, Michelle Monje, Michelle Erickson, Laura Pellegrini*
- **Aging and Neurodegeneration** *Marco Prinz, Li-Huei Tsai, Michel Desjardins, Li Gan, Alison Goate*
- **Cancers and Neuroimmune-Tumor Interactions** *Hideho Okada, Milan Chheda, Justin Lathia, Frank Winkler*
- **CNS Autoimmunity: An Expanding Disease Category** *Francisco Quintana, Jennifer Gommerman, Burkhard Becher, Dorothy Schafer*
- **Pain, Itch and Neuroimmunity** *Florent Ginhoux, Dan Kaplan, Tuan Trang, Seog Bae Oh, Diana Bautista*
- **The GRC Power Hour™** *Anne Schaefer*

## Nitric Oxide



FEB 12-17, 2023 VENTURA BEACH MARRIOTT, VENTURA, CA

CHAIR: Andrew Gow

VICE CHAIR: Miriam Cortese-Krott

- **Keynote Session: Heme and Nitric Oxide** *Jonathan Stamler, Dennis Stuehr, Kyle Lancaster*
- **Cardiovascular Function: The Role of Nitric Oxide in Physical Performance** *Jason Allen, Anni Vanhatalo, Simone Porcelli, Chris Easton*
- **Cysteine Modification** *Harry Ischiropoulos, Elizabeth Murphy, Paschalis-Thomas Doulias*
- **Nitric Oxide Production and its Sources** *David Wink, Mattias Carlstrom, Takaaki Akaike*
- **Interactions with Persulfides and Other Oxidants** *Martin Feelisch, Miriam Cortese-Krott, Melanie Madhani*
- **The Role of Nitric Oxide in Pregnancy** *Sruti Shiva, Shathiyah Kulandavelu, Phoebe Stapleton, Thea Golden*
- **Cellular Phenotype and Signaling** *Bruce Freeman, Mark Crabtree, Elizabeth Cottrell, Erika Palmieri*
- **Nitric Oxide and Respiratory Health** *Debra Laskin, Lorenzo Berra, Stacy Wendell, Serpil Erzurum*
- **Keynote Session: Nitric Oxide Signaling in Vascular Health** *Mark Gladwin, Brant Isakson, Jon Lundberg*
- **The GRC Power Hour™** *Miriam Cortese-Krott*

## Peptide Materials



JAN 15-20, 2023 GRAND GALVEZ, GALVESTON, TX

CHAIRS: Matthew Tirrell and Honggang Cui

VICE CHAIRS: Darrin Pochan and Meital Reches

- **Keynote Session: Peptides as Materials Building Units** *David Lynn, Joel Schneider, Samuel Gellman, Ronald Zuckermann*
- **Peptides Expand the Functional Space of Materials Science and Engineering** *Matthew Webber, James Schneider, Phillip Messersmith, Zhibin Guan, Jean Chmielewski, Sebastien Lecommandoux, Akif Tezcan*
- **Emerging Topics in Peptide Materials** *Nurit Ashkenasy, Ehud Gazit, David Lynn, Sarah Perry*
- **Polypeptides Push the Boundaries of Macromolecular Materials** *Sebastien Lecommandoux, Jessica Kramer, Timothy Deming, Matthew Francis, Karen Wooley, J. D. Tovar, Jianjun Cheng*

- **Strategies to Craft Next-Generation Peptide Materials** *Bing Xu, Samuel Stupp, Rein Ulijn*
- **Proteins and Peptides as Structural and Functional Units** *Tommy Pashuck, Raffaele Mezzenga, Joel Collier, Sarah Heilshorn, Etie Kokkoti, Julie Champion, Jeffrey Hartgerink*
- **Early-Career Investigator Presentations** *Meital Reches, Darrin Pochan, Lesley Chow, Handan Acar, Danielle Mai, Jing Yu, Nicholas Stephanopoulos, Herdeline Ann Ardoña*
- **Engineering Peptide Materials at the Interface of Chemistry, Biology and Medicine** *Jianfeng Cai, Dave Adams, Bing Xu, Xue Conticello, Edward Egelman, Xuehai Yan*
- **Keynote Session: Peptides and Proteins as Functional Materials** *Michael Yu, Ashutosh Chilkoti, David Tirrell*
- **The GRC Power Hour™** *Lesley Chow*

## Physical Science of Cancer



FEB 5-10, 2023 GRAND GALVEZ, GALVESTON, TX

CHAIRS: David Odde and Jennifer Munson

VICE CHAIRS: Kandice Tanner and Erik Sahai

- **Signaling Across Boundaries** *Kristen Naegle, Douglas Lauffenburger, Stacey Finley, Elana Fertig*
- **Mechano-Genomics** *John Marko, Karmella Haynes, Matthieu Piel*
- **Cells at Rest: Proliferation and Dormancy** *Maria Sosa, Scott Manalis, Shelly Peyton*
- **The Biophysics of Tumor Immunity** *Heiko Enderling, Li Tang, Eduardo Reategui*
- **Invasion and Metastasis** *Kandice Tanner, Pere Roca-Cusachs, Kimberly Stroka, Gordana Vunjak-Novakovic*
- **Tumor Mechanics: Transport and Forces Across Scales** *Maisa Santinoranon, Rebecca Shipley, Jeremy Teo*
- **Connecting Physics with Metabolism** *Michael Murrell, Claudia Fischbach, Cynthia Reinhart-King*
- **Stromal Dynamics** *Catherine Whittington, Marvin Doyle, David Basanta*
- **Clinical Applications Toward Personalized Detection and Therapy** *Erica Pratt, Kristin Swanson, Clayton Yates*
- **The GRC Power Hour™** *Claudia Fischbach, Nastaran Zahir*

## Physical Virology



JAN 22-27, 2023 RENAISSANCE TUSCANY IL CIOCCO, LUCCA (BARGA), ITALY

CHAIRS: Michael Hagan and Charlotte Uetrecht

VICE CHAIR: Frank Sainsbury

- **Virus Dynamics and Mechanics to Breaking Symmetry** *Roya Zandi, Juan Perilla, Wouter Roos, Audrey Harris*
- **Virus Inspired Designs: From Materials to Other Organisms** *Danielle Tullman-Ercek, Fasseli Coulibaly, Seth Fraden, Tobias Giessen, Cheryl Kerfeld*
- **Biomedical Applications** *Reidun Twarock, Laura Palomares, Antonette Bennett, Priscilla Yang*
- **Principles that Govern Virus Assembly and Disassembly** *Jodi Hadden-Perilla, Carolyn Teschke, Shee-Mei Lok, Vikram Jadhao*
- **How Viruses Capture and Release Cargo** *Paul van der Schoot, Mauricio Comas-Garcia, Tuli Mukhopadhyay, Robijn Bruinsma*
- **From Viruses and Host Immune Interactions to Better Vaccines** *Tobias Beck, Arup Chakraborty, Hanneke Schuitemaker, Aleksandra Walczak*
- **Virus-Host Protein Interaction Networks** *Kelly Lee, Alfredo Castello, Philippe Lemey*
- **Viruses and Membrane Compartments** *Nicole Tischler, Margaret Johnson, Montserrat Barcena, Stefanie Barbiz, Urs Greber*
- **Keynote Session: Connecting Fundamental and Applied Physical Virology** *Rudolf Podgornik, Stephen Harrison, Chantal Abergel*
- **The GRC Power Hour™** *Johnna Frierson*

## Physiology, Biology and Pathology of Phosphate



FEB 12-17, 2023 GRAND GALVEZ, GALVESTON, TX

CHAIRS: Sharon Moe and Christian Faul

VICE CHAIRS: Carsten Wagner and Aline Martin

- **Keynote Session: Phosphate in Health and Disease** *Aline Martin, Carsten Wagner, Orson Moe, Joachim Ix*
- **Organs Contributing to Phosphate Homeostasis and Endocrine Regulators** *Heini Murer, Outi Makitie, Reinhold Erben, Nati Hernandez, Monzur Murshed*
- **Disorders of Phosphate Homeostasis** *Farzana Perwad, Michael Econs, Qiaoli Li, Harald Jueppner*
- **Organ Crosstalk in the Regulation of Phosphate Balance** *Myles Wolf, Petra Simic, Kenneth White, Valentin David, Chou-Long Huang, Hannes Olauson*
- **Phosphate Sensing, Uptake, Signaling and Effects in Cells** *Michael Mannstadt, Clemens Bergwitz, Todd Alexander, Laurent Beck, George Beck*
- **Pathologic Effects of Phosphate on Cells** *Jason Stubbs, Mohammed Razaque, Elena Aikawa, Daniel Bondeson, Tally Naveh, Timo Rieg*
- **Biology of Phosphate Containing Complexes** *Steve Holt, Sagar Nigwekar, Marc Vervloet, Dorothea Fiedler, Andreas Mayer*
- **Measurement and Models** *Jakob Voelkl, Michel Chonchol, Rosa Maria Alfonso Moya, Tamara Isakova, Angel Orte, Johan Thevelein, Jieyu Chen*
- **Diet, Microbiome and Intestinal Phosphate Absorption** *Ziad Massy, Jaime Uribarri, Orlando Gutierrez, Kathleen Hill Gallant, Annabel Biruete*
- **The GRC Power Hour™** *Eleanor Lederer, Cassianne Robinson-Cohen*

## Plant Lipids: Structure, Metabolism and Function



JAN 29 - FEB 3, 2023 GRAND GALVEZ, GALVESTON, TX

CHAIRS: Rebecca Roston and Yonghua Li-Beisson

VICE CHAIR: Aruna Kilaru

- **Membrane Contact Sites and Their Functions** *Juliette Jouhet, Noemi Ruiz-Lopez, Will Prinz*
- **Lipids on the Edge, Cutin Suberin and Waxes** *Dylan Kosma, Sarah McKim, Christiane Nawrath*
- **Lipid Synthesis and Modification** *Philip Bates, Jantana Blanford, Tegan Haslam*
- **Lipid-Based Signaling** *Ana Laxalt, Ingo Heilmann, Jingzhe Guo*
- **Innovative Technical Advances in Lipid Analysis** *Ruth Welti, Marie-Cecile Caillaud, Annemarie Perez Boerema*
- **Isoprenoids, Sterols and Lipid-Derived Products** *Peter Doermann, Natalia Dudareva, Eric Moellering*
- **Lipids for Storage, Biofuels and Bioproducts** *Mie Shimojima, Agnieszka Zienkiewicz, Meng Zhang, Itay Budin*
- **Lipid Dynamics, Synthesis, Flux and Degradation** *Marina Gavilanes-Ruiz, Susanne Hoffmann-Benning, Patrick Horn*
- **Gaps in Translating Basic Lipid Science to Human Benefit** *Aruna Kilaru, John Browse, Mee Len Chye, Johnathan Napier*
- **The GRC Power Hour™** *Yonghua Li-Beisson, Rebecca Roston*

## Plant-Herbivore Interaction



FEB 26 - MAR 3, 2023 FOUR POINTS SHERATON / HOLIDAY INN EXPRESS, VENTURA, CA

CHAIR: Jennifer Thaler

VICE CHAIR: Noah Whiteman

- **Keynote Session: Synthesis in Plant-Herbivore Interactions** *Noah Whiteman, Julia Koricheva*
- **Plant Perception and Defense** *Vered Tzin, Adam Steinbrenner, Consuelo De Moraes, Gen-ichiro Arimura, Saskia Hogenhout*
- **Sensory Biology of Host Plant Selection** *Carolina Reisenman, Anne Leonard, Markus Knaden*
- **Effects of Plant Diversity on Herbivores and their Natural Enemies** *Lora Richards, Luis Abdala-Roberts, Tobias Züst, Katja Poveda, Jared Ali*
- **Tradeoffs Between Attracting Mutualists and Defending Against Antagonists** *Monica Kersch-Becker, Florian Schiestl, Kim Valenta*
- **Communities, Ecosystems and Conservation Biology** *Amy Dunham, Sally Archibald, Christopher Fettig, Orou Gaoue, Shuqing Xu*
- **Herbivores as Drivers of Plant Evolution** *Diego Salazar, Erika de Castro, Caroline Stromberg*
- **Microbial Mediation of Plant-Herbivore Interactions** *Rachel Vannette, Aileen Berasategui, Donovan German, Mark Hay, Neena Mitter*
- **Networking From Genes to Communities** *Serguei Saavedra, Matt Barbour, Sarah O'Connor*
- **The GRC Power Hour™** *Karina Boege, Deane Bowers*

## Polar Marine Science



MAR 5-10, 2023 FOUR POINTS SHERATON / HOLIDAY INN EXPRESS, VENTURA, CA

CHAIRS: Klaus Meiners and Patricia Matrai

- **Status, Trends and Emerging Physical Properties of Polar Oceans** *Kristina Brown, Michael Steele, Andrew Meijers*
- **Drivers and Impacts of Changing Sea Ice Dynamics** *Marilyn Raphael, Lettie Roach, Will Hobbs, Sohey Nihashi*
- **Changes in Polar Ocean Biogeochemistry: Paleo- and Future States** *Patricia Yager, Elizabeth Shadwick, Juliane Müller*
- **Impacts of a Changing Cryosphere on Polar Marine Biogeochemistry and Ecosystem Function** *Letizia Tedesco, Sebastien Moreau, Mathieu Ardyna, Jose Luis Iriarte*
- **Complexity, Connectivity and Change in Polar Marine Foodwebs** *Camilla Svensen, Maxime Geoffroy, Andrew Brierley*
- **The Role of Interactive Effects of Multiple Drivers in Structuring Polar Marine Ecosystems** *Philip Boyd, Clara Jule Marie Hoppe, Erin Bertrand, Vonda Cummings*
- **Crossing Boundaries in Observing Coupled Ocean-Ice-Atmosphere Systems** *Leo Lacour, Manuel Dall'Osto, Alison Gray*
- **Predicting Habitat Changes, Range Shifts and Impacts on Populations** *Ryan Reisinger, Huw Griffiths, Mónica Muelbert, Jilda Caccavo*
- **Assessing Climate Change Impacts on Coupled Social-Ecological Systems** *Nadja Steiner, Cassandra Brooks, Henry Huntington*
- **The GRC Power Hour™** *Martine Lizotte*

## Quantitative Genetics and Genomics



FEB 12-17, 2023 FOUR POINTS SHERATON / HOLIDAY INN EXPRESS, VENTURA, CA

CHAIR: Guilherme Rosa

VICE CHAIRS: Josephine Pemberton and Na Cai

- **Genetic Architecture of Quantitative Traits** *Jack Dekkers, Chris-Carolin Schoen, Gustavo de los Campos*
- **Prediction of Complex Traits** *Ivian Breen, Miguel Perez-Enciso, Daniela Lourenco, Charlie Messina*
- **Epigenetic Variation** *Libertat Tusell Palomero, Hasan Khatib, Nathan Springer*
- **Evolution of Quantitative Traits** *Bruce Walsh, Matthew Hufford, Suzanne McCaugh*

- **Selection and Breeding Strategies** *Aniek Bouwman*, Maria Martínez Castellero, Edward Buckler
- **Use of Functional Annotation** *Clare Gill*, Angela Cánovas, David Houle
- **Gene Mapping and Functional Genomics** *Ana Vazquez*, Marylyn Ritchie, Loic Yengo
- **High-Throughput Phenotyping** *Alexander Lipka*, Luiz Brito, Jonathan Lynch
- **Health and Welfare Traits** *Andrea Doeschl-Wilson*, Juan Steibel, Gosia Trynka
- **The GRC Power Hour™** *Rita Mumm*

## Quantum Biology

NEW!

MAR 19-24, 2023 GRAND GALVEZ, GALVESTON, TX

CHAIRS: Youngchan Kim and Clarice Aiello

VICE CHAIRS: Jonathan Woodward and Wendy Beane

- **Keynote Session: Successes and Challenges in Quantum Biology** *Johnnoe McFadden*, Judith Klinman, Alexandra Olaya-Castro
- **Electron and Nuclear Magnetic Resonance Methods** *Alex Jones*, Kininori Maeda, Graham Timmins, Yasuhiro Kobori, Yun Chen
- **Quantum Sensing and Imaging** *Greg Engel*, Scott Cushing, Theodore Goodson, Stan Botchway
- **Ultrafast Spectroscopy** *Jennifer Ogilvie*, Elisabet Romero, Tom Oliver, Elad Harel, Greg Engel
- **Biological Model Systems** *Francisco Laurindo*, Masakazu Iwai, Steven Vogel, Margaret Ahmad
- **Quantum-Enhanced Measurements** *Luke Lee*, Gregory Scholes, Warwick Bowen, Kasturi Saha, Romana Schirhagl, Justin Caram, Christoph Lambert
- **Frontier Approaches to Quantum Biology** *Daniel Kattnig*, Paul S. Weiss, Michael Wasielewski, Lydia Kisley
- **Quantum and Classical Effects in Biology: Theoretical Approaches** *Philip Kurian*, Susana Huelga, Ilya Sinayskiy, Sharon Hammes-Schiffer, Ilya Solov'yov, Mike Reppert
- **Quantum and Classical Effects in Biology: Computational Methods** *Birgitta Whaley*, Thorsten Ritz, Marco Sacchi, Philip Kurian
- **The GRC Power Hour™** *Lydia Kisley, Yun Chen*

## RNA Editing

+ GFS

MAR 19-24, 2023 VENTURA BEACH MARRIOTT, VENTURA, CA

CHAIRS: Peter Beal and Linda Chelico

VICE CHAIRS: Joshua Rosenthal and Ute Kothe

- **Keynote Session: Physiological Functions of Editing and Modifications** *Ute Kothe*, Wendy Gilbert, Reuben Harris, Kazuko Nishikura
- **Dynamics and Mechanism of Editing and Modification Reactions** *Joshua Rosenthal*, Heather Hundley, Eric Phizicky, Sebastian Leidel, Jane Jackman, Juan Alfonso, Kristin Koutmou
- **Evolution of Editing and Modification Systems** *Silvo Conticello*, Eli Eisenberg, Mareike Schallenberg-Ruedinger, Valerie De Crecy-Lagard, Javier Di Noia
- **New Tools for the Study and Detection of Nucleic Acid Modifications** *Eric Phizicky*, *F. Nina Papavasiliou*, Jordan Meier, Peter Dedon, Andrea Rentmeister, Rahul Kohli, Ronald Micura, Eugene Yeo, Mark Helm
- **Structures of Editing and Modification Enzymes** *Jin Billy Li*, Andrew Fisher, Xiaojiang Chen, Stewart Shuman, Tsutomu Suzuki
- **Engineering Novel Base Editors and Modification Systems** *Ronald Emeson*, Holly Rees, Alexis Komor, Thorsten Stafforst, Prashant Mali, Yi-Tao Yu, Mani Larjani, Audrone (Audrey) Lapinaite
- **Modification and Editing in Immunity** *Mary O'Connell*, F. Nina Papavasiliou, Jin Billy Li, Stacy Horner, Erez Levanon
- **Defects in Editing and Modification in Disease** *F. Nina Papavasiliou*, *Brenda Brass*, Michael Jantsch, Polly Leille Chen, Yunsun Nam, Qingfei Jiang, Ruslan Afasizhev, Denis Lafontaine, Catriona Jamieson
- **Keynote Session: Editing and Modification Pathways as Therapeutic Modality or Target** *Reuben Harris*, Chuan He, Jennifer Heemstra, Chandra Vargeese
- **The GRC Power Hour™** *Alexis Komor, Jane Jackman*

## RNA Nanotechnology

+ GFS

JAN 8-13, 2023 FOUR POINTS SHERATON / HOLIDAY INN EXPRESS, VENTURA, CA

CHAIRS: Sarah Woodson and Louise Laurent

VICE CHAIRS: Mark Bathe and Dolores Di Vizio

- **RNA Structure and Assembly** *Donovan Chin*, William Greenleaf, Rhiju Das, Peter Stockley, Silvi Rouskin
- **RNA Therapeutics** *Tushar Patel*, Xandra Breakfield, Judy Lieberman, Muthiah (Mano) Manoharan
- **RNA Aptamers and Riboswitches** *Kirill Afonin*, Ming Hammond, Julius Lucks, Netz Arroyo
- **RNA Encapsulation and Delivery** *Thomas Hermann*, Drew Weissman, Anil Sood
- **RNA Modifications and Biotypes** *Jorgen Kjems*, Wendy Gilbert, Ryan Flynn, Todd Lowe
- **RNA Imaging** *Nils Walter*, Amy Palmer, Tijana Jovanovic-Talman, Andres Jäschke, David Shechner
- **RNA Cargo Selection in EVs** *Xandra Breakfield*, Samir El Andaloussi, Aissa Weaver, Jayanta Debnath
- **RNA-Based Biomarkers and Diagnostics** *Kendall Van Keuren-Jensen*, Saumya Das, Yu-Hwa Lo, Müller Fabbri
- **Synthetic and Programmed Nucleic Acid Assemblies** *Peixuan Guo*, Friedrich Simmel, Rebecca Schulman, Chengde Mao
- **The GRC Power Hour™** *Wendy Gilbert*

## Salivary Glands and Exocrine Biology + GFS

JAN 29-FEB 3, 2023 FOUR POINTS SHERATON / HOLIDAY INN EXPRESS, VENTURA, CA

CHAIRS: Olga Baker and Jay Chiorini

VICE CHAIRS: Isabelle Lombaert and Gordon Proctor

- **Keynote Session: Systems Biology and Stem Cells: From Aging to Cancer** *Stefan Ruhl*, Sarah Knox, J. Silvio Gutkind, Leanne Jones
- **Virus Infection of the Salivary Glands** *Jennifer Webster-Cyriaque*, Qing Yu, Nihal Altan-Bonnet, Kevin Byrd, Wendy Maury
- **Salivary Protein Secretion and Glycobiology** *Walter Siqueira*, Marcelo Catalan, Markus Hardt, Malin Johansson, Anwsha Sarkar, Kelly Ten Hagen
- **The Immune System: Sjögren's Disease Pathogenesis** *Umesh Deshmukh*, *Shmuel Muallem*, Michele Bombardiere, Jill Kramer, Fei Liu, Gary Weisman
- **Salivary Gland Regeneration and Tissue Repair: From Cells to Organs** *Marit Aure*, *Mary Farach-Carson*, Danielle Benoit, Sarah Knox, Maike Sander
- **Use of Emerging Technologies in Salivary Glands** *Kirsten Limesand*, *David Yule*, Nagarajan (Raj) Kannan, Megha Padi, Rose-Anne Romano
- **Advances in the Clinic: New Therapies for Exocrine Gland Dysfunction** *Alan Baer*, *Brij Singh*, Rob Coppes, Michael Passineau
- **Genomics and Biomarkers of Exocrine Gland Diseases** *Chris Lessard*, *Cuong Nguyen*, Darise Farris
- **Keynote Session: Resolution of Inflammation** *Isabelle Lombaert*, *Gordon Proctor*, Charles Serhan
- **The GRC Power Hour™** *Belinda Hauser*

## Sex Differences in Immunity

NEW!

APR 2-7, 2023 FOUR POINTS SHERATON / HOLIDAY INN EXPRESS, VENTURA, CA

CHAIR: Sabra Klein

VICE CHAIR: Igho Ofotokun

- **Sex Differences in Autoimmunity** *Jayne Danska*, *Janilyn Arsenio*, Shannon Dunn, Jean-Charles Guéry
- **Genetic and Hormonal Mediators of Sex Differences in Respiratory Diseases** *William Bishai*, Dawn Newcomb, Qian Zhang, Djeneba Dabitao
- **Sex Differences in Cancer Outcomes and Responses to Treatments** *Fabio Conforti*, Paul Boutros, Josh Rubin
- **Sex Differences in Immunity to Vaccines Across the Life Course** *Inna Ovsyannikova*, *Lauren Collins*, Christine Stabell Benn, Mihai Netea
- **Sex Differences in Mucosal Immunity** *Ed Lavelle*, *Michal Tal*, Molly Ingersoll, Christopher Robinson
- **Development of Sex Differences in Neuroimmunity** *Jaclyn Schwarz*, Margaret McCarthy, Louise McCullough
- **Sex and Gender-Based Differences in HIV** *Elizabeth Connick*, Marcus Altfeld, Eileen Scully
- **Hormonal and Metabolic Influences on Sex Differences in Immunity** *Maureen Su*, Durga Singer, Suresh Mishra, Josh Thaler
- **Genetic Modifiers of Sex Differences in Immunity** *Christine Disteche*, Tal Shay, Jennifer Regan
- **The GRC Power Hour™** *Janine Clayton*

## Speciation

+ GFS

JAN 29 - FEB 3, 2023 RENAISSANCE TUSCANY IL CIOCCO, LUCCA (BARGA), ITALY

CHAIR: Katie Peichel

VICE CHAIR: Daniel Bolnick

- **Macroevolutionary Patterns of Species Origin, Persistence and Extinction** *Sonal Singhal*, Tiago Quental, Lindell Bromham
- **Ecological Divergence as a Driver of Speciation** *Rosemary Gillespie*, Craig Moritz, Luke Harmon, Rebecca Safran
- **Ecological Persistence after Speciation** *Rachel Germain*, Anita Narwani, Sebastian Schreiber
- **Reproductive Divergence as a Driver of Speciation** *Erik Svensson*, Rike Stelkens, Andrea Schweigart, Krushnamegh Kunte
- **Reproductive Persistence after Speciation** *Sharon Strauss*, Kathleen Kay, Daniel Ortiz-Barrientos
- **Conflict and Cooperation in the Origin and Maintenance of Species** *Salvatore Cozzolino*, Naomi Pierce, Tim Barraclough, Hanna Kokko
- **Speciation Genetics: From Reproductive Isolation to Coexistence** *Jun Kitano*, Daven Presgraves, Patrik Nosil
- **Introgression's Role in Speciation and Persistence** *Jonna Kulmuni*, Christelle Fraisse, Konrad Lohse, Ricardo Pereira
- **Keynote Session: Mesoevolution as a Link Between Microevolutionary Divergence and Macroevolutionary Patterns** *Christopher Martin*, Bree Rosenblum, Nicholas Barton, Dolph Schluter
- **The GRC Power Hour™** *Jenn Coughlan*

## Stochastic Physics in Biology

+ GFS

JAN 15-20, 2023 FOUR POINTS SHERATON / HOLIDAY INN EXPRESS, VENTURA, CA

CHAIR: Jie Xiao

VICE CHAIR: Andrew Mugler

- **Stochastic Physics in Gene Expression** *Ertugrul Ozbudak*, Natalia Komarova, Leor Weinberger
- **Sensing and Signaling** *Wallace Marshall*, Thierry Emonet, Christine Payne, Pieter Ten Wolde, Yuhai Tu
- **Modeling of Cellular Processes** *Zaida Luthey-Schulten*, Jay Newby, Moumita Das, Jian Liu
- **Thermodynamics of Biological Systems** *Herbert Levine*, Ken Dill, Albert Lau, Ben Machta, Hong Qin, Jian Wang
- **Inference of Biological Models and Pathways** *Andrew Mugler*, Arvind Murugan, Hilary Collier, Thierry Mora

- **Protein Interactions in Singles and in Communities** *Wenying Shou*, Jing Yan, Vermita Gordon, Linda Kenney, Srividya Iyer-Biswas, Lingchong You
- **Pattern Formation in Biological Systems** *Margaret Johnson*, Orit Peleg, Keng-hui Lin, Cristina Marchetti
- **Growth and Development** *Elizabeth Read*, Lev Tsimring, Madhav Mani
- **Spatial Organization of Biological Functions and Activities** *Michelle Mayalu*, Bin Zhang, Sarah Yeatch
- **The GRC Power Hour™** *Srividya Iyer-Biswas, Hong Qian*

## Translation Machinery in Health and Disease

+ GFS

FEB 19-24, 2023 GRAND GALVEZ, GALVESTON, TX

CHAIR: Tao Pan

VICE CHAIRS: Zoya Ignatova and Katherine Borden

- **Keynote Session: Beyond the Canonical View of Protein Translation** *Zoya Ignatova*, Susan Ackerman
- **Pathogens and Immunity** *Maria Hatzoglou*, Christine Dunham, Noam Stern-Ginossar, Philippe Pierre, Alexander Mankin, Jonathan Yewdell
- **Translation in and at Organelles** *Xiang-Lei Yang*, Aleksandra Filipovska, Robert Keenan
- **Innovative Technologies for Translation Research** *Chuan He*, Arvind Subramaniam, Daniel Zenklusen, Scott Blanchard, Rachel Green, John Christodoulou
- **Stress and Aging** *Robert Schneider*, Maria Hatzoglou, Motomasa Tanaka, Vadim Gladyshev, Shu-Bing Qian
- **Cancer** *Katherine Borden*, Davide Ruggero, Shobha Vasudevan, Robert Schneider, Anne Willis, Chuan He
- **Ribosomopathies and Rare Diseases** *Alexander Mankin*, Alan Warren, Dragony Fu, Susan Baserga
- **Neurological Diseases** *Susan Ackerman*, Eric Klann, Daryl Bosco, Erik Storkebaum, Xiang-Lei Yang
- **Condensates and Complexes** *Rachel Green*, Stephen Floor, Mofang Liu, Sunghoon Kim
- **The GRC Power Hour™** *Xiang-Lei Yang*

## Tropical Infectious Diseases

+ GFS

MAR 12-17, 2023 GRAND GALVEZ, GALVESTON, TX

CHAIR: Maria Elena Bottazzi

VICE CHAIR: Flaminia Catteruccia

- **Keynote Session: Pathogen-Derived Modulators and the Interaction with Host Immunity** *Jesus Valenzuela*, Henry McSorley, Patricia Aguilar, David Corry
- **Microbiota, Infection and Immune Regulation** *Pedro Gazzinelli-Guimaraes*, Stacey Burgess, James Collins, Ricardo Fujiwara, Momar Ndao, Elizabeth McGraw
- **Disrupting Transmission and Advances in Disease Control and Elimination** *Fabiano Oliveira*, Cheolho Sim, Rhoel Dinglasan, Jayhun Lee, Sarah Fortune
- **High-Throughput Approaches for the Understanding of Tropical Infections** *Pai-Yong Shi*, Makedonka Mitreva, Gustavo Fontecha, Sebastian Louder, Laura-Isobel McCall, Philip Felgner
- **Systems Biology, Big Data and the Role of Artificial Intelligence** *Joel Vega-Rodriguez*, Galit Alter, Kamal Rawal, Hayden Metsky, Anne De Groot
- **Technology Innovations for the Detection, Prevention and Treatment of Tropical Infections** *Serap Aksoy*, Mattie Pawlowic, Paul Brindley, Kelli Barr, Cristina Poveda, Timothy Anderson
- **Ecology and Field-Based Epidemiology** *Ana Sanchez*, Eric Dumontell, Andrea Graham, Tamar Carter, Sarah Gunter
- **Tropical Disease Interactions, Synergy and Interference** *Julie Gutman*, Antonio Marcilla, Alfredo Torres, Vanessa Ezenwa, Carmenta Spadafora, Melissa Lodoen
- **Keynote Session: Pathogen Modulators and Host Immunity** *Fabian Gusovsky*, Igor Almeida, R. Kip Guy, Bruce Y. Lee
- **The GRC Power Hour™** *Sara Lustigman, Luis Martinez*

## Vascular Cell Biology

+ GFS

JAN 15-20, 2023 VENTURA BEACH MARRIOTT, VENTURA, CA

CHAIR: Zoltan Arany

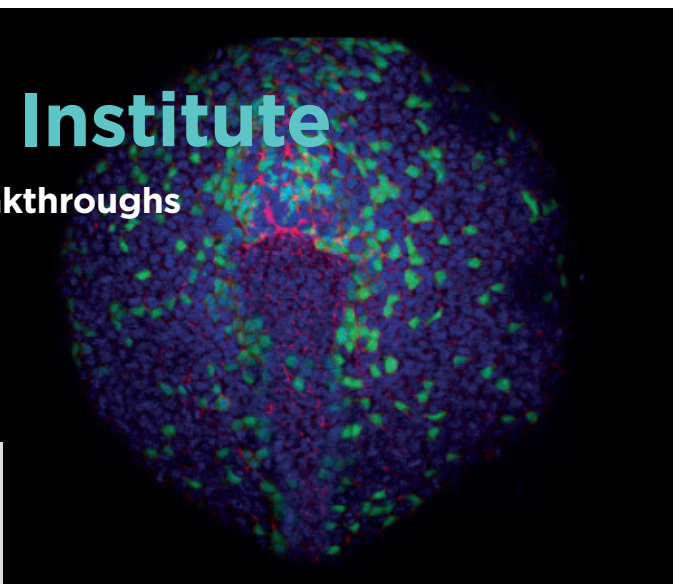
VICE CHAIR: Karen Hirschi

- **Vascular Heterogeneity and Development** *Anne Eichmann*, Holger Gerhardt, Christiana Ruhrberg, Ondine Cleaver, Nathan Lawson, Victoria Bautch
- **Vascular Complications of Pregnancy** *Mary Wallingford*, Ananth Karumanchi, Kathleen Caron, Hal Dietz
- **Inflammation and Vascular Heterogeneity** *Luisa Iruela-Arispe*, Jalees Rehman, Laura Benjamin
- **Lipids and Vasculature** *Timothy Hla*, Ira Goldberg, Katrien De Boek
- **Mechanobiology and Bioengineering** *Martin Schwartz*, Arndt Siekmann, Christopher Chen, Ellie Zizma
- **Vascular Metabolism and Pulmonary Disease** *Mariona Graupera*, Stephen Chan, Vinicio de Jesus Perez
- **Development and Disease in the Cardiovascular Tree** *Kenneth Walsh*, Sarah De Val, Iris Jaffe, Rui Benedetto, Saptarsi Halder
- **Vessels and Neurovascular Disease** *Mukesh Jain*, Mark Kahn, Chenghua Gu, Christer Betsholtz
- **Vascular Aging** *Ralf Adams*, Myriam Grunewald, Zoltan Ungvari, Napoleone Ferrara, Susan Quaggin
- **The GRC Power Hour™** *Luisa Iruela-Arispe*

# Sloan Kettering Institute

Celebrating over 75 years of breakthroughs

Join our faculty and help set the pace of biomedical science.



## JOIN US

Successful candidates will hold an appointment in one of SKI's research programs. Candidates may apply to up to two programs. MSK is an equal opportunity and affirmative action employer committed to diversity and inclusion in all aspects of recruiting and employment.

### **Cancer Biology & Genetics**

Chair: Scott Lowe, PhD

### **Cell Biology**

Chair: Tobias Walther, PhD

### **Chemical Biology**

Chair: Derek Tan, PhD

### **Computational & Systems Biology**

Chair: Dana Pe'er, PhD

### **Developmental Biology**

Chair: Anna-Katerina Hadjantonakis, PhD

### **Immunology**

Chair: Alexander Rudensky, PhD

### **Molecular Biology**

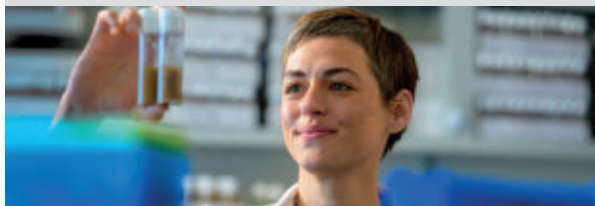
Chair: John Petrin, PhD

### **Molecular Pharmacology**

Chair: David Scheinberg, MD, PhD

### **Structural Biology**

Chair: Christopher Lima, PhD



Memorial Sloan Kettering  
Cancer Center

## AREAS OF BASIC AND TRANSLATIONAL RESEARCH

- Stem Cell Biology
- Developmental Oncology
- Regenerative Medicine
- Machine Learning
- 3D Single-Cell Modeling and Analysis
- Biophysics & Imaging
- Organelle Biology
- Chromatin & Gene Regulation
- Genome Integrity and Functional Genomics
- Chemistry & Chemical Biology
- Metastasis & Tumor Microenvironment
- Immunity, Host-Microbial Interactions and Microbiomes
- Tumor Immunobiology
- Experimental Therapeutics, Imaging and Bioengineering
- Protein Structure & Function
- Cancer Genetics

## RESEARCH AND TRAINING

- 100 research laboratories housed in state-of-the-art buildings
- 26 Core facilities offering cutting-edge scientific services
- More than 900 pre- and postdoctoral trainees
- Appointments in the Gerstner Sloan Kettering Graduate School of Biomedical Sciences and the Weill Cornell Graduate School of Medical Sciences

Visit [www.ski.edu](http://www.ski.edu) to learn more.



MSK is an equal opportunity and affirmative action employer committed to diversity and inclusion in all aspects of recruiting and employment. All qualified individuals are encouraged to apply and will receive consideration without regard to race, color, gender, gender identity or expression, sexual orientation, national origin, age, religion, creed, disability, veteran status or any other factor which cannot lawfully be used as a basis for an employment decision.

Application deadline: **October 17, 2022** | Apply at: <https://facultysearch.ski.edu>



## TENURE-TRACK FACULTY POSITION IN MOLECULAR AND SYSTEMS BIOLOGY

The Department of Molecular and Systems Biology at Geisel School of Medicine at Dartmouth invites applications for a tenure-track **Assistant** or **Associate Professor** position. We seek applicants who will direct an independent and innovative research program to understand complex problems in molecular, cell, or developmental biology, regeneration, neuroscience, or mechanisms of disease using approaches in genetics, genomics, epigenetics, metabolomics, bioinformatics, or computational systems biology.

Dartmouth is highly committed to fostering a diverse and inclusive population of students, faculty, and staff and we seek applicants who are able to work effectively with individuals from all backgrounds, including but not limited to racial and ethnic minorities, women, those who identify with LGBTQ+ communities, persons with disabilities, are from lower income backgrounds, veterans, and first-generation college graduates.

Applicants should state in their cover letter how their research, service, and/or life experiences prepare them to advance Dartmouth's commitments to diversity, equity, and inclusion.

Our department offers a dynamic and interactive environment where faculty members benefit from collaborative and collegial interactions across campus, with foundational and clinical departments at Geisel, the School of Arts & Sciences, the Thayer School of Engineering, and the Guarini School of Graduate and Advanced Studies.

A generous start-up package and access to state-of-the-art research facilities will be provided. Individuals will be given opportunities for mentoring and teaching graduate students in relevant PhD programs [e.g., Molecular and Cellular Biology (MCB), Quantitative Biomedical Sciences (QBS), and Integrative Neuroscience at Dartmouth (IND)]. The successful candidate may, as appropriate, also benefit from association with NIH-sponsored Centers for Biomedical Research Excellence (COBRE) in Quantitative Biomedical Sciences, Biomolecular Targeting, Molecular Epidemiology or Cystic Fibrosis and the NCI-designated Dartmouth Cancer Center.

Candidates must have a Ph.D. and/or M.D. degree and relevant postdoctoral research experience. Applicants should upload a cover letter, a curriculum vitae, a description of proposed research (<3 pages) and a statement on how their teaching, research, service, and/or life experiences prepare them to advance diversity, equity, and inclusion at Dartmouth (<1 page) to <http://apply.interfolio.com/112307>. Letters of recommendation should be provided from three referees.

In addition, applicants should submit a fully anonymized description of their three most significant contributions to science (<1 page) and take care not to include details such as publications, impact factors, mentors' names, institutions, awards, or any other information that may reveal their identity. The goal of this anonymous narrative is to minimize bias by allowing the search committee an initial level of evaluation focused solely on research.

The Geisel School of Medicine at Dartmouth is located on neighboring campuses in Hanover and Lebanon New Hampshire, surrounded by a vibrant, academic, and professional community offering excellent schools, lively arts, and an outstanding quality of life. Boston MA, Burlington VT, and Montreal, QC are all within a few hours' drive.

Dartmouth College is an equal opportunity/affirmative action employer with a strong commitment to diversity and inclusion. We prohibit discrimination on the basis of race, color, religion, sex, age, national origin, sexual orientation, gender identity or expression, disability, veteran status, marital status, or any other legally protected status. Applications by members of all underrepresented groups are encouraged.

The application deadline is **November 1, 2022**.



Located in Waco, Texas, Baylor University is the oldest college in Texas. With a population of around 21,000 students, Baylor is one of the top universities in the nation, having just been named an R1 institution by the Carnegie Classification in 2022. Baylor is also on the honor roll of the "Great Colleges to Work For" from The Chronicle of Higher Education. The University offers competitive salaries and benefits while giving faculty and staff the chance to live in one of the fastest-growing parts of the state. Our strategic plan, Illuminate, guides the University as we continue to live up to Baylor's mission of educating men and women for worldwide leadership and service by integrating academic excellence and Christian commitment within a caring community.

Baylor seeks to fill the following **tenure track and non-tenure-track faculty positions in the Department of Biology within the College of Arts & Sciences**.

**Microbial Ecology, Tenure Track, Assistant Professor** - [apply.interfolio.com/109905](http://apply.interfolio.com/109905), Inquiries – Dr. Thad Scott

**Evolutionary Medicine, Tenure Track, Assistant Professor** - [apply.interfolio.com/109934](http://apply.interfolio.com/109934), Inquiries – Dr. Myeongwoo Lee

**Tropical Disease Virology, Tenure Track, Assistant Professor** - [apply.interfolio.com/109928](http://apply.interfolio.com/109928), Inquiries – Dr. Cheolho Sim

**Lecturer, Non-Tenure Track, Biology** - [apply.interfolio.com/109838](http://apply.interfolio.com/109838), Inquiries - Dr. Marcie Moehnke

The Department of Biology is building a strong interdisciplinary biomedical research focus while maintaining strength in ecological, evolutionary and organismal approaches in biology. Our motto, "Understanding our World • Healing our World", captures a distinct perspective with which our department approaches teaching, research and service. Biology faculty have active Federal and non-Federal grants that fund significant research projects. Aquatic researchers collaborate with the Center for Reservoir and Aquatic Systems Research (CRASR), a research and education partnership between Baylor University and the City of Waco that focuses on aquatic resources. The department is housed in the Baylor Sciences Building, with advanced research laboratories and state-of-the-art core facilities. The Department of Biology strongly values gender, racial and ethnic diversity in its faculty ranks.

Baylor University is a private not-for-profit university affiliated with the Baptist General Convention of Texas. As an Affirmative Action/Equal Opportunity employer, Baylor is committed to compliance with all applicable anti-discrimination laws, including those regarding age, race, color, sex, national origin, pregnancy status, military service, genetic information, and disability. As a religious educational institution, Baylor is lawfully permitted to consider an applicant's religion as a selection criterion. Baylor encourages women, minorities, veterans, and individuals with disabilities to apply.

### *EEO/MF/Vets/Disabled*

*Baylor University is a private not-for-profit university affiliated with the Baptist General Convention of Texas. As an Affirmative Action/Equal Opportunity employer, Baylor is committed to compliance with all applicable anti-discrimination laws, including those regarding age, race, color, sex, national origin, pregnancy status, military service, genetic information, and disability. As a religious educational institution, Baylor is lawfully permitted to consider an applicant's religion as a selection criterion. Baylor encourages women, minorities, veterans, and individuals with disabilities to apply.*

# What's Your Next Career Move?

From networking to mentoring to evaluating your skills, find answers to your career questions on *Science Careers*

To view the complete collection, visit [ScienceCareers.org/booklets](http://ScienceCareers.org/booklets)



## Science Careers

AAAS



## DEPARTMENT OF MOLECULAR AND HUMAN GENETICS AND DAN L. DUNCAN COMPREHENSIVE CANCER CENTER

### TENURED/TENURE TRACK FACULTY POSITIONS IN GENETICS/GENOMICS

The Department of Molecular and Human Genetics and the Dan L. Duncan Comprehensive Cancer Center (DLCCCC) at Baylor College of Medicine are seeking the following positions:

- **GENOME INSTABILITY** - an individual for faculty appointment at rank appropriate for achievement and experience, working in any organism on problems in genomic instability, development of novel genetic/genomic tools or other fundamental genetic topics.

Successful candidates will have strong basic research programs related to genetic/genomic stability or instability, genome organization, genomics, genome engineering including, but not limited to DNA replication, repair, mutation, genome rearrangements, DNA damage response, mechanisms of heritability and evolution, studied in any organism from bacteria to human. This individual will join the Mechanisms in Cancer Evolution Program in the DLCCCC. However, outstanding individuals in any research area will be considered. Generous start-up support is available, and candidate will be put forward for a CPRIT award. The weekly Genome Instability Group meeting, supported by the Department and DLCCCC, includes labs from throughout the Texas Medical Center discussing work in progress.

- **CANCER GENETICIST** - an individual for faculty appointment at rank appropriate for achievement and experience in cancer research. Applicants' research programs may focus on broad ranging topics in cancer genetic research including cancer genomics, mechanisms of cancer therapeutics, cancer model organisms, genome instability, epigenetics and gene expression, and others. Applicants with expertise in computational biology, in combination with basic and/or translational cancer research, are strongly encouraged to apply. Candidates will join a team of multidisciplinary research investigators studying cancer stem cell biology, genomics, epigenetics, and metabolic aberrations in cancer.

Both appointments will be at the **Assistant, Associate, or Full Professor** level depending on experience.

The Department's research interests include genomics, mechanisms of DNA replication and repair, mechanisms of transcription, mutation, DNA recombination, genomic instability and cancer, behavioral genetics, bioinformatics, gene therapy, gene structure and expression, bacterial evolution and antibiotics resistance and the biology of aging. Department research includes strengths in bacterial, yeast, Dictyostelium, worm, fly, mouse and human genetics.

Among genetics departments at U.S. medical schools, the Department of Molecular and Human Genetics at Baylor College of Medicine (<https://www.bcm.edu/departments/molecular-and-human-genetics>) ranks first in both number of grants and total funding from the National Institutes of Health (NIH). The Department includes basic and clinical research, a new joint venture diagnostic laboratory, long-standing association with an NIH human genome sequencing center, an NIH-funded graduate program, and residency/fellowship training in medical genetics. The Department has 70 primary tenured and tenure-track research faculty members and a total of 150 primary faculty members, who are engaged in a variety of missions including basic and translational research, clinical diagnostic services, and prenatal, pediatric, and adult clinical care.

The Dan L. Duncan Comprehensive Cancer Center (DLCCCC) includes over 270 research members in seven different programs who bring in \$180M in total cancer relevant funding including nearly \$90M from NIH. Twelve state-of-the-art Shared Resources are supported by the DLCCCC and, in total, BCM has more than 30 core facilities supporting research (<https://www.bcm.edu/centers/cancer-center/research/shared-resources>).

Houston is the fourth largest US city, the most internationally diverse US city, "is widely considered to be one of the most culturally diverse cities in the world"—NY Times, and is on the New York Times' 50 Places To-Go list in the world for food and culture.

Baylor College of Medicine promotes principles of diversity, inclusion, and equity across research, education, and training programs as well as with respect to recruitment (in employment and education) of individuals from diverse backgrounds.

Curriculum vitae, a brief summary of research plans, along with the names, addresses, and phone numbers of at least three references to the following email address: [mhgfacultyrecruits@bcm.edu](mailto:mhgfacultyrecruits@bcm.edu).

Department of Molecular and Human Genetics  
Baylor College of Medicine  
One Baylor Plaza, ABBR Room R830  
Houston, TX 77030  
Phone: 713-798-5443  
Fax: 713-798-8515

*Equal Opportunity, Affirmative Action and Equal Access Employer*



**CHAIR OF BIOENGINEERING DEPARTMENT  
Northeastern University**

The College of Engineering at Northeastern University invites applications for the position of Chair of the Bioengineering Department. The Chair will provide vision to direct the hiring of faculty, the nurturing of research foci, and the development of educational curricula. The Bioengineering Department (<https://bioe.northeastern.edu/>) is the newest department (founded in 2014) at Northeastern University and is rapidly expanding its international reputation. The Department comprises 30 world-class core (tenured/tenure-track) faculty, with active research programs spanning systems biology, mechanobiology, biomechanics, bioimaging, molecular engineering, single-cell proteomics and cell engineering. There are also five full-time teaching faculty, 5 co-operative education coordinators, and 6 staff members. The departmental spirit is collegial, vibrant, and growing and is home to 94 Ph.D. students, 122 M.S. students, and 582 undergraduate students.

Candidates are expected to have demonstrated strategic vision through leadership of a well-established, nationally and internationally recognized research program, with a strong record of externally-funded research. Candidates will have demonstrated excellence and significant experience in teaching, with a commitment to high-quality teaching in bioengineering, and interest in advancing education programs with a balance between undergraduate and graduate levels.

Applicants should submit a cover letter, detailed curriculum vitae and four professional references. Please include a strategic vision statement for where you believe bioengineering is headed and statements of Diversity, Equity, Inclusion and Belonging, your own research, teaching, and leadership philosophies. Your CV should highlight positions of leadership in particular. Please limit the combined statements to three pages. Consideration of applications will begin Fall 2022. The target starting date is July 1, 2023, but the position will remain open until filled.

Inquiries and nominations for the position should be submitted to **Prof. Jeff Ruberti** [j.ruberti@northeastern.edu](mailto:j.ruberti@northeastern.edu). You can apply through the Northeastern Human Resources Portal: [https://northeastern.wd1.myworkdayjobs.com/en-US/careers/job/Professor-and-Chair---Bioengineering\\_R107597](https://northeastern.wd1.myworkdayjobs.com/en-US/careers/job/Professor-and-Chair---Bioengineering_R107597)

**For more information, contact Esther Cohen at [e.cohen@northeastern.edu](mailto:e.cohen@northeastern.edu) or 617-373-6405**



**DEPARTMENT OF BIOCHEMISTRY, VANDERBILT UNIVERSITY**

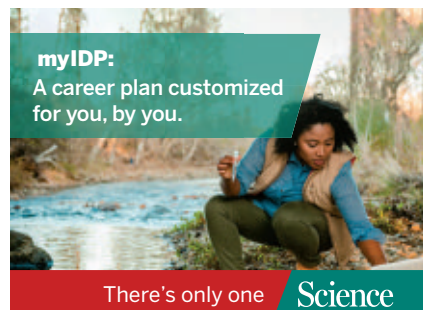
The Department of Biochemistry at Vanderbilt University (<https://medschool.vanderbilt.edu/biochemistry>) invites applications for a tenure-track faculty position at the rank of **Assistant Professor**; exceptional applicants at the rank of **Associate** or **Full Professor** will also be considered. We seek candidates who are using innovative approaches to address important and challenging problems in all aspects of biology at the molecular level. Candidates are expected to develop a strong research program and participate in the education of graduate students and postdoctoral scientists. We are especially interested in scientists that complement current department and institution strengths, which include DNA and RNA metabolism, chromatin biology, signal transduction, protein misfolding diseases, and molecular cancer biology. Investigators developing and utilizing innovative approaches including computational biology, single molecule biochemistry, and chemical biology are especially encouraged to apply.

The successful candidate will join a vibrant and diverse research community. The Biochemistry department has exceptional faculty who have received major international awards, election to the National Academy of Sciences, and a Nobel Prize in Physiology or Medicine (Stanley Cohen, 1986). Incoming faculty will have a supportive peer group and extensive mentoring. We are a welcoming community of collaborative investigators dedicated to excellence in research, training, and service.

Biochemistry is part of the Basic Sciences within the School of Medicine at Vanderbilt University. This unique structure provides an outstanding environment for discovery science that includes state-of-the-art core facilities (<https://tinyurl.com/y3s24nds>) and several trans-institutional centers and institutes (<https://tinyurl.com/yyqdq3t3>; <https://tinyurl.com/y2cvu27g>). Trainees in the appointee's lab also are eligible for stipend support from over 25 NIH-supported T32 training programs (<https://tinyurl.com/y3fnhzst>).

Applicants should apply through Interfolio by following this link: [apply.interfolio.com/112443](https://apply.interfolio.com/112443). Please submit a (i) curriculum vitae, (ii) 2-3 page research plan, (iii) a one page description of your mentoring philosophy including your commitment to advancing equity, diversity and inclusion, (iv) reprints of three recent publications, (v) three recommendation letters to be sent directly by referees via Interfolio (information is provided in the link). **Evaluation of applicants will begin October 15, 2022.**

*Vanderbilt University is an Equal Opportunity/Affirmative Action employer committed to recruiting and retaining an academically and culturally diverse community of faculty. Vanderbilt has a strong institutional commitment to diversity in all areas and particularly encourages applications from minorities, women, individuals with disabilities, and members of other underrepresented groups.*



**Features in myIDP include:**

- Exercises to help you examine your skills, interests, and values.
- A list of 20 scientific career paths with a prediction of which ones best fit your skills and interests.



Visit the website and start planning today!  
[myIDP.sciencecareers.org](https://myIDP.sciencecareers.org)

**Science Careers** In partnership with: **M.A.A.S.**



Where  
Science  
Gets  
Social.

AAAS.ORG/  
COMMUNITY

AAAS' Member  
Community is a one-stop  
destination for scientists  
and STEM enthusiasts  
alike. It's "Where  
Science Gets Social": a  
community where facts  
matter, ideas are big and  
there's always a reason  
to come hang out, share,  
discuss and explore.

Member  
COMMUNITY  
AAAS



## FACULTY POSITIONS IN BIOCHEMISTRY & MOLECULAR BIOLOGY THE UNIVERSITY OF TEXAS MEDICAL BRANCH

The Department of Biochemistry and Molecular Biology (<https://bmb.utmb.edu>) at the University of Texas Medical Branch (UTMB Health), Galveston, Texas, seeks outstanding candidates for tenure-track positions at the rank of Assistant Professor in the broad research areas of biochemistry, molecular and cellular biology. A Ph.D. degree (or equivalent) is required and postdoctoral experience is desirable. The applicants are expected to create and develop externally funded research programs. Minorities and members of underrepresented groups are especially encouraged to apply. The positions will begin in **Fall 2023**.

The Department of Biochemistry and Molecular Biology is a diverse biomedical research community with strengths in molecular virology, RNA biology, mechanobiology, structural biology, biophysics and quantitative biology. In addition to a highly collaborative environment, UTMB offers outstanding research facilities for next-generation sequencing, mass spectrometry, optical microscopy, flow cytometry, solution biophysics, NMR, X-ray crystallography, cryo-electron microscopy, scientific computing, and bioinformatics. Excellent opportunities for scientific interactions also exist through sister institutions in the Greater Houston area, Gulf Coast Consortia, and the Keck Center for Interdisciplinary Bioscience.

An attractive recruitment package of competitive salary, generous start-up funding, and renovated laboratory space will be offered. Interested applicants should submit a single PDF (<10 MB) containing the following: **1)** cover letter, **2)** curriculum vitae, **3)** summary of research accomplishments and future goals (2-3 pages), **4)** diversity statement which follows the NIH PEDP guidelines, **5)** teaching and mentoring statement (1 page) and **6)** contact information for three references. The PDF should be sent by email to: Mariano A. Garcia-Blanco M.D., Ph.D. at **BMB.Recruiting@utmb.edu**. We will begin the review of applications immediately and will continue to accept new applications until **December 1st, 2022**.

*"UTMB Health strives to provide equal opportunity employment without regard to race, color, national origin, sex, age, religion, disability, sexual orientation, gender identity or expression, genetic information or veteran status. As a Federal Contractor, UTMB Health takes affirmative action to hire and advance women, minorities, protected veterans and individuals with disabilities."*



## CALL FOR NOMINATIONS: SCOLNICK PRIZE IN NEUROSCIENCE

The McGovern Institute for Brain Research is accepting nominations for the **19th annual Edward M. Scolnick Prize in Neuroscience**. The Prize recognizes an outstanding discovery or significant advance in the field of neuroscience. The prize is \$200,000. The recipient presents a public lecture at MIT, hosted by the McGovern Institute and followed by a dinner in Spring 2023.

**Nomination Deadline:** December 15, 2022

### Nomination procedures:

Candidates for the award must be nominated by individuals affiliated with universities, hospitals, medical schools, or research institutes, with a background in neuroscience. Self-nomination is not permitted. Each nomination should include:

- A biosketch or CV of the nominee;
- A letter of nomination with a summary and analysis of the major contributions of the nominee to the field of neuroscience.
- Up to two representative reprints will be accepted.

### Selection Procedure:

- Members of the selection committee and faculty affiliated with MIT are not eligible.
- Announcement of the award recipient will be made in January 2023.
- Recipient must attend all events to be awarded the prize.

### Past Scolnick Prize Recipients:

2022: David Ginty, Harvard University; 2020: Joshua Sanes, Harvard University; 2019: Richard Huganir, Johns Hopkins University; 2018: David J. Anderson, HHMI, Caltech; 2017: Catherine Dulac, HHMI, Harvard University; 2016: Cornelia Bargmann, HHMI, The Rockefeller University; 2015: Charles Gilbert, The Rockefeller University; 2014: Huda Zoghbi, HHMI, Baylor University; 2013: Thomas Jessell, HHMI, Columbia University; 2012: Roger Nicoll, UCSF; 2011: Bruce McEwen, The Rockefeller University; 2010: Lily and Yuh-Nung Jan, UCSF; 2009: Jeremy Nathans, Johns Hopkins University; 2008: Michael Davis, Emory University; 2007: David Julius, UCSF; 2006: Michael Greenberg, Children's Hospital/HMS; 2005: Judith Rapoport, NIH; 2004: Masakazu Konishi, CalTech

Send nomination packet to: [gwolf@mit.edu](mailto:gwolf@mit.edu)

## FACULTY IN CHEMISTRY, BIOCHEMISTRY, AND CHEMICAL ENGINEERING

Division of Chemistry and Chemical Engineering  
California Institute of Technology  
<https://applications.caltech.edu/job/chemistry>

The Division of Chemistry and Chemical Engineering at the California Institute of Technology invites applications for a **faculty position** at all levels and in all areas of chemistry, biochemistry, and chemical engineering. Candidates with strong commitments to research and teaching excellence are encouraged to apply. The appointment is contingent upon completion of all requirements for a Ph.D. Exceptionally well-qualified applicants at the tenured level will be considered.

Interested candidates should apply at <https://applications.caltech.edu/job/chemistry>. Applications should include a curriculum vita, publication list, teaching statement, a description of proposed research, and three letters of recommendation. Applicants should submit a diversity and inclusion statement that discusses past and/or anticipated contributions to improving diversity, equity, and inclusion in the areas of research, teaching, and/or outreach. Applications should be received by **November 1, 2022**.

*We are an equal opportunity employer, and all qualified applicants will receive consideration for employment without regard to age, race, color, religion, sex, sexual orientation, gender identity, or national origin, disability status, protected veteran status, or any other characteristic protected by law.*

The Department of Chemistry invites applications for three new endowed professorship positions.

- Applicants are sought for **two tenure-track Assistant Professor** positions in the areas of experimental Physical Chemistry and/or Inorganic Chemistry, broadly defined, to possibly hold positions as the inaugural Marvin Fellows of Chemistry, starting **July 1, 2023** or later. Candidates are expected to have a PhD, establish an outstanding program of original research, and be an effective teacher at the graduate and undergraduate levels.
- Applicants at the **associate or full professor** rank representing any area of Chemistry will also be considered for the Marshall D. Gates, Jr. Chair in Chemistry. Gates Chair applicants are expected to have a substantial, significant, and internationally recognized record of scholarly achievement. Tenure upon appointment for qualified senior candidates may be granted, contingent on favorable review of the candidate's dossier by the department, the dean and the provost.

Application materials including curriculum vitae, three letters of recommendation, statement of research interests and plans, statement on teaching, and a statement of your commitment to advancing equity and fostering an inclusive and diverse community in academia, including past work and future goals should be submitted online at <http://www.rochester.edu/faculty-recruiting/positions>.

To learn more about the Department of Chemistry, visit <http://www.sas.rochester.edu/chm/>. Questions may be sent to [facrec@chem.rochester.edu](mailto:facrec@chem.rochester.edu).

Review of completed applications will begin on **October 1, 2022**.

*The University of Rochester has a strong commitment to diversity and actively encourages applicants from groups underrepresented in higher education. The University is an Equal Opportunity Employer committed to providing employment opportunity without regard to an individual's age, color, disability, genetic information, gender, gender identity, national origin, race, religion, sexual orientation, or veteran status.*

## UNIVERSITY OF MASSACHUSETTS CHAN MEDICAL SCHOOL FACULTY POSITION DEPARTMENT OF SYSTEMS BIOLOGY

The Department of Systems Biology at the University of Massachusetts Chan Medical School invites applications from outstanding candidates for a **tenure-track or senior tenured** professor position. We offer competitive start-up funds, laboratory space and salary. For more information, please visit the Department website at <https://www.umassmed.edu/DSB/>.

The candidate will be expected to develop and maintain an innovative, externally funded research program. We are seeking an energetic and collaborative individual who will develop a strong research program to tackle important problems in one of the following areas in systems biology: Network Biology, Single Cell Systems Biology, Genome Biology, Evolution, Variation, Immunology and Neurobiology. Exceptionally strong candidates in other areas will also be considered. Candidates should have a PhD or MD in biomedical research with a minimum of two years post-doctoral research experience that resulted in high-quality peer-reviewed publications.

The Department of Systems Biology is housed in the state-of-the-art Albert Sherman Center that opened early in 2013. The Department has high-performance computing facilities, state-of-the-art laboratory space and equipment and a full-time administrator to support the research activities of its Faculty.

Applicants should submit a cover letter explaining their interest in the Department, a curriculum vitae that includes honors, publications, and a succinct research plan to <https://academicjobsonline.org/ajo/jobs/22151> (Position ID#22151). Deadline for applications is **October 15, 2022**. To expedite the review process, applicants should invite three individuals who are familiar with their work and potential for success to upload their recommendation letters at the same web address. Inquiries, but not application materials, may be directed to Professor Job Dekker ([job.dekker@umassmed.edu](mailto:job.dekker@umassmed.edu)). The position remains open until filled.

*UMass Chan Medical School is committed to being an equal opportunity and affirmative action employer and recognizes the power of a diverse community. We encourage applications from protected veterans, individuals with disabilities and those with varied experiences, perspectives and backgrounds to consider UMass Chan Medical School as their employer of choice.*

**Position Description:** Division of Immunobiology in the Department of Pathology and Immunology at Washington University School of Medicine invites applications for a **tenure-track Assistant Professor** position. The Division of Immunobiology within the Department of Pathology and Immunology at Washington University School of Medicine in St. Louis is seeking exceptional candidates with PhD, MD/PhD, or MD in basic and/or translational immunology. This is an open call and candidates in all areas of immunology are welcome to apply. Immunobiology at WashU has a long tradition of excellence with breakthrough and pioneering research on many aspects of the immune system that are part of immunology textbooks. We invite you to become part of this truly remarkable group, contributing to and benefiting from this intellectually rich environment. The selected candidate(s) will also become integrated into the larger WashU immunology community with a highly collaborative atmosphere and covering essentially all basic, applied, and clinical aspects of immunology. The successful candidate will have access to shared equipment, state-of-the-art cores throughout the school of medicine, and access to an outstanding graduate program.

**Special Instructions:** Applicants should submit a cover letter expressing their interest, current CV, ½ page description of their one most important paper to date highlighting the novelty of the findings (accepted, published or BioRxiv deposited papers only), 2-page research statement, and the names/contact information of 3 references. Kindly send all requested material in one single PDF to Elizabeth Moore ([melizab@wustl.edu](mailto:melizab@wustl.edu)). The committee will begin to meet in September to review the candidates, and the position will remain open until filled.

*An Equal Opportunity Affirmative Action Employer, Washington University in St. Louis is committed to the principles and practices of equal employment opportunity and affirmative action. It is the university's policy to recruit, hire, train, and promote persons in all job titles without regard to race, color, age, religion, gender, sexual orientation, gender identity or expression, national origin, veteran status, disability, or genetic information. Washington University seeks an exceptionally qualified and diverse faculty; women, minorities, protected veterans and candidates with disabilities are strongly encouraged to apply.*



## Yale SCHOOL OF MEDICINE

Department of Neuroscience



The Department of Neuroscience at Yale University seeks to hire multiple new **tenure track faculty members** with interests in molecular, cellular, systems or cognitive neuroscience in health or disease. We are enthusiastic about candidates bridging between traditional conceptual or methodological boundaries.

The successful candidates will be embedded in a richly collaborative community supporting intellectual creativity. The Yale Neuroscience Department realizes that the full potential of our research lies in the power that diverse perspectives bring to the field. We are working to foster an environment where individuals of any race, gender identity, ethnicity, religion, socioeconomic class, sexual orientation, and geographical background feel supported and empowered to push forward the frontiers of neuroscience based on the principles of inclusivity, equity and belonging. We therefore strongly encourage applicants from historically minoritized backgrounds to apply.

Emphasis will be placed on recruiting at the level of **Assistant Professor**, but applicants at Associate Professor level will also be considered. The neuroscience community at Yale is dynamic and expanding, and includes the Kavli Institute for Neuroscience, the Wu Tsai Institute, the Program in Cellular Neuroscience, Neurodegeneration and Repair (CNNR) and the Swartz Program in Theoretical Neuroscience. The Interdepartmental Neuroscience Program provides robust Ph.D. training to a large group of students. The Department provides outstanding support to researchers via shared facilities such as microscopy and neurotechnology cores, and growing cores in iPSC biology and data science, as well as resources for nonhuman primate research. By mid 2023, the Department will occupy new space optimized for modern science and maximal interaction and collaboration. New faculty will be supported by a generous start-up package and ongoing salary support. Faculty are expected to develop a productive and innovative research program that will include the opportunity to participate in graduate and medical education.

Candidates must hold a Ph.D., M.D., or equivalent degree. Please send a cover letter, a diversity statement, a research statement, a curriculum vitae, and arrange for submission of 3 letters of recommendation.

- Cover letter: Indicate your desired level of appointment (Assistant or Associate Professor).
- Diversity statement (1-page max): Describe your understanding of the challenges facing historically underrepresented groups in science, as well as your lived experience, commitment, and ideas for addressing these inequities.
- Research statement (3-page max, including optional figures and references): Describe your most significant scientific discoveries and accomplishments to date, as well as the focus and goals of your future research program.
- Curriculum Vitae: Include links to publications or website.

All application materials should be submitted electronically to <http://apply.interfolio.com/110309>. Any questions regarding the application process may be addressed to [Pauline.charbogne@yale.edu](mailto:Pauline.charbogne@yale.edu). Applications will be reviewed as they are received until the positions are filled with priority given to those applications received by **October 15, 2022**.

*Yale University is an Affirmative Action/Equal Opportunity employer. Yale values diversity among its students, staff, and faculty and strongly welcomes applications from women, persons with disabilities, protected veterans, and underrepresented minorities.*



### DEPARTMENT OF PHYSIOLOGY FACULTY POSITIONS

The Department of Physiology at the Perelman School of Medicine at the University of Pennsylvania seeks highly qualified candidates for faculty positions in the tenure track at the **Assistant Professor rank**. Applicants must have a Ph.D. and/or M.D. or equivalent degree. Teaching responsibilities may include graduate and medical student instruction and training graduate students and postdoctoral fellows. Research responsibilities include developing a successful extramurally-supported research program. We seek investigators with demonstrated excellence in research grounded in fundamental mechanistic investigation that leverages molecular, biophysical, structural and cell-biological insights to inform physiological functions, particularly those emphasizing emerging areas, novel technologies, and interdisciplinary research.

Applicants in the early stage of career development are encouraged to apply. Please apply no later than **November 30, 2022**.

Apply online: <http://apply.interfolio.com/110740>

The Perelman School of Medicine, one of the top ranked medical schools in the country for NIH funding, is a highly collaborative environment with state-of-the-art core facilities (<https://www.med.upenn.edu/cores/>), There are opportunities for appointments in numerous thematic institutes and centers (<https://www.med.upenn.edu/psom/centers.html/>), including the Cardiovascular Institute, Mahoney Institute for Neurosciences, Pennsylvania Muscle Institute, and Abramson Cancer Center. The School of Medicine is integrated within the campus of the University of Pennsylvania, a world-class institution with an easily walkable campus located near central Philadelphia. We seek candidates who embrace and reflect diversity in the broadest sense.

*The University of Pennsylvania is an EOE. Minorities/Women/Individuals with disabilities/Protected Veterans are encouraged to apply.*



### FACULTY POSITION IN BACTERIAL PATHOGENESIS

The Department of Microbiology at the University of Texas Southwestern Medical Center (UTSW) seeks a new faculty member at the **Assistant Professor** (tenure track) level. Ideal candidates will develop a front-rank, competitive, and independent research program in the field of bacterial pathogenesis.

At present, research in the department spans a wide range of topics including host-pathogen interactions, prokaryotic sensing, signal transduction, gene regulation, antibiotic resistance, bacterial immunity, mechanisms of co-infection, cellular microbiology, and microbial communities (microbiome). An important academic responsibility will be the instruction and mentoring of graduate students.

An attractive start-up package, including a competitive salary and generous laboratory space in a modern building, is available to conduct research within a highly dynamic environment of a leading microbiology department (<https://www.utsouthwestern.edu/education/medical-school/departments/microbiology>). Candidates will be considered for our \$2.15M Endowed Scholars (start-up) Program (<http://www.utsouthwestern.edu/education/programs/nondegree-programs/other-programs/endowed-scholars/index.html>).

Candidates should have a Ph.D. and/or M.D. degree with at least 3-4 years of postdoctoral experience and an exceptional publication record.

Please send a cover letter, C.V., contact information for three letters of recommendation, and a brief statement of current and future research interests to: [BacterialPathogenesisSearchCommittee@utsouthwestern.edu](mailto:BacterialPathogenesisSearchCommittee@utsouthwestern.edu)

*UT Southwestern Medical Center is committed to an educational and working environment that provides equal opportunity to all members of the University community. As an equal opportunity employer, UT Southwestern prohibits unlawful discrimination, including discrimination on the basis of race, color, religion, national origin, sex, sexual orientation, gender identity, gender expression, age, disability, genetic information, citizenship status, or veteran status. To learn more, please visit: <https://jobs.utsouthwestern.edu/why-work-here/diversity-inclusion/>.*



## FACULTY POSITIONS – BIOCHEMISTRY DEPARTMENT OF BIOLOGICAL CHEMISTRY

The Department of Biological Chemistry at the University of Michigan Medical School invites applications for tenure-track or tenured faculty positions at the **Assistant/Associate/Full Professor** levels. We seek outstanding colleagues whose research defines and addresses cutting-edge questions in any area of biochemistry to join our inclusive and richly collaborative community that prioritizes both transformative science and training the next generation of scientific leaders.

Successful candidates will be part of a vibrant interdisciplinary environment with interests that span a wide range of fundamental questions and molecular, cellular, and organismal systems. Qualifications include a Ph.D. and/or M.D., a strong record of research accomplishments, and a commitment to diversity and inclusion in the biomedical sciences. Applicants for Associate and Full Professor should have a history of exceptional independent research, funding, and contributions to the scientific community. Further information about the Department is available at <http://www.biochem.med.umich.edu/>

Applications should include a cover letter, a curriculum vitae, a description of past and current research activities (up to 2 pages), a summary of future research plans (up to 2 pages), a summary of commitment to and plans for creating a diverse and inclusive scientific environment (1 page), and contact information including email address of three references. Materials should be addressed to Dr. Phyllis Hanson, Chair of Biological Chemistry and submitted via Interfolio at <http://apply.interfolio.com/110681>

Applications will be reviewed on a rolling basis with a deadline of **November 1, 2022** for full consideration. Please address any questions to Amanda Howard ([amanhova@umich.edu](mailto:amanhova@umich.edu)).

*Michigan Medicine seeks to recruit and retain a diverse workforce as a reflection of our commitment to serve the diverse people of Michigan and to maintain the excellence of the University. We welcome applications from anyone who would bring additional dimensions to the University's research and teaching mission, including women, members of minority groups, protected veterans, and individuals with disabilities. The Department and the University are committed to a policy of nondiscrimination and equal opportunity for all persons and will not discriminate against any individual because of race, color, national origin, age, marital status, sex, sexual orientation, gender identity, gender expression, disability, religion, height, weight, or veteran status. The University of Michigan is an Equal Employment Opportunity/Affirmative Action Employer.*



## DEPARTMENT OF MOLECULAR BIOLOGY

The Department of Molecular Biology and the Hamon Center for Regenerative Science and Medicine (CRSM) at the University of Texas Southwestern Medical Center are seeking applicants for tenure track faculty positions at the level of **Assistant Professor**. Candidates should have a Ph.D. or M.D., postdoctoral experience, and a demonstrated record of research excellence.

We are seeking creative and interactive individuals with strong research programs focused on mechanistic aspects of gene regulation and cellular signaling, cell growth and differentiation, developmental and stem cell biology, or disease pathogenesis. Successful applicants may apply diverse approaches to these problems, including biochemical, cellular, or animal model systems. Attractive recruitment packages, state-of-the-art core facilities, and exceptional laboratory space are available. UT Southwestern has a vibrant graduate program and an atmosphere of collegiality and collaboration.

Candidates should apply online at <https://jobs.utsouthwestern.edu/> (search for **Job# 656906**). Applicants should also submit a curriculum vitae containing a summary of past research accomplishments, a statement of future objectives, and names of three references via email to:

**MolBioSearch@UTSouthwestern.edu**  
Department of Molecular Biology  
Hamon Center for Regenerative Science and Medicine  
University of Texas Southwestern Medical Center

Applications will be reviewed on a rolling basis and early applications are encouraged.

*UT Southwestern Medical Center is committed to an education and working environment that provides equal opportunity to all members of the University community. As an equal opportunity employer, UT Southwestern prohibits unlawful discrimination, including discrimination on the basis of race, color, religion, national origin, sex, sexual orientation, gender identity, gender expression, age, disability, genetic information, citizenship status, or veteran status. To learn more, please visit: <https://jobs.utsouthwestern.edu/why-work-here/diversity-inclusion/>*

## FACULTY POSITIONS THE ROCKEFELLER UNIVERSITY

The Rockefeller University seeks exceptional, creative scientists to join its faculty. We invite applications from outstanding candidates for tenure-track positions, and also welcome applications from tenured scientists at an early stage of their career. The University is committed to a diverse community, and we strongly encourage applications from individuals from groups that are underrepresented in biomedical science.

The University has a laboratory centered rather than department based organizational structure that fosters interdisciplinary research. We encourage applications in the following areas:

- **Biochemistry, Biophysics, Chemical Biology, and Structural Biology**
- **Cancer Biology**
- **Cell Biology**
- **Genetics and Genomics**
- **Immunology, Virology, and Microbiology**
- **Mechanisms of Human Disease**
- **Neurosciences and Behavior**
- **Organismal Biology and Evolution**
- **Physical, Mathematical, and Computational Biology**
- **Stem Cells, Development, Regeneration, and Aging**

The Rockefeller University provides strong support for the work of its faculty including 100% faculty salary support, benefits that include subsidized housing and an on-site childcare center from 3 months of age through preschool, generous start-up funds, new or renovated laboratory space and state-of-the-art core facilities, and support for all graduate students as well as continuing lab support. There are extensive opportunities for collaboration within the University and with neighboring institutions.

Visit <http://www.rockefeller.edu/facultysearch> to submit your application online and view further information about the positions.

**Application deadline is September 30, 2022.**

Address questions to [facultysearch@rockefeller.edu](mailto:facultysearch@rockefeller.edu).

As an equal opportunity employer, we will consider all qualified applicants for employment without regard to race, color, religion, sex, sexual orientation, gender identity, national origin, disability or protected veteran status.



## TENURE-TRACK POSITION – DEPARTMENT OF PHYSIOLOGY THE UNIVERSITY OF TEXAS SOUTHWESTERN MEDICAL CENTER

The Department of Physiology invites outstanding scientists with Ph.D., M.D., or equivalent degrees to apply for tenure-track faculty positions at the level of **Assistant Professor**. Candidates who bring innovative approaches to the study of any under-explored/unexplored questions broadly related to physiology are encouraged to apply. The scientific excellence of the candidates is more important than the specific area of research. These positions are part of the continuing growth of the Department at one of the country's leading academic medical centers. They will be supported by significant laboratory space, competitive salaries, state-of-the-art core facilities and exceptional start-up packages. The University of Texas Southwestern Medical Center is the scientific home to six Nobel Prize laureates since 1985, 25 members of the National Academy of Sciences, and 17 members of the National Academy of Medicine. UT Southwestern conducts more than 5,800 research projects annually totaling more than \$554 million. Additional information about the Department of Physiology can be found at <http://www.utsouthwestern.edu/education/medical-school/departments/physiology/index.html>.

Applicants should submit a CV, a brief statement of current and proposed research, and a summary of your two most significant publications describing the importance of the work (100-150 words each). Please arrange to have three letters of recommendation sent on his/her behalf. All items should be submitted to: <http://academicjobsonline.org/ajo/jobs/22277>. Completed applications will be reviewed starting **November 1, 2022**. You may email questions to [ron.doris@utsouthwestern.edu](mailto:ron.doris@utsouthwestern.edu).

*UT Southwestern Medical Center is committed to an educational and working environment that provides equal opportunity to all members of the University community. In accordance with federal and state law, the University prohibits unlawful discrimination, including harassment, on the basis of: race; color; religion; national origin; sex, including sexual harassment; age; disability; genetic information; citizenship status; and protected veteran status. In addition, it is UT Southwestern policy to prohibit discrimination on the basis of sexual orientation, gender identity, or gender expression.*

# HOWARD HUGHES MEDICAL INSTITUTE

## 2023 Hanna H. Gray Fellows Program

hhmi

The Howard Hughes Medical Institute (HHMI) is pleased to announce the 2023 Hanna H. Gray Fellows Program competition. This program seeks to increase diversity in biomedical science by recruiting and retaining individuals from groups currently underrepresented in the life sciences. HHMI is committed to creating inclusive environments in which all scientists can thrive.

Hanna Gray Fellows receive funding for their postdoctoral training and may continue to receive funding during their early career years as independent faculty. In total, Fellows may receive up to \$1.4 million over eight years. Fellows participate in professional development, receive culturally aware mentorship, and enjoy networking with their peers and HHMI's broader community of scientists, across career stages.

The Institute will select and support up to 25 fellows in the 2023 competition. The competition is open to all eligible applicants and no nomination is required.

### Eligibility:

The program is open to individuals who:

- are from gender, racial, ethnic, and other groups currently underrepresented in the life sciences, including those individuals from disadvantaged backgrounds.
- hold a PhD and/or MD (or equivalent), which must be conferred by the start of the grant term.
  - US citizens must have a degree from a research institution in the US (including Puerto Rico) or an international research institution.
  - Non-US citizens and applicants with other nationalities must have a degree from a research institution in the US (including Puerto Rico).
- have no more than 18 months of postdoctoral research experience at the time of the application due date.

*The postdoctoral training mentor must hold a tenured or tenure-track position (or equivalent) at an institution in the US (including Puerto Rico).*

**Applications are due by December 7, 2022. Mentor and reference letters must be received by December 14, 2022.**

Further details: <https://www.hhmi.org/hgf> or contact [fellows@hhmi.org](mailto:fellows@hhmi.org).



### POSITIONS IN BIOLOGY AND BIOLOGICAL ENGINEERING: CALTECH, PASADENA, CA, UNITED STATES

The Division of Biology and Biological Engineering (BBE) at Caltech is seeking new faculty in all areas of biological science and biological engineering, with particular interest in individuals who are pursuing research that would benefit from and add to the interdisciplinary environment of Caltech's BBE division and its linkages to other disciplines at Caltech. Areas of interest include, but are not limited to (alphabetically): biological engineering; cellular, developmental and regulatory biology; ecological and biosphere science and engineering; neural and behavioral biology; organismal and integrative biology; and virology, immunology and infectious disease.

Successful applicants are expected to develop innovative research programs and to be committed to high quality teaching. Preference will be given to candidates at the Assistant Professor level; however, well-qualified applicants at the associate or full professor level may also be considered. The appointment is contingent upon completion of the Ph.D. degree.

Please submit on-line applications at: <https://www.bbe.caltech.edu/jobs>, and include a brief cover letter; curriculum vitae; relevant publications, a description of proposed research; and a statement of teaching interests. Applicants should also submit a diversity and inclusion statement that discusses past and/or anticipated contributions to improving diversity, equity, and inclusion in the areas of research and teaching.

Applicants should arrange to have 3-4 reference letters uploaded.

Applications must be submitted no later than **1 November, 2022**.

*We are an equal opportunity employer and all qualified applicants will receive consideration for employment without regard to race, color, religion, sex, sexual orientation, gender identity, or national origin, disability status, protected veteran status, or any other characteristic protected by law.*



### FACULTY POSITION

Susan L. Cullman Laboratory for Cancer Research, Department of Chemical Biology, Ernest Mario School of Pharmacy, Rutgers, The State University of New Jersey, Piscataway, NJ is seeking an outstanding investigator for a tenure-track faculty position at the assistant or associate professor level with preference given to those whose work complements and enhances our current research programs in cancer metabolism, cancer biology, cancer prevention, and neurodegenerative biology.

The successful candidate should hold the equivalent of a Ph.D. and/or M.D. degree and is expected to develop and maintain a strong extramurally funded research program and participate in departmental teaching at the undergraduate, graduate and professional levels. The position provides a strong start-up package of funding, laboratory space, and highly competitive salary and benefits. Applicants should apply at <https://jobs.rutgers.edu/postings/136917> and include a cover letter, curriculum vitae, brief research plan, and names and addresses of three references.



### DEPARTMENT OF BIOCHEMISTRY

The University of Missouri (MU) invites applications for two tenure-track faculty positions in the Department of Biochemistry. Both positions will be in areas of fundamental biochemistry, one focused on plant biochemistry, and one focused on biomedical problems. Candidates should have an earned doctorate and the ability to lead a federally funded research group. Applications at the Assistant Professor level are encouraged. Candidates at a higher level will be considered if there is a record of extramural research funding, publications, teaching, and service expected of tenured faculty at a research-intensive university, and such candidates in Plant Biochemistry will be considered for the O'Dell endowed professorship.

The department has an undergraduate teaching mission in the College of Agriculture and Natural Resources (CAFNR), provides pre-clinical training in the School of Medicine, and supports graduate education in both units. As a department in a Land Grant University that bridges two colleges, the Department of Biochemistry is home to fundamental molecular science and to its translation into both agricultural and biomedical applications. Areas of interest include fundamental biochemistry and/or applications such as synthetic biology; metabolic engineering; transgenic technology; and spatio-temporal biochemistry involving transcriptomics, proteomics, and other genome-wide approaches. The candidates will join highly collaborative research communities in plant biology and precision medicine that are supported by outstanding core facilities. For additional information, visit <http://biochem.missouri.edu>.

#### APPLICATION:

To apply, visit <https://biochem.missouri.edu/open-positions/>, click on Open Positions and submit: (1) a cover letter; (2) curriculum vitae; (3) a one-page summary of research accomplishments with two pages of future plans; (4) a one-page narrative of teaching philosophy and commitment to diversity, equity, and inclusion; and (5) names and contact information of four references. Review of applications will begin on November 28, 2022, and will continue until the position is filled. For information, contact [biochemchair@missouri.edu](mailto:biochemchair@missouri.edu).

*The University of Missouri is an Equal Access, Equal Opportunity, and Affirmative Action Employer. We are fully committed to achieving the goal of a diverse and inclusive academic community of faculty, staff, and students. We seek individuals who are committed to this goal and our core campus values of respect, responsibility, discovery, and excellence.*

## Fellowships for Postdoctoral Scholars

AT WOODS HOLE OCEANOGRAPHIC INSTITUTION

New or recent doctoral recipients are encouraged to submit **applications prior to October 15, 2022**, to start after January 1 and before December 1, 2023.

Awards will be in the following areas: **Applied Ocean Physics & Engineering; Biology; Geology & Geophysics; Marine Chemistry & Geochemistry; Physical Oceanography; interdepartmental research; and a joint USGS/WHOI award.**

Awards are aimed at advancing applicants' research careers. Scholarships are 18-months (annual stipend of \$68,500, plus health and travel allowances and a research budget). Recipients will pursue their own research interests, mentored by resident staff. Communication with potential WHOI advisors prior to submitting applications is encouraged. The Postdoctoral Scholar Program is committed to broadening participation in ocean science and engineering.

For further information: <https://go.whoi.edu/pdscholarship>



### Science Careers helps you advance your career. Learn how!

- Register for a free online account on ScienceCareers.org.
- Search hundreds of job postings and find your perfect job.
- Sign up to receive e-mail alerts about job postings that match your criteria.
- Upload your resume into our database and connect with employers.
- Watch one of our many webinars on different career topics such as job searching, networking, and more.

Visit [ScienceCareers.org](https://ScienceCareers.org) today — all resources are free



**Science Careers**  
FROM THE JOURNAL SCIENCE

SCIENCECAREERS.ORG



## DEPARTMENT OF MOLECULAR AND HUMAN GENETICS FACULTY POSITIONS

Among genetics departments at U.S. medical schools, the Department of Molecular and Human Genetics at Baylor College of Medicine (<https://www.bcm.edu/departments/molecular-and-human-genetics>) ranks first in both number of grants and total funding from the National Institutes of Health (NIH). The Department of Molecular and Human Genetics provides a fully integrated environment for physicians and basic scientists, promoting a cross-species approach to functional genetics and a commitment to technology transfer. Activities within the Department include clinical genetics, basic and clinical research, a joint venture diagnostic laboratory, long-standing association with an NIH-large scale human genome sequencing center, medical student teaching, an MS Genetic Counseling program, a Ph.D. graduate program, and residency/fellowship training in medical genetics.

The Department has over \$100 million in total research funding, 70 primary tenured and tenure-track research faculty members and a total of 150 primary faculty members, who are engaged in a variety of missions including basic and translational research, clinical diagnostic services, and prenatal, pediatric, and adult clinical care. To expand our translational impact, we established a uniquely structured and governed joint venture diagnostic laboratory, Baylor Genetics, and a Baylor College of Medicine/Chinese University of Hong Kong Center for Medical Genetics in Hong Kong that together has expanded our clinical, diagnostic, and educational mission to a world-wide audience.

Faculty will have an opportunity to interact with the vigorous ABMGG residency and clinical laboratory fellowship training programs that include over 40 clinical and diagnostic laboratory faculty and over 50 genetic counseling faculty and staff. The training programs attract four to six individuals per year for resident training in categorical Medical Genetics, Combined Pediatrics/Medical Genetics, Combined Internal Medicine/Medical Genetics, and Maternal Fetal Medicine/Medical Genetics, as well as three to four individuals for ABMGG-approved clinical laboratory fellowship training in the following areas: clinical biochemical genetics and laboratory genetics and genomics.

The Department staffs clinical genetics programs at Texas Children's Hospital, Baylor St. Luke's Medical Center, Harris Health System, and the Michael E. DeBakey Veteran Affairs Medical Center.

Baylor College of Medicine promotes principles of diversity, inclusion, and equity across research, education, and training programs as well as with respect to recruitment (in employment and education) of individuals from diverse backgrounds.

The Department is seeking individuals for faculty appointments at rank appropriate for achievement and experience. We are currently recruiting for the following positions:

- **Physician Scientist Geneticist** - The Department is seeking MD or MD/PhD trained individuals who have clearly demonstrated their ability to conduct high-impact basic, translational and/or clinical research and compete for scientific funding in the area of medical genetics and model organism genetics. Start-up package commensurate for experience will be provided.
- **Clinical Geneticist** - The Department is seeking MD or MD/PhD trained, ABMGG eligible and/or certified physicians in the areas of clinical genetics and medical biochemical geneticist.
- **Research Geneticist** - The Department is seeking PhD trained basic and translational research geneticists (studying any model system), statistical geneticists, and computational geneticists who are focused on elucidating the underlying genetic and genomic mechanisms of rare and common diseases.

Appointments will be at the **Assistant, Associate, or Full Professor** levels depending on experience.

Applicants should email a pdf version of their curriculum vitae and cover letter stating the position for which they are applying to the following email address: [mhgfacultyrecruits@bcm.edu](mailto:mhgfacultyrecruits@bcm.edu), Department of Molecular and Human Genetics, Baylor College of Medicine, One Baylor College of Medicine, ABBR Room R830, Houston, TX 77030, Phone: 713-798-5443, Fax: 713-798-8515

*Equal Opportunity, Affirmative Action and Equal Access Employer*



## 2023-2024 POSTDOCTORAL FELLOWSHIPS FOR ACADEMIC DIVERSITY

The Postdoctoral Fellowships for Academic Diversity are competitive programs intended to increase the diversity of the academic research community at the University of Pennsylvania (Penn) and Children's Hospital of Philadelphia (CHOP). Both organizations seek to attract promising researchers and educators from different backgrounds, races, ethnic groups, and other diverse populations whose life experiences, research experiences and employment backgrounds will contribute significantly to their academic missions. Fellowships are available for postdoctoral training in all areas of study at either Penn or CHOP. STEM applications are encouraged.

### Eligibility

- Candidates must be US citizens or permanent residents
- Graduate students from Penn and other institutions who have completed, or will complete their requirements for Ph.D. by the Fellowship start date (**July 1, 2023**)
- Postdoctoral scholars from other institutions who have completed their graduate degree within the last two years
- Professional applicants (M.D., D.M.D., V.M.D., J.D., etc.) within a year of completing their post-degree professional training
- Postdocs, residents and fellows who currently have a position at Penn or CHOP are ineligible for this program

Application deadline: **Wednesday, November 16, 2022 (5pm EST)**

### Awards

Fellows starting in July 2023 will receive a stipend of \$57,000 a year in year 1 with \$2,000 increases in years 2 and 3. Additionally, the fellow will receive annual allowances for travel (\$2,000) and research (\$4,000), and, may be eligible for a one-time relocation expense of up to \$5,000. Penn and CHOP also provide a medical, vision, dental and life insurance benefits package. Successful candidates will receive highly mentored scholarly and research training as well as workshops to enhance their research and professional skills.

The program is designed to provide postdocs with time to focus on research, and publishing activities that will enhance their career prospects for either a faculty appointment in an academic institution or in other sectors of the economy such as industry, government or nonprofit organizations.

Start dates will be arranged in consultation with the faculty mentor and will begin as early as **July 2023**.

To find out more and to apply, please visit <https://research.upenn.edu/postdocs-and-students/penn-provosts-postdoctoral-fellowships/>

By Daria Boglaienko

## The meaning of home

**A**t work after a sleepless night, I was suspended between two realities. The previous evening, my hometown, Kharkiv, had been bombed. I spent the night endlessly refreshing the news; sleep was out of the question. The next morning, I went into the lab. My manager suggested I stay home, but I was determined to carry on as usual. I hoped getting back to work would serve as a distraction. Ever since I left Ukraine to come to the United States for graduate school, work and study had provided a home for me. But as the days of the war turned to weeks turned to months and I witnessed from afar the destruction of my city and country, I began to reconsider what home really means.

My life in Kharkiv was culturally rich and inspiring—literally “breathed in,” as if the air itself was full. Every day after work as a university instructor and part-time Ph.D. student in chemical engineering and industrial ecology, I hurried to English class or dance class or chose a path home through the city center so I could stop at an art gallery or walk by a theater to note what performance to attend next. Occasionally I even performed at dance festivals myself. And I was surrounded by friends—from early childhood, university, hiking and kayaking trips, dance classes, church, and my kind and erudite colleagues.

Through it all, I dreamed of furthering my education beyond the borders of my city and country. So, when I was 28, I left everyone and everything that could be called home to pursue additional graduate training in the United States.

I was alone in a country that was not my own, but my work made me feel as if I was at home. Being immersed in research and discoveries filled my life with meaning and gave me strength. I had no regrets.

After finishing my Ph.D., I decided to stay in the United States to continue my research career. By this point I knew my journey was going to continue far from family and old friends, but scientific discovery inspired me, easing the loneliness. Hope that my research would in some way serve future scientists and the world kept me going despite the distance from the people who are dear to me.

The war showed me what home really means. Seeing the destruction of apartment buildings, parks, markets, hospitals, churches—places that hold my most precious memories—felt like being punched in the chest. My own deep roots were being destroyed. I checked the news from



**“I am trying to fill my life with some of the inspiration it had in Kharkiv.”**

Kharkiv every few hours, and I was never far from my phone. Reading “I’m OK” texts from family while I prepared for experiments or read papers became a necessary part of my routine.

I used to take my heritage for granted. I cherished it, but I set it aside in my daily life. I imagine many immigrants building a new life in a new country cope the same way. Now, I have started to feel responsible for that cultural heritage—and I am trying to recapture its spirit in my new country. Instead of focusing so singlemindedly on studying and work, I am trying to fill my life with some of the inspiration it had in Kharkiv. For example, I recently returned to whitewater kayaking, which I had fallen in love with after a memorable first experience with friends on the Southern Bug River

back in Ukraine. I’ve also revived my dormant passion for literature and started to read more for pleasure, especially books by contemporary Ukrainian writers. And at the end of August I was able to bring my mother and sister to the United States through the U.S. Uniting for Ukraine program, which brings me some relief and peace of mind.

Amid the horrors of the war, the world has seen how brave and strong Ukrainians are. In re-embracing my heritage, I feel I, too, am taking a stand for Ukraine, even though I am far from the war. I generally think of myself as shy and lacking confidence. But perhaps a streak of independence and resourcefulness is hidden underneath. I am realizing I was shaped by the culture of my city and the spirit of my country more than I ever knew. ■

Daria Boglaienko is a chemist at the Pacific Northwest National Laboratory. Send your career story to [SciCareerEditor@aaas.org](mailto:SciCareerEditor@aaas.org).



PRIZE FOR IMMUNOLOGY

REWARDING HIGH-RISK RESEARCH.  
SUPPORTING EARLY-CAREER SCIENTISTS.  
HELPING TO FIND CURES FASTER.  
**APPLY TODAY**

**Now accepting applications for the Michelson Philanthropies & Science Prize for Immunology.**

The Michelson Philanthropies and Science Prize for Immunology focuses on transformative research in human immunology, with trans-disease applications to accelerate vaccine and immunotherapeutic discovery. This international prize supports investigators 35 and younger, who apply their expertise to research that has a lasting impact on vaccine development and immunotherapy. It is open to researchers from a wide range of disciplines including computer science, artificial intelligence/machine learning, protein engineering, nanotechnology, genomics, parasitology and tropical medicine, neurodegenerative diseases, and gene editing.

**Application deadline: Oct. 1, 2022.**

For more information visit:  
[www.michelsonmedicalresearch.org](http://www.michelsonmedicalresearch.org)

**#MichelsonPrizes**



*"The Michelson Philanthropies & Science Prize for Immunology will greatly impact my future work. As I am just starting my scientific career, it will illuminate my work, spark interest and support me to continue my research in this field."*

**Paul Bastard, MD, PhD,**  
Laboratory of Human Genetics of Infectious Diseases, Imagine Institute (INSERM, University of Paris), Paris, France; and The Rockefeller University, New York.

Dr. Bastard received the inaugural Grand Prize for his essay: "Why do people die from COVID-19: Autoantibodies neutralizing type I interferons increase with age."

**GRAND PRIZE:  
\$30,000**

**FINALIST PRIZE:  
\$10,000**



The Samsung Ho-Am Prize was established in 1990 to honor both the philosophy of putting people first and the spirit of public service originally championed by “Ho-Am” Byung-chull Lee(1910-1987), the founder of Samsung. The Prize is awarded annually to outstanding researchers of Korean heritage around the world who have made important contributions to the advancement of science.

# The Samsung Ho-Am Prize ignites the passion and innovative spirit for scientific discovery

We welcome your recommendations for the 2023 Samsung Ho-Am Prize candidates.

- Award Categories : **Physics & Mathematics, Chemistry & Life Sciences, Engineering, Medicine**
- Candidate Eligibility : Researchers of Korean heritage
- Nomination Deadline : Oct. 31, 2022
- \*Learn more about the prize and nomination : [www.hoamfoundation.org](http://www.hoamfoundation.org)

**SAMSUNG**

**HOAM**  
THE HO-AM FOUNDATION